Mystery kidney disease strikes South Asia *p. 24*

Assessing young scientists' value *p. 28*

Pharmaceuticals made to order *pp. 44 & 61*

Science

$15
1 APRIL 2016
sciencemag.org

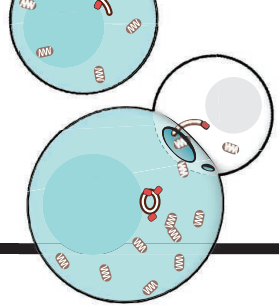
AAAS



Sequencing going ape

Higher resolution of the gorilla genome *p. 52*

CONTENTS



35 & 95
Nursing mouse eggs to maturity

1 APRIL 2016 • VOLUME 352 • ISSUE 6281

NEWS

IN BRIEF

12 News at a glance

IN DEPTH

15 EL NIÑO'S WARMTH DEVASTATING REEFS WORLDWIDE
Recent aerial surveys of Australia's Great Barrier Reef find massive coral bleaching *By D. Normile*

16 SANDY RIPPLES POINT TO MARS'S PAST
Unique dune features emerge from rover's campaign in the sand *By E. Hand*

18 BRAZIL BILL WOULD LEGALIZE RENEGADE CANCER PILL
Government races to put "fosfo" through clinical testing
By H. Escobar

19 CANADIAN SCIENTISTS SMILE AT LIBERALS' DÉJÀ VU BUDGET
Trudeau offers warm support for basic research *By W. Kondro*

20 NO-STRINGS AWARDS AT NIH DRAW CONCERN
Some recipients say they didn't expect deep cuts in funding *By J. Kaiser*

FEATURES

21 IMMUNITY GOES LOCAL
Similar to lymph nodes, but transient, tertiary lymphoid structures can drive immune responses *By M. Leslie*

24 OCCUPATIONAL HAZARD
Farm workers are dying in southern India as an epidemic of a mysterious kidney disease goes global
By R. Chatterjee

INSIGHTS

LETTERS

28 NEXTGEN VOICES

PERSPECTIVES

31 MITOCHONDRIAL DISEASE THERAPY FROM THIN AIR?
Low-oxygen treatment slows neurodegeneration in a model of a mitochondrial disorder
By E. A. Shoubridge
▸ RESEARCH ARTICLE P. 54

32 RETHINKING THE S_N2 REACTION
The gas-phase dynamics of a paradigm organic reaction are more complex than expected *By J. Xie and W. L. Hase*

34 HOW ANTARCTICA GOT ITS ICE
A complex set of interactions caused the rapid growth of the Antarctic ice sheet 34 million years ago
By C. H. Lear and D. J. Lunt
▸ REPORT P. 76

35 NURSING THE OOCYTE
Mammalian egg cells receive material from neighboring "nurse" cells via bridges and gaps *By M. E. Pepling*
▸ REPORT P. 95



24

37 AN ODD ONE OUT
An oxygen-rich white dwarf sets an important mark for stellar evolution *By B. Gänsicke*
▸ REPORT P. 67

38 ENGAGE KEY SOCIAL CONCEPTS FOR SUSTAINABILITY
Social indicators, both mature and emerging, are underused *By C. C. Hicks* et al.

40 COLLOIDAL CRYSTAL ORDERING IN A LIQUID CRYSTAL
A nematic phase promotes the formation of dilute, low-symmetry colloidal crystals *By C. Blanc*
▸ REPORT P. 69

42 A BRAIN CONDITIONED FOR SOCIAL DEFEAT
A brain circuit in vertebrates determines who wins or loses a fight
By L. Desban and C. Wyart
▸ REPORT P. 87

43 A lncRNA LINKS GENOMIC VARIATION WITH CELIAC DISEASE
A long noncoding RNA is associated with an intestinal autoimmune disorder
By M. Huarte
▸ REPORT P. 91

44 GOING WITH THE FLOW
A desktop machine allows on-demand medicine production *By R. E. Martin*
▸ RESEARCH ARTICLE P. 61

BOOKS *ET AL.*

46 BOY
By A. Ziegler; directed by L. Firman, reviewed by O. Vikbladh

47 LAB GIRL
By H. Jahren, reviewed by M. Lowman

DEPARTMENTS

11 EDITORIAL
New frontiers in bioscience
By Paul G. Allen

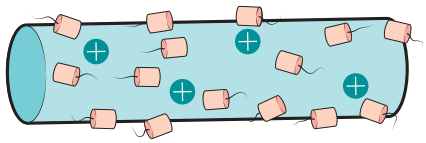
110 WORKING LIFE
Of mice and mics
By Adam Ruben

Science Staff 8
New Products 104
Science Careers 106

Downloaded from on March 31, 2016

Published by AAAS

CONTENTS



40 & 69

Orienting nanorods in liquid crystals

1 APRIL 2016 • VOLUME 352 • ISSUE 6281

RESEARCH

IN BRIEF

48 From *Science* and other journals

REVIEW

51 CELL DEATH PATHWAYS
Programmed necrosis in inflammation: Toward identification of the effector molecules *D. Wallach* et al.
REVIEW SUMMARY; FOR FULL TEXT: dx.doi.org/10.1126/science.aaf2154

RESEARCH ARTICLES

52 NONHUMAN GENOMICS
Long-read sequence assembly of the gorilla genome *D. Gordon* et al.
RESEARCH ARTICLE SUMMARY; FOR FULL TEXT: dx.doi.org/10.1126/science.aae0344

53 SYNTHETIC BIOLOGY
Genetic circuit design automation *A. A. K. Nielsen* et al.
RESEARCH ARTICLE SUMMARY; FOR FULL TEXT: dx.doi.org/10.1126/science.aac7341

54 MITOCHONDRIAL DISEASE
Hypoxia as a therapy for mitochondrial disease *I. H. Jain* et al.
▸ PERSPECTIVE P. 31

61 FLOW CHEMISTRY
On-demand continuous-flow production of pharmaceuticals in a compact, reconfigurable system *A. Adamo* et al.
▸ PERSPECTIVE P. 44; PODCAST

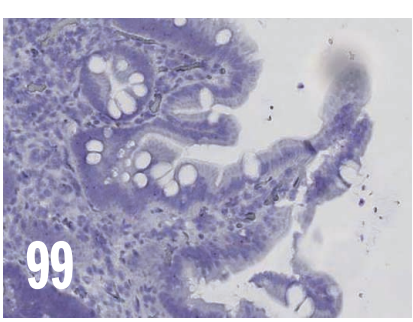
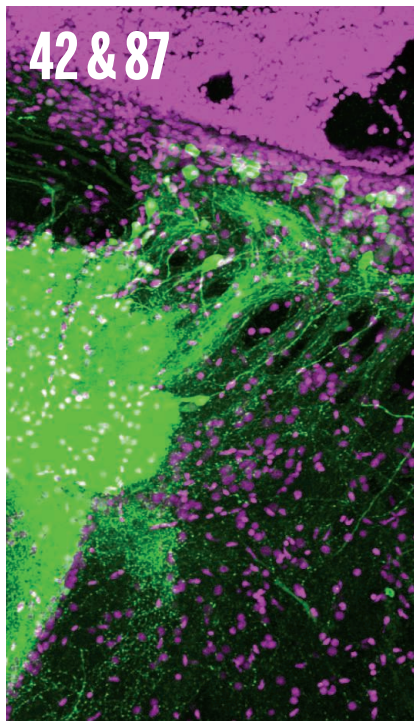


PHOTO: (BOTTOM LEFT) SANKAR GHOSH



REPORTS

67 STELLAR EVOLUTION
A white dwarf with an oxygen atmosphere *S. O. Kepler* et al.
▸ PERSPECTIVE P. 37

69 COLLOIDAL ORDERING
Triclinic nematic colloidal crystals from competing elastic and electrostatic interactions *H. Mundoor* et al.
▸ PERSPECTIVE P. 40

73 ELECTROCATALYSIS
Tuning the activity of Pt alloy electrocatalysts by means of the lanthanide contraction *M. Escudero-Escribano* et al.

76 ICE SHEETS
Antarctic Ice Sheet variability across the Eocene-Oligocene boundary climate transition *S. Galeotti* et al.
▸ PERSPECTIVE P. 34

80 ATMOSPHERIC METHANE
A 21st-century shift from fossil-fuel to biogenic methane emissions indicated by $^{13}CH_4$ *H. Schaefer* et al.

84 CLIMATE CHANGE
Consistent response of bird populations to climate change on two continents *P. A. Stephens* et al.

87 CONFLICT BEHAVIOR
Social conflict resolution regulated by two dorsal habenular subregions in zebrafish *M.-Y. Chou* et al.
▸ PERSPECTIVE P. 42

91 IMMUNE REGULATION
A long noncoding RNA associated with susceptibility to celiac disease *A. Castellanos-Rubio* et al.
▸ PERSPECTIVE P. 43

95 MAMMALIAN GERM CELLS
Mouse oocytes differentiate through organelle enrichment from sister cyst germ cells *L. Lei and A. C. Spradling*
▸ PERSPECTIVE P. 35

99 IMMUNOLOGY
The TAM family receptor tyrosine kinase TYRO3 is a negative regulator of type 2 immunity *P. Y. Chan* et al.

ON THE COVER



A female western lowland gorilla (*Gorilla gorilla gorilla*). Long-read sequencing and assembly of the gorilla genome provides a more complete picture of the gene content, genetic variation, and repeat biology in this species. This approach improves population genetic and evolutionary inferences and will allow individual laboratories to effectively generate high-quality references for complex mammalian genomes. See page 52. *Photo: © imageBROKER/Alamy*

SCIENCE (ISSN 0036-8075) is published weekly on Friday, except the last week in December, by the American Association for the Advancement of Science, 1200 New York Avenue, NW, Washington, DC 20005. Periodicals mail postage (publication No. 484460) paid at Washington, DC, and additional mailing offices. Copyright © 2016 by the American Association for the Advancement of Science. The title SCIENCE is a registered trademark of the AAAS. Domestic individual membership and subscription (51 issues): $165 ($74 allocated to subscription). Domestic institutional subscription (51 issues): $1522; Foreign postage extra: Mexico, Caribbean (surface mail) $55; other countries (air assist delivery) $89. First class, airmail, student, and emeritus rates on request. Canadian rates with GST available upon request, GST #1254 88122. Publications Mail Agreement Number 1069624. **Printed in the U.S.A.**
Change of address: Allow 4 weeks, giving old and new addresses and 8-digit account number. **Postmaster:** Send change of address to AAAS, P.O. Box 96178, Washington, DC 20090–6178. **Single-copy sales:** $15.00 current issue, $20.00 back issue prepaid includes surface postage; bulk rates on request. **Authorization to photocopy** material for internal or personal use under circumstances not falling within the fair use provisions of the Copyright Act is granted by AAAS to libraries and other users registered with the Copyright Clearance Center (CCC) Transactional Reporting Service, provided that $35.00 per article is paid directly to CCC, 222 Rosewood Drive, Danvers, MA 01923. The identification code for *Science* is 0036-8075. *Science* is indexed in the *Reader's Guide to Periodical Literature* and in several specialized indexes.

Published by AAAS

Science
AAAS
1200 New York Avenue, NW, Washington, DC 20005
Bateman House, 82-88 Hills Road, Cambridge, UK CB2 1LQ

Editor-in-Chief Marcia McNutt
Executive Editor Monica M. Bradford **News Editor** Tim Appenzeller
Managing Editor, Research Journals Katrina L. Kelner
Deputy Editors Lisa D. Chong, Andrew M. Sugden(UK), Valda J. Vinson, Jake S. Yeston

Research and Insights

DEPUTY EDITOR, EMERITUS Barbara R. Jasny **SR. EDITORS** Caroline Ash(UK), Gilbert J. Chin, Julia Fahrenkamp-Uppenbrink(UK), Pamela J. Hines, Stella M. Hurtley(UK), Paula A. Kiberstis, Marc S. Lavine(Canada), Kristen L. Mueller, Ian S. Osborne(UK), Beverly A. Purnell, L. Bryan Ray, Guy Riddihough, H. Jesse Smith, Jelena Stajic, Peter Stern(UK), Phillip D. Szuromi, Sacha Vignieri, Brad Wible, Nicholas S. Wigginton, Laura M. Zahn **ASSOCIATE EDITORS** Brent Grocholski, Keith T. Smith **ASSOCIATE BOOK REVIEW EDITOR** Valerie B. Thompson **ASSOCIATE LETTERS EDITOR** Jennifer Sills **CHIEF CONTENT PRODUCTION EDITOR** Cara Tate **SR. CONTENT PRODUCTION EDITORS** Harry Jach, Lauren Kmec **CONTENT PRODUCTION EDITORS** Jeffrey E. Cook, Chris Filiatreau, Cynthia Howe, Barbara P. Ordway, Catherine Wolner **SR. EDITORIAL COORDINATORS** Carolyn Kyle, Beverly Shields **EDITORIAL COORDINATORS** Aneera Dobbins, Joi S. Granger, Lisa Johnson, Anita Wynn **PUBLICATIONS ASSISTANTS** Jeffrey Hearn, Dona Mathieu, Le-Toya Mayne Flood, Shannon McMahon, Scott Miller, Caitlyn Phillips, Jerry Richardson, Alice Whaley(UK), Brian White **EXECUTIVE ASSISTANT** Anna Bashkirova **ADMINISTRATIVE SUPPORT** Janet Clements(UK), Lizanne Newton(UK), Maryrose Madrid

News

NEWS MANAGING EDITOR John Travis **INTERNATIONAL EDITOR** Richard Stone **DEPUTY NEWS EDITORS** Daniel Clery(UK), Robert Coontz, Elizabeth Culotta, David Grimm, David Malakoff, Leslie Roberts **CONTRIBUING EDITOR** Martin Enserink(Europe) **SR. CORRESPONDENTS** Jeffrey Mervis, Elizabeth Pennisi **NEWS WRITERS** Adrian Cho, Jon Cohen, Jennifer Couzin-Frankel, Carolyn Gramling, Eric Hand, Jocelyn Kaiser, Catherine Matacic, Kelly Servick, Robert F. Service, Erik Stokstad(Cambridge, UK), Emily Underwood **INTERNS** Hanae Armitage, Patrick Monahan, Nala Rogers **CONTRIBUTING CORRESPONDENTS** Michael Balter(Paris), John Bohannon, Warren Cornwall, Ann Gibbons, Mara Hvistendahl, Sam Kean, Eli Kintisch, Kai Kupferschmidt(Berlin), Andrew Lawler, Christina Larson(Beijing), Mitch Leslie, Charles C. Mann, Eliot Marshall, Virginia Morell, Dennis Normile(Shanghai), Heather Pringle, Tania Rabesandratana(London), Gretchen Vogel(Berlin), Lizzie Wade(Mexico City) **CAREERS** Donisha Adams, Rachel Bernstein(Editor) **COPY EDITORS** Julia Cole, Dorie Chevlen, Jennifer Levin (Chief) **ADMINISTRATIVE SUPPORT** Jessica Adams

Executive Publisher Rush D. Holt
Interim Publisher Bill Moran **Chief Digital Media Officer** Rob Covey

BUSINESS OPERATIONS AND PORTFOLIO MANAGEMENT DIRECTOR Sarah Whalen **PRODUCT DEVELOPMENT DIRECTOR** Will Schweitzer **PRODUCT DEVELOPMENT ASSOCIATE** Hal Moore **BUSINESS SYSTEMS AND FINANCIAL ANALYSIS DIRECTOR** Randy Yi **MANAGER OF FULFILLMENT SYSTEMS** Neal Hawkins **SYSTEMS ANALYST** Nicole Mehmedovich **ASSISTANT DIRECTOR, BUSINESS OPERATIONS** Eric Knott **MANAGER, BUSINESS OPERATIONS** Jessica Tierney **SENIOR BUSINESS ANALYST** Cory Lipman **BUSINESS ANALYSTS** Sandy Kim, Meron Kebede **FINANCIAL ANALYST** Robert Clark **DIRECTOR, COPYRIGHTS LICENSING SPECIAL PROJECTS** Emilie David **PERMISSIONS ASSOCIATE** Elizabeth Sandler **RIGHTS, CONTRACTS, AND LICENSING ASSOCIATE** Lili Kiser

MARKETING DIRECTOR Elise Swinehart **ASSOCIATE DIRECTOR OF ACQUISITION AND RETENTION** Julianne Wielga **MARKETING ASSOCIATE** Elizabeth Sattler **SR. MARKETING EXECUTIVE** Jennifer Reeves **ASSOCIATE DIRECTOR, CREATIVE SERVICES** Tzeitel Sorrosa **ART ASSOCIATE** Seil Lee **JR. ART ASSOCIATE** Kim Huynh **ASSISTANT COMMERCIAL EDITOR** Selby Frame **MARKETING PROJECT MANAGER** Angelissa McArthur **PROGRAM DIRECTOR, AAAS MEMBER CENTRAL** Peggy Mihelich **FULFILLMENT SYSTEMS AND OPERATIONS** membership@aaas.org **MANAGER, MEMBER SERVICES** Pat Butler **SPECIALISTS** Terrance Morrison, Latasha Russell **MANAGER, DATA ENTRY** Mickie Napoleoni **DATA ENTRY SPECIALISTS** Brenden Aquilino, Fiona Giblin

PUBLISHER RELATIONS MANAGER Catherine Holland **PUBLISHER RELATIONS, EASTERN REGION** Keith Layson **PUBLISHER RELATIONS, WESTERN REGION** Ryan Rexroth **SALES RESEARCH COORDINATOR** Aiesha Marshall **MANAGER, SITE LICENSE OPERATIONS** Iquo Edim **SENIOR OPERATIONS ANALYST** Lana Guz **FULFILLMENT ANALYST** Judy Lillibridge **ASSOCIATE DIRECTOR, MARKETING** Christina Schlecht **MARKETING ASSOCIATE** Isa Sesay-Bah

WEB TECHNOLOGIES SR. DEVELOPER Chris Coleman **DEVELOPERS** Dan Berger, Jimmy Marks, Ryan Jensen **SR. PROJECT MANAGER** Trista Smith **PROJECT MANAGER** Nick Fletcher

DIGITAL MEDIA DIRECTOR OF ANALYTICS Enrique Gonzales **DIGITAL REPORTING ANALYST** Eric Hossinger **SR. WEB PRODUCER** Sarah Crespi **WEB PRODUCER** Alison Crawford **VIDEO PRODUCER** Nguyen Nguyen **SOCIAL MEDIA PRODUCER** Brice Russ

DIRECTOR OF OPERATIONS PRINT AND ONLINE Lizabeth Harman **DIGITAL/PRINT STRATEGY MANAGER** Jason Hillman **QUALITY TECHNICAL MANAGER** Marcus Spiegler **PROJECT ACCOUNT MANAGER** Tara Kelly **DIGITAL PRODUCTION MANAGER** Lisa Stanford **ASSISTANT MANAGER DIGITAL/PRINT** Rebecca Doshi **SENIOR CONTENT SPECIALISTS** Steve Forrester, Antoinette Hodal, Lori Murphy, Anthony Rosen **CONTENT SPECIALISTS** Jacob Hedrick, Kimberley Oster

DESIGN DIRECTOR Beth Rakouskas **DESIGN EDITOR** Marcy Atarod **SENIOR DESIGNER** Garvin Grullón **DESIGNER** Chrystal Smith **GRAPHICS MANAGING EDITOR** Alberto Cuadra **SENIOR SCIENTIFIC ILLUSTRATORS** Chris Bickel, Katharine Sutliff **SCIENTIFIC ILLUSTRATOR** Valerie Altounian **SENIOR ART ASSOCIATES** Holly Bishop, Nathalie Cary, Preston Huey **PHOTOGRAPHY MANAGING EDITOR** William Douthitt **PHOTO EDITORS** Leslie Blizard, Christy Steele

DIRECTOR, GLOBAL COLLABORATION, CUSTOM PUBLICATIONS, ADVERTISING Bill Moran **EDITOR, CUSTOM PUBLISHING** Sean Sanders: 202-326-6430 **ADVERTISING MARKETING MANAGER** Justin Sawyers: 202-326-7061 science_advertising@aaas.org **ADVERTISING SUPPORT MANAGER** Karen Foote: 202-326-6740 **ADVERTISING PRODUCTION OPERATIONS MANAGER** Deborah Tompkins **SR. PRODUCTION SPECIALIST/GRAPHIC DESIGNER** Amy Hardcastle **SR. TRAFFIC ASSOCIATE** Christine Hall **SALES COORDINATOR** Shirley Young **ASSOCIATE DIRECTOR, COLLABORATION, CUSTOM PUBLICATIONS/CHINA/TAIWAN/KOREA/SINGAPORE** Ruolei Wu: +86-186 0082 9345, rwu@aaas.org **COLLABORATION/CUSTOM PUBLICATIONS/JAPAN** Adarsh Sandhu + 81532-81-5142 asandhu@aaas.org **EAST COAST/E. CANADA** Laurie Faraday: 508-747-9395, FAX 617-507-8189 **WEST COAST/W. CANADA** Lynne Stickrod: 415-931-9782, FAX 415-520-6940 **MIDWEST** Jeffrey Dembski: 847-498-4520 x3005, Steven Loerch: 847-498-4520 x3006 **UK EUROPE/ASIA** Roger Goncalves: TEL/FAX +41 43 243 1358 **JAPAN** Katsuyoshi Fukamizu(Tokyo): +81-3-3219-5777 kfukamizu@aaas.org **CHINA/TAIWAN** Ruolei Wu: +86-186 0082 9345, rwu@aaas.org

WORLDWIDE ASSOCIATE DIRECTOR OF SCIENCE CAREERS Tracy Holmes: +44 (0) 1223 326525, FAX +44 (0) 1223 326532 tholmes@science-int.co.uk **CLASSIFIED** advertise@sciencecareers.org **U.S. SALES** Tina Burks: 202-326-6577, Nancy Toema: 202-326-6578 **EUROPE/ROW SALES** Sarah Lelarge **SALES ASSISTANT** Kelly Grace **JAPAN** Hiroyuki Mashiki(Kyoto): +81-75-823-1109 hmashiki@aaas.org **CHINA/TAIWAN** Ruolei Wu: +86-186 0082 9345 rwu@aaas.org **MARKETING MANAGER** Allison Pritchard **MARKETING ASSOCIATE** Aimee Aponte

AAAS BOARD OF DIRECTORS, CHAIR Geraldine L. Richmond **PRESIDENT** Barbara A. Schaal **PRESIDENT-ELECT** Susan Hockfield **TREASURER** David Evans Shaw **CHIEF EXECUTIVE OFFICER** Rush D. Holt **BOARD** Cynthia M. Beall, May R. Berenbaum, Carlos J. Bustamante, Stephen P.A. Fodor, Claire M. Fraser, Michael S. Gazzaniga, Laura H. Greene, Elizabeth Loftus, Mercedes Pascual

SUBSCRIPTION SERVICES For change of address, missing issues, new orders and renewals, and payment questions: 866-434-AAAS (2227) or 202-326-6417, FAX 202-842-1065. Mailing addresses: AAAS, P.O. Box 96178, Washington, DC 20090-6178 or AAAS Member Services, 1200 New York Avenue, NW, Washington, DC 20005

INSTITUTIONAL SITE LICENSES 202-326-6730 **REPRINTS:** Author Inquiries 800-635-7181 **COMMERCIAL INQUIRIES** 803-359-4578 **PERMISSIONS** 202-326-6765, permissions@aaas.org **AAAS Member Services** 202-326-6417 or http://membercentral.aaas.org/discounts

Science serves as a forum for discussion of important issues related to the advancement of science by publishing material on which a consensus has been reached as well as including the presentation of minority of conflicting points of view. Accordingly, all articles published in *Science*—including editorials, news and comment, and book reviews—are signed and reflect the individual views of the authors and not official points of view adopted by AAAS or the institutions with which the authors are affiliated.

INFORMATION FOR AUTHORS See pages 624 and 625 of the 5 February 2016 issue or access www.sciencemag.org/authors/science-information-authors

SENIOR EDITORIAL BOARD
Gary King, *Harvard University,* **Susan M. Rosenberg,** *Baylor College of Medicine,*
Ali Shilatifard, *Northwestern University Feinberg School of Medicine*

BOARD OF REVIEWING EDITORS (Statistics board members indicated with **(S)**)

Adriano Aguzzi, *U. Hospital Zürich*
Takuzo Aida, *U. of Tokyo*
Leslie Aiello, *Wenner-Gren Foundation*
Judith Allen, *U. of Edinburgh*
Sonia Altizer, *U. of Georgia*
Sebastian Amigorena, *Institut Curie*
Kathryn Anderson, *Memorial Sloan-Kettering Cancer Center*
Meinrat O. Andreae, *Max-Planck Inst. Mainz*
Paola Arlotta, *Harvard U.*
Johan Auwerx, *EPFL*
David Awschalom, *U. of Chicago*
Clare Baker, *University of Cambridge*
Nenad Ban, *ETH Zurich*
Jordi Bascompte, *University of Zurich*
Ray H. Baughman, *U. of Texas, Dallas*
David Baum, *U. of Wisconsin*
Carlo Beenakker, *Leiden U.*
Kamran Behnia, *ESPCI-ParisTech*
Yasmine Belkaid, *NIAID, NIH*
Philip Benfey, *Duke U.*
May Berenbaum, *U. of Illinois*
Gabriele Bergers, *U. of California, San Francisco*
Bradley Bernstein, *Massachusettes General Hospital*
Peer Bork, *EMBL*
Bernard Bourdon, *Ecole Normale Supérieure de Lyon*
Chris Bowler, *École Normale Supérieure*
Ian Boyd, *U. of St. Andrews*
Emily Brodsky, *U. of California, Santa Cruz*
Ron Brookmeyer, *U. of California Los Angeles* **(S)**
Christian Büchel, *U. Hamburg-Eppendorf*
Joseph A. Burns, *Cornell U.*
Carter Tribley Butts, *U. of California, Irvine*
Gyorgy Buzsaki, *New York U. School of Medicine*
Blanche Capel, *Duke U.*
Mats Carlsson, *U. of Oslo*
Ib Chorkendorff, *U. of Denmark*
David Clapham, *Children's Hospital Boston*
Joel Cohen, *Rockefeller U., Columbia U.*
James J. Collins, *MIT*
Robert Cook-Deegan, *Duke U.*
Lisa Coussens, *Oregon Health & Science U.*
Alan Cowman, *Walter & Eliza Hall Inst.*
Robert H. Crabtree, *Yale U.*
Roberta Croce, *Vrije Universiteit*
Janet Currie, *Princeton U.*
Jeff L. Dangl, *U. of North Carolina*
Tom Daniel, *U. of Washington*
Frans de Waal, *Emory U.*
Stanislas Dehaene, *Collège de France*
Robert Desimone, *MIT*
Claude Desplan, *New York U.*
Dennis Discher, *U. of Pennsylvania*
Gerald W. Dorn II, *Washington U. School of Medicine*
Jennifer A. Doudna, *U. of California, Berkeley*
Bruce Dunn, *U. of California, Los Angeles*
William Dunphy, *Caltech*
Christopher Dye, *WHO*
Todd Ehlers, *U. of Tuebingen*
David Ehrhardt, *Carnegie Inst. of Washington*
Tim Elston, *U. of North Carolina at Chapel Hill*
Gerhard Ertl, *Fritz-Haber-Institut, Berlin*
Barry Everitt, *U. of Cambridge*
Ernst Fehr, *U. of Zurich*
Anne C. Ferguson-Smith, *U. of Cambridge*
Michael Feuer, *The George Washington U.*
Toren Finkel, *NHLBI, NIH*
Kate Fitzgerald, *U. of Massachusetts*
Peter Fratzl, *Max-Planck Inst.*
Elaine Fuchs, *Rockefeller U.*
Daniel Geschwind, *UCLA*
Karl-Heinz Glassmeier, *TU Braunschweig*
Ramon Gonzalez, *Rice U.*
Julia R. Greer, *Caltech*
Elizabeth Grove, *U. of Chicago*
Nicolas Gruber, *ETH Zurich*
Kip Guy, *St. Jude's Children's Research Hospital*
Taekjip Ha, *U. of Illinois at Urbana-Champaign*
Wolf-Dietrich Hardt, *ETH Zurich*
Christian Haass, *Ludwig Maximilians U.*
Sharon Hammes-Schieff, *U. of Illinois at Urbana–Champaign*
Michael Hasselmo, *Boston U.*
Martin Heimann, *Max-Planck Inst. Jena*
Yka Helariutta, *U. of Cambridge*
James A. Hendler, *Rensselaer Polytechnic Inst.*
Janet G. Hering, *Swiss Fed. Inst. of Aquatic Science & Technology*
Kai-Uwe Hinrichs, *U. of Bremen*
David Hodell, *U. of Cambridge*
Lora Hooper, *UT Southwestern Medical Ctr. at Dallas*
Tamas Horvath, *Yale University*
Raymond Huey, *U. of Washington*
Fred Hughson, *Princeton U.*
Auke Ijspeert, *EPFL Lausanne*
Stephen Jackson, *USGS and U. of Arizona*
Steven Jacobsen, *U. of California, Los Angeles*
Kai Johnsson, *EPFL Lausanne*
Peter Jonas, *Inst. of Science & Technology (IST) Austria*
Matt Kaeberlein, *U. of Washington*
William Kaelin Jr., *Dana-Farber Cancer Inst.*
Daniel Kahne, *Harvard U.*
Daniel Kammen, *U. of California, Berkeley*
Abby Kavner, *U. of California, Los Angeles*
Masashi Kawasaki, *U. of Tokyo*
V. Narry Kim, *Seoul National U.*
Joel Kingsolver, *U. of North Carolina at Chapel Hill*
Robert Kingston, *Harvard Medical School*
Etienne Koechlin, *Ecole Normale Suprieure*
Alexander Kolodkin, *Johns Hopkins U.*
Thomas Langer, *U. of Cologne*
Mitchell A. Lazar, *U. of Pennsylvania*
David Lazer, *Harvard U.*
Thomas Lecuit, *IBDM*
Virginia Lee, *U. of Pennsylvania*
Stanley Lemon, *U. of North Carolina at Chapel Hill*
Ottoline Leyser, *Cambridge U.*
Wendell Lim, *U.C. San Francisco*
Marcia C. Linn, *U. of California, Berkeley*
Jianguo Liu, *Michigan State U.*
Luis Liz-Marzan, *CIC biomaGUNE*
Jonathan Losos, *Harvard U.*
Ke Lu, *Chinese Acad. of Sciences*
Christian Lüscher, *U. of Geneva*
Laura Machesky, *CRUK Beatson Inst. for Cancer Research*
Anne Magurran, *U. of St. Andrews*
Oscar Marin, *CSIC & U. Miguel Hernández*
Charles Marshall, *U. of California, Berkeley*
C. Robertson McClung, *Dartmouth College*
Graham Medley, *U. of Warwick*
Tom Misteli, *NCI*
Yasushi Miyashita, *U. of Tokyo*
Mary Ann Moran, *U. of Georgia*
Richard Morris, *U. of Edinburgh*
Alison Motsinger-Reif, *NC State U.* **(S)**
Thomas Murray, *The Hastings Center*
Daniel Neumark, *U. of California, Berkeley*
Kitty Nijmeijer, *U. of Twente*
Pär Nordlund, *Karolinska Inst.*
Helga Nowotny, *European Research Advisory Board*
Ben Olken, *MIT*
Joe Orenstein, *U. of California Berkeley & Lawrence Berkeley National Lab*
Harry Orr, *U. of Minnesota*
Pilar Ossorio, *U. of Wisconsin*
Andrew Oswald, *U. of Warwick*
Steve Palumbi, *Stanford U.*
Jane Parker, *Max-Planck Inst. of Plant Breeding Research*
Giovanni Parmigiani, *Dana-Farber Cancer Inst.* **(S)**
John H. J. Petrini, *Memorial Sloan-Kettering Cancer Center*
Samuel Pfaff, *Salk Institute for Biological Studies*
Joshua Plotkin, *U. of Pennsylvania*
Albert Polman, *FOM Institute AMOLF*
Philippe Poulin, *CNRS*
Jonathan Pritchard, *Stanford U.*
David Randall, *Colorado State U.*
Felix Rey, *Institut Pasteur*
Trevor Robbins, *U. of Cambridge*
Jim Roberts, *Fred Hutchinson Cancer Research Ctr.*
Barbara A. Romanowicz, *U. of California,Berkeley*
Amy Rosenzweig, *Northwestern University*
Mike Ryan, *U. of Texas, Austin*
Mitinori Saitou, *Kyoto U.*
Shimon Sakaguchi, *Kyoto U.*
Miquel Salmeron, *Lawrence Berkeley National Lab*
Jürgen Sandkühler, *Medical U. of Vienna*
Alexander Schier, *Harvard U.*
Vladimir Shalaev, *Purdue U.*
Robert Siliciano, *Johns Hopkins School of Medicine*
Denis Simon, *Arizona State U.*
Uri Simonsohn, *U. of Pennsylvania*
Alison Smith, *John Innes Centre*
Richard Smith, *U. of North Carolina* **(S)**
John Speakman, *U. of Aberdeen*
Allan C. Spradling, *Carnegie Institution of Washington*
Jonathan Sprent, *Garvan Inst. of Medical Research*
Eric Steig, *U. of Washington*
Paula Stephan, *Georgia State U. and National Bureau of Economic Research*
Molly Stevens, *Imperial College London*
V. S. Subrahmanian, *U. of Maryland*
Ira Tabas, *Columbia U.*
Sarah Teichmann, *Cambridge U.*
John Thomas, *North Carolina State U.*
Shubha Tole, *Tata Institute of Fundamental Research*
Christopher Tyler-Smith, *The Wellcome Trust Sanger Inst.*
Herbert Virgin, *Washington U.*
Bert Vogelstein, *Johns Hopkins U.*
Cynthia Volkert, *U. of Göttingen*
David Wallach, *Weizmann Inst. of Science*
Ian Walmsley, *U. of Oxford*
Jane-Ling Wang, *U. of California, Davis* **(S)**
David A. Wardle, *Swedish U. of Agric. Sciences*
David Waxman, *Fudan U.*
Jonathan Weissman, *U. of California, San Francisco*
Chris Wikle, *U. of Missouri* **(S)**
Ian A. Wilson, *The Scripps Res. Inst.* **(S)**
Timothy D. Wilson, *U. of Virginia*
Rosemary Wyse, *Johns Hopkins U.*
Jan Zaanen, *Leiden U.*
Kenneth Zaret, *U. of Pennsylvania School of Medicine*
Jonathan Zehr, *U. of California, Santa Cruz*
Len Zon, *Children's Hospital Boston*
Maria Zuber, *MIT*

BOOK REVIEW BOARD
David Bloom, *Harvard U.,* **Samuel Bowring,** *MIT,* **Angela Creager,** *Princeton U.,* **Richard Shweder,** *U. of Chicago,* **Ed Wasserman,** *DuPont*

Published by AAAS

EDITORIAL

New frontiers in bioscience

In 1975, when relatively powerful microprocessors first became available, many young entrepreneurs—including myself—were inspired to create companies, platforms, and programming tools that helped make computing available to everyone. This in turn helped spark the information revolution. Today, thanks to the increasing sophistication, speed, and power of computer modeling and other new tools such as optogenetics and multiple forms of microscopy, we are on the brink of another revolution—this time in bioscience.

In laboratories around the world, some of the brightest scientists—well-established and those early in their careers—are conceiving novel theories at the very forefront of knowledge. In tissue regeneration, multilevel function, multiscale modeling, longevity, and other cutting-edge fields, breakthrough research will soon enable us to improve human health and perhaps even reveal the deepest mechanisms of life itself. It is this promise that motivates my own investment, and I imagine that of others, in the new frontiers of bioscience.



Modeling human infection

"...all of us...must invest much more in...out-of-the-box approaches at the very edges of knowledge."

The complexity of biology is a fascinating challenge, and I am keen to see the field deconstruct its mysteries, establish reliable and predictive models, and put that knowledge to work. Such innovative and creative work drives human progress, and it is this belief that fuels my ongoing support for basic science. Toward this end, I've invested in the Allen Institute for Brain Science and the Allen Institute for Cell Science, and just last week launched the new Frontiers Group—a part of the Allen Institute—which supports researchers at academic institutions around the world. In recent years, organizations such as the Howard Hughes Medical Institute, W. M. Keck Foundation, Kavli Foundation, Gordon and Betty Moore Foundation, and Simons Foundation have also made important investments in groundbreaking bioscience.

Such investments in bioscience are catalysts for change. But to make the transformational advances we seek, all of us—philanthropists, governments, universities, and private companies alike—must invest much more in basic, fundamental science and in the intrepid scientists who are willing to pursue out-of-the-box approaches at the very edges of knowledge.

We should also be working more aggressively to break down scientific silos by backing more collaborative, interdisciplinary teams that include experts in bioscience, mathematics, computer science, medicine, engineering, and other fields. For example, the Human Genome Project succeeded because of the convergence of massive computing power, new algorithms, expertise in laboratory biology, and broad support from the public and private sectors. We need more of that, more often, to keep advancing bioscience.

This type of bold, sweeping, integrative research inevitably entails the likelihood of setbacks and sometimes outright failure. As a consequence, some consider such science as too risky to support with the level of investments that I advocate. But what they fail to recognize is that the much larger risk to society lies in not committing enough to tackle the most complex or daunting frontiers. Without risk, there is rarely reward, and unless we attempt more "bleeding edge" approaches, efforts to prevent pandemics, defeat dementia, or cure cancer may take much longer than they should.

We must do better, and we can. If we champion new research pioneers, cultivate a spirit of open collaboration, and aggressively fund science at the frontiers, the 21st century will ultimately yield answers to the biggest questions in bioscience. A much brighter future lies just over the horizon—if we commit to charting a bolder course.

– **Paul G. Allen**



Paul G. Allen is the cofounder of Microsoft, the chief executive officer of Vulcan Inc., a recipient of the 2015 Carnegie Medal of Philanthropy, and the founder of the Allen Institute for Brain Science, Institute for Cell Science, and Institute for Artificial Intelligence. Twitter @PaulGAllen. E-mail: Frontiers@AllenInstitute.org

Downloaded from on March 31, 2016

PHOTOS: (INSET) DENISE MONACK/STANFORD UNIVERSITY; (TOP) BEATRICE DE GEA/VULCAN INC.

10.1126/science.aaf7711

Published by AAAS

NEWS

> “WPA believes strongly in evidence-based treatment. There is no sound scientific evidence that innate sexual orientation can be changed.”
>
> Statement released 23 March by the **World Psychiatric Association**, calling for an end to the practice of “conversion therapy.”

IN BRIEF

A much older ‘hobbit’



Liang Bua cave on Flores, where the “hobbit” fossils were discovered in 2003.

In 2003, scientists excavating a cave on the Indonesian island of Flores unearthed the skull and skeleton of an adult female hominin who stood about a meter tall. The hominin, they said, was a new, primitive species, dubbed *Homo floresiensis*; dating of the sediments in which the fossils were found suggested that *H. floresiensis* lived as recently as 18,000 years ago. The discovery of the “hobbit” has sparked fierce debate, with some scientists arguing that it was merely a diseased *H. sapiens*. Now, a new paper by many of the same scientists who made the original discovery may put that debate to rest: New stratigraphic data from the cave suggest that *H. floresiensis* actually lived between 100,000 and 60,000 years ago; *H. sapiens*, however, didn’t reach the region until about 60,000 to 50,000 years ago. The new data come from further excavations conducted between 2007 and 2014. Near the cave’s center, the team found a series of sedimentary layers that reveal a clear time sequence of fossil-bearing sediments, volcanic sediments, and others that they used to reconstruct the cave’s history. Dating of the sediments showed that the fossils couldn’t be younger than 60,000 years, the team reports this week in *Nature*. The original excavations were conducted at the edges of the cave, where erosion had turned the sedimentary layers into a confusing jumble, leading to an erroneous age for the hobbit.

AROUND THE WORLD

A plan to reshuffle U.S. science

WASHINGTON, D.C. | The U.S. Department of Commerce (DOC) would be eliminated, and many research programs at the National Science Foundation (NSF) and the Department of Energy (DOE) would be sharply curtailed, under a plan released last week by the budget committee of the U.S. House of Representatives. A faction of congressional Republicans has so far prevented the House from passing a 2017 budget resolution, the first step in deciding how much money each agency will receive next year. But if the budget committee has its way, the science programs at DOC—including the National Institute of Standards and Technology, the National Oceanic and Atmospheric Administration, and the Census Bureau—would be dispersed across the government. Legislators also favor giving stable funding to only three of NSF’s six research directorates—effectively giving second-class status to the other three—and having DOE defer to industry in funding several areas of high-risk, basic research. **http://bit.ly/cutComm**

Galápagos waters now a sanctuary

QUITO | The Ecuadorian government last week declared waters surrounding part of the Galápagos Islands to be the country’s first marine sanctuary. The islands are famous for Charles Darwin’s studies and for their biodiversity—25% of Earth’s species are packed onto this South American archipelago—says conservation



The Galápagos sanctuary aims to curtail overfishing.

PHOTOS: (LEFT TO RIGHT) LIANG BUA TEAM; © BRANDON COLE MARINE PHOTOGRAPHY/ALAMY STOCK PHOTO

Downloaded from on March 31, 2016

Published by AAAS

biologist Hugo Arnal, head of Ecuador's World Wildlife Fund, which lobbied hard for the zoning changes. In 2001, Ecuador made the waters a marine reserve, but fishing still took its toll on the wildlife. Now, with zoning changes and creation of the 39,000-square-kilometer Darwin and Wolf Marine Sanctuary, the government has made 33% of the island's local waters off-limits to fishing and other sea-life removal. That area in the northern Galápagos harbors the largest density of sharks in the world and already is a mecca for shark researchers. "This is just the beginning of a new chapter in the conservation history of the archipelago," Arnal says. But successful restoration of declining fished species will require enforcement of no-take areas, Arnal and others note, and stronger regulations on shark fishing, particularly of migratory species such as the hammerhead.

Yellow fever outbreak

LUANDA | A vaccine shortage is hampering efforts by the World Health Organization (WHO) to fight an outbreak of yellow fever in Angola. More than 450 people have been infected, most of them in Luanda, the capital; 178 people have died. The outbreak, reported in December 2015, is the first i n the country in 50 years. Epidemiologists worry that the country's poor record of routine immunizations, along with the widespread distribution of the *Aedes aegypti* mosquitoes that carry the disease, could allow the virus to spread quickly. WHO has spearheaded a vaccination campaign that has already reached 6 million of Luanda's 7.3 million people. However, WHO's emergency stockpile of the vaccine, maintained since 2002, has been depleted by the outbreak, and millions more doses may be needed as the virus spreads beyond the city. WHO is now discussing with vaccine manufacturers plans to divert shipments that were to be used for routine immunization elsewhere to replenish the emergency fund.

X-ray observatory status unknown

KANAGAWA PREFECTURE, JAPAN | The Japan Aerospace Exploration Agency (JAXA) is desperately trying to reestablish communications with its recently launched Hitomi x-ray observatory (formerly known as ASTRO-H) following a loss of contact on 26 March. Hitomi, which was launched 17 February, is a groundbreaking telescope that will be able to image emissions from black holes, the swirl of hot gas in galaxy clusters, and supernova remnants through high-energy photons—including x-rays and gamma rays—with unprecedented accuracy. The U.S.-based Joint Space Operations Center (JSpOC), which tracks orbiting objects with radar, reported on 27 March seeing five separate objects at Hitomi's location; meanwhile, ground-based amateur satellite watchers reported seeing Hitomi in a slow spin. But JAXA spokesperson Azusa Yabe says that the agency had received short signals from Hitomi after JSpOC reported its possible breakup. "We are still trying to recover communication with Hitomi, and trying to find out the status and causes of this communication failure," Yabe says. **http://bit.ly/Hitomicomm**



A seafaring people from south Sulawesi likely brought dingoes to Australia.

PHOTO: CRAIG DINGLE/ISTOCK PHOTO

Who let the dingoes in?

Canines and people have been traveling the world together for possibly 30,000 years—but archaeological evidence, from bones to rock art paintings, suggests that Australia's native dog, *Canis dingo*, didn't arrive down under until 3500 to 5000 years ago. So who brought them? Australian archaeologists Paul Tacon of Griffith University, Gold Coast, in Brisbane and Melanie Fillios of the University of New England in Armidale reviewed archaeological evidence and genetic data for the dingo's origin, and then assessed potential candidates, including early farmers, hunter-gatherers, and sea-faring traders. Early farmers, for example, were ruled out because dingoes lack a gene for digesting starch, found in farmed grains. Instead, the "likely suspects" are the Toalean, a sophisticated maritime hunting and gathering people from the Indonesian island of Sulawesi, the researchers report this month in the *Journal of Archaeological Science: Reports*. Between 8000 and 1500 years before present, the Toalean traveled vast distances by sea; they likely brought the dingoes from Borneo, where dingo remains have been found, to Australia. The "big implications of this work aren't just for dingo origins," says the University of Sydney in Australia wildlife biologist Mathew Crowther—it will help tease out historical movements of people throughout Asia and the Pacific.

KAGRA starts its test run

GIFU PREFECTURE, JAPAN | Last week, Japanese scientists began a test run of their Kamioka Gravitational Wave Detector, known as KAGRA. This first run of the telescope, located more than 200 meters underground

Published by AAAS

at the Kamioka mine site to minimize noise, comes just a month after a U.S.-led team of scientists announced it had for the first time directly detected gravitational waves, confirming a 100-year-old prediction in Albert Einstein's general theory of relativity. KAGRA will cooperate with the United States's Laser Interferometer Gravitational-Wave Observatory and the European Gravitational Observatory's Virgo interferometer to look for gravitational waves; having three detectors will allow greater precision in locating the sources of the waves. The test run, with a low-power laser, is a construction milestone but actual observations are still 2 years away.

FINDINGS

Long-term drugs no help for Lyme

The effect of long-term antibiotics on Lyme disease has been long debated. Proponents argue that taking antibiotics for months or even years can alleviate chronic pain, fatigue, and neurological troubles, based on individual cases and some studies, although a handful of small-scale trials have suggested otherwise. Now, a much larger clinical trial suggests that long-term antibiotics don't make a difference. Dutch researchers recruited 280 patients with persistent Lyme symptoms: They either had antibodies to Lyme bacteria or had symptoms like a rash associated with acute Lyme disease. Each volunteer received 2 weeks of intravenous antibiotics; then, some participants received oral antibiotics for 12 more weeks, while others received a placebo. At the end of the study, all of the patients were in somewhat better health based on certain measures of mental and physical functioning, though still below normal, regardless of whether they received treatment, the authors report in this week's issue of *The New England Journal of Medicine*. Whether that improvement is a result of the 2-week course of antibiotics, a placebo effect, or some other reason is unclear.



Ticks spread Lyme bacteria.

NEWSMAKERS

Surgeon Paolo Macchiarini fired

The curtain has finally fallen for trachea surgeon **Paolo Macchiarini** at the Karolinska Institute (KI) in Stockholm. Last week, the university announced that Macchiarini will be dismissed, effective immediately, after its disciplinary board found that he "engaged in conduct and research that is incompatible with a position of employment at KI." Once hailed as a surgical pioneer for attempts to replace damaged tracheae with artificial ones that combined stem cells with polymer scaffolds, Macchiarini survived a misconduct investigation at KI last year. But a documentary that aired on Swedish television in January suggested that Macchiarini had exaggerated the success of his operations in published papers, and triggered serious questions about the way KI had handled its investigation. Macchiarini, who has shaken off misconduct allegations several times before, vows to fight on. "I do not accept any of the findings of the Disciplinary Board," he wrote in an email to *Science*. "I have instructed lawyers and will be taking immediate steps to restore my reputation." **http://bit.ly/KIfiresMacc**

Testing limits on Mount Everest

Five years ago, Welsh rugby player–turned–mountain climber Richard Parks ascended to the roof of the world. Next month, he hopes to do it again—this time, without the aid of supplemental oxygen, and as part of a research project (Project Everest Cynllun) conducted with scientists at the University of South Wales, Pontypridd, in the United Kingdom. "We've got some very ambitious science that we're proposing," says physiologist Damian Bailey, who is leading the science team. Upon reaching the summit around the end of May, Parks will take a number of samples, including the world's highest blood sample and the world's highest muscle biopsy (which Parks will perform on himself). "We're looking to record the lowest blood-gas samples, the lowest partial pressures of oxygen, arguably, shown in the circulation so far," Bailey says. But the expedition isn't just about recording firsts, he adds. "What we're really talking about is trying to understand the factors that control oxygen transport"—specifically, how oxygen gets to the brain. Studying how an ultrafit climber manages the severely limited oxygen supply in the so-called "death zone" above 8000 meters' altitude could provide clues to the mechanisms linking hypoxia, cognitive decline, and dementia. **http://bit.ly/EverestBailey**



Richard Parks ascends Everest in 2011; next month, he plans to do it again, without supplemental oxygen.

BY THE NUMBERS

154

Increase in tuberculosis (TB) cases in the United States from 2014 to 2015, bringing the 2015 total to 9564, according to the Centers for Disease Control and Prevention. The United States last recorded an increase in TB cases 23 years ago.

328

Number of times two scientists aboard the *JOIDES Resolution* ran around the ship's helideck this week, matching the 21 kilometers covered by colleagues simultaneously embarking on a Cardiff University World Half Marathon back home in Wales.

PHOTOS: (TOP TO BOTTOM) VOLKER STEGER/SCIENCE SOURCE; RICHARD PARKS

Published by AAAS



Images from December 2014 (left) and February 2015 show coral bleaching in the Pacific waters around American Samoa.

PHOTO: XL CATLIN SEAVIEW SURVEY

ECOLOGY

El Niño's warmth devastating reefs worldwide

Recent aerial surveys of Australia's Great Barrier Reef find massive coral bleaching

By **Dennis Normile**

Even as recently as early March, Australian coral reef scientists still hoped that the legendary Great Barrier Reef (GBR) would get off lightly in the current El Niño, the climate phenomenon that brings unusually warm water to the equatorial Pacific, stressing and often killing corals. No such luck. On 20 March, the GBR Marine Park Authority in Townsville, Australia, reported that divers were finding extensive coral bleaching—the loss of symbiotic algae—in remote northern areas of the reef. Many sections were already dead.

Subsequent flyover surveys have confirmed an unfolding disaster: "Only four reefs out of 520 [observed] had no bleaching," says Terry Hughes, director of the Australian Research Council Centre of Excellence for Coral Reef Studies in Townsville, who personally checked the northernmost 1000 kilometers of the 2300-kilometer reef system over 4 days last week. "It was the saddest reef trip of my career."

The GBR joins a lengthening list of reefs bleached because of the El Niño that started in late 2014. It is now the longest bleaching event ever, and this El Niño, which helped make 2015 the planet's hottest year on record, "isn't even close to being over," says Mark Eakin, a coral reef ecologist at the U.S. National Oceanic and Atmospheric Administration (NOAA) in College Park, Maryland. Even though the El Niño is now weakening, its lingering effects could cause bleaching for another year, he adds.

Eakin says it is too early to tell whether this current event will match the infamous bleaching event of 1998, when 16% of reefs worldwide perished. But it is surely a sign of what's to come, he and others contend.

With global warming raising ocean temperatures, even relatively weak El Niños will be enough to make corals uncomfortably hot, Eakin warns. "If bleaching events continue to increase in both frequency and intensity, there will be a step-wise decline in the health of the reefs; the frequency of bleaching events can overwhelm the ability of the corals to recover," says coral ecologist Alexandra Dempsey of the Khaled bin Sultan Living Oceans Foundation in Annapolis.

> *"It was the saddest reef trip of my career."*
>
> **Terry Hughes**, Australian Research Council Centre of Excellence for Coral Reef Studies

Ove Hoegh-Guldberg, director of the Global Change Institute at the University of Queensland, St. Lucia, in Brisbane, Australia, suggests that the world is on course to lose coral reefs entirely by 2040. "This is not in the future, it's happening right now," he says.

Corals harbor colorful symbiotic algae called zooxanthellae, which use photosynthesis to produce nutrients for themselves and their hosts. When the water gets too hot the corals expel the zooxanthellae and turn white, or bleach. If the water cools soon enough, the algae return. But prolonged bleaching can kill the corals—and much more. The loss of coral cover makes reefs less hospitable for many marine organisms and fish, leading to a dramatic loss of biodiversity.

Bleaching occurs occasionally because of local conditions—in 2002, for example, local hot weather drove widespread bleaching on the GBR. But an El Niño drives up temperatures all across the Pacific and influences waters and weather patterns worldwide. The record-setting 1998 bleaching resulted from a particularly powerful El Niño. A 2010 El Niño also caused extensive global bleaching.

In late 2014, NOAA's Eakin, who runs the agency's Coral Reef Watch, predicted a "global-scale bleaching event" because of the then-emerging El Niño. The reports started flowing in at the beginning of 2015. That April, Dempsey and other researchers reported extensive bleaching in the British Indian Ocean Territory, a speck of isles in the Indian Ocean halfway between Africa

Downloaded from on March 31, 2016

Published by AAAS

and Indonesia. "More than 50% of branching corals, some as large as 2 meters in diameter, were beginning to show the early onset of bleaching," says Dempsey, who was part of a team surveying the remote and rarely visited reefs.

Extensive bleaching hit Hawaii in November 2015 and then Fiji and New Caledonia in February of this year. "Bleaching is going on right now across half the globe in the Southern Hemisphere," Eakin says. "We expect the warming to continue its northward movement in the Indian Ocean, and the long-range outlook is calling for bleaching in the Caribbean this summer," he adds.

The fate of the GBR will be documented best, thanks to Australia's scientific resources. About 6 months ago, Hughes laid plans for a National Coral Bleaching Taskforce, which swung into action last week with aerial surveys and teams of divers. The team uses a zero-to-five scoring system, where zero is no bleaching, three is 30% to 60%, and four is more than 60% bleaching. Hughes notes that 95% of the reefs they checked were scored as three or four. For comparison, in 2002 only 18% of the reefs were bleached that badly. "Without a doubt, [the damage] is much more extreme than in 2002 or 1998," he says.

A tropical cyclone in early March cooled off the central and southern sections of the reef. But coral scientists don't know exactly how far south the bleaching extends; to find out, they plan more aerial surveys of the GBR this week.

It is not clear what percentage of the bleached corals will die. But Hoegh-Guldberg was surprised by the bleaching at the GBR's pristine remote northern tip, which is least subject to fishing and tourism pressure. "We were feeling somehow that the northern end of the reef would be more robust," he says.

The optimistic view, Hughes notes, is that the pristine reefs "should bounce back faster, but the level of bleaching will take a decade to recover from."

Australian studies of this and the other major bleaching events, in 1998 and 2002, could yield clues about reef resilience. "Some lucky reefs haven't been hit and some have been clobbered three times," Hughes says. He and his colleagues will start looking for patterns, including how distant a particular reef is from the coast, its water quality, and the impacts of fishing and tourism, "to see if we can get some clues why some reefs are more vulnerable." If water quality proves to be a determining factor, "that would point to an obvious management imperative," Hughes says.

But improving water quality will have only a minor impact, given global warming. "The only way out of this bind is to rapidly contain further increases in global warming" by implementing the carbon dioxide emission cuts pledged at last year's Paris climate conference, Hoegh-Guldberg says. He is hopeful that the 500 million people worldwide who rely on reefs for their livelihoods will start making their voices heard. The damage to the GBR and other reefs, he adds, shows the "graphic alternative if we don't deal with this issue." ■



Aerial surveys in March of the Great Barrier Reef revealed extensive bleaching of corals (white).

PHOTO: TERRY HUGHES

PLANETARY SCIENCE

Sandy ripples point to Mars's past

Unique dune features emerge from rover's campaign in the sand

By **Eric Hand**, *in The Woodlands, Texas*

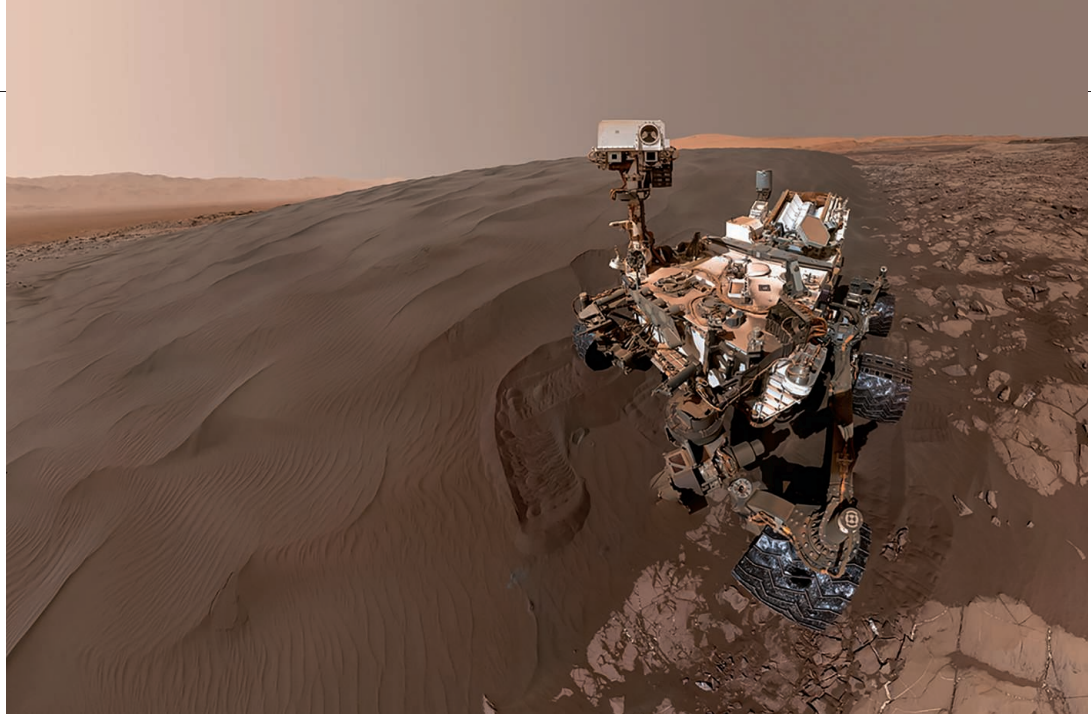
The Martian was only a movie, but the blowing sand that drove the plot really does influence Mars today—and is now a source of intrigue for scientists studying the planet. Investigators with NASA's Curiosity rover are exploring the planet's dark sand dunes and have discovered structures thought to be unlike any on Earth: ripples spaced about 3 meters apart, intermediate in size between the little ripples and big dunes found on both planets. Scientists aren't sure how they form, but they think the density of the thin martian atmosphere plays a role in shaping them.

"Something in the martian environment is begging for these to form," says Lori Fenton, a planetary scientist who studies dunes at the SETI Institute in Mountain View, California, and who wasn't involved in the research. Even before scientists can puzzle out what that is, they hope to use fossilized ripples in rocks that hardened from ancient dunes to glean clues about the thicker atmosphere of early Mars, according to Mathieu Lapotre, a graduate student at the California Institute of Technology (Caltech) in Pasadena, who presented the work here last week at the Lunar and Planetary Science Conference (LPSC).

Researchers had seen the large ripples in pictures taken from orbit, "but nobody thought hard enough" about them, Fenton says. In the end it took up-close observations by Curiosity, which is exploring Gale Crater. When the rover neared dark, billowy dunes girding the mountain that it aims to climb, some researchers on the rover's science team considered them a potentially hazardous obstacle. But others saw an opportunity. "We have not visited an active sand dune field on another planet," says Bethany Ehlmann, a participating scientist on the rover team at Caltech. "I don't think it's conscionable to be 100 meters away and drive by without stopping to take a look."

Downloaded from on March 31, 2016

Published by AAAS



Ripples 3 meters apart mingle with centimeter-scale ripples on the flanks of Mars's Namib Dune, which spans hundreds of meters.

So Ehlmann and others pushed for a campaign of pictures, wind measurements, and chemical analyses over several weeks in December 2015 and January. The scientists presented their initial results at the LPSC: images of 5-meter-tall dunes that would not look out of place in Namibia. Imprinted on top of the large dunes were typically tiny ripples and the mysterious, larger ones.

On terrestrial beaches and deserts, small sand ripples form centimeters apart. They take shape when windborne sand grains hop and strike sand downwind, scattering yet more grains. Once a ripple begins to form, it protects sand on its downwind slope from being dislodged by further impacts. Meanwhile, scattered sand continues to be deposited on the upwind side of the ripple. Larger dunes, which can sit hundreds of meters apart, grow through a different process involving the aerodynamics of the atmosphere. As wind approaches a pile of sand, its streamlines are compressed, whipping up speeds and piling up more sand toward the crest. Eventually, the leading edge becomes too steep and collapses, allowing a new crest to form and the dune to inch along.

In the solar system, dunes are found on Earth, Mars, Venus, Titan, and perhaps even Pluto. Planetary scientists study them from orbit to infer wind directions—like a "free wind sock," says Jani Radebaugh, who studies Titan's dunes at Brigham Young University in Provo, Utah. They can also use them to infer wind speed. From theoretical models and wind tunnel tests using crushed walnut shells to mimic sand blowing in Mars's weak gravity, researchers have estimated that wind speeds need to reach about 15 to 20 meters a second for martian dunes to form. Researchers hope to check those numbers by studying a handful of Curiosity's images of moving dunes snapped on days when the rover also took wind measurements, says Nathan Bridges, a planetary scientist at Johns Hopkins University Applied Physics Laboratory (APL) in Laurel, Maryland.

Other scientists on the Curiosity team are studying the size, chemistry, and color of martian dune sand. On Earth, dunes consist mainly of quartz grains, eroded from the granite that makes up much of the continental crust. On Mars, by contrast, dunes are made up mostly of dark, dense minerals like olivine, from volcanic basalt. The dunes get darker with time as finer dust, which contains lighter-colored feldspar minerals, blows away. Ehlmann says studying how the martian wind sorts grains by size and composition will help researchers understand other changes that occur as the sediment turns into stone.

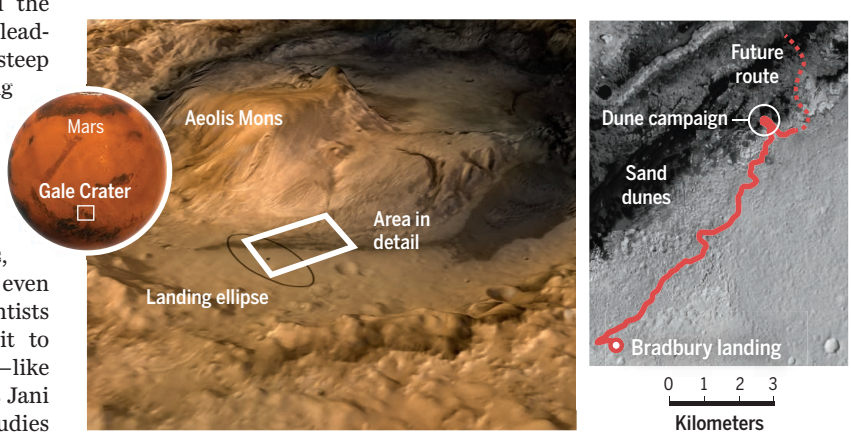
But at the LPSC, scientists were most excited by the discovery of the large ripples. In addition to spotting them in the Curiosity images, Lapotre and his colleagues have identified them at dozens of sites all over the planet in images taken from orbit. They found that at higher elevations, where the atmosphere is thinner, the ripples are farther apart. If these ripples can be found in old rocks, Radebaugh says, "you can get a good sense of what the paleoatmosphere was like."

If the large ripples are forming because of atmospheric influences rather than the impact mechanics of hopping sand grains, then, technically, they would be dunes rather than ripples. Lapotre says they seem to be similar to dunes found in riverbeds on Earth. Just as waves on the water's surface shape the bottom, invisible "boundary layers" in the atmosphere may sculpt ripples on the surface of Mars.

Not everyone is convinced that the ripples are a new type of dune. "They could just be big ripples" left over from a windier martian past, says Ralph Lorenz, an APL planetary scientist. But Fenton says Lapotre and colleagues have spotted slip faces—signs of miniavalanches—on the lee sides of some of them. Larger dunes share such slumping features, but small ripples lack them. The new-dune scenario is "plausible," she says. "I'm happy that somebody has put forward an explanation, because it has bugged me." ■

Crossing the dunes

Since landing in 2012, NASA's Curiosity rover has trundled toward its mountain target, Aeolis Mons (also called Mount Sharp), but it must cross potentially hazardous sand dunes. For several weeks this past December and January, the rover stopped to investigate the dunes.



CREDITS: (IMAGES, TOP TO BOTTOM) NASA/JPL-CALTECH/MSSS; NASA (3) (DIAGRAM) C. BICKEL/*SCIENCE*

Published by AAAS

CANCER RESEARCH

Brazil bill would legalize renegade cancer pill

Government races to put "fosfo" through clinical testing

By **Herton Escobar**, *in São Paulo, Brazil*

A showdown over a controversial cancer therapy has intensified, pitting Brazil's scientists against its congress. Last week, responding to a clamor from politicians and desperate patients, the congress voted to legalize the production and distribution of synthetic phosphoethanolamine, even though the putative cancer drug has not been clinically tested or registered with the Brazilian Health Surveillance Agency (Anvisa).

Scientists blast the legislation as a travesty. Apart from patient testimonials and a few preliminary studies in tumor cell lines and in mice, critics say, there is no evidence for safety or efficacy of the compound, popularly known as the "cancer pill" or "fosfo." The Brazilian Society for the Advancement of Science called the bill "a grave affront to the scientific community," and urged Brazilian President Dilma Rousseff to veto it.

The pressure couldn't come at a worse time for the embattled president, who is facing a series of corruption scandals that have undermined public support for her administration. She is also fighting an impeachment process in congress, related to allegations of fiscal improprieties. Vetoing the bill would mean defying public opinion and the congress on an emotionally charged issue. Signing it would draw opprobrium from the scientific community and compromise the authority of Brazil's regulatory agencies. She has until 13 April to decide.

Phosphoethanolamine is a common molecule in the body. Gilberto Chierice, an analytical chemist at the University of São Paulo in Brazil, developed the synthetic version in the early 1990s. In press interviews, he has explained that he became interested in the molecule after reading about its association with tumors. He hypothesized that the compound induces programmed cell death and tags malignant cells for the immune system to attack. Chierice, now retired, did not respond to requests for comment, but he has stated to other media that for about 20 years—starting long before the first studies on the compound's putative anticancer effects appeared in peer-reviewed journals in 2011—his lab freely gave it to patients without authorization from Anvisa or the university. Observers estimate it was several thousand.

In June 2014, a University of São Paulo directive forced Chierice's lab to shut down the operation. Outraged that the drug was no longer available, patients and their families started suing the university. The number of lawsuits skyrocketed after June 2015, when national media began running stories about people claiming that the compound alleviated their symptoms or even cured them of cancer. Several judges have ruled in favor of plaintiffs. The university says it already has received close to 15,000 court orders obligating it to continue supplying individual patients with the now iconic blue-and-white "cancer pills."

The university is fighting the injunctions while waiting for the issue to be settled, either by a ruling from the Supreme Federal Court or by the pending legislation. Until then, the compound continues to be produced in an artisanal process at Chierice's former lab and given to patients free of charge under court order. Only one scientist there now knows how to make it.

In the meantime, the federal government is racing to get the compound tested properly. Initial results from preclinical studies at four independent labs, released on 18 March, were not promising. The labs found that the pills contain only 30% phosphoethanolamine. The substance doesn't appear to be toxic—but it doesn't appear to kill cancer cells, either. Chierice and his group asserted in interviews and in a court brief that the results are invalid, because concentrations of the compound in the experiments were too low and it must be metabolized to acquire its antitumor properties.



For 20 years, synthetic phosphoethanolamine was made in this University of São Paulo lab and distributed to cancer patients without regulatory approval.

PHOTO: CECILIA BASTOS/JORNAL DA USP

The discouraging results have not deterred a clinical trial, funded by the São Paulo state government, that's set to begin this spring. The drug will be tested against 10 tumor types, including breast, prostate, liver, pancreatic, and skin cancer, in up to 1000 patients at four public hospitals. "We really hope this works," says Paulo Hoff, an oncologist and director of the Institute of Cancer of São Paulo who is leading the trial. But, he says, "we can't ignore the absence of data and turn that into a legitimate treatment, sanctioned by the state."

Even the first author of six papers that describe the compound's potential anticancer effects says congress's move was "premature." "Congress is not the competent forum to say whether a drug should be given to patients. It undermines the authority of Anvisa and the credibility of the scientific community," says Adilson Kleber Ferreira, a pharmaceutical chemist at the University of São Paulo. He is no longer connected with Chierice's group, but he believes the compound is promising and worthy of further study.

Many scientists remain deeply skeptical that fosfo will live up to its reputation. Although it may yet prove to have therapeutic benefits, it's unlikely that one substance works against so many tumor types, says Ademar Lopes, vice-president of the A.C. Camargo Cancer Center in São Paulo. "I don't believe in miracles when it comes to cancer." ■

Herton Escobar is a writer in São Paulo, Brazil.

Downloaded from on March 31, 2016

Published by AAAS



The Experimental Lakes Area project in northwestern Ontario benefits from a new budget.

PHOTO: L. HAYHURST/IISD-ELA

SCIENCE FUNDING

Canadian scientists smile at Liberals' déjà vu budget

Trudeau offers warm support for basic research

By **Wayne Kondro**

What a difference a government makes. Last week the Canadian research community felt it was stepping out of the darkness and into the sunshine after Prime Minister Justin Trudeau unveiled his first budget since taking office last November.

The 2015–16 fiscal blueprint pumps up the country's three funding councils after years of static or declining budgets. It also resurrects several initiatives from the last budget a Liberal government presented, in 2005, before the Conservatives took power under Stephen Harper and launched what many scientists regarded as a "war on science."

On 22 March Finance Minister Bill Morneau presented a budget that includes a host of scientific goodies—and promised more to come—as part of what he called "a new vision for Canada's economy as a center of global innovation, renowned for its science, technology, resourceful citizens, and globally competitive companies." Morneau also said the new policies would be "evidence-based," a parting shot at what Liberals regarded as Harper's ideologically driven decisions to shift resources away from basic research and into applied areas and muzzle discussion of climate change.

"Overall I am quite impressed," says Katie Gibbs, who leads Evidence for Democracy, a pro-science advocacy group based in Ottawa. "I think it shows strong support for science, and it marks a significant turning point for science in Canada compared with previous budgets."

The new spending plan adds $23 million apiece to the budgets of two granting councils—the Canadian Institutes of Health Research (CIHR) and the Natural Sciences and Engineering Research Council of Canada (NSERC)—and $12 million to the Social Sciences and Humanities Research Council (SSHRC). The boosts augment a $37 million increase for all three councils announced last year by Harper that goes into effect this year. NSERC's budget will rise to $866 million, CIHR's to $789 million, and SSHRC's to $559 million. Support for the indirect costs of research at universities will rise by $15 million, to $261 million.

Trudeau also announced that he has asked his science minister, medical geographer Kirsty Duncan, to conduct "a comprehensive review of all elements of federal support for fundamental science." One important goal is to make sure that Canada continues to participate in big-science projects and other international collaborations. The new budget, for example, includes a promise to shell out $290 million over 4 years to secure Canadian participation in the International Space Station through 2024. Duncan will also examine the status of young scientists and the operations of the granting councils.

"I think they're trying to at least signal through this exercise that they're paying attention to the concerns of the science community," says Paul Dufour of the Institute for Science, Society and Policy at the University of Ottawa. Of course, he adds, "how that's going to translate into more money and resources is another story."

In the meantime, scientists are pleased with many details in an overall budget of $243 billion, a nearly 7% boost in spending. As expected, the government touted its climate change agenda. The budget blueprint includes $1.532 billion over 2 years for initiatives that reduce greenhouse gas emissions, $100 million over 5 years for "clean technology research, development and demonstration activities," and $15 million over 8 years to create two Canada Excellence Research Chairs in "clean and sustainable technology."

In another reversal of Conservative policies, Morneau announced plans to spend $151 million over 5 years to reinvigorate ocean and freshwater sciences. That amount includes an unspecified amount for the Experimental Lakes Area (ELA), a freshwater research facility in northern Ontario whose $1.53-million-per-year federal appropriation was axed by Harper in 2013. No longer a federal facility, ELA has broadened its funding base to sustain operations.

The Trudeau government will also resurrect two other big initiatives killed by the Conservatives. The first, a "Post-Secondary Institutions Strategic Investment Fund," revives a 2005 plan for improving university infrastructure. It will provide $1.53 billion over 3 years for universities and colleges to "modernize research labs, retrofit buildings used for advance training, and expand on-campus incubators that support startups as they grow their businesses."

The other resurrected plan will promote more university-industry linkages by way of "large-scale integrated facilities." They would serve as sort of incubator-centers for startup companies, venture capitalists, and business service providers located near a university or government research institute. The Trudeau government plans to provide $612 million over 4 years for such innovation clusters.

To Dufour, however, the new emphasis on basic research is the best news of all. "There's the famous phrase from the former prime minister, that 'science powers commerce.' And for the Conservative administration, that's all that mattered," he says. "Whereas this government has made it clear that they respect and value science and scientists, and that basic science is important to the economy and society." ■

Wayne Kondro is a writer based in Ottawa; Brian Owens, a writer in New Brunswick, Canada, provided additional reporting.

Downloaded from on March 31, 2016

Published by AAAS

BIOMEDICINE

No-strings awards at NIH draw concern

Some recipients say they didn't expect deep cuts in funding

By **Jocelyn Kaiser**

After years of roller-coaster funding for her lab, yeast geneticist Sue Jinks-Robertson of Duke University Medical Center in Durham, North Carolina, was thrilled early last year when her sole funding source, the National Institute of General Medical Sciences (NIGMS), announced a new kind of award that promised stability. She could trade her three small, project-based grants, which had to be renewed every 4 years, for a single award that would provide 5 years of steady funding. But when NIGMS called Jinks-Robertson in February to tell her she had won this new option, the Maximizing Investigators' Research Award (MIRA), her excitement quickly turned to shock. Her funding, she learned, would be cut 20% compared with her average over the last 5 years, from $427,300 to $345,000 a year.

Jinks-Robertson, 61, isn't the only mid-career or senior investigator who feels duped. Two disillusioned recipients at Memorial Sloan Kettering Cancer Center in New York City, Maria Jasin and Christopher Lima, say they've been in touch with at least 16 of their fellow awardees who have serious concerns about the impact of the cuts on their labs. About five investigators have turned down MIRAs, for various reasons, NIGMS says.

Most of the unhappy MIRA recipients who corresponded with *Science* did not want to be quoted by name because they didn't want to be seen as "whiners," or they worried NIGMS would cut their funding further. But one mid-career investigator who had a large program on cell biology slashed by 40% says she feels like "my legs were cut out from under me." She will now write proposals to other National Institutes of Health (NIH) institutes to make up the difference—an outcome the MIRA program was intended to avoid.

> ***"[I feel like] my legs were cut out from under me."***
>
> **A MIRA recipient**

MIRAs are part of an effort across NIH to expand the agency's use of awards that support people based on their track record, not projects, a model long followed by the Howard Hughes Medical Institute (*Science*, 25 July 2014, p. 366). To pilot test the program, in January 2015 NIGMS invited established investigators with at least two standard R01 research grants to apply for a MIRA, which promised 5 years of support—longer than the usual 4-year R01 grant—in exchange for "somewhat less" funding. Of 710 eligible investigators, 179 applied and NIGMS expects to make at least 115 awards.

On average, the new awards amount to a 12% cut in a recipient's overall average NIGMS funding for the past 5 years, with much deeper cuts for some. Small labs expect to get even smaller; large ones are preparing to downsize or scramble for other funds. Jinks-Robertson, for instance, says unless she can scrape up other funds, her six-person lab will drop to no more than a technician, graduate student, and postdoc. And because NIGMS rules did not allow her to apply to renew her standard R01 grants as a backup option, she felt she had no choice but to accept the new award. "It was, take it or leave it," she says. Researchers at medical schools, like Jinks-Robertson, are being hit particularly hard because, unlike their colleagues at universities, they usually must get at least half their salary from their grants.

NIGMS Director Jon Lorsch, in Bethesda, Maryland, says only a "small minority" have complained, and that NIGMS was "very clear" that a MIRA would entail less money overall in exchange for an extra year of stable funding and freedom to pursue new ideas not tied to a specific project. By saving money, he adds, the program aims to free up funds for younger investigators. But some have complained that the award seems intended to accomplish that by persuading senior investigators to wind down their labs and retire.

One "irony," Lorsch says, is that when the program was first discussed, the fear was that it would be "a big giveaway to already well-funded investigators that would make disparities worse." Instead, it will redistribute the wealth, NIGMS says: The notice for a first round of MIRAs for early career investigators promises awards "somewhat larger" than the average NIGMS R01 grant for new investigators.

Despite the grumbling from some MIRA recipients, members of NIGMS's advisory council, who approved the program earlier and recently received an update, remain supportive of the program, says council member Rick Horwitz, executive director of the Allen Institute for Cell Science in Seattle, Washington. "My own view is we need to spread resources enough to support a critical mass of labs with diverse approaches," he says.

Still, NIGMS is responding to the concern that MIRAs may not work for everyone by giving more leeway to established investigators who apply for the next round of MIRA grants: Applicants will have more time to renew their R01s if they don't get a MIRA or decide not to accept it. And at least one MIRA recipient thinks the program will remain a popular option. Howard Ochman of the University of Texas, Austin, who studies microbial genome evolution, says that although his six-person lab will probably go down by one postdoc, "It's a relief. I know I can continue [supporting] those who remain." ■

Security, at a price

Some scientists say that a new type of federal grant that promises stable support, the Maximizing Investigators' Research Award (MIRA), offers less funding than expected.

179
Number of program applicants for NIGMS' first MIRA round

115
Number of program awardees

~5
Recipients who declined award

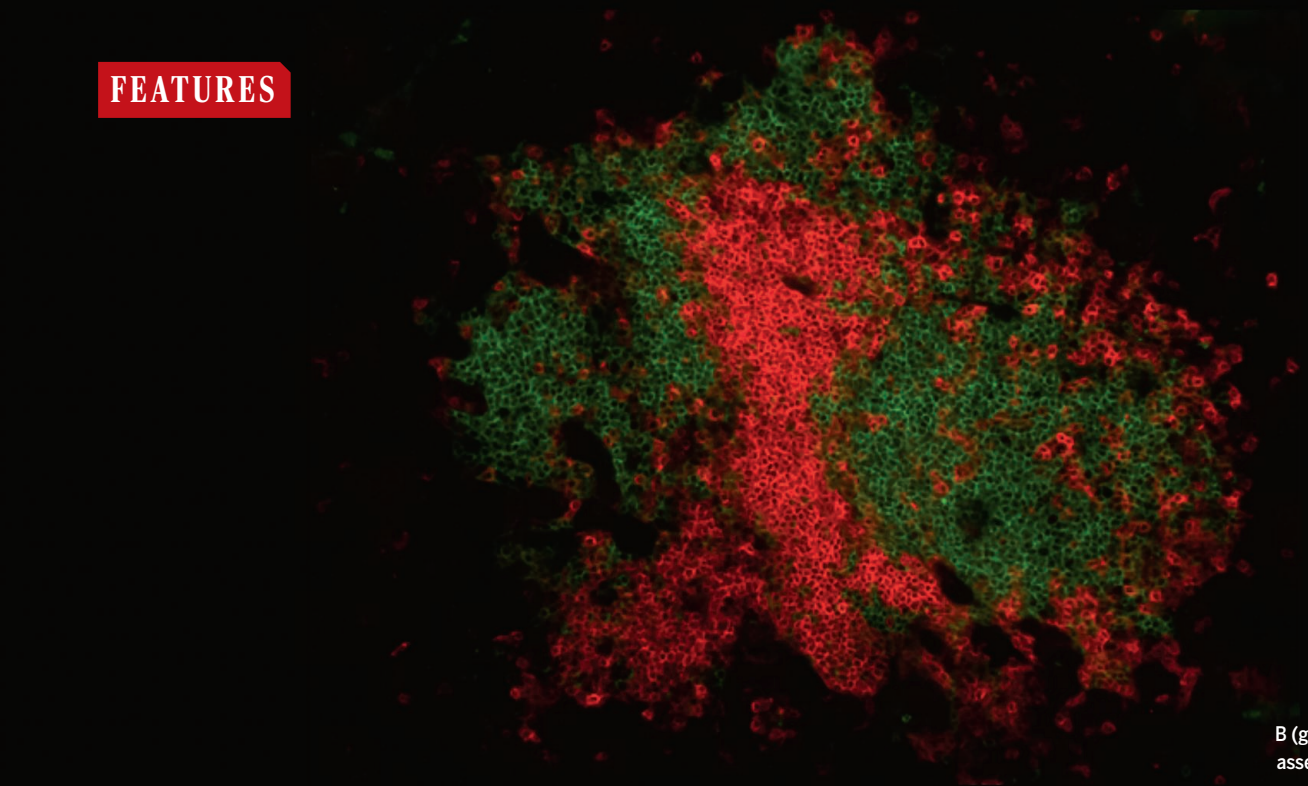
$420k
Median size of two NIGMS R01s (direct costs)

$400k
Median size of MIRA award (direct costs)

12%
Average cut, for MIRA recipient, in 5-year funding level

Downloaded from on March 31, 2016

Published by AAAS



B (green) and T cells (red) assemble inside a tertiary lymphoid structure.

IMAGE: N. RUDDLE *ET AL. PROCEEDINGS OF THE NATIONAL ACADEMY OF SCIENCES* **11**. (13 MARCH 2007)

Downloaded from on Ma 31, 2016

IMMUNITY GOES LOCAL

The temporary immune command posts that form near infections or inflammation draw clinical interest

By **Mitch Leslie**

Nancy Ruddle just could not make her mice get sick. During the 1990s, the immunologist at Yale University School of Medicine and her colleagues spent months trying to create a strain of diabetic mice. In hopes of inducing the hallmark of type I diabetes—destruction of the insulinmaking β cells by the immune system—they had genetically altered the animals to trigger inflammation in the pancreas, where the cells reside. But the mice—and their β cells—remained stubbornly healthy. "At first we were rather disappointed with them," Ruddle recalls. "We said we'd better find out what was going on."

Peering through a microscope at pancreatic tissue from one of the mice, a colleague of Ruddle's spotted something unexpected. He announced, "this is a lymph node," Ruddle says. She was certain he was wrong because the pancreas doesn't contain these immune system outposts, where cells muster before being activated to fight microbes. Ruddle figured he had just seen one of the loose gatherings of immune cells that sometimes appear at sites of inflammation.

But after studying his find and other similar structures in the animals' kidneys and skin, she and her lab members had to admit that the structures looked a lot like lymph nodes. They showed the same segregation of two main kinds of immune cells, B and T cells, and the same distinctive small veins that allow immune cells to enter the nodes. "That was one of the things that convinced me" that the objects weren't just flash mobs of immune cells, Ruddle says.

Two decades later, immunologists are convinced that these structures are far more important to the body's immune defenses, and to strategies for manipulating them, than Ruddle could have imagined. Researchers now call what she and her colleagues observed tertiary lymphoid structures (TLS) or tertiary lymphoid organs: organized congregations of immune tissue that can sprout at sites of inflammation

Published by AAAS

or infection almost anywhere in the body. They appear to serve as local command centers that instigate immune system counterattacks against pathogens and tumors—and may also promote the self-directed attacks of autoimmune diseases and the rejection of transplanted organs.

These days, research on TLS "is exploding," says immunologist Andreas Habenicht of the University of Munich in Germany. Armed with new understanding of the signals that create these structures, drug companies have even begun testing compounds to block TLS formation in people with autoimmune diseases.

RUDDLE'S LAB WASN'T THE FIRST to discern TLS—and, it turns out, the structures didn't explain the diabetes-free mice. Researchers noted these oddities as far back as the early 1900s but largely ignored them. But her group's rodent findings, published in 1996, made the structures impossible to overlook, others say. "In hindsight you went, 'Wow, that's an amazing observation,'" says immunologist Troy Randall of the University of Alabama, Birmingham.

For decades, scientists thought that the defensive responses of B and T cells began in the lymph nodes, spleen, and related tissues—the so-called secondary lymphoid organs. (The bone marrow and thymus are the primary lymphoid organs.) At these sites, B and T cells meet up with antigens, distinctive molecular bits from invading microbes or tumors that trip the immune system's alarms. These encounters, along with stimulatory signals from other immune cells, switch on T cells' pathogen-fighting capabilities and spur B cells to mature into antibody producers.

Researchers have determined, however, that B and T cells can interact with antigens and receive marching orders within a TLS as well. In a 2009 study, for instance, immunologist Reinhold Förster of Hannover Medical School in Germany and colleagues exposed mice to a virus and then found that T cells that could react to it were activated in TLS. "They are local sites of organization of attack against a virus or other pathogen," says immunologist Bart Lambrecht of Ghent University in Belgium.

Although secondary lymphoid organs assemble only at defined locations during embryonic development, TLS form whenever and wherever they are needed, at trouble spots throughout the body. TLS appear, for example, in the lungs of tuberculosis patients as well as near or inside tumors. Immunologist Jorge Caamaño of the University of Birmingham in the United Kingdom and colleagues reported that fat within the abdominal cavity is riddled with the structures, which may help battle pathogens that escape from the gut. TLS also arise in several autoimmune diseases—in the brains of people with multiple sclerosis and in the joints of people with rheumatoid arthritis—and in transplanted organs being rejected.

Researchers have a general picture of how TLS assemble. The process begins when inflammation draws immune cells to the site of an infection or injury. By producing signals, which can include a molecule called lymphotoxin, those cells in turn stimulate stromal cells, residents of the local tissue, to provide a scaffold for the incipient TLS and lure T and B cells. But many details of TLS formation remain mysterious, including which cells are key to building them. "The challenge is to understand what are the driving cells," says immunologist Simon Jones of Cardiff University in the United Kingdom. "There are a number of candidates."

Although most TLS are microscopic, they can grow much larger—in the rare condition follicular bronchiolitis, they can be big enough to clog the tubes that bring air into the lungs. But unlike secondary lymphoid organs, which are permanent, TLS typically disassemble, sometimes within a few weeks, after inflammation or infection clear.

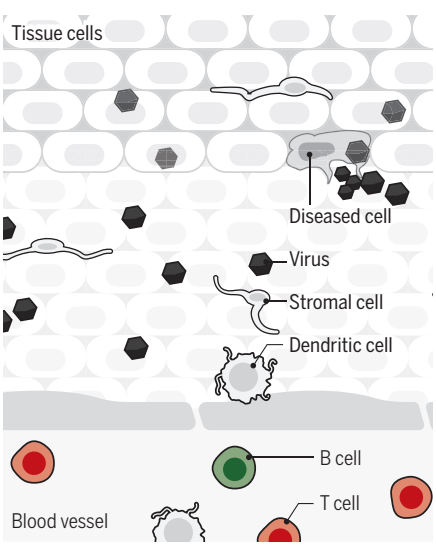
Positioning TLS on the battlefields where immune cells are fighting pathogens or tumors could provide some strategic advantages. "It's nice to have a factory nearby," where immune defenses, such as antibodies, are forged, Lambrecht says. Local command posts could make it easier for roused immune cells to track down their

Immunity's MASH units

Tertiary lymphoid structures (TLS) organize on-the-spot immune responses.

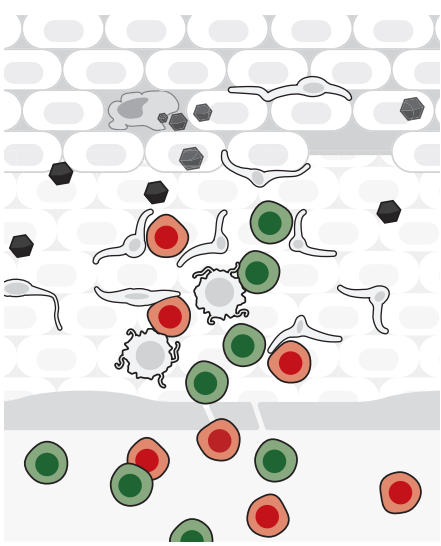
1 Infection begins

A virus has begun invading and killing cells in one part of the body. Their presence alerts dendritic cells and other immune sentinels.



2 Cells congregate

Immune cells swarm into the site of the infection. They interact with local stromal cells that will help organize the TLS.



3 Structure forms

A completed TLS contains activated T cells that can recognize the virus (inset). B cells that matured there have begun releasing antibodies.

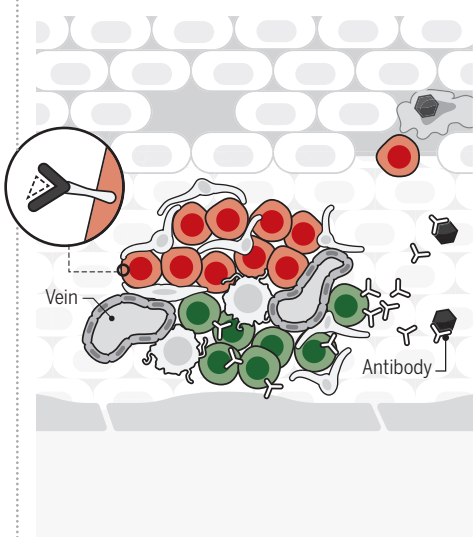


ILLUSTRATION: V. ALTOUNIAN/*SCIENCE*

Published by AAAS

targets, says immunologist Walter Storkus of the University of Pittsburgh in Pennsylvania. "The cells are being activated in the environment in which they are supposed to act." TLS may also bolster defenses for parts of the body, such as the lungs, that are regularly exposed to pathogens but don't have a lot of secondary lymphoid organs, Förster says.

BUT THOSE ADVANTAGES are far from certain. Indeed, one of the most important questions about TLS is how much they contribute to immune responses. The hundreds of lymph nodes in our bodies are perfectly good at arranging liaisons between antigens and B and T cells, so what do TLS add?

One direct test demonstrated that, at least in mice, TLS can substitute for secondary lymphoid organs. In a 2006 study, Randall and colleagues surgically removed the spleens of mice that had been genetically modified to lack lymph nodes. They then infected the mice with the flu. Randall expected that a lack of secondary lymphoid organs would leave them defenseless. But the mice survived. "In fact, they did way better than the normal mice," he says.

Randall recalls he was taken aback by the findings and suspected a mix-up. "I'll bet the cages got switched," he told his offended lab technician, insisting that she redo the experiment. Three months later she returned in triumph with the same results. The mice could still generate TLS—which were enough to sustain a strong immune defense. "The immune response was amazingly functional with just [TLS]," Randall says.

Although similar experiments aren't possible in humans, indirect evidence suggests that TLS take part in our immune defenses as well. Studies in cancer patients have typically shown that the more TLS they have in or near their tumors, the higher their odds of survival. "I liken them to MASH units that take up positions at the border of the tumor," Storkus says. In people with autoimmune diseases, on the other hand, increased numbers of TLS signal more severe tissue damage, several studies indicate.

So far, however, "we have a correlation" between TLS abundance and the severity of various conditions but no understanding of mechanism, Randall says. Instead of driving tissue destruction in autoimmune diseases, he notes, TLS could represent the body's attempt to stop it. "The evidence on whether they are good or bad is still very much debated," says immunologist Francesca Barone of the University of Birmingham in the United Kingdom.

Two recent studies underscore that uncertainty. When cancer biologist Eli Pikarsky of Hebrew University-Hadassah Medical School in Jerusalem and colleagues tested 82 people who'd had surgery for liver cancer, they discovered to their surprise that larger numbers of TLS indicated an increased likelihood of tumor recurrence and a greater risk of dying. The researchers suspected that the TLS were somehow aiding tumor growth.

To find out how, the team genetically modified mice to trigger inflammation in their livers. Inflammation drives liver cancer in people, and it spurred the mice to develop tumors in the organ—and to produce TLS there as well. The researchers reported in *Nature Immunology* last year that instead of fighting cancer cells, TLS in the rodents served as cradles, or niches, where precancerous cells could develop into tumors. "You can actually see the tumors bud out of the niche—I don't know if it's beautiful or sad," Pikarsky says.

> ***"In hindsight you went, 'Wow, that's an amazing observation.'"***
>
> **Troy Randall**, University of Alabama, Birmingham

The second study, published in *Immunity* last year, challenged the conventional wisdom about the role of TLS in atherosclerosis. Because the structures may worsen inflammation in autoimmune diseases, researchers assumed that they promote atherosclerosis, in which vessels become inflamed as well as clogged. But when Habenicht and colleagues disrupted TLS in mouse arteries by engineering smooth muscle cells in the vessels to lack the lymphotoxin receptor, the animals developed more severe atherosclerosis. "We've discovered that in the arteries they seem to be protective" at least under certain conditions, Habenicht says. He and his colleagues speculate that TLS inhibit atherosclerosis because they host regulatory T cells, which dial down inflammation.

DESPITE THE UNCERTAINTIES about TLS effects, researchers and several drug companies have been trying to develop ways to manipulate these structures for disease treatments. The first drug tailored to suppress TLS to reach clinical trials is baminercept, developed by the pharmaceutical company Biogen. The drug, designed to prevent activation of the lymphotoxin receptor, has already undergone two phase II clinical trials to gauge its effectiveness against rheumatoid arthritis and Sjögren syndrome, an autoimmune disease in which immune cells attack the salivary glands and the glands that produce tears.

So far the drug, which fuses an antibody to the lymphotoxin receptor, has been a disappointment. Baminercept didn't help rheumatoid arthritis patients. And in a recent trial in people with Sjögren syndrome, it didn't increase the production of saliva, the study's standard of effectiveness. Rheumatologist E. William St. Clair of Duke University in Durham, North Carolina, one of the leaders of the trial, says that he and his colleagues are trying to determine why by testing salivary gland biopsies from the patients.

Other drugs aimed at inhibiting TLS could soon be ready for testing. VX5, an antibody designed to block a molecule that helps stimulate TLS growth, is undergoing animal studies sponsored by the biotech firm Vaccinex. Some scientists are also testing whether approved drugs, such as the B cell–killing antibody rituximab, curb TLS formation in people with autoimmune diseases, such as Sjögren syndrome.

Researchers are also investigating whether inducing TLS could be beneficial in some diseases. Immunologist Yang-Xin Fu of the University of Texas Southwestern Medical Center in Dallas and colleagues have evidence that stimulating TLS could improve the response to a set of powerful new anticancer drugs called checkpoint inhibitors. These molecules thwart a mechanism that protects tumors from T cell attacks, but only 20% to 30% of patients benefit from them.

In a study published in March in *Cancer Cell,* Fu and colleagues hitched a protein known as LIGHT, which stimulates the lymphotoxin receptor and triggers TLS creation, to an antibody that latches onto certain cancer cells. Injected into mice with cancer, the combination homed in on the tumors and induced the growth of structures that resembled TLS. The T cells that swarmed into the tumors to produce these structures ultimately eliminated the cancerous growths—something not seen in mice treated with the checkpoint inhibitor alone. If researchers can deliver LIGHT to human tumors, it might boost the percentage of patients who benefit from checkpoint inhibitors to 70% or 80%, Fu says.

Whether the efforts to harness TLS for treatments will pay off isn't clear. But interest in the structures continues to expand, and Ruddle, who is now an emeritus professor, says she is surprised at how much research her group's 20-year-old finding has spawned. After all, she and her colleagues only wanted to understand why their mice didn't get sick. ■

Published by AAAS





Downloaded from on March 31, 2016

OCCUPATIONAL HAZARD

Farm workers are dying in southern India as an epidemic of a mysterious kidney disease goes global

By **Rhitu Chatterjee**

A small crowd of villagers waits at a low-slung concrete school building in Pedda Srirampuram, a village in the southern Indian state of Andhra Pradesh. The early morning air is crisp and the men and women are dressed in light shawls and sweaters. Each holds two plastic bags—one with their medical records, the other with a clear plastic container of their urine. They line up to be seen by one of four young men at two large wooden tables.

A researcher named Srinivas Rao sits at the first table. "What's your name?" he asks a short, wiry man who is next in line. "D. Kesava Rao," the man replies, handing over his medical records. Rao, the researcher, flips through the pages, noting down details. "His kidneys are not functioning at all," Rao remarks. "Both his kidneys."

Kesava Rao, 45, has chronic kidney disease of unknown etiology (CKDu) and depends on dialysis to survive. "Every week I undergo dialysis, 4 weeks a month," Rao says. A soft-spoken man with a ready smile, Rao has worked all his life on construction sites or coconut farms. He lived a healthy life and hardly ever saw a doctor, he says, until a fever led to an exam and his diagnosis. Rao didn't have diabetes or, until his kidneys failed, hypertension, the two main causes of chronic kidney disease worldwide. Nor do most of the other villagers who have gathered here, all chronic kidney disease patients, waiting to get a free blood test for creatinine, a metabolite and a proxy for kidney function, and give samples of urine and blood for research.

This region in coastal Andhra Pradesh is at the heart of what local doctors and media are calling a CKDu epidemic. There is little rigorous prevalence data, but unpublished studies by Gangadhar Taduri, a nephrologist at the Nizam's Institute of Medical Sciences in Hyderabad, in the neighboring state of Telangana, suggest the disease af-

PHOTO: ED KASHI/VII

Published by AAAS



PHOTO: © TOM LAFFAY

Women widowed by chronic kidney disease gather in the town of Balliputtuga, India (left), where the mysterious ailment has killed some 125 people. It mainly strikes rural farm laborers, like these men husking coconuts in the hot South Indian sun.

fects 15% to 18% of the population in this agricultural region, known for rice, cashews, and coconuts. Unlike the more common kind of CKD, seen mostly in the elderly in urban areas, CKDu appears to be a rural disease, affecting farm workers, the majority of them men between their 30s and 50s. "It is a problem of disadvantaged populations," says Taduri, who is leading the team of researchers in the village.

A rash of similar outbreaks in other countries has underscored that it is a global problem. Some rice-growing regions of Sri Lanka have their own epidemic, and the disease is rampant in sugar-producing regions of Mexico and Central America (*Science,* 11 April 2014, p. 143). It has also been reported in Egypt. Just about everywhere, prevalence numbers are scarce and uncertain, but "there is a great deal of concern," says Virginia Weaver, an epidemiologist at Johns Hopkins Bloomberg School of Public Health in Baltimore, Maryland. "This is an illness that has substantial mortality. People who would [otherwise] be working, raising families, are dying. It's quite extraordinary."

Public health experts and researchers are alarmed and baffled. In Central America, which has been hit the hardest, the leading hypothesis is that this is an occupational disease, caused by chronic exposure to heat and dehydration in the cane fields. Here in Andhra Pradesh, Taduri and his colleagues think natural toxins in the drinking water—lithium, for example—could contribute. Using the blood and urine samples from Pedda Srirampuram, "we're going to evaluate whether [trace elements] are really present in the body or not," says C. Prabhakar Reddy, one of the researchers collecting the samples.

Published by AAAS

But in India, as in Sri Lanka and Central America, researchers trying to explain CKDu are pursuing a wide range of ideas, including excessive use of over-the-counter painkillers and exposure to pesticides. Nephrologist Ajay Singh of Harvard Medical School in Boston has found high levels of silica, present in some pesticides, in the region's drinking water, and thinks it could be responsible. "There's a smoking gun," he says, though he concedes, "I don't know whether the smoking gun is responsible."

As the global scale of the disease becomes clear, the search for answers is accelerating. The beginnings of an international scientific network to study CKDu are taking shape, and researchers are working on simple, accurate diagnostics so that they can map incidence around the globe—and try to correlate it with potential causes.

LIKE MOST PLACES where CKDu is rampant, India doesn't have a good idea how many people have the disease (also known as CKDnT, for nontraditional causes). But the anecdotal evidence from Andhra Pradesh is sobering. We have "almost 126 widows" of men who have died from CKD, says Rajni Kumar Dolai, the chief of the village of Balliputtuga. The total population of his village is 3270, which implies that almost 4% of its inhabitants have died of the disease.

By screening village populations in a van equipped with an ultrasound machine and other diagnostic equipment, Taduri and his colleagues came up with their estimated incidence of 15% or more in this region. Most people diagnosed with CKDu "didn't have any complaints that suggested a kidney problem," Taduri says. "But … their creatinine was high." Ultrasound exams revealed that they had "shrunken" kidneys.

CKDu is so deadly in part because it is hard to detect. "It is a silent killer," says A. K. Chakravarthy, a nephrologist in Nellore, Andhra Pradesh. In the disease's early stages, people show no symptoms. "By the time they find out, it is too late," he says. Their kidneys are already beyond repair, leading to high blood pressure, weakness, and other symptoms. Access to dialysis here remains limited, even though the state government of Andhra Pradesh has added facilities in recent years. For many patients, death comes not long after their diagnosis.

Those lucky enough to get dialysis survive for several years, but are unable to earn a living, pushing their families deeper into poverty. His strength and endurance sapped by the disease and dialysis, Kesava Rao can no longer provide for his family of five. His eldest son, now 20, has had to step into his father's shoes. "He finished high school, and then stopped studying," Rao says. "He's the primary breadwinner of the family now."

In India, several research groups are on the trail of a cause. But each team has used its own methods and tools, often in isolation, making it hard to compare findings. Taduri and Singh, for example, have both worked in Andhra Pradesh for years, and both have pursued the hypothesis that the high levels of silica in drinking water could be responsible. Silica dust is known to damage lungs and kidneys when inhaled, but no one knows what it does when ingested.

Yet the two researchers had never met until recently. "I wasn't even aware that this work was going on," Singh says about Taduri's work. Whereas Singh thinks the silica comes from pesticides, Taduri believes it leaches into the groundwater from bedrock. Singh admits the researchers could have benefitted from a collaboration. "We need to develop a coordinated approach."

That is true beyond India. As scientists and public health experts realize that CKDu is a global disease or set of diseases, they are casting a wider net for possible causes. "We need to look at this from a global perspective," Weaver says.

SOME 30 INDIAN and international scientists, physicians, and public health experts sit at a round table in a nondescript conference room at The Energy and Resources Institute in New Delhi. The group is here for a CKD workshop spearheaded by the La Isla Foundation, a nonprofit group that works with affected communities in Central America. The goal of the January meeting: to create a global network of scientists studying the disease.

The first task for the network is to determine prevalence, says Ben Caplin, a nephrologist at University College London who works in Nicaragua. "We need to know where are the hot spots of CKDnT," he says. "Are there common environmental, occupational, and social factors shared between CKDnT hot spots?"

But participants differ about how to define the disease. Caplin proposes a working definition: "no alternative cause of CKD diagnosed by medical professional, absence of diabetes, absence of hypertension." But Singh says that the condition may well be a collection of diseases caused by different factors in different places. By insisting on a single definition, we are "already starting to have a bias on what the causes may be."

Neil Pearce of the London School of Hygiene & Tropical Medicine, the only epidemiologist in the room, says screening for impaired kidney function can be done without making assumptions about causes. "We're trying to find populations with high prevalence and low prevalence. This says nothing about the individual."

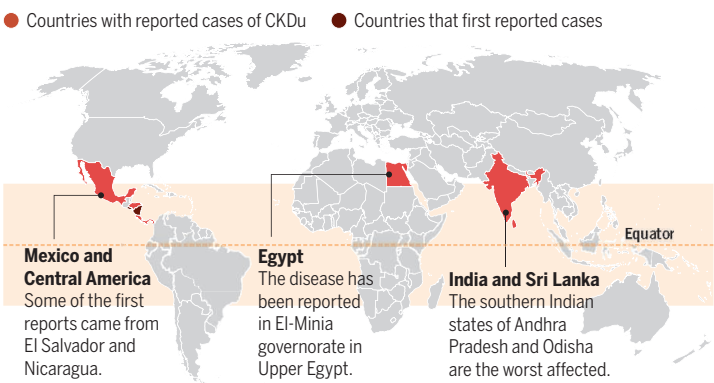
Getting a handle on prevalence will require a standard screening test, however. Caplin, Pearce, and their colleagues are developing a protocol that can be adapted for different populations: a blood test for kidney function, a urine test, and a basic questionnaire recording the participant's age, sex, occupation, and income. The team is trying to keep it simple and inexpensive, Caplin says. "We don't want to make it too complicated and put people off."

The team hopes to publish the protocol in a peer-reviewed journal, so that scientists in any country can use it to screen local or regional populations with their own funds. "I think that using a simple protocol that will be affordable in different settings would really shed light on the extent and global distribution of the disease," says Catharina Wesseling, an occupational and environmental health expert at the Karolinska Institute in Stockholm.

Wesseling studies CKDnT in Central America, where it takes an even heavier toll than in India. "Just look at the mortal-

Hot spots of kidney failure

The mysterious new form of chronic kidney disease strikes mainly poor, agricultural areas in the tropics. It takes its heaviest toll in Central America, but it has now been reported in other regions.



MAP: G. GRULLÓN/SCIENCE

Published by AAAS





In the village of Pedda Srirampuram in India, a mobile testing team studying the causes of chronic kidney disease interviews villagers and collects blood and urine samples. D. Kesava Rao (left) has no remaining kidney function. The former construction worker and farm laborer can no longer work and survives thanks to dialysis treatments.

PHOTOS: ED KASHI/VII

ity numbers," says Jason Glaser of La Isla. In Chichigalpa, Nicaragua, for example, "46% of all male deaths are due to CKD," he says. "Seventy-five percent of deaths of men between 35 and 55 years are due to CKD." By some estimates, the disease has already killed at least 20,000 people in the region.

If the disease hitting India is identical, research in Central America could narrow the search for a cause. Recent studies there have bolstered the hypothesis that CKDu results from long hours of work in the heat with too little drinking water, leading to chronic dehydration. Last year, for example, a study by Wesseling and her colleagues showed that the disease has existed in Costa Rica at least since the 1970s, but that the death rate in Guanacaste province has shot up from 4.4 per 100,000 men between 1970 and 1972 to 38.5 in 2008 to 2012 with the expansion of industrial-scale sugarcane farms. In another study, the same group showed that the kidney function of cane cutters in one Nicaraguan community declined through a single harvest period. "These people have a very scary deterioration of kidney function over the harvest time," Wesseling says.

A pilot study she and her colleagues did last year hinted at how chronic dehydration does its damage. They found high levels of uric acid crystals in cane cutters' urine, especially at the ends of their shifts. Those crystals could be injuring the kidneys, the researchers proposed. "This is an important mechanism we hadn't thought about," says Richard Johnson, a nephrologist at the University of Colorado, Denver, and an author on the study.

But the case is far from closed. "I absolutely don't think that heat stress and dehydration are the only part of the story," Glaser says. "You see different severity [of the disease] in different places." Like him, most scientists are not yet ruling out other factors.

EVEN BEFORE scientists know for sure what causes the disease, Taduri says communities can take steps to reduce the risks. Providing clean surface water sources for drinking, urging people to drink more water at work, and advising them to stay away from painkillers will improve their health anyway, he contends. In El Salvador, Glaser and his colleagues are working to expand a pilot study called the Worker Health and Efficiency program, which prescribes frequent rest and hydration for workers.

Meanwhile, in CKDu-affected communities in southern India, fear and frustration are on the rise. Now, says Taduri, villagers in Andhra Pradesh refuse to come for screening, fearing stigma. When a man is diagnosed with the kidney condition, "his entire family will feel him as a burden," explains Dolai, the village chief in Balliputtuga.

On a nearby farm, a group of men stand in a circle peeling coconuts. Most are sweating in the midmorning sun. Each stands over a blade longer than his forearm, its wooden handle planted firmly in the soil. They pluck coconuts from a pile and swiftly pull each one over the blade, peeling the thick husk away from the hard, brown inner shell.

The men talk as they work, and the conversation turns to their creatinine levels. "Mine is 1.4," says a young man in his 30s. "Mine is 1.3," another says. "One point nine." "Two." For half the men, the levels are either borderline or high. All work long hours under the sun, with too little water to drink. Their legs and backs often hurt when they return home in the evenings, and they turn to painkillers or alcohol, even though they know both are bad for their kidneys.

The men understand they are at risk of chronic kidney disease, but believe they can do little to stop it from progressing. Rest is not an option, one says. "We have the disease, but we still have to work to earn a living." ■

Rhitu Chatterjee is a writer in New Delhi.

Published by AAAS

INSIGHTS

Understanding Antarctica's less icy past *p. 34* ▸

Going with the flow for medicines on demand *p. 44*





LETTERS

Edited by **Jennifer Sills**

NEXTGEN VOICES

Measures of success

In January, we asked young scientists this question: **Do publications (number and impact) convey the true value of an early-career scientist?** Out of the almost 200 (self-selected) scientists who replied, about 75% did not think that publications conveyed a scientist's true value. About 25% said that publications were indeed the most important metric. Among those who disagreed, several themes emerged:

- Publication record does not account for the many intangible traits that make a good scientist.
- A young scientist's publication record reflects his or her country, institution, and adviser more than his or her own skills.
- Publications overlook good work that led to negative results.
- Quantity does not equal quality.

Below, we have printed some of the most interesting responses. In some cases, we have printed excerpts of submissions (indicated by ellipses) and lightly copyedited original text for clarity. To read the complete versions, as well as many more, go to http://scim.ag/NG_18R. Follow *Science's* NextGen VOICES survey on Twitter with the hashtag #NextGenSci.

...YOUNG RESEARCHERS HAVE limited control over the number and impact of their publications. But being a good scientist is not just about impact factor; it is asking the right questions, helping your peers find solutions, discussing your work, and sharing negative results....

Claudia S. Barz

Institute for Neuroscience and Medicine, INM-2, Research Centre Jülich, 52428, Jülich, Germany and RWTH Aachen, Medical School, 52074, Aachen, Germany. E-mail: c.barz@fz-juelich.de

...UNTIL SCIENCE BECOMES a true meritocracy, and until equality in terms of race, gender, lifestyle, and economic background

ILLUSTRATION: JAMES STEINBERG

Downloaded from on March 31, 2016

Published by AAAS

becomes a reality, the system is inherently flawed. Young scientists should be valued by their commitment to education, their dedication to fighting inequality in science, and their efforts to democratize science.

Melodie Elane Benford

Pearland, TX 77584, USA.
E-mail: melodie.benford@gmail.com

A SCIENTIST SHOULD be evaluated with respect to his work environment. This can include country, institutions, group, and people with whom he is working. Then his performance should be normalized with these factors.

Manoj Kumar Mishra

Space Physics Laboratory, VSSC, Thiruvananthapuram, 695022, India.
E-mail: manojkmishra79@gmail.com

YOUNG SCIENTISTS SHOULD be evaluated based on their ability to convey ideas, interpret data, resolve problems, and generate novel scientific ideas. These values can be easily overlooked if one focuses only on publications and impact factors. A mediocre young scientist may have good publications merely by being at the right place, with the right person, and at the right time....

Tiong Sun Chia

Harry Perkins Institute of Medical Research, Perth, 6009, Australia. E-mail: tiongsun@gmail.com

...IT IS IMPORTANT to consider achievement relative to opportunity and not to reward opportunity as if it were achievement. For example, success in a rich country or institution is easier than in a poor one; researching in a prestigious institute is an opportunity, not an achievement.

Endymion Cooper

School of Biological and Chemical Sciences Queen Mary University of London, London, E1 4NS, UK. E-mail: endymion.dante.cooper@gmail.com

NUMBER AND IMPACT of publications at this stage depend too much on external factors: quality of supervision; public interest in research area; and, more than anything, luck. There is much more to being a good scientist than simply publishing research. Evaluation of young scientists must adopt a holistic approach, taking into account the challenges faced, their level of commitment, plus involvement in nonresearch–focused activities, such as teaching and public engagement.

Kate Newton

Department of Earth Sciences, University of Birmingham, Edgbaston, B15 2TT, UK.
E-mail: ken155@bham.ac.uk

SUBMIT NOW:
SCIENCE LIFE IN SIX WORDS

Add your voice to *Science*! Our new NextGen VOICES survey is now open:

"For sale: Baby shoes, never worn." This classic story, widely attributed to Ernest Hemingway, paints a detailed picture in just six words. Now it's your turn! Use exactly six words to create a story about the life of a scientist in your field. (Please do not send a list of words that do not create a story.)

To submit, go to http://scim.ag/NG_19

Deadline for submissions is 13 May. A selection of the best responses will be published in the 1 July issue of *Science*. Submissions should be exactly six words! Anonymous submissions will not be considered.

THE TRUE VALUE of a young scientist's career would be better explained by a "networking index." This would let us know if rookies could establish new contacts and successfully collaborate with other research groups...rather than just being restricted to their immediate circle....

Nicolás Bonel

División Zoología de Invertebrados I, Departamento de Biología, Bioquímica y Farmacia, Universidad Nacional del Sur-CONICET, Bahía Blanca, Buenos Aires (RA-B8000ICN), Argentina.
E-mail: nicobonel@gmail.com

...WE NEED A modified h index that also takes into account the number of authors: First three and last three positions get standard h index evaluation. The value for an author in the middle should be the impact factor divided by the number of authors. The h index should be for only the past 5 years. This way, it is not a function of age.

Charles de Bock

Vlaams Instituut voor Biotechnologie (VIB), 3000, Leuven, Belgium.
E-mail: charles.debock@cme.vib-kuleuven.be

[SCIENTISTS] ARE NEVER remembered for the number of papers we've published, but for how we advance our fields. Suggesting otherwise to young scientists—the future of science—will distract from our true purpose and discourage future Boltzmanns, Faradays, and Bohrs....

Kelsey Farenhem

Vagelos Scholars Program in Molecular Life Sciences, University of Pennsylvania, Philadelphia, PA 19104, USA.
E-mail: farek@sas.upenn.edu

QUANTIFICATION OF WORK published during the Ph.D. candidacy does not convey the true value due to the large impact of the guidance of the adviser. Therefore, in the years after the Ph.D., ...researchers should be funded directly from national agencies. This would allow them...to prove their ability to set their own research goals, manage their work, and lead others in pursuit of new scientific discoveries. After this period, their independently achieved results can be quantified in the same way as those of their more established peers.

Jernej Zupanc

Seyens Ltd., 1000, Ljubljana, Slovenia.
E-mail: jernej.zupanc@seyens.com

RESEARCH ADDRESSING REAL societal problems and the ability to engage the public convey the true value of a scientist....We can measure the public interest of the author's work through media circulation of the news or altimetrics....

Esraa Elsanadidy

Department of Chemistry, University of Connecticut, Storrs, CT 06268, USA.
E-mail: esraa_elsanadidy@yahoo.com

NEITHER NUMBER NOR impact factor of the candidate's publication is sufficient to assess the true value of an early-career scientist. If this were the case, a number of well-known scientists who published path-breaking results after a long lull, as well as Nobel laureates, would have been labeled as underachievers....

Suchitra D. Gopinath

Translational Health Science and Technology Institute, NCR Biotech Science Cluster, Faridabad, 121001, India. E-mail: sgopinath@thsti.res.in

...SOMETIMES THERE IS a huge time lag when measuring publication impact. How long did it take before the first climate change papers really made an impact? Ideas might take a while until they become relevant, known, or established.

Marten Winter

German Centre for Integrative Biodiversity Research (iDiv) Halle-Jena-Leipzig, sDiv—Synthesis Centre, 04103, Leipzig, Germany.
E-mail: marten.winter@idiv.de

...IT WOULD BE far better to look at an early-career scientist's publication list in relation to a metric that correlates years since publication and citations received. This metric would...reinforce desirable traits such as scientific accuracy (longevity) and applicability (influence).

K. Christian Kemp

POSTECH, Pohang, 37662, South Korea.
E-mail: ckemp@postech.ac.kr

Published by AAAS



"...scientists should be valued by papers—by quality, not quantity..."

...NOT HAVING high-impact publications...may indicate discipline-crossing, boundary-breaking work.... Hiring young scholars based on the value of their high-impact publications alone thus risks reinforcing normal science while deferring paradigmatic shifts.

Rense Nieuwenhuis

Swedish Institute for Social Research (SOFI) of Stockholm University, 10691, Stockholm, Sweden. E-mail: rense.nieuwenhuis@sofi.su.se

"IMPACT" SHOULD BE JUDGED qualitatively by experts by assessing papers, documentation for public data sets (especially experimental designs and protocols), software and data analysis code, and/or outreach and communication efforts....

J. Steen Hoyer

Computational and Systems Biology Program, Washington University in St. Louis, St. Louis, MO 63132, USA and Donald Danforth Plant Science Center, St. Louis, MO 63132, USA. E-mail: j.s.hoyer@wustl.edu

...EARLY-CAREER scientists should also be evaluated by how many revisions and resubmissions they have completed after rejection. Those metrics are an indicator of scientific grit, or the ability to persevere when met with adversity....

Rosa Li

Departments of Psychology and Neuroscience, Center for Cognitive Neuroscience, Duke University, Durham, NC 27708, USA. E-mail: rosa.li@duke.edu

YOUNG RESEARCHERS SHOULD be evaluated on their ability to execute solid and honest science, rather than on how flashy their findings are. There needs to be less of a gap in reward between the competent execution of a well-planned experiment that ultimately leads to a negative result and one that leads to a positive one. To that end, evaluations could be partly based on project proposals that demonstrate the ability to plan and think through relevant topics for the field.

Grace Lindsay

Neurobiology and Behavior Program, Columbia University, New York, NY 10032, USA. E-mail: gwl2108@columbia.edu

THEORETICALLY ORIENTED early-career scientists should be valued by papers—by quality, not quantity; by citation rates, not impact factors.... Meanwhile,...doctors should be appraised based on their success in curing their patients, and R&D personnel should be valued based on their new product development.

Dayuan Li

Collaborative Innovation Center of Resource-conserving and Environment-Friendly Society and Ecological Civilization, Central South University, Changsha, 410083, China. E-mail: bigolee@163.com

...WITH REGARD TO hiring and promotion, factors such as enthusiasm, collegiality, mentoring qualities, and the ethical conduct of research must be evident. It is upon these attributes that a satisfying and influential scientific career will be built....

Anthony O'Mullane

School of Chemistry, Physics, and Mechanical Engineering, Queensland University of Technology, Brisbane, QLD 4001, Australia. E-mail: anthony.omullane@qut.edu.au

...DOES TEACHING 33 credits a year prohibit me from being considered a scientist? If publications are the measure, it most certainly does, yet I think I do play an important role in the scientific community: educating future scientists....

Keah C. Schuenemann

Department of Earth and Atmospheric Sciences, Metropolitan State University of Denver, Denver, CO 80217, USA. E-mail: kschuene@msudenver.edu

...IN MANY CASES, we are allowed authorship on a publication simply because we are in charge of cleaning the laboratory glassware and helping with very simple experiments. Such a publication is not comparable to a publication on which there are very few authors and the young scientist is the primary contributor.

Daniel Ramirez

Centro de Investigación, Innovación y Desarrollo de Materiales, University of Antioquia, Medellín, Colombia. E-mail: estiben.ramirez@udea.edu.co

...A BETTER APPROACH will be to subject all scientists to Yelp-like review criteria. Anonymous...reviewers will be able to grade a scientist based on their past interactions, on a number of points including bench-related criteria (methodology and efficiency), thinking ability (innovativeness of ideas and creativity), and mentorship and leadership abilities. Of course, the scientists themselves can respond directly to reviews posted about them. Furthermore, the quality of the reviewers contributes to the weight of their rating....

Shann S. Yu

École Polytechnique Fédérale de Lausanne, Swiss Institute for Experimental Cancer Research (ISREC), CH-1015, Lausanne, Switzerland. E-mail: shann.yu@epfl.ch

PUBLICATIONS ARE THE key parameters for assessing young scientists. During their training phase, they need to learn literature searches, find research questions or problems, design a study...and, of course, learn hands-on techniques for the experiments. Analyzing and interpreting the results is a key part of the process. Building a story based on the data output and publicizing it to the scientific community is the final phase of training....

Matiram Pun

EURAC Institute of Mountain Emergency Medicine, European Academy of Bolzano, Bozen, 39100, Italy. E-mail: matiram.pun@eurac.edu

ALTHOUGH NO ONE factor can quantify the "value" of a scientist, publications are a crucial part of the job. If a scientist cannot communicate through writing, even the most groundbreaking research will have no impact....The number and impact of one's publications can therefore differentiate those who have great ideas from those who are able to influence the scientific community with those great ideas.

Catherine Y. Li

Vagelos Scholars Program in Molecular Life Sciences, University of Pennsylvania, Philadelphia, PA 19104, USA. E-mail: catli@sas.upenn.edu

ILLUSTRATION: JAMES STEINBERG

Published by AAAS

MITOCHONDRIA

Mitochondrial disease therapy from thin air?

Low-oxygen treatment slows neurodegeneration in a model of a mitochondrial disorder

By **Eric A. Shoubridge**

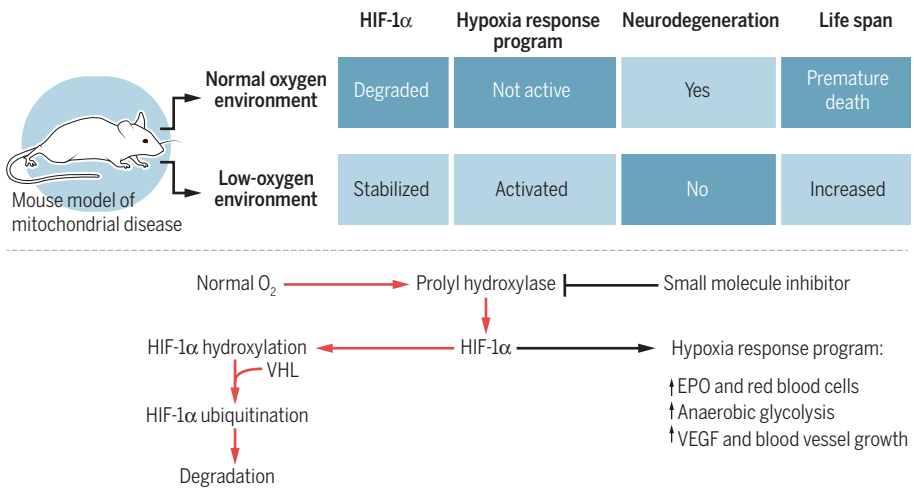
The mitochondrial oxidative phosphorylation (OXPHOS) system supplies most of the adenosine 5′-triphosphate (ATP) in the human body. Defects in this system are among the most common genetic metabolic diseases, and many are associated with fatal, early-onset neurodegenerative conditions for which there are no effective treatments. On page 54 of this issue, Jain *et al.* (*1*) propose that restricting the oxygen supply to patients, who already have a defect in aerobic ATP synthesis, may be a form of therapy. This seems counterintuitive. How did the authors reach that conclusion?

The OXPHOS machinery consists of four enzyme complexes in the respiratory chain that transport electrons obtained from the oxidation of carbohydrates and fats to molecular oxygen; a fifth enzyme complex uses the energy derived from this process to drive ATP synthesis. Jain *et al.* first sought to identify genetic targets that might be useful in treating OXPHOS disorders using a clustered regularly interspaced short palindromic repeats (CRISPR)–Cas9–mediated genome-wide screen in a human cell culture model of disease. The authors mimicked mitochondrial disease by adding antimycin A, an inhibitor of one of the respiratory chain complexes, to the culture medium. Under this condition, cell growth is slowed and the cells turn to glycolysis for some of their ATP needs, producing lactic acid from glucose.

To identify genetic suppressors of the growth phenotype caused by the respiratory chain defect, Jain *et al.* performed a CRISPR-Cas9-based screen, using guide RNAs that disrupt most human genes. They then looked for enrichment of those guide RNAs that allowed cells to grow in the presence of the inhibitor, reasoning that whatever gene or genes had been disrupted would be potential targets for treating OXPHOS diseases. Strikingly, the most enriched RNAs were those targeting different coding regions in the gene encoding Von Hippel–Lindau (VHL) factor, an E3 ubiquitin ligase that plays a key role in the hypoxia response pathway (*2*).

The hypoxia response pathway, which is conserved in all metazoans, is directed by hypoxia-inducible factor 1α (HIF-1α), a transcription factor that orchestrates gene expression to compensate for low ambient oxygen (*3*). Genes that become activated include erythropoietin (*EPO*), a factor that promotes the synthesis of red blood cells, glycolytic enzymes, and the glucose transporter to increase the potential for anaerobic glycolysis; and vascular endothelial growth factor (*VEGF*), which promotes the growth of new blood vessels. Under normoxic conditions, HIF-1α is hydroxylated by prolyl hydroxylase, an enzyme whose activity is oxygen dependent. VHL recognizes the hydroxylated form of HIF-1α, polyubiquinates it, and sends it for destruction in the proteasome. During hypoxia, prolyl hydroxylase is inactive, and the stabilized HIF-1α can translocate to the nucleus to activate the hypoxia response program. Jain *et al.* added a prolyl hydroxylase inhibitor, which should constitutively activate the hypoxia response pathway, to cells treated with respiratory chain poisons and showed that it improved growth rates. Notably, the treatment decreased cellular oxygen consumption by half, likely due to the activation of pyruvate dehydrogenase kinase, slowing the entry of pyruvate into the tricarboxylic acid cycle (the chemical reactions linked to the respiratory chain) (*4*, *5*). The authors also showed improved survival of zebrafish embryos with respiratory chain defects that lacked VHL, or in the presence of the prolyl hydroxylase inhibitor.

The critical test was carried out in a mouse model of Leigh syndrome, an early-onset, fatal neurodegenerative disease, and the most common presentation of mitochondrial disease in the pediatric population. The mouse model is a germline deletion of *Ndufs4*, a structural subunit of mitochondrial complex I (*6*), which results in a severe global decrease in complex I activity but, interestingly, no decrease in whole-body oxygen consumption. Mice lacking *Ndufs4* develop neuropathology similar to that seen in Leigh syndrome; most die by 50 to 60 days of age. Because the prolyl hydroxylase inhibitor tested by Jain *et al.* does not cross the blood-brain barrier, they instead investigated whether exposing the animals to long-term hypoxia would rescue the neurological phenotype and increase survival. They chose oxygen tensions that humans experience in high-altitude regions like the Andes or Himalayas. This exposure



Low oxygen helps. (**Top**) Mice with a mutation in the mitochondrial respiratory chain develop progressive neurodegeneration. A low-oxygen environment increases their life span and prevents the neuropathology. The mechanism is unknown. (**Bottom**) Inhibiting prolyl hydroxylase activates the hypoxia response program.

Montreal Neurological Institute, Department of Human Genetics, McGill University, Montreal, Quebec, Canada. E-mail: eric@ericpc.mni.mcgill.ca

GRAPHIC: P. HUEY/*SCIENCE*

Downloaded from on March 31, 2016

Published by AAAS

activated a strong hypoxic response, which included a marked increase in EPO and a 50% increase in hematocrit, and the activation of several hypoxia response enzymes. Although hypoxic exposure did not alter complex I activity, it increased survival, rescued the strength and balance defects, and partially rescued spontaneous locomotor activity (see the figure). Mice succumbed faster when exposed to hyperoxia, suggesting that oxygen itself might be the culprit, but the mechanism is far from clear.

Although it is reasonable to assume that exposure to hypoxia somehow limited oxygen consumption in the tissues of the *Ndufs4*-deficient mice, there is no direct evidence of this. Circulating lactate concentrations decreased under hypoxia in both wild-type and *Ndufs4*-deficient mice, indicating that there was less demand for anaerobic glycolysis under oxygen-limiting conditions. It would be very informative to measure how much oxygen is extracted from the blood by different tissues in these mice, in addition to whole-body oxygen consumption, because part of the rescue may simply result from decreasing overall metabolic rate, as implied by studies performed by Jain *et al.* on cells treated with the prolyl hydroxylase inhibitor. If this is the case, one would predict substantial improvements in the phenotype of the genetically altered mice by pharmacological activation of the hypoxia response pathway, even under normoxic conditions. This idea could also be tested genetically by crossing the *Ndufs4*-deficient mice with mice in which the hypoxia response pathway is constitutively active.

Jain *et al.* are appropriately cautious about translating their results to the clinical setting. Chronic hypoxia is not medically benign, and loss-of-function mutations in VHL predispose to cancer (*7*). Further, the authors have only demonstrated efficacy in a single animal model, and it is not clear what level or duration of hypoxia might be necessary to slow or arrest the disease. Although questions about the mechanism and potential side effects remain to be studied, the striking response in the mouse model of a mitochondrial disease suggests that this observation will be of great interest to investigators in the field. Families with children affected by mitochondrial disease, who have few therapeutic options, will be anxious to fast-track these investigations. ■

REFERENCES

1. I. H. Jain *et al.*, *Science* **352**, 54 (2016).
2. P. H. Maxwell *et al.*, *Nature* **399**, 271 (1999).
3. G. L. Semenza, *Cell* **148**, 399 (2012).
4. I. Papandreou *et al.*, *Cell Metab.* **3**, 187 (2006).
5. J. W. Kim *et al.*, *Cell Metab.* **3**, 177 (2006).
6. S. E. Kruse *et al.*, *Cell Metab.* **7**, 312 (2008).
7. L. Gossage *et al.*, *Nat. Rev. Cancer* **15**, 55 (2015).

10.1126/science.aaf5248

ORGANIC CHEMISTRY

Rethinking the S_N2 reaction

The gas-phase dynamics of a paradigm organic reaction are more complex than expected

By **Jing Xie**[1] *and* **William L. Hase**[2]

The S_N2 nucleophilic substitution reaction, $X^- + RY \rightarrow XR + Y^-$, is a paradigm reaction in organic chemistry (*1*). The modern understanding of the S_N2 reaction mechanism is based on work of Hughes and Ingold (*2*), who proposed that the nucleophile (X^-) approaches the carbon atom that bears the leaving group (Y^-). As a result, the bond between the carbon atom and the leaving group becomes weakened. As this bond breaks and a new bond forms between the nucleophile and the carbon atom, the configuration of the carbon atom is inverted. Analyses of gas-phase reaction rates led to the suggestion of a potential energy surface (PES) with two wells connected by a central barrier transition state (*3*). Electronic structure calculations have confirmed this picture for some S_N2 reactions (*4*), but recent studies have shown that the actual reaction dynamics may be considerably more complex (see the figure) (*5*–*8*).

"...subtle features, such as the dipole of the molecular reactant and the depth of the frontside potential energy well, may have pronounced effects on S_N2 reaction dynamics."

To obtain a detailed understanding of S_N2 mechanisms, scientists, including Angela Merkel, have performed extensive experimental and computational studies of $X^- + CH_3Y \rightarrow XCH_3 + Y^-$ gas phase reactions (*5*, *9*–*12*). The traditional model for these reactions assumes that the reactive system becomes temporarily trapped in potential energy wells for pre- and postreaction ion-dipole complexes. Given rapid and complete statistical intramolecular vibrational energy distribution in the complexes, the RRKM (Rice-Ramsperger-Kassel-Marcus) theory may be used to model S_N2 reaction kinetics and calculate S_N2 rate constants.

Recent work has shown that although the indirect, double-well mechanism may occur, the RRKM model for the complexes may be invalid and, thus, the S_N2 reaction dynamics may be non-RRKM (*5*, *9*). There are also direct mechanisms such as stripping, rebound, and frontside attack, and additional indirect mechanisms such as the roundabout (see the figure) (*5*, *13*). The relative importance of the indirect and direct mechanisms depends on the specific S_N2 reaction and the collision energy (*13*). For the indirect, double-well mechanism, recrossing of the central barrier may also be important, violating the fundamental assumption of transition state theory (*5*, *9*). For $OH^- + CH_3I$, both the S_N2 and $OH^- + CH_3I \rightarrow H_2O + CH_2I^-$ proton transfer reactions occur, and the atomistic mechanisms are coupled for the two reactions. This complicates interpretation of the S_N2 reaction dynamics (*6*).

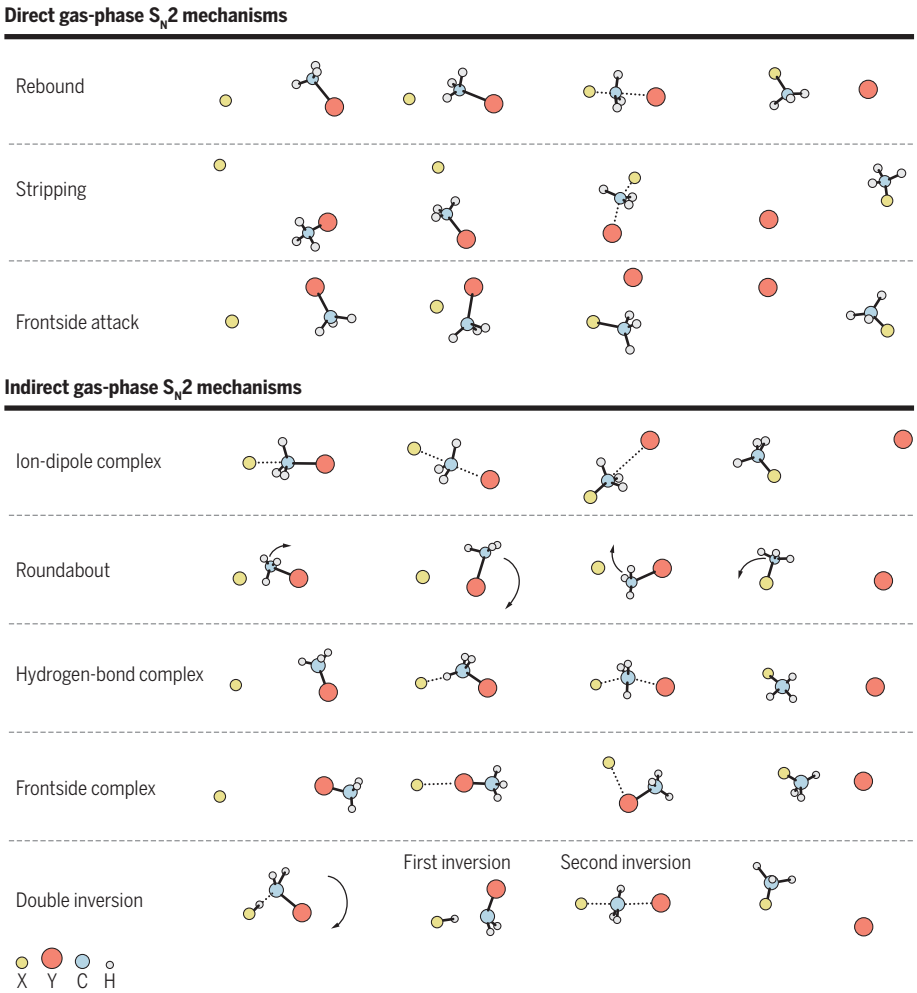
Stepwise addition of solvent molecules to the bare reactant anion offers a bottom-up approach to learn more about the transition of chemical reactions from the gas to liquid phase. To investigate the role of solvation in S_N2 reactions, Otto *et al.* have performed crossed molecular beam studies of the microsolvated $OH^-(H_2O)_n + CH_3I$ reaction (n = 1, 2) for a range of collision energies (*14*). The results show that the dynamics for $OH^-(H_2O)$ differ dramatically from those for the unsolvated OH^- anion. For the unsolvated reaction, the indirect mechanism is of minor importance. For $OH^-(H_2O)$, indirect mechanisms are important at low energies, but at energies above 1 eV the dynamics switch to the rebound mechanism. Adding a second water molecule to OH^-, for the $OH^-(H_2O)_2 + CH_3I$ reaction, leads to isotropically distributed products in the experiments, with no evidence for a direct S_N2 reaction in this case.

These different dynamics for solvated and unsolvated OH^- may be related to properties of the reactants as they begin to interact. The unsolvated reaction proceeds from a non-traditional hydrogen-bonded OH^----HCH_2I pre-reaction complex, whereas the $OH^-(H_2O)$ pre-reaction complex is similar to the traditional ion-dipole structure, with OH^- almost collinear with the C–I axis. This latter geometry favors direct backside attack, promoting

[1]*Department of Chemistry, University of Minnesota, Minneapolis, MN 55455, USA.* [2]*Department of Chemistry and Biochemistry, Texas Tech University, Lubbock, TX 79406, USA. E-mail: bill.hase@ttu.edu*

Downloaded from on March 31, 2016

Published by AAAS



A multitude of mechanisms. According to the traditional picture, S_N2 reactions proceed via a double-well mechanism. Recent studies have shown that, depending on the reactants and the reaction conditions, numerous other mechanisms, including those shown here, can also occur.

the rebound mechanism. The isotropic scattering for $OH^-(H_2O)_2$ and CH_3I is suggestive of a long-lived pre-reaction complex.

Two quite recent studies have provided more detail concerning the atomic-scale dynamics of $X^- + CH_3Y$ reactions (*7*, *8*). Retention of configuration in the S_N2 reaction has been assumed to only occur by a frontside attack mechanism (see the figure), but Szabó and Czakó have observed a double inversion mechanism (see the figure) in a chemical dynamics simulation of the $F^- + CH_3Cl$ reaction on an accurate global PES (*7*). The double inversion only contributes 1 to 2% to the total S_N2 reaction rate. Nevertheless, the finding of this pathway is important and intriguing. The double-inversion mechanism results from coupling between the proton transfer and S_N2 pathways. The relationships between the double-inversion pathway and the minima and transition states on the $F^- + CH_3Cl$ PES remain to be elucidated.

In combined crossed molecular beam, ion imaging experiments and chemical dynamics simulations, Stei *et al*. have studied the influence of the leaving group on the dynamics of the $F^- + CH_3Cl$ and $F^- + CH_3I$ S_N2 reactions (*8*). The two reactions have very similar PESs and energetics. Both have hydrogen-bonded and traditional backside pre-reaction complexes, which are very similar in energy and connected by a low-barrier transition state. The pre-reaction region of the PES is connected to the S_N2 products by the traditional $[F\text{--}CH_3\text{--}X]^-$ transition state. The reactions are barrierless and highly exothermic.

Yet, despite these similarities, the two reactions have decidedly different reaction dynamics. The rebound mechanism is important for the chlorine reaction but not for the iodine reaction. Direct stripping is a dominant mechanism for the iodine reaction but only plays a minor role for the chlorine reaction. The occurrence of the rebound mechanism for the chlorine reaction at large impact parameters suggests that F^- orients CH_3Cl more efficiently than CH_3I. This is consistent with the larger dipole moment of CH_3Cl as compared with CH_3I, which would result in enhanced orientation for CH_3Cl with backside attack and the rebound mechanism at large impact parameters. In addition, the iodine reaction has a frontside complex with a potential energy minimum of 22 kcal/mol; the equivalent minimum for the chlorine reaction is only 3 kcal/mol. This deep frontside potential energy minimum for the F^----ICH_3 complex may suppress backside attack and the rebound mechanism. These are salient explanations for the differences in the $F^- + CH_3Cl$ and $F^- + CH3I$ reaction dynamics, but further studies will be needed for a complete understanding of the origins of their different dynamics.

These recent studies and previous work illustrate the incompleteness of the traditional S_N2 reaction model, in which the dynamics are mediated by complex formation. The traditional mechanism does play a role, particularly at low collision energies, but other reaction mechanisms such as the indirect roundabout and the direct rebound and stripping (see the figure) are often more important. The very different dynamics for the $F^- + CH_3Cl$ and $F^- + CH_3I$ reactions show how subtle features, such as the dipole of the molecular reactant and the depth of the frontside potential energy well, may have pronounced effects on S_N2 reaction dynamics. Additional work needs to be done to probe the generality of the double-inversion mechanism found for $F^- + CH_3Cl$. Solvation adds further complications: The $OH^-(H_2O) + CH_3I$ reaction has 28 different indirect mechanisms (*6*). Much work remains to be done to establish theoretical models that capture all the atomistic details of the dynamics of S_N2 reactions. ■

ILLUSTRATION: P. HUEY/*SCIENCE*

REFERENCES

1. C. K. Ingold, *Structure and Mechanisms in Organic Chemistry* (Cornell Univ. Press, Ithaca, NY, 1953).
2. W. A. Cowdrey, E. D. Hughes, C. K. Ingold, S. Masterman, A. D. Scott, *J. Chem. Soc.* **1937**, 1252 (1937).
3. W. M. Olmstead, J. I. Brauman, *J. Am. Chem. Soc.* **99**, 4219 (1977).
4. K. Ishida, K. Morokuma, A. Komornicki, *J. Chem. Phys.* **66**, 245 (1977).
5. P. Manikandan, J. Zhang, W. L. Hase, *J. Phys. Chem. A* **116**, 3061 (2012).
6. J. Xie, R. Otto, R. Wester, W. L. Hase, *J. Chem. Phys.* **142**, 244308 (2015).
7. I. Szabó, G. Czakó, *Nat. Commun.* **6**, 5972 (2015).
8. M. Stei, E. Carrascosa, M. A. Kainz, A. H. Kelkar, J. Meyer, I. Szabó, G. Czakó, R. Wester, *Nat. Chem.* **8**, 151 (2016).
9. W. L. Hase, *Science* **266**, 998 (1994)
10. M. L. Chabinyc, S. L. Craig, C. K. Regan, J. I. Brauman, *Science* **279**, 1882 (1998).
11. J. K. Laerdahl, E. Uggerud, *Int. J. Mass Spectrom.* **214**, 277 (2002).
12. A. Merkel, Z. Havlas, R. Zahradník, *J. Am. Chem. Soc.* **110**, 8355 (1988).
13. J. Xie, R. Otto, J. Mikosch, J. Zhang, R. Wester, W. L. Hase, *Acc. Chem. Res.* **47**, 2960 (2014).
14. R. Otto, J. Brox, S. Trippel, M. Stei, T. Best, R. Wester, *Nat. Chem.* **4**, 534 (2012).

10.1126/science.aaf5172

Published by AAAS

CLIMATE

How Antarctica got its ice

A complex set of interactions caused the rapid growth of the Antarctic ice sheet 34 million years ago

By **Caroline H. Lear**[1] *and* **Dan J. Lunt**[2]

Ice sheets such as those on Greenland and Antarctica today not only respond to changing climate but can also cause climate to change. Their sizes have fluctuated substantially in the past. In particular, Antarctica was effectively ice-free until its ice cover began to expand rapidly at the Eocene-Oligocene boundary around 34 million years ago (see the figure). Recent research, including a report by Galeotti *et al.* on page 76 of this issue (*1*), helps to identify the mechanisms that led to this rapid ice sheet growth.

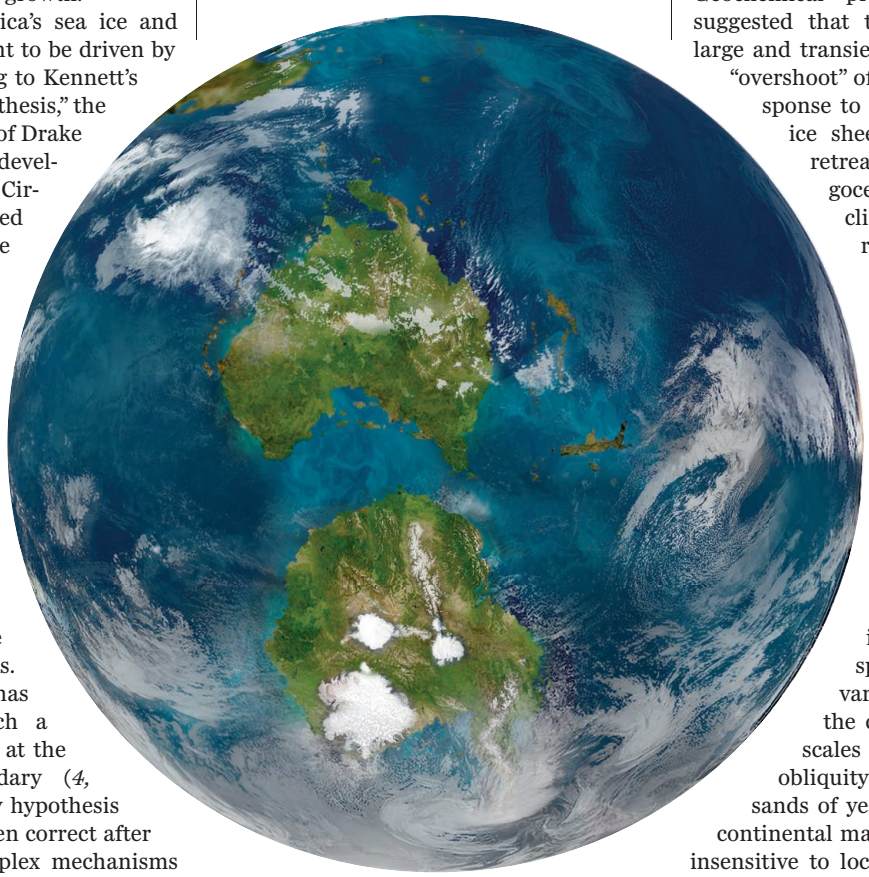
The extent of Antarctica's sea ice and ice sheet was long thought to be driven by tectonic forces. According to Kennett's influential "gateway hypothesis," the widening and deepening of Drake Passage that led to the development of the Antarctic Circumpolar Current caused Antarctica to become thermally isolated, promoting ice sheet growth (*2*). However, this hypothesis has been out of favor since DeConto and Pollard's pioneering modeling work (*3*) instead implicated a fall in atmospheric carbon dioxide as the main driver, with the resulting growth of the Antarctic ice sheet accelerated by positive ice sheet–climate feedbacks. Observational evidence has been mounting for such a drop in atmospheric CO_2 at the Eocene-Oligocene boundary (*4, 5*). But Kennett's gateway hypothesis may yet prove to have been correct after all, albeit via more complex mechanisms than the one he originally imagined.

What caused the drop in CO_2 at the Eocene-Oligocene transition? Recently, there have been some tantalizing indications that tectonically driven gateway changes may have caused the CO_2 changes. In early work, Zachos *et al.* (*6*) found evidence for an increase in ocean productivity at the Eocene-Oligocene boundary, attributed to changes in ocean circulation and upwelling associated with the opening of the Tasman Seaway (*7*). Based on increased silicic acid use by diatoms in the Late Eocene, Egan *et al.* (*8*) have suggested that deepening and/or widening of the Southern Ocean gateways increased the strength of the Antarctic circumpolar current and led to increased upwelling south of the polar front. The resulting increase in surface-water nutrient concentration could have led to diatom proliferation, more organic carbon burial, and hence CO_2 drawdown.

A recent modeling study (*9*) has also indicated that gateway changes could be important for the global carbon cycle. Using an Earth system climate model, Fyke *et al.* showed that the opening of Drake Passage can lead to an increase in Atlantic overturning circulation and a decrease in Pacific overturning circulation. As a result, the characteristic residence times in the two basins change, such that the Atlantic reservoir of dissolved inorganic carbon becomes smaller and that of the Pacific grows. The net effect is a global increase in the ocean carbon reservoir, and hence an increase in CO_2 drawdown from the atmosphere.

Galeotti *et al.* now present sedimentological evidence from Antarctica that calls for a reinterpretation of the ice sheet history across the Eocene-Oligocene transition. Geochemical proxy records previously suggested that the early ice sheet was large and transient, perhaps reflecting an "overshoot" of the climate system in response to a rapid forcing (*10*). The ice sheet was thought to have retreated after this "Early Oligocene Glacial Maximum," as climate feedback processes resulted in a new steady state with a smaller ice sheet (*10*). Instead, Galeotti *et al.* suggest that the early ice sheet did not reach the coast at the Ross Sea. Rather than retreating, it subsequently advanced, reaching the Ross Sea continental margin 32.8 million years ago. Galeotti *et al.* propose that the initial, smaller ice sheet was able to respond dynamically to local variations in insolation on the comparatively short time scales of orbital precession and obliquity changes (tens of thousands of years). Once it reached the continental margin, it became relatively insensitive to local insolation forcing, instead fluctuating in size on the longer eccentricity time scale (hundreds of thousands of years), in conjunction with other components of the global climate system.

Climate itself is influenced by changes in ice sheets, both directly through changing albedo and surface height, which lead to local cooling and atmospheric circulation changes, and indirectly through changes



A green Antarctica. At the time of the Eocene-Oligocene boundary, about 34 million years ago, the Antarctic ice sheet was still small but about to expand. The paleogeography in the image is based on the reconstructions in (*15*). Vegetation and cloud cover are based on (*11*), the Antarctic ice caps are based on (*3*), and the phytoplankton blooms indicating increased productivity are based on the ideas in (*6, 7*).

ILLUSTRATION: ALAN KENNEDY/UNIVERSITY OF BRISTOL

[1]*School of Earth and Ocean Sciences, Cardiff University, Cardiff CF10 3AT, UK.* [2]*School of Geographical Sciences and the Cabot Institute, University of Bristol, Bristol BS8 1SS, UK. E-mail: learc@cardiff.ac.uk; d.j.lunt@bristol.ac.uk*

Downloaded from on March 31, 2016

Published by AAAS

to the carbon cycle. Several recent model studies have explored the response of the climate system to an expansion of the Antarctic ice sheet (*11*–*13*). All models agree that an ice sheet causes substantial local cooling caused by the higher altitude and more reflective surface. However, beyond Antarctica, the models provide different predictions for which regions of the Southern Ocean warm or cool due to the ice sheet. It therefore remains unclear whether growth and retreat of the Antarctic ice sheet is dominated by positive or negative feedbacks associated with ocean temperatures at its marine margin.

However, very recent work indicates that the sign of the feedback could depend on the configuration of the Drake Passage and Tasman Seaway. Kennedy *et al.* (*11*) modeled the response of the climate system under two different gateway configurations. Before 34 million years ago, the expansion of the Antarctic ice sheet led to a strong warming (and therefore a potential negative feedback on ice growth) in the Pacific and central Indian sectors of the Southern Ocean. After 34 million years ago, it led to a cooling in large parts of these regions (and thus a potential positive feedback on ice growth). Thus, the timing of glaciation could be determined, in part, by paleogeographic and gateway changes.

"To understand climate–ice sheet interactions on geological time scales, we must consider the entire coupled climate, ice sheet, and carbon cycle system..."

Ice sheets likely affect the global carbon cycle through numerous processes operating on different time scales. These effects include changes to ocean productivity and carbon burial, deep-water formation and carbon storage, continental weathering and CO_2 drawdown, sea-level change and carbonate deposition, and permafrost area and terrestrial carbon storage. Galeotti *et al.* emphasize the difference between the dynamic behavior of the initial, smaller Antarctic ice sheet and the increased stability of the subsequent larger ice sheet. Meanwhile, Middle Miocene geochemical records suggest that different regions of the Antarctic may have different sensitivities to pCO_2 (*14*).

The work by Galeotti *et al.* is consistent with the notion that the Antarctic ice sheet formed when a key carbon dioxide threshold was passed near the Eocene-Oligocene boundary. The authors conclude that CO_2 concentrations also control the sensitivity of the ice sheet to orbital forcing. However, the results of this study and that of Greenop *et al.* (*14*) raise questions about how the ice sheet itself affects the carbon cycle. For example, to what extent do the size and stability of the Antarctic ice sheet affect CO_2 variability on orbital time scales?

To understand climate–ice sheet interactions on geological time scales, we must consider the entire coupled climate, ice sheet, and carbon cycle system, including both tectonic and orbital forcings. Important advances toward this goal have already been made by both observational and modeling communities. However, on its own, each approach has its limitations. State-of-the-art Earth system models that include the necessary climate–carbon–ice sheet processes are often designed to be run for hundreds, not millions, of years; thus, modeling studies must use approximations that need to be considered when interpreting their results. Observational studies are often carried out at single locations and focus on measuring one part of the system. It can be challenging to correctly interpret these records in a global and system-wide perspective. However, combining insight from both modeling and data together allows the strengths of the two approaches to be maximized—the veracity of the data with the system-wide interpretation from the modeling. Only an integrated model and data approach will allow the complex web of interconnected processes associated with Antarctic ice sheet growth and decay to be untangled. ■

REFERENCES

1. S. Galeotti *et al.*, *Science* **352**, 76 (2016).
2. J. P. Kennett, *J. Geophys. Res.* **82**, 3843 (1977).
3. R. M. DeConto, D. Pollard, *Nature* **421**, 245 (2003).
4. A. M. C. Heureux, R. E. M. Rickaby, *Earth Planet. Sci. Lett.* **409**, 329 (2015).
5. P. N. Pearson, G. L. Foster, B. S. Wade, *Nature* **461**, 1110 (2009).
6. J. C. Zachos, T. M. Quinn, K. A. Salamy, *Paleoceanography* **11**, 251 (1996).
7. L. Diester-Haass, R. Zahn, *Palaeogeogr. Palaeoclimatol. Palaeoecol.* **172**, 153 (2001).
8. K. E. Egan, R. E. M. Rickaby, K. R. Hendry, A. N. Halliday, *Earth Planet. Sci. Lett.* **375**, 34 (2013).
9. J. G. Fyke, M. d'Orgeville, A. J. Weaver, *Global Planet. Change* **128**, 72 (2015).
10. J. C. Zachos, L. R. Kump, *Global Planet. Change* **47**, 51 (2005).
11. A. T. Kennedy, A. Farnsworth, D. J. Lunt, C. H. Lear, P. J. Markwick, *Philos. Trans. R. Soc. Lond. A* **373**, 20140419 (2015).
12. A. Goldner, N. Herold, M. Huber, *Nature* **511**, 574 (2014).
13. J.-B. Ladant, Y. Donnadieu, C. Dumas, *Clim. Past* **10**, 1957 (2014).
14. R. Greenop, G. L. Foster, P. A. Wilson, C. H. Lear, *Paleoceanography* **29**, 845 (2014).
15. D. J. Lunt *et al.*, *Clim. Past Discuss.* **11**, 5683 (2015).

Published online 10 March 2016

10.1126/science.aad6284

DEVELOPMENT

Nursing the oocyte

Mammalian egg cells receive material from neighboring "nurse" cells via bridges and gaps

By **Melissa E. Pepling**

The generation of a mature egg, or oocyte, is essential for fertility. The oocyte requires the production of considerable quantities of messenger RNA (mRNA), protein, and organelles during its formation, a store needed for the subsequent development of the fertilized egg. In some species, these components are provided by neighboring cells called nurse cells (*1*). The role of nurse cells during oocyte development has been well studied in the fruit fly, *Drosophila melanogaster*, but it has been unclear if mammalian species also have nurse cells. On page 95 of this issue, Lei and Spradling (*2*) provide evidence for nurse cells during mouse oogenesis, adding to our understanding of mammalian oocyte development and raising hope for new infertility treatments.

The *Drosophila* oocyte forms from a germline stem cell that divides to form a daughter germline stem cell and a cyst-forming cell called a cystoblast (*1*). The cystoblast undergoes exactly four rounds of mitosis without cytokinesis, the physical process of cells dividing from one another, to form an interconnected cyst of 16 cells. One cell becomes the oocyte while the other 15 serve as nurse cells, supporting the oocyte by supplying the needed mRNAs, proteins, and organelles, transporting them across intercellular bridges called ring canals. These materials move along microtubules that span the bridges, presumably driven by microtubule motors (*3*). The nurse cells eventually undergo programmed cell death. In other species such as the worm *Caenorhabditis elegans*, cytoplasmic contents are shared between germ cells and only some survive (*4*), but whether some germ cells serve as nurse cells in mammals was unknown.

Mammalian oocytes also develop in clusters called germ cell cysts and possess many of the same characteristics as *Drosophila* germ-

Department of Biology, Syracuse University, 107 College Place, Syracuse, NY 13244, USA. E-mail: mepeplin@syr.edu

Downloaded from on March 31, 2016

Published by AAAS

line cysts, such as intercellular bridge connections and synchrony of their cell divisions (*5*). Mouse oocytes originate as primordial germ cells that migrate from their initial position in the embryo to arrive at the developing ovary at about 10.5 days after fertilization [referred to as days postcoitum (dpc)] (*6*). They then undergo several rounds of mitosis without cytokinesis to form cysts. At ~13.5 dpc, the germ cells begin to enter meiosis and subsequently form oocytes. Some of the oocytes in each cyst survive and become enclosed in primordial follicles, whereas the remaining cells undergo programmed cell death (*7*). The possibility has been raised that the dying germ cells serve a supportive role for the surviving oocytes, as in *Drosophila*. Mitochondria have been found in the intercellular bridges by electron microscopy, suggesting that organelles are transported between cells of the cyst. However, our understanding has been limited because mouse cysts are tightly packed together and difficult to distinguish.

Here, Lei and Spradling first used lineage tracing, a technique they had previously applied to the analysis of mouse germ cell cysts (*8*), to investigate how the mouse germ cells are physically connected to one another. In *Drosophila*, the connections are such that the cell that will become the oocyte has four ring canals. Lineage tracing in conjunction with labeling for the mammalian intercellular bridge component TEX14 revealed that a small number of germ cells in cysts made three or four bridges with neighboring cells and were selectively preserved during development, suggesting that they would become the surviving oocytes.

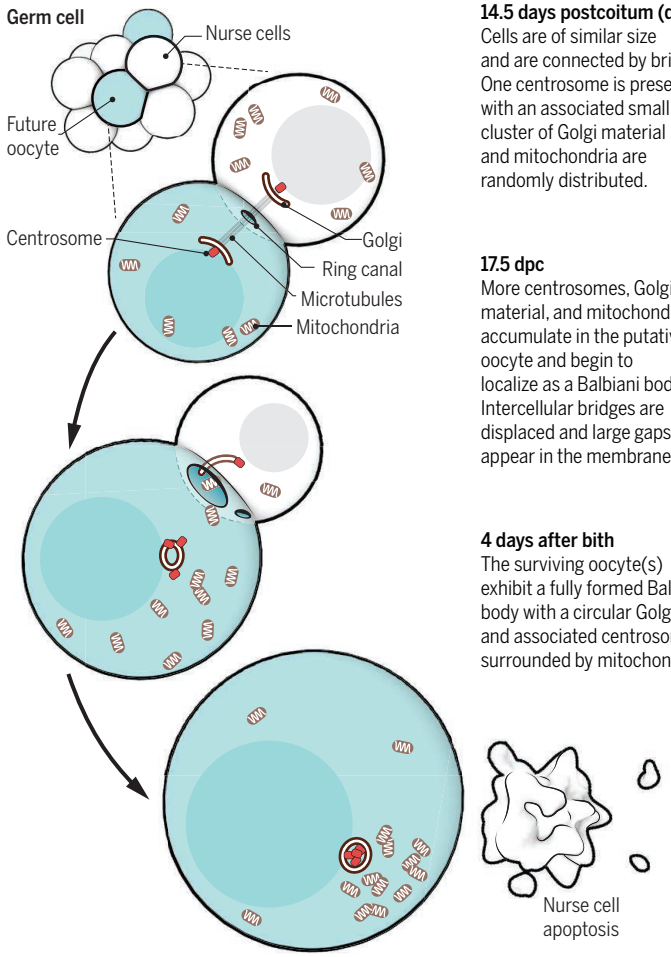
Next, the authors looked for evidence of organelle transport using markers for centrosomes, Golgi, and mitochondria. In *Drosophila*, organelles are transported into the oocyte and accumulate in a region known as the Balbiani body (*3*). Mouse oocytes also have a Balbiani body (*9*), but in the mouse it was unknown how the Balbiani body formed. Lei and Spradling observed centrosomes, Golgi material, and mitochondria accumulating in a subset of oocytes during mouse perinatal oocyte development (see the figure). The Balbiani body–containing oocytes appear larger and do not express a cell death marker, further supporting the idea that these cells will become the mature oocytes. The oocytes without Balbiani bodies look smaller, lose most of their cytoplasm, and appear to be undergoing apoptosis analogous to *Drosophila* nurse cells.

The functional significance of germ cell development in the mouse cysts was unknown and might have been little more than an evolutionary remnant of that seen in organisms like *Drosophila*. In fact, female Tex14 mutants are fertile and have normal oocyte development, calling into question the importance of germ cell cysts (*10*). However, Lei and Spradling now show that TEX14 is not expressed in the intercellular bridges when they first appear and thus is not required for their formation.

In *Drosophila*, the ring canals grow in size as cytoplasm is transferred. No such growth in the mouse bridges has been observed. Instead, Lei and Spradling observed gaps in the membranes of the cyst cells. This suggests that although some transport occurs through the mammalian bridges, the gaps allow the transfer of large amounts of additional material from the supporting cells to the oocyte in the cysts.

To find out if microtubules and microtubule motors are important for transporting organelles into oocytes and whether this is necessary for oocyte development, Lei and Spradling used inhibitors in ovary organ culture to block microtubule polymerization or dynein microtubule motor activity. In either case, they found a reduction in organelle enrichment and Balbiani body formation. They also found that the normal germ cell loss that occurs during primordial follicle formation was reduced. The additional surviving cells are presumably the nurse-like cells of the cyst. It would be interesting to determine if the extra surviving germ cells can become functional oocytes.

Many questions remain regarding early oocyte development in mammals. In particular, it is unclear whether specific maternal mRNAs are provided by the supporting germ cells to the future oocytes and if they are localized to the Balbiani body as in other species. Also unclear are the mechanisms used to localize molecules to the surviving oocytes. In addition, development of tools for the live imaging of organelle transport would shed light on transport dynamics. A more complete understanding of early oocyte development is essential for developing treatments of infertility and other reproductive disorders. ■



Building an egg, mouse-style. (Top) A germ cell cyst that will give rise to a few oocytes and several nurse cells. Each oocyte is thought to be associated with about four nurse cells. (Middle) Organelles are initially transported along microtubules, but as bridges are displaced, materials travel through large gaps in the plasma membrane. (Bottom) An oocyte with a fully formed Balbiani body and a nurse cell undergoing programmed cell death.

REFERENCES

1. W. Deng, H. Lin, *Int. Rev. Cytol.* **203**, 93 (2001).
2. L. Lei, A. C. Spradling, *Science* **352**, 95 (2016).
3. R. T. Cox, A. C. Spradling, *Development* **130**, 1579 (2003).
4. J. S. Baum, J. P. St George, K. McCall, *Semin. Cell Dev. Biol.* **16**, 245 (2005).
5. M. E. Pepling, A. C. Spradling, *Development* **125**, 3323 (1998).
6. M. E. Pepling, *Reproduction* **143**, 139 (2012).
7. M. E. Pepling, A. C. Spradling, *Dev. Biol.* **234**, 339 (2001).
8. L. Lei, A. C. Spradling, *Development* **140**, 2075 (2013).
9. M. E. Pepling, J. E. Wilhelm, A. L. O'Hara, G. W. Gephardt, A. C. Spradling, *Proc. Natl. Acad. Sci. U.S.A.* **104**, 187 (2007).
10. M. P. Greenbaum *et al.*, *Biol. Reprod.* **80**, 449 (2009).

10.1126/science.aaf4943

ILLUSTRATION: V. ALTOUNIAN/*SCIENCE*

Published by AAAS

ASTRONOMY

An odd one out

An oxygen-rich white dwarf sets an important mark for stellar evolution

By **Boris Gänsicke**

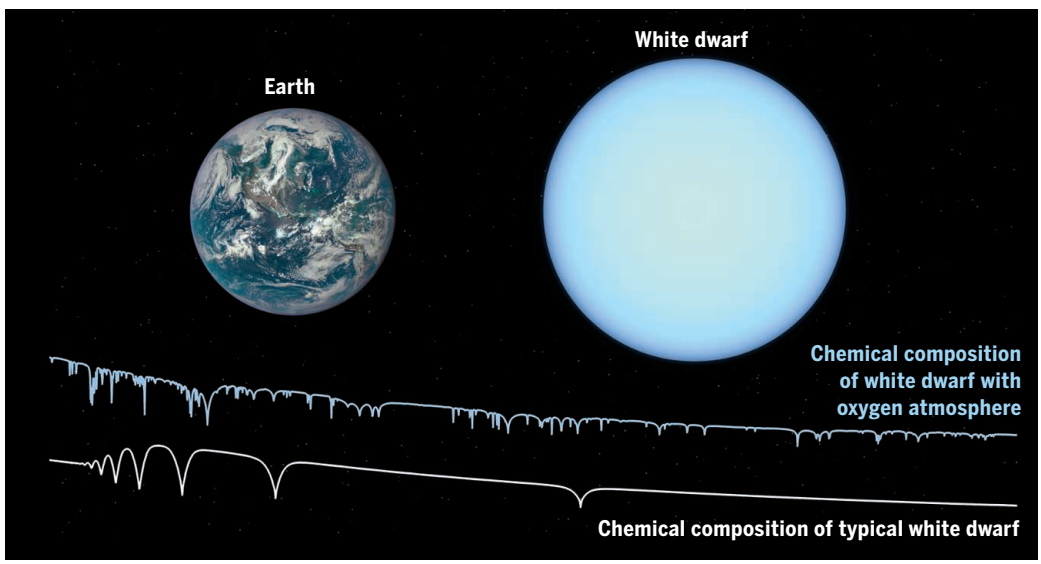
Most stars in the universe are in the process of burning hydrogen into helium via nuclear fusion deep inside their cores, which powers their luminosity and provides the thermal pressure that stops them from collapsing under their own weight. Stars end their lives once the nuclear fuel runs out, at which point they will either explode in a supernova, or, much more commonly, shed most of their mass and leave behind a white dwarf. On page 67 of this issue, Kepler *et al.* (*1*) announce the identification of a white dwarf called SDSSJ1240+6710 that has an almost pure oxygen atmosphere, diluted only by traces of neon, magnesium, and silicon. This white dwarf challenges the textbook wisdom of single stellar evolution and may provide a link to some of the types of supernovae discovered over the past decade.

White dwarfs are roughly Earth-sized, but still have ~0.4 to 1.2 times the mass of the Sun. The resulting strong surface gravity leads to a chemical stratification (*2*). The heaviest elements concentrated in the core of a white dwarf are typically carbon and oxygen, produced by helium burning, whereas the outermost layers are made up of helium and hydrogen. The chemical composition derived by Kepler *et al.* is extremely unusual and requires that the outer layers of the stellar core containing hydrogen, helium, and carbon were forcefully removed during the formation of the white dwarf. A mixture of oxygen, neon, and magnesium is thought to be produced in a small number of stars through the nuclear burning of carbon; however, the white dwarfs formed through this process should be fairly massive (*3*), whereas Kepler *et al.* find that SDSSJ1240+6710 has just the average mass for a white dwarf. Most striking, perhaps, is the detection of silicon, which indicates that nuclear burning could have proceeded to the stage where oxygen is consumed as well, in which case classical evolution models predict the collapse into a neutron star (see the figure).

Although there is currently no published model that predicts the existence of white dwarfs similar to SDSSJ1240+6710, its observational properties suggest that its origin is the partial nuclear burning of heavier elements either in a binary system or a single star near the mass boundary that leads to the collapse into neutron stars (e.g., *4*, *5*). The search for optical transients by many different groups has led to a rapid growth in the variety of thermonuclear supernovae, and some of the new subclasses may leave behind bound remnants with exotic chemical compositions (*6*). Unambiguously identifying and characterizing such remnants would be a major step toward a more complete understanding of these stellar explosions.

Besides the implications for the theories of stellar evolution, the discovery made by Kepler *et al.* also demonstrates the power of combining technological advances with human ingenuity. The authors made use of the data that the Sloan Digital Sky Survey (SDSS) (*7*) collected over the past 15 years. Although SDSS was never designed to find exotic white dwarfs, the sheer number of available fibers in its state-of-the-art multi-object spectrographs allowed the gathering of vast amounts of serendipitous observations. The identification of SDSSJ1240+6710 involved something that is common to many important discoveries in astronomy: analyzing the data with an open mind, neither driven by a particular agenda nor searching for the answer to a particular question. Simple scientific curiosity and attention to detail led them to spot the subtle difference between the spectrum of this white dwarf and the 32,000 or so others that they inspected.

Following up SDSSJ1240+6710 with high-quality spectroscopy in the optical and ultraviolet will provide measurements of the abundances of other nuclear burning products, such as sulfur or phosphorus, which will allow us to constrain the nuclear burning processes that its progenitor underwent. SDSS has only wedged open the door into massive spectroscopic surveys. Several next-generation instruments, such as WEAVE (the wide-field multi-object spectrograph for the William Herschel Telescope), 4MOST (the 4-m Multi-Object Spectroscopic Telescope), and DESI (Dark Energy Spectroscopic Instrument), are gearing up to take data for tens of millions of galaxies and stars. What other needles will be found in those haystacks? Stay open-minded. ■



A space oddity. White dwarfs are the Earth-sized burnt out cores of stars like the Sun and lock up the ashes of nuclear fusion. In most cases, a very thin layer of hydrogen (gray line) on the surface prevents the spectroscopic measurement of the chemical composition of the end products produced by fusion. Using spectroscopy from the SDSS, Kepler *et al.* (*1*) discovered a white dwarf with an atmosphere dominated by oxygen with small traces of neon, magnesium, and silicon. This chemical composition is unique among ~32,000 known white dwarfs and must arise from an extremely rare process of stellar evolution.

GRAPHIC: MARK HOLLANDS, UNIVERSITY OF WARWICK. NASA (EARTH) AND DETLEV KOESTER (WHITE DWARF MODEL SPECTRA)

Department of Physics, University of Warwick, Coventry, CV4 7AL, UK. E-mail: boris.gaensicke@warwick.ac.uk

REFERENCES

1. S. O. Kepler *et al.*, *Science* **352**, 67 (2016).
2. E. Schatzman, *Ann. Astrophys.* **8**, 143 (1945).
3. I. Iben *et al.*, *Astrophys. J.* **489**, 772 (1997).
4. C. L. Doherty *et al.*, *Mon. Not. R. Astron. Soc.* **446**, 2599 (2014).
5. S. Jones *et al.*, http://arxiv.org/abs/1602.05771 (2016).
6. R. J. Foley *et al.*, *Astrophys. J.* **138**, 376 (2009).
7. D. G. York *et al.*, *Astrophys. J.* **120**, 1579 (2000).

10.1126/science.aaf3768

Downloaded from on March 31, 2016

Published by AAAS



SOCIAL SCIENCE AND SUSTAINABILITY

Engage key social concepts for sustainability

Social indicators, both mature and emerging, are underused

By **Christina C. Hicks,[1,2,3*] Arielle Levine,[4] Arun Agrawal,[5] Xavier Basurto,[6] Sara J. Breslow,[7] Courtney Carothers,[8] Susan Charnley,[9] Sarah Coulthard,[10] Nives Dolsak,[11] Jamie Donatuto,[12] Carlos Garcia-Quijano,[13] Michael B. Mascia,[14] Karma Norman,[7] Melissa R. Poe,[7,15] Terre Satterfield,[16] Kevin St. Martin,[17] Phillip S. Levin[7]**

With humans altering climate processes, biogeochemical cycles, and ecosystem functions (*1*), governments and societies confront the challenge of shaping a sustainable future for people and nature. Policies and practices to address these challenges must draw on social sciences, along with natural sciences and engineering (*2*). Although various social science approaches can enable and assess progress toward sustainability, debate about such concrete engagement is outpacing actual use. To catalyze uptake, we identify seven key social concepts that are largely absent from many efforts to pursue sustainability goals. We present existing and emerging well-tested indicators and propose priority areas for conceptual and methodological development.

POLICY

Indicators represent a particularly powerful tool. They are scalable across geographic areas and, when designed well, reduce complex phenomena to simple measures (*3*). Social indicators can be used to ensure accountability or track progress toward normative goals, for example, increasing well-being (*3*, *4*). Further, they can evaluate local conditions to direct decision-making for more desirable futures, for example, by identifying if local values are conducive to collective management approaches. Indicators can thus describe what exists, and in doing so, they define what is important. Conversely, that which is not measured can disappear from public debate and political consciousness (*3*). Bias toward easily quantifiable concepts, coupled with the tendency for indicators to direct change, can hinder progress, particularly where biases ignore key determinants of human equity and action (*5*). Consequently, suitable indicators are required for key social phenomena fundamental to a sustainable future.

PROMISING SOCIAL INDICATORS. Human well-being is dependent on healthy ecosystems, yet short-term pursuit of well-being may negatively affect those same ecosystems (*6*). Tracking only economic growth has been detrimental to social and environmental progress (*4*), which demonstrates the need for broader understanding and assessment of human well-being. The recent surge of interest in measuring well-being from local to national scales has tended toward consensus around what to measure and how (*4*, *7*). Human well-being remains variously defined but can be thought of as a state of being with others, where human needs are met, when individuals can act meaningfully to pursue self-defined goals, and when they can enjoy a satisfactory quality of life (*4*, *8*). Well-being is thus multidimensional (i.e., more than gross domestic product or happiness) and consists of both objective and subjective elements (i.e., it reflects what people have or have achieved and how they feel about this). Although well-being manifests differently across contexts, three components appear universal: material well-being, quality of

[1]*Center for Ocean Solutions, Stanford University, CA, USA.* [2]*Australian Research Council Centre of Excellence for Coral Reef Studies, James Cook University, Australia.* [3]*Lancaster Environment Centre, Lancaster University, UK.* [4]*Geography, San Diego State University, CA, USA.* [5]*School of Natural Resources and the Environment, University of Michigan, USA.* [6]*Nicholas School of the Environment, Duke University, NC, USA.* [7]*Northwest Fisheries Science Center, NOAA, WA, USA.* [8]*School of Fisheries and Ocean Sciences, University of Alaska Fairbanks, USA.* [9]*U.S. Department of Agriculture, Forest Service, USA.* [10]*Northumbria University, UK.* [11]*School of Marine and Environmental Affairs, University of Washington, USA.* [12]*Swinomish Indian Tribal Community, WA, USA.* [13]*Anthropology and Marine Affairs, University of Rhode Island, USA.* [14]*Moore Center for Science, Conservation International, VA, USA.* [15]*Washington Sea Grant, University of Washington, USA.* [16]*The Institute for Resources, Environment and Sustainability, University of British Columbia, Canada.* [17]*Department of Geography, Rutgers University, NJ, USA.* **Corresponding author. E-mail: christina.hicks@lancaster.ac.uk*

ILLUSTRATION: DAVIDE BONAZZI/@SALZMANART

Downloaded from on March 31, 2016

Published by AAAS

life, and relational well-being (*7*). These established, multidimensional elements have well-tested indicators (see the table).

Material well-being, quality of life, and relational well-being can in part be understood from people's values. Values reflect the importance something holds for us and, in doing so, guide human thinking, feeling, and behavior to frame the pursuit of well-being. Social psychologists in particular have developed systematic approaches to assess values. Values in this sense are transsituational goals that vary in importance and serve as guiding principles in people's lives, such as conformity or compassion (*8*). Broad agreement has emerged that a limited number of values exist, that they relate to each other in a consistent manner, and that specific values are similar to one another, whereas others conflict. Analogous to the agreed upon constituents of well-being, all identified values are considered present, in varying degrees of importance, in all human societies (*8*). Academics and international agencies have measured a common set of values, across nearly 100 countries, that represent more than 85% of the world's population (*8*) (see the table).

The success of sustainability polices will be influenced by agency: the ability to act (and achieve) on the basis of what one values and has reason to value (*9*). People often strive to adapt to their social systems (e.g., laws and policies) and their natural environments (e.g., resource availability) as they pursue greater well-being for themselves and their families. Where people have agency, they may reject policies that impinge on their values or their ability to improve well-being. Where people lack agency, they may be unable to take advantage of the potential for desirable change or may be coerced into undesirable situations. Trajectories to desirable futures can falter because people have, or lack, agency, even when values have been used to inform policy. Measures for agency are less developed than those for human well-being or values, but progress has been made (*10*). Indicators often measure assets (e.g., education); control over specific domains (e.g., household decision-making); or global proxies (e.g., the "ladder of power") (*10*) (see the table). There is mounting evidence that multidimensional process-based measures of agency are necessary to account for people's (i) direct control or effective power; (ii) ability to pursue and achieve goals; (iii) capacity to direct their pursuits toward what they value or have reason to value; and (iv), ability to improve their own, or others', well-being (*10*).

Inequality—the unequal distribution of costs, benefits, power, and access to resources—exacerbates both socialand environmental conditions; it undermines sustainability (*11*). Inequalities shape who has agency and who lacks it (*11*). Consequently, reduction of inequality is a central theme in the United Nation's Sustainable Development Goals. Indicators of inequality have not been specified, but, analytical lenses have been developed (see the table).

Social measures for sustainability

Promising indicators for measuring well-being, values, agency, and inequality

WELL-BEING

1. OECD's "how's life" framework (*7*). Quality of life: Eight elements (e.g., health status, subjective well-being). Material conditions: Three elements (e.g., income): Sustainability of well-being over time: Four capitals (e.g., human, economic, social, and natural).
2. Millennium Ecosystem Assessment 2003 from "voices of the poor" (*7*). Material well-being (e.g., enough food); bodily well-being (e.g., health); security (e.g., civil peace); freedom of choice and action; social well-being (including psychological well-being, self-respect and dignity, peace, harmony, and good relations).
3. Ten universal capabilities [e.g., Nussbaum 2001 (*7*)]. Life; bodily health; bodily integrity; senses, imagination, and thought; emotions; practical reason; affiliation; other species; play; control over one's environment (e.g., political and material).

VALUES

1. Human values [e.g., Schwartz *et al*., 2012 in (*8*)]. Two dimensions capturing self-enhancement to self-transcendence and openness-to-change to traditionalism that contain 10 value types.
2. World values survey [e.g., Inglehart and Welzel 2005 in (*8*)]. Two dimensions capturing traditionalism to secularism and survival to self-expression.
3. Cultural dimensions theory [e.g., Hofstede 2001 in (*8*)]. Six dimensions capturing individualism to collectivism; uncertainty avoidance; social hierarchy; masculinity to femininity; long-term orientation; indulgence to self-restraint.

AGENCY

1. Moving out of poverty's "ladder of power" [Narayan and Petesch 2007 in (*10*)]. Assesses one's power up a hypothetical ladder.
2. Agency and empowerment [Alsop and Heinsohn 2005 in (*10*)]. Reflects asset endowments (e.g., psychological, informational, organizational, material, social, financial, and human).
3. Demographic and health survey [Orc-Macro 2006 in (*10*)]. Determines control over six domains (own earnings, partners earnings, own health care, major household purchases, daily household purchases, visits to family).

INEQUALITY

1. Gini index [e.g., (*11*)]. Measures the extent to which the distribution of income deviates from perfectly equal.
2. Social mobility indices [e.g., (*11*)]. Measures the movement of individuals, families, households, across a social layer (e.g., changes in income levels, education levels).
3. Fractionalization indices: Measures the social heterogeneity and conflict in a group.

CONCEPTUAL AND METHODOLOGICAL NEEDS. Power, the ability to influence or control the beliefs or actions of others, is created by, and recreates, many inequalities, which include the ability to exercise agency (*12, 13*). Power at different scales can be exerted over others, through various means (e.g., knowledge or policies), or to achieve certain ends. Understanding and monitoring power that is exerted in both overt ways (e.g., state control) and diffuse ways (e.g., hegemonic ideas) is central to crafting a sustainable future. Work is needed to determine how elements of power, in the context of sustainability, can be measured and monitored through time. These efforts may draw from progress in related fields; for example, the Herfindahl-Hirschman index measures the extent to which market shares are concentrated within a few companies and could be adapted to measure the extent to which influence is concentrated within a few individuals, organizations, or states. Social network analyses can be used to measure the influence of a group, organization, or idea.

Existing measures of values may provide broad context for well-being but may lack the depth and breadth that an understanding of culture enables. Culture is a multifaceted concept that includes the shared language, knowledge, meanings, values, beliefs, norms, customs, and practices that are transmitted through social learning (*14*). Culture is expressed through social, political, and economic systems, as well as through symbols, artifacts, and landscapes, such as the British badger or suburban American lawn, that serve to reinforce beliefs or norms of behavior. Comprehensive indicators of culture are yet to be developed, but indicators exist for elements of culture, such as place attachment. A comparative cultural database, based on in-depth ethnographic work, exists for nearly 300 cultures, and it could inform a measurement-based indicator system (ehrafworldcultures.yale.edu).

Although inequality may persist, the extent to which this represents an injustice determines when conflict may arise and action is necessary. Thus, progress toward sustainability goals must be evaluated through the lens of justice, a normative principle centered on how people should be treated (*15*). Existing indicators assess distributional and procedural justice in workplaces, or environmental injustice in federal jurisdictions; however,

Published by AAAS

adequately addressing justice will require additional assessments of what is considered "fair," to and by whom, and programmatic steps regarding how justice can be achieved and maintained (*15*).

Progress has been made toward development of some indicators, and in many instances, relevant data and expertise exist within national and international, official and unofficial statistics bureaus (e.g., national censuses, representative surveys, and polling reports). Further work is needed to understand and communicate desirable directions of change. Reasonable consensus exists that it is desirable to increase well-being and agency and to reduce inequality, injustice, and imbalances of power. In contrast, although extreme values are detrimental to sustainability goals, there is no desirable direction of change for values or culture. Instead, these concepts facilitate understandings of how sustainability goals manifest and how policies can be crafted. Although critical gaps remain with concepts in need of indicator development, quantitative indicators are alone insufficient for understanding these concepts. Complementary, qualitative, and reflexive assessments will remain critical for development, implementation, and interpretation of robust measurement systems. ■

REFERENCES AND NOTES

1. W. Steffen *et al.*, *Science* **347**, 1259855 (2015).
2. N. Castree *et al.*, *Nature Clim. Change* **4**, 763 (2014).
3. J. G. Kelley, B. A. Simmons, *Am. J. Pol. Sci.* **59**, 55 (2015).
4. Organization for Economic Cooperation and Development, *Guidelines for Measuring Subjective Well-being* (OECD Publishing, Paris, 2013)
5. J. C. Scott, *Seeing Like a State* (Yale Univ. Press, New Haven, CT, 1998).
6. Millennium Ecosystem Assessment, *Ecosystems and Human Well-Being: Biodiversity Synthesis* (World Resources Institute, Washington, DC, 2005).
7. A. McGregor, S. Coulthard, L. Camfield, "Measuring what matters: The role of well-being methods in development policy and practice" (Project 04, Overseas Development Institute, London, 2015).
8. T. Brosch, D. Sander, Eds., *Handbook of Value Perspectives from Economics, Neuroscience, Philosophy, Psychology, and Sociology* (Oxford Univ. Press, Oxford, 2016).
9. A. Sen, *J. Philos.* **82**, 169 (1985).
10. S. Ibrahim, S. Alkire, *Oxf. Dev. Stud.* **35**, 379 (2007).
11. T. Piketty, *Capital in the 21st Century* (Harvard Univ. Press, Cambridge, 2014).
12. S. Lukes, *Power: A Radical View* (Palgrave Macmillan, Hampshire, UK, ed. 3, 2005).
13. N. Kabeer, *Dev. Change* **30**, 435 (1999).
14. L. Kroeber, C. Kluckhohn, *Culture, A Critical Review of Concepts and Definitions* (Peabody Museum of Archaeology and Ethnology, Harvard Univ., Cambridge, MA, 1952).
15. G. Walker, *Environmental Justice: Concepts, Evidence Politics* (Routledge, New York, 2012).

ACKNOWLEDGMENTS

Funding was provided by Washington Sea Grant and NOAA Fisheries. This is a contribution of the California Current Integrated Ecosystem Assessment Program. N. Graham, R. Martone, R. Hicks, and three anonymous reviewers provided invaluable insights to earlier versions.

10.1126/science.aad4977

SELF-ASSEMBLY

Colloidal crystal ordering in a liquid crystal

A nematic phase promotes the formation of dilute, low-symmetry colloidal crystals

By **Christophe Blanc**

Nanoparticles (NPs) can now be synthesized with a wide array of controlled sizes, shapes, and properties. However, turning them into nanomaterials often requires packing them into ordered assemblies to manifest specific electronic or optical properties for applications in nanoelectronics, optics, and metamaterials. Colloidal self-assembly (*1*) of NPs is relatively simple but is often restricted to high-symmetry crystals by the lack of specific directional bonds, especially for dilute NP solutions. To obtain lower symmetries that confer useful optical or electronic properties, long-range directional interactions must be imparted. On page 69 of this issue, Mundoor *et al.* (*2*) make clever use of an anisotropic host fluid, a liquid crystal, to promote the formation of a low-symmetry crystal in a dilute dispersion of nanorods.

In simple fluids, the absence of directional interactions between dispersed particles tends to favor the formation of only a few types of crystals. For example, concentration of hard spherical colloids mainly produces high-symmetry face-centered cubic or hexagonal close-packed lattices. Progress in colloidal engineering has partially lifted this limitation with the introduction of colloidal particles that can organize via directional interactions because of the specific control of their shape or of their surface patterns (*3*). Such "shape-anisotropic" or patchy colloids can promote preprogrammed structures when they are in close contact, but their interactions in dilute dispersions remain mostly isotropic.

Mundoor *et al.* show that the situation can be very different in a liquid crystalline matrix when the proper combination of interactions is present. They studied the dispersion and self-assembly of semiconductor nanorods in an aligned nematic liquid crystal. In thermotropic nematic phases, rodlike molecules develop a long-range orientational order caused by the spontaneous molecular alignment. The alignment occurs only over a given temperature range, and is a time average as the molecules can still move and fluctuate. Uniformly aligned domains are easily obtained at large scale in thin films formed over suitable substrates.

The spontaneous formation of colloidal crystals of the triclinic pinacoidal symmetry class (almost the lowest symmetry possible) was observed at very low concentrations (<<1%). In crystals of this class, none of the unit cell edges are equal, and none of the angles between the edges are equal, nor are they right angles. Repulsive electrostatic interactions between the NPs compete with attractive interactions mediated by the orientational elasticity of the liquid crystal (see the figure). The NPs have positive surface charges, and although they are elongated rods, the electrostatic interaction is effectively isotropic at large distances. However, each particle also gives rise to an elastic distortion of the matrix with a quadrupolar symmetry. This distortion creates the long-range and anisotropic elastic interactions between the NPs. The mesophase nature of the host is essential to the formation of the low-symmetry crystal because only the electrostatic repulsion remains if the liquid is heated into the isotropic phase, where the orientational ordering disappears.

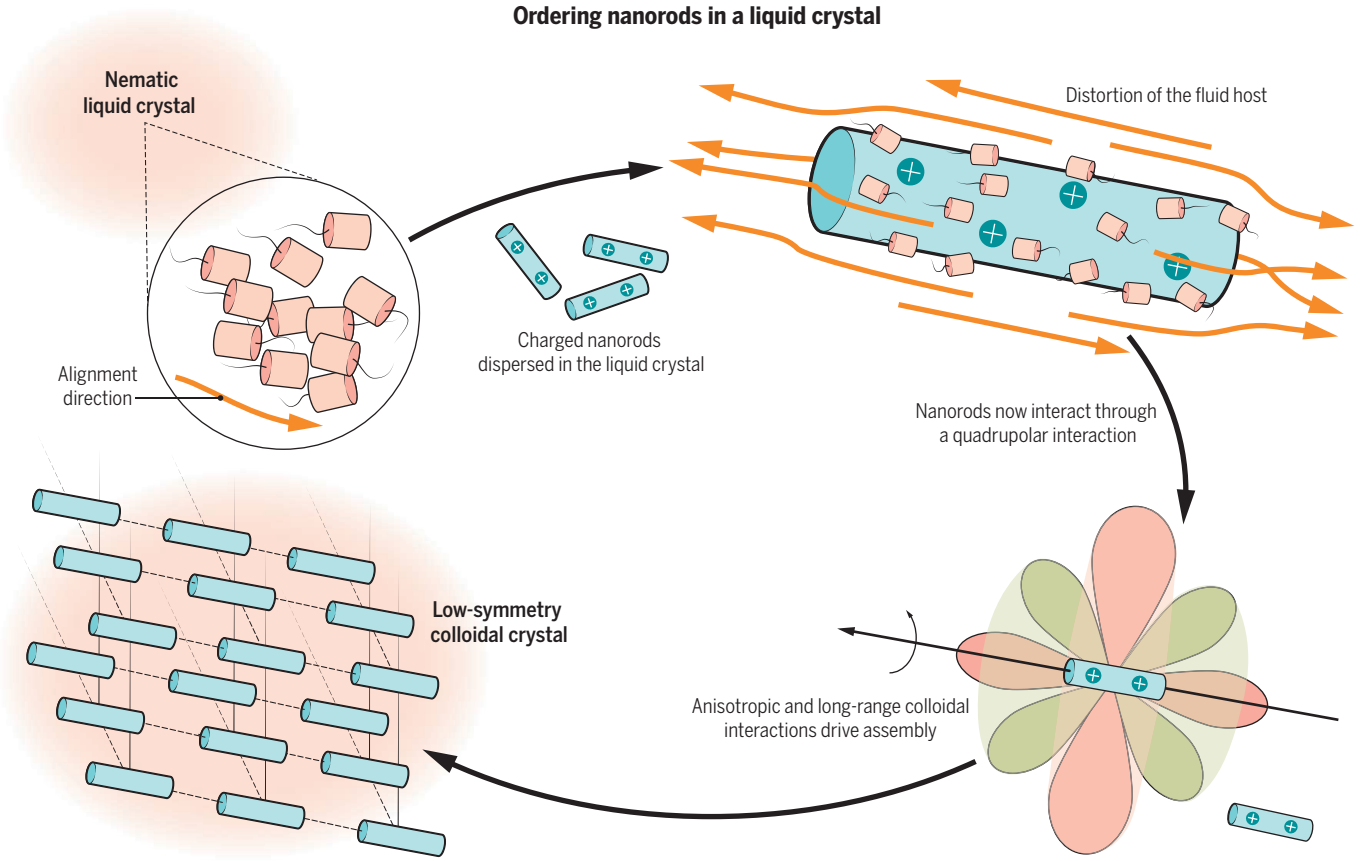
> ***"The mesophase nature of the host is essential to the formation of the low-symmetry crystal..."***

The control of the organization of solid inclusions by means of mesophases already has a long history. For example, spontaneous alignment of nanorods by the nematic phase is well known and is caused by a restoring torque created by a preferred orientation of the host fluid molecules at the surface of the particles (a phenomenon called anchoring). This phenomenon was discussed theoretically as early as the 1970s

Laboratoire Charles Coulomb (L2C), UMR 5221 CNRS–Université de Montpellier, Montpellier, France.
E-mail: christophe.blanc@umontpellier.fr

Downloaded from on March 31, 2016

Published by AAAS



A liquid-crystal assist. Schematic of the strategy developed by Mundoor *et al.* to design colloidal crystals with low symmetry. When charged nanorods are dispersed in a nematic liquid crystal, they spontaneously align along its orientation direction but also distort it locally. This results in strongly anisotropic elastic colloidal interactions (here sketched as a multilobed quadrupole). Provided that a sufficiently repulsive isotropic force between particles is also present, directional bonding develops that favors low-symmetry crystals.

(*4*), but experimental realization with NPs was satisfactorily achieved only recently. This experimental realization has opened up the possibility of new switchable NP-based devices (*5*). Various positional ordering mechanisms based on thermotropic liquid crystals have also been successfully achieved in the past few years. At the molecular scale, particles have been directly combined with mesogens in hybrid architectures (*6*), which offers many possibilities for molecular self-assembly. However, such an approach is limited to NPs only a few nanometers in size; larger NPs must be considered as embedded in a continuous anisotropic medium. Templated structures could nonetheless still be formed in a host showing strong and periodic distortions. Cubic lattices of NPs have thus been recently obtained in a blue phase (*7*), a special mesophase that spontaneously forms ordered three-dimensional defect structures.

Mundoor *et al.* have exploited another phenomenon highlighted in 1997, when Poulin *et al.* (*8*) showed that controlled anchoring conditions on micrometer-sized inclusions combined with the host orientational elasticity not only generated local distortions of the matrix and defects, but also gave rise to well-defined long-range anisotropic colloidal forces. Although the importance of such mechanisms for colloidal self-assembly was rapidly recognized, most investigations focused on the formation of two-dimensional crystals of micrometer-sized colloids (*9*) in thin liquid-crystal cells. The elastic interactions predominated and were usually much greater than the thermal energy. Additional techniques, such as optical tweezing, were needed to direct the colloidal assembly into ordered structures with lattice constants comparable to the colloidal size. The same techniques were used to produce three-dimensional colloidal crystals of a few units with tetragonal symmetry (*10*), but such a directed approach was difficult to apply to NPs and poorly scalable.

The main innovation of Mundoor *et al.* is combining the elastic interaction with a well-defined electrostatic repulsion to enable the easy, nondirected self-assembly of colloidal crystals for NPs dispersed in a nematic liquid crystal. The approach is general and can be applied to many other NPs, provided that surface anchorings and electric charges can be sufficiently controlled; hence, their work should enable various artificial colloidal crystals of low symmetry to be designed with NPs. Another characteristic of liquid crystals is their extreme sensitivity to weak external stimuli such as electric fields. Lattice parameters and crystal orientations should be easily tuned in a colloidal crystal formed in a liquid crystal. This aspect remains to be explored in depth in the system described here, but this also opens the possibility of a whole class of simple reconfigurable devices in which both the orientation and ordering of NPs could be easily controlled. ■

ILLUSTRATION: P. HUEY/*SCIENCE*

REFERENCES

1. F. Li, D. P. Josephson, A. Stein, *Angew. Chem. Int. Ed.* **50**, 360 (2011).
2. H. Mundoor, B. Senyuk, I. I. Smalyukh, *Science* **352**, 69 (2016).
3. Y. Wang *et al.*, *Nature* **491**, 51 (2012).
4. F. Brochard, P. G. De Gennes, *J. Phys.* **31**, 691 (1970).
5. Y. Zhang *et al.*, *ACS Nano* **9**, 3097 (2015).
6. M. Draper *et al.*, *Adv. Funct. Mater.* **21**, 1260 (2011).
7. M. A. Gharbi *et al.*, *ACS Nano* **10**, 3410 (2016).
8. P. Poulin *et al.*, *Science* **275**, 1770 (1997).
9. I. Muševič *et al.*, *Science* **313**, 954 (2006).
10. A. Nych *et al.*, *Nat. Commun.* **4**, 1489 (2013).

10.1126/science.aaf4260

Published by AAAS

BEHAVIOR

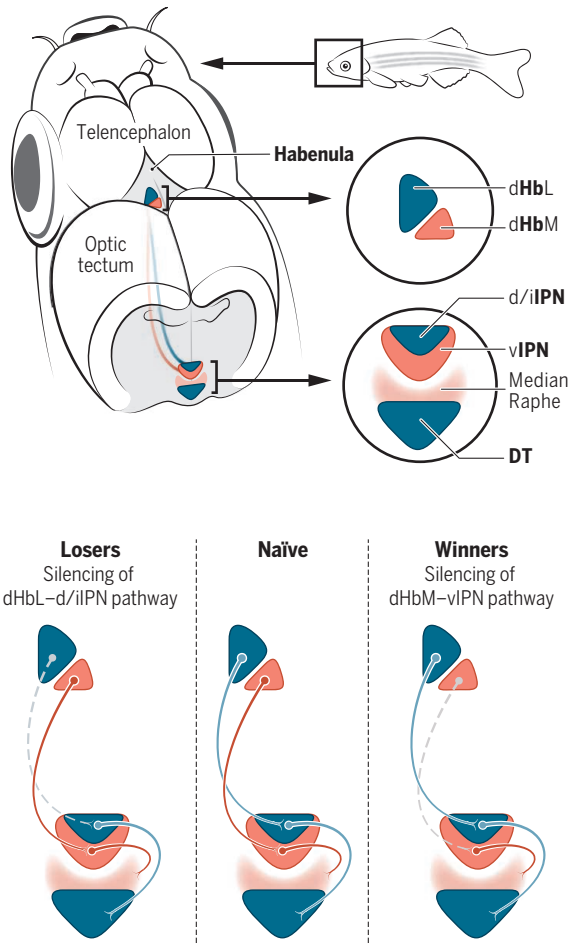
A brain conditioned for social defeat

A brain circuit in vertebrates determines who wins or loses a fight

By **Laura Desban** *and* **Claire Wyart**

Aggression is common in the animal kingdom, even though agonistic behaviors can lead to chronic stress or pain. So how does aggression remain conserved evolutionarily? In 1859, Darwin argued in his book *On the Origin of Species* that the conservation of any behavioral trait is ultimately explained by its necessity for survival and reproduction. To survive with limited resources, individuals express aggressive behaviors against competitors to pass on their genes. For social animals, dominance hierarchies establish rapidly (*1*), avoiding the cost of recurrent fighting within the group. Hierarchy formation and maintenance rely on the effect of prior experience (*2*). However, the underlying mechanisms and neural circuitry remain elusive. On page 87 of issue, Chou *et al.* (*3*) identify a key role for the dorsal habenula (dHb) region of the brain in zebrafish to determine who wins and who loses in a fight. This region is highly conserved across vertebrates, raising the possibility of manipulating neuronal circuits that govern innate social behaviors.

The social status of an individual determines the quality and the quantity of its opportunities. Individuals usually keep their social rank over time by means of positive or negative reinforcement induced by prior experience, referred to as the winner effect or loser effect, respectively. During dyadic fighting, zebrafish males show agonistic behavior with a stereotypic sequence (*4*): first display behaviors by erecting its fins along with body flaring, then circle and bite until dominance is established. The fight ends with the surrender of the losing fish, who exhibits fleeing behavior. By imaging calcium (as a readout for neuron activity) in acute brain slices obtained from fish immediately after fighting, Chou *et al.* observed differences between winners and losers at the level of the dorsal habenula–interpeduncular nucleus (dHb–IPN) pathway (see the figure). In losers, neuronal activity originating from dHb onto the dorsal and intermediate IPN (d/iIPN) was reduced. The authors confirmed by in vivo electrophysiology (that is, by inserting electrodes to record local field potentials in the IPN) that dominance status is associated with activity levels in the dHb-IPN circuitry.



Habenular circuitry implicated in the outcome of fighting. (**Top**) Schematic showing a dorsal view of habenular connections onto the IPN in the zebrafish brain. The dHbL–d/iIPN–DT pathway (blue) and the dHbM–vIPN–median raphe pathway (orange) are involved in fear behavior. (**Bottom**) Selective inactivation of dHb–IPN pathways affects behavior. Silencing of the projection from dHbL onto d/iIPN triggers the fish to lose (left); silencing of the projection from dHbM onto vIPN triggers the fish to win (right). Naïve fish are those who did not previously fight (middle).

In mammals, the habenula is a multitask brain region that integrates aversive inputs processed by the limbic system and the basal ganglia and adapts motor responses accordingly (*5*). To find homologous structures in zebrafish, Chou *et al.* drew upon knowledge of connections in the mammalian brain. Recent studies using anterograde tracers in zebrafish had provided evidence for the conservation of habenular pathways (*6*) and associated functions (*7*). The dHb–IPN pathway of zebrafish corresponds to the medial Hb–IPN pathway of mammals and is similarly involved in fear responses (*7*, *8*). Furthermore, the dIPN projects onto the dorsal tegmental (DT) region corresponding to the mammalian periaqueductal gray (PAG) (*7*). The PAG regulates fleeing behavior in mammals (*9*), providing further support for the idea that the zebrafish circuit contributes to loser-like behavior.

Chou *et al.* used transgenic zebrafish lines to target neurons of either the lateral or medial subnucleus of the dHb (dHbL and dHbM) and block their synaptic transmission to distinct regions of the IPN. Reduction of transmission in one pathway (dHbL–d/iIPN) increased the tendency to lose fights, whereas in the other pathway, dHbM–ventral IPN (vIPN), the tendency to lose was decreased. Selective manipulations of habenular transmission to the IPN were therefore sufficient to determine the winner (and loser) without prior experience—an effect that persisted over time and was reinforced during subsequent fights. These results suggest that the dHb–IPN pathway acts as a neural switch that conditions the outcome of social fighting, depending on differential transmission onto dorsal or ventral IPN subnuclei. This study, however, does not rule out the potential role of many other brain regions acting in concert with the habenula (*10*).

Because the manipulation of synaptic transmission within the dHb–IPN pathway led to antagonistic outcomes during social

[1]Institut du Cerveau et de la Moelle épinière, GH Pitié-Salpêtrière, 75013 Paris, France. E-mail: claire.wyart@icm-institute.org

ILLUSTRATION: K. SUTLIFF/*SCIENCE*

Downloaded from on March 31, 2016

Published by AAAS

fighting, the habenula seemingly can induce differential motor responses. This is concordant with recent studies describing the habenula as a hub integrating multiple sensory cues (*11*) to produce an adapted motor response. How this signal is relayed at the molecular and neuronal level is not yet known. Multiple modulatory neurotransmitters and peptides are associated with aggressive behavior (*10*, *12*), but their diversity in the habenula and IPN is most likely underappreciated. The dissection of neuromodulatory systems using innovative genome-editing technologies may reveal the full circuitry governing social defeat in vertebrates.

Zebrafish has emerged as a powerful system to study social interactions (*13*), and there are many social behaviors in this animal to unravel (14). For example, the recent observation of social preference in juvenile zebrafish (*15*), at stages when whole-brain imaging is feasible, opens new paths of investigation into the sensory cues and the genes and circuits mediating these early social interactions. It should be possible to find out why some individuals are reluctant to go toward others when the majority are attracted by conspecifics.

Although zebrafish have a short generation time and are easy to maintain in captivity, the bottleneck often lies in the fine description and quantitative analysis of complex behaviors. The study of Chou *et al.* illustrates how the genetic manipulation of pathways governing innate behaviors in zebrafish can inspire investigations in other model organisms by providing new working hypotheses and brain regions to target. The next step will be to combine whole-brain imaging, optogenetic manipulations, and CRISPR-mediated genome editing to unravel the complete circuits underlying social behaviors in vertebrates. ■

REFERENCES

1. I. D. Chase, K. Seitz, *Adv. Genet.* **75**, 51 (2011).
2. C. Rutte, M. Taborsky, M. W. Brinkhof, *Trends Ecol. Evol.* **21**, 16 (2006).
3. M.-Y. Chou *et al.*, *Science* **352**, 87 (2016).
4. R. F. Oliveira, J. F. Silva, J. M. Simoes, *Zebrafish* **8**, 73 (2011).
5. O. Hikosaka, *Nat. Rev. Neurosci.* **11**, 503 (2010).
6. R. Amo *et al.*, *J. Neurosci.* **30**, 1566 (2010).
7. M. Agetsuma *et al.*, *Nat. Neurosci.* **13**, 1354 (2010).
8. T. Yamaguchi, T. Danjo, I. Pastan, T. Hikida, S. Nakanishi, *Neuron* **78**, 537 (2013).
9. R. Misslin, *Neurophysiol. Clin.* **33**, 55 (2003).
10. R. F. Oliveira *et al.*, *Proc. Natl. Acad. Sci. U.S.A.* **113**, E654 (2016).
11. E. Dreosti, N. Vendrell Llopis, M. Carl, E. Yaksi, S. W. Wilson, *Curr. Biol.* **24**, 440 (2014).
12. T. N. deCarvalho *et al.*, *Genesis* **52**, 636 (2014).
13. R. F. Oliveira, *Front. Neural Circuits* **7**, 131 (2013).
14. R. D. Fernald, *Cold Spring Harb. Symp. Quant. Biol.* **79**, 229 (2014).
15. E. Dreosti, G. Lopes, A. R. Kampff, S. W. Wilson, *Front. Neural Circuits* **9**, 39 (2015).

10.1126/science.aaf6016

ILLUSTRATION: P. HUEY/*SCIENCE*

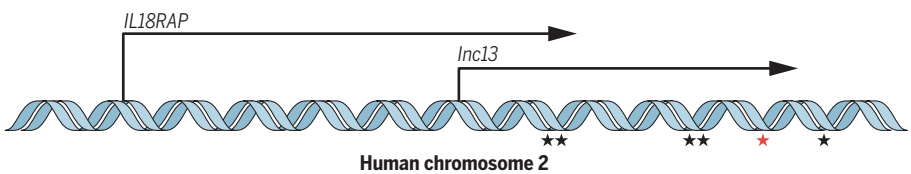
RNA

A lncRNA links genomic variation with celiac disease

A long noncoding RNA is associated with an intestinal autoimmune disorder

By **Maite Huarte**

The majority of human single-nucleotide polymorphisms (SNPs) associated with increased disease risk map to noncoding regions of the genome. The nucleotide variations therefore cannot be directly related to changes in the function of proteins. Indeed, SNPs frequently localize to DNA regulatory elements such as enhancers or promoters, or within intergenic regions that are transcribed to produce long noncoding RNAs (lncRNAs). LncRNAs are RNA molecules longer than 200 nucleotides that do not encode proteins; in many instances, they regulate gene expression through diverse mechanisms. On page 91 of this issue, Castellanos-Rubio *et al.* (*1*) report that a relationship between the function of a lncRNA and the SNPs within its locus underlies celiac disease, an autoimmune disorder that causes intolerance to gluten.



Location overlap. The genomic loci of *IL18RAP* and *lnc13* overlap in human chromosome 2. SNPs associated with celiac disease are indicated with blue stars. A red star shows the specific SNP, rs917997.

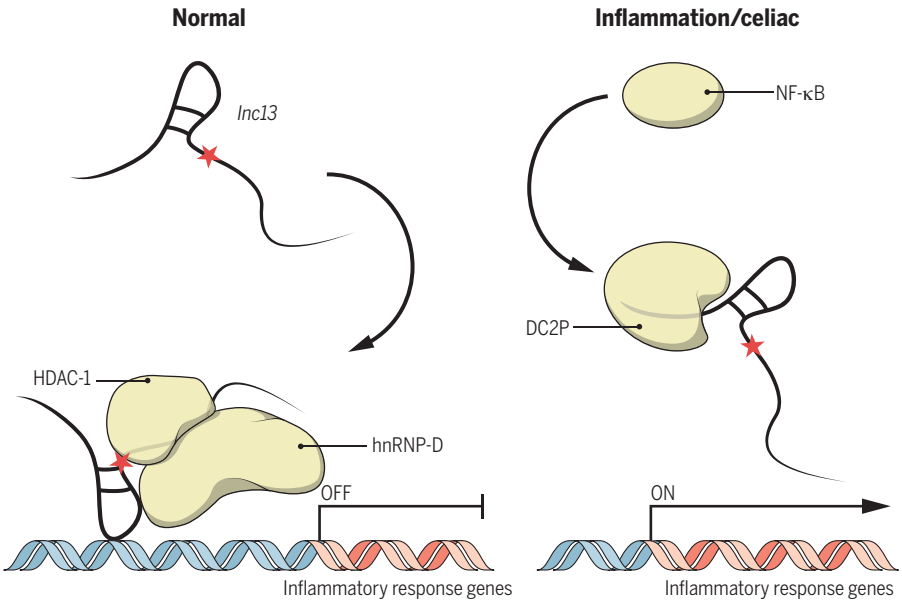
Genome-wide association studies revealed that six SNPs that are linked to increased risk of suffering from gluten intolerance form a haploblock (closely associated SNPs) located in chromosome 2 (*2*). One of the SNPs (rs917997) is positioned 1.5 kb downstream of interleukin-18 receptor accessory protein (IL18RAP), a gene that has been associated with susceptibility to celiac disease and other autoimmune diseases (*2*–*4*). In the mouse genome, a previously annotated lncRNA, *lnc13*, is transcribed in this position. Castellanos-Rubio *et al.* identified a lncRNA in the equivalent position of the human genome and showed that both human and murine lnc13 regulate the expression of genes of the inflammatory response. Despite limited DNA sequence conservation, the function and mechanism of lnc13 is conserved between mouse and human.

The fine regulation of lnc13 expression is probably crucial for its proper function. It is transcribed from the same strand of DNA as IL18RAP, and its 5′ end overlaps with the 3′ end of IL18RAP (see the first figure). However, despite this overlap, both genes have independent promoters and are independently regulated. IL18RAP expression is induced in the intestinal epithelium of celiac patients and in lipopolysaccharide (LPS)–stimulated macrophages (a treatment that mimics the inflammatory response). However, under these conditions, the expression of lnc13 is diminished. Reduction in the amount of lnc13 is a posttranscriptional event dependent on the signaling pathway controlled by the transcription factor nuclear factor kappa B (NF-κB). Indeed, despite not being translated, lnc13 is highly stable in nonstimulated macrophages. By contrast, in LPS-activated macrophages, NF-κB induces the expression of Dcp2, a negative regulator of the stability of capped RNAs. Dcp2 thereby keeps lnc13 amounts low (see the second figure). Thus, the co-inherited IL18RAP and lnc13 are transcribed from the same locus and take part in the same biological process. However, their regulation is independent, in part because of the posttranscriptional control of lnc13.

The expression levels of lnc13 correlate negatively with the expression of several genes of the inflammatory response, some of which are up-regulated in celiac disease patients' biopsies. In fact, lnc13 inhibits the expression of these genes in cells where the inflammatory response is inactive. Similar to several other characterized lncRNAs, lnc13 is preferentially present in the nucleus

Downloaded from on March 31, 2016

Published by AAAS



Gluten triggers inflammation. The action of *lnc13* in a normal macrophage or a macrophage with an active inflammatory response is shown. A decrease in available *lnc13* (due to its increased association with DC2P) is linked to celiac disease. *lnc13* function is impaired by the change in RNA sequence caused by a risk-related SNP, rs917997 (red star).

of the cells, and through binding to chromatin factors, it mediates gene silencing (*5*). In particular, lnc13 forms a complex with heterogeneous nuclear ribonucleoprotein D (hnRNPD) and the histone deacetylase HDAC-1. In nonstimulated macrophages, this lnc13-containing repressor complex is localized to the promoters of pro-inflammatory genes, keeping them transcriptionally silent. In agreement with this model, Castellanos-Rubio *et al.* have shown that lnc13, hnRNPD, and HDAC-1 are associated to those gene promoters. However, it remains unknown whether these are the only targets of lnc13, or whether it regulates the expression of additional genes of the inflammatory response, or even of other cellular pathways.

The activity of lnc13 seems to depend on the interaction with the RNA binding protein hnRNPD. hnRNPD is an abundant protein that functions at different levels of RNA metabolism and is also involved in transcriptional regulation. hnRNPD binds with high affinity to RNA molecules that contain AU-rich (A, adenine; U, uracil) elements (AREs) (*6*). Interestingly, the interaction between lnc13 and hnRNPD is affected by the sequence variation of the SNP rs917997. The interaction is substantially decreased when the genomic sequence variant is the disease-associated "TT" instead of the wild-type "CC" (T, thymine; C, cytosine). However, it is not clear whether the nucleotides corresponding to the allelic variants of lnc13 are part of an ARE. Thus, the nucleotide change may be affecting RNA structure rather than being localized to the protein-RNA interface. This not only highlights the relevance of RNA structure, but also shows how minimal changes in RNA sequence may have a functional impact.

The study by Castellanos-Rubio *et al.* demonstrates that lncRNAs play an active role in celiac disease and represents an exciting example of how a disease-associated SNP can directly affect the function of a lncRNA. It may be that other SNPs associated with risk of disease act in a similar manner. Unfortunately, it is still not possible to predict how long RNA molecules fold, and whether and how they interact with RNA binding proteins or genomic regions. At present, only individual detailed experimental analyses can deliver that information. Such studies will hopefully help us to infer the molecular principles that govern the function of lncRNAs and allow the design of lncRNA-targeting therapies. ■

REFERENCES AND NOTES

1. A. Castellanos-Rubio *et al.*, *Science* **352**, 91 (2016).
2. L. D. Ward, M. Kellis, *Nucleic Acids Res.* **40**, D930 (2012).
3. D. J. Smyth *et al.*, *N. Engl. J. Med.* **359**, 2767 (2008).
4. A. Zhernakova *et al.*, *Am. J. Hum. Genet.* **82**, 1202 (2008).
5. J. L. Rinn, H. Y. Chang, *Annu. Rev. Biochem.* **81**, 145 (2012).
6. K. Mazan-Mamczarz *et al.*, *Nucleic Acids Res.* **37**, 204 (2009).

ACKNOWLEDGMENTS

Supported by European Research Council grant ERC-2011-StG 281877 and Spanish Ministry of Science grant SRYC1100I008347XV0.

10.1126/science.aaf6015

Center for Applied Medical Research (CIMA), Department of Gene Therapy and Regulation of Gene Expression, University of Navarra, Pamplona, Spain, and IdiSNA, Institute of Health Research of Navarra, Pamplona, Spain. E-mail: maitehuarte@unav.es

CHEMICAL SYNTHESIS

Going with the flow

A desktop machine allows on-demand medicine production

By **Rainer E. Martin**

Imagine it is the middle of the night. A severe snow storm has hit the region, and your 3-year-old's fever is rising. You suspect a serious infection and cannot wait until the next morning to go to the pharmacy, yet the roads are impassable. No problem—you were recently granted access to a prototype machine no larger than a kitchen microwave that allows the user to synthesize their pharmaceutical of choice. You start up a smartphone app that has access to the family medical history and other relevant parameters, such as allergies and body weight. A few minutes later, you have consulted an emergency pediatrician through the app, inserted the relevant capsule, and pressed the start button. After a short wait, a single, personalized dose of the necessary antibiotic is ready for use. All this may sound like science fiction, but the report by Adamo *et al.* on page 61 of this issue (*1*) proves that this scenario might become reality in the not-too-distant future.

The authors have created an on-demand synthesis platform that can produce thousands of formulated, ready-to-use liquid drug doses per day. Currently, the end user can choose from four key drugs, but the drug catalog can be extended. The fully integrated machine is roughly the size of a refrigerator and contains individual synthesis, purification, and formulation modules. Once a drug is selected, the required synthesis steps are conducted automatically by guiding starting materials and reagents through a flow reactor network that is established within the machine for the selected drug. Complex, laborious, and time-consuming steps such as phase separation, precipitations, and crystallizations, which are required to get to the purified pharmaceutical, are all conducted in a fully automated fashion.

Since the early days of Justus von Liebig (1803 to 1873), the art of organic synthesis

Medicinal Chemistry, Roche Pharmaceutical Research and Early Development (pRED), Roche Innovation Center Basel, F. Hoffmann-La Roche Ltd, Grenzacherstrasse 124, CH-4070 Basel, Switzerland. E-mail: rainer_e.martin@roche.com

ILLUSTRATION: P. HUEY/*SCIENCE*

Downloaded from on March 31, 2016

Published by AAAS

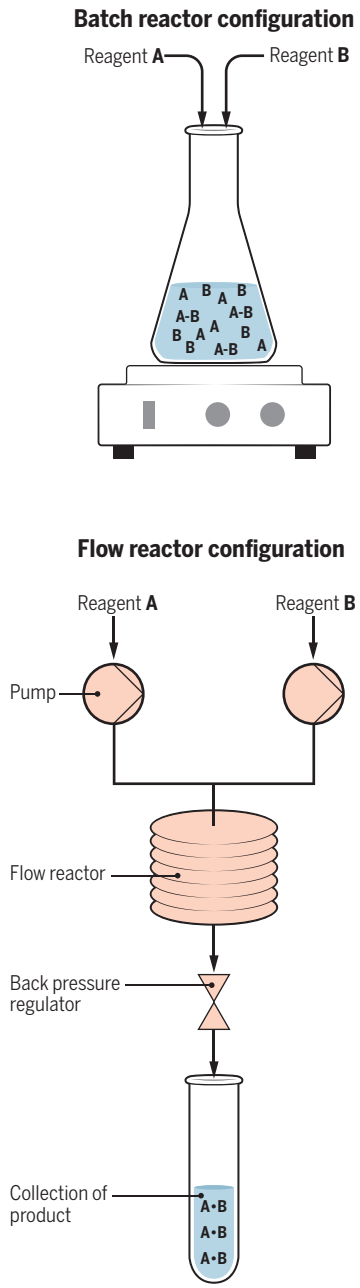
has relied on batch processing (see the figure) (*2*). Generations of chemists have been trained to perform chemical reactions in a process similar to cooking. Reagents, catalysts, and solvents are added into a flask and then stirred and heated for a given time, after which the chemical composition is analyzed to see if the reaction is complete, and the product is isolated. Modern lab equipment is much more specialized, but the guiding principle is still the same. Sequential batch processing remains the most commonly applied methodology for the production of chemicals that we need for our society, such as active pharmaceutical ingredients, fine chemicals, food additives, and agrochemicals (*3*).

A conceptually different approach to chemical synthesis is to pump the reagents in a continuous flow through a tubular or chip-based reactor (see the figure). The reactor can be cooled, heated, or irradiated with light and can contain immobilized reagents, catalysts, or scavengers that remove unwanted side products or trace metals. The increased surface-to-volume ratio of flow reactors results in certain advantages over classical batch processing such as improved heat and mass transfer. This reduces synthesis time, increases efficiency, considerably improves mixing of reaction partners, and avoids the formation of hot spots, which can lead to unwanted side products (*4*).

The closed nature of flow reactors offers many other advantages. For example, it allows superheating of solvents beyond their boiling point, shortening production times by increasing reaction rates. Using temperatures and pressures that are classically inaccessible provides a novel process window (*2, 5*). Hazardous and highly toxic compounds or unstable reaction intermediates are kept in a closed system, increasing process safety and moving the process toward closer agreement with the principles of green chemistry (*6*).

By nature, flow processes are suitable for automation. This offers interesting possibilities, such as running sequential reaction steps consecutively without isolation of intermediates, real-time inline diagnostics for optimum reaction parameter control, minimization of compound and solvent consumption by miniaturization, and continuous operation (*7*). Flow principles can be applied to reaction scales ranging from nanograms to tons. Even relatively small reactors can generate kilograms of material per day.

Flow processes have been used for many years for the production of a number of commodity chemicals, particularly in the petrochemical industry. However, flow chemistry has only recently become an accepted and enabling tool for the modern medicinal chemist (*8, 9*). Its adoption in medicinal synthesis has been facilitated by the advent of several vendors providing specialized modular and rapidly reconfigurable devices for running different types of reactions. Flow chemistry has expanded synthetic capabilities and opened new avenues for the efficient assembly of complex natural compounds and important medicines (*10*–*13*).



Pharmaceuticals on demand. Medicinal chemistry has traditionally relied on batch synthesis. Adamo *et al.* instead use flow chemistry for on-demand production of medicine doses in a desktop machine. The work illustrates the potential of flow chemistry for fine-chemicals production.

Flow technologies have the potential to be very powerful not only for the synthesis and purification of novel compounds, but also for merging chemical, analytical, and biological procedures into a single continuous process. This would minimize spatiotemporal barriers and foster a cost-efficient lead discovery process. Werner *et al.* have shown that a flow-based biochemical assay can be seamlessly integrated into a fully automated flow synthesis, purification, compound quantification, and biological testing system (*14*). An hour after the injection of starting materials, potency data against a given biological target are available. This unprecedented reduction in synthesis-testing cycle times could help to speed up the generation of structure-activity relationship data, thereby accelerating the drug discovery process.

How will flow technologies influence the way we produce pharmaceuticals in the future? Advances in flow technology such as that demonstrated by Adamo *et al.* are pushing the boundaries of synthetic capability. The pharmaceutical industry has already devoted substantial resources to transferring traditionally batch-style processes to flow-type architecture to reduce infrastructure investments and make the industry fit for on-demand production.

The work by Adamo *et al.* offers tantalizing prospects of on-demand drug delivery in emergency and specialized cases, such as epidemics of rare diseases in refugee camps or after natural disasters. Issues remain with regard to accessibility of cartridge refills, waste disposal, and how to avoid the production of illicit substances. However, the major advance in this work lies not in the delivery of a desktop drug synthesis machine, but in demonstrating the great potential of flow chemistry in drug production. This brings the prospect of safer, more efficient, and sustainable pharmaceutical production through flow technologies closer to reality. ■

REFERENCES

1. A. Adamo *et al.*, *Science* **352**, 61 (2016).
2. J. Wegner, S. Ceylan, A. Kirschning, *Chem. Commun.* **47**, 4583 (2011).
3. S. Kobayashi, *Chem. Asian J.* **11**, 425 (2016).
4. D. Tyler McQuade, P. H. Seeberger, *J. Org. Chem.* **78**, 6384 (2013).
5. V. Hessel, D. Kralisch, N. Kockmann, T. Noël, Q. Wang, *ChemSusChem* **6**, 746 (2013).
6. P. T. Anastas, J. C. Warner, *Green Chemistry: Theory and Practice* (Oxford Univ. Press, New York, 1998), p.30.
7. D. Webb, T. J. Jamison, *Chem. Sci.* **1**, 675 (2010).
8. L. Malet-Sanz, F. Susanne, *J. Med. Chem.* **55**, 4062 (2012).
9. C. Wiles, P. Watts, *Future Med. Chem.* **1**, 1593 (2009).
10. I. R. Baxendale *et al.*, *Chem. Commun.*, 2566 (2006).
11. S. Newton *et al.*, *Angew. Chem. Int. Ed.* **53**, 4915 (2014).
12. F. Lévesque, P. H. Seeberger, *Angew. Chem. Int. Ed.* **51**, 1706 (2012).
13. M. D. Hopkin, I. R. Baxendale, S. V. Ley, *Chem. Commun.* **46**, 2450 (2010).
14. M. Werner *et al.*, *Angew. Chem. Int. Ed.* **53**, 1704 (2014).

10.1126/science.aaf3065

ILLUSTRATION: P. HUEY/*SCIENCE*

Published by AAAS

BOOKS *et al.*

THEATER

Identity theft

Inspired by true events, a new play explores a controversial case of gender reassignment

By **Oliver Vikbladh**

In 1966, when David Reimer and his twin brother were only 7 months old, they were brought to a local hospital to be circumcised. A piece of equipment malfunctioned, and David emerged from the operation with his penis obliterated. Desperate and devastated, his parents turned to John Money, a well-known clinical psychologist and influential researcher of human sexuality at Johns Hopkins University, often credited with coining the term "gender identity."

Money had developed a theory on how gender roles emerge, one that emphasized the primacy of nurture over nature. He advised the Reimers to allow doctors to surgically construct female genitalia from David's remaining tissues and to raise him as a girl, unaware of what had transpired.

Money had previously overseen similar interventions on intersex individuals. It is unclear, however, whether the Reimers understood that David would be the first child unambiguously born a boy to receive the treatment.

In the end, the Reimers followed Money's recommendations—a decision they would later regret. By his own adult account, David spent a traumatic early childhood feeling like a boy trapped in the body of a girl (*1*). At the age of 38, he took his own life, having lived as male since age 13.

In her new play, *Boy*, now on stage at the Clurman Theatre in New York City, playwright Anna Ziegler presents an engrossing, fictionalized account of the Reimer case. In one of the opening scenes, a woman composes a letter to Dr. Wendell Barnes: "You said we are shaped by society and not biology … and for the first time in a long time I felt some…hope," she writes, after relaying the tragic story of her son's botched circumcision. "[O]ne should do whatever one can to ease unnecessary suffering, however radical," Barnes later replies.

The play unfolds through two parallel narratives. One depicts the complex relationship and growing affection between Barnes and Samantha, a young patient struggling with her identity. The other is a story of burgeoning love between Jenny and Adam, a young man with a dark past.



Bobby Steggert (left) and Ted Koch in a scene from *Boy*

The cast delivers a strong performance of a complex script that, although clear and sometimes moving, occasionally suffers from excessive exposition. Particularly impressive is Bobby Steggert, the actor cast in the story's central role, who excels at expressing a childlike innocence infused with confusion and bitterness. Steggert is aided by Linsay Firman's steady direction, which allows the two narratives to seamlessly intermix.

Perhaps the most complex character in the play is Barnes: highly educated, but naive, with a tendency for overabstraction. Discussing literature with Samantha, he remarks about Jane Eyre, "She is such a wonderful symbol, isn't she …," which prompts the confused response: "I didn't think she was a symbol. I thought she was a person."

The reviewer is at the Center for Neural Sciences, New York University, New York, NY 10003, USA. E-mail: omv208@nyu.edu

Boy
Anna Ziegler; directed by Linsay Firman
The Clurman Theatre, New York, NY
Through 9 April 2016



Barnes's pretensions are presented in sharp contrast with Doug, Sam's working-class father, who serves as a voice of reason throughout the play. Eventually, Doug confronts Barnes, questioning his motivation for taking on the case. "[W]e both know you never really cared about Sam. All you wanted was a doll to play dress-up with. To prove your theories with."

Similar accusations were leveled at John Money, who, despite evidence that all was not well, declared the David Reimer experiment a success. His work on the case amplified his fame and influenced the thinking of both scientists and doctors until David Reimer went public with his own account in 1997 (*2*).

Unfortunately, debates over medical and scientific misconduct are hardly a thing of the past. The current scandal surrounding Italian surgeon Paolo Macchiarini similarly highlights the ethical hazards that exist at the frontiers of biomedicine. Although Macchiarini was originally cleared of misrepresenting the success of a series of experimental trachea implants (*3*), subsequent revelations have called into question whether his patients, most of whom died, were sufficiently informed about the risks of his procedure.

It is, of course, almost impossible to know with certainty what motivates a doctor or scientist to take unjustifiable risks. Personal ambition, ideological zeal, or an appeal to some greater good might coexist within the same person. With *Boy*, however, Ziegler has opted for a generous, and perhaps therefore even more tragic, interpretation of the doctor's motives, depicting Barnes as acting out of misguided benevolence and love for the "daughter" he helped create. Ultimately, he faces his patient and the consequences of his methods in a cathartic exchange of the kind that the real David Reimer was never afforded.

REFERENCES

1. J. Colapinto, *As Nature Made Him: The Boy Who Was Raised as a Girl* (Harper Perennial, New York, 2001).
2. J. Colapinto, "The True Story of John/Joan," *Rolling Stone* (11 Dec. 1997), p. 54.
3. G. Vogel, *Science* **351**, 546 (2016).

10.1126/science.aaf6089

PHOTOS: (TOP) ZACK DEZON; (BOTTOM) CAROL ROSEGG

Downloaded from on March 31, 2016

Published by AAAS



PHOTO: SHIRONOSOV/ISTOCKPHOTO

SCIENCE LIVES

Life in the lab

A new memoir revels in the joys, sorrows, and occasional absurdities that come with a career in science

By **Meg Lowman**

"You may think a mushroom is a fungus. This is exactly like believing that a penis is a man." If this evocative statement does not capture your attention, then perhaps nothing will. Hope Jahren, the woman who wrote it, could be described as the Jane Goodall of botany. Whereas Goodall's writing elevated chimps to the top of our lists of charismatic megafauna, Jahren has set out to draw attention to a much more challenging group of organisms. In her new book, *Lab Girl*, she has transformed the sedentary, slow-growing lives of plants into a vibrant series of stories that are interwoven with tales of her own research career in the field of paleo-plant physiology.

As a field biologist myself, with the entire forest as my laboratory, I gained enormous insights into the world of the indoor laboratory from this book. Jahren sets the record straight about the value of having a scientific "base camp" as a place to ask pivotal questions. "My lab is the place where I put my brain out on my fingers and I do things. My lab is a place where I move. I stand, walk, sit, fetch, carry, climb, and crawl. My lab is a place where it's just as well that I can't sleep, because there are so many things to do in the world besides that," she writes. "All the baffling things that arrived unwelcome with adulthood—tax returns and car insurance and pap smears—none of them matter when I am in the lab."

The reviewer is at the California Academy of Sciences, San Francisco, CA 94118, USA. E-mail: canopymeg@gmail.com

Lab Girl
Hope Jahren
Knopf, 2016. 300 pp.



Jahren tells it like it is, mincing no words to describe the loneliness and uncertainty she experienced early in her scientific career. Recalling her first semester as an assistant professor, she writes, "I think I made more mistakes on the homework than the students did."

She is equally frank about the creative efforts that went into setting up her first laboratory. "We went to the Salvation Army and got old camping equipment for the lab and amateur oil paintings for my office. We visited the state surplus warehouse, where anyone with a Georgia state employee ID card could help themselves to the mountain of outdated equipment that had been discarded by local government agencies."

The characters who populate Jahren's world are as lively as the drought-stressed plants she studies. Her longtime friend and lab manager, Bill, is central to the narrative, playing the part of the quiet and reliable fixer and confidant.

"Science has taught me that everything is more complicated than we first assume," writes Jahren.

The stories she shares are compelling because they are relatable. How many of us have a "Bill" in our lives: a Renaissance man or woman who can resolve seemingly hopeless dilemmas and is there to listen during times of doubt? And although not all of us have had a student who crashed the university van en route to a conference, we all have at least a few student-related tales of woe.

I must admit to reading this book twice—once for the incredible descriptions of plant physiology and botanical experiments and the second time to focus on Jahren's life as a woman working in a field that is predominantly male. In the end, I am not sure which is more extraordinary, the plants or the woman who studies them. If the next generation of scientists have role models like Jahren, then the world of science will be better off indeed.

Our libraries are full of books written by Darwin, Pasteur, Leakey, Ehrlich, and many hundreds of acclaimed male scientists. The shelf of titles by women doing science is much smaller, yet it is growing. As a woman who has written a book about her own (mis) adventures in science (*1*), I look forward to the day when my bookshelf reflects the rich diversity of all those who are engaged in the scientific enterprise.

REFERENCES

1. M. Lowman, *Life in the Treetops: Adventures of a Woman in Field Biology* (Yale Univ. Press, New Haven, CT, 1999).

10.1126/science.aaf2161

Downloaded from on March 31, 2016

Published by AAAS

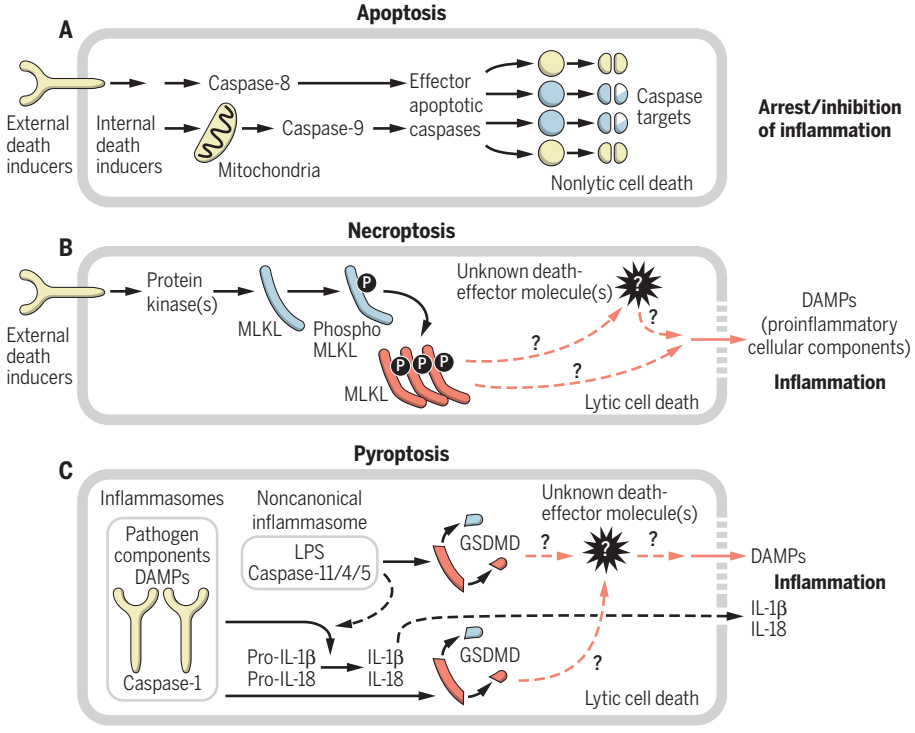
REVIEW SUMMARY

CELL DEATH PATHWAYS

Programmed necrosis in inflammation: Toward identification of the effector molecules

David Wallach,* Tae-Bong Kang, Christopher P. Dillon, Douglas R. Green*

BACKGROUND: Inflammatory lesions often contain dead cells. Cell death in developmental processes characteristically occurs by apoptosis, a form of programmed cell death in which dying cells are phagocytized before undergoing membrane damage. In inflammation, however, cell death is often necrotic, where cellular constituents are released after membrane rupture. The death of cells in inflammation was until recently thought to result from other changes in the inflamed tissue. This view has changed, however, owing to several findings: that necrotic cell death can be induced by biomolecules known to initiate inflammation [such as the cytokine tumor necrosis factor (TNF) or the pathogen component lipopolysaccharide (LPS)]; that it can be dictated in a programmed manner by distinct sets of signaling mechanisms; and that it yields release of some cellular components capable of facilitating inflammation. It now seems probable that necrotic cell death is not always a consequence of inflammation, but is sometimes rather its trigger. To confirm this notion, we need reliable tools for detection of programmed necrosis in vivo. Because programmed necrosis cannot be distinguished morphologically from accidental cell death, its identification in inflamed tissues must be based on its distinctive molecular details.



Effector mechanisms in lytic and nonlytic cell death (**A**) In apoptosis, caspases cleave substrate proteins that orchestrate the cell-death process. (**B**) In necroptosis, protein kinases phosphorylate MLKL, thereby activating it. Phospho-MLKL then causes cell lysis. (**C**) In pyroptosis, other caspases cleave and hence activate gasdermin-D (GSDMD), thus causing death. These caspases also activate cytokines IL-1β and IL-18. In both necroptosis and pyroptosis, the cell membrane ruptures, releasing cellular components that may trigger inflammation.

ADVANCES: We now have quite detailed knowledge of the mechanisms initiating apoptotic cell death and those initiating two forms of programmed necrosis—necroptosis and pyroptosis. Apoptosis is triggered by proteases of the caspase family. Necroptosis is triggered by specific protein kinases, most crucially receptor-interacting protein kinase–3 (RIPK3). Pyroptosis is triggered by caspases distinct from those mediating apoptosis, and whose activation yields proteolytic activation of the inflammatory cytokines interleukin-1β (IL-1β) and IL-18. All of these molecular initiators of death programs, however, also contribute to the initiation of nondeadly cell functions and are thus not specific markers for death. Two proteins were recently found to act further downstream in the signaling pathways leading to programmed necrosis. One, the pseudokinase mixed lineage kinase domain–like protein (MLKL), is crucial for necroptosis. The other, gasdermin-D (GSDMD), after cleavage by the pyroptosis-mediating caspases, is a major player in their induction of death. Mere expression of activated MLKL, or of the N-terminal proteolytic fragment of GSDMD, can trigger necrotic death. The finding that MLKL and GSDMD play roles in necroptosis and pyroptosis raises hopes that we are approaching the identification of molecules that exclusively serve these forms of death.

ON OUR WEBSITE

Read the full article at http://dx.doi.org/10.1126/science.aaf2154

OUTLOOK: What are the parameters that can reliably allow us to define a cause-effect relationship between necrotic death and inflammation—and more generally, to define the causal relationships between any disease and its co-occurring pathogenic events? In the case of cell death, this question boils down to the need to identify molecular events that contribute specifically enough to allow their use as definitive molecular probes. The effectors of death—proteins found to mediate deadly changes in the cell—are likely to have that absolute specificity. Whether MLKL and GSDMD are such death effectors has yet to be established. Some studies suggest that MLKL directly permeabilizes membranes, whereas others suggest that it does not. Regarding GSDMD, there is still no knowledge of the mechanisms by which its N-terminal fragment triggers death. Identifying death-effector molecules will be of immense importance to medicine. Such molecules will not only be the best markers for detecting programmed necrosis, but will also serve as the optimal targets for its pharmaceutical arrest in disease. ■

The list of author affiliations is available in the full article online.
*Corresponding author. E-mail: d.wallach@weizmann.ac.il (D.W.); douglas.green@stjude.org (D.R.G.)
Cite this article as D. Wallach *et al.*, Science 352, aaf2154 (2016). DOI: 10.1126/science.aaf2154

Downloaded from on March 31, 2016

REVIEW

CELL DEATH PATHWAYS

Programmed necrosis in inflammation: Toward identification of the effector molecules

David Wallach,[1]* Tae-Bong Kang,[2] Christopher P. Dillon,[3] Douglas R. Green[3]*

Until recently, programmed cell death was conceived of as a single set of molecular pathways. We now know of several distinct sets of death-inducing mechanisms that lead to differing cell-death processes. In one of them—apoptosis—the dying cell affects others minimally. In contrast, programmed necrotic cell death causes release of immunostimulatory intracellular components after cell-membrane rupture. Defining the in vivo relevance of necrotic death is hampered because the molecules initiating it [such as receptor-interacting protein kinase–1 (RIPK1), RIPK3, or caspase-1] also serve other functions. Proteins that participate in late events in two forms of programmed necrosis [mixed lineage kinase domain–like protein (MLKL) in necroptosis and gasdermin-D in pyroptosis] were recently discovered, bringing us closer to identifying molecules that strictly serve in death mediation, thereby providing probes for better assessing its role in inflammation.

"When I use a word…it means just what I choose it to mean—neither more nor less." This declaration from Lewis Carroll's *Through the Looking Glass* aptly describes a common practice of scientists. By defining terms and deciding what they stand for, they spur interest in testing the validity of their hypotheses; unlike Humpty Dumpty's assertion, however, terms defined by scientists often turn out to mean more than initially conceived.

The term "programmed cell death" has made a huge and persisting impact on cell death research (*1*). However, recent developments in cell death research have altered our view of what this term means. Until recently, programmed cell death was thought to occur only in one form, called "apoptosis." This form is characterized by induced changes that yield death in a way that minimizes its impact on neighboring living cells. Recent findings have revealed, however, that another form of death, "necrosis" or "oncosis," can also be dictated by defined molecular pathways. Necrosis involves release of the dying cell's intracellular components, and the effects of this release on neighboring cells can yield inflammation (*2*).

Based on the findings regarding apoptosis, programmed cell death was initially viewed as a set of mechanisms that act exclusively within the dying cell and serve only to dictate its demise. In programmed necrosis, the end of the plan of action toward death is believed to be not only death induction but also induction of inflammation, another complex programmed process capable of causing death in other ways. Here, we address the challenges faced in the study of programmed necrosis in vivo and the attempts to overcome them by harnessing the knowledge gained ex vivo. While there are various pathways by which necrosis can be "programmed," we focus here on those of necroptosis and pyroptosis. (See glossary in Box 1.)

[1]Department of Biomolecular Sciences, The Weizmann Institute of Science, 76100 Rehovot, Israel. [2]Department of Biotechnology, College of Biomedical and Health Science, Konkuk University, Chung-Ju 380-701, Korea. [3]Department of Immunology, St. Jude Children's Research Hospital, Memphis, TN 38105, USA.
*Corresponding author. E-mail: d.wallach@weizmann.ac.il (D.W.); douglas.green@stjude.org (D.R.G.)

Possible roles of lytic and nonlytic cell death in inflammation

Inflammation is a multicellular process that destroys pathogens and promotes recovery from injury through a variety of cooperating changes, including cell death (*2*). Initially identified as a pathological phenomenon, cell death is still often described in pathology textbook chapters on tissue damage. Indeed, some of the most harmful consequences of infection and inflammation, including the massive damage to tissues in necrotizing fasciitis ("flesh-eating" syndrome) and the functional arrest of regions in the heart and brain pursuant to infarct and stroke, can be ascribed to massive cell death.

Various manifestations of the pathology of inflammation are known to be mediated by cellular functions that are potentially beneficial, yet cause damage when induced in excess. Similarly, when cell death in inflammation occurs in a restricted manner, its role can be beneficial, as in the elimination of injured or infected cells, which are taken up by phagocytosis as they die (*3*, *4*).

Phagocytic uptake of a dying infected cell, however, might not suffice to eradicate the pathogens that infected it, and might instead have the opposite effect. Being able to survive and replicate within cells, intracellular pathogens may continue to survive in the cells that engulf them and might thus exploit this uptake for their further spread. This is particularly true of pathogens that can withstand destructive activities within professional phagocytes. Indeed, a variety of harmful intracellular pathogens prosper in phagocytic cells, including *Mycobacterium tuberculosis*, *Shigella flexneri*, and others. In order for cell death to assist in destroying such pathogens, these pathogens must permeate through the cell membrane into the extracellular milieu, where they might be unable to grow and/or be exposed to other defensive mechanisms.

Lytic cell death can also contribute to defense in another way. Various intracellular components, once released from dying cells, can trigger inflammatory activities in other cells. By allowing the release of such "damage associated molecular patterns" (DAMPs), lytic cell death may self-amplify or even initiate the inflammatory process.

Thus, depending on the role that cell death might play in inflammation, it should optimally occur in one of two ways. For eliminating intracellular pathogens that resist destruction by intracellular defense mechanisms, death of the cells would preferably involve rupture of their membranes. In contrast, death destined to eliminate pathogens that are easily destroyed within professional phagocytes, or facilitation of repair by phagocytic uptake of malfunctioning cells, would be better served without membrane rupture (nonlytic cell death), thus maximizing removal of the cellular constituents and preventing DAMP-mediated perpetuation of inflammation.

Cell death also plays a role in promoting adaptive immune responses to antigens associated with the dying cells (e.g., produced by an infecting organism or by cancer-associated mutations). This "immunogenic cell death" is distinct from inflammation per se (*5*). Immunogenic cell death involves activation of dendritic cells and a process of "cross-priming," in which molecules in the dying cell are processed and presented on class I major histocompatibility complex (MHC) molecules in the dendritic cell for recognition by $CD8^+$ T lymphocytes (*6*).

Apoptosis—a nonlytic form of death mediated by proteases of the caspase family

The characteristics of apoptotic cell death minimize disturbance of living cells by the dying cells. This cell death program is prevalent in development and tissue remodeling, processes not associated with inflammation. When apoptosis occurs in inflammatory lesions, it might actually serve to terminate the inflammation. In apoptosis, a group of structurally related proteases called "effector" (or "executioner") caspases (in humans, caspase-3, -6, and -7) cleave specific target sites in numerous cellular proteins. These caspases initiate multiple enzymatic and structural changes that lead to the morphological and functional changes characteristic of apoptosis. As expected for a programmed process, the various molecular pathways that are targeted for cleavage by the

Box 1. Glossary of terms.

Apoptosis: a programmed form of nonlytic cell death resulting from the activation of effector caspases via a variety of upstream signals

Caspases: cysteine-dependent aspartate-directed proteases that cleave numerous targets in the cell after activation by upstream signals

Cross-priming: the process of uptake and presentation of antigen on class I MHC by phagocytic cells such as dendritic cells in order to activate CD8 response

Damage associated molecular patterns (DAMPs): a series of intracellular components released upon cellular damage that induce inflammatory activities in other cells

Effector caspase: a caspase activated via an initiator caspase that targets cellular proteins for cleavage and orchestrates the process of apoptosis; also referred to as an executioner caspase

IL-1β: an inflammatory cytokine produced in proform requiring caspase cleavage for maturation and release

Immunogenic cell death: cell death that directly activates the immune response through uptake of the dying cells and presentation of associated antigens to T lymphocytes

Inflammasome: a general term for macromolecular complexes acting as activation platforms for caspase-1, -4, -5, or -11

Inflammation: a complex biological response involving production of cytokines to recruit innate and adaptive immune cells in order to eliminate the initial insult, clear out damaged tissue, and initiate the repair process through a variety of cooperating functional changes

Inflammatory caspases: caspases 1 and 11 in mouse and 1, 4, and 5 in human whose activation leads to the processing of IL-1β

Initiator caspase: a regulatory caspase that requires the formation of a macromolecular complex for activation, and functions to activate effector caspases

Koch postulates: a set of four criteria published by the German physician Robert Koch in 1890 designed to evaluate the causative link between a microbe and disease

Lytic cell death: cell death that results in the acute permeabilization of the plasma membrane

Necroptosis: programmed form of lytic cell death in which RIPK3 activation leads to downstream activation of MLKL and the acute permeabilization of the plasma membrane

Nonlytic cell death: cell death in which cells are packaged for disposal by phagocytes, generally preventing the release of intracellular contents

Phagocytosis: the process of a cell (i.e., macrophages, dendritic cells) ingesting cell fragments or microorganisms, leading to the formation of a vacuole to degrade the engulfed components

Pleiotropy: the phenomenon in which something, such as a protein, plays more than one, often opposing, role in cellular processes; for example, caspase-8 is necessary for death receptor–mediated apoptosis, but restrains necroptosis

Programmed cell death: originally referred specifically to cell death that is "programmed" in development, but now taken to mean any cell death engaged by an active predestined molecular mechanism

PRR: pattern recognition receptor; cellular proteins evolved to specifically bind components of pathogens and to initiate signaling for defense

Pyroptosis: lytic form of cell death characterized by activation of inflammatory caspases and usually associated with secretion of IL-1β and IL-18

effector caspases are evolutionarily conserved (*7*). Some of these molecular pathways serve to safeguard against the release of DAMPs, limiting the initiation of inflammation; other molecular features actively suppress inflammatory activity by leukocytes (*8*).

The ability of a wide range of different inducers to activate the same apoptotic program has been ascribed to the existence of molecular hubs that convey activating signals to the effector caspases through some other members of the caspase family defined as "initiator caspases." In the so-called "intrinsic cell death pathway," effects of intracellular death inducers converge, mainly through the function of members of the Bcl-2 protein family. The latter act to permeabilize the outer membranes of the mitochondria, releasing cytochrome c and other intermembrane space proteins. Cytochrome c triggers the oligomerization of an adapter protein, APAF1, which then binds and thereby activates the initiator caspase, caspase-9 (*9*, *10*).

In the extrinsic cell death pathway, signals emanating from the receptors for tumor necrosis factor (TNF) and from some other membranous receptors converge to oligomerize the adapter protein FADD/MORT1. This in turn binds and thus activates another initiator caspase, caspase-8 (*11*).

In both the intrinsic and the extrinsic cell death pathways, the triggering of apoptotic death occurs by imposed dimerization of the initiator caspases within distinct signaling complexes. Association of the caspases with their adapter proteins in these complexes is mediated by homotypic binding domains encompassing one of four related "death-fold" motifs (*12*). Once activated, caspase-8 and -9 proteolytically process and activate effector caspases.

Necroptosis—a regulated, lytic cell death involving specific kinases

The term "necrosis" (or "oncosis") refers to all forms of death that are characterized by swelling of the cells and their organelles, followed by permeabilization of the cellular membranes. This is the typical pattern of death of cells in response to accidental damage, and also of the two forms of programmed cell death described here—necroptosis and pyroptosis. Whereas the morphologic features of apoptosis, both in vivo and in cell culture, distinguish it clearly from other forms of cell death, there is currently no way to distinguish necroptosis or pyroptosis from accidental necrotic death merely by visual inspection of the cells. Our knowledge of those forms of programmed death and their consequences is therefore largely restricted to information based on identifying the molecules involved, either in vitro or through the use of genetically modified animals in vivo.

The discovery of necroptosis can be traced back to the seminal finding in 1965 that certain leukocyte-produced cytokines, called lymphotoxins, cytotoxins, or TNF, can trigger cell death (*13*, *14*). This death was initially reported to occur by apoptosis. By 1988 it had been clarified, however, that in some cells, TNF also triggers necrotic death (*15*).

The most upstream signaling activity required for induction of necroptosis by a TNF ligand family member is the protein kinase function of receptor-interacting protein kinase–1 (RIPK1) (*16*, *17*) (Fig. 1). Several other biological stimuli trigger necroptosis independently of RIPK1: the interferons (IFNs) exert necroptotic effects that depend on the interferon-induced protein kinase PKR (*18*, *19*). Also, Toll-like receptor 3 (TLR3), a membrane-anchored receptor for viral nucleic acid, induces necroptosis via the adapter protein TRIF (*20*). Some viruses can also trigger necroptosis independently of RIPK1. The cell death response to mouse cytomegalovirus (MCMV) infection, for example, employs the IFN-induced protein DAI (*21*–*23*). Unlike RIPK1, neither TRIF nor DAI possesses protein-kinase or any other enzymatic activity.

The protein kinase RIPK3 acts downstream of RIPK1 in the necroptotic signaling pathway (*24*–*26*). It is activated by associating with RIPK1, TRIF or DAI, with which it associates via a RIP homotypic interacting motif, RHIM. Strong negative regulation of the initiation of signaling for necroptosis is mediated by caspase-8 together with a caspase-like molecule, c-FLIP$_L$ (*16*, *27*, *28*), and by the ubiquitin ligases cIAP1 and cIAP2 (*29*). The last two mediate their effect by facilitating the anchorage of K63-linked polyubiquitin chains to RIPK1, thereby arresting the integration of RIPK1 into the signaling protein complex that initiates necroptosis.

RIPK3 mediates necroptosis by binding mixed lineage kinase domain–like protein (MLKL), a

protein kinase homolog that, despite binding adenosine 5′-triphosphate, is devoid of protein kinase activity (*30*, *31*). RIPK3 phosphorylates MLKL, thereby imposing a conformational change that negates a self-inhibitory effect of the kinase-homologous C-terminal region in MLKL. This allows the N-terminal coiled-coil region to impose oligomerization of the MLKL molecules and subsequent cell lysis (*32*–*34*). Mere expression of the coiled-coil portion of MLKL, or of MLKL mutants in which the coiled-coil region is constitutively exposed, is toxic to cells (*33*, *35*, *36*). MLKL is therefore currently believed to be the major and perhaps the only RIPK3 target that mediates this form of death.

However, RIPK3 also participates in signaling to other processes, including other forms of cell death, independently of MLKL. Kinase-inactive RIPK3 can signal, via RIPK1, to trigger caspase-8–mediated apoptosis (*37*–*39*). Several metabolic enzymes (*24*), as well as PGAM5, a mitochondrial protein with serine-threonine phosphatase activity (*40*), bind RIPK3 and contribute to induction of reactive oxygen species (ROS) and production of inflammatory cytokines. In addition, RIPK3 binds Ca^{2+}-calmodulin–dependent protein kinase (CaMKII) and activates it. Induction of necrotic death of cardiomyocytes by oxidative stress appears to depend on the RIPK3-mediated activation of CaMKII and on the above metabolic enzymes. This death also appears to involve the generation of ROS and the function of cyclophilin-D—a key regulator of the mitochondrial permeability transition (MPT) pore—but not MLKL (*41*). MPT-mediated regulated necrosis is believed to occur by mechanisms distinct from those mediating necroptosis (*42*). In some cells, induction of necroptosis can be suppressed by ROS scavengers (*43*), suggesting a cell-specific requirement for synergism of the two pathways in death induction.

That necroptosis is induced by TNF, a ligand for which almost all cells express receptors, might appear to suggest that this form of death is exerted in all cells. In reality, the situation is the opposite; almost all cells are normally resistant to the death-inducing activities of TNF. The cytotoxic activities of this cytokine are therefore usually assessed either by the use of certain transformed cell lines that are uniquely sensitive to them or in the presence of drugs that sensitize cells to those activities (inhibitors of caspase action, or of the function of the ubiquitin ligases cIAP1 and cIAP2, of RNA synthesis, or of protein synthesis).

This strict dependence of necroptosis on sensitizing mechanisms endows it with selectivity. Infection of cells by certain viruses sensitizes them to the cytotoxic activities of TNF and IFN (*44*, *45*). In the case of several of these viruses and some bacteria, the form of death so enhanced is necroptosis. One molecular effect through which these pathogens facilitate necroptosis is prevention of caspase action (and apoptosis) by caspase-inhibitory proteins that they express (Fig. 1). There are also viruses that facilitate necroptosis through the direct action of viral proteins that mimic the function of signaling proteins in the pathway.

On the basis of these observations, it is believed that necroptotic death has evolved to serve as a second line of defense, to assure that immune-mediated killing of pathogen-infected

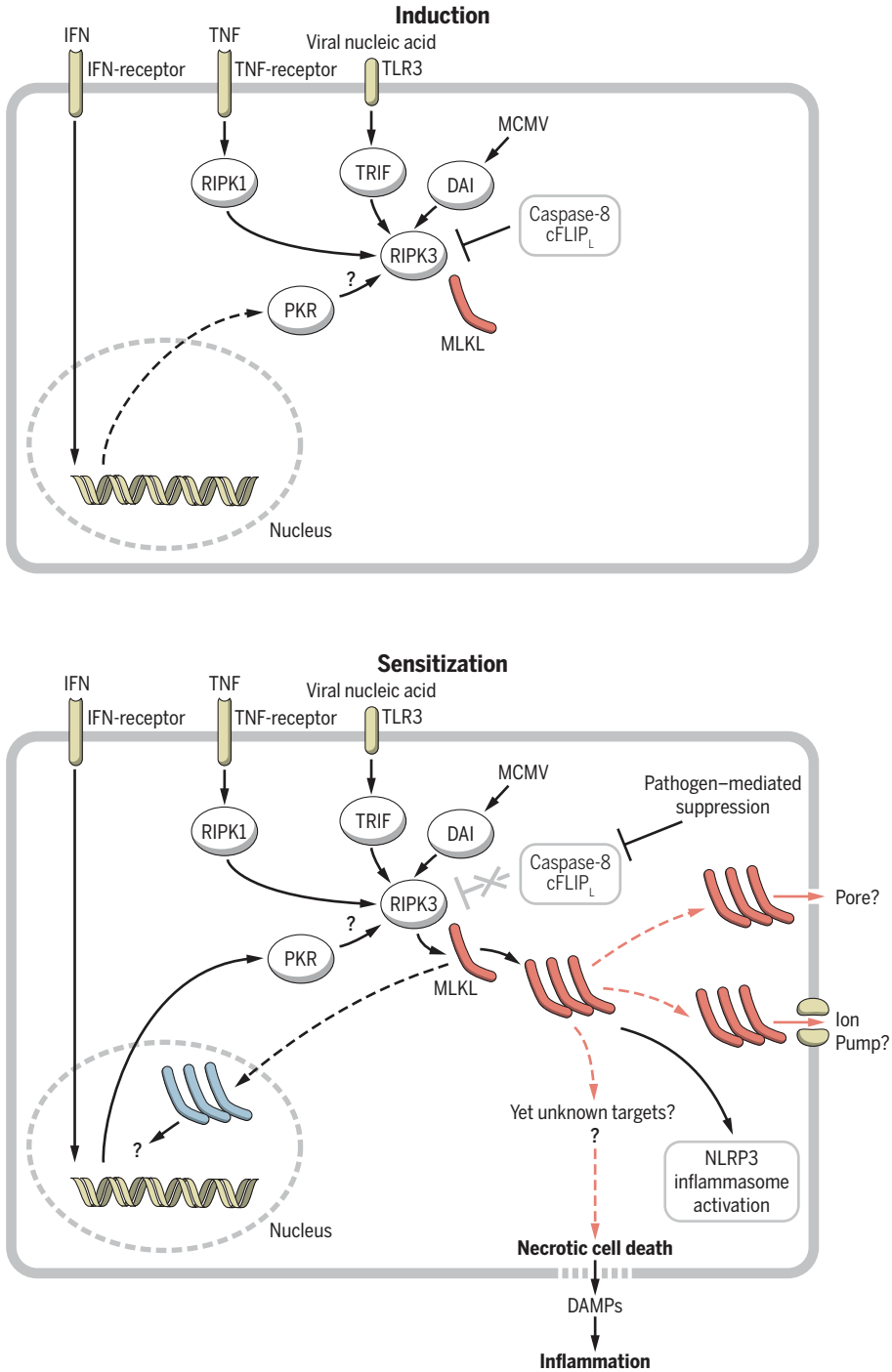


Fig. 1. Initiation of necroptosis: distinct roles of inducing ligands and sensitizing factors. Activation of the proteins that initiate signaling for necroptosis is controlled at two mechanistic levels. The first is induction, mainly by extracellular host-derived ligands such as TNF. This induction does not affect healthy cells because it is normally blocked by cellular inhibitory activities, such as that mediated by the proteolytic function of the caspase-8/cFLIP$_L$ complex (upper panel). The second level is sensitization, by pathogens and other agents that counteract the cellular inhibitory activities, allowing phosphorylation and oligomerization of MLKL and hence triggering of necrotic cell death (lower panel). The figure also depicts the various reported molecular consequences of MLKL activation. Those that might contribute to the induction of cell death are marked in orange.

cells occurs whenever the pathogen acts to block signaling for caspase-mediated apoptotic death. Some pathogens have further evolved to express proteins that block the induction of necroptosis. Conversely, some have usurped mechanisms of necroptosis induction for their own benefit [reviewed in (*46*)].

Pyroptosis—a pathogen-induced lytic form of death, associated with generation of inflammatory cytokines

Pyroptosis was discovered as a form of death that is inflicted on cells upon their infection by certain pathogens. It is usually associated with secretion of IL-1β and IL-18, proinflammatory cytokines generated by proteolyic processing of precursors located within the cytoplasm. Similarly to apoptosis, pyroptosis, as well as its accompanying generation of processed forms of IL-1β and IL-18, is mediated by specific members of the caspase family of cysteine proteases (the "inflammatory caspases"). These caspases—caspase-1 and -11 in mice and caspase-1 and two orthologs of caspase-11 (caspase-4 and -5) in humans—are structurally similar to the initiator caspases that signal for apoptosis. As alluded to in the term "pyroptosis" ("pyro" relating to fire or fever), the effects of DAMPs released from the dying cells, in combination with effects of the mature forms of IL-1β and IL-18, are believed to trigger inflammation. Such induced inflammation following rupture of the cellular membrane can effectively facilitate destruction of intracellular pathogens that have triggered the death program upon their exposure to the extracellular milieu (*47*).

Whereas necroptosis occurs in a wide variety of cell types, pyroptosis was observed mostly in professional phagocytes—macrophages, monocytes, and dendritic cells, where it contributes to defense against pathogens (*47*)—although it has also been reported in other cells. Similarly to necroptosis, pyroptosis can be triggered by intracellular pathogens—bacteria, viruses, and nucleated parasites—and, like necroptosis, it is facilitated by exposure of the cell to extracytoplasmic stimuli such as IFNs, TLR ligands, or TNF. However, the way in which these two groups of stimuli contribute to pyroptosis differs diametrically from how they contribute to necroptosis. In necroptosis, death signaling is usually initiated by extracytoplasmic ligands, and is facilitated by pathogens via the effects of pathogen-derived proteins that release the inhibition of this signaling by host-derived proteins. In contrast, extracytoplasmic ligands like TNF or those of the TLRs do not trigger signaling for pyroptosis, but only "prime" the cell for death induction by facilitating synthesis of the proteins that signal it. The actual triggering event is the recognition of intracellular pathogen components by "pattern recognition receptors" (PRRs), cellular proteins that have evolved to specifically bind components of pathogens, and consequently to initiate signaling for defense (Fig. 2).

Caspase-4, -5, and -11 are themselves PRRs; they are directly activated by Gram-negative bacteria in the cytoplasm within macromolecular signaling complexes called "noncanonical inflammasomes." This activation is mediated by binding of the lipid-A portion of lipopolysaccharide (LPS) to the caspases (*48*).

In the case of caspase-1, however, activation by pathogen components (as well as by DAMPs) occurs through the function of distinct proteins with PRR activity. These proteins bind caspase-1 by death-fold associations within "canonical inflammasomes." The currently known caspase-1–activating PRRs belong to three protein families: the NOD-like receptor (NLR) and the tripartite motif–containing (TRIM) families that mediate activation of caspase-1 by bacterial proteins such as the flagellin of *Legionella pneumophila* and by DAMPs, and the Pyrin and HIN domain (PYHIN; also known as AIM2-like receptors, ALRs) family of PRRs that mediate activation of caspase-1 by cytoplasmic or nuclear DNA of pathogens or by misplaced host nucleic acids.

Some of the caspase-1–activating PRRs bind caspase-1 directly. Others employ ASC (apoptosis-associated speck-like protein containing a CARD), an intermediate adapter protein that serves as a means of signaling amplification. Upon activation, ASC self-associates, forming in each cell a single huge aggregate ("Spek") that massively activates caspase-1 and also induces its self-processing [reviewed in (*49*)].

The functional roles of caspase-1 and of caspase-4, -5, and -11, although interrelated, are apparently somewhat different. Whereas all of them cause pyroptosis, the accompanying processing of IL-1β and IL-18 appears to require caspase-1. The processing of IL-1β and IL-18 by caspase-4, -5, and -11 is indirectly mediated via activation of caspase-1 by the inflammasome containing the PRR NLRP3 (*49*).

Besides cleaving the precursors for IL-1β and IL-18, the inflammatory caspases also cleave several other proteins. This cleavage serves various functions (*50*, *51*). Recent studies revealed that cleavage of gasdermin-D (GSDMD) by these caspases contributes to death induction (*52*–*54*). The N-terminal fragment of GSDMD generated by this cleavage is by itself cytotoxic. Moreover, cells deficient in GSDMD are fully resistant to the induction of pyroptosis by caspase-11. They are also less sensitive to the pyroptotic effect of caspase-1, but are not fully resistant to it (*52*–*54*).

Identifying programmed necrosis in inflamed tissues: A chicken-and-egg conundrum

As mentioned above, inflammation is frequently associated with cell death. This phenomenon has attracted particular attention in situations where cell death is a major pathological determinant—for example, in the massive destruction of liver tissue in acute hepatitis, the loss of lymphocytes in septic shock, or damage to the heart muscle as a result of infarct or to the brain as an outcome of stroke. The identification of distinct sets of mechanisms that dictate programmed death raises hopes that drugs designed to target these mechanisms will be therapeutic in such pathological situations (*42*, *55*). Moreover, the finding that specific molecules control certain forms of necrotic death that can initiate inflammation suggests that drugs targeting these molecules might allow arrest of some inflammatory processes.

To achieve such goals, however, we must first find ways to identify those pathological situations in which specific forms of programmed cell death occur. We must then identify those situations in which these death programs serve an initiating role. Acquiring such knowledge is hampered, however, by the lack of means to distinguish between necrotic death that was inflicted in a programmed and in a nonprogrammed manner. Nonprogrammed necrotic death is likely to occur in inflammation, which characteristically involves isolation of the injured site. Restriction of the access of nutrients and oxygen to the isolated cells may suffice to cause their death. Mere dissociation of cells through effects of extracellular digestive enzymes generated by leukocytes may also result in death, because cells must constantly receive survival signals from their neighbors and from the extracellular matrix. Cells can be killed by toxic compounds released by leukocytes, by ROS produced by leukocytes, by complement proteins, and by other agents generated at the site of inflammation [reviewed in (*2*)].

In the absence of a reliable analytical tool to distinguish necrotic death inflicted by any of the above-mentioned causes from necrotic death induced in a programmed manner, we will continue to encounter a chicken-and-egg conundrum. We will be unable to tell whether the co-occurrence of necrotic death and inflammation in a particular situation reflects an initiating role of the death in the observed inflammation or elicitation of this death by the inflammatory process. Because the morphological analysis of cells that die in the course of inflammation does not suffice to permit this distinction, we must base it on our mechanistic knowledge of programmed necrotic processes. For this, however, we must identify molecular parameters that are specific enough to allow definitive identification of such processes.

Rigorous definition of parameters is always required for specifying causal relationships between disease and co-occurring, potentially pathogenic, events. An example of such rigorous definition is the set of "Koch postulates" formulated over a century ago in an attempt to define the causal roles of specific infectious agents in diseases. Similar rigorous criteria must be applied to the molecular probes used to identify distinct forms of programmed cell death and establishing the causal role of these death forms in inflammation (Table 1).

Are we approaching identification of molecular probes specific to distinct forms of programmed cell death?

Attempts over the years to define molecular probes specific to programmed cell death have been hampered by the fact that those same molecules with important roles in death also contribute to various functions of living cells (*56*).

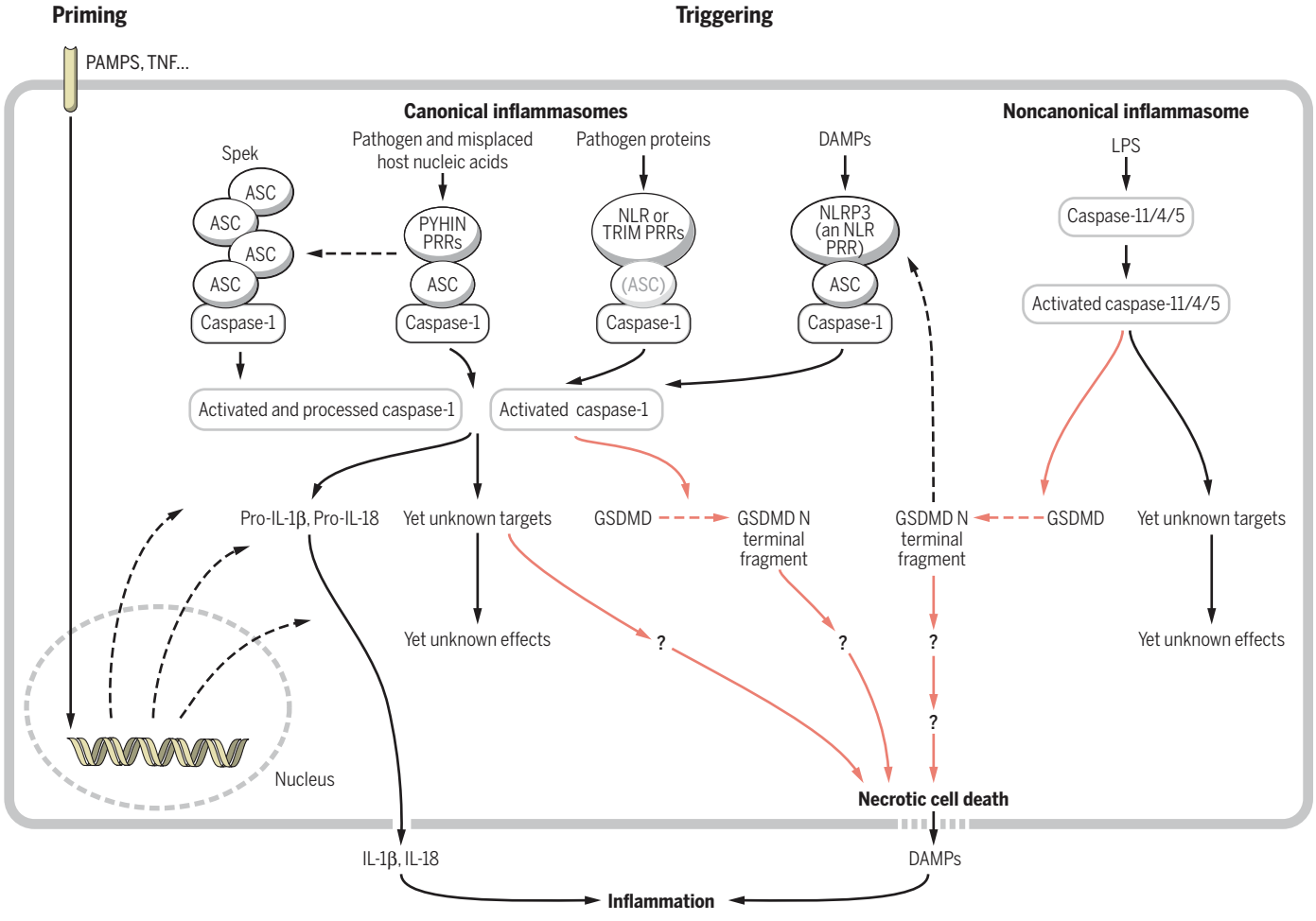


Fig. 2. Induction of pyroptosis: distinct roles of priming and triggering stimuli and of "canonical" and "noncanonical" inflammasomes. Signaling for pyroptosis is regulated on two mechanistic levels, as in the case of necroptosis, but in a sort of inverse manner. The first level has to do with effects of extracytoplasmic ligands like TNF and PAMPs that "prime" the cell by activating genes encoding the signaling proteins. The second level is the actual triggering of signaling by components of intracellular pathogens and by DAMPs. This induction involves two distinct groups of signaling mechanisms. Most of the agents that induce pyroptosis do so by binding specific PRRs of the NLR, TRIM, or PYHIN families, thereby triggering the activation of caspase-1 within macromolecular complexes called the "canonical inflammasomes." Some of these inflammasomes also contain the protein ASC, which, once activated, self-associates in a huge complex ("Spek") that both activates caspase-1 and facilitates its self-processing. In addition, intracellular LPS triggers pyroptosis by directly binding caspase-11 (in the mouse) or caspase-4 or -5 (in humans), activating these inflammatory caspases within the so-called "noncanonical inflammasome." The caspases cleave a variety of target proteins that serve different functions. Their cleavage of GSDMD triggers pyroptosis through a yet-unknown effect of the GSDMD N-terminal domain. Other yet-unknown targets of caspase-1 also trigger pyroptotic death. Activation of IL-1β and IL-18 in the course of pyroptosis is mediated by processing of the precursors of these inflammatory cytokines by caspase-1. Caspase-11, -4, and -5 are incapable of processing these precursors. However, they impose this processing indirectly via activation of caspase-1.

The function of the protein kinase RIPK1 provides a typical example of the pleiotropic effects of proteins serving proximal roles in signaling pathways activated by TNF. A C-terminal death-domain motif in RIPK1 mediates activation of the extrinsic apoptotic pathway through association with the adapter protein FADD/MORT1. Another region within it (the "intermediate domain") is targeted to ubiquitination, and then initiates signaling for nuclear factor κB (NF-κB) activation and hence induction of inflammatory and death-inhibitory genes. It also blocks activation of the extrinsic apoptotic death pathway through mechanisms independent of gene activation. Association of the RHIM domain in RIPK1 with a homologous region in RIPK3 has a dual effect on necroptosis induction: It restricts the spontaneous activation of RIPK3 and hence its spontaneous initiation of necroptosis, but is also required for necroptosis initiation by TNF and by some other inducing agents (*57*).

This complexity of RIPK1 function is underscored in recent studies of immunogenic cell death that occurs when cells undergo necroptosis. As discussed above, upon engulfment of a dying cell by a dendritic cell, antigens associated with the dying cell can be transferred to the class I MHC of the dendritic cell by "cross-priming," a process important for activation of antigen-specific T cells. Cells that have undergone necroptosis are particularly good at inducing such cross-priming. One study (*58*) suggested, however, that this process is dependent upon the activation of NF-κB by RIPK1 and that necroptotic cells that do not engage in such activation do not cross-prime, even though they induce inflammatory effects in dendritic cells.

Pleiotropy has also been observed in the functions of all other molecules found to participate in the proximal events of programmed cell death induction. The ubiquitin ligases cIAP1 and cIAP2 and the protease caspase-8, prominent negative players in necroptosis initiation, each has a variety of other functional roles. Such is also the case with RIPK3; this protein kinase, apparently crucial for the induction of necroptosis, also contributes, independently of cell death, to a growing number of other cellular activities (*59*–*62*).

Table 1. Defining "Koch postulates"–like rigorous tests for identification of death-effector molecules and their causative roles in inflammation.

Criteria that are indicative of causative role	Criteria indicative of a causative role of microbes in disease: the Koch postulates	Criteria indicative of the identity of death-effector molecules and their causative role in inflammation		
			The case of MLKL	The case of GSDMD
Documentation of co-occurrence	The microorganism is found in abundance in all organisms suffering from the disease, but not in healthy organisms.	The molecule is generated or activated in the dying cell prior to death.	Phosphorylation and membrane translocation of MLKL co-occur with necroptosis.	Caspase-mediated generation of an N-terminal fragment of GSDMD co-occurs with pyroptosis.
Characterization of the potentially causative element/effector molecule	The microorganism can be isolated from a diseased organism and grown in pure culture.	(a) Functional studies of the molecule demonstrate cell-killing potential. (b) Studies of the particular form of death induced by the molecule confirm the potential induction of inflammation by it.	*(a) MLKL might be able to form pores in membranes or activate ion channels.* (b) The expected release of DAMPs by necroptotic cells can potentially initiate inflammation.	*(a) No "deadly feature" of the GSDMD N-terminal fragment as yet identified.* (b) The expected release of DAMPs by pyroptotic cells can potentially initiate inflammation. Generation of IL-1β and IL-18
Documentation of exclusive cause-and-effect relationship	(a) The cultured microorganism causes disease when introduced into a healthy organism. (b) The microorganism can be re-isolated from the inoculated diseased experimental host and identified as identical to the original specific causative agent.	(a) Expression/activation of the molecule alone suffices to inflict death and consequent inflammation. (b) Ablation of the expression of the molecule prevents cell death and consequent inflammation. (c) The molecule can be shown to be incapable of triggering inflammation independently of death.	(a) Mere expression or mutational exposure of the MLKL coiled-coil domain triggers necroptosis *but has not yet been shown to trigger inflammation.* (b) Knockout and knockdown of MLKL block induction of necroptosis in vitro and of some inflammatory processes in vivo. *(c) MLKL seems also to have nondeadly functions. Those functions might yield inflammation in vivo.*	(a) Mere expression of the GSDMD N-terminal fragment triggers death *but has not yet been shown to trigger inflammation.* (b) GSDMD knockout abolishes caspase-11–mediated pyroptosis and decreases caspase-1–mediated pyroptosis. *(c) Generation of the GSDMD N-terminal fragment by caspase-11 triggers NLRP3-inflammasome–mediated generation of inflammatory cytokines, apparently independently of death.*

The caspases that serve crucial roles in the induction and execution of apoptosis, as well as those that induce pyroptosis, are also not death specific. Restrained activation of the "apoptotic caspases" contributes to induction of cell growth and differentiation (*63*). Activation of the inflammatory caspase-1, besides inducing pyroptosis, activates IL-1β and IL-18. It also has other functions; for example, it triggers activation of the sterol regulatory element–binding proteins (SREBPs), transcription factors that up-regulate lipogenic genes and thus promote cell survival, probably by facilitating membrane repair (*64*). Caspase-4, -5, and -11 not only induce pyroptosis but also trigger activation of IL-1β and IL-18 through the NLRP3 inflammasome. Their reported ability to cleave various other target proteins suggests that they serve other functions as well (*50*, *65*).

Among the nondeadly functions of the proteins that signal for programmed necrotic death are several that affect inflammation. Through such effects, these proteins might therefore also inflict necrotic cell death indirectly [e.g., (*55*, *66*)].

Of the early components of the pathways leading to programmed cell death, none has been found that is sufficiently specific to serve as a probe for its identification. It might nevertheless be possible to design such probes, based on our knowledge of those later events that are the most directly related to death. Recent developments in elucidation of the mechanisms underlying necroptosis and pyroptosis raise hopes that we are nearing the identification of such "death-specific" late events. MLKL, the last known component of the necroptotic signaling pathway, might be an effector molecule of death. The N-terminal coiled-coil region in MLKL, whose oligomerization is necessary and sufficient for induction of necroptosis, can bind certain lipids. This may suggest that it causes death by forming holes in the plasma membrane (*34*–*36*, *67*). Other reports suggest, however, that MLKL affects cell function and viability by association with intracellular membranes and specific protein targets (*32*, *40*, *68*). Activated MLKL molecules also translocate to the nucleus, and contain a nuclear localization signal in the C-terminal part. The nuclear translocation occurs independently of cell death and might contribute to some nondeadly functions (*69*). MLKL has also been reported to mediate activation of the inflammasome in dendritic cells, without any apparent association with cell death (*60*) (Fig. 1).

The recent discovery of the central role of GSDMD in pyroptosis has probably made a similar contribution to our state of knowledge of the mechanisms of programmed necrosis. There are still major gaps in our knowledge of this role. The biochemical activity of the caspase-generated fragment of GSDMD that induces death is unknown. It also seems that signaling for pyroptosis is not the only functional consequence of GSDMD cleavage, because cells deficient in GSDMD also fail to display caspase-11–mediated activation of IL-1β and IL-18 through the NLRP3 inflammasome (*52*). Besides, although GSDMD deficiency prevents induction of pyroptosis via caspase-11, it only partly decreases such induction by caspase-1, implying that its role in pyroptotic death is not absolute (*52*).

Box 2. Are MLKL and GSDMD the effector molecules in necroptosis and pyroptosis?

Table 1 summarizes the evidence pointing to MLKL and GSDMD as effectors of programmed necrosis, as well as the evidence indicating that, as a consequence, they are potential inducers of inflammation. Italic type indicates that the evidence is uncertain or lacking, or might argue against the above notions.

With regard to their effector abilities: Activated MLKL can associate with membranes in cells and form pores in artificial membranes, but it is not yet known whether the latter also occurs in living cells. Some studies provide evidence that MLKL might also mediate cell death in other ways.

For GSDMD, as yet, no evidence of a potential effector function of its death-inducing N-terminal fragment has been reported.

Also lacking is evidence that release of DAMPs in response to MLKL or GSDMD indeed yields inflammation. Nor is there any in vivo evidence that activation of MLKL alone or expression of its N-terminal fragment alone can initiate inflammation.

Concerning whether the functions of these two proteins are restricted to induction of necrotic death or inflammation, there is some evidence that they can serve other, nondeadly functions as well.

It has yet to be determined whether MLKL and GSDMD are indeed the actual effector molecules in the induction of necroptosis and pyroptosis (Table 1 and Box 2). However, the knowledge acquired about these molecules has undoubtedly brought us closer to identifying such effectors, and hence to establishing reliable tools for defining the in vivo relevance of programmed necrotic cell death.

REFERENCES AND NOTES

1. R. A. Lockshin, Z. Zakeri, Programmed cell death and apoptosis: Origins of the theory. *Nat. Rev. Mol. Cell Biol.* **2**, 545–550 (2001). doi: 10.1038/35080097; pmid: 11433369
2. D. Wallach, T. B. Kang, A. Kovalenko, Concepts of tissue injury and cell death in inflammation: A historical perspective. *Nat. Rev. Immunol.* **14**, 51–59 (2014). doi: 10.1038/nri3561; pmid: 24336099
3. A. Hochreiter-Hufford, K. S. Ravichandran, Clearing the dead: Apoptotic cell sensing, recognition, engulfment, and digestion. *Cold Spring Harb. Perspect. Biol.* **5**, a008748 (2013). doi: 10.1101/cshperspect.a008748; pmid: 23284042
4. K. Segawa, S. Nagata, An apoptotic 'eat me' signal: Phosphatidylserine exposure. *Trends Cell Biol.* **25**, 639–650 (2015). doi: 10.1016/j.tcb.2015.08.003; pmid: 26437594
5. G. Kroemer, L. Galluzzi, O. Kepp, L. Zitvogel, Immunogenic cell death in cancer therapy. *Annu. Rev. Immunol.* **31**, 51–72 (2013). doi: 10.1146/annurev-immunol-032712-100008; pmid: 23157435
6. A. Giodini, M. L. Albert, A whodunit: An appointment with death. *Curr. Opin. Immunol.* **22**, 94–108 (2010). doi: 10.1016/j.coi.2010.01.023; pmid: 20171862
7. E. D. Crawford *et al.*, Conservation of caspase substrates across metazoans suggests hierarchical importance of signaling pathways over specific targets and cleavage site motifs in apoptosis. *Cell Death Differ.* **19**, 2040–2048 (2012). doi: 10.1038/cdd.2012.99; pmid: 22918439
8. V. A. Fadok *et al.*, Macrophages that have ingested apoptotic cells in vitro inhibit proinflammatory cytokine production through autocrine/paracrine mechanisms involving TGF-beta, PGE2, and PAF. *J. Clin. Invest.* **101**, 890–898 (1998). doi: 10.1172/JCI1112; pmid: 9466984
9. S. W. Tait, D. R. Green, Mitochondria and cell death: Outer membrane permeabilization and beyond. *Nat. Rev. Mol. Cell Biol.* **11**, 621–632 (2010). doi: 10.1038/nrm2952; pmid: 20683470
10. T. Moldoveanu, A. V. Follis, R. W. Kriwacki, D. R. Green, Many players in BCL-2 family affairs. *Trends Biochem. Sci.* **39**, 101–111 (2014). doi: 10.1016/j.tibs.2013.12.006; pmid: 24503222
11. I. Budihardjo, H. Oliver, M. Lutter, X. Luo, X. Wang, Biochemical pathways of caspase activation during apoptosis. *Annu. Rev. Cell Dev. Biol.* **15**, 269–290 (1999). doi: 10.1146/annurev.cellbio.15.1.269; pmid: 10611963
12. H. H. Park *et al.*, The death domain superfamily in intracellular signaling of apoptosis and inflammation. *Annu. Rev. Immunol.* **25**, 561–586 (2007). doi: 10.1146/annurev.immunol.25.022106.141656; pmid: 17201679
13. G. A. Granger, W. P. Kolb, Lymphocyte in vitro cytotoxicity: Mechanisms of immune and non-immune small lymphocyte mediated target L cell destruction. *J. Immunol.* **101**, 111–120 (1968). pmid: 5690881
14. N. H. Ruddle, B. H. Waksman, Cytotoxicity mediated by soluble antigen and lymphocytes in delayed hypersensitivity. *J. Exp. Med.* **128**, 1267–1279 (1968). doi: 10.1084/jem.128.6.1267; pmid: 5693925
15. S. M. Laster, J. G. Wood, L. R. Gooding, Tumor necrosis factor can induce both apoptic and necrotic forms of cell lysis. *J. Immunol.* **141**, 2629–2634 (1988). pmid: 3171180
16. N. Holler *et al.*, Fas triggers an alternative, caspase-8-independent cell death pathway using the kinase RIP as effector molecule. *Nat. Immunol.* **1**, 489–495 (2000). doi: 10.1038/82732; pmid: 11101870
17. A. Degterev *et al.*, Identification of RIP1 kinase as a specific cellular target of necrostatins. *Nat. Chem. Biol.* **4**, 313–321 (2008). doi: 10.1038/nchembio.83; pmid: 18408713
18. R. J. Thapa *et al.*, Interferon-induced RIP1/RIP3-mediated necrosis requires PKR and is licensed by FADD and caspases. *Proc. Natl. Acad. Sci. U.S.A.* **110**, E3109–E3118 (2013). doi: 10.1073/pnas.1301218110; pmid: 23898178
19. C. P. Dillon *et al.*, RIPK1 blocks early postnatal lethality mediated by caspase-8 and RIPK3. *Cell* **157**, 1189–1202 (2014). doi: 10.1016/j.cell.2014.04.018; pmid: 24813850
20. W. J. Kaiser *et al.*, Toll-like receptor 3-mediated necrosis via TRIF, RIP3, and MLKL. *J. Biol. Chem.* **288**, 31268–31279 (2013). doi: 10.1074/jbc.M113.462341; pmid: 24019532
21. J. W. Upton, W. J. Kaiser, E. S. Mocarski, DAI/ZBP1/DLM-1 complexes with RIP3 to mediate virus-induced programmed necrosis that is targeted by murine cytomegalovirus vIRA. *Cell Host Microbe* **11**, 290–297 (2012). doi: 10.1016/j.chom.2012.01.016; pmid: 22423968
22. Z. Huang *et al.*, RIP1/RIP3 binding to HSV-1 ICP6 initiates necroptosis to restrict virus propagation in mice. *Cell Host Microbe* **17**, 229–242 (2015). doi: 10.1016/j.chom.2015.01.002; pmid: 25674982
23. X. Wang *et al.*, Direct activation of RIP3/MLKL-dependent necrosis by herpes simplex virus 1 (HSV-1) protein ICP6 triggers host antiviral defense. *Proc. Natl. Acad. Sci. U.S.A.* **111**, 15438–15443 (2014). doi: 10.1073/pnas.1412767111; pmid: 25316792
24. D. W. Zhang *et al.*, RIP3, an energy metabolism regulator that switches TNF-induced cell death from apoptosis to necrosis. *Science* **325**, 332–336 (2009). doi: 10.1126/science.1172308; pmid: 19498109
25. Y. S. Cho *et al.*, Phosphorylation-driven assembly of the RIP1-RIP3 complex regulates programmed necrosis and virus-induced inflammation. *Cell* **137**, 1112–1123 (2009). doi: 10.1016/j.cell.2009.05.037; pmid: 19524513
26. S. He *et al.*, Receptor interacting protein kinase-3 determines cellular necrotic response to TNF-alpha. *Cell* **137**, 1100–1111 (2009). doi: 10.1016/j.cell.2009.05.021; pmid: 19524512
27. D. Vercammen *et al.*, Inhibition of caspases increases the sensitivity of L929 cells to necrosis mediated by tumor necrosis factor. *J. Exp. Med.* **187**, 1477–1485 (1998). doi: 10.1084/jem.187.9.1477; pmid: 9565639
28. A. Oberst *et al.*, Catalytic activity of the caspase-8-FLIP(L) complex inhibits RIPK3-dependent necrosis. *Nature* **471**, 363–367 (2011). doi: 10.1038/nature09852; pmid: 21368763
29. T. Tenev *et al.*, The Ripoptosome, a signaling platform that assembles in response to genotoxic stress and loss of IAPs. *Mol. Cell* **43**, 432–448 (2011). doi: 10.1016/j.molcel.2011.06.006; pmid: 21737329
30. L. Sun *et al.*, Mixed lineage kinase domain-like protein mediates necrosis signaling downstream of RIP3 kinase. *Cell* **148**, 213–227 (2012). doi: 10.1016/j.cell.2011.11.031; pmid: 22265413
31. J. Zhao *et al.*, Mixed lineage kinase domain-like is a key receptor interacting protein 3 downstream component of TNF-induced necrosis. *Proc. Natl. Acad. Sci. U.S.A.* **109**, 5322–5327 (2012). doi: 10.1073/pnas.1200012109; pmid: 22421439
32. Z. Cai *et al.*, Plasma membrane translocation of trimerized MLKL protein is required for TNF-induced necroptosis. *Nat. Cell Biol.* **16**, 55–65 (2014). doi: 10.1038/ncb2883; pmid: 24316671
33. J. M. Murphy *et al.*, The pseudokinase MLKL mediates necroptosis via a molecular switch mechanism. *Immunity* **39**, 443–453 (2013). doi: 10.1016/j.immuni.2013.06.018; pmid: 24012422
34. J. M. Hildebrand *et al.*, Activation of the pseudokinase MLKL unleashes the four-helix bundle domain to induce membrane localization and necroptotic cell death. *Proc. Natl. Acad. Sci. U.S.A.* **111**, 15072–15077 (2014). doi: 10.1073/pnas.1408987111; pmid: 25288762
35. X. Chen *et al.*, Translocation of mixed lineage kinase domain-like protein to plasma membrane leads to necrotic cell death. *Cell Res.* **24**, 105–121 (2014). doi: 10.1038/cr.2013.171; pmid: 24366341
36. H. Wang *et al.*, Mixed lineage kinase domain-like protein MLKL causes necrotic membrane disruption upon phosphorylation by RIP3. *Mol. Cell* **54**, 133–146 (2014). doi: 10.1016/j.molcel.2014.03.003; pmid: 24703947
37. Y. Dondelinger *et al.*, RIPK3 contributes to TNFR1-mediated RIPK1 kinase-dependent apoptosis in conditions of cIAP1/2 depletion or TAK1 kinase inhibition. *Cell Death Differ.* **20**, 1381–1392 (2013). doi: 10.1038/cdd.2013.94; pmid: 23892367
38. K. Newton *et al.*, Activity of protein kinase RIPK3 determines whether cells die by necroptosis or apoptosis. *Science* **343**, 1357–1360 (2014). doi: 10.1126/science.1249361; pmid: 24557836
39. P. Mandal *et al.*, RIP3 induces apoptosis independent of pronecrotic kinase activity. *Mol. Cell* **56**, 481–495 (2014). doi: 10.1016/j.molcel.2014.10.021; pmid: 25459880
40. Z. Wang, H. Jiang, S. Chen, F. Du, X. Wang, The mitochondrial phosphatase PGAM5 functions at the convergence point of multiple necrotic death pathways. *Cell* **148**, 228–243 (2012). doi: 10.1016/j.cell.2011.11.030; pmid: 22265414
41. T. Zhang *et al.*, CaMKII is a RIP3 substrate mediating ischemia- and oxidative stress-induced myocardial necroptosis. *Nat. Med.* **22**, 175–182 (2016). doi: 10.1038/nm.4017; pmid: 26726877
42. M. Pasparakis, P. Vandenabeele, Necroptosis and its role in inflammation. *Nature* **517**, 311–320 (2015). doi: 10.1038/nature14191; pmid: 25592536
43. K. D. Marshall, C. P. Baines, Necroptosis: Is there a role for mitochondria? *Front. Physiol.* **5**, 323 (2014). doi: 10.3389/fphys.2014.00323; pmid: 25206339
44. W. K. Joklik, T. C. Merigan, Concerning the mechanism of action of interferon. *Proc. Natl. Acad. Sci. U.S.A.* **56**, 558–565 (1966). doi: 10.1073/pnas.56.2.558; pmid: 5229977
45. D. Aderka, D. Novick, T. Hahn, D. G. Fischer, D. Wallach, Increase of vulnerability to lymphotoxin in cells infected by vesicular stomatitis virus and its further augmentation by interferon. *Cell. Immunol.* **92**, 218–225 (1985). doi: 10.1016/0008-8749(85)90003-6; pmid: 2986852
46. E. S. Mocarski, H. Guo, W. J. Kaiser, Necroptosis: The Trojan horse in cell autonomous antiviral host defense. *Virology* **479-480**, 160–166 (2015). doi: 10.1016/j.virol.2015.03.016; pmid: 25819165
47. E. A. Miao *et al.*, Caspase-1-induced pyroptosis is an innate immune effector mechanism against intracellular bacteria. *Nat. Immunol.* **11**, 1136–1142 (2010). doi: 10.1038/ni.1960; pmid: 21057511
48. J. Shi *et al.*, Inflammatory caspases are innate immune receptors for intracellular LPS. *Nature* **514**, 187–192 (2014). pmid: 25119034
49. I. Jorgensen, E. A. Miao, Pyroptotic cell death defends against intracellular pathogens. *Immunol. Rev.* **265**, 130–142 (2015). doi: 10.1111/imr.12287; pmid: 25879289

50. N. J. Agard, D. Maltby, J. A. Wells, Inflammatory stimuli regulate caspase substrate profiles. *Mol. Cell. Proteomics* **9**, 880–893 (2010). doi: 10.1074/mcp.M900528-MCP200, pmid: 20173201
51. K. Labbé, M. Saleh, in *Progress in Inflammation Research: The Inflammasomes*, I. Couillin, V. Pétrilli, F. Martinon, Eds. (Springer Basel AG, Basel, 2011), pp. 17–36.
52. N. Kayagaki *et al*., Caspase-11 cleaves gasdermin D for non-canonical inflammasome signalling. *Nature* **526**, 666–671 (2015). doi: 10.1038/nature15541; pmid: 26375259
53. J. Shi *et al*., Cleavage of GSDMD by inflammatory caspases determines pyroptotic cell death. *Nature* **526**, 660–665 (2015). doi: 10.1038/nature15514; pmid: 26375003
54. W. T. He *et al*., Gasdermin D is an executor of pyroptosis and required for interleukin-1β secretion. *Cell Res.* **25**, 1285–1298 (2015). doi: 10.1038/cr.2015.139; pmid: 26611636
55. D. E. Christofferson, Y. Li, J. Yuan, Control of life-or-death decisions by RIP1 kinase. *Annu. Rev. Physiol.* **76**, 129–150 (2014). doi: 10.1146/annurev-physiol-021113-170259; pmid: 24079414
56. D. Wallach, T.-B. Kang, A. Kovalenko, The extrinsic cell death pathway and the élan mortel. *Cell Death Differ.* **15**, 1533–1541 (2008). doi: 10.1038/cdd.2008.41; pmid: 18794887
57. R. Weinlich, D. R. Green, The two faces of receptor interacting protein kinase-1. *Mol. Cell* **56**, 469–480 (2014). doi: 10.1016/j.molcel.2014.11.001; pmid: 25459879
58. N. Yatim *et al*., RIPK1 and NF-κB signaling in dying cells determines cross-priming of $CD8^+$ T cells. *Science* **350**, 328–334 (2015). doi: 10.1126/science.aad0395; pmid: 26405229
59. J. E. Vince *et al*., Inhibitor of apoptosis proteins limit RIP3 kinase-dependent interleukin-1 activation. *Immunity* **36**, 215–227 (2012). doi: 10.1016/j.immuni.2012.01.012; pmid: 22365665
60. T. B. Kang, S. H. Yang, B. Toth, A. Kovalenko, D. Wallach, Caspase-8 blocks kinase RIPK3-mediated activation of the NLRP3 inflammasome. *Immunity* **38**, 27–40 (2013). doi: 10.1016/j.immuni.2012.09.015; pmid: 23260196
61. X. Wang *et al*., RNA viruses promote activation of the NLRP3 inflammasome through a RIP1-RIP3-DRP1 signaling pathway. *Nat. Immunol.* **15**, 1126–1133 (2014). doi: 10.1038/ni.3015; pmid: 25326752
62. K. Moriwaki *et al*., The necroptosis adaptor RIPK3 promotes injury-induced cytokine expression and tissue repair. *Immunity* **41**, 567–578 (2014). doi: 10.1016/j.immuni.2014.09.016; pmid: 25367573
63. E. Kuranaga, M. Miura, Nonapoptotic functions of caspases: Caspases as regulatory molecules for immunity and cell-fate determination. *Trends Cell Biol.* **17**, 135–144 (2007). doi: 10.1016/j.tcb.2007.01.001; pmid: 17275304
64. L. Gurcel, L. Abrami, S. Girardin, J. Tschopp, F. G. van der Goot, Caspase-1 activation of lipid metabolic pathways in response to bacterial pore-forming toxins promotes cell survival. *Cell* **126**, 1135–1145 (2006). doi: 10.1016/j.cell.2006.07.033; pmid: 16990137
65. B. F. Py *et al*., Caspase-11 controls interleukin-1β release through degradation of TRPC1. *Cell Rep.* **6**, 1122–1128 (2014). doi: 10.1016/j.celrep.2014.02.015; pmid: 24630989
66. D. Wallach, T. B. Kang, S. H. Yang, A. Kovalenko, The in vivo significance of necroptosis: Lessons from exploration of caspase-8 function. *Cytokine Growth Factor Rev.* **25**, 157–165 (2014). doi: 10.1016/j.cytogfr.2013.12.001; pmid: 24411566
67. Y. Dondelinger *et al*., MLKL compromises plasma membrane integrity by binding to phosphatidylinositol phosphates. *Cell Rep.* **7**, 971–981 (2014). doi: 10.1016/j.celrep.2014.04.026; pmid: 24813885
68. W. Chen *et al*., Diverse sequence determinants control human and mouse receptor interacting protein 3 (RIP3) and mixed lineage kinase domain-like (MLKL) interaction in necroptotic signaling. *J. Biol. Chem.* **288**, 16247–16261 (2013). doi: 10.1074/jbc.M112.435545; pmid: 23612963
69. S. Yoon, K. Bogdanov, A. Kovalenko, D. Wallach, Necroptosis is preceded by nuclear translocation of the signaling proteins that induce it. *Cell Death Differ.* **23**, 253–260 (2016). doi: 10.1038/cdd.2015.92; pmid: 26184911

10.1126/science.aaf2154

RESEARCH ARTICLE SUMMARY

NONHUMAN GENOMICS

Long-read sequence assembly of the gorilla genome

David Gordon,* John Huddleston,* Mark J. P. Chaisson,* Christopher M. Hill,* Zev N. Kronenberg,* Katherine M. Munson, Maika Malig, Archana Raja, Ian Fiddes, LaDeana W. Hillier, Christopher Dunn, Carl Baker, Joel Armstrong, Mark Diekhans, Benedict Paten, Jay Shendure, Richard K. Wilson, David Haussler, Chen-Shan Chin, Evan E. Eichler†

INTRODUCTION: The accurate sequence and assembly of genomes is critical to our understanding of evolution and genetic variation. Despite advances in short-read sequencing technology that have decreased cost and increased throughput, whole-genome assembly of mammalian genomes remains problematic because of the presence of repetitive DNA.

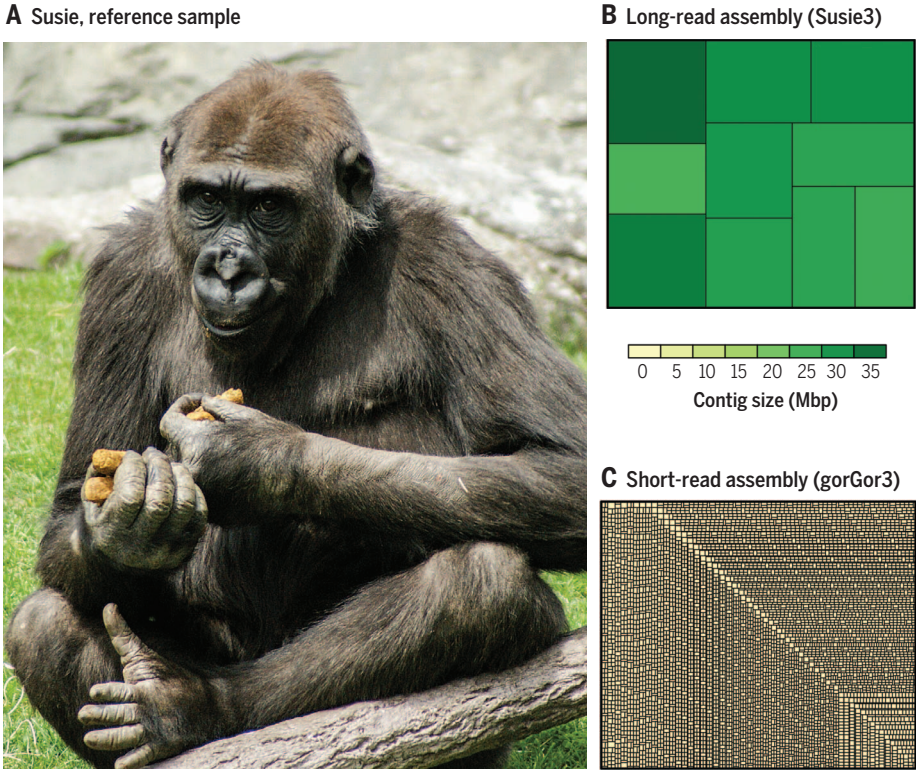
RATIONALE: The goal of this study was to sequence and assemble the genome of the western lowland gorilla by using primarily single-molecule, real-time (SMRT) sequencing technology and a novel assembly algorithm that takes advantage of long (>10 kbp) sequence reads. We specifically compare the properties of this assembly to gorilla genome assemblies that were generated by using more routine short sequence read approaches in order to determine the value and biological impact of a long-read genome assembly.

RESULTS: We generated 74.8-fold SMRT whole-genome shotgun sequence from peripheral blood DNA isolated from a western lowland gorilla (*Gorilla gorilla gorilla*) named Susie. We applied a string graph assembly algorithm, Falcon, and consensus algorithm, Quiver, to generate a 3.1-Gbp assembly with a contig N50 of 9.6 Mbp. Short-read sequence data from an additional six gorilla genomes was mapped so as to reduce indel errors and improve the accuracy of the final assembly. We estimate that 98.9% of the gorilla euchromatin has been assembled into 1854 sequence contigs. The assembly represents an improvement in contiguity: >800-fold with respect to the published gorilla genome assembly and >180-fold with respect to a more recently released upgrade of the gorilla assembly. Most of the sequence gaps are now closed, considerably increasing the yield of complete gene models. We estimate that 87% of the missing exons and 94% of the incomplete genes are recovered. We find that the sequence of most full-length common repeats is resolved, with the most significant gains occurring for the longest and most G+C–rich retrotransposons. Although complex regions such as the major histocompatibility locus are accurately sequenced and assembled, both heterochromatin and large, high-identity segmental duplications are not because read lengths are insufficiently long to traverse these repetitive structures. The long-read assembly produces a much finer map of structural variation down to 50 bp in length, facilitating the discovery of thousands of lineage-specific structural variant differences that have occurred since divergence from the human and chimpanzee lineages. This includes the disruption of specific genes and loss of predicted regulatory regions between the two species. We show that use of the new gorilla genome assembly changes estimates of divergence and diversity, resulting in subtle but substantial effects on previous population genetic inferences, such as the timing of species bottlenecks and changes in the effective population size over the course of evolution.

ON OUR WEBSITE

Read the full article at http://dx.doi.org/10.1126/science.aae0344

CONCLUSION: The genome assembly that results from using the long-read data provides a more complete picture of gene content, structural variation, and repeat biology, improving population genetic and evolutionary inferences. Long-read sequencing technology now makes it practical for individual laboratories to generate high-quality reference genomes for complex mammalian genomes. ■



Long-read sequence assembly of the gorilla genome. (**A**) Susie, a female western lowland gorilla, was used as the reference sample for full-genome sequencing and assembly [photograph courtesy of Max Block]. (**B** and **C**) Treemaps representing the differences in fragmentation of the long-read and short-read gorilla genome assemblies. The rectangles are the largest contigs that cumulatively make up 300 Mbp (~10%) of the assembly.

The list of author affiliations is available in the full article online.
*These authors contributed equally to this work.
†Corresponding author. E-mail: eee@gs.washington.edu
Cite this article as D. Gordon *et al.*, *Science* 352, aae0344 (2016). 10.1126/science.aae0344

Downloaded from on March 31, 2016

RESEARCH ARTICLE

NONHUMAN GENOMICS

Long-read sequence assembly of the gorilla genome

David Gordon,[1,2]* John Huddleston,[1,2]* Mark J. P. Chaisson,[1]* Christopher M. Hill,[1]* Zev N. Kronenberg,[1]* Katherine M. Munson,[1] Maika Malig,[1] Archana Raja,[1,2] Ian Fiddes,[3] LaDeana W. Hillier,[4] Christopher Dunn,[5] Carl Baker,[1] Joel Armstrong,[3] Mark Diekhans,[3] Benedict Paten,[3] Jay Shendure,[1,2] Richard K. Wilson,[4] David Haussler,[3] Chen-Shan Chin,[5] Evan E. Eichler[1,2]†

Accurate sequence and assembly of genomes is a critical first step for studies of genetic variation. We generated a high-quality assembly of the gorilla genome using single-molecule, real-time sequence technology and a string graph de novo assembly algorithm. The new assembly improves contiguity by two to three orders of magnitude with respect to previously released assemblies, recovering 87% of missing reference exons and incomplete gene models. Although regions of large, high-identity segmental duplications remain largely unresolved, this comprehensive assembly provides new biological insight into genetic diversity, structural variation, gene loss, and representation of repeat structures within the gorilla genome. The approach provides a path forward for the routine assembly of mammalian genomes at a level approaching that of the current quality of the human genome.

High-quality sequence and assembly of genomes is a lynchpin to our understanding of the genetic diversity and evolution of species. The development of massively parallel sequencing technologies has drastically reduced the cost and increased the throughput of genome sequencing (*1*, *2*). Although these advances have enabled sequencing of many more species and individuals, assemblies are left incomplete and fragmented in large part because the underlying sequence reads are too short [<200 base pairs (bp)] to traverse complex repeat structures (*3*). This has led to incomplete gene models, less accurate representation of repeats, and biases in our understanding of genome biology. The published western lowland gorilla genome assembly, for example, was generated by a mix of ABI capillary sequence and whole-genome shotgun Illumina short sequencing read pairs (*4*). Although the accuracy is high and many important inferences regarding the evolution of the species could be made, the resulting assembly contains more than 400,000 sequence gaps (Table 1) (*4*). Moreover, the use of the human genome to help guide the assembly of the gorilla genome created an artificially low number of structural rearrangements (*5*). The effect of these misassemblies and missing data becomes exacerbated when genomic comparisons are made among multiple primate genomes. For example, nearly 20% of the human genome could not be readily aligned in a four-way comparison among apes in large part because of the draft nature of nonhuman primate genomes (*2*). The recent development and application of long-read sequencing technologies has shown considerable promise in improving human genome assemblies as well as our understanding of genetic variation (*3*, *6*, *7*). We applied this long-read sequencing technology to generate an alternate genome assembly of the western lowland gorilla.

SMRT sequence and assembly of the gorilla genome

We generated 74.8-fold whole-genome shotgun sequence coverage using a single-molecule, real-time (SMRT) sequencing platform from peripheral blood DNA isolated from a western lowland gorilla (*Gorilla gorilla gorilla*) named Susie. All data were generated by using P6-C4 sequence chemistry from genomic libraries (>20 kbp in length), with an average subread length of 12.9 kbp. We applied a string graph assembly algorithm, Falcon (v.0.3.0), and consensus algorithm, Quiver (*8*), to generate a 3.1-Gbp assembly with a contig N50 of 9.6 Mbp (Table 1 and Figs. 1 and 2). Falcon leverages error-corrected long "super-reads" to generate a string graph representation of the genome that is subsequently refined by using a series of operations designed to break spurious edges and bridge across repetitive regions. The assembly produced 16,073 sequence contigs, including 889 contigs >100 kbp. Compared with a recent diploid assembly of a human genome (NA12878; N50 = 906 kbp) (*7*), the Falcon assembly represents a 10-fold improvement. We estimate that 98.9% of the gorilla euchromatin assembled into 1854 sequence contigs on the basis of alignment to human (GRCh38). The contigs were ordered and oriented into scaffolds (scaffold N50 = 23.1 Mbp) with bacterial artificial chromosome (BAC)– and fosmid-end sequences. Sequence analysis reveals that most of the smaller contigs (<100 kbp) consist of either centromeric or telomeric satellite sequence or collapsed segmental duplications (Fig. 1B). Chromosomal regions with higher segmental duplication content tended to be enriched for shorter sequence contigs. In fact, we observed a strong correlation [correlation coefficient (r) = 0.76] between the remaining euchromatic gaps and the presence of gorilla or human segmental duplications (fig. S15).

Compared with a previous gorilla genome assembly (gorGor3), this assembly represents a substantial decrease in assembly fragmentation (433,861 versus 16,073 contigs, >96% reduction in total contig number) (Fig. 3). Using the N50 contig length as a metric, we estimate a contiguity improvement of >819-fold with respect to the published gorilla genome assembly and >180-fold with respect to a more recently released upgrade of this Illumina-based assembly (Table 1 and table S4). When we aligned our sequence to the

Table 1. Gorilla assembly statistics.

	gorGor3*	Susie3
Individual	Kamilah	Susie
Total genome length (bp)	3,035,660,144	3,080,414,926
Number of contigs	464,874	16,073
Total sequence (bp)	2,828,866,575	3,080,414,926
Placed contig length (bp)	2,718,960,062	2,790,620,487
Unplaced contig length (bp)	109,906,513	289,794,439
Maximum contig length (bp)	191,556	36,219,563
Contig N50 (bp)	11,661	9,558,608
Number of scaffolds	57,196	554
Maximum scaffold length	10,247,101*	110,018,866
Scaffold N50 (bp)	913,458	23,141,960

*Values are taken from previously published gorilla genome paper (*4*).

[1]Department of Genome Sciences, University of Washington School of Medicine, Seattle, WA 98195, USA. [2]Howard Hughes Medical Institute, University of Washington, Seattle, WA 98195, USA. [3]Genomics Institute, University of California Santa Cruz and Howard Hughes Medical Institute, Santa Cruz, CA 95064, USA. [4]McDonnell Genome Institute, Department of Medicine, Department of Genetics, Washington University School of Medicine, St. Louis, MO 63108, USA. [5]Pacific Biosciences of California, Menlo Park, CA 94025, USA.
*These authors contributed equally to this work. †Corresponding author. E-mail: eee@gs.washington.edu

published gorilla genome reference (gorGor3), we closed 94% of the 433,861 gorGor3 gaps (fig. S13), resulting in the addition of least 164 Mbp of euchromatic sequence. This additional sequence dramatically improved gene annotation, including the discovery of thousands of exons and putative regulatory elements (Fig. 1C).

An analysis of the gaps in gorGor3 showed that they were enriched 3.8-fold for Alu short interspersed nuclear element (SINE) repeats, revealing that this G+C–rich primate repeat was particularly problematic in the initial gorilla assembly. Overall, there was a positive correlation between gap size and repeat content, especially for segmental duplications (three- to fivefold enrichment). For example, 10,959 gorGor3 gaps were in excess of 2 kbp; of these, 21% (2298) mapped to segmental duplications (table S12). Although heterochromatic regions could still not be resolved in the new gorilla assembly, our analysis of the underlying sequence data indicates that 10% of the gorilla genome consists of satellite repeats (table S15). A 32-bp satellite (pCht7) (*9*) associated with subterminal caps of gorilla chromosomes was more abundant than α-satellite repeats (4.0 versus 2.3%) within the genome sequence data (table S15). In contrast to other apes, these data suggest that telomeric-associated heterochromatic repeats are more abundant than centromeric repeats in gorilla.

Quality assessment

We assessed the quality of the assembly using two independent sources of data. First, we used paired-end sequence data generated during the sequencing and assembly of the first western lowland gorilla (Kamilah) to assess the assembly integrity. Our analysis showed that 98.6% of the new gorilla assembly was supported by concordant paired-end sequence data generated from either large-insert BAC or fosmid gorilla clones (table S2). An analysis of aligned high-quality Sanger sequence data (54.5 Mbp) revealed high sequence identity (99.71%) within the potential range of allelic diversity expected among western lowland gorillas (*10*) (table S10). In order to more precisely assess sequencing accuracy, we generated and aligned Illumina whole-genome sequence data from the same gorilla (Susie) and used sequence differences to estimate an initial error of one per 1000 base pairs [quality value (QV) = 30]. The most frequent errors observed were a threefold excess of single base pair insertions. We used Illumina whole-genome sequence data from Susie as well as six additional western lowland gorilla genomes (*10*) to correct these indel errors. Using these additional genomes, we created a "pan" gorilla reference genome (Susie3), correcting indel errors and identifying the most common single-nucleotide polymorphism variants. After error correction, we estimate that Susie3 has less than one error per 5000 bp (QV > 35) (table S7).

Comparative analyses between human and gorilla genomes

To determine the potential biological utility of this new reference gorilla genome, we measured the increased yield in gene content from gap closures in the gorilla reference by identifying human RefSeq (*11*) exons that map within gap regions of gorGor3 that are closed in Susie3. Using this projection, we estimate that 87% (11,105 of 12,754) of the missing RefSeq exons are recovered and that 94% of the incomplete gorilla genes are resolved for at least one isoform in Susie3. More generally, we found that an additional 1 to 3% of Illumina RNA-sequencing (RNA-seq) data and an additional 6 to 7% of gorilla ESTs are mapped by standard mapping methods to this more complete genome assembly (table S13). The assembly also improves the contiguous representation of genes predicted by human GENCODE (*12*). Compared with other nonhuman primate genomes, Susie3 has far fewer assembly errors, making it one of the most complete primate genomes after human (Fig. 4). We found that 88% of protein-coding transcripts (GENCODE) have >99% identity against Susie3 compared with ~55% in gorGor3 (fig. S18). We leveraged the new assembly, available RNA-seq data, and Augustus TransMap (*13*–*15*) alignments to define a new set of 45,087 consensus gene models for protein-coding transcripts (isoforms from 19,633 genes) in the gorilla genome.

The greater sequence contiguity of the genome assembly provided an opportunity to comprehensively assess structural variation between gorilla and human genomes at a fine-scale resolution, down to ~50 bp. Comparison of the gorilla (Susie3) and human (GRCh38) assemblies revealed a total of 117,512 insertions and deletions (92 Mbp) and 697 inversion variants (Table 2 and table S20). More than 86% of these events were previously unidentified (fig. S47) (*16*, *17*), and 72% of the events were determined to represent fixed differences specific to the gorilla lineage. Variants ranged in size from small structural variants within the coding sequence of genes to large, complex, gene-rich structural variant events spanning hundreds of kilobase pairs (Fig. 4, C

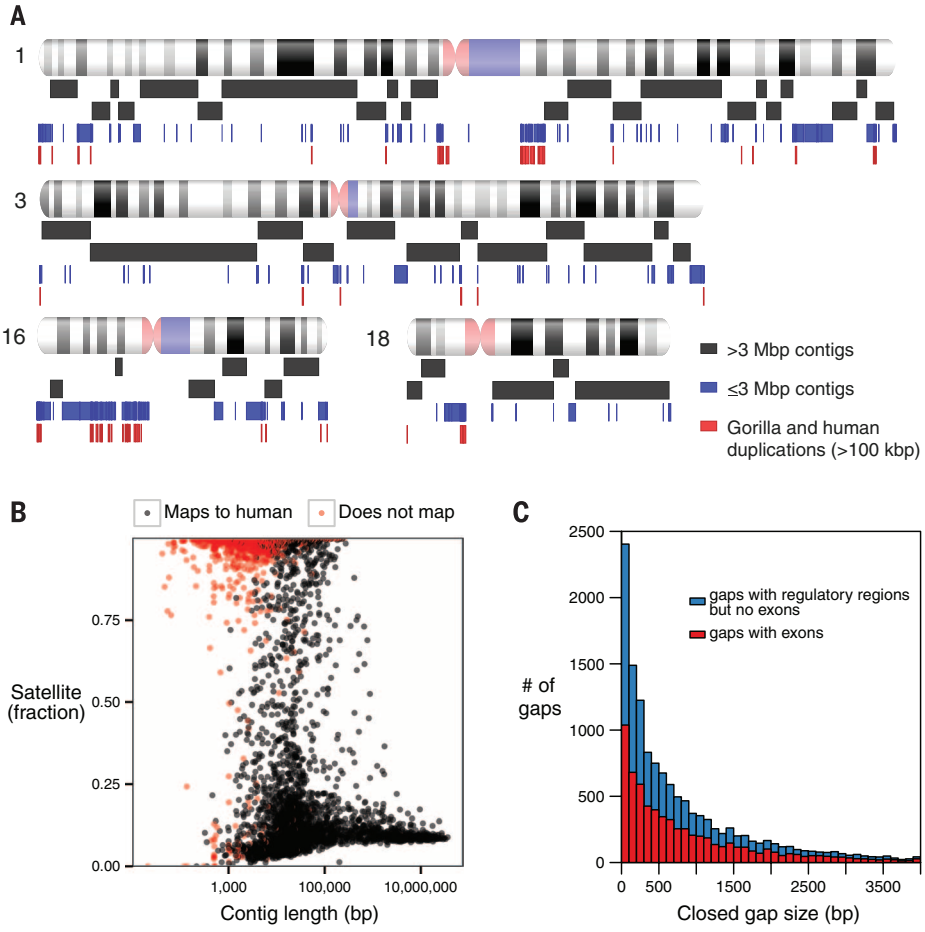


Fig. 1. Gorilla genome assembly. (**A**) Schematic depicting assembly contig lengths (contig N50 = 9.6 Mbp) mapped to human GRCh38 chromosomes. The first two rows of black rectangles represent contigs >3 Mbp, the blue rectangles correspond to contigs ≤3 Mbp, and red rectangles correspond to blocks of human/gorilla segmental duplications >100 kbp. (**B**) Mappability and satellite content of Susie3 contigs. Satellite content defined by use of RepeatMasker (*28*) and Tandem Repeats Finder (*29*). Contigs that are unable to map to GRCh38 by using BLASR (colored red) (*30*) contain a high fraction of satellite sequence. (**C**) Length distribution of gaps in the published gorilla assembly gorGor3 closed by Susie3 and containing exons or regulatory regions. Of the gaps in gorGor3, 94% were closed in Susie3, with thousands corresponding to missing exons (red) and putative noncoding regulatory DNA (blue).

and D). Our analysis also provided a comprehensive catalog of mobile element differences between human and gorilla (24.1% of all structural variation events). Compared with earlier gorilla genome assemblies, we found that the proportion of full-length retrotransposons is significantly greater for the longest [HERV Kolmogorov-Smirnov (KS) $P = 0.0016$, and PTERV1 KS $P < 2.2 \times 10^{-16}$] and most G+C–rich repeat elements (SVA KS $P < 2.2 \times 10^{-16}$) (Fig. 5). PTERV1 is particularly notable in this regard because its 9- to 10-kbp full-length insertions are specific to the gorilla lineage (*18*, *19*); we found a 4.8-fold increase in full-length elements, with most elements in Susie3 being previously unidentified.

A small fraction (0.3%) of the structural variants affect protein-coding genes, including those that appear to lead to a likely gene-disruptive event in gorilla when compared with human. Because such gene-disrupting events may represent polymorphisms or be enriched for errors in a reference, we restricted our analysis to previously undescribed events that were shared across an additional six western lowland gorillas (table S19). Using these criteria, we identified 145 structural variants (76 deletions and 69 insertions) that affect the coding sequence of 110 distinct RefSeq genes. Although no single functional gene category reached statistical significance for enrichment, several of the genic differences between the species were associated with sensory perception, keratin production, interleukin and cytokine secretion, reproduction, immunity, growth, transmembrane signaling, and nucleotide binding (table S19).

We also investigated structural variants that affected potential regulatory elements on the basis of recent annotations of the human genome (ENCODE). We annotated base pair–resolved variants that intersected with deoxyribonuclease I hypersensitive (DNase I HS) sites associated with open chromatin, histone H3 lysine 4 trimethylation (H3K4me3) marks associated with transcriptionally active regions/promoters, and histone H3 acetylation on lysine 27 (H3K27ac) signals associated with enhancers (*12*). Among the 10,466 insertions and deletions that intersected regulatory elements, 2151 represented fixed structural differences between humans and gorillas (GSVs). Similarly, we identified 133 GSVs that affect long intergenic noncoding RNA (lincRNA). As expected, we observed a significant (2- to 10-fold) depletion of structural variants intersecting these functional categories, with the exception of lincRNA.

We further quantified the spatial correlation between GSVs and the regulatory elements by comparing their proximity. The midpoints of the GSVs overlapped significantly less with the protein-coding genes (projection test $P = 6.0 \times 10^{-12}$) and with fetal DNase I HS sites (projection test $P = 4.3 \times 10^{-10}$), which is consistent with the action of purifying selection. We observed a modest spatial enrichment between GSVs that map within 50 to 200 bp of putative promoter and enhancer marks (projection test $P = 0.041$ and 4.1×10^{-15} for H3K4me3 and H3K27ac, respectively). This analysis identified 327 protein-coding genes within 10 kbp of an H3K4me3 mark that overlaps or maps near a GSV (<100 bp) and 672 genes that had the same spatial pattern for H3K27ac marks. We compared these fixed structural differences within putative regulatory DNA with 127 genes with differences in RNA expression and CTCF binding sites between human and gorilla (*20*). We identified nine genes in which a GSV intersected an H3K4me3 or HeK27Ac mark (*ADAMTS10*, *ALDH1L1*, *CDH1*, *COL5A1*, *GRK5*, *IGF2BP1*, *INSR*, *IQGAP2*, and *SRC*) and eight that intersected the 3′ untranslated region or a noncoding transcribed exon (*AMOTL1*, *DUSP4*, *HNF1B*, *ITGB8*, *SGPP2*, *TCL1A*, *ZDHHC19*, and *ZNF607*). None of these GSVs affected protein-coding regions of these genes, and thus, these fixed differences in noncoding regulatory DNA are strong candidates to explain the expression differences between the species.

Six inversions were identified that potentially disrupt an exon or break within a gene, in addition to 206 inversions and microinversions that map within introns. Among the insertion and deletion events, 15 of the structural variants occurred in genes that are largely intolerant to mutation in humans (residual variation intolerance score < 20 percentile) (*21*). This includes insertions within the insulin-degrading enzyme (*IDE*) and a negative regulator of WNT signaling (*AXIN1*), as well as deletions in a tubulin-specific chaperone (*TBCD*) and an extracellular sulfatase (*SULF2*) associated with cell signaling. Our analysis revealed a large number of in-frame deletions and insertions that result in the addition and loss of amino acids and protein domain differences between human and gorilla genes. Although the impact of these structural variants awaits further characterization, the greater resolution of structural variants provides a large number

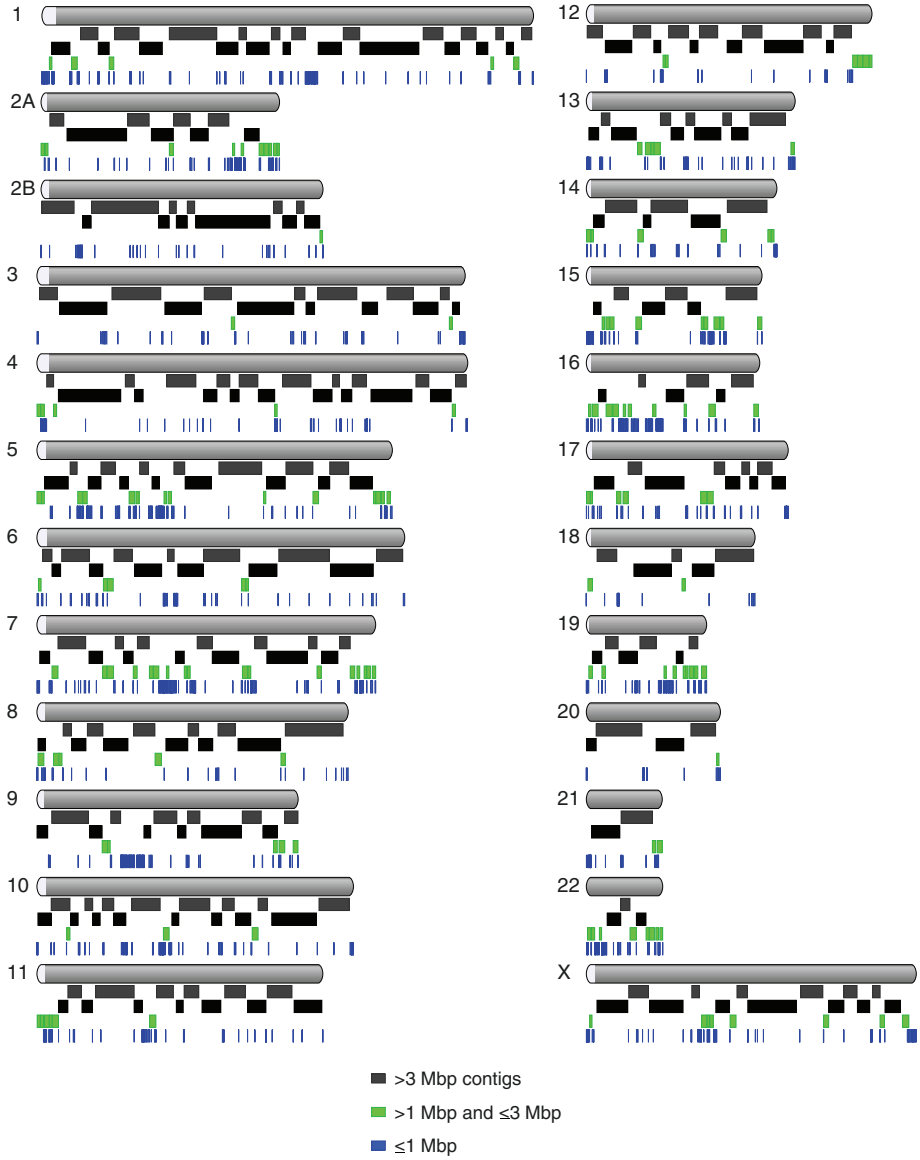


Fig. 2. Gorilla genome ideogram. Schematic depicting assembly contig lengths mapped to gorilla chromosomes. The first two rows of black rectangles represent contigs >3 Mbp, the green rectangles correspond to contigs >1 Mbp and ≤3 Mbp, and blue rectangles correspond to contigs ≤1 Mbp.

Table 2. Gorilla genome structural variants. Contigs greater than 200 kbp were mapped to GRCh38 by using BLASR (30). Nonrepetitive sequences contained at most 70% of sequence annotated as repeat by RepeatMasker (3.3.0) (28) or Tandem Repeats Finder 4.07b (29). Mosaic repeats are defined as one or more different repeat annotations; however, mosaic structural variants composed solely of Alu are listed separately because of their frequency.

	Insertion					Deletion				
Repeat element	Count	Fixed	Average length (bp)	Standard deviation length (bp)	Total bases	Count	Fixed	Average length (bp)	Standard deviation length (bp)	Total bases
Complex, not repetitive	15,383	13,190	709.31	1807.29	10911284	13,749	10,250	763.17	1,954	10492765
Complex, repetitive	7,552	7,243	2716.96	2746.63	20,518,484	7,450	5,934	2757.39	2906.61	20,542,529
AluY	6,418	5,878	284.36	65.2	1,825,012	9,422	7,882	294.58	60.04	2,775,515
AluS	990	950	160.64	85.98	159,036	1,053	845	159.84	82.05	168,315
L1Hs	86	50	262.67	582.37	22,590	220	179	235.51	358.93	51,813
L1	1,339	1,256	438.5	737.1	587,147	1,181	874	450.84	744.1	532,441
L1P	1,891	1,660	278.26	487.86	526,192	1,430	1,098	312.81	493.88	447,317
SVA	1,498	1,097	1561.2	1007.55	2,338,672	1,194	786	1279.32	914.18	1,527,511
HERV	324	285	241.06	498.09	78,104	260	194	362.79	797.4	94,325
PTERV	190	179	2973.22	3427	564,912	1	1	188	0	188
Mosaic-Alu	1,433	1,355	320.11	262.59	458,717	1,514	1,177	307.92	260.53	466,194
STR	11,049	4,152	228.73	313.35	2,527,257	10,564	4,573	156.93	175.96	1,657,802
Tandem Repeats	7,351	4,520	367.74	811.03	2,703,261	7,828	4,225	323.38	558.5	2,531,424
Satellite	1,757	1,613	437.46	1072.08	768,617	1,768	1,437	426.73	1047.71	754,455
Other	1,319	1,184	201.01	247.8	265,130	1,196	896	180.49	227.79	215,872
Not base-pair resolved	41	N/A	49,496	23817.46	2029323	61	N/A	55,971	43,496	3,414,209
Total	58,621	44,653	789.54	2183.43	46,283,738	58,891	40,482	775.55	2804.21	45,672,675

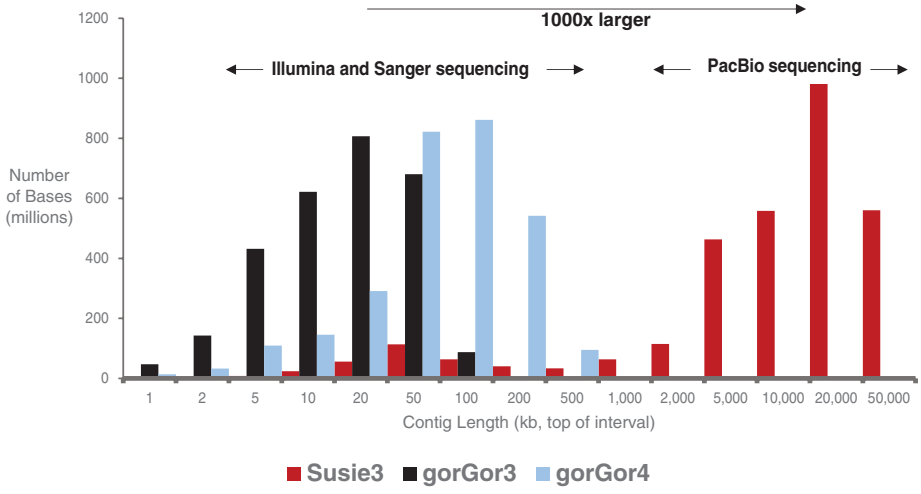


Fig. 3. Comparison of gorilla genome assemblies. The contig length distribution for the resulting long-read assembly (Susie3) is 2 to 3 orders of magnitude larger when compared with previous gorilla genome assemblies (gorGor3 and gorGor4) that were generated by using Illumina and Sanger sequencing technology.

of likely high-impact species differences for future investigation.

Sequence and assembly of the major histocompatibility locus

As a test of the enhanced structural variation detection and its potential biomedical relevance, we compared the organization of the major histocompatibility complex (MHC) II locus between gorilla and human (GRCh37). MHC encodes genes that are critical for antigen presentation on immune cells, and its content and structure are known to differ radically between closely related primates (22). We found that segmental duplication has expanded the locus in gorilla relative to human so that in the assembly, there are 79,166 (~10%) duplicated base pairs, compared with 53,084 bp (~8%) in human. We identified three large gorilla insertions across the ~1 Mbp region (15, 48, and 52 kbp) that correspond to 14% of the locus (Fig. 4C), including several previously unidentified MHC genes. In terms of assembly statistics, the MHC region in gorGor3 has 168 gaps that are filled in Susie3, eight of which mapped within 100 bp of 27 distinct genes (human RefSeq).

To verify the organization of the HLA region in Susie3, we sequenced a tiling path of BACs derived from another gorilla, Kamilah, who previously contributed to the published gorGor3 assembly (table S6). We generated two high-quality, clone-based sequence haplotypes for the region (MHC haplotype 1, 863,324 bp; MHC haplotype 2, 289,560 bp). Both Kamilah MHC haplotypes mapped with higher sequence identity to Susie3 (99.6 and 99.9%) than gorGor3 (98.1 and 98.9%), which is consistent with assembly improvements for this complex region of the genome.

Population genetic inferences based on the new assembly

Last, we assessed whether the new gorilla genome assembly would have any influence on previous population genetic inferences as a result of potential changes in estimates of divergence and diversity. Although the difference was subtle, we found that human versus gorilla sequence alignments were significantly less divergent ($P < 2.2 \times 10^{-16}$; Welch two-sample t test) with Susie3 (1.60% divergent) when compared with the published gorilla assembly (1.65% divergent) (Fig. 6). Both regional and chromosomal analyses showed that the different estimates of gorilla-human divergence were nonrandomly distributed. In particular, we observed that specific gene-rich regions and chromosomes (such as chromosomes 19 and

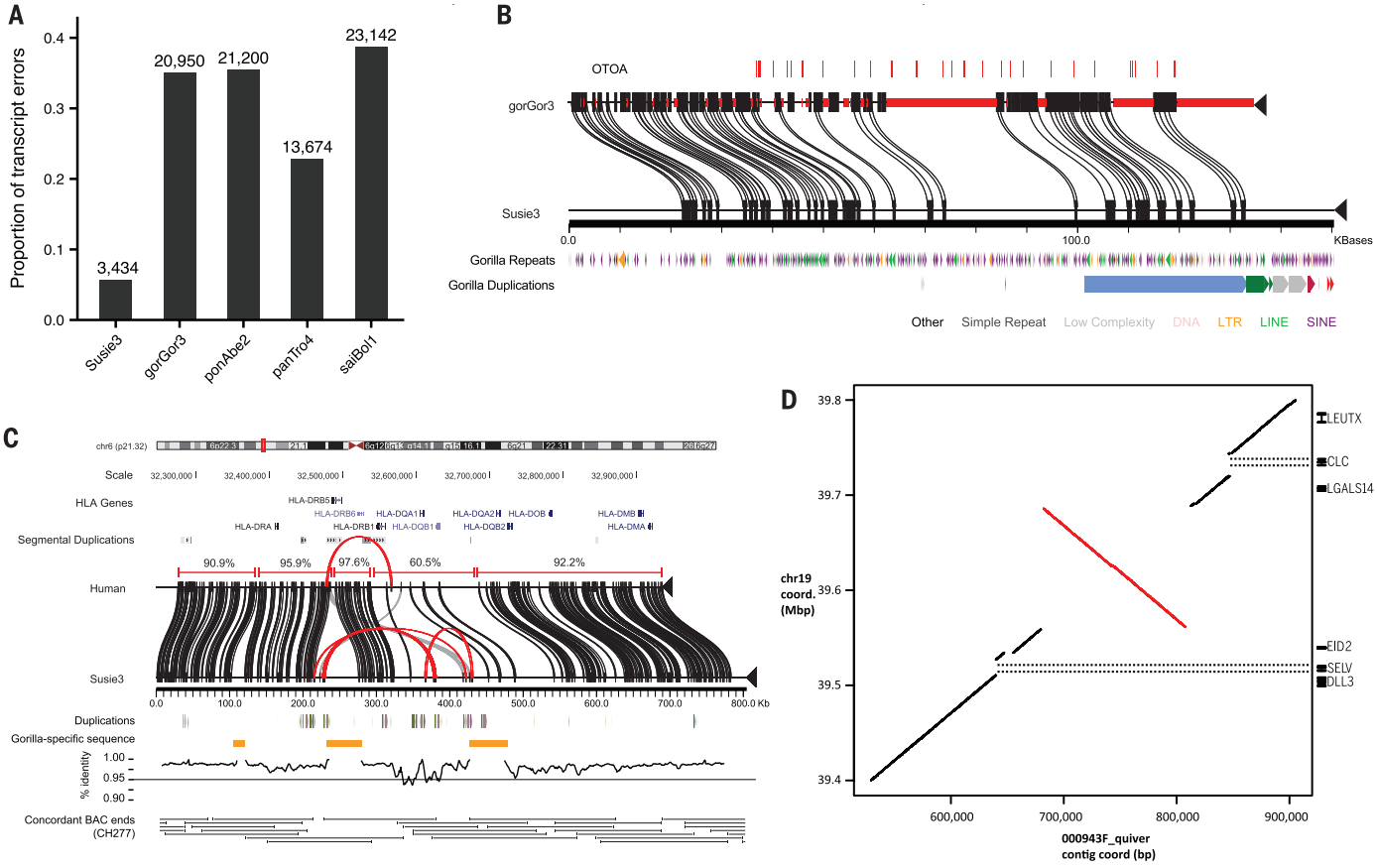


Fig. 4. Gene annotation and structural variation. (**A**) Proportion of GENCODE transcripts with assembly errors when aligned with gorilla assemblies Susie3 and gorGor3, and three reference assemblies, including orangutan (ponAbe2), chimpanzee (panTro4), and squirrel monkey (saiBol1). Examples of assembly errors include transcript mappings extending off the end of contigs/scaffolds, containing unknown bases, or incomplete transcript mapping. (**B**) An example of a gene, otoancorin (*OTOA*), with complete exon representation (red ticks) resolved in the new assembly. Red bars on gorGor3 sequence indicate gaps in the assembly. Alignments between gorilla assemblies are based on Miropeats (*31*). (**C**) Alignment of MHC Class II locus in Susie3 against GRCh37 with Miropeats. Alignment identities of collinear blocks between assemblies are shown above the corresponding GRCh37 sequence. Repeats internal to Susie3 are shown in red along the coordinates. Alignment identity across the entire locus is shown below the Susie3 contigs in 5-kbp windows (1 kbp sliding). Support for the proper organization of the Susie3 sequence is shown by the tiling path of concordant BAC end sequences from the Kamilah BAC library (CHORI-277). (**D**) A sequence-resolved complex gorilla genome structural variation orthologous to human chromosome 19:38,867,213–39,866,620 (GRCh38). The dot-matrix plot shows a 125,375-bp inversion flanked by a proximal 16-kbp deletion and 8-kbp insertion, and a 23-kbp distal deletion. The deletions remove the entire sequences of the *SELV* and *CLC* genes in gorilla when compared with human.

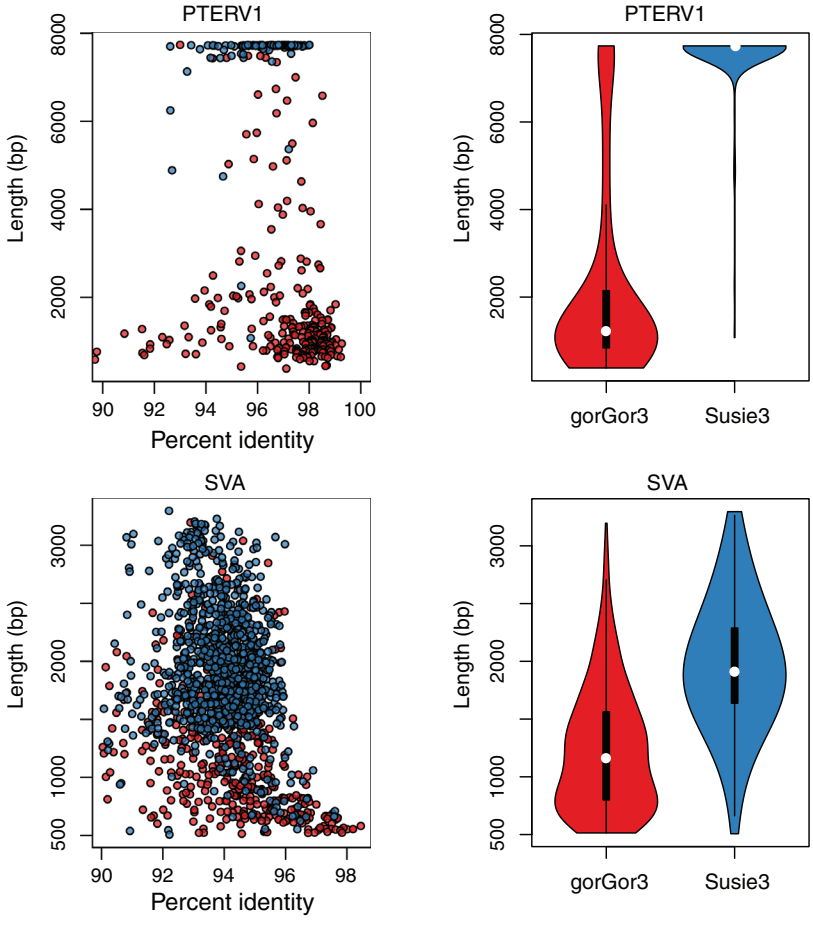
22) showed the largest difference between the two assemblies (fig. S61B). We found a strong correlation with the difference in divergence and regions enriched for Alu and G+C content (r = –0.60; Pearson's, $P < 0.001$) (Fig. 6B), suggesting that mismapping, collapse, or underrepresentation within these regions of the Illumina-based assemblies may be contributing to this excess of divergence (Fig. 6B).

We also assessed the effect of the new assembly on estimates of diversity by comparing the pattern of single-nucleotide variants for six western lowland gorillas against Susie3 and gorGor3. Although a greater fraction of the Illumina paired-end reads mapped with higher mapping quality to Susie3 (table S8), we observed a higher ratio of heterozygous genotypes in gorGor3 (mean, 0.35) as compared with Susie3 (mean, 0.33). Next, we examined the average observed heterozygosity across both assemblies in 100-kbp windows (fig. S62). The largest difference in observed heterozygosity between the assemblies was on the X chromosome, in which the average gorGor3 heterozygosity was 0.27 versus 0.23 in Susie3.

It is likely that the increased gorGor3 heterozygosity is due to mapping errors owing to fewer reads successfully mapping (gorGor3 has more than 400,000 gaps, many of which contain repetitive sequences). Mapping software errs on the side of sensitivity, meaning reads derived from underrepresented regions may be incorrectly placed. To test this idea, we identified the reads (including mate-pairs) from Coco, a female gorilla, corresponding to heterozygous positions in gorGor3 and remapped them to both gorGor3 and Susie3. We found that only 87% of the heterozygous calls in gorGor3 resulted in heterozygous calls in Susie3 (table S33). The "lost" heterozygous genotypes correspond to regions with lower Illumina read depth as compared with that of gorGor3, supporting the notion that mapping error is likely inflating heterozygosity in the original assembly (fig. S63).

Accurate estimates of population histories are important for understanding how climate change, disease, and human activity shaped the genetic diversity within western lowland gorillas. Such estimates are critically dependent on genetic measures such as heterozygosity. We fit a pairwise sequentially Markovian coalescent (PSMC) model to Illumina data from four western lowland gorillas mapped against Susie3 and gorGor3 (Fig. 6). Comparing the two assemblies, we observed two statistically significant differences in the predicted effective population size of the gorilla species at ~50 thousand years ago (ka) and ~5 million years ago (ma) (Fig. 6). The effects occur in opposite directions. We observed a significant decrease in the effective population size at more ancient time periods ($P < 0.0001$; Welch two-sample t test), possibly because of a greater fraction of repetitive sequence and segmental duplications being resolved in Susie3. In contrast, use of Susie3 as a reference predicts a significantly greater effective population size at 50 ka ($P < 0.0001$; Welch two-sample t test). Our results suggest that the most recent bottleneck of the western lowland

Fig. 5. Improved mobile element resolution. (**Left**) PTERV1 and SVA insertion length and percent identity distributions in Susie3 (blue) and gorGor3 (red). The PTERV1 and SVA elements in gorGor3 are biased toward short but on average higher identity alignments to the consensus sequence because the more divergent long terminal repeat sequences are not resolved. (**Right**) The mean and median insertion lengths for gorGor3 and Susie3 are PTERV1, 2194.93, 7565.85 (median 1223 and 7725) and SVA, 1240.1, and 1965.63 (median 1162 and 1909).



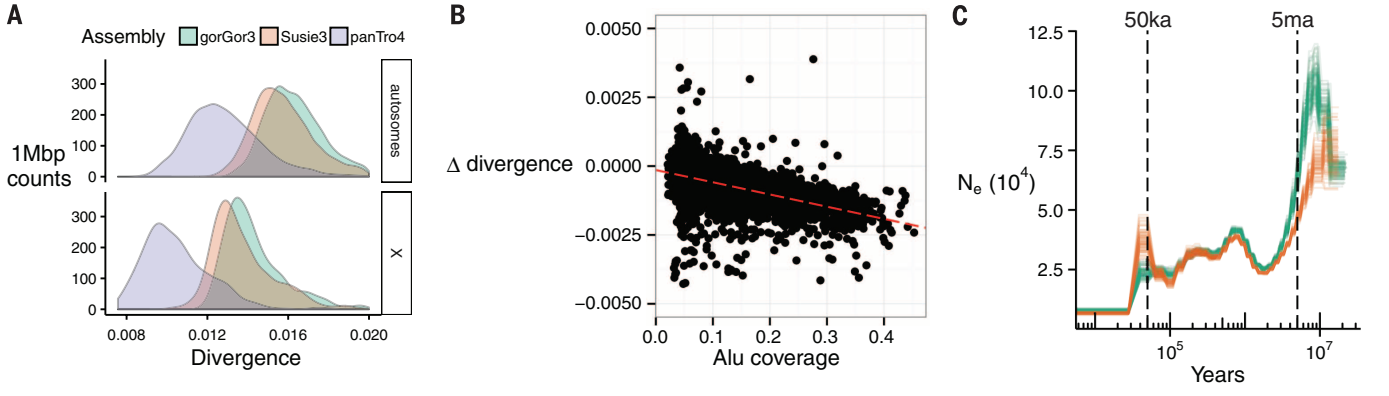
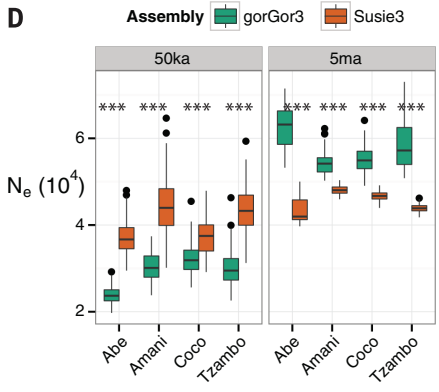


Fig. 6. Population genetic analyses. (**A**) Density of average divergence within 1-Mbp windows between human (GRCh38) and gorGor3, Susie3, or chimpanzee (panTro4) autosomes. (**B**) A comparison of human-gorGor3 and human-Susie3 divergence over 1-Mbp windows. The *x* axis is Alu coverage in each window, and the *y* axis is the difference in human-gorilla divergence between gorGor3 and Susie3. Positive *y* axis values indicate increased human–Susie3 divergence relative to human–gorGor3. The increased divergence of human–gorGor3 correlates with Alu content (slope, −0.0044094; intercept, 0.0001486; Pearson's correlation, −0.60). (**C**) The effective population size (N_e) shown over time. A PSMC model was applied to the western lowland gorilla based on different genome assemblies. Illumina genome sequence data from western lowland gorillas (Abe, Amani, Coco, Tzambo) was mapped against gorGor3 (green) and Susie3 (orange), and PSMC was fit to the genome alignments (-N25 -t15 -r5 -b -p "4+25*2+4+6"; mutation rate = 1.25×10^{-8}; generation time = 19 years). There are 100 bootstrap replicates for each gorilla and model. (**D**) The distribution of the bootstrap intervals that overlap 50 ka and 5 ma. At 50 ka, Susie3 estimates of the effective population size are significantly higher than that for gorGor3; the inverse pattern is true for 5 ma. All differences between Susie3 and gorGor3 are significant (***$P \leq 0.0001$; Welch two-sample *t* test).



gorilla may have been underestimated by a factor of ~1.5, highlighting the importance of using higher-quality assemblies when fitting demographic models.

Our results demonstrate the utility of long-read sequence technology to generate high-quality working draft genomes of complex vertebrate genomes without guidance from preexisting reference genomes. Comparisons against recent published human genomes that used alternate assemblers indicate that Falcon provides superior performance with respect to assembled contig length, repeat resolution, and computational time (*6*, *7*). The genome assembly that results from using the long-read data provides a more complete picture of gene content, structural variation, and repeat biology as well as allows us to refine population genetic and evolutionary inferences. Notwithstanding the dramatic improvements to the sequence contiguity of euchromatin, gaps still remain. Our analysis suggests that both heterochromatin and large, high-identity segmental duplications remain largely unresolved because read lengths are insufficiently long to traverse these repetitive structures (Fig. 1C). Although all long-read assembly algorithms should still be considered work in progress, it is clear that both sequencing and computational technologies have now advanced to a stage that allows individual laboratories to generate high-quality mammalian genomes with vastly higher contiguity of the euchromatin. This capability promises to revolutionize our understanding of genome evolution and species biology.

Materials and methods

High-quality DNA was extracted (Qiagen Puregene kit, Valencia, CA) from peripheral blood drawn from a captive female western lowland gorilla (Susie) from the Lincoln Park Zoo (Chicago, IL). We generated SMRTbell genomic libraries (>20 kbp in length) and SMRT sequence data (P6C4 chemistry, RSII platform) with average subread lengths of 12.9 kbp. A gorilla genome assembly, Susie3, was generated by using Falcon (v0.3.0) (https://github.com/PacificBiosciences/FALCON-integrate). The Falcon assembly method operates in two phases: First, overlapping sequence reads are compared [DALIGNER (*23*)] to generate 97 to 99% accurate consensus sequences for reads with lengths in the top percentile (>15 kbp). Next, overlaps between the corrected longer reads are used to generate a string graph (*24*). The graph is reduced so that multiple edges formed by heterozygous structural variation are replaced to represent a single haplotype. Contigs are formed by using the sequences of nonbranching paths. Two supplemental graph cleanup operations are defined so as to improve assembly quality by removing spurious edges from the string graph: tip removal (*25*) and chimeric duplication edge removal. Tip removal discards sequences with errors that prevent 5′ or 3′ overlaps. Chimeric duplication edges may result from the raw sequence information or during the first sequence cleanup step and artificially increase the copy number of a duplication. Indel errors in the assembly were corrected by aligning Illumina (HiSEq. 2500 and NextSeq) sequence data generated from six additional western lowland gorillas (*10*), including 14-fold sequence data generated from the new gorilla reference genome (Susie). Consensus gene models were built with Augustus (*13*) by use of TransMap (*14*, *15*) alignments of GENCODE transcripts to Susie3 and previously published RNA-seq data (*26*, *27*).

REFERENCES AND NOTES

1. H. Y. K. Lam *et al*., Performance comparison of whole-genome sequencing platforms. *Nat. Biotechnol.* **30**, 78–82 (2012). doi: 10.1038/nbt.2065; pmid: 22178993
2. J. Rogers, R. A. Gibbs, Comparative primate genomics: Emerging patterns of genome content and dynamics. *Nat. Rev. Genet.* **15**, 347–359 (2014). doi: 10.1038/nrg3707; pmid: 24709753
3. M. J. P. Chaisson, R. K. Wilson, E. E. Eichler, Genetic variation and the de novo assembly of human genomes. *Nat. Rev. Genet.* **16**, 627–640 (2015). doi: 10.1038/nrg3933; pmid: 26442640
4. A. Scally *et al*., Insights into hominid evolution from the gorilla genome sequence. *Nature* **483**, 169–175 (2012). doi: 10.1038/nature10842; pmid: 22398555
5. L. Carbone *et al*., Gibbon genome and the fast karyotype evolution of small apes. *Nature* **513**, 195–201 (2014). doi: 10.1038/nature13679; pmid: 25209798
6. K. Berlin *et al*., Assembling large genomes with single-molecule sequencing and locality-sensitive hashing. *Nat. Biotechnol.* **33**, 623–630 (2015). doi: 10.1038/nbt.3238; pmid: 26006009
7. M. Pendleton *et al*., Assembly and diploid architecture of an individual human genome via single-molecule technologies. *Nat. Methods* **12**, 780–786 (2015). doi: 10.1038/nmeth.3454; pmid: 26121404
8. C.-S. Chin *et al*., Nonhybrid, finished microbial genome assemblies from long-read SMRT sequencing data. *Nat. Methods* **10**, 563–569 (2013). doi: 10.1038/nmeth.2474; pmid: 23644548
9. N. J. Royle, D. M. Baird, A. J. Jeffreys, A subterminal satellite located adjacent to telomeres in chimpanzees is absent from the human genome. *Nat. Genet.* **6**, 52–56 (1994). doi: 10.1038/ng0194-52; pmid: 8136835
10. J. Prado-Martinez *et al*., Great ape genetic diversity and population history. *Nature* **499**, 471–475 (2013). doi: 10.1038/nature12228; pmid: 23823723
11. N. A. O'Leary *et al*., Reference sequence (RefSeq) database at NCBI: Current status, taxonomic expansion, and functional annotation. *Nucleic Acids Res.* **44** (D1), D733–D745 (2016). doi: 10.1093/nar/gkv1189; pmid: 26553804
12. J. Harrow *et al*., GENCODE: The reference human genome annotation for The ENCODE Project. *Genome Res.* **22**, 1760–1774 (2012). doi: 10.1101/gr.135350.111; pmid: 22955987
13. M. Stanke, M. Diekhans, R. Baertsch, D. Haussler, Using native and syntenically mapped cDNA alignments to improve de novo gene finding. *Bioinformatics* **24**, 637–644 (2008). doi: 10.1093/bioinformatics/btn013; pmid: 18218656
14. A. Siepel *et al*., Targeted discovery of novel human exons by comparative genomics. *Genome Res.* **17**, 1763–1773 (2007). doi: 10.1101/gr.7128207; pmid: 17989246
15. J. Zhu *et al*., Comparative genomics search for losses of long-established genes on the human lineage. *PLOS Comput. Biol.* **3**, e247 (2007). doi: 10.1371/journal.pcbi.0030247; pmid: 18085818
16. M. Ventura *et al*., Gorilla genome structural variation reveals evolutionary parallelisms with chimpanzee. *Genome Res.* **21**, 1640–1649 (2011). doi: 10.1101/gr.124461.111; pmid: 21685127
17. P. H. Sudmant *et al*., Evolution and diversity of copy number variation in the great ape lineage. *Genome Res.* **23**, 1373–1382 (2013). doi: 10.1101/gr.158543.113; pmid: 23825009
18. C. T. Yohn *et al*., Lineage-specific expansions of retroviral insertions within the genomes of African great apes but not humans and orangutans. *PLOS Biol.* **3**, e110 (2005). doi: 10.1371/journal.pbio.0030110; pmid: 15737067
19. N. Polavarapu, N. J. Bowen, J. F. McDonald, Identification, characterization and comparative genomics of chimpanzee endogenous retroviruses. *Genome Biol.* **7**, R51 (2006). doi: 10.1186/gb-2006-7-6-r51; pmid: 16805923
20. Y. Xue *et al*., Mountain gorilla genomes reveal the impact of long-term population decline and inbreeding. *Science* **348**, 242–245 (2015). doi: 10.1126/science.aaa3952; pmid: 25859046
21. S. Petrovski, Q. Wang, E. L. Heinzen, A. S. Allen, D. B. Goldstein, Genic intolerance to functional variation and the interpretation of personal genomes. *PLOS Genet.* **9**, e1003709 (2013). doi: 10.1371/journal.pgen.1003709; pmid: 23990802
22. A. M. Little, P. Parham, Polymorphism and evolution of HLA class I and II genes and molecules. *Rev. Immunogenet.* **1**, 105–123 (1999). pmid: 11256568
23. E. W. Myers, Efficient local alignment discovery amongst noisy long reads. *Lect. Notes Comput. Sci.* **8701**, 52–67 (2014). doi: 10.1007/978-3-662-44753-6_5
24. E. W. Myers, The fragment assembly string graph. *Bioinformatics* **21** (suppl. 2), ii79–ii85 (2005). doi: 10.1093/bioinformatics/bti1114; pmid: 16204131
25. P. A. Pevzner, H. Tang, G. Tesler, De novo repeat classification and fragment assembly. *Genome Res.* **14**, 1786–1796 (2004). doi: 10.1101/gr.2395204; pmid: 15342561
26. D. Brawand *et al*., The evolution of gene expression levels in mammalian organs. *Nature* **478**, 343–348 (2011). doi: 10.1038/nature10532; pmid: 22012392
27. A. Necsulea *et al*., The evolution of lncRNA repertoires and expression patterns in tetrapods. *Nature* **505**, 635–640 (2014). doi: 10.1038/nature12943; pmid: 24463510
28. A. Smit, R. Hubley, P. Green, RepeatMasker Open-3.0 (1996); available at www.repeatmasker.org.
29. G. Benson, Tandem repeats finder: A program to analyze DNA sequences. *Nucleic Acids Res.* **27**, 573–580 (1999). doi: 10.1093/nar/27.2.573; pmid: 9862982
30. M. J. Chaisson, G. Tesler, Mapping single molecule sequencing reads using basic local alignment with successive refinement (BLASR): Application and theory. *BMC Bioinformatics* **13**, 238 (2012). pmid: 22988817
31. J. D. Parsons, Miropeats: Graphical DNA sequence comparisons. *Comput. Appl. Biosci.* **11**, 615–619 (1995). pmid: 8808577

ACKNOWLEDGMENTS

We are grateful to A. Scally and Z. Ning for early access to the upgraded Kamilah gorilla assembly (gorGor4) and for discussion regarding its assembly. We thank M. Duyzend, L. Harshman, and C. Lee for technical assistance and quality control in generating sequencing data and H. Li for helpful suggestions for the PSMC analysis. The authors thank M. Heget, K. Gillespie, and M. Shender from the Lincoln Park Zoo for providing gorilla peripheral blood and T. Brown for assistance in editing this manuscript. This work was supported, in part, by grants from the U.S. National Institutes of Health (NIH grant HG002385 to E.E.E. and HG007635 to R.K.W. and E.E.E.; HG003079 to R.K.W.; HG007990 to D.H. and B.P.; and HG007234 to B.P.). E.E.E., J.S., and D.H. are investigators of the Howard Hughes Medical Institute. E.E.E. is on the scientific advisory board (SAB) of DNAnexus and was a SAB member of Pacific Biosciences. (2009–2013); E.E.E. is a consultant for Kunming University of Science and Technology (KUST) as part of the 1000 China Talent Program. M.J.P.C. is a former employee of (2009–2012) and owns shares in Pacific Biosciences. On 24 February 2011, Pacific Biosciences filed a patent entitled "Sequence assembly and consensus sequence determination" (U.S. patent no. US20120330566, issued 27 December 2012); M.J.P.C. is identified as inventor of this patent. Pacific Biosciences has filed two patents related to the Falcon assembler algorithm entitled "String graph assembly for polyploid genomes" (U.S. patent no. US2015/0169823 A1 filed 18 December 2014, and U.S. patent no. US2015/0286775 A1 filed 18 June 2015); C.C. is identified as inventor for both patents. The Susie3 assembly, PacBio and Illumina sequencing data for Susie, and clone sequences have been deposited in the European Nucleotide Archive under the project accession PRJEB10880. E.E.E., D.G., J.H., M.J.P.C., C.M.H., and Z.N.K. designed experiments; K.M.M., M.M., and C.B. prepared libraries and generated sequencing data; D.G., J.H., M.J.P.C., C.M.H., Z.N.K., L.W.H., and A.R. performed bioinformatics analyses; I.F., J.A., M.D., B.P., R.K.W., and D.H. analyzed gene accuracy. J.S. helped in the evaluation of Hi-C data. C.D. and C.-S.C. aided in Falcon assembler modifications. J.H. deposited SMRT sequencing data into SRA. E.E.E., D.G., J.H., M.J.P.C., C.M.H., and Z.N.K. wrote the manuscript.

SUPPLEMENTARY MATERIALS

www.sciencemag.org/content/352/6281/aae0344/suppl/DC1
Supplementary Text
Figs. S1 to S63
Tables S1 to S36
References (*32*–*67*)

7 December 2015; accepted 26 February 2016
10.1126/science.aae0344

RESEARCH ARTICLE SUMMARY

SYNTHETIC BIOLOGY

Genetic circuit design automation

Alec A. K. Nielsen, Bryan S. Der, Jonghyeon Shin, Prashant Vaidyanathan, Vanya Paralanov, Elizabeth A. Strychalski, David Ross, Douglas Densmore, Christopher A. Voigt*

INTRODUCTION: Cells respond to their environment, make decisions, build structures, and coordinate tasks. Underlying these processes are computational operations performed by networks of regulatory proteins that integrate signals and control the timing of gene expression. Harnessing this capability is critical for biotechnology projects that require decision-making, control, sensing, or spatial organization. It has been shown that cells can be programmed using synthetic genetic circuits composed of regulators organized to generate a desired operation. However, the construction of even simple circuits is time-intensive and unreliable.

ON OUR WEBSITE

Read the full article at http://dx.doi.org/10.1126/science.aac7341

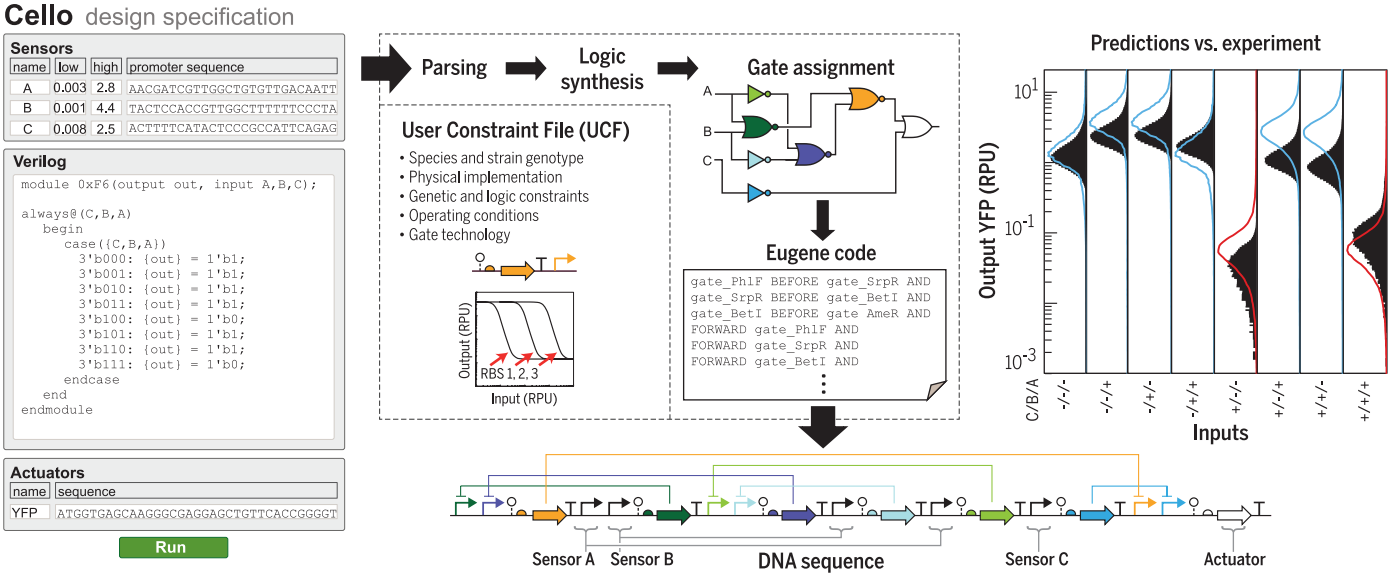
RATIONALE: Electronic design automation (EDA) was developed to aid engineers in the design of semiconductor-based electronics. In an effort to accelerate genetic circuit design, we applied principles from EDA to enable increased circuit complexity and to simplify the incorporation of synthetic gene regulation into genetic engineering projects. We used the hardware description language Verilog to enable a user to describe a circuit function. The user also specifies the sensors, actuators, and "user constraints file" (UCF), which defines the organism, gate technology, and valid operating conditions. Cello (www.cellocad.org) uses this information to automatically design a DNA sequence encoding the desired circuit. This is done via a set of algorithms that parse the Verilog text, create the circuit diagram, assign gates, balance constraints to build the DNA, and simulate performance.

RESULTS: Cello designs circuits by drawing upon a library of Boolean logic gates. Here, the gate technology consists of NOT/NOR logic based on repressors. Gate connection is simplified by defining the input and output signals as RNA polymerase (RNAP) fluxes. We found that the gates need to be insulated from their genetic context to function reliably in the context of different circuits. Each gate is isolated using strong terminators to block RNAP leakage, and input interchangeability is improved using ribozymes and promoter spacers. These parts are varied for each gate to avoid breakage due to recombination. Measuring the load of each gate and incorporating this into the optimization algorithms further reduces evolutionary pressure.

Cello was applied to the design of 60 circuits for *Escherichia coli*, where the circuit function was specified using Verilog code and transformed to a DNA sequence. The DNA sequences were built as specified with no additional tuning, requiring 880,000 base pairs of DNA assembly. Of these, 45 circuits performed correctly in every output state (up to 10 regulators and 55 parts). Across all circuits, 92% of the 412 output states functioned as predicted.

CONCLUSION: Our work constitutes a hardware description language for programming living cells. This required the co-development of design algorithms with gates that are sufficiently simple and robust to be connected by automated algorithms. We demonstrate that engineering principles can be applied to identify and suppress errors that complicate the compositions of larger systems. This approach leads to highly repetitive and modular genetics, in stark contrast to the encoding of natural regulatory networks. The use of a hardware-independent language and the creation of additional UCFs will allow a single design to be transformed into DNA for different organisms, genetic endpoints, operating conditions, and gate technologies. ■

The list of author affiliations is available in the full article online.
*Corresponding author. E-mail: cavoigt@gmail.com
Cite this article as A. A. K. Nielsen *et al.*, *Science* **352**, aac7341 (2016). DOI: 10.1126/science.aac7341



Genetic programming using Cello. A user specifies the desired circuit function in Verilog code, and this is transformed into a DNA sequence. An example circuit is shown (0xF6); red and blue curves are predicted output states for populations of cells, and solid black distributions are experimental flow cytometry data. The outputs are shown for all combinations of sensor states; plus and minus signs indicate the presence or absence of input signal. RBS, ribosome binding site; RPU, relative promoter unit; YFP, yellow fluorescent protein.

Downloaded from on March 31, 2016

RESEARCH ARTICLE

SYNTHETIC BIOLOGY

Genetic circuit design automation

Alec A. K. Nielsen,[1] Bryan S. Der,[1,2] Jonghyeon Shin,[1] Prashant Vaidyanathan,[2] Vanya Paralanov,[3] Elizabeth A. Strychalski,[3] David Ross,[3] Douglas Densmore,[2] Christopher A. Voigt[1]*

Computation can be performed in living cells by DNA-encoded circuits that process sensory information and control biological functions. Their construction is time-intensive, requiring manual part assembly and balancing of regulator expression. We describe a design environment, Cello, in which a user writes Verilog code that is automatically transformed into a DNA sequence. Algorithms build a circuit diagram, assign and connect gates, and simulate performance. Reliable circuit design requires the insulation of gates from genetic context, so that they function identically when used in different circuits. We used Cello to design 60 circuits for *Escherichia coli* (880,000 base pairs of DNA), for which each DNA sequence was built as predicted by the software with no additional tuning. Of these, 45 circuits performed correctly in every output state (up to 10 regulators and 55 parts), and across all circuits 92% of the output states functioned as predicted. Design automation simplifies the incorporation of genetic circuits into biotechnology projects that require decision-making, control, sensing, or spatial organization.

Electronic design automation (EDA) software tools aid engineers in the design and analysis of semiconductor-based electronics. Prior to EDA, integrated circuit design was a manual process performed by hand. This was accelerated by the development of hardware description languages (e.g., Verilog) that enabled a user to design an electronic system through textual commands that are transformed into a circuit patterned on silicon. We applied this approach to genetic circuits, so that a Verilog design is transformed into a linear DNA sequence that can be constructed and run in living cells. The design environment, referred to as Cello (an abbreviation of Cellular Logic), implements algorithms that derive the detailed physical design from the textual specification (Fig. 1). Cello requires genetic logic gates that are sufficiently modular and reliable such that their interconnection can be automated.

Moving computing into cells enables programmable control over biological functions (*1*–*5*). This is crucial for fully realizing the potential of engineering biology, where applications require that different sets of genes be active under different conditions (*6*–*9*). Cells are naturally able to respond to their environment, make decisions, construct intricate structures, and coordinate to distribute tasks. These functions are controlled by a regulatory network of interacting proteins, RNA, and DNA. Patterns of such interactions generate computational operations analogous to those used in electronic circuits (*10*–*14*), and regulators can be combined to build synthetic genetic circuits (*15*–*18*). This approach has led to digital logic gates (*19*–*24*), memory devices (*25*–*29*), analog computation (*30*), and dynamic circuits (e.g., timers and oscillators) (*15*, *16*, *31*–*33*). These have begun to be integrated into biotechnological applications (*34*, *35*)—for example, to implement feedback control in a metabolic pathway (*36*). However, the construction of simple circuits consisting of only a few regulators remains a time-consuming task, and this has limited their widespread implementation.

Genetic circuit design is challenging for several reasons (*37*, *38*). First, circuits require precise balancing of regulator expression (*22*, *39*). Second, many parts are combined to build a circuit and their function can vary depending on genetic context, strain, and growth conditions (*40*–*46*). Third, circuits are defined by many states (their response to different inputs or how they change over time), and this can be cumbersome to characterize (*15*, *47*–*49*). Finally, many regulators are toxic when overexpressed, and even mild effects can combine to drive negative selection against the circuit (*50*). Balancing these issues is difficult to do by hand. Thus, computational tools have been developed for the study of natural networks and to aid circuit design by predicting how parts or devices will perform when connected (*51*–*58*).

We developed Cello to accelerate circuit design, allow increased complexity of circuits, and enable non-experts to incorporate synthetic gene regulation into genetic engineering projects (Fig. 1). The focus is on the design of a circuit that performs a desired computational operation, which connects to cell-based sensors and cellular functions (actuators). A user provides three specifications to Cello. The first are the DNA sequences for the sensors: the sequences of their output promoters and data for their ON/OFF signal strengths in standardized units (see below) (*59*). The second is the "user constraints file" (UCF), which contains the functional details of the gate library, the layout of the genetic system, the organism and strain, and the operating conditions for which the circuit design is valid. The third is Verilog code that captures the desired computational operation. Cello uses this information to automatically design a DNA sequence encoding the desired genetic circuit by connecting a set of simpler gates that implement Boolean logic to the sensors and each other. The output of the circuit can be connected to cellular processes by directing the output promoter to control a cellular function (e.g., a metabolic pathway), either directly or through an intermediate (e.g., a phage RNA polymerase) (*60*, *61*). The sensors, circuit, and actuator are inserted into specific genetic locations and transformed into a strain, both of which are defined in the UCF (Fig. 1B).

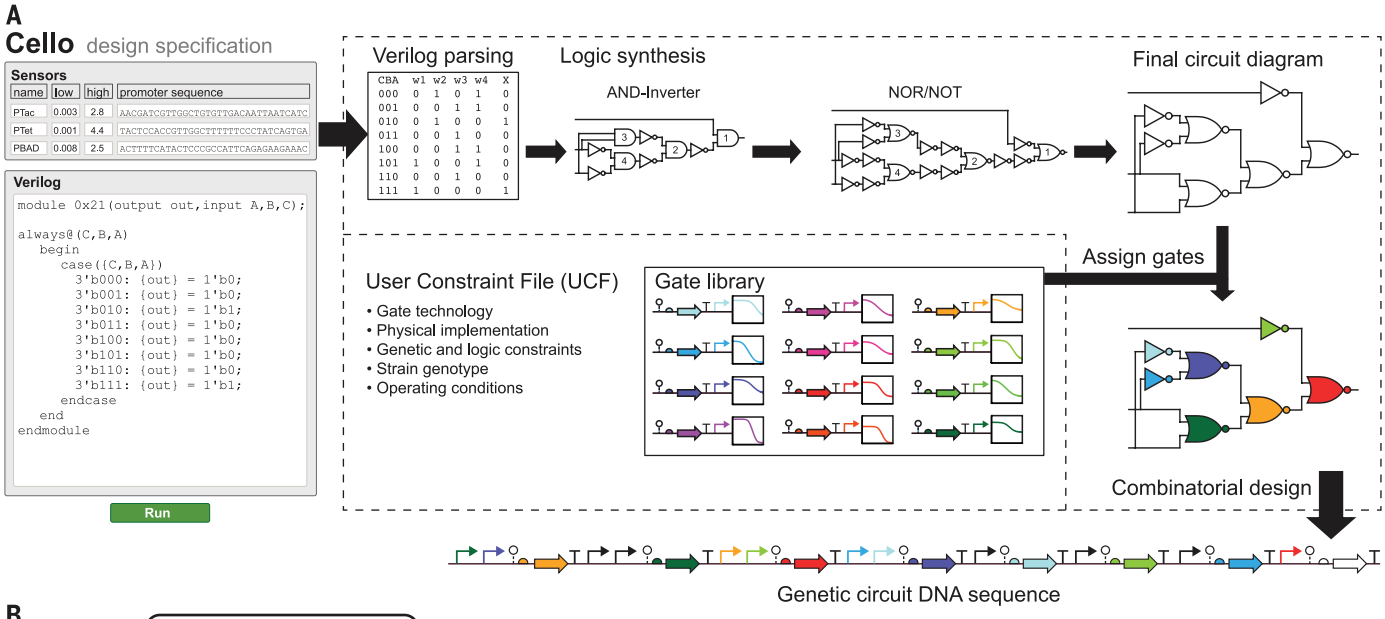
Cello builds circuits by connecting transcriptional gates, whose common signal carrier is RNA polymerase (RNAP) flux on DNA (*62*). This conversion allows gates to be layered by having the output promoter from one gate serve as the input to the next. This modularizes the design, so that a circuit is defined by a pattern of promoters in front of regulators on a linear DNA strand (Fig. 2A). Within this paradigm, the regulators performing the gate biochemistry could be transcription factors (*21*, *63*), RNA-based regulation (*64*–*66*), protein-protein interactions (*19*, *67*), CRISPR/Cas-based regulation (*68*–*71*), or recombinases (*25*, *26*, *72*).

We developed a set of insulated NOT and NOR gates based on prokaryotic repressors (*21*). These repressor-based gates were characterized in isolation as NOT gates. To facilitate the connection of gates and sensors, we adopted the BBa_J23101 constitutive promoter as a standard (*59*). The output of an insulated version of this promoter (*73*) is defined as 1 RPU (relative promoter unit); working with National Institute of Standards and Technology (NIST) collaborators, this output was measured to correspond to 24.7 ± 5.7 mRNAs per cell, which is approximately 0.02 RNAP s^{-1} promoter^{-1} (fig. S33). These data were used by Cello to automatically generate a large set of circuits. The sequences were built as specified by the software output with no additional tuning, which facilitates the iterative improvement of the quality of the gates and design rules.

Cello design environment

Verilog is a commonly used hardware description language for electronic system design (*74*). It is hardware-independent, meaning that a circuit can be described by abstract textual commands and then transformed into different physical implementations (i.e., chip types). Verilog is often accompanied by a simulation package that aids the evaluation of a design in silico before building the system. Verilog code has a hierarchical organization centered on modules that communicate

[1]Synthetic Biology Center, Department of Biological Engineering, Massachusetts Institute of Technology, Cambridge, MA 02139, USA. [2]Biological Design Center, Department of Biomedical Engineering, Department of Electrical and Computer Engineering, Boston University, Boston, MA 02215, USA. [3]Biosystems and Biomaterials Division, Material Measurement Laboratory, National Institute of Standards and Technology, Gaithersburg, MD 20817, USA.
*Corresponding author. E-mail: cavoigt@gmail.com



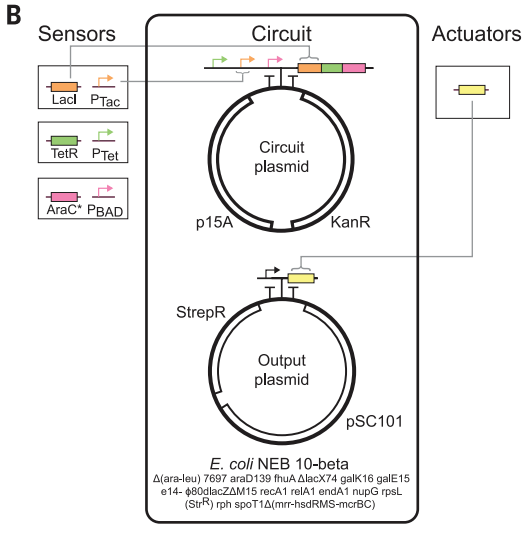


Fig. 1. Overview of Cello. (**A**) Cello users write Verilog code and select or upload sensors and a UCF. On the basis of the Verilog design, a truth table is constructed from which a circuit diagram is synthesized. Regulators are assigned from a library to each gate (each color is a different repressor). Combinatorial design is then used to concatenate parts into a linear DNA sequence. SBOL Visual (*101*) is used for the part symbols. Raised arrows are promoters, circles on stems are ribozyme insulators, hemispheres are RBSs, large arrows are protein-coding sequences, and "T"s are terminators. Part colors correspond to physical gates. (**B**) The physical specification for the Eco1C1G1T1 UCF. The circuit and sensors are inserted into one plasmid; the other plasmid contains the circuit output promoter, which can be used to drive the expression of a fluorescent protein or other actuator. Both plasmids must be present in the specified strain for the design to be valid.

through wires to propagate signals. In our implementation, circuit function can be defined by Case, Assign, or Structural statements within modules (fig. S23). Initially, our focus with Cello is on the creation of asynchronous combinational logic without feedback. This is useful in the design of genetic circuits that can process multiple environmental sensors in order to choose among different cellular functions. However, Verilog provides the framework to extend the designs to include more complex circuits, including those with specified timing and signal strengths as well as analog (Verilog-AMS) functions.

The philosophy behind Cello is to generate circuits for highly specified physical systems and operating conditions. This paradigm is captured by the UCF, which specifies (i) the gate technology, including DNA sequences and functional data; (ii) defined physical locations for the circuit (e.g., plasmid or genomic locus); (iii) the organism, strain, and genotype; (iv) operating conditions where the circuit design is valid; (v) architectural rules to constrain the part arrangement; and (vi) preferred logic motifs to be incorporated during logic synthesis.

The UCF follows the JSON (JavaScript Object Notation) standard (*75*), which is both human- and machine-readable and is convertible with SBOL (Synthetic Biology Open Language) (*76*). We developed the Eco1C1G1T1 UCF (data file S1) for *E. coli* (NEB 10-beta) and gate technology based on a set of 12 prokaryotic repressors (*21*). The development of additional UCFs would enable a circuit design to be transferred to other organisms, conditions, or gate technologies.

When a user selects a UCF and synthesizes a circuit from Verilog code, the corresponding DNA sequence is designed in three steps (Fig. 1). First, the textual commands are converted to a circuit diagram. Algorithms parse the Verilog code and derive a truth table (fig. S23), which is converted to an initial circuit diagram by the logic synthesis program ABC (*77*) and subsequently modified to only contain logic operations for gates available in the UCF (fig. S25). The second step is to assign specific regulators to each gate in the diagram. Functionally connecting gates requires that the outputs from the first gate span the input threshold of the second gate (Fig. 2B). Because gates based on different regulators have different response functions, not all pairs can be functionally connected (Fig. 2C). Identifying the optimal assignment is an NP-complete problem (Fig. 2D) (*78*–*81*). We implemented a Monte Carlo simulated annealing algorithm to rapidly identify an assignment that produces the desired response (Fig. 2E and fig. S28). The third step is to create the linear DNA sequence based on the circuit diagram and gate assignment. The assignment is converted into a set of parts and constraints between the parts [written with the Eugene language (*82*)]. The UCF can also include additional constraints on the genetic architecture—for example, to forbid a particular combination of parts. A combinatorial design algorithm (*83*) is used to build a genetic construct that conforms to the constraints (fig. S29). This allows a user to design multiple constructs containing the same circuit function and genetic constraints while varying

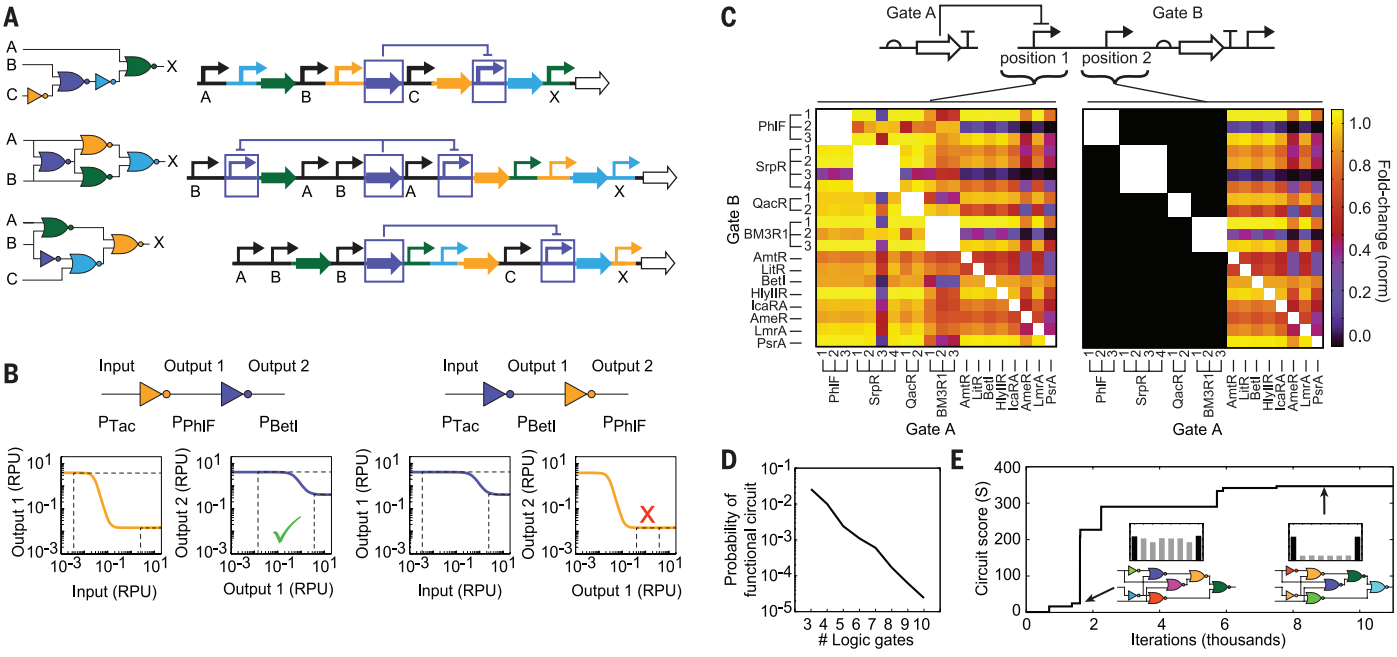


Fig. 2. Assignment of genetic gates to the circuit diagram. (**A**) A set of four gates based on different repressors (colors) connected in various permutations to build different circuit functions. The inputs (A, B, and C) are sensor input promoters; the circuit output promoter (X) controls the actuating gene. (**B**) The shapes of the gate response functions determine whether they can be functionally connected. The orange gate (PhlF) has a large dynamic range (dashed lines) that spans the threshold of the purple gate (BetI). However, in the reverse order, the gates do not functionally connect. (**C**) Combinatorial relations of repressors from the insulated gate library are shown in the upstream (gate A) and downstream (gate B) positions. Color scale at right indicates relative change (normalized), calculated as the maximum output range that can be achieved by connecting gate A to gate B. Numbers denote different RBSs. The left and right graphs show when gate A regulates position 1 and position 2, respectively. Gates that are excluded from position 2 because of roadblocking are shown in black (fig. S9). (**D**) The probability of finding a functional circuit versus the number of logic gates. The probability of a functional circuit is defined as the likelihood that a random assignment passes input threshold analysis (fig. S31) and has no roadblocking combinations. (**E**) The convergence of the simulated annealing gate assignment algorithm (fig. S28). Bar graph insets: Black bars should be ON, gray bars should be OFF; the *y* axis is the output in RPU on a log scale, and the *x* axis is the input state (from left to right: 000, 001, 010, 011, 110, 101, 110, 111). The circuit score (*S*) is defined as the ratio of the lowest predicted ON state to the highest predicted OFF state (fig. S26 and eq. S2). An example search is shown for the circuit diagram in the insets; colors correspond to repressors assigned to each gate (Fig. 3B).

unconstrained design elements to build a library that can be screened.

Cello then simulates the performance of the genetic circuit. When flow cytometry data are provided in the UCF for the gates, this provides the cell-to-cell variation in the response for a population of cells. We developed a computational approach to quantify how population variability propagates from the sensors through the gates to the output promoters (fig. S30). Cello applies a simple algorithm to determine how signals propagate from the sensors through the gates to the output promoters. This generates predicted cytometry distribution for all combinations of input states, which can be directly compared to experiments. Finally, for each gate, the load on the cell for carrying the gates is estimated on the basis of their impact on growth [percent reduction of optical density at 600 nm (OD_{600})] as a function of the activity of the input promoter (*84*). For any combination of inputs, if the predicted growth reduction exceeds a threshold, this information can guide multiobjective circuit optimization or be provided as a warning to the user (fig. S27).

Initial gate assembly and failure modes

We constructed a gate library based on a set of 16 Tet repressor (TetR) homologs that are orthogonal; that is, they do not bind to each other's promoters (*21*). These can be converted into simple NOT/NOR gates by having the input promoter(s) drive the expression of the repressor, after which there is a terminator and output promoter. Because of a lack of strong terminators when these gates were built, the same terminator (BBa_B0015) was reused for each one. Each repressor had a different ribosome binding site (RBS), chosen to maximize the dynamic range.

These gates could be connected to form simple functional circuits; however, in each case additional tuning was required and the dynamic range of the output was low (*21*). We tested the ability of the response functions of the gates to predict circuit behavior as a whole with no additional tuning. We designed a set of eight simple circuits from these gates that required between one and four repressors (Fig. 3A) (*84*). Nearly all of the circuits generated an incorrect response. Only the (A NIMPLY B) gate functioned properly, and six of eight circuits had their output states either all OFF or all ON for every input condition. Across all the circuits, 13 of 32 output states were correct, which is comparable to what would be expected from a process that generates random outputs.

We used this test set to determine common causes for circuit failure (figs. S6 to S10). When paired with different promoters, gates often generated an unpredictable response, and this was apparent even for circuits based on a single repressor (*42*). The promoters generated transcripts with different 5′-untranslated regions (5′UTRs), which can strongly influence gene expression (*40*, *85*). A second problem was that some promoters in the downstream "position 2" of a NOR gate (Fig. 2C) can reduce transcription from the upstream promoter, a phenomenon we refer to as "roadblocking." Third, some circuits had growth defects, which were caused by repressors that become toxic when expressed past a threshold (Fig. 3D). Fourth, several circuits were genetically unstable because of homologous recombination of parts reused in the same circuit (*86*, *87*).

Insulated gates

A second generation of gates was constructed to address the observed failure modes (Fig. 3B). Changes took two forms: (i) New parts were added to gates to insulate them from genetic context, and (ii) rules were included in the UCF that disallow certain parts, positions, and part combinations that lead to unpredictable behavior. Transcriptional insulation was achieved for gates by adding a different strong terminator with sufficiently diverse sequences to avoid homologous recombination

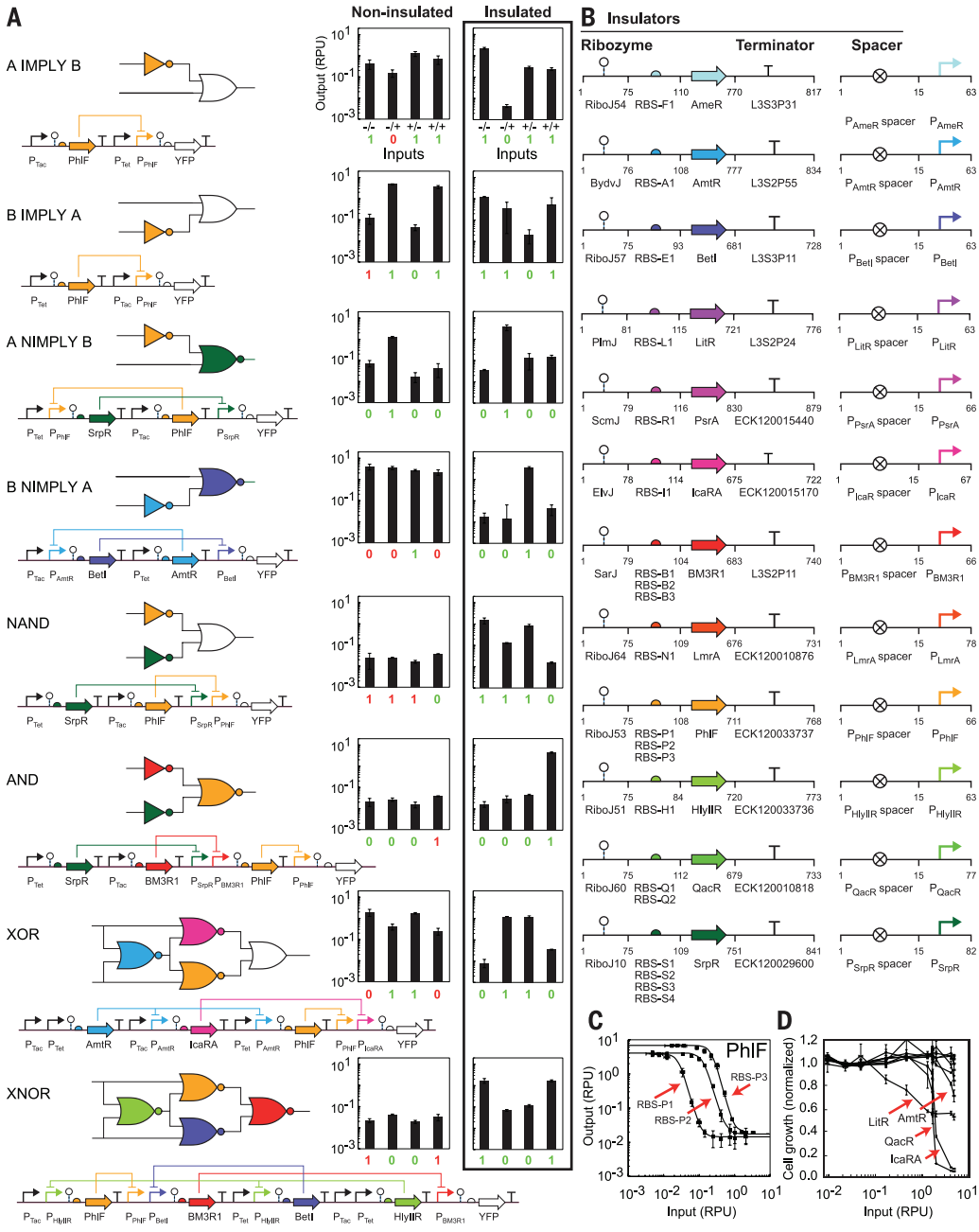


Fig. 3. Impact of gate insulation. (**A**) The logic function, circuit diagram, and DNA construct are shown for each genetic circuit. Only the insulated circuit schematics are shown; the equivalent information for the non-insulated circuits is shown in fig. S5. The expected output for each circuit is shown at the bottom of each bar graph as 1 for ON and 0 for OFF. The numbers are colored according to whether the state is predicted correctly (green) or incorrectly (red). For noninsulated circuits, inputs correspond to the absence or presence of 1 mM isopropyl-β-D-thiogalactopyranoside (IPTG; right −/+) and 20 μM 3-oxohexanoyl-homoserine lactone (3OC6HSL; left −/+). For insulated circuits, inputs correspond to the absence or presence of 1 mM IPTG (right −/+) and aTc (2 ng/ml; left −/+) (*84*). (**B**) The architectures of the insulated gates. Some gates have multiple versions with different RBS sequences. The gate DNA sequences are provided in table S8. (**C**) An example of a response function for a NOT gate based on the PhlF repressor. The change in the threshold for the three RBSs is shown. Data for all insulated gates are shown in fig. S4. (**D**) The impact of each gate on cell growth as a function of its input promoter activity. Cell growth was measured as OD_{600} and normalized by the growth of the no-inducer control 6 hours after induction (*84*). The four gates that reduced growth by >20% are indicated. Error bars are one SD of normalized cell growth [*y* axis in (D)] and the median [*y* axis in (A) and (C); *x* axis in (C) and (D)] for three independent experiments performed on the same day.

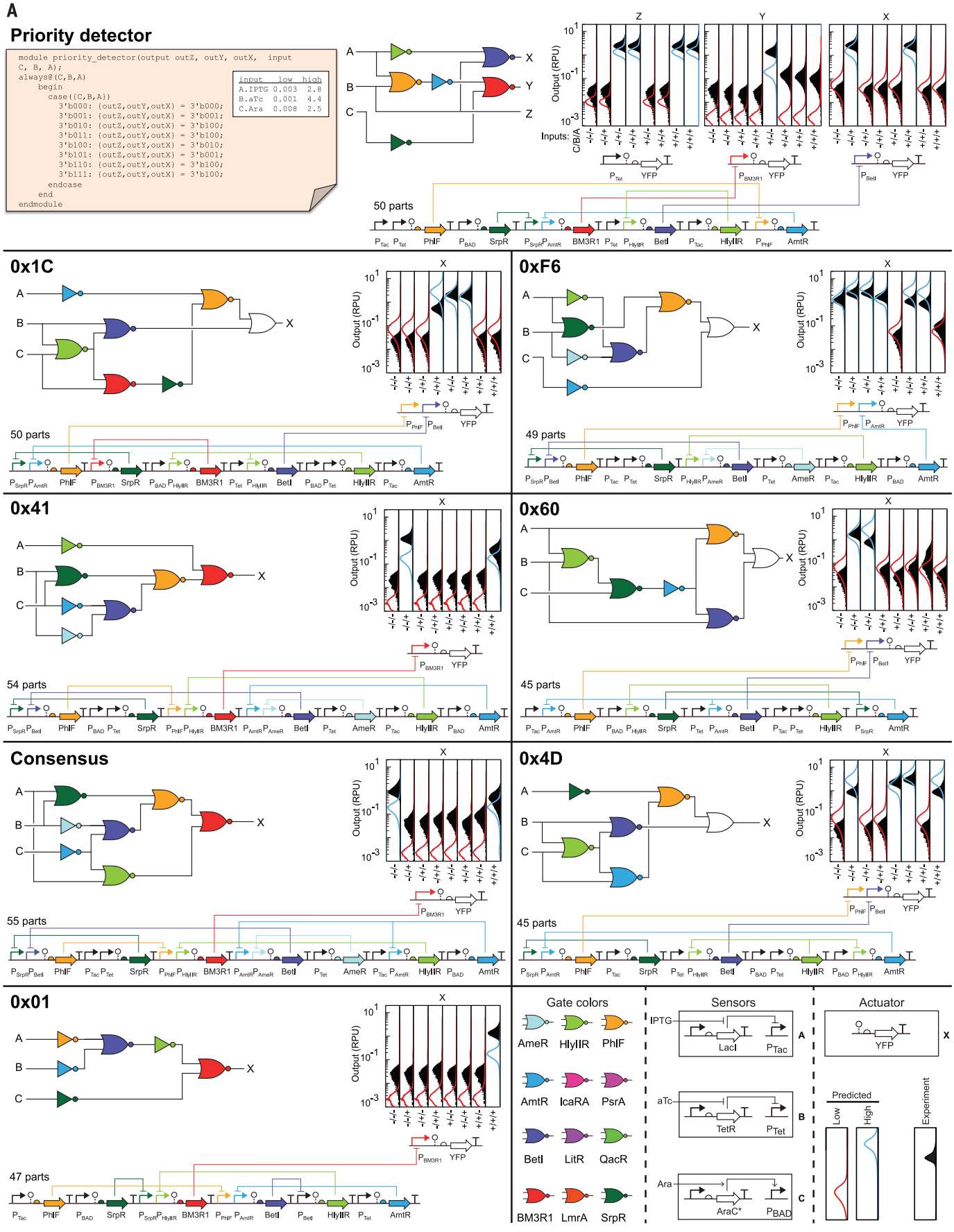
(table S2) (*87*). The output promoters were also insulated on both sides from changes to their upstream and downstream context. Insulators consisting of a hammerhead ribozyme and downstream hairpin (RiboJ) ensure that a promoter generates the same response function irrespective of the downstream gene (*42*). As with the terminators, to avoid recombination we had to create a library of RiboJ variants that are functionally identical but sequence-diverse so that each gate had a unique insulator sequence (fig. S3 and table S1). To insulate the promoter from the upstream sequence, we added 15 nucleotides (nt) of randomly generated DNA to extend the promoters to −50 so as to include regions with an impact on strength (table S8) (*88*). Finally, the propensity for repressible promoters to roadblock was measured (fig. S9) and these data were used to create Eugene rules in the UCF that disallow these promoters from position 2 in NOR gates (Fig. 2C).

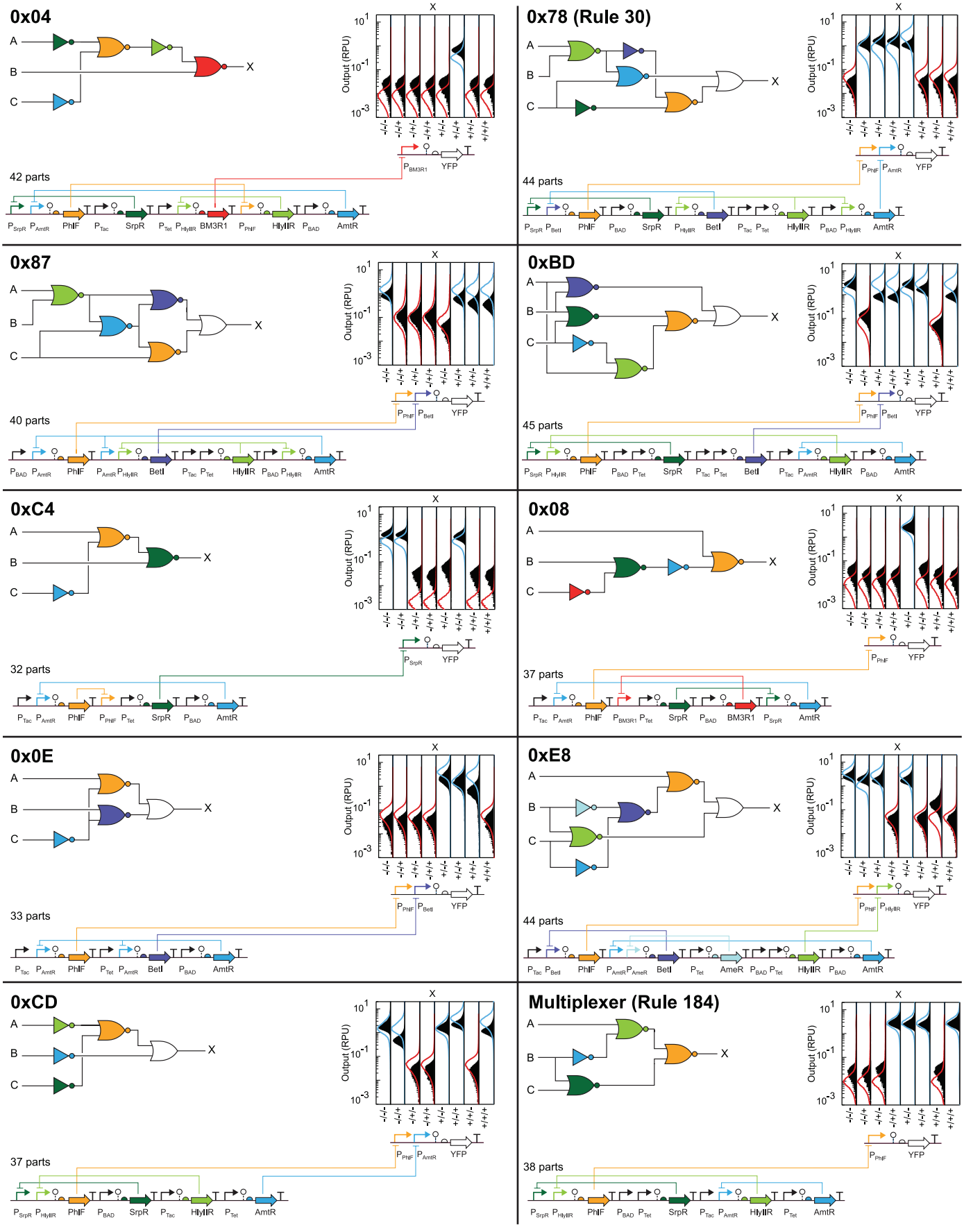
The response functions were then experimentally measured for all the gates (Fig. 3C, fig. S4, and table S4). Several of the first-version gates had response functions that were difficult to connect functionally to sensors or other gates (Fig. 2B). To increase the likelihood of finding a connection, we made versions of the gates with different RBSs that shift the response threshold (table S3). The growth impact of each gate was then measured as a function of the input promoter activity to determine whether there is a toxicity threshold that should be avoided (Fig. 3D and fig. S10). To eliminate toxic or cross-reacting repressors, we reduced the original set of 16 TetR homologs to 12. Only four of these caused a growth defect at high inputs, and this could be avoided by the assignment algorithm (fig. S27).

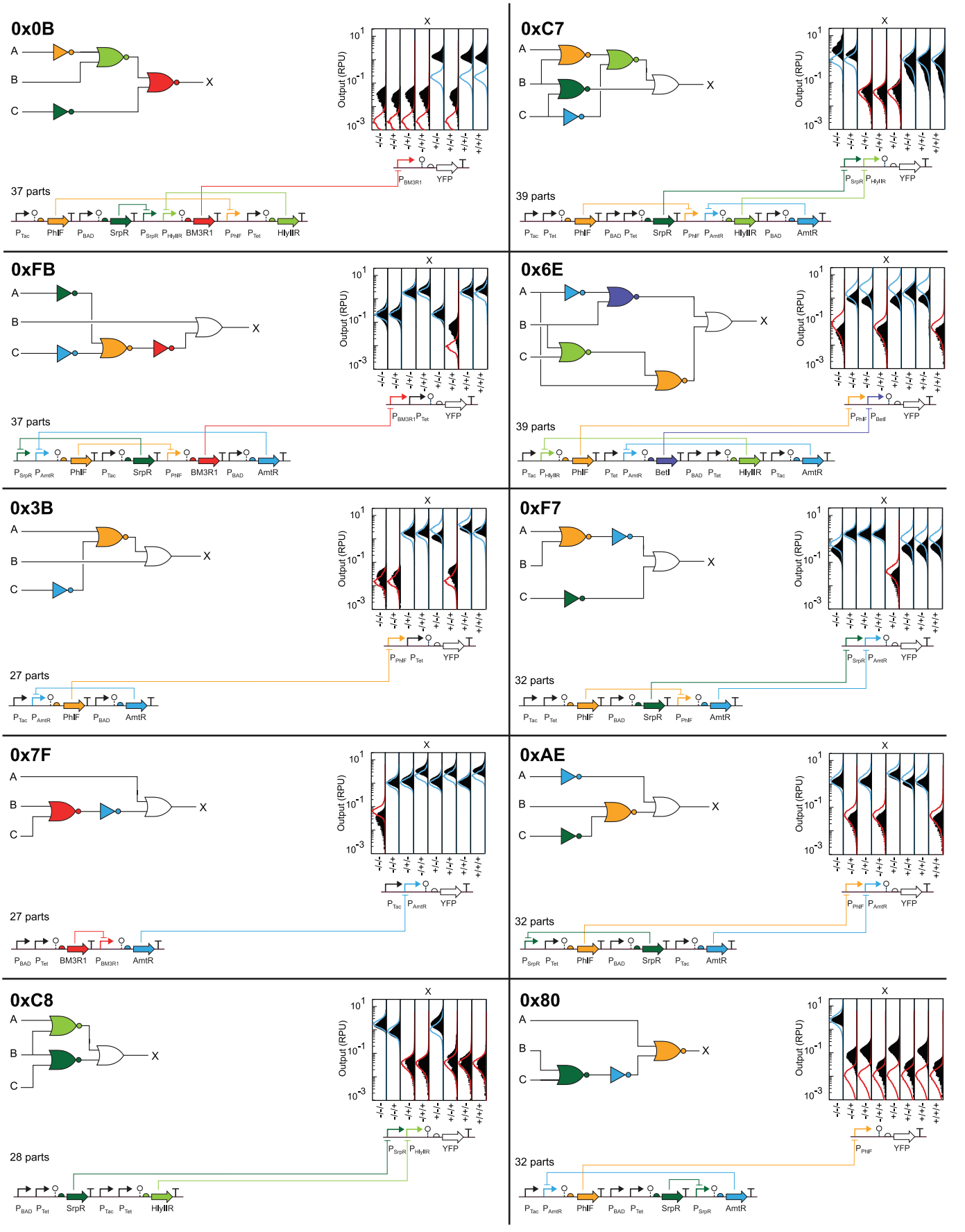
The eight simple circuits were redesigned with the new gate library (*84*). The sequences were constructed as designed, with no post-design tuning. All of the circuits functioned correctly, corresponding to a total of 32/32 correct output states (Fig. 3A).

Circuit design automation using Cello

Cello was used to design a large set of 52 additional circuits based on the insulated gates (Fig. 4) (*84*). These circuits include a Priority Detector (that prioritizes the inputs and selects which output is ON based on the highest-priority input that is ON), well-known functions (e.g., a multiplexer), and logic underlying cellular automaton pattern


A
Priority detector
module priority_detector(output outZ, outY, outX, input C, B, A);
always@(C,B,A)
begin
case({C,B,A})
3'b000: {outZ,outY,outX} = 3'b000;
3'b001: {outZ,outY,outX} = 3'b001;
3'b010: {outZ,outY,outX} = 3'b100;
3'b011: {outZ,outY,outX} = 3'b100;
3'b100: {outZ,outY,outX} = 3'b010;
3'b101: {outZ,outY,outX} = 3'b001;
3'b110: {outZ,outY,outX} = 3'b100;
3'b111: {outZ,outY,outX} = 3'b100;
endcase
end
endmodule
input low high
A.IPTG 0.003 2.8
B.aTc 0.001 4.4
C.Ara 0.008 2.5
A
B
C
X
Y
Z
Output (RPU)
Inputs: C/B/A
YFP
50 parts
0x1C
49 parts
0xF6
54 parts
0x41
45 parts
0x60
55 parts
Consensus
45 parts
0x4D
47 parts
0x01
Gate colors
AmeR HlyIIR PhlF
AmtR IcaRA PsrA
BetI LitR QacR
BM3R1 LmrA SrpR
Sensors
IPTG
LacI
aTc
TetR
Ara
AraC*
Actuator
Predicted
Low
High
Experiment


0x04
A
B
C
X
42 parts
P_{SrpR} P_{AmtR} PhlF P_{Tac} SrpR P_{Tet} P_{HlyIIR} BM3R1 P_{PhlF} HlyIIR P_{BAD} AmtR
Output (RPU)
10^{1}
10^{-1}
10^{-3}
-/-/-
-/-/+
-/+/-
-/+/+
+/-/-
+/-/+
+/+/-
+/+/+
P_{BM3R1} YFP
0x78 (Rule 30)
44 parts
P_{SrpR} P_{BetI} PhlF P_{BAD} SrpR P_{HlyIIR} BetI P_{Tac} P_{Tet} HlyIIR P_{BAD} P_{HlyIIR} AmtR
P_{PhlF} P_{AmtR} YFP
0x87
40 parts
P_{BAD} P_{AmtR} PhlF P_{AmtR} P_{HlyIIR} BetI P_{Tac} P_{Tet} HlyIIR P_{BAD} P_{HlyIIR} AmtR
P_{PhlF} P_{BetI} YFP
0xBD
45 parts
P_{SrpR} P_{HlyIIR} PhlF P_{BAD} P_{Tet} SrpR P_{Tac} P_{Tet} BetI P_{Tac} P_{AmtR} HlyIIR P_{BAD} AmtR
P_{PhlF} P_{BetI} YFP
0xC4
32 parts
P_{Tac} P_{AmtR} PhlF P_{PhlF} P_{Tet} SrpR P_{BAD} AmtR
P_{SrpR} YFP
0x08
37 parts
P_{Tac} P_{AmtR} PhlF P_{BM3R1} P_{Tet} SrpR P_{BAD} BM3R1 P_{SrpR} AmtR
P_{PhlF} YFP
0x0E
33 parts
P_{Tac} P_{AmtR} PhlF P_{Tet} P_{AmtR} BetI P_{BAD} AmtR
P_{PhlF} P_{BetI} YFP
0xE8
44 parts
P_{Tac} P_{BetI} PhlF P_{AmtR} P_{AmeR} BetI P_{Tet} AmeR P_{BAD} P_{Tet} HlyIIR P_{BAD} AmtR
P_{PhlF} P_{HlyIIR} YFP
0xCD
37 parts
P_{SrpR} P_{HlyIIR} PhlF P_{BAD} SrpR P_{Tac} HlyIIR P_{Tet} AmtR
P_{PhlF} P_{AmtR} YFP
Multiplexer (Rule 184)
38 parts
P_{SrpR} P_{HlyIIR} PhlF P_{BAD} P_{Tet} SrpR P_{Tac} P_{AmtR} HlyIIR P_{Tet} AmtR
P_{PhlF} YFP


0x0B
A
B
C
X
37 parts
P_Tac PhlF P_BAD SrpR P_SrpR P_HlyIIR BM3R1 P_PhlF P_Tet HlyIIR
Output (RPU)
10^1
10^-1
10^-3
-/-/-
-/-/+
-/+/-
-/+/+
+/-/-
+/-/+
+/+/-
+/+/+
P_BM3R1
YFP
0xC7
A
B
C
X
39 parts
P_Tac P_Tet PhlF P_BAD P_Tet SrpR P_PhlF P_AmtR HlyIIR P_BAD AmtR
Output (RPU)
P_SrpR P_HlyIIR
YFP
0xFB
A
B
C
X
37 parts
P_SrpR P_AmtR PhlF P_Tac SrpR P_PhlF BM3R1 P_BAD AmtR
Output (RPU)
P_BM3R1 P_Tet
YFP
0x6E
A
B
C
X
39 parts
P_Tac P_HlyIIR PhlF P_Tet P_AmtR BetI P_BAD P_Tet HlyIIR P_Tac AmtR
Output (RPU)
P_PhlF P_BetI
YFP
0x3B
A
B
C
X
27 parts
P_Tac P_AmtR PhlF P_BAD AmtR
Output (RPU)
P_PhlF P_Tet
YFP
0xF7
A
B
C
X
32 parts
P_Tac P_Tet PhlF P_BAD SrpR P_PhlF AmtR
Output (RPU)
P_SrpR P_AmtR
YFP
0x7F
A
B
C
X
27 parts
P_BAD P_Tet BM3R1 P_BM3R1 AmtR
Output (RPU)
P_Tac P_AmtR
YFP
0xAE
A
B
C
X
32 parts
P_SrpR P_Tet PhlF P_BAD SrpR P_Tac AmtR
Output (RPU)
P_PhlF P_AmtR
YFP
0xC8
A
B
C
X
28 parts
P_BAD P_Tet SrpR P_Tac P_Tet HlyIIR
Output (RPU)
P_SrpR P_HlyIIR
YFP
0x80
A
B
C
X
32 parts
P_Tac P_AmtR PhlF P_BAD P_Tet SrpR P_SrpR AmtR
Output (RPU)
P_PhlF
YFP

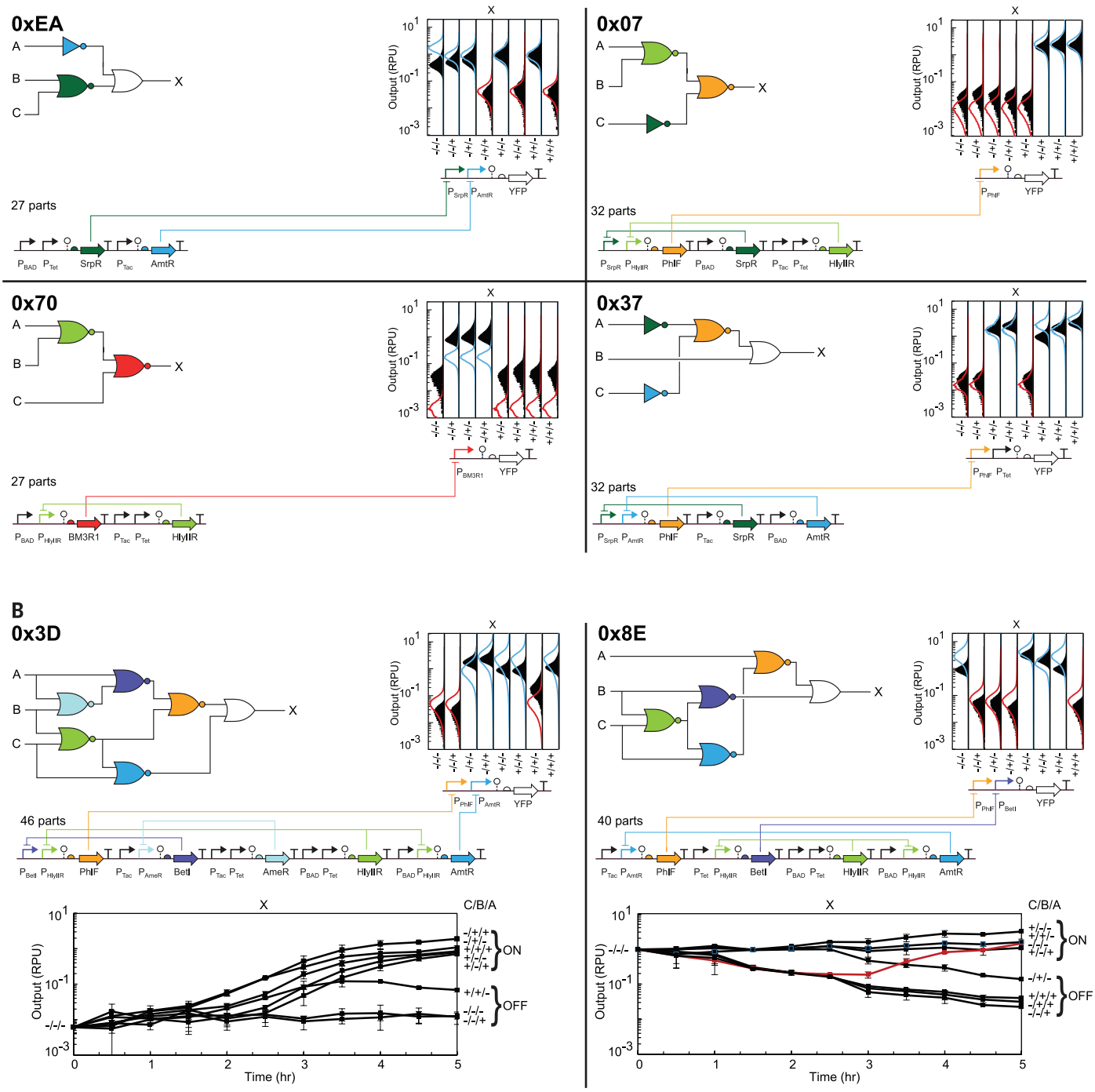


Fig. 4. Automated design of circuits by Cello. (**A**) An example of the code along with the input states (in RPU) is shown for the Priority Detector circuit. All circuits designed by Cello that had correct output states are shown along with their genetic schematics, output predictions, and experimental measurements. The inputs A, B, and C correspond to the P_{Tac}, P_{Tet}, and P_{BAD} sensor promoter activities; their corresponding regulators (LacI, TetR, and AraC*) are not shown in the schematics. The outputs (X, Y, and Z) correspond to YFP driven from output promoters in separate experiments. Solid black distributions are experimental data; blue and red line distributions are computational predictions from Cello (fig. S30). The number of parts for each circuit includes all functional DNA parts in the circuit (promoters, ribozymes, RBSs, protein-coding sequences, and terminators), plus eight parts for the sensor block and two parts for the plasmid backbones. Inputs correspond to the absence or presence of 1 mM IPTG, aTc (2 ng/ml), and 5 mM L-arabinose (Ara). Replicates are provided in fig. S19. The DNA sequence for each circuit is provided in data file S2. When the circuit does not have a common name (e.g., Priority Detector), a hexadecimal naming system is used [e.g., 0x41 (*84*)]. The names starting with "Rule" refer to Wolfram's cellular automaton convention (*89*). (**B**) Time-course data are included for two circuits. The circuits are maintained in the −/−/− state for 3 hours before induction and then switched to the other eight possible states at time = 0 hours (*84*). Error bars are one SD of RPU median performed on three separate days.

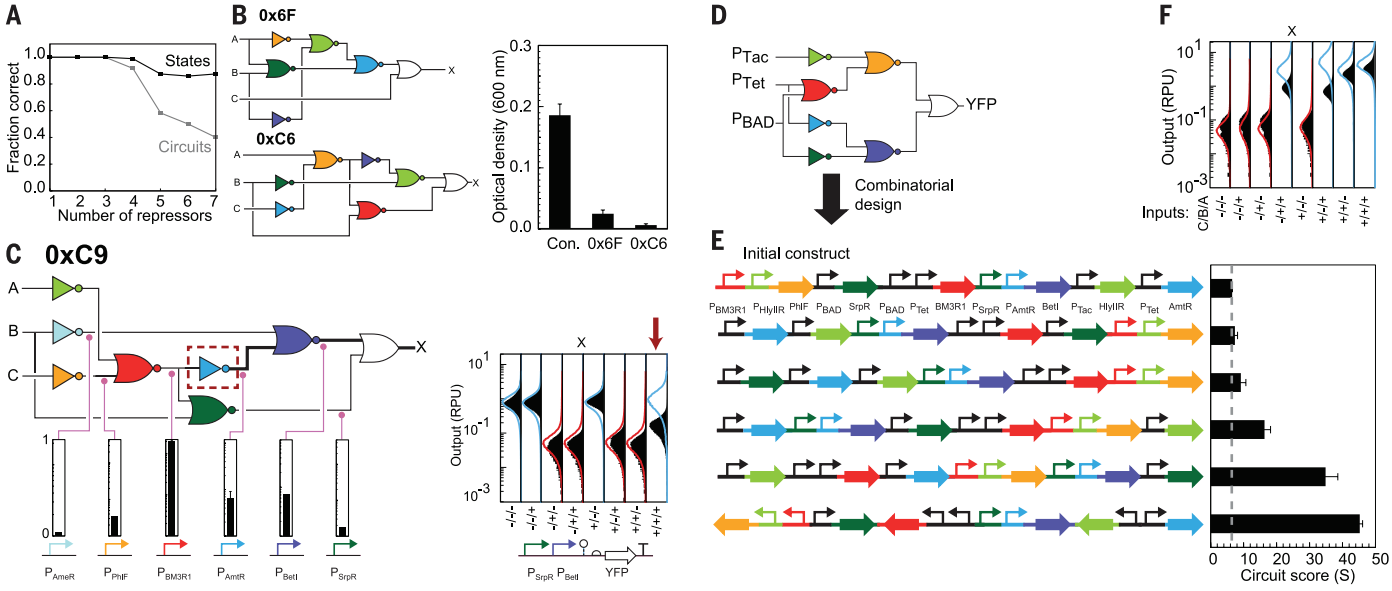


Fig. 5. Analysis of circuit failures and the design of multiple constructs by combinatorial design. (**A**) For the library of 60 circuits (Fig. 3A, Fig. 4, and figs. S12, S13, S14, and S17), the fraction of correct states (black) and the fraction of fully correct circuits (gray) are shown versus the number of repressors in the circuit. (**B**) Impact on cell growth for the two circuits that failed because of toxicity. The control bar is for cells containing the RPU standard plasmid only. Data are average values from three experiments performed on different days; error bars denote SD. (**C**) An example of circuit debugging. All combinations of inputs for all wires were tested; for clarity, only a subset of debugging for the failed state (+/+/+) is shown. The data are normalized to [0, 1] to correct for the dynamic range across gates. In this case, the failure originated when the AmtR gate produced an intermediate response that then propagated through the circuit. (**D**) The circuit diagram for a Majority circuit. Colors correspond to repressors. (**E**) Six layouts for this circuit were designed that maintain the same repressor assignments but allow the order and orientation of the gates to vary. The circuit score (*S*) is defined as the ratio of the lowest ON state's median to the highest OFF state's median. Error bars are one SD for two experiments performed on different days. Cytometry distributions for each design are shown in fig. S15. The dashed line marks the lowest circuit score in the library. (**F**) Predictions and cytometry distributions for the final design. The format and inducer concentrations are as described in Fig. 4. The red line is a transient fault state.

formation (e.g., "Rule 30") (*89*). Additional three-input, one-output logic circuits were built that demonstrate the ability to integrate inputs in different ways. These circuits could be used to turn a cellular function on or off in response to an environment defined by multiple signals. Each of the 52 circuits was specified either by using behavioral Verilog (with Cello performing the logic minimization step) or by performing a separate enumeration to identify the global minimum number of gates and specifying the circuit diagram using structural Verilog (*90*). Subsequently, the global minimum three-input logic gates were included in the UCF so that they could be incorporated as motifs in larger circuits in future designs (fig. S25). For each circuit, the sensor promoters and ON/OFF values were specified, the Eco1C1G1T1 UCF was selected, and a DNA sequence was automatically generated by Cello. DNA synthesis (*91*) and assembly were used to build each sequence; sequences contained up to 10 regulators and 55 parts. The output states of each circuit were measured by flow cytometry and compared with the Cello predictions. No additional tuning was done to diverge from the Cello-predicted sequence.

Of these 52 circuits, 37 functioned as predicted, such that all of the output states matched desired ON and OFF levels (Fig. 4A). Further, the predicted cytometry distributions closely matched those measured experimentally. Of 412 output states across all circuits we built, 92% were correct. The Consensus circuit (output is ON only when all three inputs agree) is the largest, containing 10 regulatory proteins (seven repressors from NOT/NOR gates and three from the inducible systems) and 55 genetic parts. Two of the circuits with four layers (0x3D and 0x8E) were selected to characterize the switching dynamics between states (Fig. 4B). Interestingly, 0x8E shows a transient incorrect state, known as a "fault" in electronics, when the inputs are changed from −/−/− to +/−/+. This is consistent with the last NOR gate transiently receiving ON/OFF inputs until one of the signals transits two layers.

Of the 52 circuits, seven were incorrect in one state, two were incorrect in two states, and five had ≥3 failures (figs. S12 to S14 and fig. S20). As more gates were included in a design, there was a higher probability of failure (Fig. 5A). Two circuits were found to cause a growth defect (Fig. 5B). The circuits that failed in a few states tended to match the remaining states closely, so the initial design could be used as the basis for further rounds of optimization. To this end, debugging experiments were performed to determine which gates failed. This was done by creating a set of plasmids that contained each gate's output promoter fused to yellow fluorescent protein (YFP). These plasmids were transformed with the circuit in lieu of the output plasmid, and the response of the internal gate was measured for all combinations of inputs. An example of this is shown in Fig. 5C; several other examples are shown in fig. S21. From this analysis, most of the circuit failures point to unexpected behavior from the anhydrotetracycline (aTc) sensor (seven circuits) or AmtR gate (two circuits).

Screening design variants has the potential to increase the probability of success, particularly for larger circuits. To do this, Cello outputs a Eugene file that contains architectural rules from the UCF as well as constraints to enforce the circuit diagram and repressor assignments (fig. S29). The user can specify the size of the library, and a combinatorial design algorithm (*83*) generates the target number of constructs. Although all of the systems should be functionally equivalent, subtle changes in their composition may affect circuit function through hidden effects (e.g., transcriptional read-through or promoter interference). We tested this approach by designing a Majority circuit (Fig. 5D), whose output is ON when a majority of its inputs are ON. We built a small library of six constructs that maintained the same circuit diagram and repressor assignments, but in which the order and orientation of genes was allowed to vary (Fig. 5E). Several of these circuits functioned correctly; the response of the best of these is shown in Fig. 5F.

Discussion

The design of synthetic regulatory networks has been dominated by manual trial-and-error tinkering at the nucleotide level. Cello automates the selection and concatenation of parts and balancing

the associated constraints. By doing this, it enables more rapid design of larger multipart systems; the circuits that we present here are larger and more complex than most that have been built by hand. Of 60 circuits designed automatically, 45 functioned as designed (Fig. 2A, Figs. 4 and 5, and fig. S17). Our largest circuit has 12 regulated promoters, doubling a plateau first noted in 2009 regarding a limit on the complexity of circuits that could be designed by hand (*38*). The DNA sequence output represents a testable prediction that either validates the underlying theory or reveals failure modes that can be addressed in the gate design. Previous experiments in which repressors were used to build synthetic logic gates showed that this often led to nonsensical functions that could not be predicted from the known interactions (*92*). Quantifying why predictions fail, where systems break, and how the host evolves provides failure modes that can be addressed through engineering. Iterative co-development of robust gates and software converged on genetic systems that are highly repetitive and modular, in stark contrast to the encoding of natural networks.

The future of engineering biology will require integrated design across many subcellular systems, including the creation of sensors that can process many stimuli, management of resources and metabolites, and control over multiple cellular functions (communication, stress response, chemotaxis, etc.). Within this greater framework, our approach is to separate the design and construction of synthetic circuits from engineering considerations for other cellular processes (e.g., metabolic engineering). Working with transcriptional circuits establishes a discrete boundary that other methods can engage to create a desired circuit to specification. For example, circuits could be built for which the sensors had been designed using all-atom biophysical models (*93*–*96*) and the outputs used to control enzyme expression levels, as determined via metabolic flux models (*97*, *98*). Integration with amorphous computing would enable spatial and community design (*58*, *99*, *100*). Integrating across these computer-aided design (CAD) tools in a way that automates design choices and balances constraints will be critical to advancing the complexity of genetic engineering projects.

REFERENCES AND NOTES

1. J. Hasty, D. McMillen, J. J. Collins, Engineered gene circuits. *Nature* **420**, 224–230 (2002). doi: 10.1038/nature01257; pmid: 12432407
2. D. Sprinzak, M. B. Elowitz, Reconstruction of genetic circuits. *Nature* **438**, 443–448 (2005). doi: 10.1038/nature04335; pmid: 16306982
3. D. A. Drubin, J. C. Way, P. A. Silver, Designing biological systems. *Genes Dev.* **21**, 242–254 (2007). doi: 10.1101/gad.1507207; pmid: 17289915
4. D. Endy, "Taking Faster and Smarter to New Physical Frontiers." *N.Y. Times*, 6 December 2011; www.nytimes.com/2011/12/06/science/drew-endy-better-computing-for-the-things-we-care-about-most.html.
5. D. G. Gibson *et al*., Creation of a bacterial cell controlled by a chemically synthesized genome. *Science* **329**, 52–56 (2010). doi: 10.1126/science.1190719; pmid: 20488990
6. W. Weber, M. Fussenegger, Emerging biomedical applications of synthetic biology. *Nat. Rev. Genet.* **13**, 21–35 (2012). pmid: 22124480
7. W. C. Ruder, T. Lu, J. J. Collins, Synthetic biology moving into the clinic. *Science* **333**, 1248–1252 (2011). doi: 10.1126/science.1206843; pmid: 21885773
8. P. M. Boyle, P. A. Silver, Parts plus pipes: Synthetic biology approaches to metabolic engineering. *Metab. Eng.* **14**, 223–232 (2012). doi: 10.1016/j.ymben.2011.10.003; pmid: 22037345
9. W. J. Holtz, J. D. Keasling, Engineering static and dynamic control of synthetic pathways. *Cell* **140**, 19–23 (2010). doi: 10.1016/j.cell.2009.12.029; pmid: 20085699
10. H. H. McAdams, A. Arkin, Simulation of prokaryotic genetic circuits. *Annu. Rev. Biophys. Biomol. Struct.* **27**, 199–224 (1998). doi: 10.1146/annurev.biophys.27.1.199; pmid: 9646867
11. H. H. McAdams, L. Shapiro, Circuit simulation of genetic networks. *Science* **269**, 650–656 (1995). doi: 10.1126/science.7624793; pmid: 7624793
12. M. Ptashne, A genetic switch: Gene control and phage. lambda (1986) (available at www.osti.gov/scitech/biblio/5413898).
13. U. Alon, *An Introduction to Systems Biology: Design Principles of Biological Circuits* (CRC Press, 2007).
14. N. E. Buchler, U. Gerland, T. Hwa, On schemes of combinatorial transcription logic. *Proc. Natl. Acad. Sci. U.S.A.* **100**, 5136–5141 (2003). doi: 10.1073/pnas.0930314100; pmid: 12702751
15. M. B. Elowitz, S. Leibler, A synthetic oscillatory network of transcriptional regulators. *Nature* **403**, 335–338 (2000). doi: 10.1038/35002125; pmid: 10659856
16. J. Stricker *et al*., A fast, robust and tunable synthetic gene oscillator. *Nature* **456**, 516–519 (2008). doi: 10.1038/nature07389; pmid: 18971928
17. S. Basu, Y. Gerchman, C. H. Collins, F. H. Arnold, R. Weiss, A synthetic multicellular system for programmed pattern formation. *Nature* **434**, 1130–1134 (2005). doi: 10.1038/nature03461; pmid: 15858574
18. W. A. Lim, Designing customized cell signalling circuits. *Nat. Rev. Mol. Cell Biol.* **11**, 393–403 (2010). doi: 10.1038/nrm2904; pmid: 20485291
19. T. S. Moon, C. Lou, A. Tamsir, B. C. Stanton, C. A. Voigt, Genetic programs constructed from layered logic gates in single cells. *Nature* **491**, 249–253 (2012). doi: 10.1038/nature11516; pmid: 23041931
20. A. Tamsir, J. J. Tabor, C. A. Voigt, Robust multicellular computing using genetically encoded NOR gates and chemical 'wires'. *Nature* **469**, 212–215 (2011). doi: 10.1038/nature09565; pmid: 21150903
21. B. C. Stanton *et al*., Genomic mining of prokaryotic repressors for orthogonal logic gates. *Nat. Chem. Biol.* **10**, 99–105 (2014). doi: 10.1038/nchembio.1411; pmid: 24316737
22. J. C. Anderson, C. A. Voigt, A. P. Arkin, Environmental signal integration by a modular AND gate. *Mol. Syst. Biol.* **3**, 133 (2007). doi: 10.1038/msb4100173; pmid: 17700541
23. S. Ausländer, D. Ausländer, M. Müller, M. Wieland, M. Fussenegger, Programmable single-cell mammalian biocomputers. *Nature* **487**, 123–127 (2012). pmid: 22722847
24. W. S. Teo, M. W. Chang, Development and characterization of AND-gate dynamic controllers with a modular synthetic GAL1 core promoter in *Saccharomyces cerevisiae*. *Biotechnol. Bioeng.* **111**, 144–151 (2014). doi: 10.1002/bit.25001; pmid: 23860786
25. P. Siuti, J. Yazbek, T. K. Lu, Synthetic circuits integrating logic and memory in living cells. *Nat. Biotechnol.* **31**, 448–452 (2013). doi: 10.1038/nbt.2510; pmid: 23396014
26. J. Bonnet, P. Yin, M. E. Ortiz, P. Subsoontorn, D. Endy, Amplifying genetic logic gates. *Science* **340**, 599–603 (2013). doi: 10.1126/science.1232758; pmid: 23539178
27. J. Bonnet, P. Subsoontorn, D. Endy, Rewritable digital data storage in live cells via engineered control of recombination directionality. *Proc. Natl. Acad. Sci. U.S.A.* **109**, 8884–8889 (2012). doi: 10.1073/pnas.1202344109; pmid: 22615351
28. L. Yang *et al*., Permanent genetic memory with >1-byte capacity. *Nat. Methods* **11**, 1261–1266 (2014). doi: 10.1038/nmeth.3147; pmid: 25344638
29. B. P. Kramer, M. Fussenegger, Hysteresis in a synthetic mammalian gene network. *Proc. Natl. Acad. Sci. U.S.A.* **102**, 9517–9522 (2005). doi: 10.1073/pnas.0500345102; pmid: 15972812
30. R. Daniel, J. R. Rubens, R. Sarpeshkar, T. K. Lu, Synthetic analog computation in living cells. *Nature* **497**, 619–623 (2013). doi: 10.1038/nature12148; pmid: 23676681
31. T. Danino, O. Mondragón-Palomino, L. Tsimring, J. Hasty, A synchronized quorum of genetic clocks. *Nature* **463**, 326–330 (2010). doi: 10.1038/nature08753; pmid: 20090747
32. S. Basu, R. Mehreja, S. Thiberge, M.-T. Chen, R. Weiss, Spatiotemporal control of gene expression with pulse-generating networks. *Proc. Natl. Acad. Sci. U.S.A.* **101**, 6355–6360 (2004). doi: 10.1073/pnas.0307571101; pmid: 15096621
33. M. Tigges, T. T. Marquez-Lago, J. Stelling, M. Fussenegger, A tunable synthetic mammalian oscillator. *Nature* **457**, 309–312 (2009). doi: 10.1038/nature07616; pmid: 19148099
34. T.-M. Lo, M. H. Tan, I. Y. Hwang, M. W. Chang, Designing a synthetic genetic circuit that enables cell density-dependent auto-regulatory lysis for macromolecule release. *Chem. Eng. Sci.* **103**, 29–35 (2013). doi: 10.1016/j.ces.2013.03.021
35. T. Ellis, X. Wang, J. J. Collins, Diversity-based, model-guided construction of synthetic gene networks with predicted functions. *Nat. Biotechnol.* **27**, 465–471 (2009). doi: 10.1038/nbt.1536; pmid: 19377462
36. F. Zhang, J. M. Carothers, J. D. Keasling, Design of a dynamic sensor-regulator system for production of chemicals and fuels derived from fatty acids. *Nat. Biotechnol.* **30**, 354–359 (2012). doi: 10.1038/nbt.2149; pmid: 22446695
37. R. Kwok, Five hard truths for synthetic biology. *Nature* **463**, 288–290 (2010). doi: 10.1038/463288a; pmid: 20090726
38. P. E. M. Purnick, R. Weiss, The second wave of synthetic biology: From modules to systems. *Nat. Rev. Mol. Cell Biol.* **10**, 410–422 (2009). doi: 10.1038/nrm2698; pmid: 19461664
39. Y. Yokobayashi, R. Weiss, F. H. Arnold, Directed evolution of a genetic circuit. *Proc. Natl. Acad. Sci. U.S.A.* **99**, 16587–16591 (2002). doi: 10.1073/pnas.252535999; pmid: 12451174
40. S. Kosuri *et al*., Composability of regulatory sequences controlling transcription and translation in *Escherichia coli*. *Proc. Natl. Acad. Sci. U.S.A.* **110**, 14024–14029 (2013). doi: 10.1073/pnas.1301301110; pmid: 23924614
41. D. B. Goodman, G. M. Church, S. Kosuri, Causes and effects of N-terminal codon bias in bacterial genes. *Science* **342**, 475–479 (2013). doi: 10.1126/science.1241934; pmid: 24072823
42. C. Lou, B. Stanton, Y.-J. Chen, B. Munsky, C. A. Voigt, Ribozyme-based insulator parts buffer synthetic circuits from genetic context. *Nat. Biotechnol.* **30**, 1137–1142 (2012). doi: 10.1038/nbt.2401; pmid: 23034349
43. V. K. Mutalik *et al*., Precise and reliable gene expression via standard transcription and translation initiation elements. *Nat. Methods* **10**, 354–360 (2013). doi: 10.1038/nmeth.2404; pmid: 23474465
44. F. Moser *et al*., Genetic circuit performance under conditions relevant for industrial bioreactors. *ACS Synth. Biol.* **1**, 555–564 (2012). doi: 10.1021/sb3000832; pmid: 23656232
45. B. Yordanov *et al*., A computational method for automated characterization of genetic components. *ACS Synth. Biol.* **3**, 578–588 (2014). doi: 10.1021/sb400152n; pmid: 24628037
46. S. Cardinale, M. P. Joachimiak, A. P. Arkin, Effects of genetic variation on the *E. coli* host-circuit interface. *Cell Rep.* **4**, 231–237 (2013). doi: 10.1016/j.celrep.2013.06.023; pmid: 23871664
47. N. Rosenfeld, J. W. Young, U. Alon, P. S. Swain, M. B. Elowitz, Gene regulation at the single-cell level. *Science* **307**, 1962–1965 (2005). doi: 10.1126/science.1106914; pmid: 15790856
48. T. S. Gardner, C. R. Cantor, J. J. Collins, Construction of a genetic toggle switch in *Escherichia coli*. *Nature* **403**, 339–342 (2000). doi: 10.1038/35002131; pmid: 10659857
49. F. K. Balagaddé, L. You, C. L. Hansen, F. H. Arnold, S. R. Quake, Long-term monitoring of bacteria undergoing programmed population control in a microchemostat. *Science* **309**, 137–140 (2005). doi: 10.1126/science.1109173; pmid: 15994559
50. A. P. Arkin, D. A. Fletcher, Fast, cheap and somewhat in control. *Genome Biol.* **7**, 114 (2006). doi: 10.1186/gb-2006-7-8-114; pmid: 16942631
51. R. Ghamari, thesis, Boston University (2011).
52. D. Chandran, F. T. Bergmann, H. M. Sauro, TinkerCell: Modular CAD tool for synthetic biology. *J. Biol. Eng.* **3**, 19 (2009). doi: 10.1186/1754-1611-3-19; pmid: 19874625
53. C. J. Myers *et al*., iBioSim: A tool for the analysis and design of genetic circuits. *Bioinformatics* **25**, 2848–2849 (2009). doi: 10.1093/bioinformatics/btp457; pmid: 19628507
54. J. Beal, T. Lu, R. Weiss, Automatic compilation from high-level biologically-oriented programming language to genetic regulatory networks. *PLOS ONE* **6**, e22490 (2011). doi: 10.1371/journal.pone.0022490; pmid: 21850228
55. M. J. Czar, Y. Cai, J. Peccoud, Writing DNA with GenoCAD. *Nucleic Acids Res.* **37**, W40–W47 (2009). doi: 10.1093/nar/gkp361; pmid: 19429897

56. M. A. Marchisio, J. Stelling, Automatic design of digital synthetic gene circuits. *PLOS Comput. Biol.* **7**, e1001083 (2011). doi: 10.1371/journal.pcbi.1001083; pmid: 21399700
57. H. M. Sauro *et al*., Next generation simulation tools: The Systems Biology Workbench and BioSPICE integration. *OMICS* **7**, 355–372 (2003). doi: 10.1089/153623103322637670; pmid: 14683609
58. T. J. Rudge, P. J. Steiner, A. Phillips, J. Haseloff, Computational modeling of synthetic microbial biofilms. *ACS Synth. Biol.* **1**, 345–352 (2012). doi: 10.1021/sb300031n; pmid: 23651288
59. J. R. Kelly *et al*., Measuring the activity of BioBrick promoters using an in vivo reference standard. *J. Biol. Eng.* **3**, 4 (2009). doi: 10.1186/1754-1611-3-4; pmid: 19298678
60. T. H. Segall-Shapiro, A. J. Meyer, A. D. Ellington, E. D. Sontag, C. A. Voigt, A 'resource allocator' for transcription based on a highly fragmented T7 RNA polymerase. *Mol. Syst. Biol.* **10**, 742 (2014). doi: 10.15252/msb.20145299; pmid: 25080493
61. H. H. Wang *et al*., Genome-scale promoter engineering by coselection MAGE. *Nat. Methods* **9**, 591–593 (2012). doi: 10.1038/nmeth.1971; pmid: 22484848
62. B. Canton, A. Labno, D. Endy, Refinement and standardization of synthetic biological parts and devices. *Nat. Biotechnol.* **26**, 787–793 (2008). doi: 10.1038/nbt1413; pmid: 18612302
63. R. Weiss, thesis, Massachusetts Institute of Technology (2001).
64. A. A. Green, P. A. Silver, J. J. Collins, P. Yin, Toehold switches: De-novo-designed regulators of gene expression. *Cell* **159**, 925–939 (2014). doi: 10.1016/j.cell.2014.10.002; pmid: 25417166
65. V. K. Mutalik, L. Qi, J. C. Guimaraes, J. B. Lucks, A. P. Arkin, Rationally designed families of orthogonal RNA regulators of translation. *Nat. Chem. Biol.* **8**, 447–454 (2012). doi: 10.1038/nchembio.919; pmid: 22446835
66. J. Chappell, M. K. Takahashi, J. B. Lucks, Creating small transcription activating RNAs. *Nat. Chem. Biol.* **11**, 214–220 (2015). doi: 10.1038/nchembio.1737; pmid: 25643173
67. D. Chen, A. P. Arkin, Sequestration-based bistability enables tuning of the switching boundaries and design of a latch. *Mol. Syst. Biol.* **8**, 620 (2012). doi: 10.1038/msb.2012.52; pmid: 23089683
68. L. S. Qi *et al*., Repurposing CRISPR as an RNA-guided platform for sequence-specific control of gene expression. *Cell* **152**, 1173–1183 (2013). doi: 10.1016/j.cell.2013.02.022; pmid: 23452860
69. D. Bikard *et al*., Programmable repression and activation of bacterial gene expression using an engineered CRISPR-Cas system. *Nucleic Acids Res.* **41**, 7429–7437 (2013). doi: 10.1093/nar/gkt520; pmid: 23761437
70. A. A. Nielsen, C. A. Voigt, Multi-input CRISPR/Cas genetic circuits that interface host regulatory networks. *Mol. Syst. Biol.* **10**, 763 (2014). doi: 10.15252/msb.20145735; pmid: 25422271
71. K. M. Esvelt *et al*., Orthogonal Cas9 proteins for RNA-guided gene regulation and editing. *Nat. Methods* **10**, 1116–1121 (2013). doi: 10.1038/nmeth.2681; pmid: 24076762
72. T. S. Ham, S. K. Lee, J. D. Keasling, A. P. Arkin, Design and construction of a double inversion recombination switch for heritable sequential genetic memory. *PLOS ONE* **3**, e2815 (2008). doi: 10.1371/journal.pone.0002815; pmid: 18665232
73. The standard differs from the Kelly standard and contains an insulating upstream terminator, a different spacer upstream of the promoter (as opposed to a BioBricks prefix), RiboJ, RBS B0064, a different terminator, and three silent mutations to YFP.
74. D. E. Thomas, P. R. Moorby, *The Verilog Hardware Description Language* (Springer Science & Business Media, 2002).
75. D. C. Crockford, "The application/json Media Type for JavaScript Object Notation (JSON)"; https://tools.ietf.org/html/rfc4627.
76. M. Galdzicki *et al*., The Synthetic Biology Open Language (SBOL) provides a community standard for communicating designs in synthetic biology. *Nat. Biotechnol.* **32**, 545–550 (2014). doi: 10.1038/nbt.2891; pmid: 24911500
77. R. Brayton, A. Mishchenko, in *Computer Aided Verification*, T. Touili, B. Cook, P. Jackson, Eds. (Springer, 2010), pp. 24–40; http://link.springer.com/chapter/10.1007/978-3-642-14295-6_5.
78. N. Roehner, C. J. Myers, Directed acyclic graph-based technology mapping of genetic circuit models. *ACS Synth. Biol.* **3**, 543–555 (2014). doi: 10.1021/sb400135t; pmid: 24650240
79. F. Yaman, S. Bhatia, A. Adler, D. Densmore, J. Beal, Automated selection of synthetic biology parts for genetic regulatory networks. *ACS Synth. Biol.* **1**, 332–344 (2012). doi: 10.1021/sb300032y; pmid: 23651287
80. G. Rodrigo, A. Jaramillo, AutoBioCAD: Full biodesign automation of genetic circuits. *ACS Synth. Biol.* **2**, 230–236 (2013). doi: 10.1021/sb300084h; pmid: 23654253
81. L. Huynh, I. Tagkopoulos, Optimal part and module selection for synthetic gene circuit design automation. *ACS Synth. Biol.* **3**, 556–564 (2014). doi: 10.1021/sb400139h; pmid: 24933033
82. E. Oberortner, S. Bhatia, E. Lindgren, D. Densmore, A rule-based design specification language for synthetic biology. *J. Emerg. Technol. Comput. Syst.* **11**, 25:1–25:19 (2014). doi: 10.1021/sb400139h; pmid: 24933033
83. M. J. Smanski *et al*., Functional optimization of gene clusters by combinatorial design and assembly. *Nat. Biotechnol.* **32**, 1241–1249 (2014). doi: 10.1038/nbt.3063; pmid: 25419741
84. See supplementary materials on *Science* Online.
85. H. M. Salis, E. A. Mirsky, C. A. Voigt, Automated design of synthetic ribosome binding sites to control protein expression. *Nat. Biotechnol.* **27**, 946–950 (2009). doi: 10.1038/nbt.1568; pmid: 19801975
86. S. C. Sleight, H. M. Sauro, Visualization of evolutionary stability dynamics and competitive fitness of *Escherichia coli* engineered with randomized multigene circuits. *ACS Synth. Biol.* **2**, 519–528 (2013). doi: 10.1021/sb400055h; pmid: 24004180
87. Y.-J. Chen *et al*., Characterization of 582 natural and synthetic terminators and quantification of their design constraints. *Nat. Methods* **10**, 659–664 (2013). doi: 10.1038/nmeth.2515; pmid: 23727987
88. V. A. Rhodius, V. K. Mutalik, C. A. Gross, Predicting the strength of UP-elements and full-length *E. coli* σ^E promoters. *Nucleic Acids Res.* **40**, 2907–2924 (2012). doi: 10.1093/nar/gkr1190; pmid: 22156164
89. S. Wolfram, *A New Kind of Science* (Wolfram Media, Champaign, IL, 2002), vol. 5.
90. This was done for 0x0E, 0x19, 0x1C, 0x38, 0x3D, 0x6E, 0x81, 0xB9, 0xC6, 0xC7, 0xBD, and 0xC8.
91. S. Kosuri, G. M. Church, Large-scale de novo DNA synthesis: Technologies and applications. *Nat. Methods* **11**, 499–507 (2014). doi: 10.1038/nmeth.2918; pmid: 24781323
92. R. S. Cox, M. G. Surette, M. B. Elowitz, Programming gene expression with combinatorial promoters. *Mol. Syst. Biol.* **3**, 145 (2007). doi: 10.1038/msb4100187
93. B. I. Dahiyat, S. L. Mayo, De novo protein design: Fully automated sequence selection. *Science* **278**, 82–87 (1997). doi: 10.1126/science.278.5335.82; pmid: 9311930
94. L. L. Looger, M. A. Dwyer, J. J. Smith, H. W. Hellinga, Computational design of receptor and sensor proteins with novel functions. *Nature* **423**, 185–190 (2003). doi: 10.1038/nature01556; pmid: 12736688
95. C. E. Tinberg *et al*., Computational design of ligand-binding proteins with high affinity and selectivity. *Nature* **501**, 212–216 (2013). doi: 10.1038/nature12443; pmid: 24005320
96. W. R. Whitaker, S. A. Davis, A. P. Arkin, J. E. Dueber, Engineering robust control of two-component system phosphotransfer using modular scaffolds. *Proc. Natl. Acad. Sci. U.S.A.* **109**, 18090–18095 (2012). doi: 10.1073/pnas.1209230109; pmid: 23071327
97. C. S. Henry, L. J. Broadbelt, V. Hatzimanikatis, Thermodynamics-based metabolic flux analysis. *Biophys. J.* **92**, 1792–1805 (2007). doi: 10.1529/biophysj.106.093138; pmid: 17172310
98. A. M. Feist *et al*., A genome-scale metabolic reconstruction for *Escherichia coli* K-12 MG1655 that accounts for 1260 ORFs and thermodynamic information. *Mol. Syst. Biol.* **3**, 121 (2007). doi: 10.1038/msb4100155
99. S. S. Jang, K. T. Oishi, R. G. Egbert, E. Klavins, Specification and simulation of synthetic multicelled behaviors. *ACS Synth. Biol.* **1**, 365–374 (2012). doi: 10.1021/sb300034m; pmid: 23651290
100. A. E. Blanchard, V. Celik, T. Lu, Extinction, coexistence, and localized patterns of a bacterial population with contact-dependent inhibition. *BMC Syst. Biol.* **8**, 23 (2014). pmid: 24576330
101. J. Y. Quinn *et al*., SBOL Visual: A graphical language for genetic designs. *PLOS Biol.* **13**, e1002310 (2015). doi: 10.1371/journal.pbio.1002310; pmid: 26633141

ACKNOWLEDGMENTS

All data described in this paper are presented in the supplementary materials. Cello can be accessed at www.cellocad.org; the code is open source and maintained via the Nona Research Foundation (www.nonasoftware.org). The insulated gates, circuits, and plasmids defined in the UCF can be obtained via Addgene (www.addgene.org). The *E. coli* strain used in this UCF is available from New England Biolabs (C3019). D.D. is president and part owner of Lattice Automation, which works on software for synthetic biology. Supported by Office of Naval Research, Multidisciplinary University Research Initiative grant N00014-13-1-0074 (C.A.V. and A.A.K.N.); a Siebel Scholarship (Class of 2015) and Air Force Office of Scientific Research, National Defense Science and Engineering Graduate fellowship FA9550-11-C-0028 (A.A.K.N.); National Institute of General Medical Sciences grant P50 GM098792 and NSF Synthetic Biology Engineering Research Center grant SynBERC EEC0540879 (C.A.V. and J.S.); NSF grant 1147158 (D.D. and P.V.); the NIST Strategic and Emerging Research Initiative (V.P., E.A.S., and D.R.); the National Research Council postdoctoral program (V.P.); an AWS in Education Grant; and Thermo Fischer (Life Technologies, A114510). We thank S. Bhatia (Boston University) for his work to enumerate the three-input, one-output logic motifs; R. Ghamari (Boston University) for early work on the Cello software foundation and design approach; N. Roehner for technical assistance with SBOL; and E. Oberortner for technical assistance with Eugene. The National Institute of Standards and Technology notes that certain commercial equipment, instruments, and materials are identified in this paper to specify an experimental procedure as completely as possible. In no case does the identification of particular equipment or materials imply a recommendation or endorsement by NIST, nor does it imply that the materials, instruments, or equipment are necessarily the best available for the purpose. The University of California, San Francisco, holds a patent application associated with this work (US20130005590 A1). The set of insulated gates, the plasmid backbones for the circuit and output plasmids (Fig. 1), and the standard RPU plasmid are available via Addgene (www.addgene.org/Christopher_Voigt/). Cello can be accessed as a web-based application (www.cellocad.org), the code for which will be open source and provided on Github (https://github.com/CIDARLAB/cello).

SUPPLEMENTARY MATERIALS

www.sciencemag.org/content/352/6281/aac7341/suppl/DC1
Supplementary Text
Materials and Methods
Figs. S1 to S44
Tables S1 to S10
Supplementary References
Data Files S1 to S4

4 June 2015; accepted 21 January 2016
10.1126/science.aac7341

RESEARCH ARTICLES

MITOCHONDRIAL DISEASE

Hypoxia as a therapy for mitochondrial disease

Isha H. Jain,[1,2,3] Luca Zazzeron,[4] Rahul Goli,[1,2,3] Kristen Alexa,[5] Stephanie Schatzman-Bone,[5] Harveen Dhillon,[1,2,3] Olga Goldberger,[1,2,3] Jun Peng,[1,2,3] Ophir Shalem,[3,6,7] Neville E. Sanjana,[3,6,7] Feng Zhang,[3,6,7] Wolfram Goessling,[3,5,8,9] Warren M. Zapol,[4] Vamsi K. Mootha[1,2,3]*

Defects in the mitochondrial respiratory chain (RC) underlie a spectrum of human conditions, ranging from devastating inborn errors of metabolism to aging. We performed a genome-wide Cas9-mediated screen to identify factors that are protective during RC inhibition. Our results highlight the hypoxia response, an endogenous program evolved to adapt to limited oxygen availability. Genetic or small-molecule activation of the hypoxia response is protective against mitochondrial toxicity in cultured cells and zebrafish models. Chronic hypoxia leads to a marked improvement in survival, body weight, body temperature, behavior, neuropathology, and disease biomarkers in a genetic mouse model of Leigh syndrome, the most common pediatric manifestation of mitochondrial disease. Further preclinical studies are required to assess whether hypoxic exposure can be developed into a safe and effective treatment for human diseases associated with mitochondrial dysfunction.

Mitochondria are ancient organelles that are essential for normal physiology and health. The respiratory chain (RC) is crucial to mitochondrial function and generates approximately 90% of cellular adenosine triphosphate (ATP) via oxidative phosphorylation (*1*). In the oxidative step, four large protein complexes transfer electrons from NADH (the reduced form of nicotinamide adenine dinucleotide) or FADH (the reduced form of flavin adenine dinucleotide) to oxygen while generating a proton gradient. Approximately 90% of the oxygen we breathe is used as a substrate for the RC (*1*). In the phosphorylation step, the proton gradient is dissipated by a fifth and final complex to generate ATP. Numerous additional chemical reactions and transport processes are intimately coupled to the redox and proton-pumping activities of the RC.

A spectrum of human diseases result from a faulty RC (*2*–*4*). Virtually all age-related disorders, including type 2 diabetes, neurodegeneration, and sarcopenia, are accompanied by a quantitative decline in the activity of the mitochondrial RC. The aging process itself is associated with a gradual decrease of oxidative phosphorylation in multiple tissues. Monogenic disorders of the mitochondrial RC represent the largest class of inborn errors of metabolism. To date, lesions in over 150 genes, encoded by the nuclear or mitochondrial (mtDNA) genomes, have been identified as disease-causing. Mutations in these genes lead to a biochemical deficiency of one or more of the RC complexes, resulting in either tissue-specific or multisystem disease with devastating effects on human health. Patients with RC disorders can present with blindness, deafness, gray- or white-matter brain disease, cardiomyopathy, skeletal muscle myopathy, gastrointestinal dysmotility, anemia, ataxia, liver disease, and kidney disease.

Management of these disorders remains challenging (*5*, *6*). Although individual mutations are rare, the overall disease burden of mitochondrial disease is significant, with an estimated prevalence of 1 out of 4300 live births (*7*). Therefore, a general and effective therapeutic is needed. The current mainstay of managing mitochondrial disease involves the use of vitamin cofactors (such as coenzyme Q, α-lipoic acid, riboflavin, or L-carnitine) (*8*). Other proposed strategies include the use of small-molecule bypass of defective RC components, using electron carriers such as idebenone, and antioxidants. None of these approaches have demonstrated efficacy in randomized controlled clinical trials.

Several lines of evidence point to the existence of endogenous coping mechanisms for dealing with mitochondrial dysfunction. Mitochondrial disorders can be highly tissue-specific and episodic (*2*, *9*). These disorders are often triggered by drugs, alcohol, or viral illnesses, implying that a genetic lesion is not always sufficient to cause cellular dysfunction, but rather that the lesion may need to be compounded with an environmental insult. Such observations suggest the existence of cellular pathways or environments that buffer against mitochondrial lesions.

A genome-wide screen to spotlight suppressors of mitochondrial disease

We modeled mitochondrial disease in the human leukemic suspension cell line K562 and performed a Cas9-mediated knockout (KO) screen (*10*, *11*). We used the natural product antimycin as a complex III inhibitor of the RC. In the presence of antimycin, the RC is unable to oxidize high-energy reducing equivalents to power ATP production; however, cytoplasmic lactate dehydrogenase maintains NAD^+ redox balance. Removal of pyruvate exacerbates reductive stress, further preventing cell proliferation (*12*). We modeled mitochondrial disease with the addition of antimycin alone (moderate disease) or antimycin in combination with the removal of pyruvate (severe disease), using cell growth as a proxy for disease magnitude (Fig. 1A). We infected K562 cells with a ~65,000 single-guide RNA (sgRNA) library, targeting ~18,000 genes (*10*). After 1 week of genome editing, we transferred the pool of KO cells to experimental conditions of untreated, moderate disease, and severe disease states (Fig. 1B). We collected samples for an enrichment screen by allowing the KO pool to grow in selection conditions for 3 weeks. The relative growth between untreated and moderate disease conditions was 300-fold and between untreated and severe disease conditions was 7000-fold (Fig. 1C).

As expected, 3 weeks of genome editing in untreated cells led to a significant depletion of sgRNAs corresponding to essential genes, including those related to transcription, translation, and splicing (fig. S1). Nearly 20% of the 500 most essential genes were mitochondrial proteins, especially mitochondrial ribosomal proteins and electron transport chain subunits (table S1). Because mitochondrial proteins make up approximately 5% of the proteome (*13*), this enrichment highlights the dramatic effects of mitochondrial dysfunction on viability.

Of the ~18,000 genes tested, the KO screen identified inhibition of the Von Hippel-Lindau (VHL) factor as the most effective genetic suppressor of mitochondrial disease, in both the moderate and severe disease conditions (Fig. 1D). RIGER analysis ranked VHL KO cells as the most enriched over time in both infection replicates corresponding to severe and moderate disease (table S2). The five sgRNAs spanning all three exons of VHL ranked 1, 2, 3, 12, and 14 out of ~65,000 total guides for enrichment in disease conditions relative to pretreatment conditions (Fig. 1, D to F, and figs. S2 and S3). Furthermore, the most significant VHL sgRNAs were enriched approximately 20-fold in disease states (fig. S4). VHL KO cells were also enriched in untreated conditions over time, reflecting an overall effect on cell growth. However, this enrichment was significantly less than in disease conditions.

[1]Department of Molecular Biology and Howard Hughes Medical Institute, Massachusetts General Hospital, Boston, MA, USA. [2]Department of Systems Biology, Harvard Medical School, Boston, MA, USA. [3]Broad Institute of Harvard and MIT, Cambridge, MA, USA. [4]Department of Anesthesia, Critical Care, and Pain Medicine, Massachusetts General Hospital, Boston, MA, USA. [5]Genetics Division, Brigham and Women's Hospital, Harvard Medical School, Boston, MA, USA. [6]McGovern Institute for Brain Research, Cambridge, MA, USA. [7]Department of Brain and Cognitive Sciences and Department of Biological Engineering, Massachusetts Institute of Technology, Cambridge, MA, USA. [8]Gastrointestinal Cancer Center, Dana-Farber Cancer Institute, Boston, MA, USA. [9]Harvard Stem Cell Institute, Cambridge, MA, USA.
*Corresponding author. E-mail: vamsi@hms.harvard.edu

Downloaded from on March 31, 2016

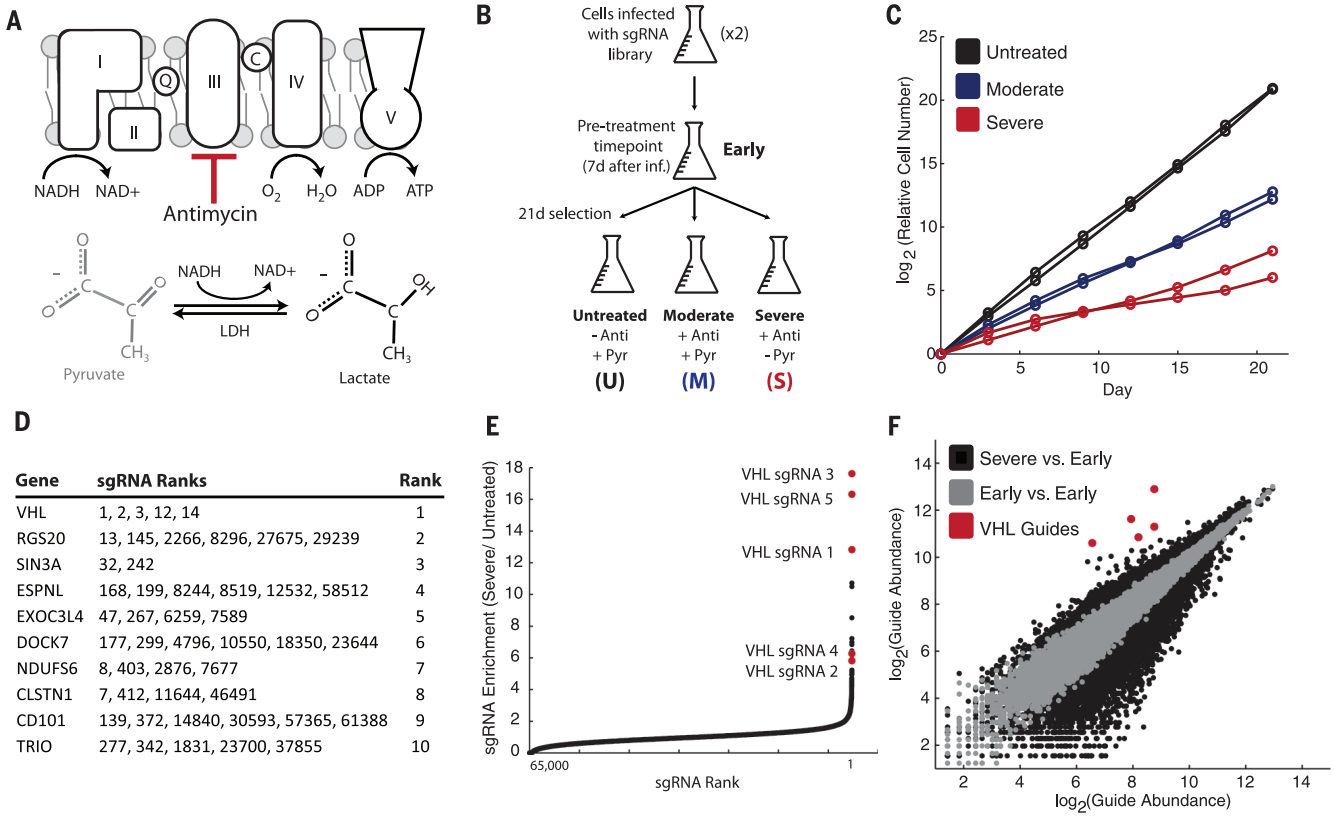
VHL activity is a key regulator of the hypoxic response pathway (*14*, *15*). Organisms have evolved elaborate mechanisms to adapt to fluctuating oxygen tensions and extreme environments. In normoxic conditions, the hypoxia-inducible transcription factors (HIFs) are constitutively made and hydroxylated by the prolyl-hydroxylase (PHD) enzymes (Fig. 2A) (*16*–*18*). The hydroxylated form is recognized by the ubiquitin ligase, VHL, and targeted for degradation. In response to environmental hypoxia, the PHD reaction does not take place, allowing HIF stabilization and activation of the hypoxia transcriptional program (Fig. 2B). VHL KO cells show HIF stabilization, even during normoxic conditions, thereby bypassing cellular oxygen-sensing mechanisms (*18*–*20*). Our screen suggested that harnessing innate responses to hypoxia may be protective in the setting of inherited mitochondrial disease.

Genetic and small-molecule proof of concept in cellular models

We validated and characterized the hypoxic response as a therapeutic target by testing the ability of VHL KO cells to withstand respiratory-chain dysfunction. VHL KO cells showed increased cell proliferation in the presence of antimycin relative to nontargeting (dummy) sgRNA-modified cells (Fig. 2C). Furthermore, there was perfect correspondence between the degree of VHL sgRNA enrichment in the CRISPR (clustered regularly-interspaced short palindromic repeats) screen and the rescue-effect size of individual sgRNAs (fig. S5). VHL KO cells were also more resistant to complex I inhibition by piericidin and complex V (ATP synthase) inhibition by oligomycin, demonstrating the potentially broad utility of our therapeutic approach (Fig. 2C).

We next explored small molecules as tools for triggering the hypoxia response. Although a VHL inhibitor has been reported (*21*), it is not cell-permeant. PHD inhibitors have been developed as investigational drugs for anemia and ischemic disorders (*22*). FG-4592 is currently in phase III clinical trials for the treatment of anemia of chronic kidney disease and acts by upregulating the canonical marker of the hypoxia response, erythropoietin (Epo). We reasoned that FG-4592 treatment would mimic VHL KO, thus triggering a broader hypoxia transcriptional program. Normal growth rates were minimally increased by FG-4592. Complex I, III, or V inhibition stunts cell growth but does not increase cell death (fig. S6) in most cell lines, including HT-29s, HEK 293Ts, and K562s. Administering ~50 μM FG-4592 in advance and during RC dysfunction nearly or completely rescued this growth defect, in a dose-dependent manner (Fig. 2, D to F, and fig. S7). The nearly full rescue of the disease state across different cell lines and across chemical lesions highlights the general utility of our approach.

We characterized the rescue mechanism of FG-4592 by studying its effect on the hypoxia response and energy metabolism. Although HIF1α is undetectable during normoxic exposure, treatment with FG-4592 stabilized the transcription factor even during normoxia. It has previously been noted that a paradox exists between severe mitochondrial dysfunction and cellular sensing of hypoxia (*23*). In cell culture, full inhibition of the RC prevents HIF stabilization,



D

Gene	sgRNA Ranks	Rank
VHL	1, 2, 3, 12, 14	1
RGS20	13, 145, 2266, 8296, 27675, 29239	2
SIN3A	32, 242	3
ESPNL	168, 199, 8244, 8519, 12532, 58512	4
EXOC3L4	47, 267, 6259, 7589	5
DOCK7	177, 299, 4796, 10550, 18350, 23644	6
NDUFS6	8, 403, 2876, 7677	7
CLSTN1	7, 412, 11644, 46491	8
CD101	139, 372, 14840, 30593, 57365, 61388	9
TRIO	277, 342, 1831, 23700, 37855	10

Fig. 1. Genome-scale Cas9-mediated knockout screen identifies VHL inhibition as protective during states of mitochondrial dysfunction. (**A**) Mitochondrial disease was modeled with the addition of the complex III inhibitor antimycin (moderate disease) or addition of antimycin and removal of pyruvate (severe disease). (**B**) K562 cells were infected in duplicate with the genome-scale Cas9-mediated knockout library and separated into conditions of untreated, moderate disease, or severe disease. Samples were taken at a pretreatment time point, as well as after 3 weeks of selection. (**C**) Growth curves for cumulative differences in growth rates in different experimental conditions for both infection replicates. (**D**) RIGER output based on enrichment of sgRNAs in severe disease condition relative to pretreatment conditions. Each row denotes a single gene, with ranks of corresponding sgRNAs in the middle column. Ranks for individual sgRNAs are out of ~65,000 total sgRNAs in the library. (**E**) sgRNA enrichment magnitude versus rank, with most enriched sgRNA shown at the far right. sgRNAs corresponding to VHL are in red. (**F**) Guide abundance in pretreatment conditions (infection 1 versus infection 2) shown in gray for each sgRNA, representative of experimental noise. Guide abundance in severe disease condition versus pretreatment condition is in black, with VHL sgRNAs in red.

even under low oxygen conditions that would otherwise trigger the hypoxia response (*23*, *24*). FG-4592 treatment bypassed this paradox and enabled HIF1α stabilization in the face of mitochondrial dysfunction, during states of normoxia or hypoxia (Fig. 3A). Further work is needed to determine whether the paradox contributes significantly to disease pathology or whether it is simply a feature of severe RC blockade in cultured cells.

The HIF transcriptional response is believed to be protective during states of hypoxia, at least in part by shifting the cell's reliance away from mitochondrial oxidative energy metabolism. The HIF1α response can preserve energy supply at low oxygen tensions in a redox-neutral manner. Indeed, treatment with FG-4592 for 24 hours up-regulated the transcription of glycolytic enzymes (Fig. 3B and fig. S8) such as glucose transporter 1 (GLUT1), hexokinase 2 (HK2), and lactate dehydrogenase A (LDHA). HIF1α activation is also known to shunt the carbon supply away from the TCA cycle and toward the LDHA reaction (*25*–*28*), as evidenced by the significant up-regulation of pyruvate dehydrogenase kinase (PDK1) (Fig. 3B). Although lesions to the RC and hypoxia can in principle limit RC activity, cells do not mount the hypoxia response upon RC inhibition, because the signal is lacking. However, FG-4592 treatment artificially triggers the hypoxia transcriptional program, even during normoxic conditions (Fig. 3B and fig. S8).

To corroborate the transcriptional changes, we also measured lactic acid production and oxygen consumption as proxies of glycolysis and oxidative phosphorylation. Glycolysis was somewhat increased by RC inhibition, probably as a result of allosteric mechanisms (Fig. 3C). Treatment with FG-4592 increased glycolysis by nearly 25% in HEK293T cells under basal conditions and beyond allosteric mechanisms in response to RC inhibition. Furthermore, basal oxygen consumption was decreased by approximately twofold with FG-4592 treatment (Fig. 3D). This may be protective in the setting of mitochondrial dysfunction, because it may limit the amount of reactive oxygen species (ROS) produced by impaired electron transport.

Genetic and small-molecule proof of concept in zebrafish models

To further establish proof of concept, we asked whether genetic or small-molecule activation of the hypoxia response would be protective against RC poisoning in zebrafish embryos. *vhl*-null zebrafish continuously up-regulate the hypoxia response throughout early development (*29*). Just as *vhl* KO cells are protected against mitochondrial dysfunction, we asked whether *vhl*-null zebrafish might be more resilient to RC poisoning. Zebrafish

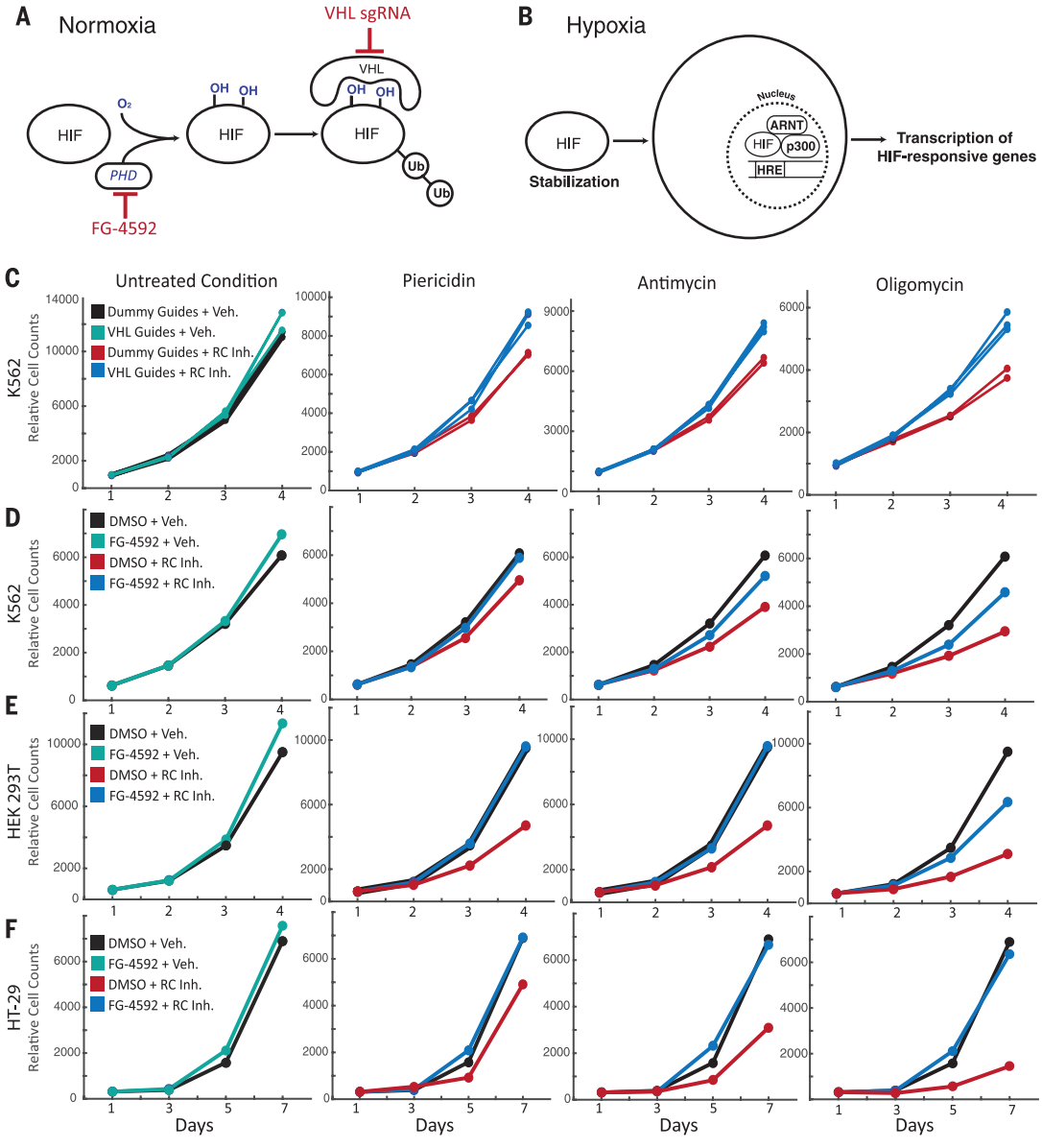


Fig. 2. Genetic or small-molecule activation of the HIF response is protective against multiple forms of RC inhibition, in multiple cell types. (**A**) Schematic for HIF degradation during normoxia. (**B**) Schematic for induction of hypoxia transcriptional program during hypoxia. (**C**) Growth curves for K562 VHL KO cells (cyan and blue) or nontargeting sgRNA cells (black and red) for untreated or disease conditions (the mean is shown). Disease conditions correspond to inhibition of complex I (piericidin), complex III (antimycin), or complex V (oligomycin). Growth curves for (**D**) K562 cells, (**E**) HEK293T cells, and (**F**) HT-29 cells ± FG-4592, in combination with untreated or disease conditions (inhibition of complexes I, III, and V), are shown. All time points were measured in duplicate, and all growth curves are representative of two or three independent experiments (the mean is shown). All final cell counts of FG-treated rescue [or VHL KO rescue in (A)] in the presence of RC inhibitor were statistically significant (one-sided *t* test *P* value < 0.05).

embryos exhibit sensitivity to multiple specific RC inhibitors, including antimycin (*30*–*32*). We demonstrated a significant improvement in the survival of *vhl*-null embryos exposed to 2.5 nM antimycin as compared to heterozygous and wild-type (WT) controls (Fig. 4A).

We then extended our small-molecule approach to the zebrafish model of RC dysfunction. A previously generated zebrafish reporter strain, Tg (*phd3::EGFP*), expresses green fluorescent protein (GFP) under the control of a HIF-responsive promoter, thereby enabling in vivo assessment of activating the hypoxia transcriptional response (*33*, *34*). FG-4592 treatment of Tg(*phd3::EGFP*) embryos at 96 hours post fertilization (hpf) resulted in a time-dependent increase in the fluorescence of individual reporter fish (Fig. 4B). Furthermore, in situ hybridization for the glycolytic HIF targets *glut1* and *ldha1* demonstrated significant up-regulation upon FG-4592 treatment (Fig. 4C), confirming that FG-4592 engages the zebrafish PHDs to trigger the hypoxia transcriptional program. We then demonstrated that cotreatment of embryos with FG-4592 rescued antimycin-induced death by nearly twofold (Fig. 4D). The genetic and small-molecule experiments in zebrafish provide proof of concept that activation of the hypoxia program can protect against insults to the mitochondrial RC.

Hypoxic breathing alleviates disease and extends life span in a mouse model of Leigh syndrome

The cellular and zebrafish models provided proof of the concept that individual components of the cellular response to hypoxia are protective

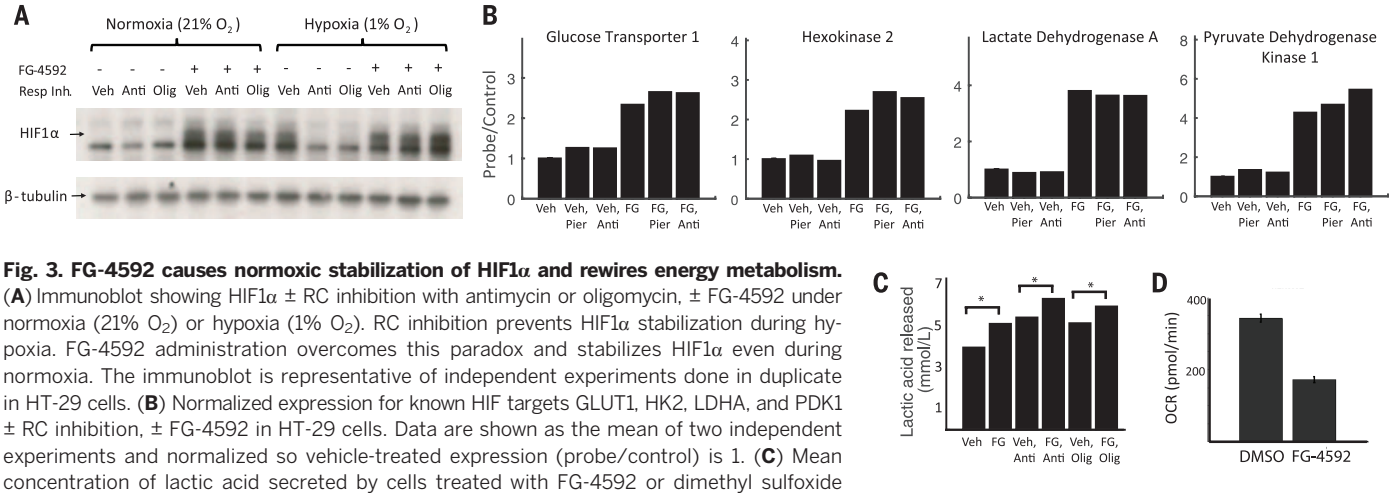


Fig. 3. FG-4592 causes normoxic stabilization of HIF1α and rewires energy metabolism. (**A**) Immunoblot showing HIF1α ± RC inhibition with antimycin or oligomycin, ± FG-4592 under normoxia (21% O_2) or hypoxia (1% O_2). RC inhibition prevents HIF1α stabilization during hypoxia. FG-4592 administration overcomes this paradox and stabilizes HIF1α even during normoxia. The immunoblot is representative of independent experiments done in duplicate in HT-29 cells. (**B**) Normalized expression for known HIF targets GLUT1, HK2, LDHA, and PDK1 ± RC inhibition, ± FG-4592 in HT-29 cells. Data are shown as the mean of two independent experiments and normalized so vehicle-treated expression (probe/control) is 1. (**C**) Mean concentration of lactic acid secreted by cells treated with FG-4592 or dimethyl sulfoxide (DMSO) ± RC inhibitors as proxy for anaerobic glycolytic flux. Data are shown for HEK293T cells (without pyruvate to eliminate a contribution from the LDHA reaction) and are representative of at least two independent experiments. (**D**) Basal oxygen consumption rates for HEK293T cells treated with FG-4592 or DMSO for >24 hours, averaged across three independent experiments (mean ± SE) [one-sided *t* test *P* value < 0.05 for all pairwise comparisons ± FG-4592 in (B) to (D)]. OCR, oxygen consumption rate.

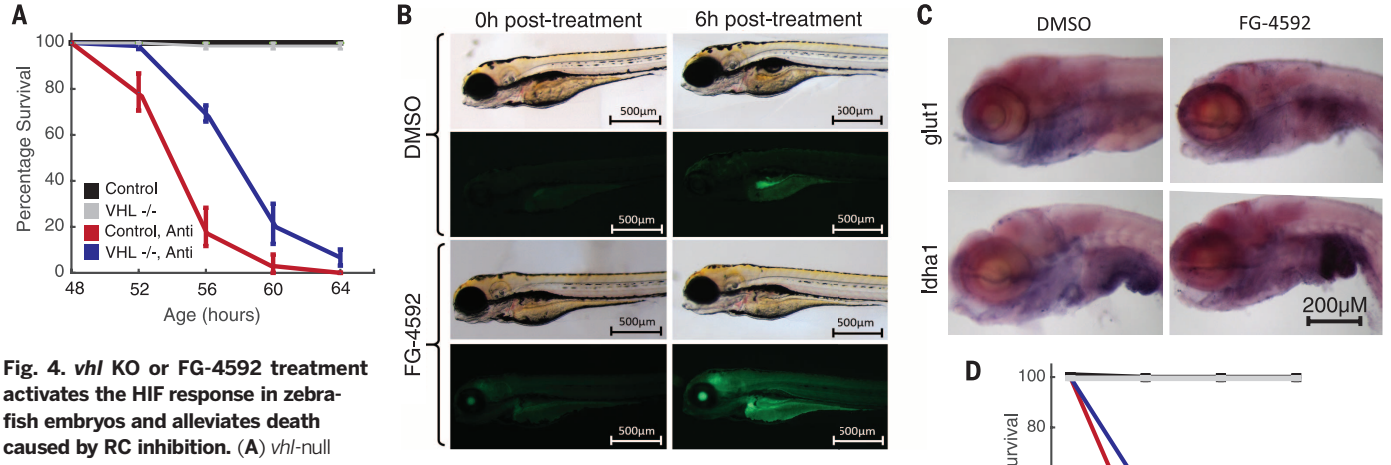


Fig. 4. *vhl* KO or FG-4592 treatment activates the HIF response in zebrafish embryos and alleviates death caused by RC inhibition. (**A**) *vhl*-null zebrafish are less sensitive to RC inhibition at 48 hpf than control (WT and Het) fish, $n \geq 75$ per treatment, $P < 0.001$ by Mantel-Cox test. (**B**) FG-4592 treatment activates expression of a HIF-responsive promoter in Tg(*phd3::EGFP*) embryos. Images are shown for embryos treated with either DMSO or 2.5 μM FG-4592 from 96 to 102 hpf. Embryos were assayed for GFP expression at 0 hours post treatment (hptx) and 6 hptx. DMSO treatment fails to activate GFP expression beyond autofluorescence in Tg(*phd3::EGFP*) transgenic embryos, whereas FG-4592 robustly initiates GFP expression by 6 hptx. (**C**) Known HIF targets *glut1* and *ldha1* are overexpressed in 96 hpf zebrafish embryos treated with FG-4592 for 6 hours. (**D**) Exposure to FG-4592 rescues antimycin-induced zebrafish embryonic death. RC inhibition by 2.5 nM antimycin in 4 days post fertilization (dpf) embryos results in significant death within the first 24 hours of treatment. Coexposure of antimycin with FG-4592 (2.5 μM) doubles embryo survival, whereas FG-4592 alone has no impact. $n = 75$ embryos per treatment, $P < 0.0001$ by Mantel-Cox test.

against mitochondrial toxins. Although small molecules are capable of activating specific branches of the hypoxia program, we reasoned that they may not have as broad and potent an effect as the naturally evolved, whole-body physiological response to hypoxia itself. Moreover, small-molecule drugs for activating the hypoxia response are currently in clinical trials for kidney disease and anemia. However, a large fraction of mitochondrial disease originates in the central nervous system, and our preliminary pharmacokinetic studies suggested limited blood-brain barrier penetration of these drugs in mice. Higher doses resulted in whole-body toxicity. Because mammals have evolved a complex homeostatic program to adapt to low oxygen tensions in their environment, we reasoned that a similarly broad hypoxic stress response might protect animal models of mitochondrial disease.

Leigh syndrome is the most common pediatric form of mitochondrial disease. Though relatively healthy at birth, patients develop irreversible neurodegeneration by 2 years of age (*6*). They suffer bilaterally symmetric lesions in the brain stem and basal ganglia, with marked gliosis. Most patients die between the ages of 3 and 16 months. To date, over 75 different genes have been implicated in this syndrome, with complex I deficiency being the most frequent biochemical cause of disease. One of the more severe recessive forms of Leigh syndrome is caused by inactivation of the *NDUFS4* gene, which codes for NADH:ubiquinone oxidoreductase subunit S4. Recently, a mouse model that recapitulates many features of Leigh syndrome was generated by disruption of the murine *Ndufs4* gene (*35*). *Ndufs4* KO mice breathing ambient air (21% O_2) display retarded growth rates, impaired visual acuity, and a delayed startle response. Their body temperature falls progressively until reaching 32°C, shortly before death at 50 to 60 days of age. Diseased mice also display locomotor deficits and failure to thrive by 50 days of age. Their neuropathology closely resembles clinical findings, with a substantial inflammatory response in the brainstem and cerebellum.

We first performed experiments to confirm that *Ndufs4* KO mice can tolerate a brief exposure to environmental hypoxia and that they activate a hypoxic response in a manner similar to WT mice. We exposed four WT mice and four KO mice to 8.5% O_2 at sea-level pressure for 6 hours. Acute exposure of WT mice to hypoxia triggers HIF stabilization, resulting in Epo transcription and translation. After a 6-hour exposure, we measured Epo protein levels in plasma and showed that both WT and KO mice up-regulated Epo production by approximately 40-fold (fig. S9). These results

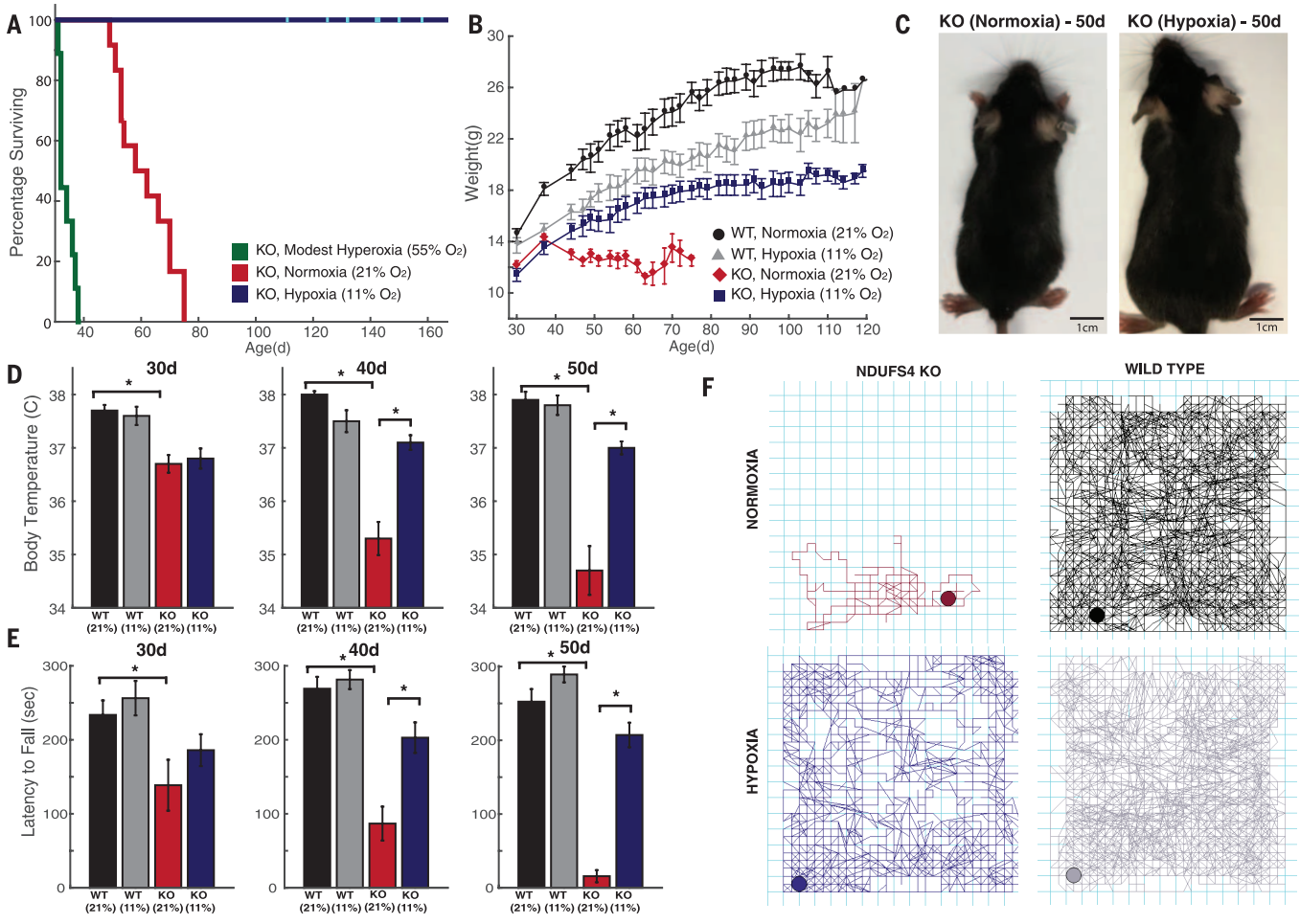


Fig. 5. Chronic hypoxia extends life span and alleviates disease in a mouse model of Leigh syndrome, whereas chronic hyperoxia exacerbates disease. (**A**) *Ndufs4* KO mice of both genders were chronically exposed to hypoxia (11% O_2), normoxia (21% O_2), or hyperoxia (55% O_2), at 30 days of age and survival was recorded (n = 12, n = 12, n = 9 mice, respectively). Cyan bars represent the current age of hypoxic KO mice. (**B**) Body weights were measured in WT and KO mice exposed to normoxia or hypoxia, three times a week upon enrollment in the study. Weights are shown as mean ± SE. (**C**) Representative images of 50-day-old KO mice exposed to normoxia or hypoxia. (**D**) Body temperature was measured in KO mice exposed to normoxia or hypoxia at age ~30, 40, and 50 days. Temperatures are shown as mean ± SE ($n \geq 7$ mice for all groups). (**E**) Latency to fall on an accelerating rod was measured as median values of triplicate trials per mouse for WT and KO mice, exposed to normoxia or hypoxia at different ages ($n \geq 7$ mice for all groups). (**F**) Representative 1-hour locomotor activity traces of sick, normoxia-treated KO mice, and age-matched hypoxia-treated KO mice, as well as controls. All data are shown as normoxia KO (maroon), hypoxia KO (blue), normoxia WT (black), and hypoxia WT (gray). *Denotes t test P value < 0.05.

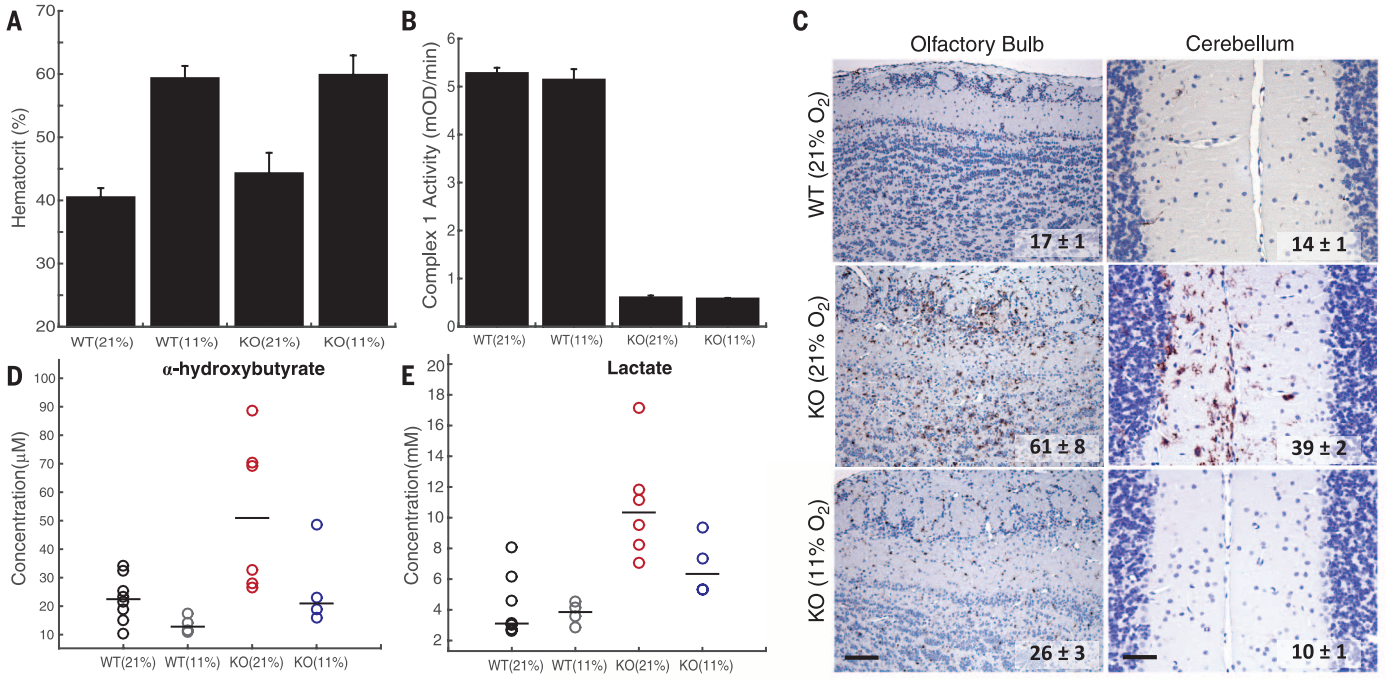


Fig. 6. Hypoxia exposure of *Ndufs4* KO mice alleviates metabolic disease markers, as well as neuropathology, without rescuing complex I activity. (**A**) Hematocrit values for WT and KO mice treated with normoxia or hypoxia for ~3 weeks (n = 3 or 4 mice per group, test P value < 0.05 for normoxia versus hypoxia for both WT and KO). (**B**) Complex I activity is significantly reduced in KO mice relative to WT mice, in both normoxic and hypoxic conditions (n = 3 or 4 mice per group, t test P value < 0.01). mOD, milli–optical density. (**C**) Representative images for immunostaining against the inflammatory marker Iba-1 in the olfactory bulb and cerebellum of *Ndufs4* KO mice treated with hypoxia or normoxia and WT mice exposed to normoxia breathing. The number of Iba-1–positive cells per 10 random fields of view is shown for each treatment group (mean ± SE, t test P value < 0.01 for normoxic versus hypoxic KO, n = 3 or 4 mice per group). Scale bar, 200 μm for the olfactory bulb and 50 μm for the cerebellum. (**D**) Plasma α-HB levels in WT and KO mice exposed to hypoxia or normoxia (n = 4 to 8 mice per group). The median is shown as a horizontal bar. (**E**) Plasma lactate in WT and KO mice exposed to hypoxia or normoxia (n = 4 to 8 mice per group). The median is shown as a horizontal bar.

indicate that the KO mice mount a hypoxic transcriptional response and that the RC inhibition–HIF stabilization paradox does not extend to this disease setting.

We next tested whether chronic exposure to moderate environmental hypoxia [breathing 11% O_2, a level known to be tolerated by humans (equivalent to 4500 m altitude)] could alleviate the disease phenotype in the *Ndufs4* KO mice. Environmental hypoxia was generated by adjusting the relative concentration of nitrogen and oxygen in the input gas mixture. This created environmental oxygen tensions similar to those found in the high mountain communities of Nepal and Peru (*36*). Continuous gas flow and CO_2 absorption by $Ca(OH)_2$ within the 11% O_2 hypoxic chamber maintained CO_2 levels below 0.4% with continuous monitoring. A control ambient environment for breathing 21% O_2 was created with an identical chamber setup. *Ndufs4* KO and control mice were continuously exposed to breathing at normoxia or 11% hypoxia after enrollment in the experiment, excluding brief exposure to normoxia for behavior tests and maintenance three times per week. Untreated *Ndufs4* KO mice typically began to show disease progression after approximately 30 days of post-birth air exposure, which is about 10 days after weaning. Because hypoxia-related vascular responses (constriction of pulmonary circulation and dilation of the ductus arteriosus) occur in early postnatal development, we initiated chronic hypoxic exposure treatments after the mice were 30 days old.

Remarkably, chronic hypoxia prevented the development of many disease symptoms in the *Ndufs4* KO mice and significantly extended their survival. All normoxia-exposed *Ndufs4* KO mice either fulfilled criteria for humane euthanasia or died at a median age of ~60 days, with none surviving past 75 days (Fig. 5A). In contrast, there were no deaths in *Ndufs4* KO mice that were chronically breathing 11% O_2. Several mice showed a mild clasping phenotype at ages greater than 120 days. At the time of submission of this manuscript, the oldest KO mice breathing 11% O_2 were 170 days old.

Hypoxia-treated mice showed an improvement in body weight gain, core temperature maintenance, and neurologic behavior. All *Ndufs4* KO mice continued to gain weight between 30 and 37 days of age (Fig. 5, B and C). At this stage, untreated KO mice lose weight, become hypothermic, and die. In contrast, *Ndufs4* KO mice breathing 11% O_2 gained weight for several weeks, at which point body weight gain slowed, similar to the growth kinetics of WT mice. The growth rate of hypoxia-treated KO mice matched that of WT mice breathing 11% O_2 upon treatment, suggesting that the primary cause of weight loss was alleviated by hypoxic exposure. At 30 days of age, untreated *Ndufs4* KO mice had similar core body temperatures to control mice. However, by 50 days there was nearly a 4°C drop in temperature (Fig. 5D). KO mice chronically breathing 11% O_2 showed no reduction of core body temperature. Thus, chronic hypoxic breathing improves the underlying metabolic phenotype that directly or indirectly results in alterations of energy and nutrient metabolism.

Ndufs4 KO mice, as well as patients suffering from Leigh syndrome, exhibit striking defects in locomotor activity. Ataxia and failure to thrive are hallmarks of mitochondrial dysfunction. Behavioral tests were performed at 10-day intervals in normoxia and hypoxia-treated WT and KO mice. The rotarod test (*37*) measures the ability of mice to maintain grip strength and balance and resist fatigue on an accelerating rotating rod. At 30 days of age, KO mice breathing air displayed a slight depression in the median time that they could stay on a rotarod (Fig. 5E). This ability declined by 40 days, and at 50 days, untreated KO mice were no longer able to stay on the rod for more than a few seconds, due to a combination of muscular weakness, inability to balance, and loss of visual acuity. Hypoxia-treated WT mice performed similarly to normoxia-treated control mice. KO mice breathing 11% O_2 displayed a near-complete rescue of this locomotor phenotype. As a further neurological behavioral

test, spontaneous locomotor activity was measured as total distance traveled within an hour (Fig. 5F). Untreated KO mice showed drastically reduced spontaneous locomotor activity and jump counts. These defects were rescued in hypoxia-treated mice, although only to 50% of the values of normoxic WT mice (fig. S10).

Modest hyperoxic breathing exacerbates disease in a mouse model of Leigh syndrome

The striking therapeutic effect of hypoxia led us to investigate whether oxygen itself was a key molecular parameter determining Leigh syndrome progression. Thus, we asked whether the converse environmental scenario of chronic mild hyperoxic exposure (55% O_2) would affect the disease. We exposed WT and *Ndufs4* KO mice to 55% normobaric oxygen starting at 30 days of age. We found that breathing 55% oxygen had no effect on the survival of the WT mice. In contrast, all *Ndufs4* KO mice breathing 55% oxygen died within 2 to 11 days of this exposure; this is significantly earlier than *Ndufs4* KO mice breathing ambient air (21% O_2), which typically succumb within 3 to 4 weeks after experimental exposures begin (Fig. 5A). The reduced survival of the KO mice breathing 55% O_2, along with the markedly extended health span of the KO mice that were breathing 11% O_2, points to the essential and previously unappreciated role of arterial oxygen tension in determining the progression of mitochondrial disease. This suggests that patients with mitochondrial disease may be highly sensitive to oxygen toxicity.

Circulating biomarkers and histopathology in a hypoxia-treated mouse model of Leigh syndrome

We further characterized *Ndufs4* KO mice after treatment with chronic hypoxia. As expected, the hematocrit in these mice was elevated from 40% during normoxia to ~60% during hypoxia, indicating EPO target engagement by hypoxic breathing (Fig. 6A). Given how effective hypoxia is in treating these mice, we asked whether they still retained a deficiency in complex I activity. Indeed, we found that although *Ndufs4* KO mice appeared healthy after hypoxia treatment, brain complex I activity remained dramatically reduced to the same levels as in untreated *Ndufs4* KO mice (Fig. 6B).

Normoxia-treated KO mice exhibited substantial neuronal degeneration. Lesions were accompanied by Iba-1$^+$ microglial proliferation within the olfactory lobes, cerebellum, and brainstem, as documented elsewhere (*38*). In contrast, KO mice breathing 11% O_2 exhibited minimal to no lesions (Fig. 6C) and were virtually indistinguishable histologically from WT controls.

Recently, α-hydroxybutyrate (α-HB) was identified as a circulating plasma marker of Leigh syndrome (*39*). Consistent with this, we found that α-HB was elevated in the plasma of *Ndufs4* KO mice breathing ambient air, but not in *Ndufs4* KO mice treated with chronic hypoxia (Fig. 6D). Similarly, plasma lactate levels were increased in *Ndufs4* KO mice breathing ambient air between 50 and 65 days of age, whereas this increase was partially prevented by 11% hypoxic exposure (Fig. 6E).

Collectively, these studies confirm that chronic hypoxic exposure to breathing 11% O_2 activates the endogenous hypoxic response. Hypoxia does not correct the proximal lesion within mitochondrial complex I, but rather prevents the onset of subsequent biochemical and histopathological defects.

Discussion

The preclinical studies described here suggest that hypoxic gas mixtures may be useful in treating or preventing mitochondrial disorders. This approach is seemingly counterintuitive, because oxygen is a key substrate for the RC. However, hypoxia activates an evolutionarily conserved adaptive program that allows mammals to cope with limited oxygen levels. This program decreases an organism's reliance on mitochondrial oxidative metabolism. Such adaptive programs are not necessarily triggered by mitochondrial disease, because the hypoxic signal is absent in those cases. Moreover, hypoxia leads to a state in which oxygen delivery and consumption are simultaneously reduced, whereas in mitochondrial disease, oxygen delivery continues in the face of impaired oxygen utilization. Such a mismatch between delivery and utilization potentially contributes to oxygen toxicity. Hence, hypoxia may represent nature's solution for overcoming mitochondrial disease pathology, both by triggering innate adaptive programs and by simultaneously limiting the substrate for oxygen toxicity.

Multiple cellular and systemic mechanisms are probably acting in concert to provide the therapeutic effect we observed in mice. First, hypoxia may be triggering the HIF-dependent transcriptional program that is known to activate key biochemical pathways, including glycolysis for redox-neutral ATP production and decreased flux through PDH to prevent mitochondrial ROS generation. Second, breathing 11% O_2 reduces the provision of oxygen to the cell—oxygen that would otherwise be available as a substrate for free radical production or aberrant signaling. Many enzymes are designed to operate under reducing conditions and are highly sensitive to ambient oxygen levels. Hypoxia may establish a new oxygen set point that is better suited to the cellular environment created by impaired RC activity, whereas hyperoxia may create an environment that is less favorable. Third, it is likely that hypoxia is also operating at the level of organ systems physiology (such as O_2 delivery and CO_2 clearance by the cardiovascular system, endocrine function, and immune signaling), which are inherently non–cell-autonomous and previously reported to be altered in humans living at high altitudes. Future studies will fully decipher the role of HIF and the cellular versus cell-autonomous mechanisms underlying the in vivo therapeutic benefit.

Our results may hold therapeutic potential for patients with mitochondrial disease. However, before the chronic hypoxia strategy described here can be evaluated in the clinical setting, additional preclinical studies are needed to establish its safety and efficacy. First, studies of additional mouse models will determine the generalizability of this approach to other rare mitochondrial disorders, common disorders of mitochondrial dysfunction, and disorders of oxidative stress. Second, in the current study, we used a treatment regimen consisting of chronic 11% inspired oxygen. Healthy humans can acclimate to high altitudes such as those encountered in Mount Blanc, Peru, and Nepal, where ambient oxygen tensions are comparable to those used in our experiments, but it is possible that these conditions would not be well tolerated by patients. Future studies should thus evaluate whether intermediate oxygen levels between 11 and 20% are effective in mouse disease models. Finally, if intermittent hypoxia proves as effective as chronic hypoxia, it may allow for a nighttime therapy for which face masks and sleeping tents have already been devised by the sports industry.

An important principle in the management of mitochondrial disease is to avoid exposures, such as aminoglycoside or tetracycline antibiotics, that are known to be toxic to mitochondria. Patients with mitochondrial disease (like many other patients) are routinely treated with supplemental oxygen and breathe high levels of inspired oxygen during general anesthesia, recovery from surgery, and intensive care. Retrospective or prospective studies may help to extend our observations to humans, and if confirmed, would imply that caution should be exercised in O_2 exposure, and that administering supplemental oxygen should be limited to those instances in which it is clinically indicated.

At present, how lesions in the RC lead to such diverse pathology remains a mystery. Given the striking therapeutic efficacy of hypoxic breathing and the detrimental effect of moderate hyperoxia we saw in our studies, we propose that aberrant oxygen metabolism, signaling, or toxicity lies at the heart of mitochondrial pathogenesis. The identification of such a critical parameter suggests that a real understanding of mitochondrial pathogenesis is within reach.

Finally, it is notable that the aging process and virtually all age-related degenerative diseases are associated with secondary mitochondrial dysfunction and oxidative stress (*40*). Although antioxidants have been proposed as a strategy to alleviate these disorders by scavenging free radicals, our work suggests that simply limiting the substrate for oxygen toxicity may prove more effective. Moreover, hypoxia can trigger an adaptive program designed to decrease our body's reliance on mitochondrial oxidative metabolism. It is conceivable that breathing hypoxic gas mixtures may prevent the onset of more common disorders.

REFERENCES AND NOTES

1. P. Rich, *Nature* **421**, 583 (2003).
2. S. B. Vafai, V. K. Mootha, *Nature* **491**, 374–383 (2012).
3. W. J. Koopman, P. H. Willems, J. A. Smeitink, *N. Engl. J. Med.* **366**, 1132–1141 (2012).
4. J. Nunnari, A. Suomalainen, *Cell* **148**, 1145–1159 (2012).

5. G. Pfeffer, K. Majamaa, D. M. Turnbull, D. Thorburn, P. F. Chinnery, *Cochrane Database Syst. Rev.* **4**, CD004426 (2012).
6. N. J. Lake, M. J. Bird, P. Isohanni, A. Paetau, *J. Neuropathol. Exp. Neurol.* **74**, 482–492 (2015).
7. G. S. Gorman *et al.*, *Ann. Neurol.* **77**, 753–759 (2015).
8. S. Parikh *et al.*, *Genet. Med.* **17**, 689–701 (2015).
9. R. H. Haas *et al.*, *Pediatrics* **120**, 1326–1333 (2007).
10. O. Shalem *et al.*, *Science* **343**, 84–87 (2014).
11. T. Wang, J. J. Wei, D. M. Sabatini, E. S. Lander, *Science* **343**, 80–84 (2014).
12. M. P. King, G. Attardi, *Science* **246**, 500–503 (1989).
13. S. E. Calvo, K. R. Clauser, V. K. Mootha, *Nucleic Acids Res.* **44**, D1251–D1257 (2016).
14. M. Ohh *et al.*, *Nat. Cell Biol.* **2**, 423–427 (2000).
15. C. M. Robinson, M. Ohh, *FEBS Lett.* **588**, 2704–2711 (2014).
16. G. L. Wang, B. H. Jiang, E. A. Rue, G. L. Semenza, *Proc. Natl. Acad. Sci. U.S.A.* **92**, 5510–5514 (1995).
17. A. J. Majmundar, W. J. Wong, M. C. Simon, *Mol. Cell* **40**, 294–309 (2010).
18. M. Ivan *et al.*, *Proc. Natl. Acad. Sci. U.S.A.* **99**, 13459–13464 (2002).
19. O. Iliopoulos, A. P. Levy, C. Jiang, W. G. Kaelin Jr., M. A. Goldberg, *Proc. Natl. Acad. Sci. U.S.A.* **93**, 10595–10599 (1996).
20. P. H. Maxwell *et al.*, *Nature* **399**, 271–275 (1999).
21. D. L. Buckley *et al.*, *J. Am. Chem. Soc.* **134**, 4465–4468 (2012).
22. M. H. Rabinowitz, *J. Med. Chem.* **56**, 9369–9402 (2013).
23. N. S. Chandel *et al.*, *Proc. Natl. Acad. Sci. U.S.A.* **95**, 11715–11720 (1998).
24. Y. L. Chua *et al.*, *J. Biol. Chem.* **285**, 31277–31284 (2010).
25. I. Papandreou, R. A. Cairns, L. Fontana, A. L. Lim, N. C. Denko, *Cell Metab.* **3**, 187–197 (2006).
26. D. Tello *et al.*, *Cell Metab.* **14**, 768–779 (2011).
27. J. W. Kim, I. Tchernyshyov, G. L. Semenza, C. V. Dang, *Cell Metab.* **3**, 177–185 (2006).
28. M. C. Simon, *Cell Metab.* **3**, 150–151 (2006).
29. E. van Rooijen *et al.*, *Blood* **113**, 6449–6460 (2009).
30. B. R. Pinho *et al.*, *Br. J. Pharmacol.* **169**, 1072–1090 (2013).
31. K. D. Stackley, C. C. Beeson, J. J. Rahn, S. S. Chan, *PLOS One* **6**, e25652 (2011).
32. J. M. Harris *et al.*, *Blood* **121**, 2483–2493 (2013).
33. K. Santhakumar *et al.*, *Cancer Res.* **72**, 4017–4027 (2012).
34. R. Chowdhury *et al.*, *ACS Chem. Biol.* **8**, 1488–1496 (2013).
35. S. E. Kruse *et al.*, *Cell Metab.* **7**, 312–320 (2008).
36. I. G. Pawson, *Proc. R. Soc. London Ser. B* **194**, 83–98 (1976).
37. J. Caston, N. Jones, T. Stelz, *Neurobiol. Learn. Mem.* **64**, 195–202 (1995).
38. A. Quintana, S. E. Kruse, R. P. Kapur, E. Sanz, R. D. Palmiter, *Proc. Natl. Acad. Sci. U.S.A.* **107**, 10996–11001 (2010).
39. J. Thompson Legault *et al.*, *Cell Rep.* **13**, 981–989 (2015).
40. R. S. Balaban, S. Nemoto, T. Finkel, *Cell* **120**, 483–495 (2005).

ACKNOWLEDGMENTS

We thank W. Kaelin Jr. and members of the Mootha lab for valuable feedback; R. Sharma, M. Ferrari, A. Rogers, and the MGH animal facility for assistance with experiments; and F. van Eeden for Tg(*phd3::EGFP*) zebrafish. I.H.J. is supported by the Department of Energy Computational Science Graduate Fellowship Program (grant DE-FG02-97ER25308). N.E.S. is supported by the National Institutes of Health (NIH) through a NHGRI Pathway to Independence Award (K99-HG008171) and a postdoctoral fellowship from the Simons Center for the Social Brain at the Massachusetts Institute of Technology. F.Z. is supported by NIH through NIMH (grants 5DP1-MH100706 and 1R01-MH110049) and NIDDK (grant 5R01DK097768-03); a Waterman Award from NSF; the New York Stem Cell, Simons, Paul G. Allen Family, and Vallee Foundations; and B. Metcalfe. F.Z. is a New York Stem Cell Foundation Robertson Investigator. W.G. is supported by NIH grants R01DK090311 and R24OD017870 and is a Pew Scholar in the Biomedical Sciences. This work was supported by a gift from the Marriott Mitochondrial Disorders Research Fund (V.K.M.) and a gift in memory of Daniel Garland (V.K.M.). V.K.M. is an Investigator of the Howard Hughes Medical Institute. V.K.M. is a founder of and paid scientific advisor for Raze Therapeutics. W.G. is a paid consultant for FATE Therapeutics. F.Z. is a founder of and a scientific advisor for Editas Medicine and a scientific advisor for Horizon Discovery. V.K.M., I.H.J., L.Z., and W.M.Z. are listed as inventors on a patent application filed by Massachusetts General Hospital related to technology reported in this paper on the use of hypoxia and the hypoxia response in the treatment of mitochondrial dysfunction. F.Z., O.S., and N.E.S. are listed as inventors on a patent application (PCT/US2013/074800) filed by The Broad Institute/MIT related to the genome-scale CRISPR knockout screening technology used in this study. The CRISPR knockout library is available through a Uniform Biological Materials Transfer Agreement from Addgene. The *Ndufs4* KO mice were a kind gift of R. Palmiter and are available under a materials transfer agreement with the University of Washington, Seattle.

SUPPLEMENTARY MATERIALS

www.sciencemag.org/content/352/6281/54/suppl/DC1
Materials and Methods
Figs. S1 to S10
Tables S1 and S2
References (*41*–*44*)

14 August 2015; accepted 9 February 2016
Published online 25 February 2016
10.1126/science.aad9642

FLOW CHEMISTRY

On-demand continuous-flow production of pharmaceuticals in a compact, reconfigurable system

Andrea Adamo,[1] Rachel L. Beingessner,[2] Mohsen Behnam,[1]* Jie Chen,[1] Timothy F. Jamison,[2]† Klavs F. Jensen,[1]† Jean-Christophe M. Monbaliu,[1]‡ Allan S. Myerson,[1]† Eve M. Revalor,[1]§ David R. Snead,[2]|| Torsten Stelzer,[1]¶ Nopphon Weeranoppanant,[1] Shin Yee Wong,[1]# Ping Zhang[2]

Pharmaceutical manufacturing typically uses batch processing at multiple locations. Disadvantages of this approach include long production times and the potential for supply chain disruptions. As a preliminary demonstration of an alternative approach, we report here the continuous-flow synthesis and formulation of active pharmaceutical ingredients in a compact, reconfigurable manufacturing platform. Continuous end-to-end synthesis in the refrigerator-sized [1.0 meter (width) × 0.7 meter (length) × 1.8 meter (height)] system produces sufficient quantities per day to supply hundreds to thousands of oral or topical liquid doses of diphenhydramine hydrochloride, lidocaine hydrochloride, diazepam, and fluoxetine hydrochloride that meet U.S. Pharmacopeia standards. Underlying this flexible plug-and-play approach are substantial enabling advances in continuous-flow synthesis, complex multistep sequence telescoping, reaction engineering equipment, and real-time formulation.

Whereas manufacturing of automobiles, electronics, petrochemicals, polymers, and food use an assembly-line and/or continuous, steady-state strategy, pharmaceutical synthesis remains one of the last industrial processes to apply a noncontinuous or "batch" approach. Moreover, pharmaceutical companies generally assemble the active pharmaceutical ingredient (API) using molecular fragments obtained from different sources, with the final synthesis steps done at the company location. The API is then often mixed with excipients and formulated in the final drug product form at a separate plant. As a result, production of a finished dosage form can require up to a total of 12 months, with large inventories of intermediates at several stages. This enormous space-time demand is one of a myriad of reasons that has led to increased interest in continuous manufacturing of APIs and drug products, as well as in the development of integrated processes that would manufacture the drug product from raw materials in a single end-to-end process (*1*–*5*).

Another major challenge facing the pharmaceutical industry is drug shortages; the U.S. Food and Drug Administration (FDA) has reported well over 200 cases per year during 2011–2014 (*6*). The root causes of these shortages often trace back to factors reflective of the limitations of batchwise manufacturing, such as variations in quality control and supply chain interruption. Moreover, the small number of suppliers for any particular medicine further exacerbates the challenges faced by batchwise manufacturing to respond to sudden changes in demand or need,

[1]Department of Chemical Engineering, Massachusetts Institute of Technology, 77 Massachusetts Avenue, Cambridge, MA 02139, USA. [2]Department of Chemistry, Massachusetts Institute of Technology, 77 Massachusetts Avenue, Cambridge, MA 02139, USA.
*Present address: Nuvera Fuel Cells, 129 Concord Road, Billerica, MA 01821, USA. **†Corresponding author. E-mail: tfj@mit.edu (T.F.J); kfjensen@mit.edu (K.F.J); myerson@mit.edu (A.S.M)**
‡Present address: Department of Chemistry, University of Liège, Quartier Agora, Allée du six Août 13, B-4000 Liège (Sart Tilman), Belgium. §Present address: Department of Chemical and Biomolecular Engineering, Faculty of Medicine, Dentistry and Health Sciences, University of Melbourne, 3010 VIC, Australia. ||Present address: Georgia-Pacific Chemicals, 2883 Miller Road, Decatur, GA 30312, USA. ¶Present address: Department of Pharmaceutical Sciences, University of Puerto Rico, Medical Sciences Campus, San Juan, PR 00936, USA. #Present address: Chemical Engineering and Food Technology Cluster, Singapore Institute of Technology, 10 Dover Drive, Singapore 138683. **Present address: Novartis Institute of Biomedical Research, 250 Massachusetts Avenue, Cambridge, MA 02139, USA.

Downloaded from on March 31, 2016

such as in epidemic or pandemic instances of influenza outbreak.

To address the above issues, we have developed a continuous manufacturing platform that combines both synthesis and final drug product formulation into a single, highly compact unit (Fig. 1). The utilization of continuous flow (*7*–*9*) within the system enables efficient heat and mass transfer, as well as process intensification (*10*) and automation. Over the past several years, the merits of flow chemistry in streamlining synthesis (*11*) have been successfully demonstrated in the preparation of many individual high-profile APIs (*12*, *13*), including artemisinin (*14*), imatinib (*15*), efavirenz (*16*), nabumetone (*17*), rufinamide (*18*), pregabalin (*19*), and (*E*/*Z*)-tamoxifen (*20*).

Work with colleagues at the Massachusetts Institute of Technology (MIT) on end-to-end, continuous manufacturing of a single API, aliskiren hemifumarate, in a shipping container–sized unit (*21*) enabled us to identify critical steps in on-demand manufacturing of pharmaceuticals. Specifically, we chose to address challenges in reconfiguration for multiple synthesis of multiple compounds, tight integration of process streams for reduced footprint, innovations in chemical reaction and purification equipment, and compact systems for crystallization and formulation. As a result, the current system is ~1/40 the size and reconfigurable, in order to enable the on-demand synthesis and formulation of not just one, but many drug products. With the necessary regulatory approvals, this proof-of-principle system could enable a gradual phase-in of pharmaceutical production in response to demand. Reproduction of the system would be simpler and less costly to operate than a full batch plant and so could produce pharmaceuticals only needed for small patient populations or to meet humanitarian needs. It could be particularly advantageous for drugs with a short shelf life. Furthermore, the ability to manufacture the active ingredient on demand could reduce formulation complexity relative to tablets needing yearlong stability.

The flexible, plug-and-play refrigerator-sized platform (Fig. 1) [1.0 m (width) × 0.7 m (length) × 1.8 m (height), ~100 kg] is capable of complex multistep synthesis, multiple in-line purifications, postsynthesis work-up and handling, semibatch crystallization, real-time process monitoring, and ultimately formulation of high-purity drug products. To demonstrate its capabilities, we produced, from raw materials, sufficient quantities to supply hundreds to thousands of consumable oral or topical liquid doses per day of four different pharmaceuticals: diphenhydramine hydrochloride (**1**), lidocaine hydrochloride (**2**), diazepam (**3**), and fluoxetine hydrochloride (**4**) (Fig. 2) (*22*). The latter API, fluoxetine hydrochloride (**4**), was synthesized as a racemic mixture, as approved by the FDA. These generic molecules from different drug classes have differing chemical structures and synthesis routes, thus challenging the capabilities and exploring the technical limits of the continuous-flow system. Moreover, they are drugs commonly found in a chief medic's toolkit. Diphenhydramine hydrochloride (**1**), for example, well known by the trade name Benadryl, is an ethanolamine-based antihistamine used to treat the common cold,



Fig. 1. Reconfigurable system for continuous production and formulation of APIs. (**A**) Labeled photograph of the stack of upstream synthesis modules. (**B**) Labeled photograph of the downstream purification and formulation modules. (**C**) Close-up examples of upstream units; PFA tube flow reactors in an aluminum shell for heating (left) and membrane surface tension–based separation units (right). (**D**) Images of some of the main components in the downstream unit including the (a) buffer tank, (b) precipitation tank, (c) filtration unit, (d) crystallization unit, (e) filtration unit, (f) formulation tank, (g) solution holding tank, and (h) formulated API. Details are in the supplementary text.

lessen symptoms of allergies, and act as a mild sleep aid. Lidocaine hydrochloride (**2**), alternatively, is a common local anesthetic and class-1b antiarrhythmic drug. Diazepam (**3**), also known as Valium, is a central nervous system depressant. Finally, fluoxetine hydrochloride (**4**) is a widely used antidepressant recognized by its trade names Prozac and Sarafem.

As shown in Figs. 3 to 5, the synthesis of each API utilizes simple starting materials and reagents readily available from commercial suppliers and highlighted advantages that flow chemistry offers relative to batch synthesis. Synthetic schemes were first developed in flow on a microliter scale before translating to the platform. The reactions leverage quick exposure at elevated temperatures (130° to 180°C) and pressures (~1.7 MPa) in controlled environments to enable faster reactions with low impurity profiles and reduce total synthesis times from hours to minutes. Reagents were in high concentrations, close to saturation, and in some cases even neat, which ensured high productivity while reducing waste and solvent amounts. This is in contrast to batch conditions that use lower concentrations, as solvents often also serve as a heat transfer medium. Moreover, in the flow system, reaction and purification occurred at the same time at different locations within the same uninterrupted reactor network. In batch, each of the operations would be physically and temporally disconnected and would have much larger time, space, and workforce requirements, hence drastically increasing the global footprint and decreasing the global output of a given process.

Assembly of the platform

The system consists of reconfigurable upstream and downstream units (Fig. 1) that, despite having many complex operations, can be managed easily by an individual user. This is unlike typical batch manufacturing, which requires many operators to oversee multiple large-scale reactors and tanks with volumes on the order of thousands of liters and the transport and formulation of the final API in a separate processing plant (*23*). As shown in Fig. 1A, the upstream unit houses reaction-based equipment for producing APIs (e.g., feeds, pumps, reactors, separators, and pressure regulators) and has a maximum power requirement of 1.5 kW, which is mainly consumed by heating the reactors and operating the pumps. The backside (in Fig. 1A), alternatively, represents the downstream unit (Fig. 1B) dedicated to purification and formulation of the drug product (e.g., tanks to precipitate the crude API from reaction mixtures, crystallizers, and filters) (Fig. 1D). Temperature, pressure, flow, and level sensors

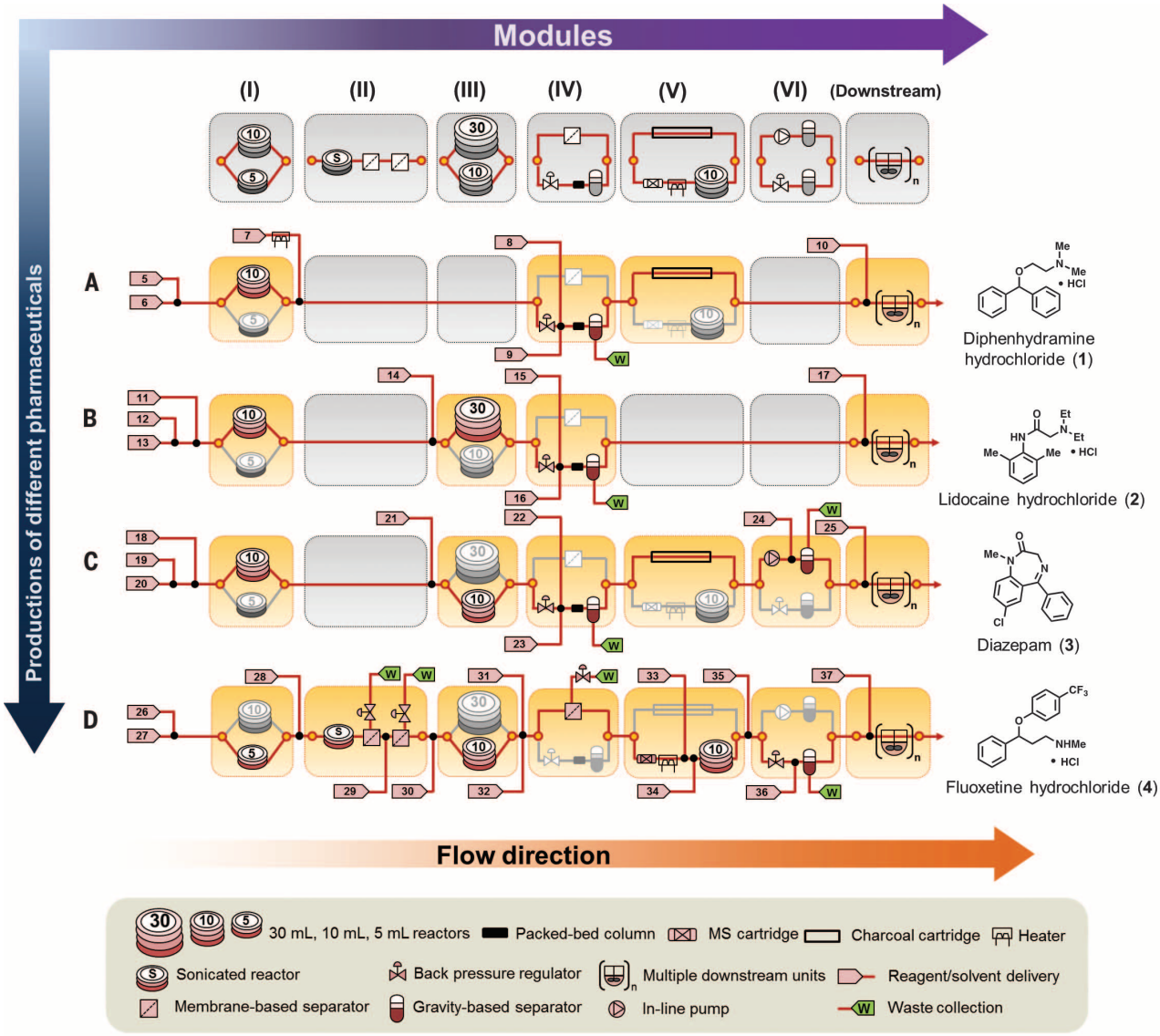


Fig. 2. Reconfigurable modules and flowcharts for API synthesis. (**A**) Diphenhydramine hydrochloride, (**B**) lidocaine hydrochloride, (**C**) diazepam, and (**D**) fluoxetine hydrochloride. The top row represents the different modules. Colored modules are active, gray boxes designate inactive modules. Reagent and solvent numbers refer to the compounds listed in table S2.

are included at strategic positions and coupled with data acquisition units to facilitate operational monitoring and support real-time production control. Because few commercial chemically compatible components were available and suitable for the gram-per-hour size scale combined with elevated temperatures and pressures, we developed most of the unit operations used in the upstream and downstream systems, as detailed in the supplementary text. These include pressure sensors, clamshell reactors with an outer aluminum body, and inner PFA (perfluoro alkoxy polymer) tubing for chemical compatibility with good heat transfer (Fig. 1C and fig. S5), surface tension liquid-liquid–driven extraction units (*24*) (Fig. 1C), multiline back pressure regulators (fig. S3), automated precipitation, filtration (Fig. 1D and fig. S6), and crystallization tanks, and automated formulation (Fig. 1D and figs. S7 and S8). The ventilation of this system was designed to have a face velocity between 0.4 and 0.5 m/s, which is typical for chemical fume hoods in the United States.

The units were arranged in modules of reactors and separators to enable reconfiguration to produce the four different drug products within the same system (Fig. 2; see table S2 for the numbering scheme). The synthesis schemes demonstrate the ability to reconfigure the system for increasing levels of chemical complexity, starting with diphenhydramine (Fig. 2A) with one reactor,

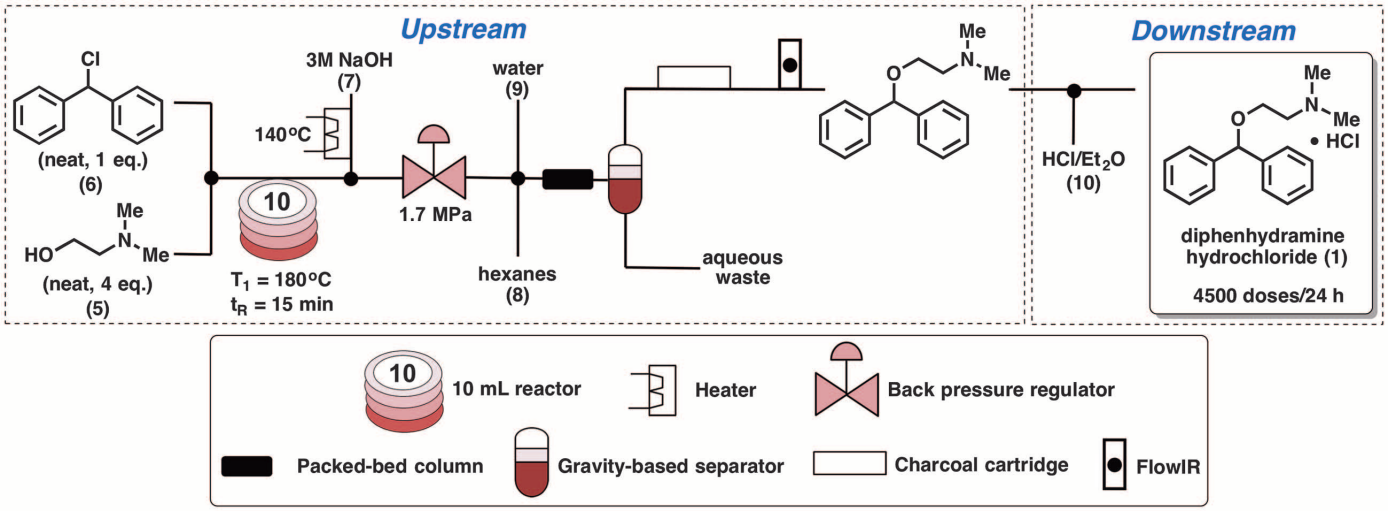


Fig. 3. Synthesis of diphenhydramine hydrochloride using the reconfigurable system. Flowchart detailing the upstream and downstream synthesis.

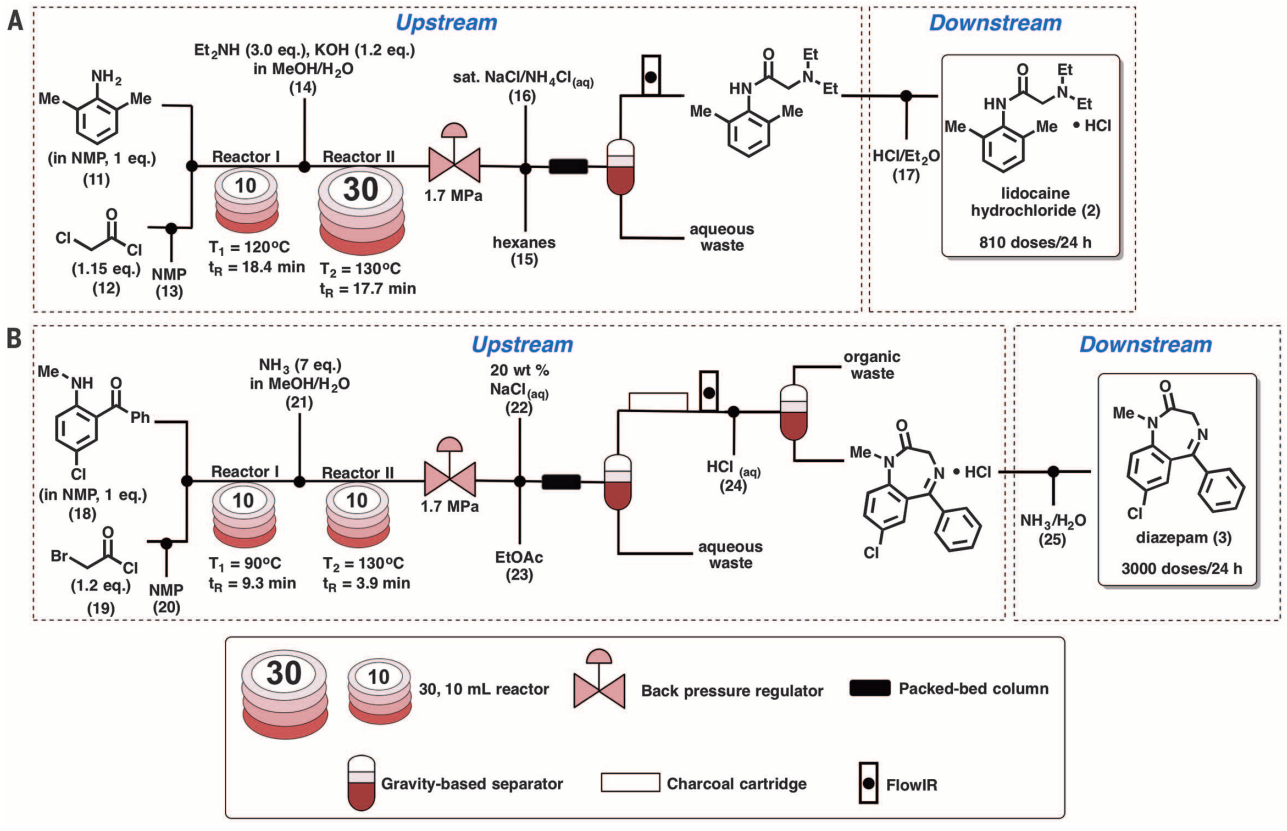


Fig. 4. Synthesis of APIs via two-step upstream configurations. (**A**) Lidocaine hydrochloride and (**B**) diazepam.

one separator, and four pumps and finishing with fluoxetine (Fig. 2D) with four reactors, four separators, and 11 pumps. An inline attenuated total reflection (ATR) Fourier transform infrared (FTIR) system (FlowIR) (figs. S9, S13, S14, S18, and S19) (*25*) provided real-time monitoring of the formed APIs. LabVIEW (National Instruments) programs were also implemented, along with the high- and fast-performance modular X Series data acquisition (DAQ) device and sensors for monitoring multiple process parameters—namely, pressure, reactor temperature, and flow rates. The same LabVIEW platform was also used to automate different units, including heating reactors, pumps, gravity-based separators, and multichannel valves. The downstream module alternatively (Fig. 2, right-hand modules) consisted of precipitation, filtration, redissolution, crystallization, filtration, and formulation units. All drug products were purified and formulated to meet U.S. Pharmacopeia (USP) standards. Consistent with the on-demand format, we focused on concentrated aqueous or alcohol-based formulations ready for dilution to target concentrations when needed and stable for at least 31 days (table S1). Solid formulations, such as tablets, would have required substantial additional space to house unit operations of drying, powder transport, solids blending, and tableting—all processes that would be difficult to implement on the gram-per-hour scale. Nevertheless, we are currently pursuing the miniaturization of these processes so that solid formulations may be prepared on the same platform.

Synthesis and formulation of diphenhydramine hydrochloride

As a first demonstration of the capabilities of this compact unit, diphenhydramine hydrochloride (**1**) was manufactured in its final liquid dosage form. As shown in Fig. 3, the process commenced with the reaction between an excess amount of neat 2-dimethylaminoethanol (**5**) and neat chlorodiphenylmethane (**6**) at a temperature of 180°C and a pressure of 1.7 MPa generated with the use of a back pressure regulator (BPR). The reaction was complete within 15 min, in contrast to typical batch processing requiring 5 or more hours at 125°C in benzene for a similar substrate (*26*). Because the product API has a melting point of 168°C, it could be handled in flow at 180°C in the absence of additional solvent, thereby minimizing the waste generated. The molten salt was then treated with a stream of preheated (140°C) aqueous NaOH (**7**). An inline purification and extraction process employing a packed-bed column to increase mass transfer, a gravity-operated liquid-liquid separator with automatic level control (fig. S1), and an activated charcoal filter to remove the colored impurities produced the diphenhydramine API as a solution in hexanes in 82% yield.

In the downstream section, the API was precipitated with HCl (**10**), and the resulting salt was filtered, washed, and dried in a specially constructed device with a Hastelloy filtration membrane (fig. S6) (*27*). After redissolving in isopropyl alcohol at 60°C, the diphenhydramine hydrochloride (**1**) was recrystallized in a crystallizer, while being cooled to 5°C. Upon filtering and drying, the crystals were dissolved in water. Real-time monitoring using an ultrasonic probe yielded the final dosage concentration (5 ml at 2.5 mg/ml). High-performance liquid chromatography analysis determined that the purity of the product conformed to USP standards (fig. S12) (*28*). Overall, the system capacity based on the optimal yield observed in each step was 4500 doses per day.

The facile transition from **1** to the production of lidocaine hydrochloride (**2**) (Fig. 4; see also Fig. 2B) was next accomplished through simple adjustments of the fluid manifolds to direct the fluids to specific reactors and separators. Whereas **1** was produced via a single upstream reaction, both **2** and **3** were generated through similar two-step upstream configurations, with modifications mainly in the purification and extraction regimens.

Synthesis and formulation of lidocaine hydrochloride

The synthesis of lidocaine hydrochloride (**2**) began with the acylation of 2,6-xylidine (**11**) in *N*-methyl-2-pyrrolidone (NMP) with neat chloroacetyl chloride (**12**), premixed inline with a stream of NMP (**13**) to avoid decomposition on standing (Fig. 4A; see also Fig. 2B). Subsequent addition of a stream of KOH and Et_2NH (**14**) in a mixture of polar protic solvents facilitated the installation of the tertiary amine to generate the crude API, without any intermediate purification. A BPR set at 1.7 MPa after reactor II enabled liquid flow at elevated temperatures (120°C and 130°C), allowing liquid operation well above the boiling point of diethylamine (55°C) and some of the solvents used (methanol and water). As a result, the reaction was complete within 5 min versus batch procedures of 60 min in refluxing toluene (*29*) or 4 to 5 hours in refluxing benzene (*30*). Overall, complete conversion (99%) of the starting materials to the crude API was realized in only 36 min. To deliver the crude lidocaine solution with sufficient purity for a streamlined downstream process, hexane (**15**) and a $NaCl/NH_4Cl$ saturated solution (**16**) were then injected through a cross-junction into the outlet product stream. Upon passing through a packed-bed column containing 0.1-mm glass beads and an inline gravity liquid-liquid separator, lidocaine was obtained in 90% yield. The downstream processing next proceeded with the formation of the HCl salt in a manner similar to that of diphenhydramine. After recrystallization, **2** (88% yield) had a purity of 97.7%, thereby meeting USP standards (fig. S17) (*31*). The API was treated with a premixed aqueous solution of 4% sodium methylcarboxycellulose to yield a final concentrate. Overall, this system can produce 810 doses (dosage strength = 20 mg/ml) of lidocaine hydrochloride per day.

Synthesis and formulation of diazepam

Following the production of lidocaine hydrochloride (**2**), we next transitioned to diazepam (**3**), through switching-in charcoal purification and gravity-based extraction units. As shown in Fig. 4B (see also Fig. 2C), the crude API was synthesized in a two-step upstream sequence initiated with the acylation of 5-chloro-2-(methylamino)

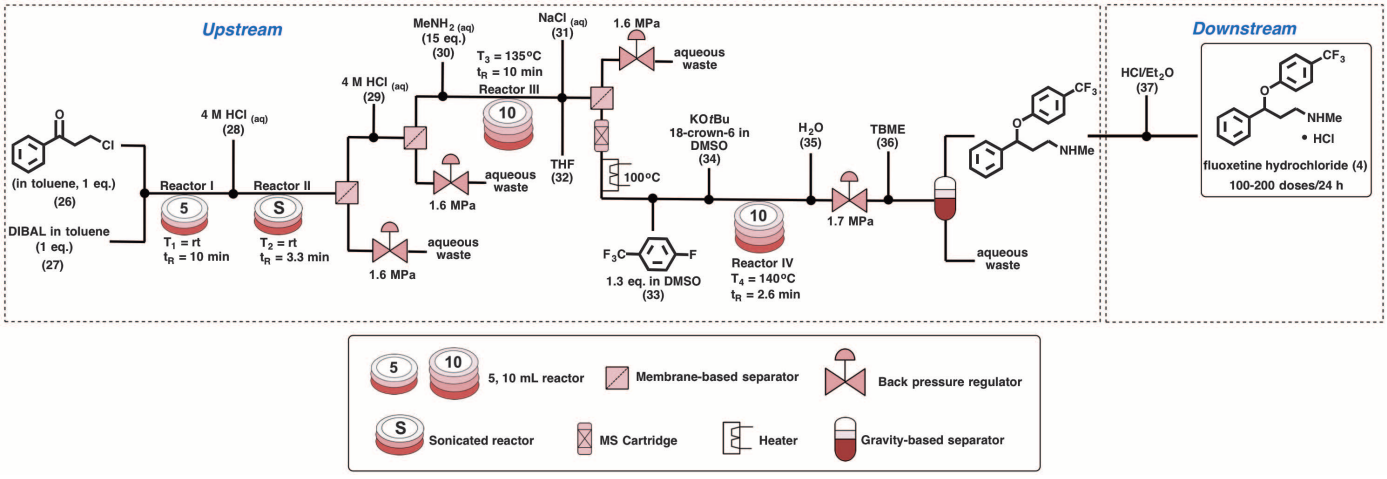


Fig. 5. Demonstration of a multistep API synthesis. Flowchart detailing the upstream and downstream synthesis of fluoxetine hydrochloride. DMSO, dimethyl sulfoxide; rt, room temperature; DIBAL, diisobutylaluminum hydride.

benzophenone in NMP (**18**) with neat bromoacetyl chloride (**19**) premixed inline with a stream of NMP (**20**). Bromine displacement, followed by an intramolecular cyclization reaction upon addition of a stream of NH_3 in MeOH/H_2O (**21**), then furnished the target molecule. Similar to lidocaine, the application of elevated pressure (1.7 MPa) and temperatures (90°C and 130°C) in this sequence enabled liquid flow and complete conversion of the starting materials in only 13 min compared to 24 hours of batch operation at room temperature (*32*). After a continuous extraction, the organic stream was then passed through the activated charcoal cartridge to remove the dark colored dimer and trimer side-products. After precipitation and recrystallization in the downstream section, the dried diazepam crystals (**3**) (94% yield) had a purity level that met USP standards (fig. S22) (*33*). Resuspending in ethanol in the formulation tank then provided a concentrate. At a dosage concentration of 1 mg/ml (one dose is 5 ml at 1 mg/ml), this system can produce ~3000 doses per day.

Synthesis and formulation of fluoxetine hydrochloride

The last of the APIs produced, fluoxetine hydrochloride (**4**), was specifically chosen to demonstrate the versatility and capacity of this system to carry out a complex, fully integrated, telescoped, multistep, biphasic synthesis (Fig. 5; see also Fig. 2D). A series of individual reactions carried out in flow, with purification and isolation of each intermediate in batch, has been previously demonstrated (*34*). By integrating four reactors and four inline separation units, however, we realized the continuous end-to-end synthesis of this API as a racemic mixture. As shown in Fig. 5, the entire upstream reactor network was maintained at 1.7 MPa through the use of multichannel BPR located near the end of the upstream unit. The synthesis commenced with a DIBAL (**27**) reduction of a close-to-saturated solution of 3-chloropropiophenone in toluene (**26**) at room temperature in the first reactor. A stream of 4 M aqueous solution of HCl (**28**) was then introduced, and the resulting mixture was subjected to ultrasound in the second reactor to enable fast dissolution of the aluminum salts and ensure long-term and stable operation of the system (*35*). A two-stage inline extraction and separation sequence with in-house–constructed membrane liquid-liquid/gas separators removed the aqueous waste and gas (*24*). An additional stream of aqueous HCl (**29**) injected into the system before the second separation ensured a complete quench of the reaction.

The intermediate alcohol next reacted with aqueous methylamine (**30**) at 135°C in the third reactor in a biphasic flow. After a residence time of 10 min, tetrahydrofuran (THF) (**32**) and aqueous NaCl (20 mol %) (**31**) efficiently extracted the resulting amino alcohol into a suitable organic solvent (THF) for nucleophilic aromatic substitution in the fourth reactor. Upon separation of the aqueous and organic phase, the latter passed through a cartridge containing 0.4-nm molecular sieves to remove residual water. After a short residence time of 2.6 min in the fourth reactor, the fluoxetine solution merged with a stream of water to prevent the precipitation of the KF salt. Extraction and separation produced a solution of fluoxetine in *tert*-butyl methyl ether (TBME) (**36**) in 43% yield and at a production rate corresponding to 1100 doses per day (one dose is 5 ml at 4 mg/ml) prior to downstream processing. Similar to the other three APIs, the downstream processing involved a precipitation and recrystallization sequence to provide fluoxetine hydrochloride crystals that met USP standards (fig. S25) (*36*). Redissolution in water yielded the final concentrate in 100 to 200 doses.

Overall, the total cycle times for the production and formulation of the APIs varied from 12.2 hours in the case of lidocaine hydrochloride to 47.7 hours for fluoxetine hydrochloride (table S3). Whereas the upsteam syntheses required three residence times (total of 0.7 to 1.3 hours) of the sequential reactions to achieve steady state, the downstream processes took much longer and were mainly dominated by the precipitation step. Because the system featured valves, convenient feed swaps (from reagents to solvents) and fast cleaning procedures between each API production were achieved. Appropriate solvent combinations were added to the reactor lines to flush the up- and downstream units. At the shortest, switching the production of lidocaine hydrochloride to diazepam required a total of 15 min for a complete flush of the internal lines in the upstream section. A switchover from the simplest to the most complex synthesis (diphenhydramine hydrochloride to fluoxetine hydrochloride) would take 2 hours. No cross-contamination was detected from run to run, and the results were reproducible within a standard deviation of 0.6% (diphenhydramine hydrochloride) to 4.7% (fluoxetine hydrochloride) yield for each API production within a single run. The downstream purification and formulation units required no reconfiguration—only the aforementioned flushing. Thus, all transitions between production runs could be completed in less than 4 hours. To meet current good manufacturing practices, one could consider replacing the perfluorinated tubing and membranes in the reactors, BPRs, and separators. The units were designed to facilitate such a replacement.

Outlook

For over a decade, the FDA has been working to stimulate modernization of small-molecule manufacturing, which is largely based on batch manufacturing processes (*37*, *38*). The vision of the FDA's Pharmaceutical Quality for the 21st Century Initiative is to create a more robust and flexible pharmaceutical sector capable of manufacturing high-quality APIs. Continuous manufacturing is one such strategy for meeting this vision (*1*, *39*). Continuous manufacturing systems benefit from integrated processing and control, which can translate to increased safety (no manual handling) and shorter processing times. The use of highly adaptable smaller equipment, which implements real-time monitoring, may also lower production costs and improve product quality (*1*, *37*, *38*). The present implementation of four well-known pharmaceutical drugs demonstrates the concept of continuous, small-scale, on-demand production of pharmaceuticals. Already-demonstrated advances in flow chemistry (*11*–*20*) could be realized on similar platforms, and with additional research, ultimately enable the continuous synthesis of modern small-molecule pharmaceuticals, including enantiopure APIs. The current system focused on liquid oral and topical dosage formulations commensurate with the on-demand approach. A complete alternative platform to current batch manufacturing would inevitably have to produce pharmaceuticals in the common dosage forms of tablets and capsules as well as sterile injectable solutions, which would require advances in downstream processing. Specifically, classical unit operations of crystallization, drying, powder transport, solids blending, and tableting would have to be miniaturized and integrated. New approaches such as three-dimensional printing of tablets could facilitate these developments. Realization and demonstration of good manufacturing practices and ultimately FDA approval will be critical to future applications of this technology, including production units for hospitals, health care organizations, pharmaceutical development, and humanitarian aid.

REFERENCES AND NOTES

1. C. Badman, B. L. Trout, *J. Pharm. Sci.* **104**, 779–780 (2015).
2. I. R. Baxendale *et al*., *J. Pharm. Sci.* **104**, 781–791 (2015).
3. S. Byrn *et al*., *J. Pharm. Sci.* **104**, 792–802 (2015).
4. R. F. Service, *Science* **347**, 1190–1193 (2015).
5. S. Mascia *et al*., *Angew. Chem. Int. Ed.* **52**, 12359–12363 (2013).
6. Food and Drug Administration, *Strategic Plan for Preventing and Mitigating Drug Shortages* (October 2013; www.fda.gov/downloads/Drugs/DrugSafety/DrugShortages/UCM372566.pdf).
7. L. Malet-Sanz, F. Susanne, *J. Med. Chem.* **55**, 4062–4098 (2012).
8. D. Webb, T. F. Jamison, *Chem. Sci.* **1**, 675–680 (2010).
9. R. L. Hartman, J. P. McMullen, K. F. Jensen, *Angew. Chem. Int. Ed.* **50**, 7502–7519 (2011).
10. V. Hessel, *Chem. Eng. Technol.* **32**, 1655–1681 (2009).
11. R. J. Ingham *et al*., *Angew. Chem. Int. Ed.* **54**, 144–148 (2015).
12. B. Gutmann, D. Cantillo, C. O. Kappe, *Angew. Chem. Int. Ed.* **54**, 6688–6728 (2015).
13. M. Baumann, I. R. Baxendale, *Beilstein J. Org. Chem.* **11**, 1194–1219 (2015).
14. F. Lévesque, P. H. Seeberger, *Angew. Chem. Int. Ed.* **51**, 1706–1709 (2012).
15. M. D. Hopkin, I. R. Baxendale, S. V. Ley, *Org. Biomol. Chem.* **11**, 1822–1839 (2013).
16. C. A. Correia, K. Gilmore, D. T. McQuade, P. H. Seeberger, *Angew. Chem. Int. Ed.* **54**, 4945–4948 (2015).
17. M. Viviano, T. N. Glasnov, B. Reichart, G. Tekautz, C. O. Kappe, *Org. Process Res. Dev.* **15**, 858–870 (2011).
18. P. Zhang, M. G. Russell, T. F. Jamison, *Org. Process Res. Dev.* **18**, 1567–1570 (2014).
19. D. Ghislieri, K. Gilmore, P. H. Seeberger, *Angew. Chem. Int. Ed.* **54**, 678–682 (2015).
20. P. R. D. Murray *et al*., *Org. Process Res. Dev.* **17**, 1192–1208 (2013).
21. P. L. Heider *et al*., *Org. Process Res. Dev.* **18**, 402–409 (2014).
22. Materials and methods are available as supplementary materials on *Science* Online.
23. D. J. am Ende, in *Chemical Engineering in the Pharmaceutical Industry*, D. J. am Ende, Ed. (Wiley, NJ, 2011), chap. 1.
24. A. Adamo, P. L. Heider, N. Weeranoppanant, K. F. Jensen, *Ind. Eng. Chem. Res.* **52**, 10802–10808 (2013).
25. C. F. Carter *et al*., *Org. Process Res. Dev.* **14**, 393–404 (2010).
26. G. Rieveschl, Dialkylaminoalkyl benzhydryl ethers and salts thereof, U.S. Patent 2,421,714A, 3 June 1947.

27. S. Y. Wong, J. Chen, L. E. Forte, A. S. Myerson, *Org. Process Res. Dev.* **17**, 684–692 (2013).
28. USP (U.S. Pharmacopeia), *Monograph* **34**, 2597 (2014).
29. T. J. Reilly, *J. Chem. Educ.* **76**, 1557 (1999).
30. N. M. Loefgren, B. J. Lundqvist, Alkyl glycinanilides, U.S. Patent 2,441,498, 11 May 1948.
31. USP (U.S. Pharmacopeia), *Monograph* **37**, 3552–3553 (2014).
32. T. Sugasawa, M. Adachi, T. Toyoda, K. Sasakura, *J. Heterocycl. Chem.* **16**, 445–448 (1979).
33. USP (U.S. Pharmacopeia), *Monograph* **37**, 2580–2581 (2014).
34. B. Ahmed-Omer, A. J. Sanderson, *Org. Biomol. Chem.* **9**, 3854–3862 (2011).
35. R. L. Hartman, J. R. Naber, N. Zaborenko, S. L. Buchwald, K. F. Jensen, *Org. Process Res. Dev.* **14**, 1347–1357 (2010).
36. USP (U.S. Pharmacopeia), *Monograph* **37**, 3035–3036 (2014).
37. Food and Drug Administration, *FDA Perspective on Continuous Manufacturing*, (February 2013; www.fda.gov/downloads/AboutFDA/CentersOffices/OfficeofMedicalProductsandTobacco/CDER/UCM341197.pdf).
38. S. L. Lee *et al.*, *J. Pharm. Innov.* **10**, 191–199 (2015).
39. S. D. Schaber *et al.*, *Ind. Eng. Chem. Res.* **50**, 10083–10092 (2011).

ACKNOWLEDGMENTS

Authors are listed in alphabetical order. We thank A. Clayton for elements of the system design, S. H. Harrison for the LabVIEW programming downstream, and A. T. Carlson for assistance with the design of the downstream units. We also thank L. M. Heckman and J. M. Noss for assistance with development of chemistry. This work was supported by the Defense Advanced Research Project Agency (DARPA) and Space and Naval Warfare Systems Center Pacific (SSC Pacific) under Contract no. N66001-I I-C-4147. We thank E. Choi, D. T. McQuade, J. Lewin, and G. Ling for their advice and support. The data reported in this paper are available in the article or in the supplementary materials. A.A. is founder of Zaiput Flow Technologies. T.F.J. is a cofounder of Snapdragon Chemistry, Inc., and a scientific adviser for Zaiput Flow Technologies, Continuus Pharmaceuticals, Paraza Pharmaceuticals, and Asymchem. K.F.J. is a scientific adviser for Snapdragon Chemistry, Inc. A.S.M. is a scientific adviser to GenSyn Technologies, Blues Spark Technologies, Continuus Pharmaceuticals, and Goddard Laboratories. MIT has filed a patent on behalf of A.A., M.B., T.F.J., K.F.J., J.C., A.S.M., J.-C.M.M., E.M.R., D.R.S., T.S., N.W., S.Y.W., and P.Z.

SUPPLEMENTARY MATERIALS

www.sciencemag.org/content/352/6281/61/suppl/DC1
Materials and Methods
Figs. S1 to S25
Tables S1 to S3
References (*40*–*43*)

21 December 2015; accepted 22 February 2016
10.1126/science.aaf1337

REPORTS

STELLAR EVOLUTION

A white dwarf with an oxygen atmosphere

S. O. Kepler,[1]* Detlev Koester,[2] Gustavo Ourique[1]

Stars born with masses below around 10 solar masses end their lives as white dwarf stars. Their atmospheres are dominated by the lightest elements because gravitational diffusion brings the lightest element to the surface. We report the discovery of a white dwarf with an atmosphere completely dominated by oxygen, SDSS J124043.01+671034.68. After oxygen, the next most abundant elements in its atmosphere are neon and magnesium, but these are lower by a factor of ≥25 by number. The fact that no hydrogen or helium are observed is surprising. Oxygen, neon, and magnesium are the products of carbon burning, which occurs in stars at the high-mass end of pre–white dwarf formation. This star, a possible oxygen-neon white dwarf, will provide a rare observational test of the evolutionary paths toward white dwarfs.

White dwarf stars are the end product of stellar evolution for all stars born with masses below 8 to 11 solar masses ($M_\odot$). The limit depends on the initial composition on the main sequence, in particular the abundances of the heavy elements (the metallicity), but also on uncertainties of the models and input physics. Among these are the nuclear reaction rates of C+He and C+C and the treatment of convection in the asymptotic giant branch (*1*, *2*). About 80% of white dwarfs have atmospheres dominated by H, and the remainder by He. All other elements are only small traces, much less abundant than in the Sun. The reason for this unusual pattern is separation in the strong gravitational field (*3*). The lightest elements present very rapidly float to the surface once the white dwarf cools below about 100,000 K effective temperature ($T_{\rm eff}$). Except for the basic division of the two groups, which suggests different evolutionary channels, the atmosphere of the white dwarfs in their later cooling evolution has thus lost all memory of the previous evolutionary phases. There are only a few, very rare, exceptions to this rule. At very high effective temperature, $T_{\rm eff}$ > 200,000 K, two stars (H1504+65 and RX J0439.8-6809) (*4*) show no visible He or H but a C/O mixture. The limits on the He abundance are rather high, and it is quite possible that these stars will develop H or He atmospheres as they cool to lower effective temperatures, when gravitational separation becomes efficient.

Between 22,000 K ≥ $T_{\rm eff}$ ≥ 18,000 K, there is a small group of stars, called Hot DQ white dwarfs (*5*, *6*), which have C-dominated atmospheres. Their origin is not yet clear, but a likely scenario is that the carbon is dredged up from below the atmosphere once the convection zone reaches deep enough (*7*). If this scenario is correct, the DQ stars demonstrate that underneath the He layer there is a C layer resulting from the previous He-burning stage on the asymptotic giant branch. Another scenario is their formation by a merger of two white dwarf stars (*8*). At lower effective temperature, around 12,000 K, there is another small group of stars with strong O lines in their spectra; they have He-dominated atmospheres, but the next most abundant element is O, followed by C (*9*–*11*). It is plausible that their composition is related to the pre–white dwarf evolution, specifically C burning, but the reason that they appear at this temperature and this O/C ratio is not understood. To aid in our understanding of the late phases of low and intermediate mass star evolution, we searched for new white dwarf stars through the 4.5 million spectra in Data Release (DR) 12 (*12*) of the Sloan Digital Sky Survey (SDSS) (*13*).

One of the results of our search was SDSS J124043.01+671034.68 (spectrum with Plate-Modified Julian Date-Fiber 7120-56720-0894), which covers 3600 to 10,400 Å with resolving power $R = \lambda/\delta\lambda \sim 2000$. The spectrum (Fig. 1) exhibits many O I spectral lines, appearing similar to the group of cool stars with strong oxygen lines in their spectra (*10*, *11*). The absence of any He lines could be understood if the stellar effective temperature were near 11,000 K. However, closer inspection shows several lines of ionized Mg II and even O II, which require $T_{\rm eff}$ > 20,000 K. Temperatures ~20,000 K are also obtained from the SDSS photometry and the ultraviolet Galaxy Evolution Explorer (GALEX) measurements (*14*). At this temperature, the H and He lines, if these elements were present in the atmosphere, should be very strong. The absence of any He and H lines is only possible if O is the most abundant element. A detailed analysis (see the supplementary materials) confirmed this, with $T_{\rm eff}$ = 21,600 K and surface gravity $\log g$ = 7.93 ± 0.17, where $g = GM/R^2$ is the surface gravity in centimeter-gram-second units, with G the gravitational constant, M the stellar mass, and R the radius. Table 1 shows the atmospheric composition ratios determined from our modeling (see the supplementary materials).

The surface gravity is typical for white dwarfs (*13*) and corresponds to a mass of 0.56 ± 0.09 $M_\odot$, using the white dwarf mass-radius relation for stars without outer H layer (*15*), but it is theoretically not expected for a star with an oxygen atmosphere. From the estimated $\log g$ solution and the SDSS photometry in the *ugriz* filters,

[1]Instituto de Física, Universidade Federal do Rio Grande do Sul, 91501-900 Porto Alegre, RS, Brazil. [2]Institut für Theoretische Physik und Astrophysik, Universität Kiel, 24098 Kiel, Germany.
*Corresponding author. E-mail: kepler@if.ufrgs.br

Downloaded from on March 31, 2016

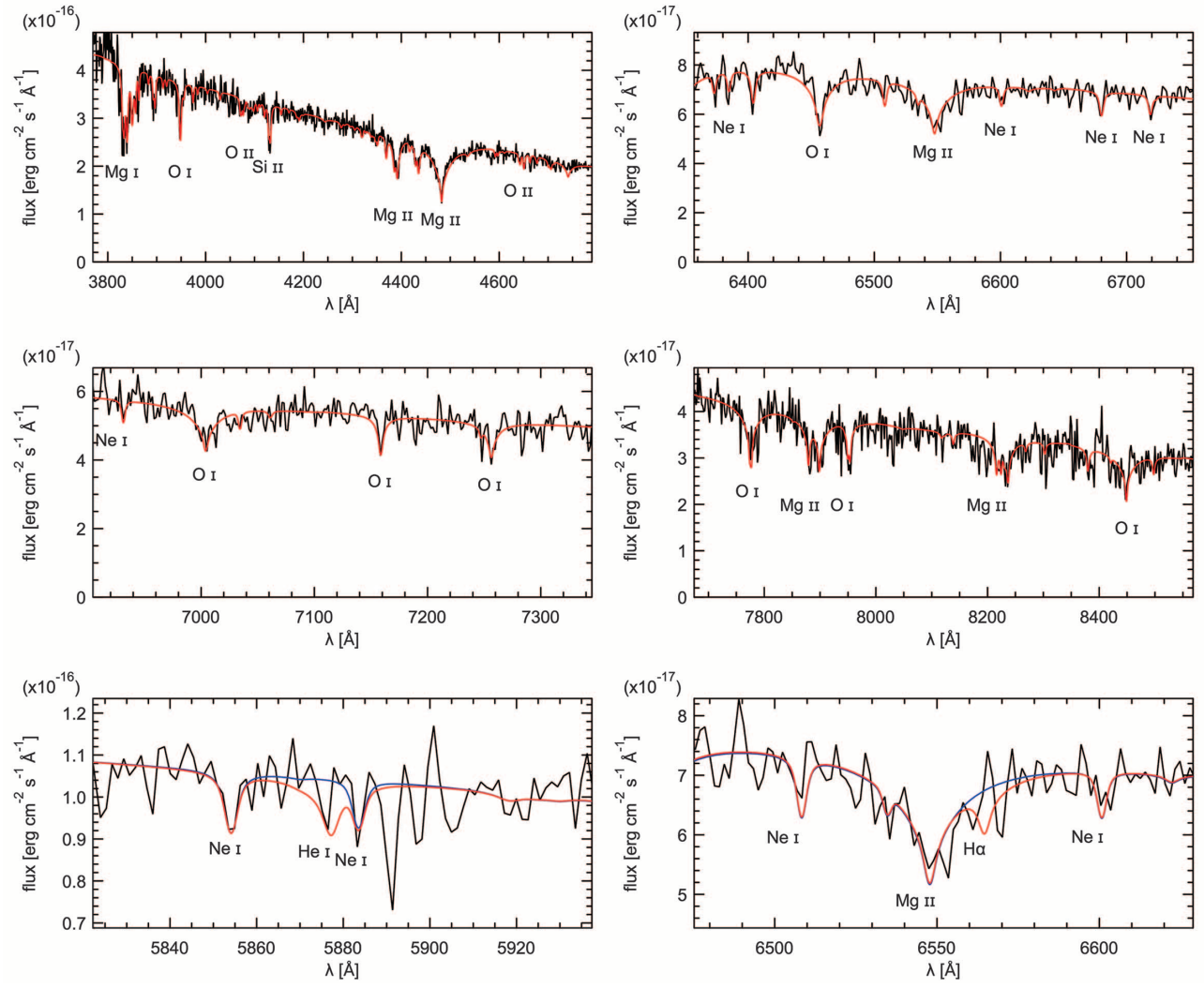


Fig. 1. Spectrum of SDSS J124043.01+671034.68. The four upper panels show important regions for O, Mg, Si, and Ne. The two lower panels show the regions of the strongest He line (5877 Å) and Hα with abundances at the upper limit (red) and without these elements (blue).

Table 1. Elemental abundance ratios by number. Abundance ratios were determined from the atmospheric modeling (see the supplementary text). Uncertainties are 69% for O/Ne, 28% for O/Mg, and 46% for O/Si; for the other elements, we only estimated upper limits.

Elements	Abundance ratio
O/Ne	25
O/Mg	55
O/Si	3200
O/H	>1000
O/He	>30
O/C	>200
O/Ca	>316,000
O/Fe	>794

we estimated the distance of the star as 360 ± 50 pc (see the supplementary materials). This is close enough that a more accurate distance, and therefore mass, should be determined once the Global Astrometric Interferometer for Astrophysics (GAIA) parallaxes become available in the next few years.

Carbon burning occurs at a temperature around T = (8 to 12) × 10^8 K, corresponding to center-of-mass energies from 1 to 3 MeV (*16*). Classical single-star evolution theory predicts that an O/Ne/Mg core composition is only produced in massive stars originally between 6 and 10.6 $M_\odot$, which reach sufficiently high core temperatures to proceed to C burning (*17*–*23*). Such high-mass main-sequence stars would result in massive (M > 1 $M_\odot$) white dwarf stars (*24*).

Single-star simulations (*25*) show that there is another possible evolutionary path. If there is a particularly violent very late thermal pulse during the post-asymptotic-giant-branch phase, it can destroy the remaining stellar envelope containing He and H. Recent simulations show that the lowest mass for C ignition occurs for a hybrid model, a C/O core surrounded by an O/Ne/Mg layer, in turn surrounded by a C/O/He/H envelope (*22*, *23*). In their model of an initial 5.5 $M_\odot$, the off-center C ignition does not reach the center, because convective boundary mixing (overshooting) causes the stalling of the C flame. In that model, the C burning ignited near the 0.3 $M_\odot$ mass coordinate and propagated upward until the first convective burning was initiated. If the

upper layers are lost, the star would be left with an O/Ne/Mg envelope (an oxygen-neon white dwarf), as we observe. For the complete removal of the H/He/C envelope, a late C-shell flash, strong mass loss, and/or close binary evolution, including mergers of white dwarfs, are possible scenarios. That several different scenarios for the late evolution might be needed is also suggested by the discussion of progenitor types and evolutionary paths observed in type Ia supernovae (*26*–*29*).

Distinct from hot pre–white dwarfs with oxygen lines (*4*) and cool oxygen line spectra white dwarfs (*10*, *11*), which have C and He rich atmospheres, we have found a star with oxygen 25 times more abundant than any other element, by number, the only one known among the roughly 32,000 SDSS white dwarf stars (*13*). Time-series spectroscopy of the object will be required to search for a close binary companion, which could point toward the evolutionary path of such a rare object.

REFERENCES AND NOTES

1. X. Meng, X. Chen, Z. Han, *Astron. Astrophys.* **487**, 625–635 (2008).
2. A. D. Romero, F. Campos, S. O. Kepler, *Mon. Not. R. Astron. Soc.* **450**, 3708–3723 (2015).
3. E. Schatzman, *Nature* **161**, 61–62 (1948).
4. K. Werner, T. Rauch, *Astron. Astrophys.* **584**, A19 (2015).
5. P. Dufour, G. Fontaine, J. Liebert, G. D. Schmidt, N. Behara, *Astrophys. J.* **683**, 978–989 (2008).
6. P. Dufour, in *White Dwarf Atmospheres and Circumstellar Environments*, D. W. Hoard, Ed. (Wiley-VCH, 2011), pp. 53–88.
7. D. Koester, J. Provencal, B. T. Gänsicke, *Astron. Astrophys.* **568**, A118 (2014).
8. B. Dunlap, J. C. Clemens, in *19th European Workshop on White Dwarfs*, P. Dufour, P. Bergeron, G. Fontaine, Eds., Astronomical Society of the Pacific Conference Series, **493**, 547 (2015).
9. J. Liebert *et al.*, *Astron. J.* **126**, 2521–2528 (2003).
10. B. T. Gänsicke, D. Koester, J. Girven, T. R. Marsh, D. Steeghs, *Science* **327**, 188–190 (2010).
11. S. O. Kepler *et al.*, *Mon. Not. R. Astron. Soc.* **446**, 4078–4087 (2015).
12. S. Alam *et al.*, *Astrophys. J. Suppl. Ser.* **219**, 12 (2015).
13. S. O. Kepler *et al.*, *Mon. Not. R. Astron. Soc.* **455**, 3413–3423 (2016).
14. L. Bianchi, A. Conti, B. Shiao, *Adv. Space Res.* **53**, 900–912 (2014).
15. L. G. Althaus *et al.*, *Astrophys. J.* **704**, 1605–1615 (2009).
16. L. Barrón-Palos *et al.*, *Nucl. Phys. A.* **779**, 318–332 (2006).
17. E. Garcia-Berro, I. Iben, *Astrophys. J.* **434**, 306 (1994).
18. K. Nomoto, C. Kobayashi, N. Tominaga, *Annu. Rev. Astron. Astrophys.* **51**, 457–509 (2013).
19. K. Nomoto, in *Supernova Environmental Impacts*, A. Ray, R. A. McCray, Eds., vol. 296 of *Proceedings of the International Astronomical Union* (2014), pp. 27–36.
20. C. L. Doherty *et al.*, *Mon. Not. R. Astron. Soc.* **441**, 582–598 (2014).
21. C. L. Doherty, P. Gil-Pons, H. H. B. Lau, J. C. Lattanzio, L. Siess, *Mon. Not. R. Astron. Soc.* **437**, 195–214 (2014).
22. P. A. Denissenkov *et al.*, *Mon. Not. R. Astron. Soc.* **447**, 2696–2705 (2015).
23. M. C. Chen, F. Herwig, P. A. Denissenkov, B. Paxton, *Mon. Not. R. Astron. Soc.* **440**, 1274–1280 (2014).
24. J. D. Cummings, J. S. Kalirai, P.-E. Tremblay, E. Ramirez-Ruiz, Two massive white dwarfs from NGC 2323 and the initial-final mass relation for progenitors of 4 to 6.5 $M_{\odot}$, http://arxiv.org/abs/1601.03053 (2016).
25. F. Herwig, T. Blöcker, N. Langer, T. Driebe, *Astron. Astrophys.* **349**, L5 (1999).
26. C. L. Fryer *et al.*, *Astrophys. J.* **725**, 296–308 (2010).
27. R. Pakmor *et al.*, *Nature* **463**, 61–64 (2010).
28. K. J. Shen, D. Kasen, N. N. Weinberg, L. Bildsten, E. Scannapieco, *Astrophys. J.* **715**, 767–774 (2010).
29. M. Dan, S. Rosswog, J. Guillochon, E. Ramirez-Ruiz, *Mon. Not. R. Astron. Soc.* **422**, 2417–2428 (2012).

ACKNOWLEDGMENTS

D.K. is supported by Science without Borders, Ministério de Ciência Tecnologia e Inovação/Ministério da Educação-Brazil. Funding for SDSS-III has been provided by the Alfred P. Sloan Foundation, the Participating Institutions, the National Science Foundation, and the U.S. Department of Energy Office of Science. The SDSS-III web site is www.sdss3.org. SDSS-III is managed by the Astrophysical Research Consortium for the Participating Institutions of the SDSS-III Collaboration, including the University of Arizona, the Brazilian Participation Group, Brookhaven National Laboratory, Carnegie Mellon University, University of Florida, the French Participation Group, the German Participation Group, Harvard University, the Instituto de Astrofísica de Canarias, the Michigan State/Notre Dame/Joint Institute for Nuclear Astrophysics Participation Group, Johns Hopkins University, Lawrence Berkeley National Laboratory, Max Planck Institute for Astrophysics, Max Planck Institute for Extraterrestrial Physics, New Mexico State University, New York University, Ohio State University, Pennsylvania State University, University of Portsmouth, Princeton University, the Spanish Participation Group, University of Tokyo, University of Utah, Vanderbilt University, University of Virginia, University of Washington, and Yale University. The spectrum can be downloaded at http://dr12.sdss3.org/sas/dr12/sdss/spectro/redux/v5_7_0/spectra/7120/spec-7120-56720-0894.fits and the SDSS photometry from http://skyserver.sdss.org/dr7/en/tools/explore/obj.asp?ra=12%2040%2043.01&dec=+67%2010%2034.68.

SUPPLEMENTARY MATERIALS

www.sciencemag.org/content/352/6281/67/suppl/DC1
Supplementary Text
Tables S1 to S11
Model Spectrum
References (*30*–*45*)

18 October 2015; accepted 19 February 2016
10.1126/science.aad6705

COLLOIDAL ORDERING

Triclinic nematic colloidal crystals from competing elastic and electrostatic interactions

Haridas Mundoor,[1] Bohdan Senyuk,[1] Ivan I. Smalyukh[1,2,3]*

The self-assembly of nanoparticles can enable the generation of composites with predesigned properties, but reproducing the structural diversity of atomic and molecular crystals remains a challenge. We combined anisotropic elastic and weakly screened electrostatic interactions to guide both orientational and triclinic positional self-ordering of inorganic nanocrystals in a nematic fluid host. The lattice periodicity of these low-symmetry colloidal crystals is more than an order of magnitude larger than the nanoparticle size. The orientations of the nanocrystals, as well as the crystallographic axes of the ensuing triclinic colloidal crystals, are coupled to the uniform alignment direction of the nematic host, which can be readily controlled on large scales. We examine colloidal pair and many-body interactions and show how triclinic crystals with orientational ordering of the semiconductor nanorods emerge from competing long-range elastic and electrostatic forces.

Since Einstein's seminal work on Brownian motion and Perrin's subsequent experiments (*1*), which showed that particles in colloidal dispersions obey the same statistical thermodynamics as atoms, the colloid-atom analogy has provided insights into the physics of atomic systems through its application in studies exploring the dynamics of colloidal crystals and glasses (*2*). This analogy has inspired the development of forms of self-assembly that attempt to reproduce the diversity of atomic crystals (*3*), although experimental realization of colloidal architectures with low symmetry, such as triclinic systems, remains challenging. At the same time, the self-assembly of colloids can be designed and controlled by exploiting aspects of particle shape (*4*) and topology (*5*), the dispersing medium's anisotropy (*6*) and composition (*7*), DNA functionalization and origami-like designs (*8*), and the facile response of particles and media to external fields (*9*, *10*). Long-range interactions are of special interest, because they can lead to the sparse but ordered assembly of colloidal composites with unusual physical behavior (*9*). Long-range electrostatic repulsions in fluids with low ionic strength (*10*–*13*) have been used to obtain crystals and plastic crystals with high-symmetry colloidal lattices. These electrostatic interactions remain relatively isotropic at large separations, despite anisotropic particles shapes (*10*). In nematic liquid crystal (NLC) hosts, highly anisotropic long-range colloidal interactions arise from the minimization of free energy associated with particle-induced elastic distortions of the NLC molecular alignment, even when particles are spherical (*6*, *14*–*16*), although the ability to control the shape of particles provides a means of

[1]Department of Physics and Soft Materials Research Center, University of Colorado, Boulder, CO 80309, USA.
[2]Department of Electrical, Computer, and Energy Engineering, Materials Science and Engineering Program, University of Colorado, Boulder, CO 80309, USA.
[3]Renewable and Sustainable Energy Institute, National Renewable Energy Laboratory and University of Colorado, Boulder, CO 80309, USA.
***Corresponding author. E-mail: ivan.smalyukh@colorado.edu**

Downloaded from on March 31, 2016

guiding self-assembly (*17*). The diversity of elastic interactions, which commonly resembles that of electrostatic dipolar and quadrupolar charge distributions (*6*, *14*, *17*), has enabled colloidal self-assembly of lamellae and dipolar crystals (*18*, *19*), although the interparticle spacing in these lamellar and crystalline assemblies could be controlled only within a range comparable to the particle sizes.

We demonstrate that competition between long-range electrostatic and elastic interactions leads to a highly unusual self-organization of rod-like nanoparticles that exhibits both long-range orientational and triclinic positional ordering. The micrometer-range colloidal crystal lattice parameters of these assemblies, as revealed by three-dimensional (3D) optical imaging, are an order of magnitude larger than the size of the constituent colloidal semiconductor nanorods (30 × 150 nm; fig. S1). We characterized pair interactions between nanorods and the structure and dynamics of their dispersions at different surface charges and volume fractions. Although various dislocations, grain boundaries, vacancies, and other defects are observed in these "soft" crystals, the crystallographic axes of triclinic lattices and colloidal nanorods tend to follow the direction of the alignment of rod-like molecules of the NLC host fluid. This preferred orientation of rod-like molecules is dubbed the "director" **n**, which can be controlled on large scales by using approaches similar to those used to manufacture displays. The mechanical coupling between the orientations of the nanorods, the lattice, and the director is due to elastic free-energy minimization at well-defined nanorod and triclinic colloidal crystal orientations relative to a far-field director $\mathbf{n}_0$ and confining surfaces; it thus has the potential to enable device-scale self-assembly of tunable composites.

Semiconductor nanorods with the composition β-$NaY_{0.5}Gd_{0.3}Yb_{0.18}Er_{0.02}F_4$, engineered to have rod-like geometric shapes and polarized up-conversion–based luminescence properties (Fig. 1 and fig. S1), were synthesized using a hydrothermal method (*20*–*23*). The dispersion of nanorods in the NLC host (*9*, *21*) was facilitated by surface functionalization of as-synthesized particles (*20*–*23*). In a typical process, 6 mg of initially oleic acid–capped nanorods in 8 ml of cyclohexane were added to 4 ml of deionized water with a small amount of hydrochloric acid to yield a pH of ~4, then stirred for 2 hours. During this process, oleic acid ligands became protonated and mixed with cyclohexane, leaving bare uncapped nanorods with positive surface charges (*21*–*23*). The nanorods were then washed with acetone four to five times, redispersed in water, and subsequently coated with methoxy-poly(ethylene glycol)silane (Si-PEG) (*21*). Typically, 5 mg of Si-PEG dissolved in 1 ml of ethanol was mixed with 5 ml of nanorod dispersion in deionized water (pH ~4) and stirred for 2 hours. After the reaction, particles were precipitated by centrifugation, dispersed in ethanol, and then redispersed in a pentylcyanobiphenyl (5CB) NLC host via mixing and subsequent solvent evaporation at an elevated temperature of 70°C; the NLC composite was then quenched to room temperature while vigorously stirring (*9*, *21*). NLC dispersions of nanorods were infiltrated into glass cells by means of capillary action. For planar boundary conditions for **n**, inner surfaces of cell substrates were coated with aqueous polyvinyl alcohol (1 weight %) and rubbed unidirectionally. The cell gap thickness within 15 to 60 μm was set using Mylar films. The surface charging of particles was characterized by probing their electrophoretic mobility within the aligned NLC cell under an electric field that was applied to in-plane electrodes (fig. S2). We controlled the effective positive surface charge per nanorod within $Z^*e \approx +(60 \text{ to } 250)e$ (*22*), the Debye screening length ξ_D in the nonpolar 5CB within 0.1 to 1.2 μm, and the nanorods' surface

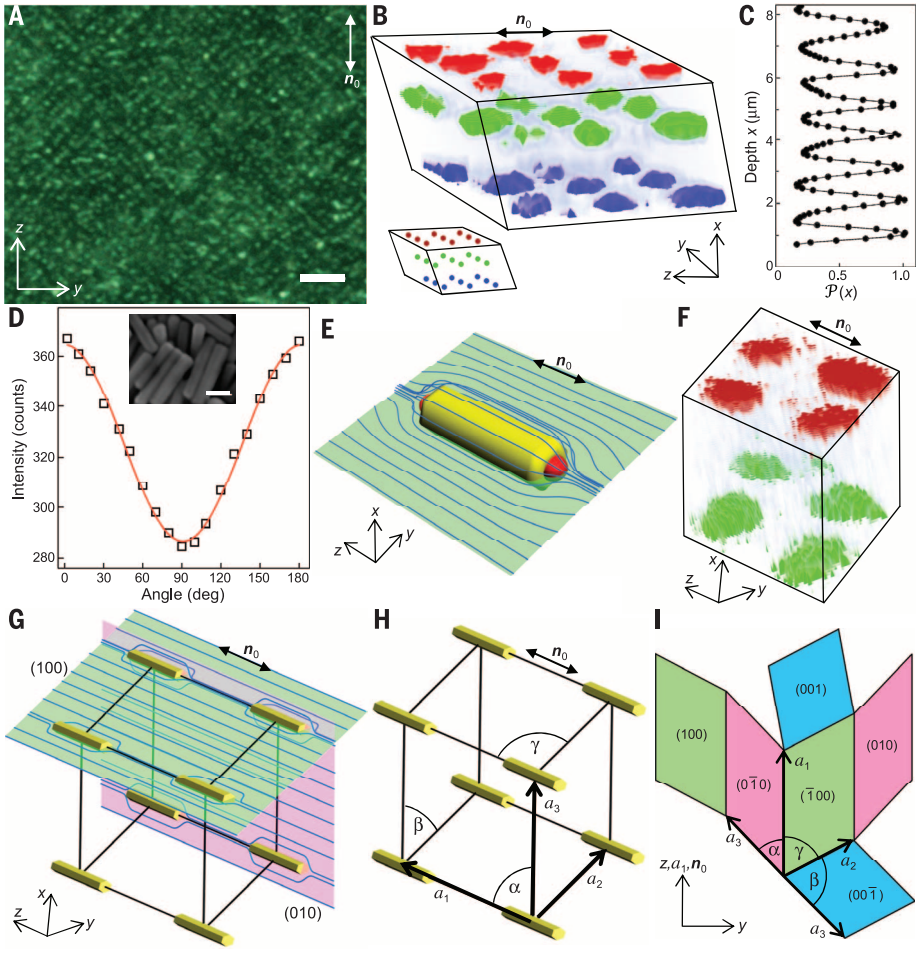


Fig. 1. Triclinic crystal self-assembly of nanorods in a NLC host. (**A**) Dark-field micrograph of a crystal assembly with lattice parameters a_1 = 1.30 ± 0.05 μm and a_2 = 1.01 ± 0.05 μm (scale bar, 5 μm). (**B**) 3D micrograph showing luminescence from a small part of a triclinic colloidal crystal, which was reconstructed from slow confocal microscopy scanning (obtained within ~3 min). It shows nanorod arrangements as they sense the potential energy landscape near their minimum-energy lattice sites. The luminescence signals from individual nanorods are shown in red, green, and blue to illustrate the locations of particles in three consecutive planes parallel to confining glass substrates. The bottom inset shows center-of-mass positions of building blocks in a triclinic crystal with the same lattice. The lattice parameters, based on averaging 18 independent local measurements, are as follows: a_1 = 1.49 ± 0.06 μm, a_2 = 0.95 ± 0.05 μm, a_3 = 1.20 ± 0.05 μm, α = 58° ± 2°, β = 69° ± 2°, and γ = 49° ± 2° [the angles α, β, and γ are defined in (H)]. (**C**) Probability ($\mathcal{P}$) distribution for finding nanorods at a depth x in the sample, relative to the center of the first colloidal layer parallel to the substrates (where x = 0). This distribution was calculated based on 3D luminescence imaging. (**D**) Luminescence intensity at 552 nm versus analyzer rotation between 0° and 180°. The inset shows a scanning electron microscopy image of the nanorods (scale bar, 50 nm). (**E**) Schematic illustration of director distortions (blue) around a single nanorod (yellow), with the red hemispheres at the poles depicting two particle-induced boojums. These quadrupolar elastic distortions are axially symmetric with respect to the nanorod axis (parallel to $\mathbf{n}_0$) and have mirror symmetry planes both parallel and orthogonal to $\mathbf{n}_0$. (**F**) 3D micrograph showing a primitive unit cell of a triclinic colloidal crystal, which was reconstructed from confocal scanning. Coloring is as in (B). (**G** to **I**) Schematics (not to scale) of a primitive cell of a triclinic colloidal crystal, (G) showing local director distortions (blue lines) induced by nanorods, (H) defining the parameters of a triclinic lattice, and (I) showing the lattice unfolded.

potential $\Phi_0 = Z^* e\xi_D/[\varepsilon_0\varepsilon(\Omega_{nr} + 4\pi l_{nr}\xi_D)]$ (*13*) within 28 to 129 mV; here, Z^* is an effective number of elementary charges $e = 1.6 \times 10^{-19}$ C, and Ω_{nr}, l_{nr}, ε, and ε_0 are the nanorod surface area, nanorod length, average dielectric constant of 5CB, and vacuum permittivity, respectively (*22*).

Dark-field and polarizing optical microscopies show the positional ordering of nanorods (Fig. 1A) and NLC alignment along $\mathbf{n}_0$ (fig. S3). The background-free 3D distribution of confocal luminescence from the nanorods, derived from an up-conversion process and collected while slowly scanning an infrared excitation laser beam (*22*), reveals colloidal crystals (Fig. 1, B, C, and F). During this 3D imaging, the nanorods sense the potential landscape and jiggle around their minimum-energy triclinic lattice sites (Fig. 1B). To investigate the orientations of nanorods within the lattice, we measured luminescence intensity while rotating the analyzer with respect to $\mathbf{n}_0$ (Fig. 1D). At all studied concentrations, the intensity of emission at 552 nm was greatest when the analyzer was parallel to $\mathbf{n}_0$, indicating that the nanorods align along $\mathbf{n}_0$ (fig. S1), as schematically depicted in Fig. 1E. This nanorod orientation is consistent with minimization of the total bulk elastic and surface anchoring free energy of NLCs around PEG-functionalized nanoparticles (*9*). Weak quadrupolar particle-induced elastic distortions are present in the NLC bulk, and the director orientation at the nanorod surfaces is compliant with tangential boundary conditions,

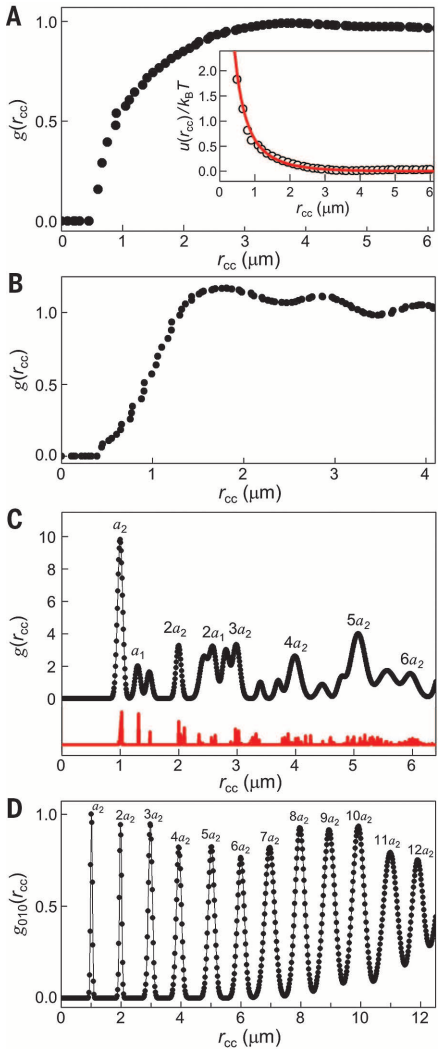


Fig. 2. Ordering of nanorods in 5CB. (**A**) Radial distribution function $g(r_{cc})$ for nanorod dispersion in the isotropic phase, consistent with the presence of long-range, repulsive, weakly screened electrostatic interactions. The inset shows pair potentials extracted from these data and fit by a screened Coulomb interactions potential (k_B, the Boltzmann constant; T, an absolute temperature) (*22*). (**B** and **C**) $g(r_{cc})$ for nanorod dispersion in the nematic phase at (B) a low ρ_N of ~0.35 μm^{-3} and (C) a high ρ_N of ~4.5 μm^{-3}, with emergent triclinic crystal ordering in the latter case. The normalized $g(r_{cc})$ (red) in (C) was calculated for the (100) plane of an ideal triclinic lattice with average dimensions determined from experiments; it serves as a visual guide for the corresponding experimental peaks. (**D**) Probability distribution $g_{010}(r_{cc})$, calculated for the experimental triclinic lattice along a_2 by averaging data for the [010] and [0$\bar{1}$0] directions. Numbers above the peaks indicate distances corresponding to integer numbers of lattice parameters a_1 and a_2.

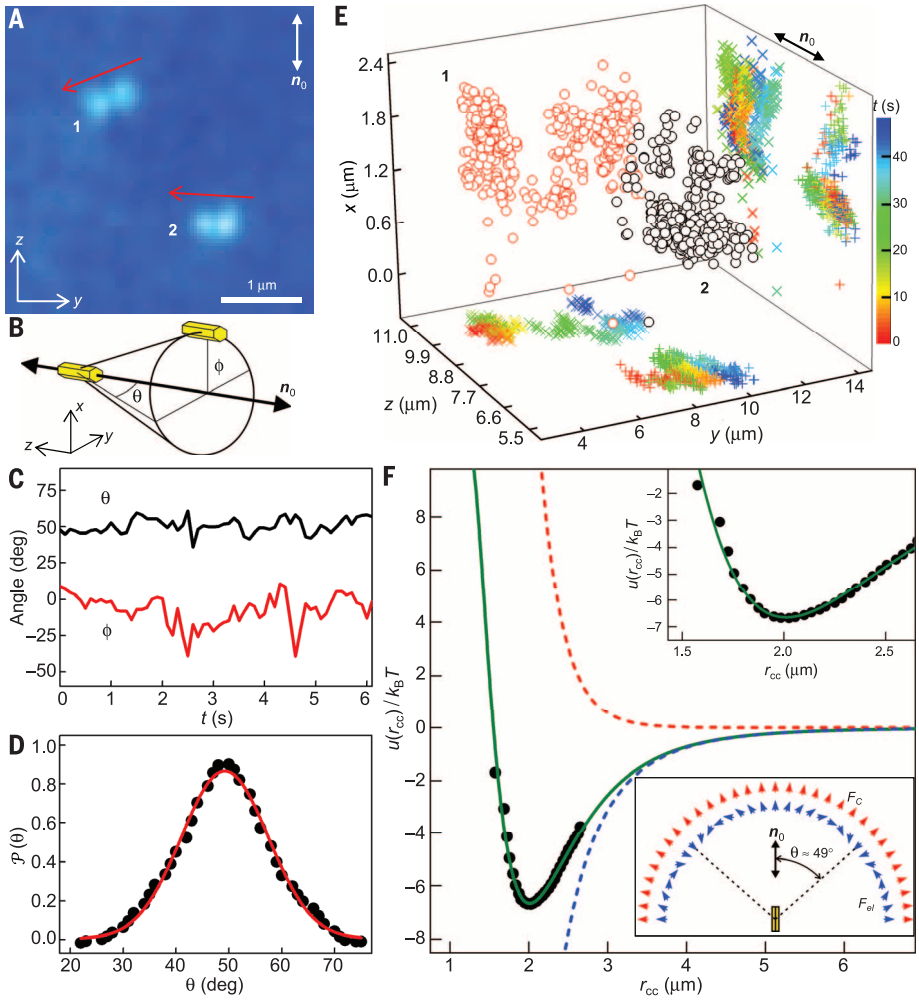


Fig. 3. Pair interactions between nanorods. (**A**) A representative DHPSF micrograph showing nanorods in 5CB at different depths of the cell, corresponding to different orientations of bright-lobe pairs 1 and 2 (marked by red arrows) (*25*). (**B**) Schematic of two nanorods with $\mathbf{r}_{cc}$ tilted with respect to $\mathbf{n}_0$ and the substrates, as characterized by angles θ and ϕ. (**C**) Typical changes in θ and ϕ over time t. (**D**) Probability distribution for measured θ; the red line is a Gaussian fit. (**E**) 3D positions of two nanorods over time, characterized with ≤10-nm precision and depicted by red (nanorod 1) and black (nanorod 2) open circles. The positions are shown projected onto the zx and zy planes, in which corresponding symbols × (nanorod 1) and + (nanorod 2) are colored according to the elapsed time. (**F**) Pair interaction potentials extracted from experimental data and fit with the sum of screened electrostatic and elastic potentials (green line). Dashed lines represent the electrostatic repulsive (red) and elastic attractive (blue) potentials. The top inset shows a close-up view near the potential well minimum. The bottom inset shows how the directions of the elastic force F_{el} (blue arrows) and screened Coulomb electrostatic repulsion force F_C (red arrows) depend on the angle between $\mathbf{r}_{cc}$ and $\mathbf{n}_0$.

except for the small surface point defect regions of discontinuity in the director field at the particle's poles, dubbed "boojums." By combining the nanorod orientation and position data, we experimentally identified a primitive lattice cell, based on confocal luminescence distributions from eight representative nanorods (Fig. 1F), and then reconstructed a triclinic pinacoidal lattice (Fig. 1, G to I), which allows for only the center inversion symmetry operation (*24*).

By examining nanorod displacements over time with video microscopy in dark-field and upconversion luminescence modes, we obtained the viscous drag coefficients (fig. S4) and the radial distribution function $g(r_{cc})$ (where r_{cc} is a center-to-center separation between nanorods) in both nematic and elevated-temperature isotropic phases (Fig. 2). Purely repulsive, direction-independent interactions are evident in the isotropic phase of the nematic host at 40°C (Fig. 2A). Once the host is cooled to the nematic phase at 28°C, $g(r_{cc})$ reveals attractive forces in both dilute and concentrated dispersions (Fig. 2, B and C). To explore the pair interactions between nanorods, we studied the trajectories of two particles that were brought close to each other with optical tweezers and then released (*22*). We used double-helix point spread function (DHPSF) microscopy (Fig. 3) (*22*, *25*) to find the 3D positions of nanorods within the cell over time with 7- to 10-nm precision (*25*), as well as to characterize the corresponding orientations of their center-to-center separation vector $\mathbf{r}_{cc}$ relative to $\mathbf{n}_0$. The nanorods equilibrate at micrometer-scale pair separations and with $\mathbf{r}_{cc}$ tilting away from the sample plane while circumscribing a cone of $\theta \approx 49° \pm 4°$ around $\mathbf{n}_0$; this would be impossible to quantify in 3D without DHPSF (Fig. 3, A to E). The pair interaction forces are highly anisotropic and long-ranged, and the angular distribution of $\mathbf{r}_{cc}$ orientations is consistent with the cone of maximum-attraction angles expected for colloidal elastic quadrupoles (Fig. 3) (*14*–*16*). Particle tracking gives the anisotropic distribution of nanorod displacements within equal intervals of elapsed time and gives the pair-interaction potential with a well-pronounced energetic minimum (Fig. 3F). Because the attractive van der Waals forces between nanorods are negligible at the relevant $\mathbf{r}_{cc}$ (*2*, *22*, *26*)—which is consistent with the fact that only repulsions persist when the host is heated to the isotropic phase (Fig. 2A)—we attribute this minimum in pair-interaction energy to the competition of elastic and electrostatic interactions. Considering the classical use of multipolar expansions in both nematic elasticity and electrostatics (*1*, *2*, *14*), we used their leading terms (i.e., a monopole for electrostatics, because of the surface charging of nanorods, and a quadrupole for nematic elasticity, because of the director distortions shown in Fig. 1E) to model these interactions. The total potential can be approximately described as a superposition $u \approx u_C + u_{el}$ of the quadrupolar elastic (u_{el}) and the electrostatic screened Coulomb (u_C) interaction potentials (*2*, *22*, *27*). This yields $u(r_{cc}) = (A_1/r_{cc})\exp(-r_{cc}/\xi_D) + A_2(9 - 90\cos^2\theta + 105\cos^4\theta)r_{cc}^{-5}$, where A_1 and A_2 are fitting parameters that are dependent on the size and charging of nanorods and on alignment, elastic, and dielectric properties (*22*). This expression fits well the distance dependence of the experimental potential (Fig. 3F) and explains the equilibrium orientation of $\mathbf{r}_{cc}$ at $\theta \approx 49° \pm 4°$ to $\mathbf{n}_0$. The Debye screening length $\xi_D = 0.34$ μm, derived from A_1 in $u(r_{cc})$ (*22*), matches the ξ_D that was independently obtained from fitting the repulsive electrostatic potential in the isotropic phase of 5CB, in which elastic forces vanish (inset of Fig. 2A). The strength of the elastic quadrupole moment derived from A_2 and the corresponding material parameters, such as elastic constants and anchoring coefficients, are consistent with theories of quadrupolar elastic interactions and independent experimental measurements (*14*–*16*, *22*).

As the concentration of nanorods increases, they exhibit gas-, liquid- and glass-like structural organizations, and crystalline order (Fig. 1 and figs. S5 to S7) emerges at concentrations that are roughly consistent with the average equilibrium separations in colloidal pairs and lattices (Figs. 1 to 3). Within the (100) crystallographic planes (Figs. 1 and 4A and table S1), $\mathbf{r}_{cc}$ tends to align at angles of ~49° to $\mathbf{n}_0$, similar to the orientation of the center-to-center separation vector of pairs of nanorods. By analyzing particle displacement distributions associated with different lattice sites in the triclinic colloidal crystal (Fig. 4B), we gained insight into the corresponding energy landscape (Fig. 4C) and obtained the average spring constant of the crystal, $k \approx 0.63$ pN μm^{-1}. Translational order in our triclinic lattices (Fig. 1A) is quantified by $g(r_{cc})$ (Fig. 2C) and the one-dimensional probability distribution function $g_{010}(r_{cc})$ (Fig. 2D), which is calculated along the direction of crystallographic axis a_2 (Fig. 1, H and I). We characterized the two-dimensional mean square displacement (MSD, $\langle\Delta r^2\rangle$) of the nanorods as a function of time t (Fig. 4D, inset). We then used it to estimate the so-called Lindemann parameter $\delta L = [3\langle\Delta r^2(t \to \infty)\rangle/4r_{nn}^2]^{1/2}$, where r_{nn} is the crystal nearest-neighbor equilibrium distance and $\langle\Delta r^2(t \to \infty)\rangle$ is the asymptotic value of the time-dependent MSD $\langle\Delta r^2(t)\rangle$ used for the estimate. This parameter is commonly used to characterize crystallization and melting transitions in terms of the MSD of particles around their ideal lattice positions, as compared with their nearest-neighbor distance. Plotting the Lindemann parameter against the nanorod number density ρ_N (Fig. 4D) shows

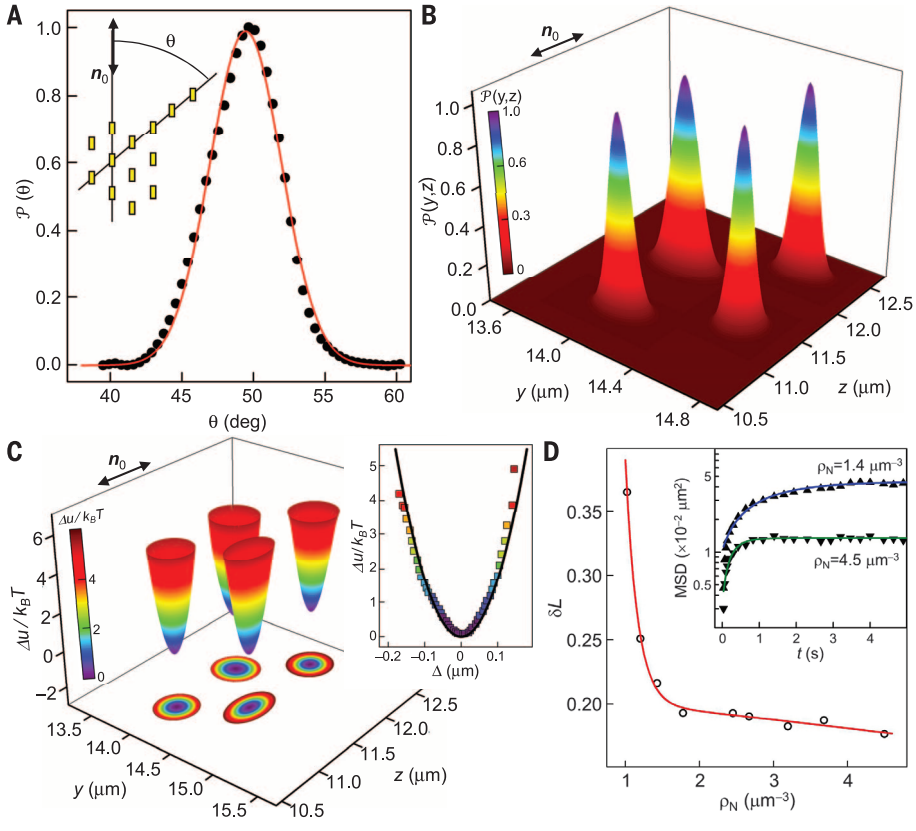


Fig. 4. Characterization of triclinic colloidal crystals. (**A**) Probability distribution of an angle θ (inset; yellow rectangles represent nanorods) measured in the (100) plane of a colloidal crystal. Its Gaussian fit is shown in red. (**B**) Probability distributions of positions within four lattice sites in the (100) plane of a triclinic crystal and (**C**) the corresponding potential landscape. The inset in (C) shows a dependence of the relative potential energy experienced by nanorods on local distance Δ. (**D**) Lindemann parameter δL versus nanorod number density ρ_N. The inset shows MSDs of nanorods over time t at $\rho_N = 1.4$ μm^{-3} (upright triangles) and 4.5 μm^{-3} (inverted triangles).

that its concentration-dependent behavior and values correspond to a crystallization transition that is consistent with that found in other condensed matter systems (*28*). A thermal expansion of ~0.01°C^{-1} of the lattice (fig. S8) stems from the decrease of an average NLC elastic constant K and quadrupolar elastic forces as temperature increases (K decreases by a factor of ~3 when the composite is heated from room temperature to ~34°C) (*22*).

Nanorods can be electrically concentrated and ordered starting from dilute initial dispersions (fig. S9), similar to the crystallization of hard sphere–like colloids when subjected to electrophoretic or dielectrophoretic forces (*29*). The triclinic crystal order is facilitated by applying 300 to 900 mV to transparent electrodes on inner substrates of the cell, which is lower than the threshold voltage needed for NLC switching. In response to these dc fields, the positively charged nanorods slowly move toward a negative electrode as a result of electrophoresis and eventually form a crystal as their concentration uniformly increases (fig. S9). These low voltages also facilitate uniform alignment of crystalline nuclei and healing of defects; in addition, they induce a giant electrostriction of the triclinic lattice, with ~25% strain at fields of 0.03 V μm^{-1} (fig. S8B). Because NLC is switched at ~1 V (*9*, *21*), colloidal crystal lattice orientations can be reconfigured while following the rotation of the director, although these processes are slow and complex. Electric fields, confinement in thin cells (thicknesses ≤15 μm) that are incompatible with an integer number of primitive cells in the colloidal crystal, variations in nanorod concentrations that exceed the range accommodated by an equilibrium triclinic lattice, and temperature changes control the primitive cell parameters (table S1) and prompt the formation of defects ranging from edge dislocations (fig. S11) to vacancies and grain boundaries (*2*, *22*, *30*).

We have introduced a highly tunable and reconfigurable colloidal system with competing long-range elastic and electrostatic interactions that lead to triclinic pinacoidal lattices of orientationally ordered nanorods. This unexpected triclinic crystallization of semiconductor particles at packing factors <<1% shows potential for the self-assembly of a wide variety of mesostructured composites on device-relevant scales, which can be tuned by weak external stimuli such as low-voltage fields and very small temperature changes. The control of particle charging allowed for tuning of the triclinic lattice periodicity between 0.5 and 1.6 μm, a range which can be extended by tuning the strength of electrostatic interactions through doping or deionizing NLCs (*10*–*13*) or through using nematics with different properties. Considering that dipolar and other multipolar elastic colloidal interactions in NLCs can be introduced and guided by controlling the boundary conditions at particle surfaces, and given that the control of NLC elastic constants may alter the angular dependencies of these interactions (*22*), our study sets the stage for explorations of mesoscopic colloidal positional and orientational ordering that can enable the engineering of material properties through spontaneous ordering of nanoparticles.

REFERENCES AND NOTES

1. H. N. W. Lekkerkerker, R. Tuinier, *Colloids and the Depletion Interaction* (Springer Netherlands, 2011).
2. P. M. Chaikin, T. C. Lubensky, *Principles of Condensed Matter Physics* (Cambridge Univ. Press, 1995).
3. V. N. Manoharan, *Science* **349**, 1253751 (2015).
4. P. F. Damasceno, M. Engel, S. C. Glotzer, *Science* **337**, 453–457 (2012).
5. B. Senyuk *et al.*, *Nature* **493**, 200–205 (2013).
6. P. Poulin, H. Stark, T. C. Lubensky, D. A. Weitz, *Science* **275**, 1770–1773 (1997).
7. S. Sacanna, W. T. M. Irvine, P. M. Chaikin, D. J. Pine, *Nature* **464**, 575–578 (2010).
8. M. R. Jones *et al.*, *Nat. Mater.* **9**, 913–917 (2010).
9. Q. Liu, Y. Yuan, I. I. Smalyukh, *Nano Lett.* **14**, 4071–4077 (2014).
10. B. Liu *et al.*, *Nat. Commun.* **5**, 3092 (2014).
11. S. K. Sainis, J. W. Merrill, E. R. Dufresne, *Langmuir* **24**, 13334–13337 (2008).
12. A. Yethiraj, A. van Blaaderen, *Nature* **421**, 513–517 (2003).
13. M. F. Hsu, E. R. Dufresne, D. A. Weitz, *Langmuir* **21**, 4881–4887 (2005).
14. T. C. Lubensky, D. Pettey, N. Currier, H. Stark, *Phys. Rev. E* **57**, 610–625 (1998).
15. R. W. Ruhwandl, E. M. Terentjev, *Phys. Rev. E* **55**, 2958–2961 (1997).
16. S. Ramaswamy, R. Nityananda, V. A. Raghunathan, J. Prost, *Mol. Cryst. Liq. Sci. Technol. A* **288**, 175–180 (1996).
17. C. P. Lapointe, T. G. Mason, I. I. Smalyukh, *Science* **326**, 1083–1086 (2009).
18. J. C. Loudet, P. Barois, P. Poulin, *Nature* **407**, 611–613 (2000).
19. A. Nych *et al.*, *Nat. Commun.* **4**, 1489 (2013).
20. F. Wang *et al.*, *Nature* **463**, 1061–1065 (2010).
21. H. Mundoor, I. I. Smalyukh, *Small* **11**, 5572–5580 (2015).
22. Materials and methods are available as supplementary materials on *Science* Online.
23. N. Bogdan, F. Vetrone, G. A. Ozin, J. A. Capobianco, *Nano Lett.* **11**, 835–840 (2011).
24. D. E. Sands, *Introduction to Crystallography* (Dover Publications, 2012).
25. D. B. Conkey, R. P. Trivedi, S. R. P. Pavani, I. I. Smalyukh, R. Piestun, *Opt. Express* **19**, 3835–3842 (2011).
26. C. A. S. Batista, R. G. Larson, N. A. Kotov, *Science* **350**, 1242477 (2015).
27. V. D. Nguyen, S. Faber, Z. Hu, G. H. Wegdam, P. Schall, *Nat. Commun.* **4**, 1584 (2013).
28. R. W. Cahn, *Nature* **413**, 582–583 (2001).
29. R. C. Hayward, D. A. Saville, I. A. Aksay, *Nature* **404**, 56–59 (2000).
30. I. I. Smalyukh, O. D. Lavrentovich, *Phys. Rev. Lett.* **90**, 085503 (2003).

ACKNOWLEDGMENTS

This research was supported by the U.S. Department of Energy, Office of Basic Energy Sciences, Division of Materials Sciences and Engineering, under award ER46921, contract DE-SC0010305 with the University of Colorado–Boulder. We acknowledge the use of electron microscopy facility at the National Institute of Standards and Technology, Boulder, and thank A. Sanders for the help with imaging. We thank P. Ackerman, Q. Liu, T. Lee, and T. Lubensky for discussions.

SUPPLEMENTARY MATERIALS

www.sciencemag.org/content/352/6281/69/suppl/DC1
Materials and Methods
Figs. S1 to S11
Table S1
Movie S1
References (*31*–*39*)

14 December 2015; accepted 26 February 2016
10.1126/science.aaf0801

ELECTROCATALYSIS

Tuning the activity of Pt alloy electrocatalysts by means of the lanthanide contraction

María Escudero-Escribano,[1,2]* Paolo Malacrida,[1] Martin H. Hansen,[3,4] Ulrik G. Vej-Hansen,[1,3] Amado Velázquez-Palenzuela,[1] Vladimir Tripkovic,[3,5] Jakob Schiøtz,[1,3] Jan Rossmeisl,[3,4] Ifan E. L. Stephens,[1,6]* Ib Chorkendorff[1]*

The high platinum loadings required to compensate for the slow kinetics of the oxygen reduction reaction (ORR) impede the widespread uptake of low-temperature fuel cells in automotive vehicles. We have studied the ORR on eight platinum (Pt)–lanthanide and Pt-alkaline earth electrodes, Pt_5M, where M is lanthanum, cerium, samarium, gadolinium, terbium, dysprosium, thulium, or calcium. The materials are among the most active polycrystalline Pt-based catalysts reported, presenting activity enhancement by a factor of 3 to 6 over Pt. The active phase consists of a Pt overlayer formed by acid leaching. The ORR activity versus the bulk lattice parameter follows a high peaked "volcano" relation. We demonstrate how the lanthanide contraction can be used to control strain effects and tune the activity, stability, and reactivity of these materials.

To reduce the Pt loading at the cathode of polymer electrolyte membrane fuel cells (PEMFCs), researchers have intensively studied alloys of Pt with late transition metals such as Ni or Co as oxygen reduction reaction (ORR) electrocatalysts (*1*–*6*). Catalysts exhibiting even greater activity and stability could be designed through the identification of the descriptors that control the performance (*7*–*10*). One single descriptor controls ORR activity, the ΔE_{OH} binding energy, by way of a Sabatier volcano: An ΔE_{OH} ~0.1 eV weaker than Pt(111) yields the optimum value (*11*). Other indirect descriptors related to ΔE_{OH} include the d-band center (*12*), the Pt-Pt

Downloaded from on March 31, 2016

interatomic distance (*4*) and the generalized coordination number (*8*). Stability is a multiparametric challenge, hence requiring several descriptors, such as the alloying energy E_a (*11*, *13*), and dissolution potential (*14*, *15*).

Our earlier studies identified alloys of Pt and rare earths, in particular Pt_xY and Pt_xGd, as active and stable catalysts for oxygen reduction, both in the bulk polycrystalline (*11*, *16*) and nanoparticle (NP) form (*17*, *18*). The exceptionally negative E_a of Pt–rare earth alloys should increase their resistance to degradation (*11*, *13*). In contrast, more commonly studied ORR alloys, such as Pt-Ni or Pt-Co, typically degrade in long-term tests via dealloying (*19*, *20*). Nevertheless, new forms of Pt-Ni–based catalysts achieve exceptional activity and stability during short-term accelerated degradation tests (*5*, *21*, *22*). Nonetheless, engendering long-term stability in fuel cells (*20*) may require materials that are inherently less prone to dealloying. Because the rare earth (e.g., Y or Gd) is unstable against dissolution, a Pt overlayer is formed on the surface, as shown on Fig. 1, A and B. We showed that on Pt_xGd and Pt_xY NPs, the bulk compressive strain correlated strongly with increased ORR activity; this result suggested that the bulk strain is imposed onto the Pt surface atoms, weakening ΔE_{OH} (*23*). These observations led us to conjecture that other Pt-lanthanide alloys, exhibiting more optimal levels of compression, would reach the peak of the Sabatier volcano. Here, we show how the decreased radius of the lanthanides with increased filling of the f-shell—i.e., the lanthanide contraction—provides us with a route to engineer such compression. We have systematically studied activity and stability trends of Pt_5La, Pt_5Ce, Pt_5Sm, Pt_5Gd, Pt_5Tb, Pt_5Dy, Pt_5Tm, and Pt_5Ca, using a combination of experiments and theory to explain our observations.

We evaluated the electrocatalytic properties of sputter-cleaned polycrystalline Pt_5M electrodes by rotating disk electrode (RDE) voltammetry in O_2-saturated 0.1 M $HClO_4$. We chose a Pt:M ratio of 5:1 because we could obtain a consistent series of alloys with the same structure, allowing for a systematic investigation. Furthermore, it corresponds to the phase that is most Pt-rich and stable (*16*). At 0.9 V, Pt_5Tb is the most active polycrystalline Pt-based catalyst reported. All of the materials exhibited activity enhancement by a factor of 3 to 6 over pure Pt (see figs. S5 and S6 and table S1 in the supplementary materials). The overall electrocatalytic ranking of ORR activity of polycrystalline Pt alloys is shown in fig. S6: $Pt_5Tb > Pt_5Gd \sim Pt_3Y > Pt_5Sm > Pt_5Ca \sim Pt_5Dy > Pt_5Tm > Pt_5Ce > Pt_5Y \sim Pt_5La >> Pt$ (*6*, *11*, *16*), demonstrating that these alloys accelerate the ORR more effectively than other polycrystalline Pt alloys. Pt_3Co and Pt_3Ni alloys prepared this way exhibited enhancement only by a factor of 2 (*12*, *24*). Accelerated stability tests consisting of 10,000 consecutive cycles between 0.6 and 1.0 V versus a reversible hydrogen electrode (RHE) were performed after the initial ORR activity measurements. The electrochemical experiments are summarized in figs. S3 to S11. Figure 1C reports the ORR activities before and after the stability test for all the Pt alloys and pure Pt. Apart from Pt_5Ca (which has a lower E_a), all of the Pt-lanthanide alloys retained enhancement by a factor of 3 over pure Pt after the accelerated stability test. Notably, Pt_5Gd exhibited a residual activity that was 5 times as great as that of pure Pt.

We characterized the structure and chemical composition of the electrocatalysts by x-ray diffraction (XRD) and x-ray photoelectron spectroscopy (XPS) in order to explain our experimental observations. All of the alloys formed stable intermetallic compounds with a hexagonal structure (figs. S1 and S2 and table S1), in agreement with previous reports (*25*). The XRD data suggest that the polycrystalline alloys may show different degrees of preferential orientation in the bulk (figs. S1 and S2). However, by presputtering the electrodes, we minimize any differences in surface orientation between the samples under investigation. Moreover, based on Watanabe and coworkers' in situ scanning tunneling microscopy measurements on sputter-deposited Pt-Fe (*26*), we expect the acid-leached Pt overlayers to be dominated by (111) terraces, typically the most stable facet termination (*27*). Most of the elements in the bulk Pt_5M alloy form a so-called kagome layer (*6*, *16*) (Fig. 2 and fig. S16), with a nearest-neighbor Pt-Pt distance $d_{Pt\text{-}Pt} = a/2$. The lattice parameter a and hence $d_{Pt\text{-}Pt}$ decreased from left to right in the lanthanide series (Fig. 2).

Figure 3, A and B, show the angle-resolved XPS (AR-XPS) depth profiles on sputter-cleaned Pt_5Tb before and after electrochemical measurements. For each of the alloys, the Pt to M ratio increased substantially, especially at the most surface-sensitive angles, as shown for Pt_5Tb on Fig. 3C, after initial electrochemistry measurements, confirming the formation of a Pt overlayer. The depth profile of Fig. 3B showed that, even after accelerated stability tests, this structure was maintained, demonstrating the stability of these materials upon potential cycling.

To quantitatively interpret our XPS data (for details, see section S4 of the supplementary materials and figs. S12 to S15), we evaluated the mean Pt overlayer thickness for the alloys. Figure 3D shows how it varied for both the initial ORR activity and after stability tests as a function of the bulk lattice parameter a. The overlayer thickness after the initial testing varied little between the different alloys. However, after stability tests, the mean Pt overlayer generally increased from Pt_5La to Pt_5Tb [Pt_5Ca lies out of the scale; the initial Pt:M ratios for Pt_5Ca, Pt_5Sm, and Pt_5Dy were in fact higher than those expected from the nominal bulk stoichiometry (fig. S13), thus inhibiting a precise calculation of the overlayer thickness]. This difference could explain the anomalous behavior of

[1]Center for Individual Nanoparticle Functionality (CINF), Department of Physics, Technical University of Denmark, 2800 Lyngby, Denmark. [2]Department of Chemical Engineering, Stanford University, Stanford, CA 94305, USA. [3]Center for Atomic-Scale Materials Design (CAMD), Department of Physics, Technical University of Denmark, 2800 Lyngby, Denmark. [4]Nano-Science Center, Department of Chemistry, University of Copenhagen, 2100 Copenhagen, Denmark. [5]Department of Energy Conversion and Storage, Technical University of Denmark, 4000 Roskilde, Denmark. [6]Department of Mechanical Engineering, Massachusetts Institute of Technology, Cambridge, MA 02139, USA.
***Corresponding author. E-mail: ibchork@fysik.dtu.dk (I.C.); ifan@fysik.dtu.dk (I.E.L.S.); maria.escudero@fysik.dtu.dk (M.E.-E.)**

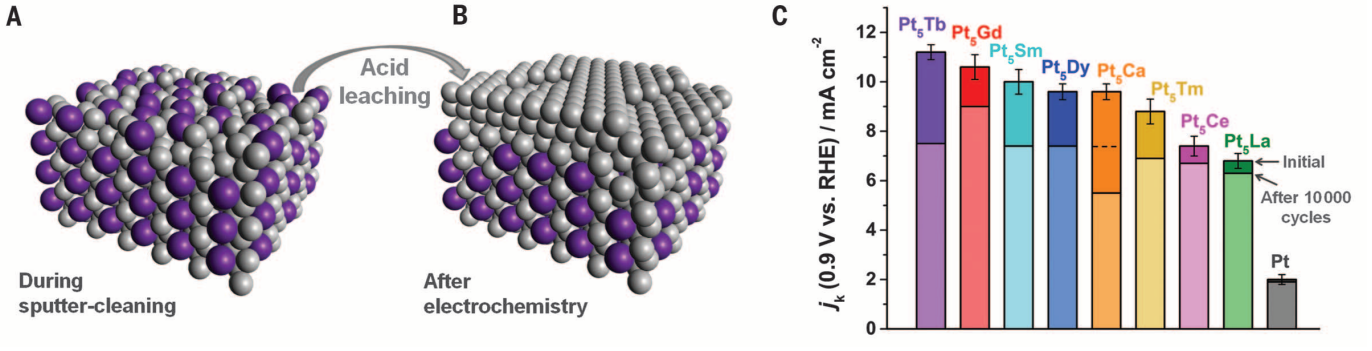


Fig. 1. Schematic views and electrochemical properties of polycrystalline Pt_5M (M = lanthanide or alkaline earth metal) electrocatalysts. Three-dimensional view of the Pt_5M structure (**A**) during sputter-cleaning and (**B**) after electrochemistry. (**C**) Kinetic current density, j_k, of Pt_5M and Pt at 23°C, 1600 revolutions per minute in O_2-saturated 0.1 M $HClO_4$, before and after a stability test consisting of 10,000 cycles between 0.6 and 1.0 V versus RHE at 100 mV s^{-1}. The activity of Pt_5Ca after the stability test has been normalized considering the increase of area after the test (see section S3.4 in the supplementary materials). The value normalized by the geometric area (dotted line) is shown for comparison.

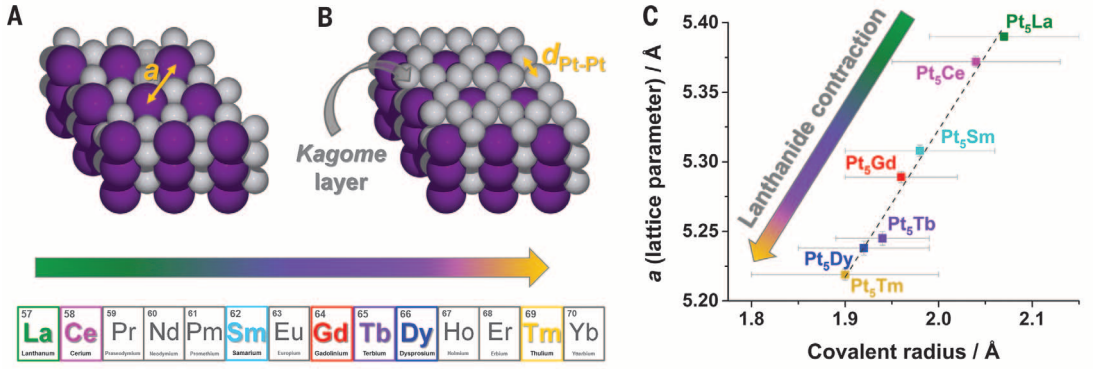


Fig. 2. Structure of Pt_5M. (**A** and **B**) Schematic view of the bulk structure of a Pt_5M (illustrated for Pt_5Tb), showing Pt_5Tb terminated by (A) a Pt and Tb intermixed layer and (B) a Pt kagome layer. Purple spheres represent Tb atoms, and gray spheres represent Pt atoms. Under ORR conditions in an acidic environment, one to two layers of M will be leached out, leaving three to five layers of Pt, as shown on Fig. 1B. (**C**) Relation between the lattice parameter *a* of Pt_5M measured by XRD (table S1) and the covalent radius of the lanthanide atoms (*31*). The dotted line shows the linear fit. The upper part of the figure shows the lanthanide contraction across the lanthanide series, the covalent radii decreasing in the same direction as d_{Pt-Pt}. The error in *a* corresponds to the uncertainty in the fit (table S1), whereas the error in the covalent radius corresponds to the estimated standard deviation from (*31*).

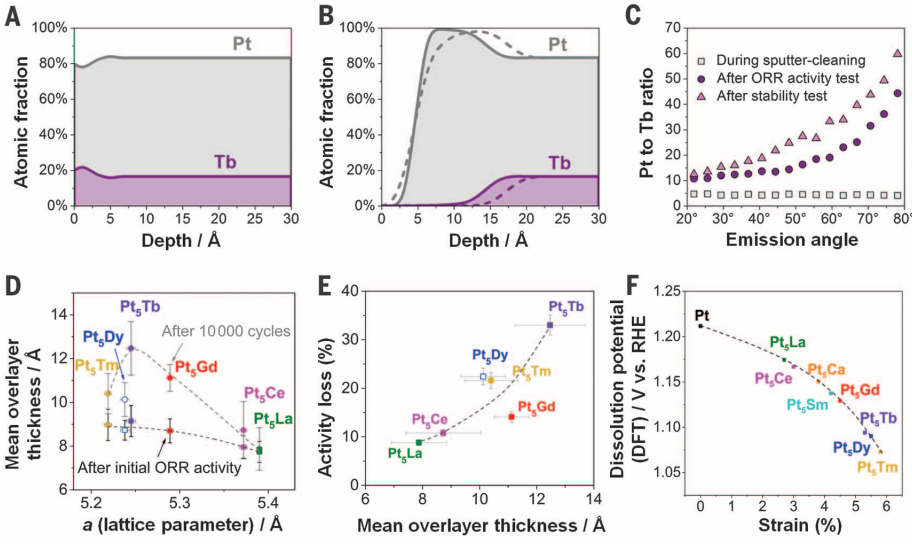


Fig. 3. XPS profiles before and after electrochemistry and Pt overlayer thickness as a function of the lattice parameter and activity loss. (**A and B**) AR-XPS profiles of polycrystalline Pt_5Tb (A) as prepared and (B) after initial ORR activity (solid line) and after stability test (dashed line). (**C**) Pt to Tb atomic ratios in Pt_5Tb from AR-XPS during sputter cleaning, after ORR initial activity, and after stability test. (**D**) Estimated average thicknesses of the Pt overlayer for Pt_5Tm, Pt_5Dy, Pt_5Tb, Pt_5Gd, Pt_5Ce, and Pt_5La after initial ORR activity and after stability test (taken from Fig. 1C), as a function of *a* lattice parameter [Pt_5Dy is shown as a hollow symbol to demarcate it as an outlier, likely because its as-prepared composition was inconsistent with that of the bulk (fig. S13)]. (**E**) Percentage of activity loss after stability test as a function of the Pt overlayer thickness. (**F**) Slab stability represented as dissolution potential versus the strain of the Pt overlayer on Pt_5M (from experimental lattice parameter *a*).

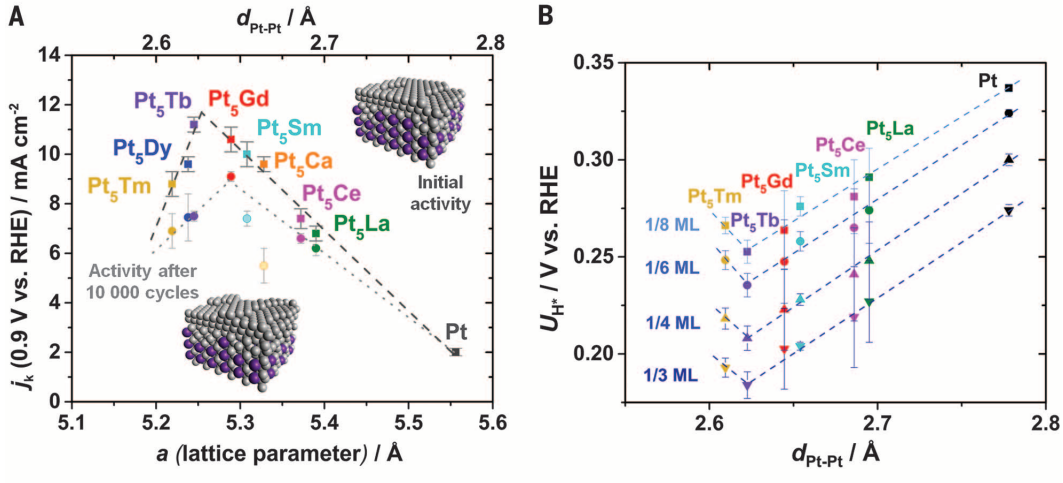


Fig. 4. Experimental volcano-type relationships between activity, H adsorption, and Pt-Pt distance. (**A**) Kinetic current density at 0.9 V (taken from Fig. 1C) on polycrystalline Pt_5M electrocatalysts versus the lattice parameter *a* of bulk Pt_5M (lower axis) and bulk d_{Pt-Pt} (upper axis), respectively. The figure shows the kinetic current density, j_k, of the alloys after the initial ORR activity (dark gray squares) and after 10,000 cycles of the stability test (colored circles). The dotted and dashed lines represent the experimental trends resulting after initial ORR activity and after stability, respectively. The activity of Pt_5Ca after 10,000 cycles has been normalized to account for the increase of area after the stability test. (**B**) Relation between the potential necessary to adsorb 1/8, 1/6, 1/4, and 1/3 monolayers (ML) of H (U_H) from the cyclic voltammograms (CVs) in the H adsorption region in N_2-saturated 0.1 M $HClO_4$ on Pt_5M (Fig. S5) and d_{Pt-Pt}.

these alloys, relative to the overall trend. The activity loss also correlates with the thickness of the overlayer (Fig. 3E) (*3*). Our density functional theory (DFT) calculations on the stability of different Pt overlayers, expressed as dissolution potential, show that the stability decreases as the compressive strain increases (Fig. 3F)—i.e., strain is a stability descriptor. We attribute the apparent thickening of the Pt overlayer with cycling to surface diffusion processes (*28*); bulk diffusion of lanthanide atoms through the overlayer will be strongly impeded by the strength of E_a (*13*). The strain-induced destabilization of the Pt overlayer could facilitate surface mobility (*28*), providing a channel for the dissolution of any residual lanthanide atoms in close vicinity to the surface. In summary, Fig. 3, D to F, shows that the overlayer thickness, activity losses, and thermodynamic stability are all a function of the bulk lattice parameter: Increased strain destabilizes the Pt overlayer and thus accelerates surface diffusion.

Figure 4A is a plot of the ORR activity as a function of the lattice parameter, a and $d_{Pt\text{-}Pt}$. Notably, all nine compounds, including the Pt-lanthanides and Pt_5Ca, follow the same volcano-type trend, with Pt_5Gd and Pt_5Tb at the apex. Because ΔE_{OH} is likely correlated with $d_{Pt\text{-}Pt}$ (*3*), the most trivial explanation for this trend is that the plot represents a Sabatier volcano: Alloys on the left bind OH too weakly, whereas on the right hand they bind ΔE_{OH} too strongly (as described by the DFT calculations in figs. S17 and S18). Alternatively, beyond a certain level of bulk strain, the overlayer could be unstable, causing the $d_{Pt\text{-}Pt}$ of the overlayer to relax toward a much lower level of surface strain. On single crystals, the destabilization is manifested as a positive shift in the "reversible" voltammetric peak for OH adsorption (*1*, *10*); however, we do not observe this shift on our polycrystalline materials, presumably because of hysteresis (electrochemical "irreversibility") or possibly coadsorption of OH and O. Conversely, the lanthanide contraction results in a clear voltammetric shift for the H adsorption region (figs. S3 and S4), plotted on Fig. 4B, which resembles the activity volcano, with Pt_5Tb exhibiting the maximum destabilization of adsorbed H. Notably, we also observe a linear relation between the experimental activity and the potential shift in the H adsorption (fig. S7).

Our DFT calculations on strain-activity-reactivity relations (section S5.4) suggest that Pt_5Tb, which is the most active electrocatalyst, should exhibit ~3% compression, approaching the optimum OH binding energy of the Sabatier volcano (*11*). By comparing our activity data and the voltammetric shift in H adsorption to the DFT predictions, we can conjecture that Pt-lanthanide alloys with a shorter $d_{Pt\text{-}Pt}$ than Pt_5Tb form a more relaxed overlayer (figs. S19 to S21]. More generally, our observations suggest that strain effects can only weaken the binding of H and OH to a certain extent. More appreciable destabilization of reaction intermediates can be afforded by ligand effects (*1*, *10*). The implementation of these catalysts in fuel cells will require scalable synthesis methods yielding high surface catalysts. Nonetheless, we have already demonstrated that Pt_xGd NPs exhibited an outstanding activity of 3.6 Å/mg Pt at 0.9 V RHE in liquid half cells (*18*, *29*) (fig. S6B), only surpassed by Pt_3Ni nanoframes (*21*) and Mo-doped Pt_3Ni nanoparticles (*22*). Careful tuning of the NP composition—for instance, by synthesizing ternary Pt-Gd-Tb alloys, in combination with a judicious choice of annealing treatment (*21*, *22*, *30*)—could yield record-breaking catalytic activity and stability over the long term in real devices.

REFERENCES AND NOTES

1. V. R. Stamenkovic *et al.*, *Science* **315**, 493–497 (2007).
2. H. A. Gasteiger, S. S. Kocha, B. Sompalli, F. T. Wagner, *Appl. Catal. B* **56**, 9–35 (2005).
3. P. Strasser *et al.*, *Nat. Chem.* **2**, 454–460 (2010).
4. S. Mukerjee, S. Srinivasan, M. P. Soriaga, J. McBreen, *J. Electrochem. Soc.* **142**, 1409–1422 (1995).
5. B. Han *et al.*, *Energy Environ. Sci.* **8**, 258–266 (2015).
6. I. E. L. Stephens, A. S. Bondarenko, U. Grønbjerg, J. Rossmeisl, I. Chorkendorff, *Energy Environ. Sci.* **5**, 6744 (2012).
7. J. K. Nørskov *et al.*, *J. Phys. Chem. B* **108**, 17886–17892 (2004).
8. F. Calle-Vallejo *et al.*, *Science* **350**, 185–189 (2015).
9. J. Suntivich, K. J. May, H. A. Gasteiger, J. B. Goodenough, Y. Shao-Horn, *Science* **334**, 1383–1385 (2011).
10. I. E. L. Stephens *et al.*, *J. Am. Chem. Soc.* **133**, 5485–5491 (2011).
11. J. Greeley *et al.*, *Nat. Chem.* **1**, 552–556 (2009).
12. V. R. Stamenkovic, B. S. Mun, K. J. J. Mayrhofer, P. N. Ross, N. M. Markovic, *J. Am. Chem. Soc.* **128**, 8813–8819 (2006).
13. U. G. Vej-Hansen, J. Rossmeisl, I. E. L. Stephens, J. Schiøtz, *Phys. Chem. Chem. Phys.* **18**, 3302–3307 (2016).
14. L. Tang *et al.*, *J. Am. Chem. Soc.* **132**, 596–600 (2010).
15. E. F. Holby, W. Sheng, Y. Shao-Horn, D. Morgan, *Energy Environ. Sci.* **2**, 865–871 (2009).
16. M. Escudero-Escribano *et al.*, *J. Am. Chem. Soc.* **134**, 16476–16479 (2012).
17. P. Hernandez-Fernandez *et al.*, *Nat. Chem.* **6**, 732–738 (2014).
18. A. Velázquez-Palenzuela *et al.*, *J. Catal.* **328**, 297–307 (2015).
19. K. J. J. Mayrhofer, K. Hartl, V. Juhart, M. Arenz, *J. Am. Chem. Soc.* **131**, 16348–16349 (2009).
20. L. Dubau *et al.*, *Appl. Catal. B* **142-143**, 801–808 (2013).
21. C. Chen *et al.*, *Science* **343**, 1339–1343 (2014).
22. X. Huang *et al.*, *Science* **348**, 1230–1234 (2015).
23. M. Mavrikakis, B. Hammer, J. K. Nørskov, *Phys. Rev. Lett.* **81**, 2819–2822 (1998).
24. V. Stamenkovic *et al.*, *Angew. Chem. Int. Ed.* **45**, 2897–2901 (2006).
25. V. Ohm *et al.*, *J. Alloy. C* **238**, 95–101 (1996).
26. L. J. Wan, T. Moriyama, M. Ito, H. Uchida, M. Watanabe, *Chem. Commun.* **2002**, 58–59 (2002).
27. L. Vitos, A. V. Ruban, H. L. Skriver, J. Kollar, *Surf. Sci.* **411**, 186–202 (1998).
28. J. Erlebacher, D. Margetis, *Phys. Rev. Lett.* **112**, 155505 (2014).
29. C. M. Pedersen *et al.*, *Electrochim. Acta* **179**, 647–657 (2015).
30. D. Wang *et al.*, *Nat. Mater.* **12**, 81–87 (2013).
31. B. Cordero *et al.*, *Dalton Trans.* **2008**, 2832–2838 (2008).

ACKNOWLEDGMENTS

The Center for Individual Nanoparticle Functionality is sponsored by the Danish National Research Foundation (DNRF54). We gratefully acknowledge EU FP7's initiative Fuel Cell and Hydrogen Joint Undertaking's project CathCat (GA 303492), as well as Danish Strategic Research's project NACORR (12-133817), for funding this work. M.E.-E. is the recipient of a Sapere Aude: DFF-Research Talent grant from the Danish Council for Independent Research. I.E.L.S. is the recipient of the Peabody Visiting Associate Professorship from the Department of Mechanical Engineering at Massachusetts Institute of Technology. We thank C. D. Damsgaard for assistance setting up the XRD measurements and O. Hansen for critically reading the manuscript. The authors declare competing financial interests: Intellectual property pertaining to the materials presented in this Report is protected by three patents (CA2877617-A1, WO2014079462-A1, and CA2767793-A1).

SUPPLEMENTARY MATERIALS

www.sciencemag.org/content/352/6281/73/suppl/DC1
Materials and Methods
Figs. S1 to S21
Table S1
References (*32*–*65*)

17 November 2015; accepted 11 February 2016
10.1126/science.aad8892

Downloaded from on March 31, 2016

ICE SHEETS

Antarctic Ice Sheet variability across the Eocene-Oligocene boundary climate transition

Simone Galeotti,[1]* Robert DeConto,[2] Timothy Naish,[3,4] Paolo Stocchi,[5] Fabio Florindo,[6] Mark Pagani,[7] Peter Barrett,[3] Steven M. Bohaty,[8] Luca Lanci,[1] David Pollard,[9] Sonia Sandroni,[10] Franco M. Talarico,[10,11] James C. Zachos[12]

About 34 million years ago, Earth's climate cooled and an ice sheet formed on Antarctica as atmospheric carbon dioxide (CO_2) fell below ~750 parts per million (ppm). Sedimentary cycles from a drill core in the western Ross Sea provide direct evidence of orbitally controlled glacial cycles between 34 million and 31 million years ago. Initially, under atmospheric CO_2 levels of ≥600 ppm, a smaller Antarctic Ice Sheet (AIS), restricted to the terrestrial continent, was highly responsive to local insolation forcing. A more stable, continental-scale ice sheet calving at the coastline did not form until ~32.8 million years ago, coincident with the earliest time that atmospheric CO_2 levels fell below ~600 ppm. Our results provide insight into the potential of the AIS for threshold behavior and have implications for its sensitivity to atmospheric CO_2 concentrations above present-day levels.

The establishment of the Antarctic Ice Sheet (AIS) is associated with an approximate +1.5 per mil increase in deep-water marine oxygen isotopic ($\delta^{18}O$) values beginning at ~34 million years ago (Ma) and peaking at ~33.6 Ma (*1*–*3*), with two positive $\delta^{18}O$ steps separated by ~200,000 years. The first positive isotopic step primarily reflects a temperature decrease (*4*); the second isotopic step has been interpreted as the onset of a prolonged interval of

maximum ice extent [Earliest Oligocene Glacial Maximum (EOGM)] between 33.6 and 33.2 Ma (*5*). Deep-water temperature cooled by 3° to 5°C (*6*) as a consequence of decreasing CO_2 levels (*7*), while the volume of ice on Antarctica expanded to either near-modern dimensions (*6*, *8*) or as much as 25% larger than present-day values (*9*, *10*). A sea-level fall of ~70 m is estimated from low-latitude shallow-marine sequences (*9*, *11*). Uncertainties in the magnitudes of these estimates in part reflect the limitations of geochemical proxy records used to deconvolve the relative contribution of ice volume and temperature at orbital resolution (*12*), as well as uncertainties inherent in the backstripping of continental margin sedimentary records (*8*). Ice sheet–proximal marine geological records from the continental margin of Antarctica can improve our understanding of the AIS evolution by providing evidence of the direct response of shallow-marine sedimentary environments (e.g., water depth changes) to ice sheet expansion and retreat.

The temporal pattern and extent of Late Eocene–Early Oligocene (~34.1 to ~31 Ma) Antarctic glacial advance and retreat is recorded in the well-dated CRP-3 drillcore, a shallow-water glaciomarine sedimentary succession deposited in the Victoria Land Basin (Fig. 1), tens of kilometers seaward of the present-day East Antarctic Ice Sheet (EAIS) in the Western Ross Sea (*13*). Thirty-seven fluvial to shallow-marine (deltaic) sedimentary cycles occur in the lower 500 m of the drillcore [330 to 780 m below sea floor (mbsf)] that record the advance and retreat of land-terminating glaciers delivering terrigenous sediment to an open wave–dominated coastline and are associated with relative sea level (RSL) oscillations of less than 20 m (*14*). These cycles, characterized as type B (Fig. 2; see also supplementary materials), do not display evidence of ice contact from glacial overriding. In contrast, 11 glaciomarine sedimentary cycles bounded by glacial surfaces of erosion in the upper 300 m of the drillcore (0 to 300 mbsf) reflect oscillations of the seaward extent of a marine-terminating ice sheet onto the Ross Sea continental shelf and across the CRP-3 drill site associated with larger RSL fluctuations of >20 m (*14*) (type A cycles in Fig. 2; see also supplementary materials). Temporal variations in lithofacies, grain size, and clast abundance primarily reflect oscillations in depositional energy that were controlled by changes in water depth and/or glacial proximity (*14*, *15*). Shallow-marine sedimentary cycles analogous to those observed in the CRP-3 drillcore have been directly linked with orbitally driven climatic cycles of the AIS across the Oligocene-Miocene boundary at a nearby Ross Sea site (*15*). Accordingly, we applied a similar approach to directly compare the timing of proximal ice volume changes during the Early Oligocene against high-resolution temperature and ice volume proxy records derived from distal deep-sea sequences.

Clast abundance (Fig. 2) reflects glacial proximity and has been shown in a previous study to be controlled by orbital forcing in conjunction with the deposition of type B cycles in the lower part of CRP-3 (*16*). To similarly test for the role of orbital forcing within the laterally extensive glacial advances within the type A cycle succession in the upper 300 m of the CRP-3 core, we applied a singular spectrum analysis (see supplementary materials) to the clast abundance time series and a new record of luminance, which reflects changing proportions of clay and sand in sedimentary environments controlled by the proximity to the ice margin and by changes in water depth associated with RSL fluctuations (*14*). An independently derived age model for CRP-3, based on biochronologic calibration of a magnetic reversal stratigraphy (*16*), together with identification of the orbital components in these records enables a one-to-one correlation of sedimentary cycles to the highly resolved, orbitally tuned $\delta^{18}O$ record from the deep sea (*2*, *17*) (Fig. 2). A key age constraint in the CRP-3 record is the precisely dated transition (±5000 years) at 31.1 Ma between magnetic polarity chrons C12n and C12r at 12.5 mbsf (*13*) (fig. S5).

Variation in facies and clast abundance within type B shallow-marine sedimentary cycles have previously been interpreted to reflect periodic advance and retreat of land-terminating alpine glaciers in the Transantarctic Mountains (*15*) in response to precession and obliquity forcing (*16*) (Fig. 2). This direct response to orbitally paced local insolation forcing indicates a highly dynamic AIS that advanced and retreated during the early icehouse phase of the EOGM. The first sedimentary evidence of ice advance onto the Ross Sea continental shelf coincides with the deposition of unconformity-bound, type A sedimentary cycles beginning at 32.8 Ma, and marks an abrupt transition in AIS sensitivity to orbital forcing that was paced by longer-duration eccentricity cycles (Figs. 2 and 3). This phase is also associated with climate cooling and increased physical weathering, as evidenced by a change in clay mineralogy (*18*). Type A cycles (Fig. 2) have been interpreted to represent cyclic alternations in both grounding-line proximity and RSL change (*14*). According to glacial isostatic adjustment (GIA) theory and given the ice marginal position of the CRP-3 site, any proximal ice thickness variation would have triggered crustal and geoidal deformations such that the resulting

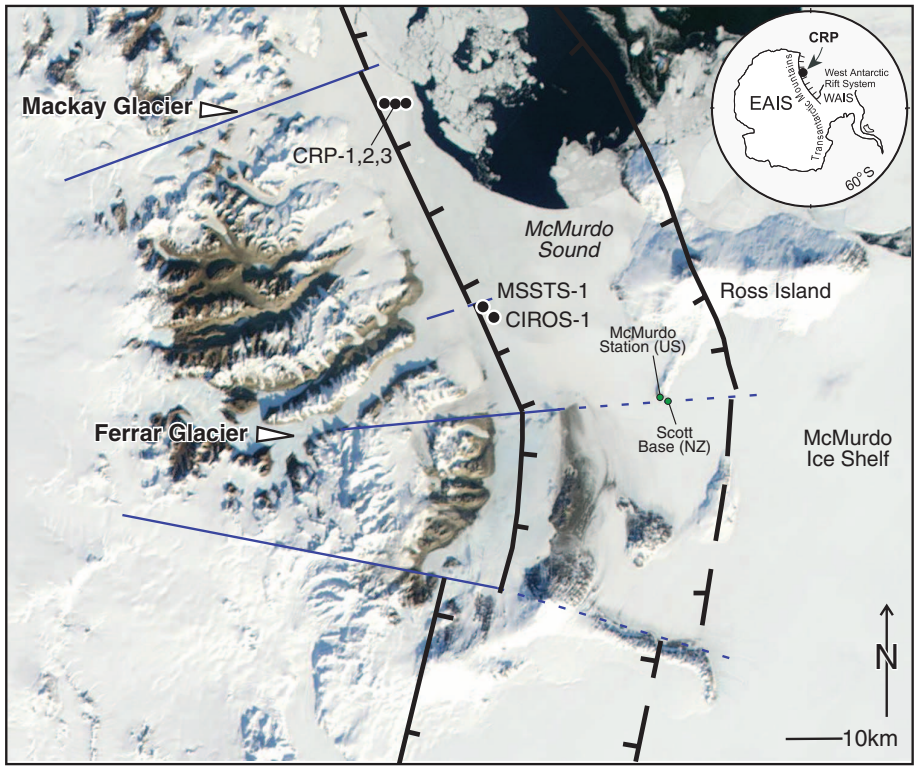


Fig. 1. Location of key geographical and geological features in Southern McMurdo Sound. Boundary faults of the southern extension of Terror Rift are shown, together with the location of the CRP, MSSTS-1, and CIROS-1 drill sites.

[1]Dipartimento di Scienze Pure e Applicate, Università degli Studi di Urbino "Carlo Bo," 61029 Urbino, Italy. [2]Department of Geosciences, University of Massachusetts, Amherst, MA, USA. [3]Antarctic Research Centre, Victoria University of Wellington, Wellington, New Zealand. [4]GNS Science, P.O. Box 30368, Lower Hutt, New Zealand. [5]NIOZ Royal Netherlands Institute for Sea Research, Department of Coastal Systems, and Utrecht University, 1790 AB Den Burg, Texel, Netherlands. [6]Istituto Nazionale di Geofisica e Vulcanologia, 00143 Rome, Italy. [7]Department of Geology and Geophysics, Yale University, New Haven, CT, USA. [8]Ocean and Earth Science, University of Southampton, National Oceanography Centre, Southampton SO14 3ZH, UK. [9]Earth System Science Center, Pennsylvania State University, State College, PA, USA. [10]Museo Nazionale dell'Antartide, Università degli Studi di Siena, 53100 Siena, Italy. [11]Dipartimento di Scienze Fisiche, della Terra e dell'Ambiente, Università degli Studi di Siena, 53100 Siena, Italy. [12]Earth Sciences Department, University of California, Santa Cruz, CA 95064, USA.
***Corresponding author. E-mail: simone.galeotti@uniurb.it**

local RSL change would be opposite in sign to eustatic trends and likely of larger amplitude (see supplementary materials). However, sedimentological evidence implies that glacial maxima and minima locally coincided with times of minimum and maximum RSL, respectively, for both type A and type B cycles (*14*). This implies that the GIA-induced RSL rise that was caused by the expansion and grounding of the ice sheet at the CRP-3 site was counterbalanced by a strong RSL drop as a consequence of the forebulge uplift driven by synchronous EAIS thickening. Therefore, we argue that the appearance of marine-grounded ice near the CRP-3 site was enhanced by flexural crustal uplift as the EAIS expanded, resulting in a RSL fall (>40 m) in phase with the hypothetical eustatic trend.

Both petrological and apatite fission track evidence (*19*) suggests that diamictites deposited as part of 400,000-year sedimentary cycles spanning ~17 to 157 mbsf (~32.0 to 31.1 Ma; Fig. 2) were derived both locally from the Mackay glacier and from the southern Transantarctic Mountains outlet glaciers during glacial overriding and downcutting. Flowlines that trend northwestward into McMurdo Sound from the Byrd, Skelton, and Mulock glaciers are implied by model simulation of the early Oligocene glacial expansion (*10*, *20*).

According to our chronology and geological evidence for ice grounding, a marine-calving ice sheet first occurred in the western Ross Embayment at ~32.8 Ma, about 1 million years after the glacial maximum (Oi1) inferred by $\delta^{18}O$ values from marine carbonate isotope records (*17*) (Figs. 2 and 3). Oxygen isotope values paired with southern high-latitude Mg/Ca records (*3*) indicate that the AIS volume was slightly larger across Oi1a (~32.8 Ma) than across the EOGM. The Oi1a shift coincides, within the degree of uncertainty shown in Fig. 3 (see also fig. S17), with the CO_2 minimum [~600 ppm by volume (ppmv)] at the end of a ~40% decline beginning in the late Eocene (*7*, *21*) (Fig. 3). Declining CO_2 levels that culminate during Oi1a are fully consistent with model-derived CO_2 thresholds for Antarctic glaciation (*20*). The Oi1a interval also corresponds to a long-term minimum in eccentricity and obliquity (*22*), similar to the orbital configuration favoring the onset of glaciation across Oi1 (Fig. 3), implying that an extended period of low seasonality with cooler summers contributed to these long-period glacial maxima.

Therefore, we argue that despite ice expansion during the EOGM, the nascent AIS was strongly sensitive to orbitally paced, local insolation forcing until a CO_2 threshold of ~600 ppmv was crossed at 32.8 Ma (Fig. 3 and fig. S17). After 32.8 Ma, an expanded continental-scale ice sheet displayed progressively stronger orbital ice sheet hysteresis; such behavior is also suggested by ice models (*20*, *23*). Our observations from the CRP-3 record are also consistent with far-field ice volume proxies that indicate RSL changes of ~25 m in the time interval 33.4 to 32.8 Ma (*9*, *11*), equivalent to ~40% of present-day AIS volume. By contrast, after 32.8 Ma, a protracted period of RSL stability is observed in $\delta^{18}O$ records, which corresponds with our proximal evidence for an AIS that was relatively insensitive to higher-frequency orbital forcing (*11*) until ~29 Ma, when CO_2 values again increased to >600 ppm (*24*) (fig. S17). Our observations of AIS history and behavior lead us to conclude that the partial pressure of atmospheric CO_2 was the primary influence on the overall climate state and variability of AIS volume, including its sensitivity to orbital forcing, which implies a close linkage between carbon cycle dynamics and AIS evolution on both long- and short-period orbital time scales. Indeed, amplification of the long-period eccentricity component—observed in the CRP-3 record at ~32 Ma—tracks the establishment of low-latitude $\delta^{13}C$ variability with a 405,000-year periodicity (*25*).

The general orbital coherence and phasing between glacial cycles and marine $\delta^{13}C$ records (Fig. 2) indicates that carbon cycle feedbacks

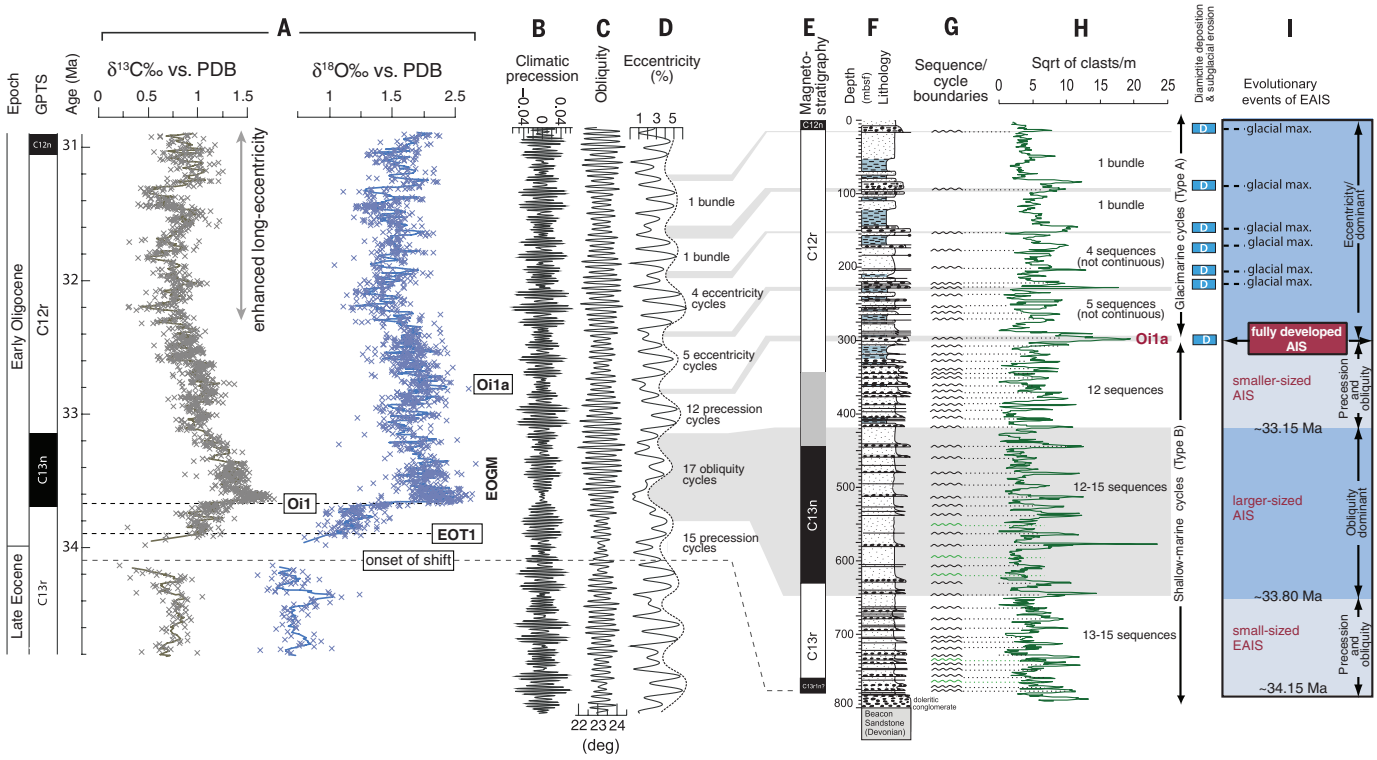


Fig. 2. Astrochronological calibration of glacial events across the Eocene-Oligocene climate transitions. (**A**) Deep-sea oxygen and carbon isotopic record from ODP Site 1218 (*2*, *17*). (**B** to **H**) Time series for climatic precession (B), obliquity (C), and eccentricity (D) correlated with magnetostratigraphy (E), lithostratigraphy (F), sequence stratigraphy (G) (*13*, *14*), and square root of clast abundance (H) (*30*) for the Late Eocene–Early Oligocene CRP-3 drillcore. Thirty-seven shallow-marine sedimentary cycles (sequences; type B) occur in the lower 500 m of the core record, controlled by advances and retreats of land-terminating glaciers associated with sea-level oscillations of less than 20 m. Eleven overlying glaciomarine sedimentary cycles (sequences; type A), each bounded by glacial surfaces of erosion, occur in the upper 300 m of the CRP-3 core, and record oscillations in the extent of a more expansive marine-terminating ice sheet in Ross Embayment. (**I**) Inferred stages and events in the development of the AIS across the Eocene-Oligocene boundary and their relationship to orbital forcing.

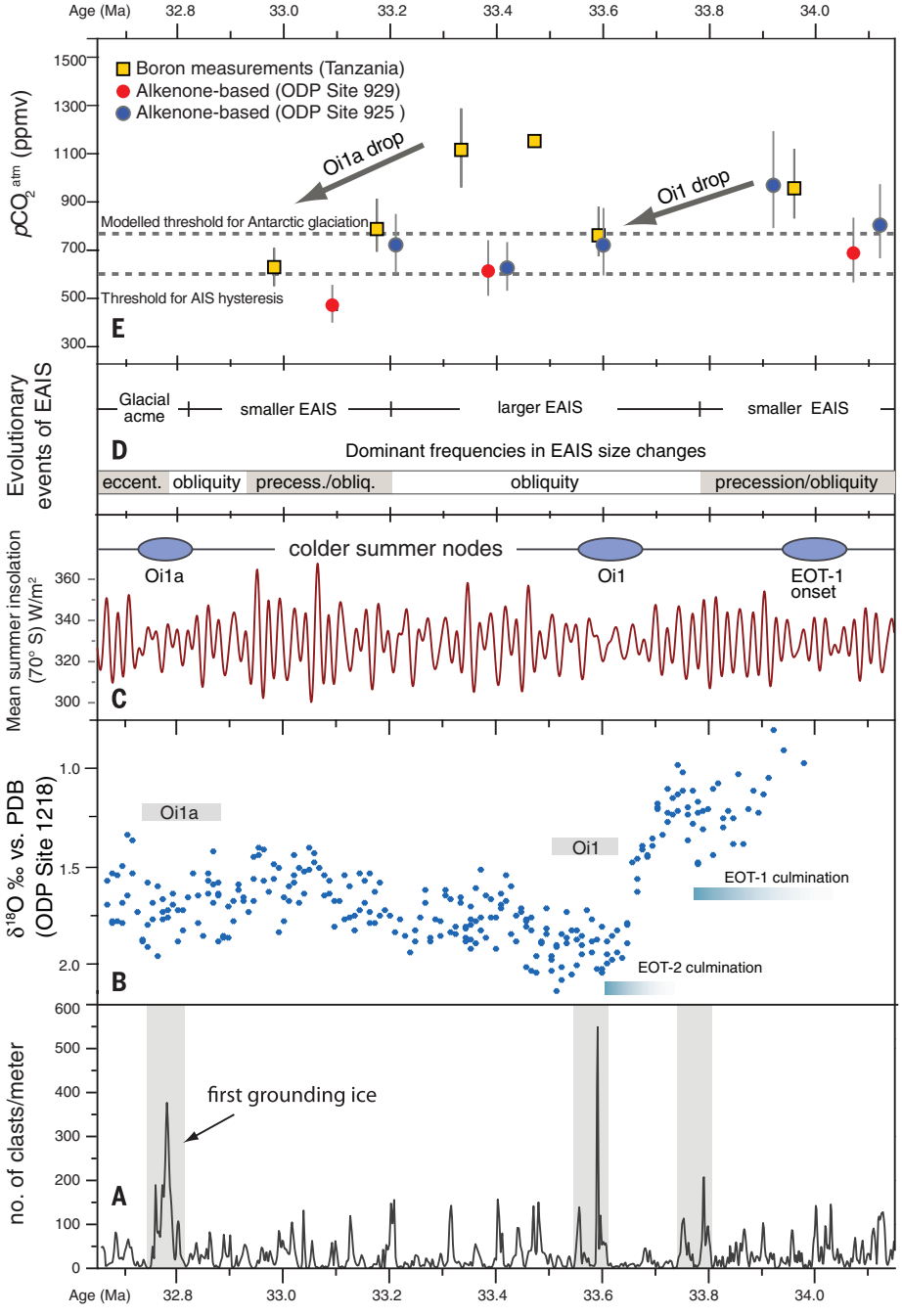


Fig. 3. Major glacial events recorded by clast abundance peaks from the CRP-3 core. (**A** and **B**) Events [gray bands in (A)] are calibrated to the astrochronologically tuned $\delta^{18}O$ record from ODP Site 1218 (B) (*2*). (**C**) Major peaks in clast abundance from CRP-3 correspond to the onset of the EOT-1 shift and glacial maxima at the Oi1 and Oi1a, and are associated with prolonged intervals characterized by cold southern high latitude summers as expressed in the 70°S mean summer insolation. (**D**) AIS volume changes recorded by the sedimentary sequences and clast abundance (see Fig. 2) are paced by the influence of obliquity and precession on a smaller-sized terrestrial ice sheet between 34.2 and 32.8 Ma. (**E**) Comparison with available atmospheric pCO_2 (partial pressure of atmospheric CO_2) records based on boron isotope (*21*) and alkenone (*7*) proxies shows that the earliest evidence of ice sheet grounding in the CRP-3 core occurs at the Oi1a event (32.9 to 32.8 Ma), coincident with a major peak in clast abundance and a longer-term drop in atmospheric CO_2 to below ~600 ppm.

contributed to CO_2 changes and amplification of short- and long-period eccentricity–paced glacial-interglacial cycles in the Early Oligocene (*26*), similar to the climate-carbon cycle dynamics associated with Northern Hemisphere glacial cycles during the Pleistocene. Coupled global climate–ice sheet models predict that the AIS should display threshold-like behavior in response to long-term trends in atmospheric CO_2 levels (*20*). For example, the stability threshold for marine-based sectors of the AIS has been shown to be ~400 ppm; between 300 and 400 ppm, marine ice sheets are highly dynamic in response to orbital forcing (*27*, *28*). Intermodel comparisons suggest a larger range of atmospheric CO_2 values (~560 to 920 ppm) for AIS glaciation (*29*). Data presented in our study imply that a CO_2 threshold for a continental-scale Antarctic ice sheet occurred at ~600 ppm, and that AIS sensitivity to insolation forcing and vulnerability to melt can be expected to increase markedly between 600 and 750 ppm.

REFERENCES AND NOTES

1. J. C. Zachos, T. M. Quinn, K. A. Salamy, *Paleoceanography* **11**, 251–266 (1996).
2. H. K. Coxall, P. A. Wilson, H. Pälike, C. H. Lear, J. Backman, *Nature* **433**, 53–57 (2005).
3. S. M. Bohaty, J. C. Zachos, M. L. Delaney, *Earth Planet. Sci. Lett.* **317–318**, 251–261 (2012).
4. C. H. Lear, T. R. Bailey, P. N. Pearson, H. K. Coxall, Y. Rosenthal, *Geology* **36**, 251 (2008).
5. Z. Liu, S. Tuo, Q. Zhao, X. Cheng, W. Huang, *Chin. Sci. Bull.* **49**, 2190–2197 (2004).
6. Z. Liu *et al.*, *Science* **323**, 1187–1190 (2009).
7. M. Pagani, J. C. Zachos, K. H. Freeman, B. Tipple, S. Bohaty, *Science* **309**, 600–603 (2005).
8. K. G. Miller *et al.*, *Bull. Geol. Soc. Am.* **120**, 34–53 (2008).
9. M. E. Katz *et al.*, *Nat. Geosci.* **1**, 329–334 (2008).
10. D. S. Wilson, D. Pollard, R. M. DeConto, S. S. R. Jamieson, B. P. Luyendyk, *Geophys. Res. Lett.* **40**, 4305–4309 (2013).
11. K. G. Miller *et al.*, *Science* **310**, 1293–1298 (2005).
12. K. Billups, D. P. Schrag, *Earth Planet. Sci. Lett.* **209**, 181–195 (2003).
13. F. Florindo, G. S. Wilson, A. P. Roberts, L. Sagnotti, K. L. Verosub, *Global Planet. Change* **45**, 207–236 (2005).
14. C. R. Fielding, T. R. Naish, K. J. Woolfe, *Terra Antarctica* **8**, 217–224 (2001).
15. T. R. Naish *et al.*, *Nature* **413**, 719–723 (2001).

16. S. Galeotti *et al.*, *Palaeogeogr. Palaeoclimatol. Palaeoecol.* **335–336**, 84–94 (2012).
17. H. K. Coxall, P. A. Wilson, *Paleoceanography* **26**, PA2221 (2011).
18. W. Ehrmann, M. Setti, L. Marinoni, *Palaeogeogr. Palaeoclimatol. Palaeoecol.* **229**, 187–211 (2005).
19. V. Olivetti, M. L. Balestrieri, F. Rossetti, F. M. Talarico, *Tectonophysics* **594**, 80–90 (2013).
20. R. M. DeConto, D. Pollard, *Nature* **421**, 245–249 (2003).
21. P. N. Pearson, G. L. Foster, B. S. Wade, *Nature* **461**, 1110–1113 (2009).
22. J. Laskar *et al.*, *Astron. Astrophys.* **428**, 261–285 (2004).
23. D. Pollard, R. M. DeConto, *Global Planet. Change* **45**, 9–21 (2005).
24. Y. G. Zhang, M. Pagani, Z. H. Liu, S. M. Bohaty, R. DeConto, *Philos. Trans. R. Soc. A* **371**, 20130096 (2013).
25. H. Pälike *et al.*, *Science* **314**, 1894–1898 (2006).
26. J. C. Zachos, L. R. Kump, *Global Planet. Change* **47**, 51–66 (2005).
27. M. O. Patterson *et al.*, *Nat. Geosci.* **7**, 841–847 (2014).
28. G. L. Foster, E. J. Rohling, *Proc. Natl. Acad. Sci. U.S.A.* **110**, 1209–1214 (2013).
29. E. Gasson *et al.*, *Clim. Past Discuss.* **9**, 5701–5745 (2014).
30. S. Sandroni, F. Talarico, *Terra Antarctica* **8**, 449–467 (2001).
10.3133/of2007-1047

ACKNOWLEDGMENTS

This research is an outcome of a 2-year project (PNRA 2004/4.09) partly funded by Programma Nazionale di Ricerche in Antartide (Italy). Also supported by NSF grants ANT-0424589, 1043018, and OCE-1202632 and by New Zealand Ministry of Business Innovation and Employment contract C05X1001(TN). Data are available from www.pangaea.de/.

SUPPLEMENTARY MATERIALS

www.sciencemag.org/content/352/6281/76/suppl/DC1
Materials and Methods
Figs. S1 to S17
References (*31–49*)

9 March 2015; accepted 24 February 2016
Published online 10 March 2016
10.1126/science.aab0669

ATMOSPHERIC METHANE

A 21st-century shift from fossil-fuel to biogenic methane emissions indicated by $^{13}CH_4$

Hinrich Schaefer,[1]* Sara E. Mikaloff Fletcher,[1] Cordelia Veidt,[2] Keith R. Lassey,[1]† Gordon W. Brailsford,[1] Tony M. Bromley,[1] Edward J. Dlugokencky,[3] Sylvia E. Michel,[4] John B. Miller,[3] Ingeborg Levin,[2] Dave C. Lowe,[1]‡ Ross J. Martin,[1] Bruce H. Vaughn,[4] James W. C. White[4]

Between 1999 and 2006, a plateau interrupted the otherwise continuous increase of atmospheric methane concentration [CH_4] since preindustrial times. Causes could be sink variability or a temporary reduction in industrial or climate-sensitive sources. We reconstructed the global history of [CH_4] and its stable carbon isotopes from ice cores, archived air, and a global network of monitoring stations. A box-model analysis suggests that diminishing thermogenic emissions, probably from the fossil-fuel industry, and/or variations in the hydroxyl CH_4 sink caused the [CH_4] plateau. Thermogenic emissions did not resume to cause the renewed [CH_4] rise after 2006, which contradicts emission inventories. Post-2006 source increases are predominantly biogenic, outside the Arctic, and arguably more consistent with agriculture than wetlands. If so, mitigating CH_4 emissions must be balanced with the need for food production.

Anthropogenic CH_4 emissions have almost tripled [CH_4] since preindustrial times (*1–3*). This contributes strongly to anthropogenic climate change through radiative forcing and impacts on atmospheric chemistry, particularly hydroxyl consumption, tropospheric ozone generation, and water vapor formation in the stratosphere (*4*). In a positive feedback to climate change, natural sources such as CH_4 hydrates, tundra, and permafrost may increase (*5*). We must therefore understand how the CH_4 budget responds to human activities and environmental change. The onset and end of the 1999–2006 [CH_4] plateau (Fig. 1) (*3*, *6*, *7*) have been studied with inverse models (top-down) (*8–14*), as well as process modeling (*6*, *8*, *15–20*) and emission estimates (bottom-up) (*21–23*). These approaches are either not emission-specific or uncertain in scaling and process representation (*8*). In contrast, the $^{13}C/^{12}C$ ratio in atmospheric CH_4 [$\delta^{13}C_{(Atm)}$; expressed in δ notation relative to the Vienna Pee Dee Belemnite standard] is controlled by the relative contributions from source types with distinctive isotope signatures $\delta^{13}C_{(So)}$ [biogenic ~–60 per mil (‰), such as wetlands, agriculture, and waste; thermogenic ~–37‰, such as fossil-fuels; pyrogenic ~–22‰, such as biomass burning] (*3*, *24*). Large and overlapping ranges for $\delta^{13}C_{(So)}$ in field studies of the main source types and even individual sources (such as wetlands) (*24*) average out at the global scale so that $\delta^{13}C_{(So)}$ is suitable to characterize emissions. Sink processes with characteristic isotopic fractionation ε (*25*) [for example, hydroxyl (OH) ε = –3.9‰; chlorine in the marine boundary layer (Cl-MBL) ε = –60‰; stratospheric loss ε = –3‰; or oxidation by soils ε = –20‰] (table S1) (*26*, *27*) also influence $\delta^{13}C_{(Atm)}$. Therefore, $\delta^{13}C_{(Atm)}$ variations indicate changes in CH_4 budgets, in which pertinent sources are industrial (thermogenic); agricultural, such as ruminants and rice cultivation (biogenic); and climate-dependent, such as biomass burning (pyrogenic) and natural wetlands, including freshwater and permafrost (biogenic). Other sources lack magnitude [termites, wild animals, ocean, and hydrates (*8*)] or known processes (geologic sources) to force abrupt and sustained changes (supplementary materials). Changes in the dominating OH sink may affect [CH_4] and $\delta^{13}C_{(Atm)}$ trends, whereas substantial changes in other sinks are unlikely or uncertain (supplementary materials).

We reconstructed [CH_4] and $\delta^{13}C_{(Atm)}$ time series by splicing measurements from ice cores, firn air, archived air (*1*, *2*), and global networks (Fig. 1, fig. S1, and tables S2 and S3) (*3*) (*25*). ^{13}C enrichment followed by stable $\delta^{13}C_{(Atm)}$ parallels [CH_4] trends until the end of the 1999–2006 plateau. Afterward, [CH_4] increases, whereas $\delta^{13}C_{(Atm)}$ becomes more ^{13}C-depleted. This suggests that the increasing emissions before and after the plateau differ in $\delta^{13}C_{(So)}$.

We used a one-box model (*25*, *27*) to quantify changes in the CH_4 budget. An inversion run derives the history of global emission strength and isotopic source signature [$\delta^{13}C_{(So)}$] from the [CH_4] and $\delta^{13}C_{(Atm)}$ reconstructions and specified sink parameters (tables S1 and S3). In forward mode, this "base source" as input reproduces measured [CH_4] and $\delta^{13}C_{(Atm)}$ until the start of an event (plateau or renewed increase). Afterward, the source is held constant, providing a "Stabilization Run" (Fig. 2A). A superimposed "perturbation source" then tests the effect of strengthening or weakening emissions with a prescribed perturbation $\delta^{13}C_{(So)}$ on $\delta^{13}C_{(Atm)}$. Alternatively, sink variability can be implemented for equivalent tests. The modeling design is detailed in section 1.3 of (*25*).

Stabilization Run 92 (SR92) tests whether emissions simply stabilized to cause the [CH_4] plateau (assuming constant sinks) (*28*). The base source is run from 1700 to 1992, during which time emission rates show steady trends (fig. S2); afterward, emissions are held constant at 1991–1992 rates and average 1982–1992 $\delta^{13}C_{(So)}$. These choices remove disruptions by the Mount Pinatubo eruption (supplementary materials). Model-data mismatches after the plateau onset (Fig. 2) suggest a changing source mix and emission reductions. The latter occur abruptly after 1992, for an average 7.2 to 11.2 Tg loss in annual global emissions

[1]Climate and Atmosphere Center, National Institute of Water and Atmospheric Research (NIWA), 301 Evans Bay Parade, Wellington 6021, New Zealand. [2]Institut für Umweltphysik, Heidelberg University, Im Neuenheimer Feld 229, 69120 Heidelberg, Germany. [3]National Oceanic and Atmospheric Administration (NOAA), Earth System Research Laboratory (ESRL), Global Monitoring Division, 325 Broadway, Boulder, CO 80305, USA. [4]Institute of Arctic and Alpine Research (INSTAAR), University of Colorado, Boulder, CO 80309, USA.
***Corresponding author. E-mail: hinrich.schaefer@niwa.co.nz**
†Present address: Lassey Research & Education, 4 Witako Street, Lower Hutt 5011, New Zealand. ‡Present address: LoweNZ, 31 Queen Street, Lower Hutt 5012, New Zealand.

Downloaded from on March 31, 2016

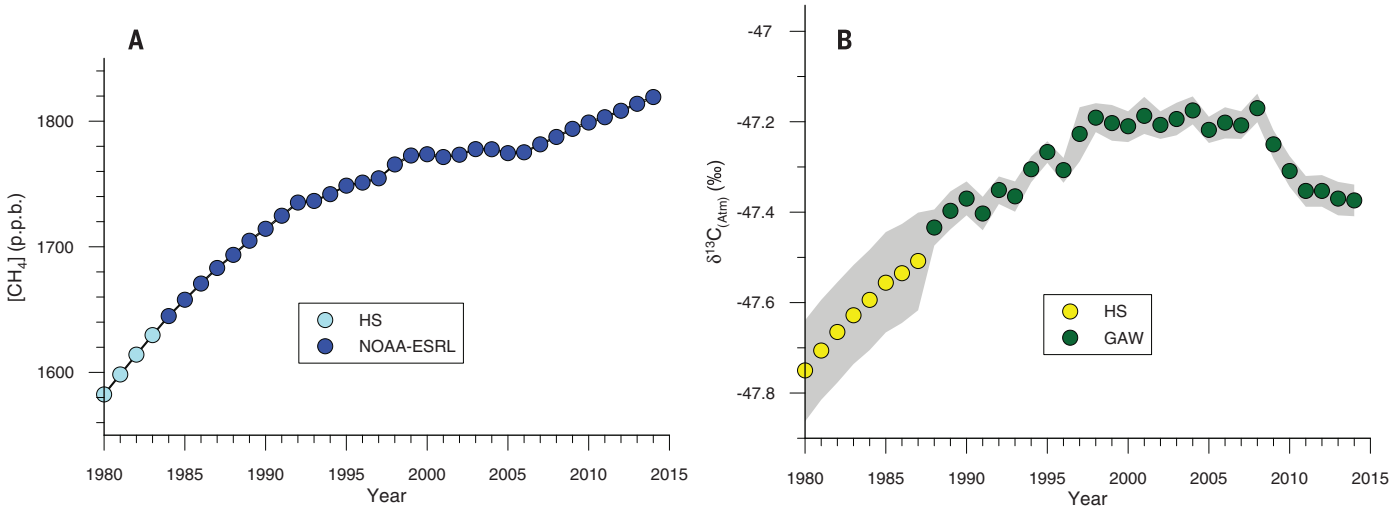


Fig. 1. Global trends in $[CH_4]$ and $\delta^{13}C_{(Atm)}$. (**A**) Spliced records of globally averaged annual values for $[CH_4]$ from a historic spline (HS) (light blue) (*1*) and the NOAA-ESRL global monitoring network (dark blue) (*3*). The uncertainty range is indicated by the thickness of the connecting line. (**B**) Spliced records of globally averaged annual values for $\delta^{13}C_{(Atm)}$ from a HS (yellow) (*2*) and atmospheric time series from contributing Global Atmosphere Watch (GAW) stations measured in our three laboratories (green). Gray shading shows the 1σ confidence interval (CI). Details on the splicing and uncertainty estimates are provided in (*25*).

over 1993–2006 relative to 1991–1992 (fig. S3). In "Perturbation Runs" (PRs92/1), this emission loss is superimposed on the SR92 source as a negative perturbation that decreases $[CH_4]$ from the SR92 values to observations (Fig. 2A). By assigning different perturbation $\delta^{13}C_{(So)}$ values in PRs92/1 to match observed $\delta^{13}C_{(Atm)}$, we fingerprinted the emissions that are no longer contributing to the total source. A perturbation $\delta^{13}C_{(So)}$ of ~–40‰ fits the plateau values within uncertainties, although without truly leveling out (Fig. 2B). The match improves for perturbation $\delta^{13}C_{(So)}$ = –53‰ for 1993–1995 and –35‰ from 1996 (PRs92/2) (Fig. 2C). Alternatively, Stabilization Run SR92/OH with OH variability, as reconstructed from methyl-chloroform (*29*), and constant 1992–2006 emissions, approximate measured $[CH_4]$ and $\delta^{13}C_{(Atm)}$ trends, so that additional source perturbations (PRs92/OH) are small and have little impact (Fig. 3). Combined OH variability and emission reductions fit observations better, but the relative weight of the two processes remains unknown, and perturbation $\delta^{13}C_{(So)}$ of –35 to –40‰ stays within uncertainties of the emissions-only scenario (figs. S4 to S7).

$\delta^{13}C_{(So)}$ ~ –35‰ is characteristic for thermogenic CH_4 (*3*, *24*, *26*), which is mainly emitted from the production of oil, natural gas, and coal (*21*, *22*). Simultaneous biogenic and pyrogenic reductions could produce the same signal as thermogenic reductions. This seems unlikely because climatic events such as El Niño–Southern Oscillation phases force opposite emission changes in wetlands (*15*)—the major biogenic source—and the total of natural and anthropogenic biomass burning (*16*). The perturbation $\delta^{13}C_{(So)}$ 1σ uncertainty (–28 to –42‰) (supplementary materials) allows for a small probability that the perturbation is pyrogenic. However, the required 20% pyrogenic drop is inconsistent with

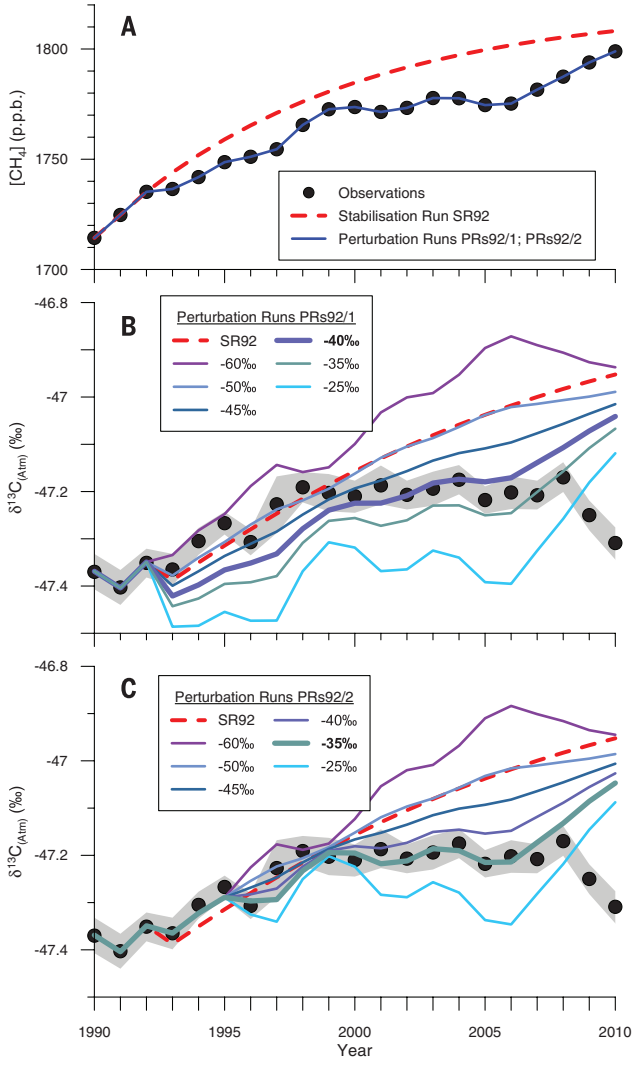


Fig. 2. Box-model results for the onset of the 1999–2006 plateau. (**A** to **C**) Observed yearly averages for $[CH_4]$ and $\delta^{13}C_{(Atm)}$ [black dots; gray shading for 1σ CI of $\delta^{13}C_{(Atm)}$]. SR92 (red dashed lines) indicates trends in $[CH_4]$ and $\delta^{13}C_{(Atm)}$ for emissions held constant at average 1991–1992 (553 Tg/year) and 1982–1992 (–53.35‰) levels, respectively. (A) Subtracting a source perturbation (yearly varying, average –9.5 Tg/year; PRs92/1 and PRs92/2) reconciles modeled $[CH_4]$ (blue line) with observations. (B) PRs92/1: $\delta^{13}C_{(Atm)}$ trends if $\delta^{13}C_{(So)}$ values between –25‰ and –60‰ (solid lines) are assigned to a set of perturbation runs starting in 1993. Thick line indicates best-fit scenario [$\delta^{13}C_{(So)}$ = –40‰] for 1999–2006 observations. (C) PRs92/2: as above, but assigning –53‰ to all perturbation runs for 1993–1995. Best-fit results from perturbation $\delta^{13}C_{(So)}$ = –35‰. Total $\delta^{13}C_{(So)}$ values for all runs are shown in fig. S14 and table S4.

reconstructions (*8*, *17*), and the preplateau reduction did not occur in the tropics (*28*), where most pyrogenic emissions originate (*8*). Sink changes may have contributed to the [CH_4] plateau, but only in concert with stagnating total emissions.

To study the renewed [CH_4] rise, another Stabilization Run SR06 runs the base source until 2006 and then holds it constant at 1999–2006 averages for emission strength and $\delta^{13}C_{(So)}$. This simulates a continuation of the [CH_4] and $\delta^{13}C_{(Atm)}$ plateaus (Fig. 4). Superimposed Perturbation Runs PRs06 with additional emissions averaging +19.7 Tg/year (fig. S3) [which is consistent with (*13*, *30*)] reproduce the [CH_4] rise and need $\delta^{13}C_{(So)}$ ~ −59‰ (−56 to −61‰, 1σ) (supplementary materials) to match the post-2006 $\delta^{13}C_{(Atm)}$ decline (Fig. 4B). Alternatively, Stabilization Run SR06/OH includes available OH reconstructions (1994–2007; constant OH assumed afterward). Associated Perturbation Runs PRs06/OH prescribe Perturbation A (2007–2011) and Perturbation B (2011–2014) to capture the marked break in slope of 2011. Best fits for Perturbation A ~ −75‰ and Perturbation B ~ −60‰ account for a ^{13}C-rich anomaly in 2008 and match the differing $\delta^{13}C_{(Atm)}$ slopes (Fig. 4C). This scenario suffers from uncertainties regarding the transition from reconstructed to constant OH in 2007 (alternative OH trends are examined in the supplementary materials). Also, matching the 2008 $\delta^{13}C_{(Atm)}$ anomaly could skew the trend for subsequent years. The resulting bias may be seen in perturbation $\delta^{13}C_{(So)}$ ~ −75‰ for 2007–2011. Such extremely ^{13}C-depleted values are only found in some boreal biogenic sources, which are unlikely to dominate the global signal. Therefore, the more conservative result is perturbation $\delta^{13}C_{(So)}$ ~ −59‰ integrated over 2007–2014 (Fig. 4B), but during 2006–2011, $\delta^{13}C_{(So)}$ was potentially more ^{13}C-depleted, as shown in Fig. 4C. OH variability may contribute to the post-2006 event, but perturbation $\delta^{13}C_{(So)}$ remains within uncertainties of the above estimates (figs. S8 to S12).

$\delta^{13}C_{(So)}$ ~ −59‰ is characteristic for biogenic sources (*3*, *24*, *26*). Thermogenic or pyrogenic emissions would require compensating changes in other sources or sinks. An atmospheric general circulation model (AGCM)–based chemistry-transport model (ACTM) study recently found post-2006 biogenic increases relative to pyrogenic ones (*12*). That study prescribed thermogenic emissions and therefore did not test all sources independently and whether thermogenic emissions are contributing to the [CH_4] growth. We calculate the possible contribution of thermogenic CH_4 in a combined increase with biogenic emissions as 0.9 ± 4.8 Tg/year (1σ) from 19.7 Tg/year total (supplementary materials). Larger thermogenic contributions require pyrogenic reductions. Process-based models (*18*) find average pyrogenic reductions by −1.5 Tg between 1999–2006 and 2007–2014. This accommodates <5.5 Tg/year additional thermogenic emissions. However, emission inventories suggest variable (*21*) or increasing pyrogenic emissions (*22*), negating thermogenic increases. Biogenic increases and pyrogenic decreases together facilitate thermogenic contributions to the total increase of 0 to 33%. A more ^{13}C-depleted perturbation $\delta^{13}C_{(So)}$, as suggested in Fig. 4C, would lower this estimate further. In all scenarios of simultaneous pyrogenic, thermogenic, and biogenic changes, increasing biogenic emissions are causing most or all of the post-2006 [CH_4] growth. This finding remains robust for potential sink changes (supplementary materials).

The global CH_4 budget is underconstrained by [CH_4] and $\delta^{13}C_{(Atm)}$. We have tested concurring and compensating changes in the pertinent and better-known [CH_4] sources and sinks. We cannot rule out that other combinations, or less understood processes (such as stratospheric-tropospheric exchange), explain or contribute to $\delta^{13}C_{(Atm)}$ trends. Three-dimensional inversions of regional variability in our data may provide further insights. Nevertheless, our findings allow for a likely reconstruction of recent CH_4 budget changes.

The $\delta^{13}C_{(Atm)}$ history suggests increasing ^{13}C-rich anthropogenic emissions since the industrial revolution (*2*). We show here that in the 1990s and early 2000s, ^{13}C-rich emissions likely stagnated or decreased. This signal is muted after the Mount Pinatubo eruption decreased OH and wetland emissions (*10*), as seen in model-data discrepancies (Figs. 2B and 3B) and possibly higher perturbation $\delta^{13}C_{(So)}$ (Fig. 2C) for 1993–1995. After 1995, the most parsimonious explanation for the observed emissions decrease is thermogenic reductions. Previous $\delta^{13}C_{(Atm)}$ studies provided contradicting results for thermogenic emissions (*9*, *11*, *31*); only (*11*) found reductions for ~1988–2002. Our result is consistent with combined bottom-up and top-down reconstructions finding "decreasing-to-stable" fossil-fuel sources during plateau onset (*8*). Also, ethane levels indicate declining annual thermogenic CH_4 emissions between 1984 and 2010 by >10 to 21 Tg (*32*), which is consistent with our 7.2 to 11.2 Tg/year average decrease. One possible cause is reduced fossil-fuel CH_4 emissions by 12 to 20 Tg/year through a collapse in production after the Soviet Union breakup in 1991 (*28*). Our results therefore support previous evidence for thermogenic reductions. Alternatively, OH variability with stagnant emissions provides an equally plausible explanation.

After 2006, the activation of biogenic emissions caused the renewed [CH_4] rise. The exact nature of this source is less clear. Possibly, emissions from waste treatment contributed, although their $\delta^{13}C_{(So)}$ ~ −55‰ is somewhat too ^{13}C-enriched, and inventories indicate no step change around 2007 (*21*, *22*). Arctic warming could have enhanced emissions from wetlands, thawing permafrost, and CH_4 hydrates (*5*). This was detected for 2007 but not afterward (*14*). The onset of the post-2006 trend in $\delta^{13}C_{(Atm)}$ in the 60° to 90°N latitude band seems to lag other latitudes (fig. S13),

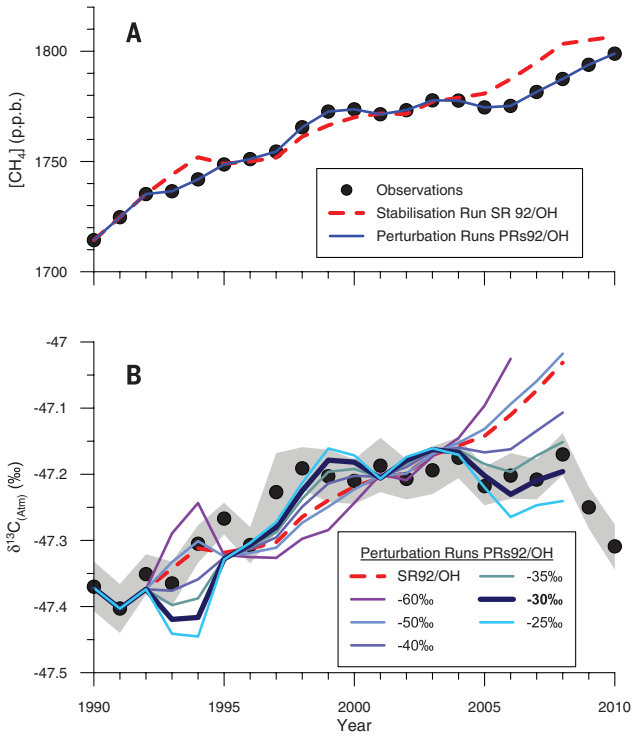


Fig. 3. OH-variability scenario for the onset of the 1999–2006 plateau. Symbols are as in Fig. 2. (**A** and **B**) SR92/OH (red dashed lines) includes OH variability (*29*) for 1994–2007, in addition to constant emissions after 1992 at average 1991–1992 and 1982–1992 levels for emission strength and $\delta^{13}C_{(So)}$, respectively. (A) In SR92/OH, sink variability (*29*) produces [CH_4] close to observations, leaving little room for source perturbations in PRs92/OH (average −2.6 Tg/year; blue line). This results from an OH-induced trend to lower atmospheric CH_4 residence time τ for 1993–1999, whereas the longer-term average (1993–2007) of τ is almost identical to the value used for the runs in Fig. 2. (B) PRs92/OH: best fit is for perturbation $\delta^{13}C_{(So)}$ = −30‰, but $\delta^{13}C_{(Atm)}$ trends for values between −25‰ and −50‰ all fit observations throughout most of the 1993–2006 perturbation period because OH variability and the associated changes in ε and τ alone can account for observed [CH_4] and $\delta^{13}C_{(Atm)}$ trends. Total $\delta^{13}C_{(So)}$ values for all runs are shown in fig. S14 and listed in table S4.

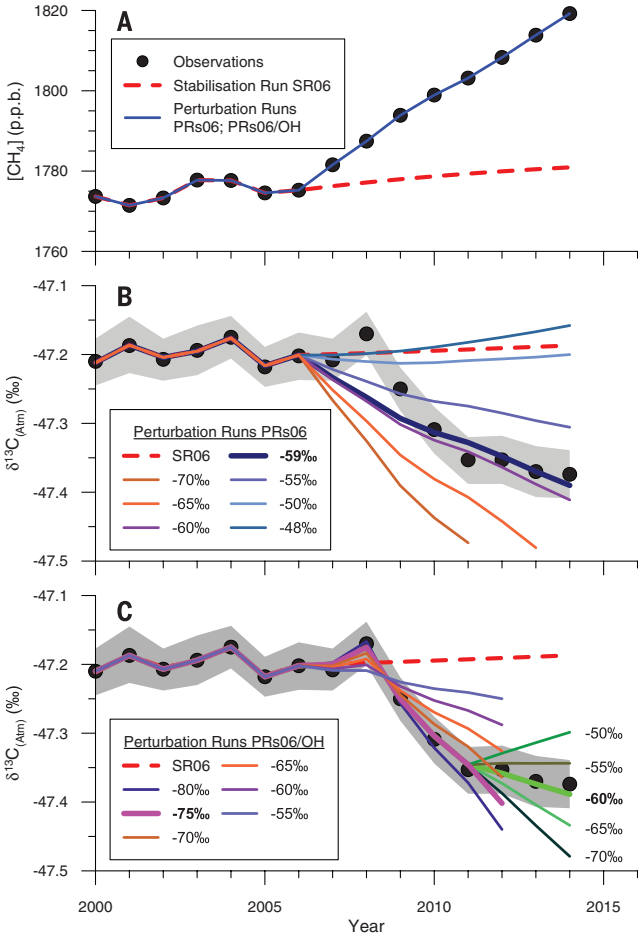


Fig. 4. Box-model results for the [CH_4] increase after 2006. Symbols are as in Fig. 2. (**A** to **C**) Two Stabilization Runs (red dashed lines) SR06 [(A) and (B)] and SR06/OH [(A) and (C)] produce the same trend in [CH_4], but different $\delta^{13}C_{(Atm)}$ for emissions held constant at average 1999–2006 levels from 2007 on. (A) PRs06 and PRs06/OH (yearly varying with average 19.7 Tg/year) reconcile modeled [CH_4] (blue line) with observations. (B) $\delta^{13}C_{(Atm)}$ trends for PRs06 with perturbation $\delta^{13}C_{(So)}$ values between −70‰ and −45‰. The thick line indicates best fit scenario for $\delta^{13}C_{(So)}$ = −59‰. (C) PRs06/OH for a combined scenario that includes (i) OH reconstructions (*29*) when available (1994–2007, no OH variability afterward); (ii) Perturbation A for 2007–2011 overlain on the OH variability (blue and orange lines), best fit for perturbation $\delta^{13}C_{(So)}$ = −75‰ (magenta line); and (iii) Perturbation B for 2011–2014 (green lines, using best-fit Perturbation A until 2011), best fit for perturbation $\delta^{13}C_{(So)}$ ~ −60‰ (bright green line). Total $\delta^{13}C_{(So)}$ values for all runs are shown in fig. S15 and table S4.

and post-2006 emissions rose mostly in the tropics, as shown in satellite CH_4 measurements (*13*). This footprint and the perturbation $\delta^{13}C_{(So)}$ fit tropical wetlands and agricultural emissions. Natural wetlands, the single largest CH_4 source, have been implicated in the post-2006 [CH_4] growth (*8*, *14*) under enduring La Niña conditions (*33*). The associated combination of higher wetland (*15*) and lower pyrogenic emissions (*16*) could explain strongly ^{13}C-depleted perturbations $\delta^{13}C_{(So)}$ for 2007–2011 (Fig. 4C). However, tropical wetland emissions are higher in the southern hemisphere (*19*), whereas remote sensing shows that [CH_4] increased mainly in the northern tropics and subtropics (*13*). Also, tropical wetlands are relatively ^{13}C-enriched (–52 to –60‰) and match our post-2006 perturbation not as well as rice cultivation (–59 to –65‰) and C_3-fed ruminants (–60 to –74‰) (*3*, *24*, *26*). This isotopic evidence against tropical wetlands is not strong, given the ranges of reported $\delta^{13}C_{(So)}$ for various sources. However, sustained source ^{13}C-depletion over 7 years with the potential for strong ^{13}C-depletion until 2011 is harder to reconcile with tropical wetlands as compared with other biogenic emissions, such as agricultural ones. Inventories report increased annual agricultural emissions over the 2000–2006 average of ~12 Tg by 2011, dominated by ruminants (*21*, *23*). This can largely account for the post-2006 [CH_4] growth, estimated at 15 to 22 Tg/year (*30*). Also, India and China's dominance in livestock emissions (*23*) and Southeast Asian rice cultivation are consistent with the location of the source increase (*13*). Although we cannot identify the specific biogenic source driving the [CH_4] increase with certainty, it is compatible with agricultural emissions. If so, feedbacks between climate change and natural CH_4 emissions (*5*) are not yet evident.

The finding of a predominantly biogenic post-2006 increase is robust. Further, it seems likely that fossil-fuel emissions stagnated or diminished in the 1990s. They are a minor contributor to the renewed [CH_4] rise. This contradicts emission inventories reporting increases of all source types between 2005 and 2010 with a major (~60%) thermogenic contribution (*21*, *22*). The predicted $\delta^{13}C_{(So)}$ ~ −48‰ (or more ^{13}C-enriched) produces a slight $\delta^{13}C_{(Atm)}$ increase that cannot be reconciled with the measured marked decline (Fig. 4B). The finding is unexpected, given the recent boom in unconventional gas production and reported resurgence in coal mining and the Asian economy (*21*, *22*). Our isotope-based analysis suggests that the [CH_4] plateau marks not a temporary suppression of a particular source but a reconfiguration of the CH_4 budget. Either food production or climate-sensitive natural emissions are the most probable causes of the current [CH_4] increase. These scenarios may require different mitigation measures in the future.

REFERENCES AND NOTES

1. C. MacFarling Meure *et al.*, *Geophys. Res. Lett.* **33**, L14810 (2006).
2. D. F. Ferretti *et al.*, *Science* **309**, 1714–1717 (2005).
3. E. J. Dlugokencky, E. G. Nisbet, R. Fisher, D. Lowry, *Philos. Trans. A Math. Phys. Eng. Sci.* **369**, 2058–2072 (2011).
4. D. T. Shindell *et al.*, *Science* **326**, 716–718 (2009).
5. E. A. G. Schuur *et al.*, *Nature* **520**, 171–179 (2015).
6. M. Rigby *et al.*, *Geophys. Res. Lett.* **35**, L22805 (2008).
7. K. R. Lassey *et al.*, *J. Integr. Environ. Sci.* **7** (suppl. 1), 109–117 (2010).
8. S. Kirschke *et al.*, *Nat. Geosci.* **6**, 813–823 (2013).
9. G. Monteil *et al.*, *Atmos. Chem. Phys.* **11**, 9141–9153 (2011).
10. N. Bândă, M. Krol, M. van Weele, T. van Noije, T. Röckmann, *Atmos. Chem. Phys.* **13**, 2267–2281 (2013).
11. P. Bousquet *et al.*, *Nature* **443**, 439–443 (2006).
12. A. Ghosh *et al.*, *Atmos. Chem. Phys.* **15**, 2595–2612 (2015).
13. S. Houweling *et al.*, *Atmos. Chem. Phys.* **14**, 3991–4012 (2014).
14. P. Bousquet *et al.*, *Atmos. Chem. Phys.* **11**, 3689–3700 (2011).
15. E. L. Hodson, B. Poulter, N. E. Zimmermann, C. Prigent, J. O. Kaplan, *Geophys. Res. Lett.* **38**, L08810 (2011).
16. G. R. van der Werf *et al.*, *Atmos. Chem. Phys.* **6**, 3423–3441 (2006).
17. M. G. Schultz *et al.*, *Global Biogeochem. Cycles* **22**, GB2031 (2008).
18. G. R. van der Werf *et al.*, *Atmos. Chem. Phys.* **10**, 11707–11735 (2010).
19. J. R. Melton *et al.*, *Biogeosciences* **10**, 753–788 (2013).
20. V. Naik *et al.*, *Atmos. Chem. Phys.* **13**, 5277–5298 (2013).
21. European Commission, Joint Research Centre/Netherlands Environmental Assessment Agency, Emission Database for Global Atmospheric Research (EDGAR) (version 4.2) (2011); available at http://edgar.jrc.ec.europa.eu.
22. U.S. Environmental Protection Agency, Global Anthropogenic Non-CO_2 Greenhouse Gas Emissions: 1990–2030 (U.S. EPA, 2012).
23. U.N. Food and Agriculture Organisation, FAOstat database (2014); available at http://faostat3.fao.org.
24. O. Bréas, C. Guillou, F. Reniero, E. Wada, *Isotopes Environ. Health Stud.* **37**, 257–379 (2001).
25. Materials and methods are available as supplementary materials on *Science* Online.
26. H. Schaefer, M. J. Whiticar, *Global Biogeochem. Cycles* **22**, GB1001 (2008).
27. K. R. Lassey, D. C. Lowe, M. R. Manning, *Global Biogeochem. Cycles* **14**, 41–49 (2000).
28. E. J. Dlugokencky *et al.*, *Geophys. Res. Lett.* **30**, 1992 (2003).
29. S. A. Montzka *et al.*, *Science* **331**, 67–69 (2011).
30. E. G. Nisbet, E. J. Dlugokencky, P. Bousquet, *Science* **343**, 493–495 (2014).
31. I. Levin *et al.*, *Nature* **486**, E3–E4 (2012).
32. I. J. Simpson *et al.*, *Nature* **488**, 490–494 (2012).
33. National Oceanic and Atmospheric Administration, C. P. C. Ocean Nino Index (2014); available at http://www.cpc.ncep.noaa.gov/products/analysis_monitoring/ensostuff/ensoyears.shtml.

ACKNOWLEDGMENTS

We thank S. Montzka for supplying OH-reconstruction data. M. Harvey and K. Steinkamp provided helpful discussions. Feedback from two anonymous reviewers improved the manuscript. Antarctica NZ supports air sampling at Arrival Heights, Antarctica (ARH). Raw data for individual stations measured by INSTAAR and NIWA are available from the World Data Centre for Greenhouse Gases http://ds.data.jma.go.jp/gmd/wdcgg/introduction.html; data from

INSTAAR are also available from ftp://aftp.cmdl.noaa.gov/data/trace_gases. Data from Heidelberg University are available from http://www.iup.uni-heidelberg.de/institut/forschung/groups/kk/en/Data_html. Data measured by University of Washington and University of California, Irvine, were taken from http://cdiac.ornl.gov/ndps/quay.html and http://cdiac.ornl.gov/epubs/db/db1022/db1022.html, respectively. Yearly δ^{13} C values for individual stations and global annual averages are presented in tables S3 and S4. This research was supported by the Marsden Fund Council from New Zealand Government funding, administered by the Royal Society of New Zealand. Further support came from NIWA under Climate and Atmosphere Research Programme CAAC1504 (2014/15 SCI). The authors declare no competing interests. H.S. designed the data analysis; G.W.B., T.M.B., R.J.M., J.B.M., D.C.L., B.H.V., C.V., and S.E.M. performed δ^{13}C measurements; C.V., J.B.M., I.L., D.C.L., and J.W.C.W. designed sampling and analytical programmes and performed data quality control; E.J.D. provided [CH_4] data; K.R.L. and H.S. designed the box model; S.E.M.F. and H.S. performed uncertainty analyses; and all authors contributed to the interpretation and the writing of the manuscript.

SUPPLEMENTARY MATERIALS

www.sciencemag.org/content/352/6281/80/suppl/DC1
Materials and Methods
Supplementary Text
Figs. S1 to S21
Tables S1 to S5
References (*34*–*47*)

19 August 2015; accepted 19 February 2016
10.1126/science.aad2705

CLIMATE CHANGE

Consistent response of bird populations to climate change on two continents

**Philip A. Stephens,[1] Lucy R. Mason,[2] Rhys E. Green,[2,3] Richard D. Gregory,[2] John R. Sauer,[4] Jamie Alison,[5] Ainars Aunins,[6] Lluís Brotons,[7,8,9] Stuart H. M. Butchart,[3,10] Tommaso Campedelli,[11] Tomasz Chodkiewicz,[12] Przemysław Chylarecki,[13] Olivia Crowe,[14] Jaanus Elts,[15,16] Virginia Escandell,[17] Ruud P. B. Foppen,[18,19,20] Henning Heldbjerg,[21] Sergi Herrando,[22] Magne Husby,[23] Frédéric Jiguet,[24] Aleksi Lehikoinen,[25] Åke Lindström,[26] David G. Noble,[27] Jean-Yves Paquet,[28] Jiri Reif,[29,30] Thomas Sattler,[31] Tibor Szép,[32] Norbert Teufelbauer,[33] Sven Trautmann,[34] Arco J. van Strien,[35] Chris A. M. van Turnhout,[19,20] Petr Vorisek,[30,36] Stephen G. Willis[1]*

Global climate change is a major threat to biodiversity. Large-scale analyses have generally focused on the impacts of climate change on the geographic ranges of species and on phenology, the timing of ecological phenomena. We used long-term monitoring of the abundance of breeding birds across Europe and the United States to produce, for both regions, composite population indices for two groups of species: those for which climate suitability has been either improving or declining since 1980. The ratio of these composite indices, the climate impact indicator (CII), reflects the divergent fates of species favored or disadvantaged by climate change. The trend in CII is positive and similar in the two regions. On both continents, interspecific and spatial variation in population abundance trends are well predicted by climate suitability trends.

Evidence that climate change is affecting biodiversity is accumulating (*1*). Most of this evidence reveals impacts on natural populations in the form of shifts in geographic ranges, changes in abundance, or changes in individual behavior or physiology (*2*, *3*). Meta-analyses have identified widespread changes, consistent with expectations, in both the distribution of populations and the timing of events in the annual cycles of organisms (*4*–*6*). A growing body of evidence also suggests that morphological changes are a common response to altered climates (*7*, *8*). However, despite some clear cases of climate-caused alterations of local population dynamics (*9*, *10*), multispecies, large-scale analyses of population responses to global climate change are rare (*11*, *12*).

One way to assess widespread population responses to anthropogenic drivers is to derive indicators from composite trends of species' abundance (*13*). Multispecies indicators are now widely used to aggregate biodiversity information in a way that is understood by policy-makers and members of the public, enabling evaluations of progress toward biodiversity targets (*14*, *15*). Less frequently, differences in composite trends for groups of species differentially affected by change are used to highlight the role of specific drivers of abundance. For example, large-scale aggregated trends in European species' abundance have been linked to expected future changes in climatic suitability within the region to produce composite trends for species that are expected either to gain or to lose climatically suitable range in the future (*16*). One shortcoming of that approach is that relating changes in a species' population at a subcontinental level to climate change ignores important information about variation in population trends in different areas within the subcontinent. A species showing climate-driven decline at the low-latitude range margin but climate-driven increase at its poleward range margin (*17*) might not show a clear overall trend in abundance across its range. Furthermore, accounting for spatial variation in species' population trends will reduce covariation between climate change and land-use change (*18*).

[1]Conservation Ecology Group, School of Biological and Biomedical Sciences, Durham University, South Road, Durham DH1 3LE, UK. [2]Royal Society for the Protection of Birds, Centre for Conservation Science, The Lodge, Sandy, Bedfordshire SG19 2DL, UK. [3]Conservation Science Group, Department of Zoology, University of Cambridge, Downing Street, Cambridge CB2 3EJ, UK. [4]United States Geological Survey, Patuxent Wildlife Research Center, 12100 Beech Forest Road, Laurel, MD 20708, USA. [5]Institute of Integrative Biology, University of Liverpool, Crown Street, Liverpool L69 3BX, UK. [6]Faculty of Biology, University of Latvia, Jelgavas iela 1, Riga, LV-1004, Latvia. [7]Center for Mediterranean Forest Research, Centre Tecnològic Forestal de Catalunya, InForest JRU, Solsona 25280, Spain. [8]REAF, Cerdanyola del Vallès 08193, Catalonia, Spain. [9]CSIC, Cerdanyola del Vallès 08193, Catalonia, Spain. [10]BirdLife International, The David Attenborough Building, Pembroke Street, Cambridge CB2 3QZ, UK. [11]MITO2000 National Committee; c/o Dream Italia, Via Garibaldi 3, 52015, Pratovecchio-Stia, Arezzo, Italy. [12]Ogólnopolskie Towarzystwo Ochrony Ptaków, Odrowąża 24,05-270 Marki, Poland. [13]Museum and Institute of Zoology, Polish Academy of Sciences, Wilcza 64, 00-679 Warszawa, Poland. [14]BirdWatch Ireland, Unit 20 Block D Bullford Business Campus, Kilcoole, County Wicklow, Ireland. [15]Institute of Ecology and Earth Sciences, University of Tartu, Vanemuise Street 46, 51014 Tartu, Estonia. [16]Estonian Ornithological Society, Veski 4, 51005 Tartu, Estonia. [17]Sociedad Española de Ornitología/BirdLife Melquiades Biencinto, 34, 28053 Madrid. Spain. [18]European Bird Census Council, Post Office Box 6521, 6503 GA Nijmegen, Netherlands. [19]Sovon Dutch Centre for Field Ornithology, Post Office Box 6521, 6503 GA Nijmegen, Netherlands. [20]Department of Animal Ecology and Ecophysiology, Institute for Water and Wetland Research, Radboud University, Post Office Box 9010, 6500 GL Nijmegen, Netherlands. [21]Dansk Ornitologisk Forening–BirdLife Denmark and University of Aarhus, Vesterbrogade 140, 1620 København V, Denmark. [22]European Bird Census Council–Catalan Ornithological Institute, Natural History Museum of Barcelona, Plaça Leonardo da Vinci 4-5, 08019 Barcelona, Catalonia, Spain. [23]Section for Science, Nord University, 7600 Levanger, Norway. [24]UMR7204 Sorbonne Universités-MNHN-CNRS-UPMC, CESCO, CRBPO, CP 135, 43 Rue Buffon, 75005 Paris, France. [25]The Helsinki Lab of Ornithology, Finnish Museum of Natural History, Post Office Box 17, 00014 University of Helsinki, Finland. [26]Biodiversity Unit, Department of Biology, Lund University, Ecology Building, S-223 62 Lund, Sweden. [27]The British Trust for Ornithology, The Nunnery, Thetford, Norfolk IP24 2PU, UK. [28]Natagora, Département Études, Rue Nanon 98, B-5000 Namur, Belgium. [29]Institute for Environmental Studies, Faculty of Science, Charles University in Prague, Czech Republic. [30]Department of Zoology and Laboratory of Ornithology, Faculty of Science, Palacký University Olomouc, 17 Listopadu 50, 771 43 Olomouc, Czech Republic. [31]Swiss Ornithological Institute, Seerose 1, 6204 Sempach, Switzerland. [32]Institute of Environmental Sciences, University of Nyíregyháza, Sóstói út 31/b, 4400 Nyíregyháza, Hungary. [33]BirdLife Austria, Museumsplatz 1/10/8, A-1070 Vienna, Austria. [34]Dachverband Deutscher Avifaunisten e.V. (Federation of German Avifaunists), An den Speichern 6, D-48157 Münster, Germany. [35]Statistics Netherlands, Post Office Box 24500, 2490 HA The Hague, Netherlands. [36]Pan-European Common Bird Monitoring Scheme, Czech Society for Ornithology, Na Bělidle 252/34, CZ-15000 Prague 5, Czech Republic.
***Corresponding author. E-mail: s.g.willis@durham.ac.uk**

Downloaded from on March 31, 2016

We developed an indicator to quantify the impacts of recent climate change on breeding range abundance in common birds, accounting for regional variation in both climate impacts and population trends. We applied this approach to two distinct subcontinents to evaluate, for the first time, how recent climate change has affected large numbers of species over extensive biogeographical regions. Developing our indicator involves six steps, including (1) selecting species abundance data for analysis; (2) fitting species' distribution models to species' occurrence data and concurrent long-term mean climate values for a single fixed time period, and applying those models to annual climate data to determine how climate suitability has changed for each species in each country or state in which it occurs; (3) checking that these climate suitability trends are informative predictors of abundance trends; (4) deriving composite multispecies abundance indices for each state or country, separately for species with positive climate suitability trends (hereafter, the CST+ group) and for those with negative climate suitability trends (the CST– group); (5) amalgamating country- or state-level information to produce subcontinental CST+ and CST– indices; and (6) contrasting the CST+ and CST– indices to produce a climate impact indicator (CII), which reflects the divergent fates of species favored and disadvantaged by climate change.

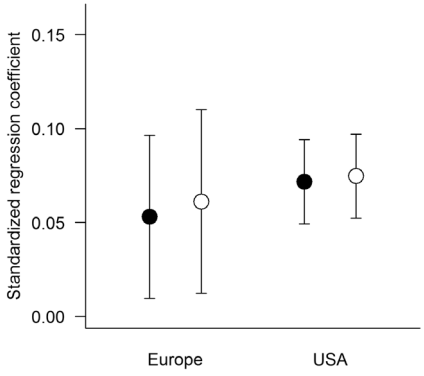


Fig. 1. Effect of climate suitability on bird population trends. Standardized regression coefficient of population trend at a country/state level on CST (with 90% confidence intervals) for European breeding birds (left two points) and U.S. breeding birds (right two points). Coefficients are from model averaging of multiple regression models (which consider body mass, habitat, and migratory behavior) of population trend on CST (solid circles) or from univariate models of population trend on CST (open circles) (*20*). All models contained the random effects of country/state and species.

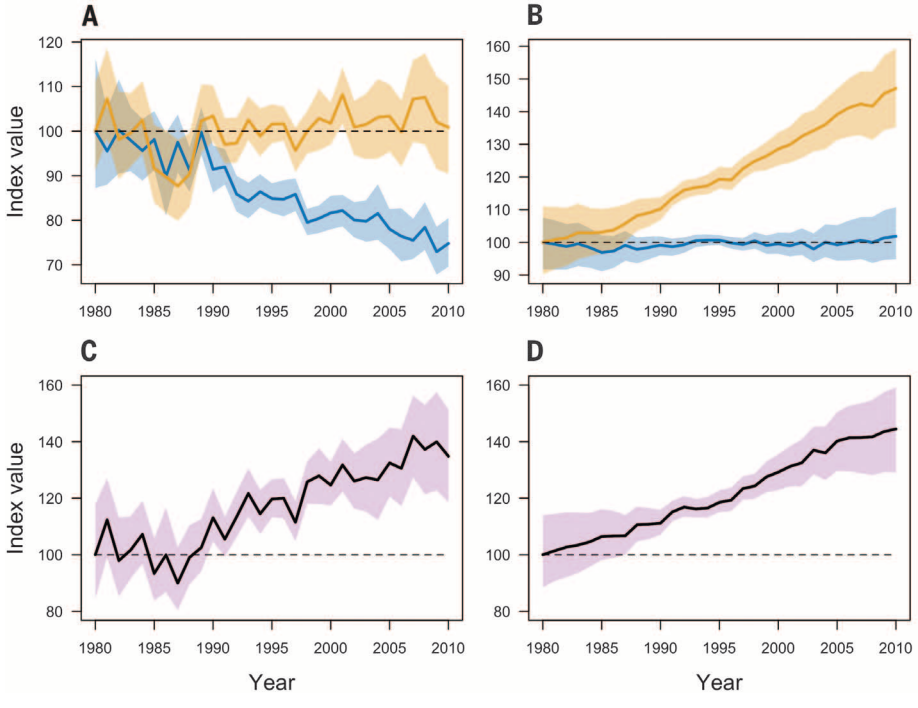


Fig. 2. Effect of climate on abundance trends of common birds. Multispecies population indices for CST+ (orange lines) and CST– (blue lines) groups combined across all eligible countries of Europe (**A**) and states of the United States (**B**). Shaded polygons in each case indicate 90% confidence intervals (produced from 2000 bootstrap replicates) (*20*). Annual values of the ratio of the CST+ index to the CST– index, the CII, are shown for Europe (**C**) and the United States (**D**). In all four panels, the index is arbitrarily set to 100 in 1980. Horizontal dashed lines at index values of 100 show the expectation if there is no trend; in (C) and (D), these indicate the expectation if climatic suitability played no role, and thus there was no difference in the composite trends for CST+ and CST– groups.

For Europe, we assessed indices of abundance for 145 species monitored by the Pan-European Common Birds Monitoring Scheme (*15*). For the United States, we used indices of abundance for 380 species monitored by the North American Breeding Bird Survey (BBS) (*19*). In both cases, we used data spanning the period from 1980 to 2010. To account for regional variation in climate impacts and species' trends, we used species' distribution models to identify the climate suitability trend for each species at the level of individual countries in Europe or states in the United States. The species' distribution models allow the calculation of probability of occurrence of the species under a particular combination of climatic conditions, represented by bioclimate variables (*20*), using species' distribution maps and concurrent long-term mean climate data. The climate suitability trend for a species represents the trend in its expected annual probability of occurrence, as derived from species' distribution models applied to annual climate data (*20*). These climate suitability trends are derived entirely independently of interannual changes in abundance within a focal species' range. We used linear mixed models to check that climate suitability trend was an informative explanatory variable for country- or state-level population trends, when potential confounding effects of life history and ecological covariates were allowed for (Fig. 1).

We allocated species at a country/state level to two groups: those expected from the species' distribution models to have been advantaged (climate suitability trend slope >0) or disadvantaged (climate suitability trend slope <0) by climate change during the study period (the CST+ and CST– groups). We derived composite population indices for both groups at the individual country or state level (see tables S1 and S2 for sample sizes in Europe and the United States, respectively). Individual species may occur in either group in different parts of their range. Within countries or states, composite population indices were derived by weighting abundance indices by the magnitude of species' climate suitability trends within CST+ and CST– groups (*20*). The result is that changes in populations of species that we expect (from species' distribution models) to be markedly affected by climate change would receive more weight in the composite index than would those of species for which the climate suitability trend was negligible. To produce subcontinental-scale composite indices for CST+ and CST– groups, composite indices for each group were combined without weighting (Fig. 2, A and B) (*20*).

The ratio of these indices (CST+:CST–), the CII (standardized to 100 in 1980), will be >100 in any year if populations expected to have been positively affected by climate change have increased more or declined less than those expected to have been negatively affected. We derived subcontinental CII values separately for Europe and the United

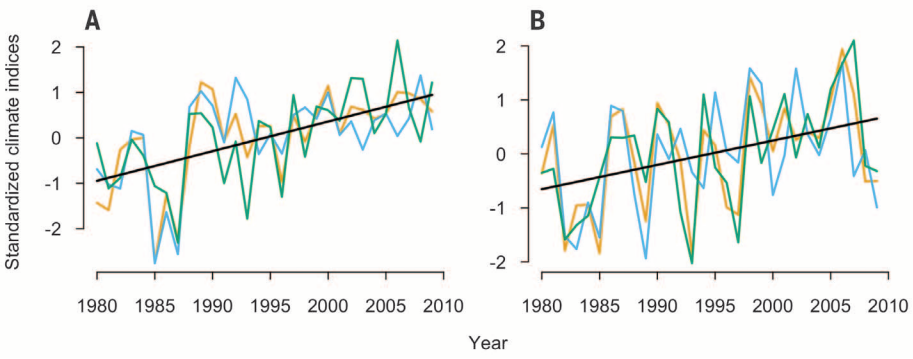


Fig. 3. Recent changes in climate in Europe and the United States. Changes in annual values of three measures of climate in the countries/states from which bird data were collected in Europe (**A**) and the United States (**B**): mean annual temperature (blue lines), mean temperature of the coldest month (orange lines), and growing degree days above 5°C (green lines). Each variable is standardized to have zero mean and unit variance. Black lines show a least-squares regression fitted to the annual standardized values for all three variables combined. Analysis of covariance provided no support for different slopes for the three climate variables or differences between Europe and the United States.

States (combining country and state CIIs, respectively) (*20*). Calculating CIIs for these geographically distinct subcontinents with very different breeding bird species assemblages allows us to examine the transferability of our approach. Plotting these CII values over time can demonstrate long-term trends in the response of species to climate. Because recent climate change is likely to have manifested itself in different ways across the two subcontinents, a common trend in the magnitude and direction of the CII would provide compelling evidence that recent climate change is affecting populations of many species across extensive areas of the world.

Overall trajectories of avian abundance in recent decades differ somewhat between the two subcontinents, suggesting rather different ecological backdrops. Specifically, the average trend of avian abundance in Europe has been largely negative since 1980 (*21*), whereas the average trend of avian abundance in the United States has been relatively stable over recent decades (*22*). This difference is reflected in the composite indices: Although the CST+ group index has been largely static in Europe and the CST– group has declined, in the United States these groups have shown a pronounced increase (CST+) or remained stable (CST–). Nevertheless, in both regions, the CST+ and CST– indices show a striking divergence, in the expected direction, with the composite population indices of species in the former group being markedly more positive than those in the latter group.

The ratio of the CST+ to CST– composite indices amalgamated to the subcontinental scale gives the subcontinental CIIs (Fig. 2, C and D). The CII for Europe is based on fewer species, fewer geographic subdivisions, and a less-consistent duration of monitoring across the region. This results in it being more variable than that for the United States. Nevertheless, trends in the two CIIs show some striking similarities. In particular, both clearly deviate from a value of 100 (indicating the divergence of the CST+ and CST– groups) by the mid- to late 1980s. Both then climb strongly to reach an index value of about 140 by 2010, highlighting the markedly stronger performance of species in the CST+ group. An analysis of standardized climate variables over the period shows no evidence for differences in the rate or scale of climate change in the two regions (Fig. 3) (*20*).

The strength and consistency of the CII across two very different assemblages (only six species are common to both), which appear to be experiencing very different overall population trends, provide evidence that this phenomenon is not peculiar to a single subcontinent. Isolating the contribution of climate change on the two subcontinents from that of other potential drivers of avian population change should stimulate further research into the factors that underlie the strong differences between the United States and Europe in the trajectories of composite multispecies trends (both CST+ and CST–) (Fig. 2, A and B). In both areas, the CII is more strongly positive than a previous index for Europe that linked multispecies trends in population size at a subcontinental level to the expected future effects of climate change (*16*). This emphasizes the value of using geographic variation of species' trends within the range and allowing a species to contribute to both the CST+ and CST– groups, according to differences in the suitability trend in different areas.

The widespread changes that we detect are based on the commonest bird species across a diversity of ecosystems in Europe and the United States. For example, the 145 European species we consider make up about 89% of the total number of individual terrestrial breeding birds in Europe (*23*). Common species dominate ecosystems, and even small changes in their abundance can lead to large changes in ecosystem structure, function, and service provision (*24*). Therefore, the changes that we have detected in common birds are already likely to be affecting ecosystems and associated services. If similar abundance changes are occurring across common species in other taxa, ecosystems may be further affected. Impacts arising from changes in bird abundances will become more pronounced if their populations continue to follow their current climate-influenced trajectories. Although our index is based on the abundance of common bird species, population trends of rare species have also been shown to be related to climatic changes (*25*). Our indicator could be applied wherever sufficient monitoring data exist. However, because long-term population monitoring data sets are rare for large tropical and subtropical regions and for the Southern Hemisphere (*26*), we cannot evaluate whether the changes we have observed apply globally. Population monitoring at low latitudes and in the Southern Hemisphere should be a future priority to identify climate-driven changes that might be occurring in these areas.

Ecological indicators, including some indicators of climate change impacts, are already being used to monitor the global state of ecosystems (*13*). Our precursor CII (*16*), based on future climate projections, has been adopted as an indicator to assess progress toward achieving the United Nations Convention on Biological Diversity's Aichi biodiversity targets (*27*), as a metric of climate change impacts on terrestrial ecosystems. The new indicators we have developed provide a first means of assessing impacts of contemporary climate on the abundance of populations, and we have shown their utility across two large areas of the world. Future updates of the CII should provide a valuable means to track the extent of impact of future climate change on species.

REFERENCES AND NOTES

1. C. B. Field *et al.*, in *Climate Change 2014: Impacts, Adaptation, and Vulnerability. Part A: Global and Sectoral Aspects. Contribution of Working Group II to the Fifth Assessment Report of the Intergovernmental Panel on Climate Change* (Cambridge Univ. Press, 2014), pp. 1–32.
2. M. M. Humphries, D. W. Thomas, J. R. Speakman, *Nature* **418**, 313–316 (2002).
3. C. Bellard, C. Bertelsmeier, P. Leadley, W. Thuiller, F. Courchamp, *Ecol. Lett.* **15**, 365–377 (2012).
4. T. L. Root *et al.*, *Nature* **421**, 57–60 (2003).
5. C. Parmesan, G. Yohe, *Nature* **421**, 37–42 (2003).
6. I. C. Chen, J. K. Hill, R. Ohlemüller, D. B. Roy, C. D. Thomas, *Science* **333**, 1024–1026 (2011).
7. J. L. Gardner, A. Peters, M. R. Kearney, L. Joseph, R. Heinsohn, *Trends Ecol. Evol.* **26**, 285–291 (2011).
8. J. A. Sheridan, D. Bickford, *Nat. Clim. Change* **1**, 401 (2011).
9. A. Ozgul *et al.*, *Nat. Clim. Change* **466**, 482 (2010).
10. M. van de Pol *et al.*, *Ecology* **91**, 1192–1204 (2010).
11. V. Devictor *et al.*, *Nat. Clim. Change* **2**, 121–124 (2012).
12. J. G. Illán *et al.*, *Glob. Change Biol.* **20**, 3351–3364 (2014).
13. S. H. M. Butchart *et al.*, *Science* **328**, 1164–1168 (2010).
14. D. P. Tittensor *et al.*, *Science* **346**, 241–244 (2014).
15. Biodiversity Indicators Partnership, www.bipindicators.net/ (2014).
16. R. D. Gregory *et al.*, *PLOS One* **4**, e4678 (2009).
17. F. Jiguet *et al.*, *Proc. Biol. Sci.* **277**, 3601–3608 (2010).
18. M. Clavero, D. Villero, L. Brotons, *PLOS One* **6**, e18581 (2011).
19. North American Breeding Bird Survey, www.pwrc.usgs.gov/bbs/ (2014).
20. See the supplementary materials on *Science* Online.
21. EBCC, www.ebcc.info/index.php?ID=510 (2014).
22. J. R. Sauer, W. A. Link, *Auk* **128**, 87–98 (2011).
23. BirdLife-International, *Birds in Europe: Population Estimates, Trends and Conservation Status* (BirdLife International, Cambridge, 2004).
24. K. J. Gaston, R. A. R. Fuller, *Trends Ecol. Evol.* **23**, 14–19 (2008).

25. R. E. Green *et al.*, *Biol. Lett.* **4**, 599–602 (2008).
26. World Wildlife Fund, *Living Planet Report 2014: Species and Spaces, People and Places* (WWF, Gland, Switzerland, 2014).
27. Aichi Targets Passport, www.bipindicators.net/resource/aichipassport (2014).

ACKNOWLEDGMENTS

The climate suitability and population trend data for individual species at the country/state level are provided as supplementary material (table S6) (*20*). Climate data are available from www.worldclim.org/. This work has been part-funded by the Royal Society for the Protection of Birds, the European Environment Agency, the European Commission, and Durham University's Grevillea Trust. We thank A. Teller and K. Biała for support; M. Flade, J. Schwarz, and C. Grüneberg for data provision; and M. Clement (U.S. Geological Survey) and two anonymous referees for comments on an earlier draft.

SUPPLEMENTARY MATERIALS

www.sciencemag.org/content/352/6281/84/suppl/DC1
Materials and Methods
Fig. S1
Tables S1 to S8
References (*28*–*64*)

5 May 2015; accepted 25 February 2016
10.1126/science.aac4858

CONFLICT BEHAVIOR

Social conflict resolution regulated by two dorsal habenular subregions in zebrafish

Ming-Yi Chou,[1] Ryunosuke Amo,[1]* Masae Kinoshita,[1] Bor-Wei Cherng,[1,2] Hideaki Shimazaki,[3] Masakazu Agetsuma,[1]† Toshiyuki Shiraki,[1] Tazu Aoki,[1] Mikako Takahoko,[1] Masako Yamazaki,[1]‡ Shin-ichi Higashijima,[4] Hitoshi Okamoto[1,2,5]§

When animals encounter conflict they initiate and escalate aggression to establish and maintain a social hierarchy. The neural mechanisms by which animals resolve fighting behaviors to determine such social hierarchies remain unknown. We identified two subregions of the dorsal habenula (dHb) in zebrafish that antagonistically regulate the outcome of conflict. The losing experience reduced neural transmission in the lateral subregion of dHb (dHbL)–dorsal/intermediate interpeduncular nucleus (d/iIPN) circuit. Silencing of the dHbL or medial subregion of dHb (dHbM) caused a stronger predisposition to lose or win a fight, respectively. These results demonstrate that the dHbL and dHbM comprise a dual control system for conflict resolution of social aggression.

Aggression is an evolutionarily conserved behavior critical for animal survival (*1*, *2*). When conflict is unavoidable, animals use aggression to establish a social hierarchy that determines how to share limited resources (*2*). Most animal conflicts aim at establishing a social hierarchy rather than causing lethal damage to opponents (*1*–*4*), which achieves the best cost-benefit for the group. However, the biological mechanisms governing the resolution of social conflict remain largely unknown. To address this question, we isolated adult male zebrafish for 24 hours and then put them together to fight in pairs (Fig. 1A) (*5*). Dyadic male zebrafish fights proceed in a stereotypic manner, starting with each animal exhibiting display behaviors, followed by circling and biting attacks, and ending when one fish shows fleeing behavior indicating surrender (Fig. 1B and movie S1) (*5*).

To investigate the neural circuits underlying the regulation of social conflict, we focused on the dorsal habenula–interpeduncular nucleus (dHb-IPN) pathway. We previously demonstrated that the lateral subregion of the zebrafish dHb (dHbL) sends axons to the dorsal IPN (dIPN) and the intermediate IPN (iIPN) (Fig. 1C), and efferent axons from the d/iIPN pass through the dorsal raphe to reach the dorsal tegmental area (DTA) (*6*, *7*) containing a putative region corresponding to the mammalian periaqueductal gray (PAG) (Fig. 2A). Because the PAG regulates fight, flight, and freezing behaviors (*8*), we wondered if the dHbL-d/iIPN pathway signals information critical for fight and flight behaviors during aggressive conflicts. We performed calcium imaging of acute brain slices to visualize neural activity after electrical stimulation of the Hb (Fig. 2A and fig. S1). In both naïve and winner fish, we found an intense activity spot in the dIPN and scattered spots in the DTA region (Fig. 2, B and C, and movies S2 and S3), reflecting activation of the dHbL-d/iIPN-DTA pathway. In contrast, in loser fish we observed intense activity mainly in the ventral IPN (vIPN) and the median raphe (MR) (Fig. 2D and movie S4). In the dIPN, the peak of fluorescence intensity in winners was similar to that in naïve fish but was significantly reduced in losers (Fig. 2E). In the vIPN, we found a higher fluorescence intensity in loser fish than in winner and naïve fish, although it did not reach statistical significance (Fig. 2E).

To further investigate neural activity of the dHbL-d/iIPN and dHbM-i/vIPN circuits in winner and loser states, we performed in vivo electrophysiological recordings of local field potential (LFP) in the IPN (Fig. 2F). In the dIPN, the LFP amplitude evoked by electrical stimulation in the left Hb was similar between winners and naïve fish but was significantly reduced in losers (Fig. 2, G and H). In contrast, naïve fish, winners, and losers showed similar LFP levels in the vIPN (Fig. 2, G and H) (*9*). Reduction in the transmission of the dHbL-d/iIPN circuit thus reflects a loser state, consistent with our calcium imaging data. The peak time latency and half decay time were similar among all conditions (fig. S2). Moreover, tract tracing results showed that the dIPN neurons coursed dorsally and caudally to extend to the DTA (Fig. 2I), whereas the vIPN neurons projected to the MR (Fig. 2J), which is consistent with our previous data (*6*) and supports our calcium imaging results.

To investigate how the dHbL-d/iIPN and dHbM-i/vIPN pathways participate in fighting behaviors, we perturbed these neural circuits in adult zebrafish. To silence the dHbL-d/iIPN pathway, we used a double transgenic line *Tg*(*narp:GALVP16*);*Tg* [*UAS:tetanus neurotoxin* (*TeNT*)] in which neurotransmission from the dHbL to the d/iIPN is selectively inhibited (*6*). We confirmed that TeNT is specifically expressed in the dHbL, by checking its expression in the *Tg*(*narp:GALVP16*);*Tg*(*UAS:TeNT*);*Tg*(*brn3a-hsp70:GFP*) zebrafish (Fig. 3A), and effectively blocks neurotransmission (fig. S3). To inhibit the dHbM-i/vIPN pathway, we first generated a transgenic line *Tg*(*gpr151:GALVP16*);*Tg* (*UAS:GFP-TeNT*) and then confirmed the gpr151: GALVP16-induced green fluorescent protein (GFP) expression in the dHb (Fig. 3B-1). Next, we crossed the *Tg*(*brn3a-hsp70:GFP-Cre*) with a glutamatergic neuron-specific line, *Tg*(*vglut2a:loxP-DsRed-loxP-GFP*) (*10*), in which glutamatergic neurons in the dHbM and ventral Hb (vHb) express GFP (Fig. 3B-2). Finally, we generated a triple transgenic line *Tg*(*gpr151:GAL4VP16*);*Tg*(*brn3a-hsp70:GFP-Cre*);*Tg*(*UAS:loxP-DsRed-loxP-GFP-TeNT*) in which GFP-TeNT was induced intersectionally only in the dHbM, and their axons could be observed in the vIPN (Fig. 3B-3 and fig. S4). These two Tg lines showed normal growth at developmental and adult stages, and the Hb-IPN circuit and structures throughout the whole brain were not affected (fig. S4) (*6*).

Next, we let the dHbL- and the dHbM-silenced fish fight against their wild-type (WT) siblings.

[1]Laboratory for Developmental Gene Regulation, RIKEN Brain Science Institute, Saitama 351-0198, Japan. [2]Department of Life Sciences, Graduate School of Arts and Sciences, University of Tokyo, Tokyo 153-8902, Japan. [3]Laboratory for Neural Computation and Adaptation, RIKEN Brain Science Institute, Saitama 351-0198, Japan. [4]National Institutes of Natural Sciences, Okazaki Institute for Integrative Bioscience, National Institute for Physiological Sciences, Aichi 444-8787, Japan. [5]Laboratory for Molecular Brain Science, Department of Life Science and Medical Bioscience, Waseda University, Tokyo 162-8430, Japan.
*Present address: Department of Molecular and Cellular Biology, Center for Brain Science, Harvard University, Massachusetts 02138, USA. †Present address: The Institute of Scientific Research and Industrial Research, Osaka University, Osaka 567-0047, Japan. ‡Present address: Department of Bioengineering, School of Engineering, University of Tokyo, Tokyo 153-8902, Japan.
§Corresponding author. E-mail: hitoshi@brain.riken.jp

Downloaded from on March 31, 2016

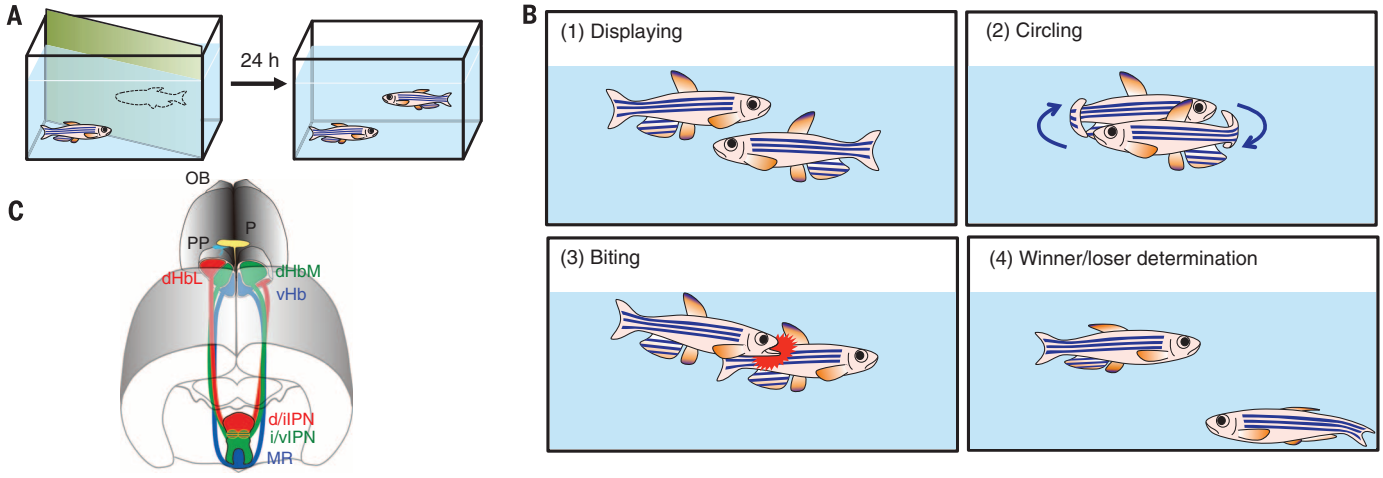


Fig. 1. Schematic illustration of fighting behavioral task and the Hb-IPN circuit. (**A**) Schematic illustration of the fighting behavioral task. (**B**) Schematic illustration of dyadic fighting behaviors in male zebrafish. (**C**) Schematic illustration showing a dorsal oblique view of the axon projections from the dHbL to the d/iIPN (red), the dHbM to the i/vIPN (green), and the vHb to the MR (blue) in the adult zebrafish brain. OB, olfactory bulb; PP, para-pineal organ.

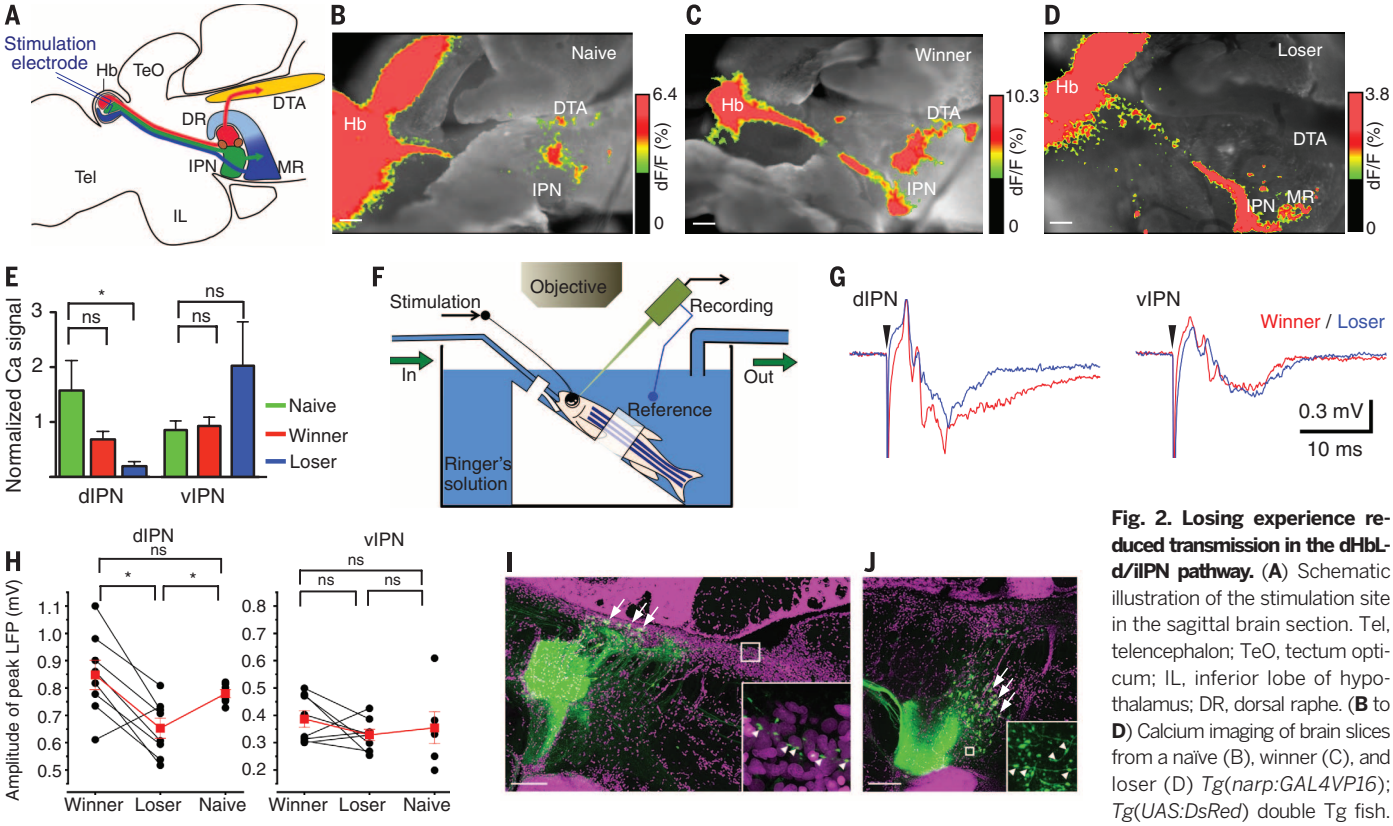


Fig. 2. Losing experience reduced transmission in the dHbL-d/iIPN pathway. (**A**) Schematic illustration of the stimulation site in the sagittal brain section. Tel, telencephalon; TeO, tectum opticum; IL, inferior lobe of hypothalamus; DR, dorsal raphe. (**B** to **D**) Calcium imaging of brain slices from a naïve (B), winner (C), and loser (D) *Tg*(*narp:GAL4VP16*); *Tg*(*UAS:DsRed*) double Tg fish. (**E**) Average peak calcium signal in the dIPN (naïve fish, 1.58 ± 0.55, n = 5 fish; winner, 0.68 ± 0.15, n = 9 fish; loser, 0.20 ± 0.08, n = 8 fish; P = 0.0132, Kruskal-Wallis test with Dunn's multiple comparison test) and the vIPN (naïve fish, 0.84 ± 0.16; winner, 0.91 ± 0.16; loser, 1.99 ± 0.78; P = 0.2034, Kruskal-Wallis test). (**F**) Schematic illustration of electrophysiology recording in vivo. (**G**) Extracellular responses evoked by electrical stimulation to the left Hb in the IPN. Five traces were averaged for each condition. The arrowheads indicate the timing of stimulation. (**H**) Comparison of the peak LFP amplitude recorded from the dIPN (naïve fish, 0.78 ± 0.02 mV, n = 6 fish; winner, 0.85 ± 0.05 mV, n = 8 fish; loser, 0.65 ± 0.04 mV, n = 8 fish; P = 0.0066, Kruskal-Wallis test with Dunn's multiple comparison test) and the vIPN (naïve fish, 0.35 ± 0.05 mV; winner, 0.39 ± 0.03 mV; loser, 0.33 ± 0.03 mV; P = 0.5685, Kruskal-Wallis test). The black circles indicate individual values, and the red squares indicate the average for each group. Data from a pair undertaking fighting behavior are linked by a black line. (**I** and **J**) Tract tracing by Neurobiotin. The efferents from the dIPN terminated in the DTA (I). The inset in (I) is a close-up view of the boxed area in (I) showing the efferents with boutons (arrowheads). Retrogradely labeled neurons were observed in the DTA (arrows). (J) The efferents from the vIPN terminated in the MR. The inset in (J) is a close-up view of the boxed area in (J) showing the efferents with boutons (arrowheads). Retrogradely labeled neurons were found in the MR (arrows). Scale bars, 100 μm. Error bars in (E) and (H), mean ± SEM. *P < 0.05; ns, not significant.

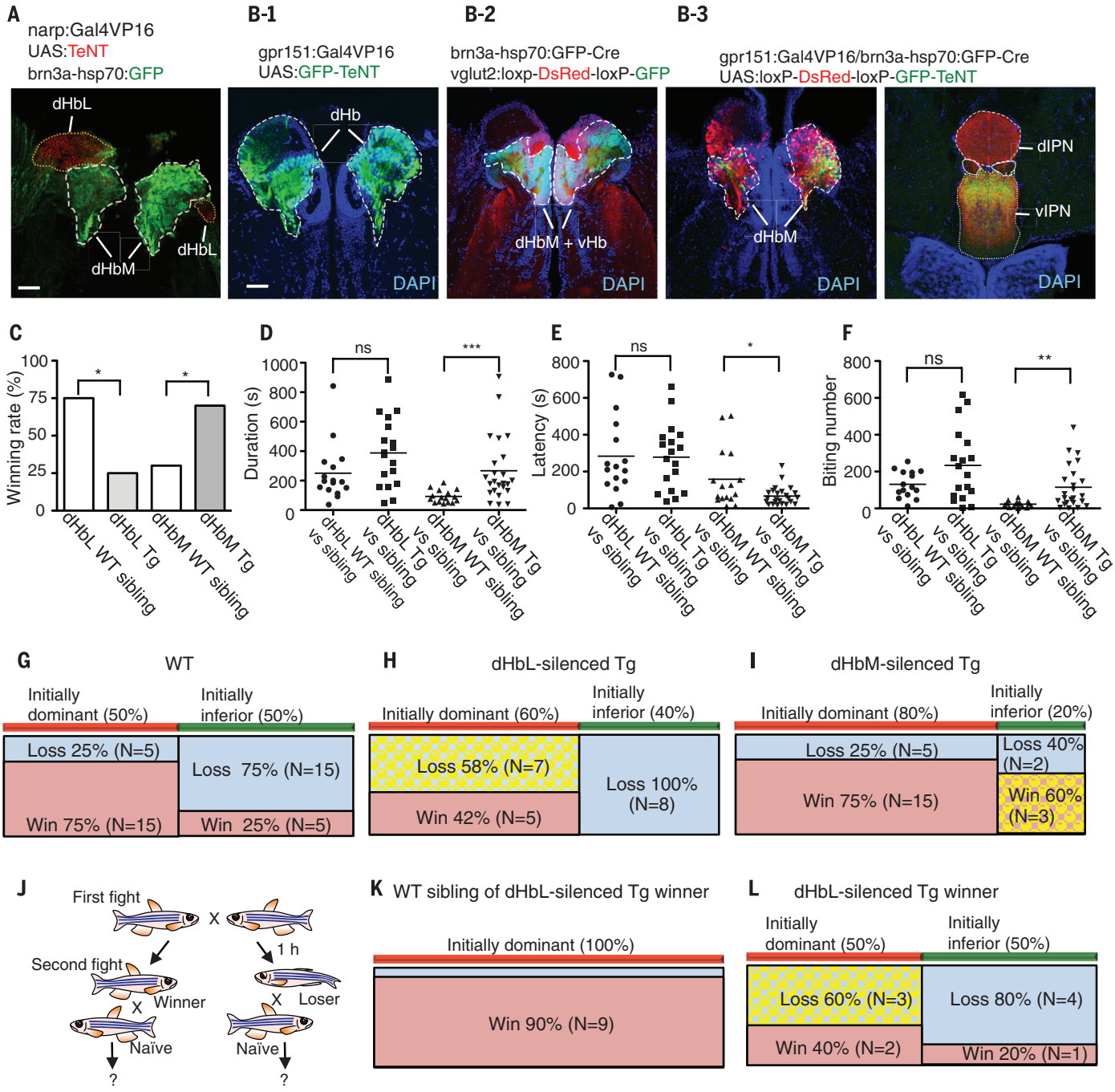


Fig. 3. Inactivation of the dHbL-d/iIPN and the dHbM-i/vIPN circuits differentially affects fight outcome. (**A**) In situ hybridization of TeNT (red) and immunofluorescent staining of GFP (green; for detection of brn3a-hsp70:GFP) in coronal sections of adult *Tg(narp:GAL VP16);Tg(UAS:TeNT);Tg(brn3a-hsp70:GFP)* fish brain. (**B**) Immunofluorescent staining of GFP (green; for detection of GFP-TeNT) and DsRed (red) in the coronal sections of adult *Tg(gpr151:GAL VP16);Tg(UAS:GFP-TeNT)* (B-1), *Tg(brn3a-hsp70:GFP-Cre);Tg(vglut2a:loxP-DsRed-loxP-GFP)* (B-2), and *Tg(gpr151:GAL VP16);Tg(brn3a-hsp70:GFP-Cre);Tg(UAS:loxP-DsRed-loxP-GFP-TeNT)* (B-3) fish brain. (**C**) The winning rate of the dHbL-silenced Tg against the WT sibling was significantly lower than the chance rate (0.5) (n = 20 fights; P = 0.02069, binomial test), and the rate of the dHbM-silenced Tg against the WT sibling was significantly higher than the chance rate (0.5) (n = 27 fights; P = 0.02612, binomial test). (**D** to **F**) Comparison of fighting duration (D) (dHbL WT sibling versus sibling, 250 ± 48.6 s, n = 15 fights; dHbL-silenced Tg versus WT sibling, 387 ± 54.9 s, n = 18 fights; P = 0.0555; dHbM WT sibling versus sibling, 962.7 ± 10.8 s, n = 16 fights; dHbM-silenced Tg versus WT sibling, 266.8 ± 45.2 s, n = 24 fights; P = 0.0008, Mann-Whitney test), latency (E) (dHbL WT sibling versus sibling, 283.6 ± 55.4 s; dHbL-silenced Tg versus WT sibling, 278.6 ± 42.3 s; P = 0.9431; dHbM WT sibling versus sibling, 158.6 ± 39.6 s; dHbM-silenced Tg versus WT sibling, 67.3 ± 10.4 s; P = 0.012, unpaired t test), and biting number (F) (dHbL WT sibling versus sibling, 130.7 ± 18.7; dHbL-silenced Tg versus WT sibling, 234.4 ± 46.1; P = 0.0638; between dHbM WT sibling versus sibling, 23.1 ± 4.1; and dHbM-silenced Tg versus WT sibling, 114.9 ± 24.1; P = 0.0039, unpaired t test). (**G** to **I**) The fighting result and initially dominant rate of WT (G), the dHbL-silenced Tg (H), and the dHbM-silenced Tg (I) fish when they fought against their WT siblings. (**J**) Schematic illustration of behavioral task for testing experience effects in zebrafish fight. (**K** and **L**) The fighting result and initially dominant rate of the dHbL WT sibling winners (K) and the dHbL-silenced winners (L) when they fought against naïve WT siblings in the second fight. Scale bars, 50 μm. Bars in (D), (E), and (F) represent the average of each group. *P < 0.05; **P < 0.01; ***P < 0.001; ns, not significant.

The dHbL-silenced fish showed a significantly higher tendency (15 out of 20, 75%) to lose fights (Fig. 3C). We also confirmed that the result does not vary among the groups that were raised separately according to different birth dates (see the supplementary text). This predisposition to losing is not simply due to weaker physical fitness of the Tg fish. The duration, latency, and number of bites ("biting number") of fights were similar between the fights of WT siblings versus WT siblings and those of the dHbL-silenced fish versus WT siblings (Fig. 3, D to F) [also see the results of a swimming performance test for physical fitness evaluation (fig. S5, movie S5, and materials and methods)]. Moreover, anxiety level, locomotion activity, and aggressiveness level (measured by the novel tank-diving test, open-field test, and mirror-biting test) of the dHbL-silenced fish were also similar to those of WT siblings (figs. S6 and S7A, and materials and methods). In contrast, the dHbM-silenced fish tended to win (19 out of 27, 70%) (Fig. 3C). The latency of a fight was significantly shorter in the fights of the dHbM-silenced fish versus WT siblings than that in those of WT siblings versus WT siblings (Fig. 3E), although the mirror-biting frequency was similar (fig. S7B). Physical fitness, anxiety level, locomotion capability, and the responses to conditioned stimuli after cued fear conditioning were similar between the dHbM-silenced fish and their WT siblings (figs. S5, S6, and S8).

We next analyzed time-lapse changes in biting frequencies during the whole fighting period. In WT fish, individuals that bit more frequently than their opponents during the first one or two minutes of the fight tended to win (15 out of 20, 75%), indicating that initial dominance could be an effective predictor of fighting results (Fig. 3G, fig. S9, and table S1). The results of fights were not caused by individual intrinsic fitness. Indeed, as previously reported, at 1 hour after the first fight, WT zebrafish exhibited "winner effects." A previous winning experience increases the probability of winning the subsequent contest (*5*). However, when we identified and separated both winner and loser for 24 hours and let them fight against another naïve fish, we found that the previous winner and loser did not show a higher probability of winning or losing the subsequent contests (figs. S10 and S11 and tables S2 and S3).

The WT siblings of the dHbL- and dHbM-silenced fish also showed a fighting pattern similar to WT fish (fig. S12 and S13 and tables S4 and S5). In the pairs of the dHbL-silenced fish versus WT siblings, all the WT siblings that showed initial dominance won the fight (Fig. 3H, fig. S14, and table S6). In contrast, only 42% of the dHbL-silenced fish that showed initial dominance won (Fig. 3H), even though these Tg fish did not show a lower rate in becoming initially dominant (n = 20 fish; P = 0.8684, binomial test) (Fig. 3H). When the dHbM-silenced fish fought against their WT siblings, they showed a significantly higher tendency to be initially dominant (80%) than their WT siblings (20%) (n = 25 fish; P = 0.002039, binomial test) (Fig. 3I, fig. S15, and table S7). Among 20 Tg fish that showed initial dominance, 15 fish won (Fig. 3I). Quite intriguingly, three out of five (60%) dHbM-silenced fish that showed initial inferiority eventually won (Fig. 3I). These results indicate that the dHbM-silenced fish showed a higher tendency to win than their WT siblings, even when they were initially inferior.

As mentioned above, at 1 hour after the first fight, WT zebrafish exhibited "winner effects." We investigated whether the same effect also held true in the dHbL-silenced fish (Fig. 3J). We found that 90% of WT siblings of the dHbL-silenced fish that won the first fight also won a second fight against a naïve fish (Fig. 3K). All WT sibling winners of the first fight showed initial dominance in the second fight (Fig. 3K, fig. S16, and table S8). In contrast, only 30% of the dHbL-silenced winners won the second fight (3 out of 10). The winning rate of the dHbL-silenced winners in the second fight was similar to that when the naïve dHbL-silenced fish fought against their WT siblings, as described above (Fig. 3C), indicating that previous winning experiences did not increase the probability for winning the subsequent fight in the dHbL-silenced fish. Only 50% of the dHbL-silenced winners of the first fight showed initial dominance in the second fight, and 60% of these lost the second fight (Fig. 3L, fig. S17, and table S9). The impairment of winner effects in the dHbL-silenced fish was not due to accumulated fatigue during the first fight, because the duration and biting number of the second fight was not reduced compared with the first fight (fig. S18). In contrast, we did not observe a higher winning tendency in the dHbM-silenced loser fish. Most the dHbM-silenced losers and their WT siblings lost in the second fight, as did most of the WT losers (loser effects).

The mechanisms by which the dHbL-d/iIPN and dHbM-i/vIPN circuits facilitate winner and loser behaviors may be due to their projections to the DTA and MR, respectively. The reduction in transmission of the dHbL-d/iIPN pathway with an accompanying reduction in the activity of the DTA (Fig. 2D) that contains a putative homologous brain region of the mammalian PAG might switch fish behaviors from attacking to fleeing. On the other hand, the dHbM-i/vIPN pathway may increase the tendency to lose through inhibitory outputs to repress the activity of the MR that was proposed to reduce anxiety- and depressive-like behaviors by increasing resilience to aversive stimuli (*11*). As the dHbL and dHbM antagonistically modulate the outcome of fights, it is possible that the interaction between these two regions determines the fighting results. Because we did not find neural connections between the dHbL and the dHbM, neural activity and interaction between the dIPN and the vIPN may play a key role in regulating fight resolution. Therefore, it is possible that the dHb-IPN pathway acts as a binary switchboard to affect fight outcomes. The left and right dHbL and dHbM are known to show characteristic size asymmetry (Fig. 1C) (*12*). A recent study demonstrated that impairment of epithalamic left-right asymmetry increases anxiety in zebrafish (*13*). Thus, it is intriguing to examine whether disruption of left-right asymmetry also influences the outcomes of fights. In addition, we found that loss of the ventral Hb (vHb)-raphe transmission impairs proper loser behaviors to avoid further attacks from the winners (see fig. S19 and movies S6 and S7 for details) (*14*). In conclusion, different parts of the Hb differentially regulate the social conflict—i.e., the two subregions of the dHb regulate the resolution of the social conflict, and the vHb contributes to the maintenance of the loser behaviors.

REFERENCES AND NOTES

1. P. Lindenfors, B. S. Tullberg, *Adv. Genet.* **75**, 7–22 (2011).
2. I. D. Chase, K. Seitz, *Adv. Genet.* **75**, 51–81 (2011).
3. E. A. Kravitz, R. Huber, *Curr. Opin. Neurobiol.* **13**, 736–743 (2003).
4. C. Rutte, M. Taborsky, M. W. Brinkhof, *Trends Ecol. Evol.* **21**, 16–21 (2006).
5. R. F. Oliveira, J. F. Silva, J. M. Simões, *Zebrafish* **8**, 73–81 (2011).
6. M. Agetsuma *et al*., *Nat. Neurosci.* **13**, 1354–1356 (2010).
7. M. F. Wullimann, B. Rupp, H. Reichert, *Neuroanatomy of the Zebrafish Brain: A Topological Atlas* (Birkhauser Verlag, 1996).
8. R. Bandler, K. A. Keay, N. Floyd, J. Price, *Brain Res. Bull.* **53**, 95–104 (2000).
9. The apparent discrepancy between LFP and calcium imaging of the vIPN may be because the LFP reflects the summation of excitatory postsynaptic potentials and calcium imaging reflects the summation of whole-cell excitation.
10. C. Satou, Y. Kimura, S. Higashijima, *J. Neurosci.* **32**, 1771–1783 (2012).
11. E. D. Paul, C. A. Lowry, *J. Psychopharmacol.* **27**, 1090–1106 (2013).
12. H. Aizawa *et al*., *Curr. Biol.* **15**, 238–243 (2005).
13. L. Facchin, E. R. Duboué, M. E. Halpern, *J. Neurosci.* **35**, 15847–15859 (2015).
14. The vHb-silenced Tg fish showed lower physical fitness and higher tendency to lose (fig. S19). The result of impairment of proper loser behaviors in the vHb-silenced fish is consistent with our previous conclusion (*15*) that the vHb activity reflects a negative expectation value and is essential for learning adaptive avoidance behavior.
15. R. Amo *et al*., *Neuron* **84**, 1034–1048 (2014).

ACKNOWLEDGMENTS

We thank K. Kawakami for providing the Tol2 and *pT2MUASTeTxLC* constructs, RIKEN Advanced Science Institute's advanced technology support division for production of experimental chambers, C. Yokoyama for advice in preparing the manuscript, and R. Nakayama for assistance in the identification of transgenic fish line. We thank all members of the Okamoto laboratory for support and advice, the Research Resource Center of RIKEN Brain Science Institute for animal care, and the National BioResource Project of Japan for fish strains. All requests for the materials (strains and plasmids) should be made to H.O. They are made available upon exchange of a materials transfer agreement. This work was supported by a Grant in Aid for Scientific Research (23120008) and Strategic Research Program for Brain Science from the Ministry of Education, Culture, Sports, Science and Technology of Japan and the Core Research for Evolutional Science and Technology, Japan Science and Technology Agency, Japan. The supplementary materials contain additional data.

SUPPLEMENTARY MATERIALS

www.sciencemag.org/content/352/6281/87/suppl/DC1
Materials and Methods
Supplementary Text
Figs. S1 to S19
Tables S1 to S9
Movies S1 to S7
References (*16*–*22*)

3 July 2015; accepted 5 February 2016
10.1126/science.aac9508

IMMUNE REGULATION

A long noncoding RNA associated with susceptibility to celiac disease

Ainara Castellanos-Rubio,[1] Nora Fernandez-Jimenez,[2] Radomir Kratchmarov,[1] Xiaobing Luo,[3] Govind Bhagat,[4,5] Peter H. R. Green,[5] Robert Schneider,[6] Megerditch Kiledjian,[3] Jose Ramon Bilbao,[2] Sankar Ghosh[1]*

Recent studies have implicated long noncoding RNAs (lncRNAs) as regulators of many important biological processes. Here we report on the identification and characterization of a lncRNA, lnc13, that harbors a celiac disease–associated haplotype block and represses expression of certain inflammatory genes under homeostatic conditions. Lnc13 regulates gene expression by binding to hnRNPD, a member of a family of ubiquitously expressed heterogeneous nuclear ribonucleoproteins (hnRNPs). Upon stimulation, lnc13 levels are reduced, thereby allowing increased expression of the repressed genes. Lnc13 levels are significantly decreased in small intestinal biopsy samples from patients with celiac disease, which suggests that down-regulation of lnc13 may contribute to the inflammation seen in this disease. Furthermore, the lnc13 disease-associated variant binds hnRNPD less efficiently than its wild-type counterpart, thus helping to explain how these single-nucleotide polymorphisms contribute to celiac disease.

Roughly 80% of the phenotype-related loci identified by genome-wide association studies (GWAS) of many human diseases map to noncoding genome regions. Long noncoding RNAs (lncRNAs) represent a large portion of noncoding regions across the genome (*1*); however, the link between the GWAS phenotype–related loci on lncRNA expression or function—and the implications for disease—remain uncharacterized (*2*, *3*). Celiac disease (CeD) is a chronic, immune-mediated intestinal disorder that is caused by intolerance to ingested gluten and develops in genetically susceptible individuals (*4*, *5*). Recent studies have revealed 39 non–human lymphocyte antigen regions associated with a risk of CeD development, including many in noncoding regions (*6*–*8*).

Among the 14 CeD-associated intergenic single-nucleotide polymorphisms (SNPs) identified by GWAS (table S1) (*9*), rs917997 is 1.5 kb apart from the 3′ end of the *IL18RAP* coding gene in chromosome 2. This region harbors a total of five other CeD-associated SNPs that are transmitted with rs917997 as a haplotype block. No transcript had been mapped to this region in the human genome, although in the positionally equivalent conserved region in mouse, a gene (lnc13) encoding a 2.8-kb transcript has been classified as noncoding, which partly sense-overlaps with the *Il18rap* gene (*10*) (fig. S1A). Using 5′ and 3′ rapid amplification of cDNA ends, we defined the ends of mouse lnc13, confirming that although the 5′ end of lnc13 overlaps with the 3′ end of Il18rap, the two RNAs are independent (fig. S1B). Polymerase chain reaction (PCR) products generated using PCR primer pairs located along the Il18rap and lnc13 cDNAs (fig. S1C), as well as Northern blot analysis (fig. S1D), further demonstrate that Il18rap and lnc13 are independent transcripts.

As this region is highly conserved between mice and humans (66.5% identity by TransMap alignment, 59% identity by pairwise alignment) (figs. S1B and S2A), we hypothesized that an equivalent lncRNA might exist in the human genome. Intestinal cell RNA sequencing (RNA-seq), histone modification, chromatin signature, and deoxyribonuclease hypersensitivity site (DHS) data, together with RNA-seq signals in different tissues (*11*), support the presence of an expressed transcript in this region (fig. S2, A and B). Although the exact ends of the human lncRNA remain to be determined, we confirmed the existence of a DHS, which typically denotes a regulatory region such as an active promoter, close to the predicted 5′ end of the human lncRNA (fig. S3A). DHSs were shown to precede both the *IL18RAP* gene and the *lnc13* gene, supporting their independent expression (fig. S3A). Expression of processed, polyadenylated, and capped human lnc13 was confirmed in the U937 myeloid cell line (fig. S3B), where lnc13 is expressed at a low level of ~10 molecules per cell (fig. S3C), similar to other lncRNAs (*12*, *13*). Moreover, RNA in situ hybridization of intestinal paraffin-embedded sections using RNAscope technology (*14*) confirmed expression of human lnc13 (Fig. 1A).

Differential expression of lnc13 in different human tissues indicates a possible tissue-specific role (fig. S3D). As our main focus was the intestinal epithelia, given its role in CeD, we examined the presence of the lnc13 transcript in situ in the lamina propria (Fig. 1A) and whole-villi sections of small intestinal biopsy samples (fig. S4A). Biopsies from CeD patients appeared to have substantially lower amounts of lnc13 compared with controls (Fig. 1A and fig. S4A). Quantitation of the decrease of lnc13 in intestinal biopsies of patients with CeD revealed that lnc13 was significantly down-regulated in tissues from patients compared with healthy controls (Fig. 1B). In contrast, the expression of the overlapping *IL18RAP* coding gene was increased in patient samples (fig. S4B). Both lamina propria lymphocytes (LPLs) and intraepithelial lymphocytes from the small intestine express lnc13, but the decreased level was observed only in the LPL fraction, pointing to a cell type–specific regulation.

We found that the subcellular localization of lnc13 is primarily nuclear in both mouse and human macrophages (fig. S4, C and D). In situ hybridization on small intestinal biopsies also showed nuclear localization of lnc13 in the mononuclear cells of the lamina propria (fig. S4E). Together, the nuclear localization, the poor Kozak consensus sequence in the predicted open reading frame, and the absence of Pfam domains as assessed by the ATGpr (*15*) and European Molecular Biology Laboratory–European Bioinformatics Institute InterPro prediction programs (*16*) strongly suggested that lnc13 is unlikely to encode a protein product.

To further characterize lnc13, we stimulated mouse bone marrow–derived macrophages (BMDMs) with lipopolysaccharide (LPS) to mimic an inflammatory environment, as evidenced by the accompanying increase in interleukin-6 (IL-6) (Fig. 1C). Consistent with observations in CeD patients, the level of lnc13 decreased significantly upon LPS stimulation (Fig. 1C and fig. S5A), whereas Il18rap levels showed a transient increase (fig. S5A). Similar results were seen in immortalized bone marrow–derived mouse macrophages (iBMMs) and monocytic cells from the human U937 line (fig. S5, B and C). The LPS-induced decrease of lnc13 is dependent on Myd88 and NF-κB (Fig. 1D and fig. S5, D and E), consistent with the observation that NF-κB is constitutively active in the mucosa of patients with CeD (*4*). The lack of Myd88 did not affect Il18rap induction but does affect IL-12 (Fig. 1D and fig. S5F). In the absence of NF-κB signaling (Fig. 1D and fig. S5, D and E), we observed an increase in lnc13 expression, which suggests that lnc13 is continuously transcribed as a stable lncRNA (fig. S5G) that is degraded by a pathway dependent on NF-κB signaling.

We compared expression changes of lnc13 with those of 92 protein-coding genes with established inflammatory roles. After LPS stimulation, differentially expressed genes were grouped by their temporal expression pattern (*17*) (table S2). The expression pattern of the *Traf2*, *Stat1*, *Stat3*, *Tnfsf10*, *Il2ra*, *Ccl12*, *Myd88*, *Csf3*, and *Il1ra* genes inversely correlated with changes in lnc13 (Fig. 2A). Expression of four of these genes (*TRAF2*, *STAT1*, *IL1RA*, and *MYD88*) was significantly increased in biopsies from CeD patients, which suggests that lnc13

[1]Department of Microbiology and Immunology, Columbia University, College of Physicians and Surgeons, New York, NY 10032, USA. [2]Department of Genetics, Physical Anthropology, and Animal Physiology, University of the Basque Country (UPV-EHU), BioCruces Research Institute, Leioa 48940, Basque Country, Spain. [3]Department of Pathology and Cell Biology, Columbia University, College of Physicians and Surgeons, New York, NY 10032, USA. [4]Center for Celiac Disease, Department of Medicine, Columbia University, College of Physicians and Surgeons, New York, NY 10032, USA. [5]Alexandria Center for Life Sciences, New York University School of Medicine, New York, NY 10016, USA. [6]Department of Cell Biology and Neuroscience, Rutgers, The State University of New Jersey, Piscataway, NJ 08854, USA.
*Corresponding author. E-mail: sg2715@columbia.edu

Downloaded from on March 31, 2016

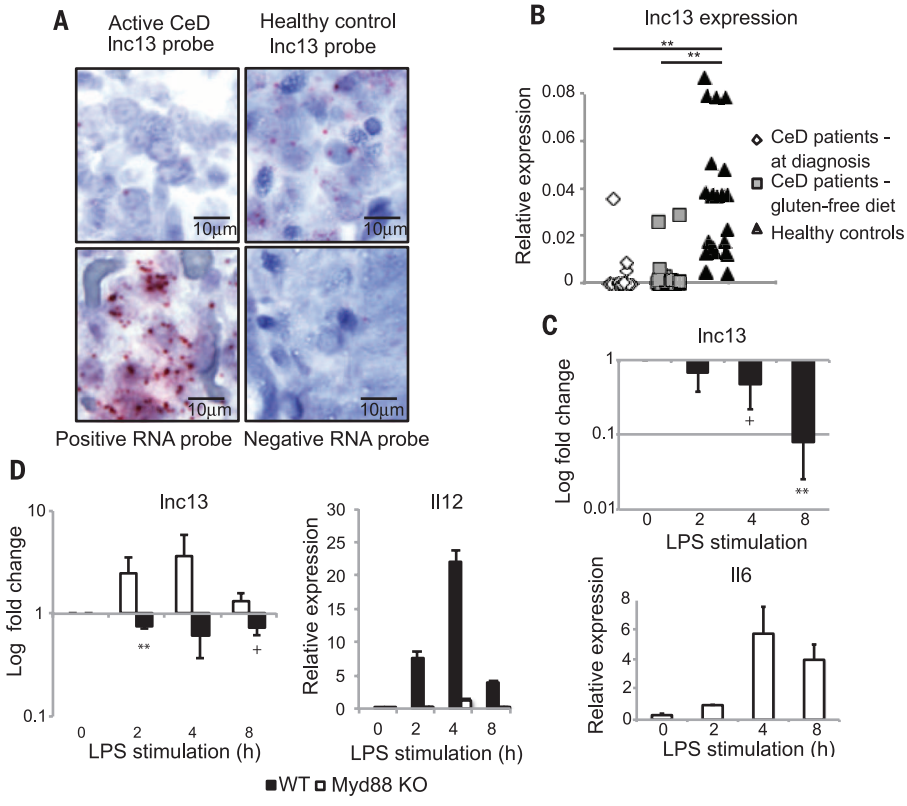


Fig. 1. Lnc13 is an inflammation-dependent lncRNA whose expression is decreased in patients with CeD. (**A**) Lnc13 expression in human intestinal lamina propria was detected by RNAscope technology. Representative pictures of five samples per condition are shown. Positive control: PPIB; negative control: bacterial dapB. (**B**) Quantitative expression ($2^{-\Delta Ct}$) of human lnc13 using a custom TaqMan expression assay in small intestinal biopsies of control and CeD patients. $^{**}P < 0.01$; unpaired two-sample *t* test. (**C**) Quantitative expression of mouse lnc13 (top) and a stimulation control (IL-6) (bottom) in response to LPS time-course stimulation in primary macrophages. Results represent average and SE (error bars) of three independent experiments. $^{**}P < 0.01$, $^{+}P < 0.1$; unpaired *t* test. (**D**) LPS-induced modulation of lnc13 (left) and IL-12 control (right) levels in WT and Myd88 KO BMDMs extracted from three pairs of mice. Data represent the average and SE of three independent experiments. $^{**}P < 0.01$, $^{+}P < 0.1$; unpaired *t* test.

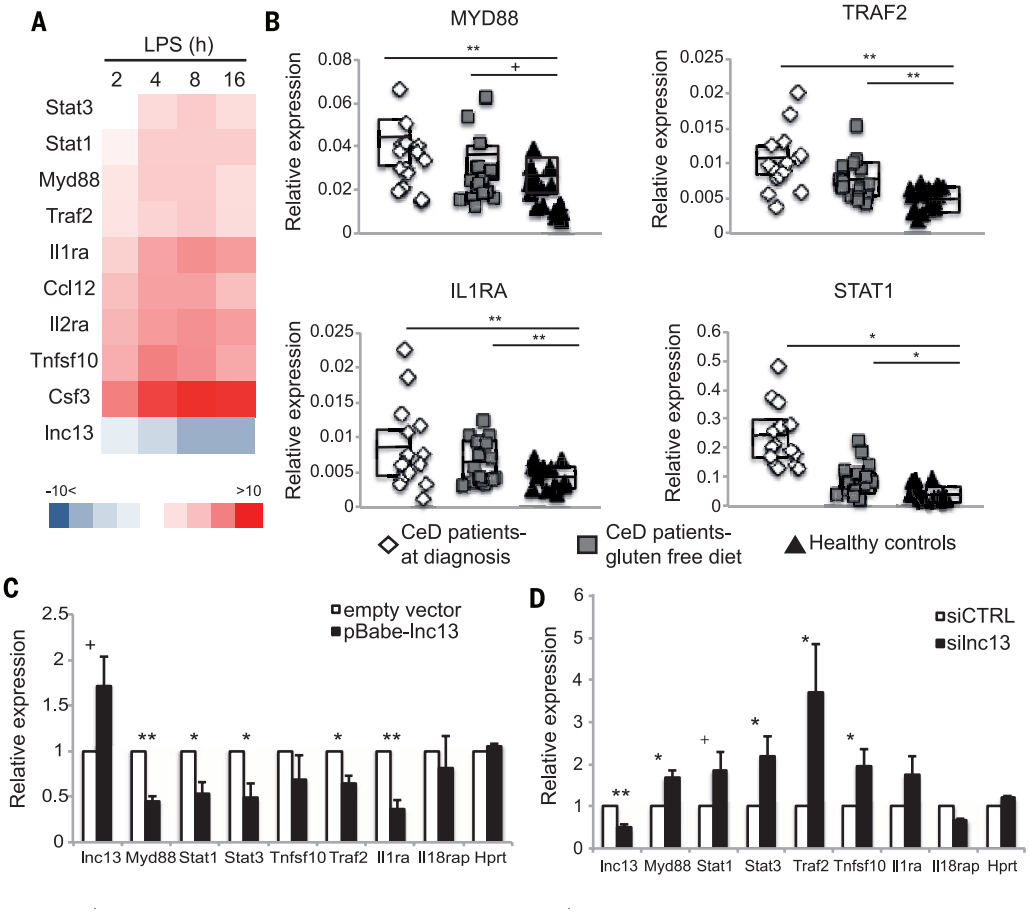


Fig. 2. Lnc13 regulates a subset of CeD-related inflammatory genes. (**A**) Heat map of the differential expression of a cluster of NF-κB–regulated genes that exhibit expression kinetics highly correlated with lnc13 expression kinetics in response to LPS stimulation (correlation coefficient $R > 0.8$) of BMDMs. (**B**) Celiac disease patients present significantly higher levels of the coexpressed genes indicated in (A), as measured by reverse transcription (RT)–QPCR. Horizontal lines represent average values; white rectangles span the 25th and 75th percentile in each group. $^{**}P < 0.01$, $^{*}P < 0.05$, $^{+}P = 0.05$; unpaired *t* test. (**C**) Immortalized macrophage cell line stably overexpressing lnc13 by a retroviral pBabe-puro vector shows decreased expression of target genes. Data represent the average and SE of four independent experiments. $^{**}P < 0.01$, $^{*}P < 0.05$, $^{+}P \leq 0.1$; unpaired *t* test. (**D**) Immortalized macrophages show lower levels of lnc13 after transfection of custom small interfering RNAs, using the HiPerfect reagent. Lower lnc13 levels result in increased expression of the target genes. Data represent the average and SE of four independent experiments. $^{**}P < 0.01$, $^{*}P < 0.05$, $^{+}P \leq 0.1$; unpaired *t* test.

levels affect this subset of inflammatory genes (Fig. 2B). Increased levels of lnc13 reduced the expression of the predicted targets, as listed above (Fig. 2C), whereas reduction of lnc13 had the opposite effect (Fig. 2D and fig. S5, H and I), demonstrating a link between lnc13 and the target genes. *IL-15* and *Il18rap* (Fig. 2, C and D, and fig. S5, I and J), which have been associated with CeD pathogenesis (*18*, *19*), did not show significant expression changes upon alteration of lnc13 levels, suggesting that lnc13 affects the expression of a certain subset, but not all the genes that have been implicated in CeD pathogenesis.

We observed that de novo transcription and protein synthesis are involved in the reduction of lnc13 observed in LPS-treated macrophages and CeD biopsies (fig. S6A). The high stability of lnc13 (fig. S5G) points to a posttranscriptional regulation of this lncRNA. Given the involvement of NF-κB (fig. S5E) and MyD88 (Fig. 1F and fig. S5D) in lnc13 regulation, we hypothesized that LPS-induced activation of NF-κB, through a MyD88-dependent pathway, leads to synthesis of a protein that is responsible and necessary for the reduction of lnc13 RNA. Decapping enzymes, which destabilize capped mRNAs and lncRNAs, have been described to regulate lncRNA levels (*20*). The expression pattern of decapping protein 2 (Dcp2) was inversely correlated with the level of lnc13 in LPS-stimulated iBMMs (Fig. 3A and fig. S5B) and BMDMs (Fig. 1C and fig. S6B). An increase of total (fig. S6, C and D) and nuclear Dcp2 (Fig. 3B and fig. S6E) after LPS stimulation in mouse and human macrophages was also observed. Furthermore, biopsies of CeD patients showed increased DCP2 expression (Fig. 3C) and relatively higher levels of nuclear Dcp2 as compared with controls (Fig. 3D). iBMMs and BMDMs from Dcp2 hypomorphic knockout (KO) mice (*21*) stimulated with LPS do not show lnc13 down-regulation (Fig. 3E and fig. S6F), and accumulation of the lnc13 transcript was seen after LPS stimulation in KO mice, strongly suggesting that Dcp2 recognizes lnc13 and causes its degradation. The same pattern was observed when we used human cell lines mutant for the Dcp2 catalytic domain or Dcp2 KO (fig. S6G). Dcp2 functions by binding RNA to recognize the cap for hydrolysis (*22*). Structural features at the 5′ end of RNA transcripts are known to be essential for Dcp2 targeting (*22*). We observed that wild-type (WT) lnc13 binds Dcp2 significantly more effectively than the 5′ lnc13 mutants (Fig. 3F), which were predicted to have an altered 5′ loop structure (fig. S6H). These results suggest that recognition of lnc13 by Dcp2 in inflamed tissue contributes to the degradation of lnc13 and the ensuing induction of a subset of inflammatory genes.

Nuclear lnc13 was almost exclusively localized to the chromatin fraction (Fig. 4A), which suggests that it might regulate expression of target genes by recruiting accessory factors to chromatin, similar to the proposed mechanism of other characterized lncRNAs such as lnc-COX2 or HOTAIR (*23*, *24*). The recently described RNA antisense purification (RAP) approach (*25*), followed by quantitative PCR (QPCR) of specific regions, confirmed the binding of lnc13 to the transcriptional start sites (TSSs) of the target genes (Fig. 4B and fig. S7A). Lnc13-bound proteins were pulled down and subjected to mass spectrometry analysis (fig. S7, B and C, and table S3). One of the major lnc13-binding proteins was an hnRNP (*23*, *24*, *26*), namely hnRNPD (also known as AUF1). Mice lacking hnRNPD develop an inflammatory skin disease (*27*). hnRNPD is able to regulate gene expression through different mechanisms, including interacting with members of the nucleosome-remodeling complex, NuRD, to regulate the epigenetic state of chromatin (*28*). BMDMs from hnRNPD KO mice did not show any effect on lnc13 down-regulation kinetics (fig. S7D), but expression of lnc13-affected genes in unstimulated and LPS-stimulated cells was increased (Fig. 4C). Human U937 cells also showed increased target gene expression when hnRNPD was knocked down (fig. S7E). Although hnRNPD is expressed as four different isoforms, we found that the p42 isoform bound most efficiently to lnc13. The p42 isoform is also known to be localized to chromatin (*29*). Chromatin immunoprecipitation (ChIP)–QPCR analysis revealed that hnRNPD binds to the same regions of chromatin as lnc13, but the bound hnRNPD is lost after LPS-stimulated lnc13 degradation (fig. S7F). The chromatin localization of both lnc13 and hnRNPD (Fig. 4A and fig. S7G), together with the enrichment of both factors in the TSSs of the target genes, further supports the hypothesis that the lnc13-hnRNPD complex functions as a regulator of expression of a subset of inflammatory genes. Interestingly, Hdac1, which is a component of the NuRD remodeling complex, was detected in the hnRNPD p42-lnc13 complex (fig. S7H). Lnc13 was seen to coimmunoprecipitate with Hdac1 in nuclear extracts from mouse and human macrophages (Fig. 4D and fig. S7I). Consistently, ChIP analysis showed enrichment of Hdac1 in the TSSs of lnc13-regulated genes in the steady state, as well as loss of Hdac1 binding after LPS stimulation when lnc13 levels were reduced (fig. S7J). Hdac1 is less efficiently bound to the lnc13 target promoters in cells lacking hnRNPD versus WT cells (Fig. 4E), suggesting that hnRNPD is necessary for Hdac1 to bind the lnc13-regulated promoters. hnRNPD and Hdac1 showed decreased enrichment in the TSSs of the target genes in lnc13 knocked-down (kd) cells compared with those with normal lnc13 levels (Fig. 4F and fig. S7K). The lnc13 kd cells showed higher levels of the target gene expression but no differences in hnRNPD expression (fig. S5J). Taken together, these data suggest that, as described for the binding of Hdac3 by *Xist* lncRNA (*30*), lnc13 acts as a link between hnRNPD, Hdac1, and

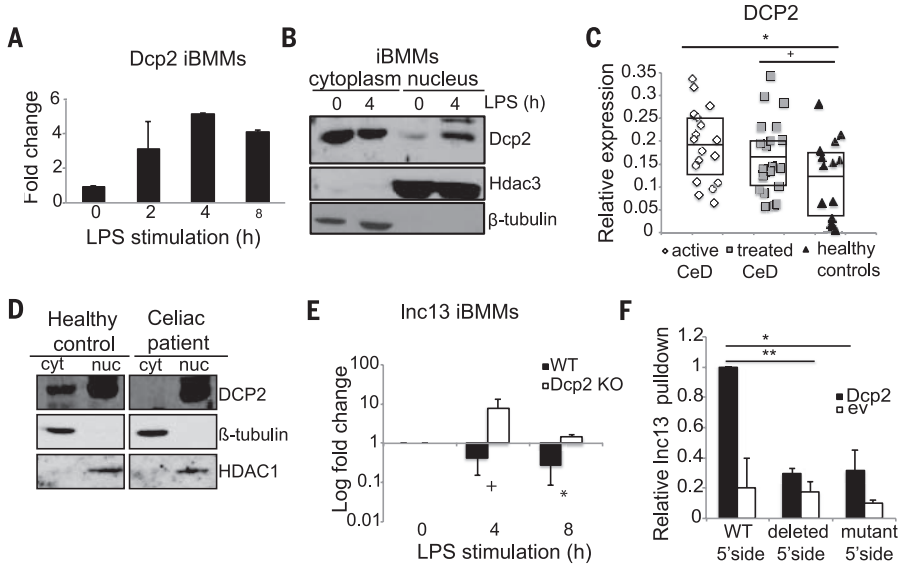


Fig. 3. The Dcp2 decapping enzyme regulates lnc13 levels. (**A**) Dcp2 expression was measured by RT-QPCR in response to LPS stimulation in iBMMs. Data represent the average and SE of three independent experiments. (**B**) Dcp2 protein levels are increased in the nucleus in response to LPS stimulation of iBMMs. (**C**) Celiac patients show higher levels of Dcp2 expression, as measured by RT-QPCR. Horizontal lines represent average values; white rectangles span the 25th and 75th percentile in each group. *P < 0.05, +P = 0.1; unpaired t test. (**D**) Localization of Dcp2 is mostly nuclear in fractions of intestinal biopsies of patients with CeD compared with healthy controls. This representative figure shows a blot performed on three samples per condition. cyt, cytoplasmic fraction; nuc, nuclear fraction. (**E**) Lnc13 expression pattern after LPS stimulation of WT (black bars) and Dcp2 KO (white bars) iBMMs. Data represent the average and SE of three independent experiments. *P < 0.05, +P < 0.1; unpaired t test. (**F**) WT or 5′ mutant forms of IVT lnc13 were incubated with lysates from cells overexpressing an empty vector (ev) or FLAG-tagged Dcp2. Dcp2 was immunoprecipitated with an antibody to FLAG, and lnc13 levels were quantified by RT-QPCR. The amount of lnc13 in the pulldown is relative to the input of the IVT RNAs and normalized to the full-length WT lnc13. Data represent the average and SE of three independent experiments, **P < 0.01, *P < 0.05; paired t test.

chromatin to regulate expression of certain inflammatory genes (fig. S9).

The direct interaction between lnc13 and hnRNPD led us to ask whether the CeD-associated SNP block within lnc13 alters this binding. In fact, the lncRNA structure is predicted to be substantially altered based on the SNP genotype (fig. S8A). Consistent with such a prediction, in vitro–transcribed (IVT) forms of WT and the CeD allele–containing lnc13 reveal dramatically different mobilities on a native agarose gel (fig. S8B). We evaluated the influence of the disease-associated SNPs in the binding between lnc13 and hnRNPD (p42) in human cell lines homozygous for different allelic variants of lnc13: "CC" (WT) and "TT"

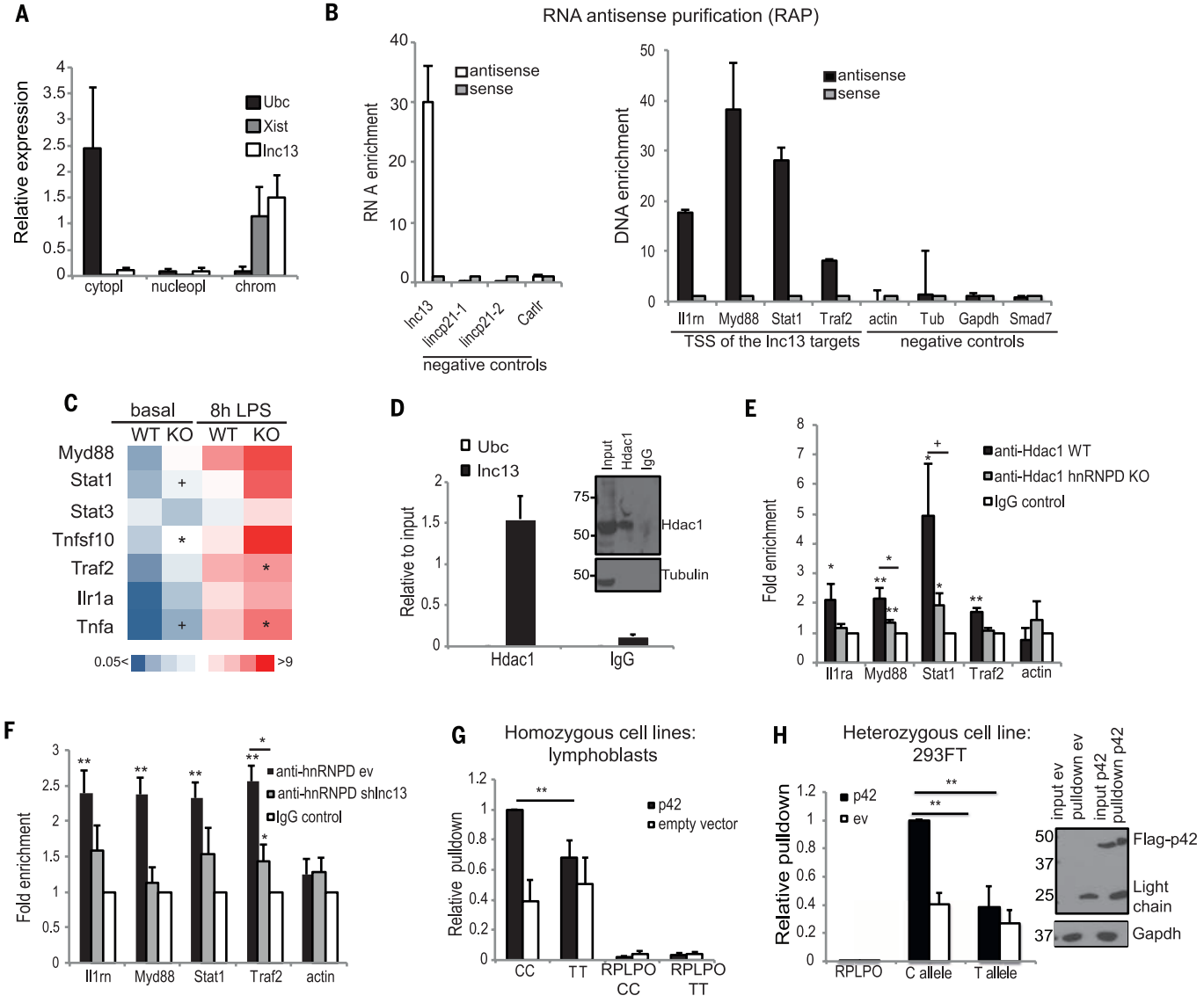


Fig. 4. Lnc13 regulates gene expression by binding to hnRNPD p42 and Hdac1 on chromatin. (**A**) Determination of lnc13 subcellular localization. Data represent the average and SE of three independent experiments. *Ubc* was used as a cytoplasmic control and *Xist* as a chromatin-associated RNA control. cytopl, cytoplasm; nucleopl, nucleoplasm; chrom, chromatin. (**B**) Lnc13 was purified by the RAP technique, using antisense oligos. Data represent the pulldown percent enrichment of RNA (left) and DNA (right) compared with the sense oligos used as controls. Average and SE of three independent experiments are represented in the graph. (**C**) Expression of lnc13 target genes in BMDMs from hnRNPD KO mice at the basal state and after LPS stimulation. Tumor necrosis factor–α was used as a positive control of overexpression in the KO cells. Data represent the average of three independent experiments. $+P = 0.1$, $*P < 0.05$; unpaired *t* test. (**D**) Interaction between Hdac1 and lnc13 by IP and RT-QPCR. Data represent the average and SE of three independent experiments. IgG, immunoglobulin G. (**E**) ChIP of Hdac1 in WT and hnRNPD KO macrophages. Data represent the average fold enrichment and SE of three independent experiments. Actin was used as a negative IP control. $+P < 0.1$, $*P < 0.05$, $**P < 0.01$; enrichment based on one-tail z-test; comparison between WT and hnRNPD KO based on two-tailed *t* test. (**F**) ChIP of hnRNPD in macrophages transduced with empty vector (ev) and with a lnc13 short hairpin RNA (sh-lnc13). Data represent the average fold enrichment and SE of five independent experiments. Actin was used as a negative IP control. $*P < 0.05$, $**P < 0.01$; enrichment based on one-tail *z* test; comparison between shlnc13 and ev based on two-tailed *t* test. (**G**) Relative binding affinity of CC- and TT-harboring RNAs to FLAG-hnRNPD, as assessed by FLAG IP and subsequent RT-QPCR. Average and SE data relative to the CC sample are from six independent pulldown experiments. $*P < 0.05$; paired *t* test. (**H**) Quantification of the amount of each allele bound to FLAG-hnRNPD in the heterozygous cell line 293FT (embryonic kidney cells). After IP, each allele was quantified by a dual-color TaqMan assay. Retrieved lnc13 was normalized to input and calculated relative to the C allele. Data represent the average and SD of three independent experiments. RPLPO was used as a negative control. $**P < 0.01$; paired *t* test. Gapdh, glyceraldehyde-3-phosphate dehydrogenase.

(disease-associated). Whereas hnRNPD was able to retrieve both forms of lnc13, disease-associated lnc13 was significantly less efficiently bound to the protein in all of the analyzed cell lines (Fig. 4G and fig. S8C). We made the same observation when IVT alleles of lnc13 were used for the pulldown (avoiding the background genomic variation of the different cell lines) (fig. S8D). Experiments using heterozygous cell lines for rs917997 and expressing both alleles confirmed the preferential binding of the C allele (Fig. 4H and fig. S8E). This observation strongly suggests a functional importance for the risk-associated lnc13 haplotype.

The studies presented here identify lnc13 as a previously unrecognized lncRNA that harbors CeD-associated SNPs; demonstrate that lnc13 is degraded by Dcp2 after NF-κB activation; and, most importantly, show that lnc13 is able to regulate the expression of a subset of CeD-associated inflammatory genes through interaction with chromatin and the multifunctional protein hnRNPD (fig. S9). We believe that lnc13 plays a role in the maintenance of intestinal mucosal immune homeostasis and that dysregulation of lnc13 expression and function—as a result of decapping and genetic polymorphisms, respectively—contributes to inflammation in autoimmune disorders such as CeD. Fully deciphering the mechanisms by which lnc13 contributes to the promotion of inflammation may shed light on the mechanisms regulating gene expression and might also reveal previously unidentified targets for use in the diagnosis or treatment of inflammatory diseases such as CeD.

REFERENCES AND NOTES

1. T. Derrien *et al.*, *Genome Res.* **22**, 1775–1789 (2012).
2. L. A. Hindorff *et al.*, *Proc. Natl. Acad. Sci. U.S.A.* **106**, 9362–9367 (2009).
3. G. Jin *et al.*, *Carcinogenesis* **32**, 1655–1659 (2011).
4. N. Fernandez-Jimenez *et al.*, *Hum. Mol. Genet.* **23**, 1298–1310 (2014).
5. P. H. Green, C. Cellier, *N. Engl. J. Med.* **357**, 1731–1743 (2007).
6. P. C. Dubois *et al.*, *Nat. Genet.* **42**, 295–302 (2010).
7. G. Trynka *et al.*, *Nat. Genet.* **43**, 1193–1201 (2011).
8. D. A. van Heel *et al.*, *Nat. Genet.* **39**, 827–829 (2007).
9. L. D. Ward, M. Kellis, *Nucleic Acids Res.* **40**, D930–D934 (2012).
10. P. Carninci *et al.*, *Science* **309**, 1559–1563 (2005).
11. M. Skipper *et al.*, *Nature* **518**, 313 (2015).
12. F. Yang *et al.*, *Mol. Cell* **49**, 1083–1096 (2013).
13. M. N. Cabili *et al.*, *Genome Biol.* **16**, 20 (2015).
14. F. Wang *et al.*, *J. Mol. Diagn.* **14**, 22–29 (2012).
15. A. A. Salamov, T. Nishikawa, M. B. Swindells, *Bioinformatics* **14**, 384–390 (1998).
16. M. Punta *et al.*, *Nucleic Acids Res.* **40**, D290–D301 (2012).
17. J. Ernst, Z. Bar-Joseph, *BMC Bioinformatics* **7**, 191 (2006).
18. V. Abadie, V. Discepolo, B. Jabri, *Semin. Immunopathol.* **34**, 551–566 (2012).
19. N. Periolo *et al.*, *Cytokine* **67**, 44–51 (2014).
20. S. Geisler, L. Lojek, A. M. Khalil, K. E. Baker, J. Coller, *Mol. Cell* **45**, 279–291 (2012).
21. Y. Li, M. Song, M. Kiledjian, *RNA* **17**, 419–428 (2011).
22. Y. Li, M. G. Song, M. Kiledjian, *Mol. Cell. Biol.* **28**, 939–948 (2008).
23. S. Carpenter *et al.*, *Science* **341**, 789–792 (2013).
24. A. M. Khalil *et al.*, *Proc. Natl. Acad. Sci. U.S.A.* **106**, 11667–11672 (2009).
25. J. Engreitz, E. S. Lander, M. Guttman, *Methods Mol. Biol.* **1262**, 183–197 (2015).
26. M. Huarte *et al.*, *Cell* **142**, 409–419 (2010).
27. N. Sadri, R. J. Schneider, *J. Invest. Dermatol.* **129**, 657–670 (2009).
28. C. Lee *et al.*, *Cereb. Cortex* **18**, 2909–2919 (2008).
29. S. Mili, H. J. Shu, Y. Zhao, S. Piñol-Roma, *Mol. Cell. Biol.* **21**, 7307–7319 (2001).
30. C. A. McHugh *et al.*, *Nature* **521**, 232–236 (2015).

ACKNOWLEDGMENTS

We thank S. Gurunathan for assistance with writing the paper and helpful discussions, B. Reizis and C. Schindler for reading the paper and providing helpful comments, and S. Zhang for the mass spectrometry analysis. The data presented here are tabulated in the main paper and the supplementary materials. The sequences reported in this paper have been deposited in the GenBank database (accession number KU712258). This work was supported by a research fellowship from the Basque government (Spain) to A.C.-R. and N.F.-J.; grants from the Basque Department of Health (2011111034) and the Spanish Instituto de Salud Carlos III (PI10/00310) to J.R.B.; NIH grant RO1-GM067005 to M.K.; and NIH grants R37-AI33443, RO1-AI093985, and RO1-DK102180 to S.G.

SUPPLEMENTARY MATERIALS

www.sciencemag.org/content/352/6281/91/suppl/DC1
Materials and Methods
Supplementary Text
Figs. S1 to S9
Tables S1 to S4
References (*31*, *32*)

17 July 2015; accepted 18 February 2016
10.1126/science.aad0467

MAMMALIAN GERM CELLS

Mouse oocytes differentiate through organelle enrichment from sister cyst germ cells

Lei Lei*† and Allan C. Spradling†

Oocytes differentiate in diverse species by receiving organelles and cytoplasm from sister germ cells while joined in germline cysts or syncytia. Mouse primordial germ cells form germline cysts, but the role of cysts in oogenesis is unknown. We find that mouse germ cells receive organelles from neighboring cyst cells and build a Balbiani body to become oocytes, whereas nurselike germ cells die. Organelle movement, Balbiani body formation, and oocyte fate determination are selectively blocked by low levels of microtubule-dependent transport inhibitors. Membrane breakdown within the cyst and an apoptosis-like process are associated with organelle transfer into the oocyte, events reminiscent of nurse cell dumping in *Drosophila*. We propose that cytoplasmic and organelle transport plays an evolutionarily conserved and functionally important role in mammalian oocyte differentiation.

Mammalian oocytes are the only cells that can develop into a mammalian embryo, but during the normal life cycle, only a small number of mature oocytes are produced. Efforts to generate functional oocytes from pluripotent stem cells or from somatic cells have met with limited success (*1*). As a result, oocytes represent the limiting component of many genetic, biotechnological, and assisted reproductive procedures. Gaining a deeper understanding of normal oocyte development might reveal processes needed to support early embryogenesis and could provide a rational framework for increasing the supply of functional, high-quality oocytes.

Oocytes differentiate in diverse species by receiving organelles and cytoplasm while joined together with sister germ cells. In many insects and lower vertebrates, synchronous mitotic divisions of precursor germ cells generate germline cysts connected by intercellular bridges known as ring canals (*2*, *3*). In *Drosophila*, organelles and RNAs move into one of the 16 cyst cells along stable microtubules that span the ring canals. The single downstream cell receiving these organelles accumulates an aggregate known as a Balbiani body and becomes an oocyte (*4*). After further growth, the other 15 cells, known as nurse cells, actively dump most of their remaining cytoplasm into the oocyte before undergoing atypical programmed cell death (*5*). In nematodes and several other insect groups, early female germ cells form a syncytium through which organelles and cytoplasm are transferred into a subset of cells that become oocytes (*2*). In hydra, early oocytes acquire extra cytoplasm by fusing with neighboring nurse cells (*2*, *6*). Genetic studies in *Drosophila* show that intercellular cytoplasmic transport is microtubule-dependent and essential for oocyte production (*7*).

Whether mammalian oocytes acquire organelles from sister cells and how this process might occur have not been decisively established (Fig. 1A). After migration to the gonad at embryonic day 10.5 (E10.5), all mouse primordial germ cells form interconnected cysts of up to 30 germ cells

Howard Hughes Medical Institute Research Laboratories, Department of Embryology, Carnegie Institution for Science, 3520 San Martin Drive, Baltimore, MD 21218, USA.
*Present address: Department of Cell and Developmental Biology, University of Michigan Medical School, 109 Zina Pitcher Place, 3045 Biomedical Science Research Building, Ann Arbor, MI 48109, USA. †Corresponding author. E-mail: spradling@ciwemb.edu (A.C.S.); leile@med.umich.edu (L.L.)

Downloaded from on March 31, 2016

(*8*, *9*). Newly formed cysts sustain ongoing apoptosis and fragment into smaller cysts (*9*). By postnatal day 4 (P4), an average of 6.4 cells (i.e., 20% from the initial 30) survive as primary oocytes containing a Balbiani body within a primordial follicle (Fig. 1A) (*10*). However, the importance of cysts for mouse oogenesis has been questioned. Female mice mutant for the ring canal protein TEX14 are still fertile, suggesting that cysts are an evolutionary relic (*11*).

The process of analyzing mouse cysts has been hampered by the tight packing of germ cells within the fetal ovary. Recently, methods of tracing the lineage of single germ cells have overcome this problem by marking just one founder germ cell's progeny (*9*). We used confocal microscopy and three-dimensional analysis software to deduce the structure of individual lineage-labeled cysts stained for TEX14. Our studies revealed a variety of interconnection patterns within mouse cysts (Fig. 1, C to E). As in many other species, ring canals differ in size (Fig. 1C) and sometimes cluster in one region of the cell membrane (Fig. 1, C to E) (*2*). On E14.5, ~14% of germ cells in cysts contain three or four ring canals (table S2), and these highly branched cells are selectively preserved (Fig. 1F) ($P < 0.05$; χ^2 test). Staining with an antibody against TEX14 did not highlight ring canals in cysts younger than E14.5 (fig. S1), consistent with the continued formation of cysts in *Tex14* mutants (*11*).

We looked for evidence of intercellular organelle movement between sister mouse germ cells marked by lineage labeling. To examine centrosome movement, a hallmark of *Drosophila* cytoplasmic transfer (*12*), we stained fetal ovaries for Pericentrin or γ-tubulin (Fig. 2, A and B). At E14.5, germ cells contained a single centrosome, as revealed by a single dotlike focus of Pericentrin staining. However, by E17.5, 20% of cells had acquired an additional centrosome, and by P0, these cells had three or four centrosomes [Fig. 2, A (arrows) and B]. Moreover, smaller putative meiotic centrosomes appeared that are distinct from the accumulating centrosomes (fig. S2). These observations suggest that centrosomes are transferred through cellular interconnections into a subset of germ cells but remain distinct from meiotic centrosomes.

Further evidence connecting intercellular transport to oocyte differentiation was obtained using GM130 staining to mark Golgi bodies (Fig. 2C). At E14.5, a small cluster of Golgi material (arrow) was found in all germ cells, often near the centrosome. However, between E17.5 and P0, some cells accumulated extra Golgi material (arrows) that later coalesced into a sphere, indicative of Balbiani body formation (arrowheads). Multiple Pericentrin-positive centrosomes accumulated at the Balbiani body, showing that the same cells accumulate extra Golgi and centrosomes. By P4, the transferred centrosomes fused together, forming a large mass in the center of the Balbiani body (arrowheads in Fig. 2, A and C). Staining with γ-tubulin could often resolve three to five individual subfoci in the Balbiani body (arrowheads in P4 panels of Fig. 2, A and C), as well as some that remain outside (arrow in P4 panel of Fig. 2A).

Quantitation of GM130 and Pericentrin staining showed that P4 oocytes contain 5.1 times as much Golgi material, 7.3 times as much Pericentrin, and 3.7 times as much γ-tubulin as E14.5 germ cells (Fig. 2, B and D). In electron micrographs (EMs) (Fig. 1, A to B′), we observed multivesicular bodies (MVBs) (yellow arrowhead) near P4 Balbiani bodies (white arrow). Mitochondria numbers also increased in cells with nascent Balbiani bodies (arrowheads in Fig. 2E), compared with other cells in the same cyst. EMs (Fig. 2F) indicated that, by P4, the number of mitochondria (arrows) in Balbiani body–containing cells had increased by a factor of 4.9 (Fig. 2G). Finally, cells containing Balbiani bodies become progressively larger after E17.5 and quadrupled in size by P4 (Fig. 2H). Thus, P4 oocytes acquire about five times as many centrosomes, Golgi, and mitochondria and four times the cytoplasmic volume of E14.5 germ cells.

Additional studies verified that cells acquiring cellular components form Balbiani bodies and become oocytes. Balbiani body–containing cells preferentially lack expression of the early apoptosis marker Annexin V (fig. S3, A and B) ($P < 0.001$; Fisher's exact test) at P0 and are selectively preserved at P4 (fig. S3C). Organelles might move between germ cells through ring canals. However, TEX14-stained structures decrease in size after E14.5 (Figs. 1, C to E, and 3A), dissociate from junctions at E17.5 (Fig. 3, D and E), and disappear entirely after E19.5. The plasma membrane separating most germ cells by E17.5 develops large gaps (Fig. 3, B, C, E, and E′, arrows). After E17.5, organelle movement appears to occur via these direct interconnections. Some germ cells contract greatly (Fig. 3G) and appear to transfer most of their cytoplasm—including centrosomes (Fig. 3, H and H′), Golgi (Fig. 3, G and H), and mitochondria (Fig. 3I)—leaving little more than a nucleus behind (Fig. 3I, asterisk, and fig. S3D). Because cysts gradually decrease in cell number throughout E17.5 to P4 (*9*) (table S1), whereas oocytes increase gradually in size (Figs. 2H and 3J), cytoplasmic transfer and programmed cell death events probably occur sequentially within cysts over several days.

Developing oocytes reorganize their nuclear heterochromatin between P0 to P4 (Fig. 4A).

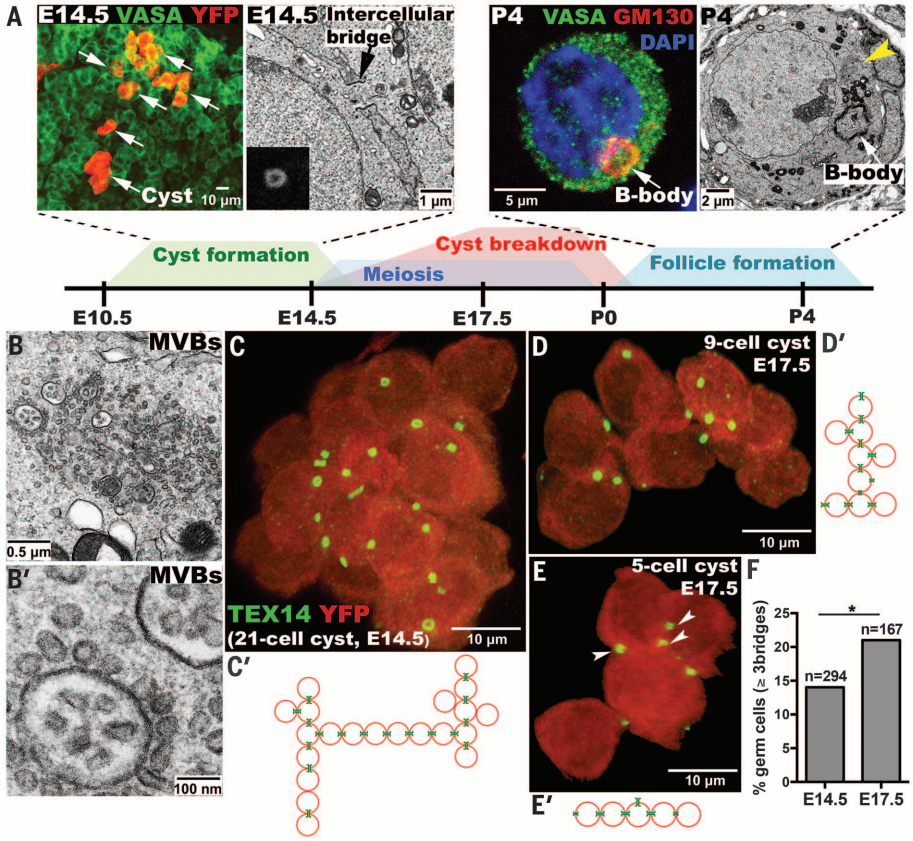


Fig. 1. Germline cysts and mouse oocyte differentiation. (**A**) Timeline of cyst formation and breakdown to form primordial follicles. (Left) Yellow fluorescent protein (YFP)–labeled single–germ cell clone showing six cysts (arrows). (Left middle) EM showing an E14.5 ring canal (arrow) and a TEX14-labeled ring canal (inset). (Right middle) GM130-labeled Balbiani body (B-body). (Right) EM of a P4 oocyte showing a Balbiani body and MVBs (yellow arrowhead). DAPI, 4′,6-diamidino-2-phenylindole. (**B** and **B′**) EMs of oocyte MVBs at higher magnifications. Lineage-labeled E14.5 (**C**) and E17.5 [(**D**) and (**E**)] cysts showing ring canals (TEX14, green). Deduced connection maps are shown in (**C′**) to (**E′**). Arrowheads in (E) indicate a branched cell with three ring canals. (**F**) Branched germ cells are selectively preserved between E14.5 and E17.5 (*$P < 0.05$; χ^2 test). *n*, number of cells.

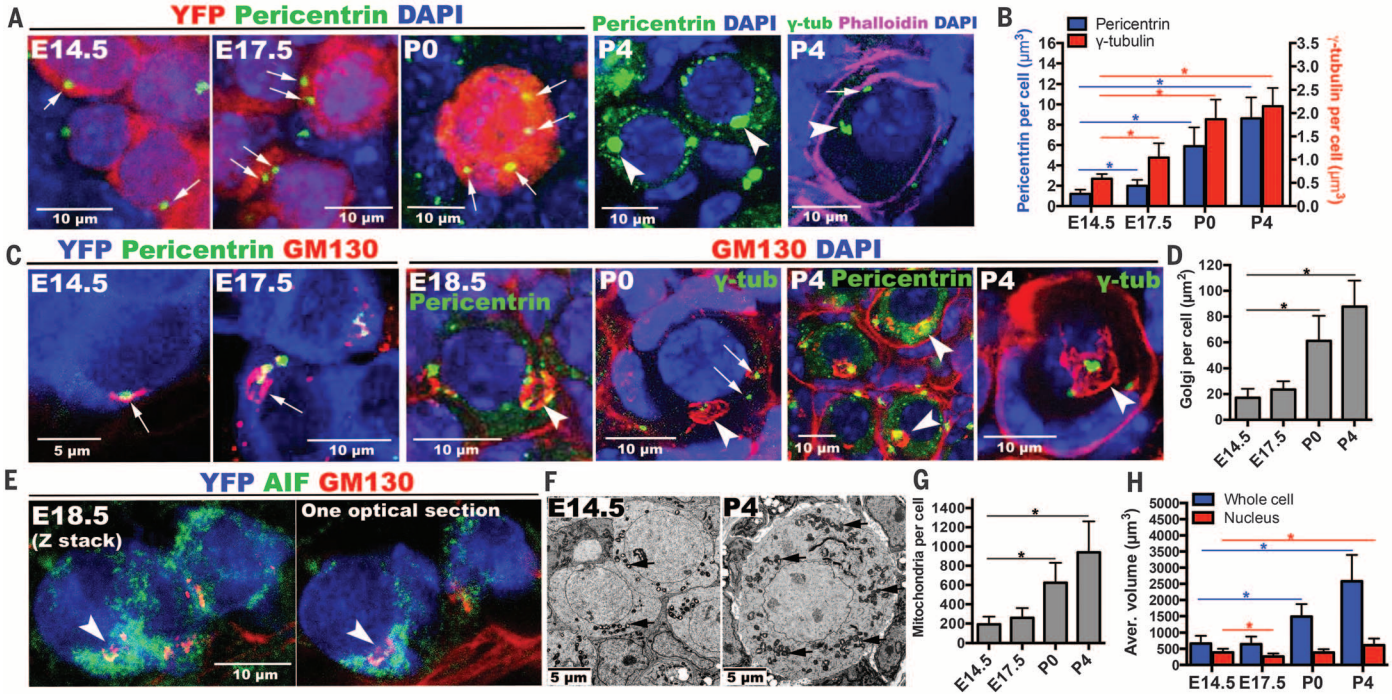


Fig. 2. Organelle enrichment and Balbiani body formation during mouse oocyte differentiation. (**A**) Pericentrin- or γ-tubulin–labeled centrosomes (green, arrows) increase in certain cyst cells (red) from E14.5 to P4. Each P4 oocyte acquires a large Pericentrin-rich mass (arrowheads). Staining with γ-tubulin shows five or six elements (arrowhead and arrow) within a P4 germ cell delimited by phalloidin staining. (**B**) Histogram summarizing centrosome accumulation. (**C**) Golgi elements (red, arrows) often associated with centrosomes (green) also increase and generate Balbiani bodies (arrowheads). By P4, Pericentrin- or γ-tubulin–labeled centrosomes (green) mostly cluster inside the Balbiani body. (**D**) Histogram of Golgi element content per cell. (**E**) Mitochondria are more abundant in the cyst cell containing a nascent Balbiani body (arrowhead). YFP is a lineage marker; AIF (apoptosis-inducing factor) denotes mitochondria. The GM130 antibody nonspecifically stains the basement membrane from E18.5 to P4. (**F**) EMs show increases in mitochondria (arrows) between E14.5 and P4, as quantitated in (**G**). (**H**) Germ cell volume increases with time. In (B), (D), (G), and (H), *$P < 0.05$; error bars indicate SD.

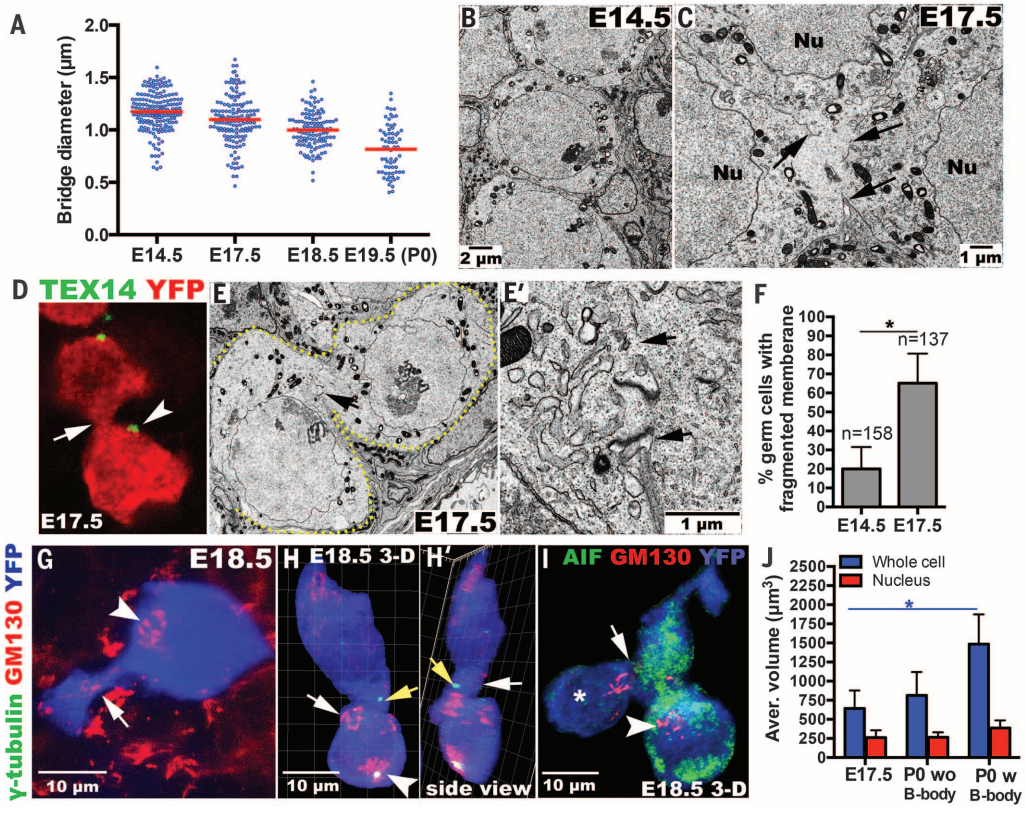


Fig. 3. Balbiani body formation and oocyte differentiation are facilitated by membrane fragmentation. (**A**) Ring canal (bridge) diameter decreases in size. Red bars denote medians. Cyst germ cells are distinct at E14.5 (**B**) but frequently contain membrane gaps by E17.5 [(**C**), arrows; (**F**)]. Nu, nucleus. (**D** to **E′**) Ring canals [(D), arrowhead; (E), arrow] detach from intercellular junctions [(D) and (E′), arrow]. Golgi material from a contracting cell [(**G**), arrow] and centrosomes [(**H**) and (**H′**), yellow arrows] move through membrane gaps into Balbiani body–containing cells (arrowhead). (**I**) A cell (asterisk indicates the nucleus) lacking most cytoplasm is connected (arrow) to mitochondria-enriched cells (green), including one with a Balbiani body (arrowhead). (**J**) P0 cells containing a Balbiani body are larger than E17.5 cells. *$P < 0.05$; error bars indicate SD [(F) and (J)].

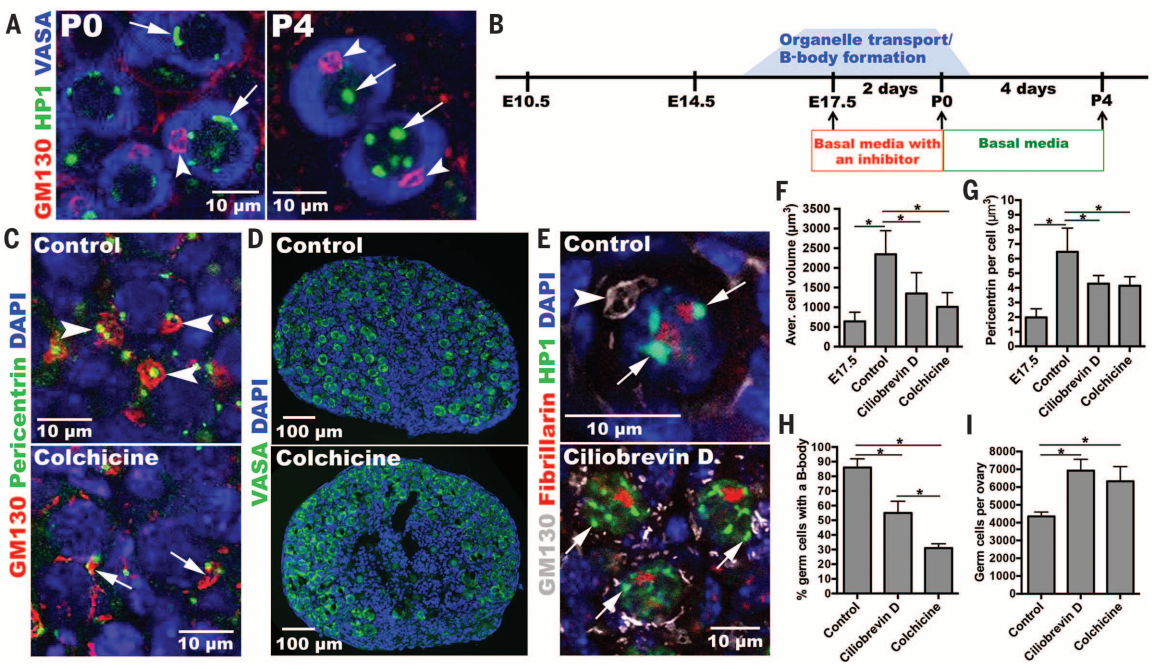


Fig. 4. Microtubule-dependent transport is important for Balbiani body formation and oocyte differentiation. (**A**) Heterochromatin (arrows) reorganizes between P0 and P4. Balbiani bodies are indicated by arrowheads. (**B**) Experimental design for oocyte differentiation in vitro. E17.5 ovaries are cultured with or without inhibitor for 2 days and then cultured for 4 days without inhibitor. Control ovaries efficiently develop primordial follicles (**C**) containing full-sized oocytes with normal Balbiani bodies (arrowheads). Ovaries treated with inhibitors form smaller cells (**F**) with fewer Balbiani bodies (**H**) and reduced Pericentrin content [(C), arrows] (**G**). (**D**) Inhibitor-treated cultures contain more germ cells (**I**). (**E**) Heterochromatin (arrows) reorganizes in controls but failed to reorganize properly in inhibitor-treated cultures. In (F) to (I), $*P < 0.05$; error bars indicate SD.

HP1 staining is juxtaposed to the nuclear lamina between E14.5 and P0, but P4 oocytes contain several nucleoplasmic aggregates (Fig. 4A). To test the role of microtubule-dependent organelle transport in oocyte differentiation, we cultured fetal ovaries in vitro, under conditions in which development proceeds normally for a week or more (Fig. 4B). When wild-type E17.5 ovarian tissue was incubated alone, cysts broke down, transferred centrosomes, formed Balbiani bodies, underwent apoptosis, and formed primordial follicles containing single primary oocytes with kinetics similar to those during development in vivo (Fig. 4, C to I, and fig. S4). When incubated in the presence of the antimicrotubule drug colchicine (10 nM) for the first 2 days of culture, corresponding to the critical period from E17.5 to E19.5 when most transport occurs, these processes were perturbed and the production of Balbiani bodies was significantly reduced, from 85% to 32% (Fig. 4, C and H). Treatment with the dynein-specific inhibitor Ciliobrevin D (25 μM) also reduced oocyte production. Normal apoptosis (Fig. 4, D and I), heterochromatin reorganization (Fig. 4E), cell volume increase (Fig. 4F), and centrosome transport (Fig. 4G) were all reduced by both inhibitors. These effects were specific, as somatic cell proliferation was not substantially affected at these same inhibitor doses (fig. S5A).

Our experiments show that mouse oocytes acquire many additional centrioles, Golgi, mitochondria, and other cytoplasmic components before primordial follicle formation (fig. S6). These materials derive by transfer from interconnected sister germ cells rather than by de novo synthesis, as organelles were observed in transit and centrosomes and Golgi were acquired sequentially in individual units before fusion, rather than by the growth of a preexisting element. The rate of organelle and cytoplasmic increase was also too large to be explained by biosynthesis in a meiotic arrested cell, and the transferred centrosomes remained distinct from a meiotic centrosome (fig. S2). Microtubule-based transport is critical for organelle transport and oocyte formation, but other pathways and the prefollicular somatic cells that surround each germ cell cluster probably also contribute. Our observation that membrane breakdown rather than ring canals facilitates most cytoplasmic transfer may explain why *Tex14*-mutant females remain fertile (*11*). These events lead to Balbiani body formation and strongly resemble cytoplasmic transfers into differentiating oocytes observed in a wide range of other species (*2*). Thus, organelle movement between the cytoplasm of connected meiotic cells, like pairing and recombination events in the nucleus, represents a conserved aspect of oocyte differentiation. Our experiments show that mammalian oogenesis is more efficient than previously believed. Intercellular transfer ensures that most germ cell cytoplasm and organelles generated during fetal development are preserved in primary oocytes, despite an 80% decline in germ cell number.

Why has cytoplasmic transfer been retained throughout evolution? The acquisition of additional organelles undoubtedly helps oocytes begin to grow into the largest cells in the mammalian body, despite possessing only a 4C DNA content (that is, four haploid genomes). Damaged organelles might simultaneously be offloaded into cells destined to die, purifying the oocyte cytoplasm (*10*). Moreover, construction of a Balbiani body by transport might serve a physiological function, such as secretion.

However, we propose that intercellular RNA transport underlies the conserved differentiation of oocytes in cysts or syncytia. Germline genomes undergo epigenetic reprogramming in preparation for a new life cycle (*13*), a process that might put the oocyte at risk by activating transposons or by fostering nonallelic recombination. In both *Drosophila* and *Xenopus*, many RNAs associate with the Balbiani body (*3*, *14*). Cytoplasmic RNA transfer may increase the concentration of reprogramming factors and protective factors, such as Piwi-interacting RNAs, that repress transposition in the oocyte. Consistent with this model, nuage has been reported to accumulate during oocyte differentiation (*15*), and mutants in genes encoding nuage proteins such as MVH, PIWIL2/MILI, and MAEL cause transposon derepression in early mouse follicles (*15*–*17*).

Our results imply that high-quality mammalian oocytes are unlikely to differentiate directly from a single precursor cell in vitro (*18*). Consequently, our findings highlight the potential for guiding more efficient in vitro differentiation by defining the critical biological processes that must take place for normal oocyte production.

REFERENCES AND NOTES

1. Y.-C. Sun, S. F. Cheng, R. Sun, Y. Zhao, W. Shen, *J. Genet. Genomics* **41**, 87–95 (2014).
2. J. Büning, *The Insect Ovary* (Chapman and Hall, 1994).
3. N. Matova, L. Cooley, *Dev. Biol.* **231**, 291–320 (2001).
4. R. T. Cox, A. C. Spradling, *Development* **130**, 1579–1590 (2003).

5. V. K. Jenkins, A. K. Timmons, K. McCall, *Trends Cell Biol.* **23**, 567–574 (2013).
6. O. Alexandrova, M. Schade, A. Böttger, C. N. David, *Dev. Biol.* **281**, 91–101 (2005).
7. J. R. Huynh, D. St Johnston, *Curr. Biol.* **14**, R438–R449 (2004).
8. M. E. Pepling, A. C. Spradling, *Development* **125**, 3323–3328 (1998).
9. L. Lei, A. C. Spradling, *Development* **140**, 2075–2081 (2013).
10. M. E. Pepling, J. E. Wilhelm, A. L. O'Hara, G. W. Gephardt, A. C. Spradling, *Proc. Natl. Acad. Sci. U.S.A.* **104**, 187–192 (2007).
11. M. P. Greenbaum, N. Iwamori, J. E. Agno, M. M. Matzuk, *Biol. Reprod.* **80**, 449–457 (2009).
12. A. P. Mahowald, J. M. Strassheim, *J. Cell Biol.* **45**, 306–320 (1970).
13. C. M. Rose, S. van den Driesche, R. R. Meehan, A. J. Drake, *Biochem. Soc. Trans.* **41**, 809–814 (2013).
14. M. Kloc, L. D. Etkin, *Development* **121**, 287–297 (1995).
15. A. K. Lim *et al.*, *Development* **140**, 3819–3825 (2013).
16. A. A. Aravin *et al.*, *PLOS Genet.* **5**, e1000764 (2009).
17. S. Malki, G. W. van der Heijden, K. A. O'Donnell, S. L. Martin, A. Bortvin, *Dev. Cell* **29**, 521–533 (2014).
18. K. Hayashi *et al.*, *Science* **338**, 971–975 (2012).

ACKNOWLEDGMENTS

This work was supported by the Howard Hughes Medical Institute. We thank E. Dikovskaia and the Carnegie mouse facility staff for invaluable advice and assistance. C.-M. Fan and C. Lepper contributed helpful advice on mouse husbandry. Members of the Spradling lab provided useful comments on the manuscript. We are grateful to Y. Zheng for providing the anti-Pericentrin antibody.

SUPPLEMENTARY MATERIALS

www.sciencemag.org/content/352/6281/95/suppl/DC1
Materials and Methods
Figs. S1 to S6
Tables S1 and S2
References (*19*, *20*)

10 August 2015; accepted 11 February 2016
Published online 25 February 2016
10.1126/science.aad2156

IMMUNOLOGY

The TAM family receptor tyrosine kinase TYRO3 is a negative regulator of type 2 immunity

Pamela Y. Chan,[1] Eugenio A. Carrera Silva,[1,2] Dimitri De Kouchkovsky,[1] Leonel D. Joannas,[1] Liming Hao,[3] Donglei Hu,[4] Scott Huntsman,[4] Celeste Eng,[4] Paula Licona-Limón,[1]* Jason S. Weinstein,[1] De'Broski R. Herbert,[5] Joseph E. Craft,[1,6] Richard A. Flavell,[1,7] Silvia Repetto,[8,9] Jorge Correale,[10] Esteban G. Burchard,[4,11] Dara G. Torgerson,[4] Sourav Ghosh,[12] Carla V. Rothlin[1]†

Host responses against metazoan parasites or an array of environmental substances elicit type 2 immunity. Despite its protective function, type 2 immunity also drives allergic diseases. The mechanisms that regulate the magnitude of the type 2 response remain largely unknown. Here, we show that genetic ablation of a receptor tyrosine kinase encoded by *Tyro3* in mice or the functional neutralization of its ortholog in human dendritic cells resulted in enhanced type 2 immunity. Furthermore, the TYRO3 agonist PROS1 was induced in T cells by the quintessential type 2 cytokine, interleukin-4. T cell–specific *Pros1* knockouts phenocopied the loss of *Tyro3*. Thus, a PROS1-mediated feedback from adaptive immunity engages a rheostat, TYRO3, on innate immune cells to limit the intensity of type 2 responses.

The type 2 immune response is the major protective mechanism against metazoan parasites and is simultaneously characteristic of allergy and allergic diseases (*1*). The mechanism that regulates the intensity of this response is not well understood. Because genetic predisposition is an important risk factor for allergic diseases, we performed a meta-analysis of three independent genome-wide association studies (GWASs) of Latinos and African Americans with asthma. Multiple intronic variants in *TYRO3* were associated with asthma (fig. S1A and table S1). The most significant association was at a single-nucleotide polymorphism (SNP) located within several putative transcription factor–binding sites in *TYRO3* (fig. S1, A and B). *TYRO3* is a member of the TAM (*TYRO3*, *AXL*, and *MERTK*) receptor tyrosine kinase (RTK) subgroup. AXL and MERTK have recently been identified as pleiotropic negative regulators of the immune response (*1*–*4*), but our meta-analysis did not reveal an association with asthma (fig. S1, C and D). The molecular functions of *TYRO3* in immune regulation remain largely uncharacterized. Because *TYRO3* shows substantial sequence identity with *AXL* and *MERTK*, we hypothesized that TYRO3 may limit the magnitude of the immune response in the context of type 2 immunity.

To test this hypothesis, we first used a house dust mite (HDM) model of allergic airway inflammation. HDM-sensitized wild-type (WT) mice developed classical signs of allergic asthma, including influx of eosinophils and lymphocytes in the bronchoalveolar lavage (BAL) fluid and lung (Fig. 1A and fig. S2, A to C), as well as expansion of $CD4^+$ T cells and effector memory cells in the mediastinal lymph nodes (medLNs) (fig. S2D). We also challenged mice lacking either TYRO3 alone or both AXL and MERTK with HDM. Remarkably, HDM-sensitized $Tyro3^{-/-}$ mice displayed a more robust type 2 response, as reflected by a further increase in leukocytes and eosinophils in BAL fluid and lung (Fig. 1A and fig. S2C). This was accompanied by increased total and effector memory $CD4^+$ T cells in the medLNs (fig. S2D); higher percentages of $CD4^+$ T cells producing type 2 cytokines—such as interleukin 4 (IL-4), IL-5, and IL-13—but not the type I cytokine interferon-γ (IFN–γ) (Fig. 1B) and higher serum immunoglobulin E (IgE) (Fig. 1C). These exacerbated cellular and humoral type 2 responses correlated with increased lung histopathological score (Fig. 1D). A role of AXL has been described in respiratory infections (*5*, *6*). However, the ablation of this receptor in conjunction with MERTK ($Axl^{-/-}Mertk^{-/-}$) did not result in increased susceptibility of mice to HDM (Fig. 1A and fig. S2).

To further evaluate if *Tyro3* was an essential component of the type 2 immune response, we infected mice with the helminth *Nippostrongylus brasiliensis*. Infected $Tyro3^{-/-}$ mice had fewer BAL red blood cells (RBCs), which indicated reduced damage (Fig. 2A). We also observed increased BAL eosinophils and enhanced alternative activation of lung interstitial macrophages (Fig. 2B and fig. S3, A and B). $Tyro3^{-/-}$ mice exhibited an accelerated and enhanced T cell response in the medLNs (fig. S3C), increased IL-4$^+$ and IL-5$^+$ $CD4^+$ T cells in the medLNs (Fig. 2C), larger amounts of type 2 cytokines from mesenteric LNs (mLNs) (fig. S3D), and enhanced L3- and L5-specific IgG1 antibodies and total IgE humoral response (Fig. 2D). By days 2, 3, and 7, $Tyro3^{-/-}$ mice had fewer worms in the lungs and small intestines, which indicates accelerated clearance of the parasite (Fig. 2E). No differences in worm burden were noted in the skin of WT and $Tyro3^{-/-}$ mice (fig. S3E). Furthermore,

[1]Department of Immunobiology, School of Medicine, Yale University, New Haven, CT 06520, USA. [2]Laboratorio de Trombosis Experimental, Instituto de Medicina Experimental, Academia Nacional de Medicina-CONICET, Buenos Aires, 1425, Argentina. [3]Department of Pathology, School of Medicine, Yale University, New Haven, CT 06520, USA. [4]Department of Medicine, University of California San Francisco, CA 94158, USA. [5]Department of Experimental Medicine, University of California San Francisco, CA 94158, USA. [6]Department of Internal Medicine (Rheumatology), School of Medicine, Yale University, New Haven, CT 06520, USA. [7]Howard Hughes Medical Institute, School of Medicine, Yale University, New Haven, CT 06520, USA. [8]Instituto de Investigaciones en Microbiología y Parasitología Médica, University of Buenos Aires-CONICET, Buenos Aires, 1121, Argentina. [9]Hospital de Clinicas Jose de San Martin, University of Buenos Aires, 1120, Argentina. [10]Center for Research on Neuroimmunological Diseases, Raúl Carrea Institute for Neurological Research (FLENI), Buenos Aires 1428, Argentina. [11]Department of Bioengineering, School of Pharmacy, University of California San Francisco, CA 94158, USA. [12]Department of Neurology, School of Medicine, Yale University, New Haven, CT 06520, USA.
*Present address: Departamento de Biología Celular y del Desarrollo, Instituto de Fisiología Celular, National Autonomous University of Mexico, D.F. México. †Corresponding author. E-mail: carla.rothlin@yale.edu (C.V.R.)

Downloaded from on March 31, 2016

ovalbumin with papain (OVA-papain) immunization, an alternative type 2 immunity model, produced an accelerated and enhanced response in *Tyro3*$^{-/-}$ mice (fig. S4). We did not, however, detect increased T helper 1 (T_H1) responses in *Tyro3*$^{-/-}$ mice (fig. S5). Taken together, these results demonstrate that TYRO3 is an essential, selective inhibitor of type 2 immunity.

Next, we investigated the cellular basis of TYRO3-mediated negative regulation of type 2 immunity. T_H2 differentiation is regulated by dendritic cells (DCs), the professional antigen-presenting cells (APCs) (*7*–*10*). A specific population of DCs that are CD11c-positive and programmed cell death protein 2 (PDL2)–positive [CD11c$^+$PDL2$^+$] has been described to induce type 2 immune responses (*11*–*14*). Bone marrow (BM)–derived CD11c$^+$PDL2$^+$ DCs expressed TYRO3. Moreover, TYRO3 expression was not restricted to PDL2$^+$ DCs as PDL2$^-$ DCs also expressed this RTK (Fig. 3A). Likewise, TYRO3 was detected in lung DCs of mice sensitized with HDM extract or infected with *N. brasiliensis*, albeit not in alveolar macrophages, eosinophils, or neutrophils (fig. S6).

To test if TYRO3 functions specifically in DCs to limit the magnitude of type 2 immunity, we used an adoptive transfer model (fig. S7A). In accordance with an inhibitory role of TYRO3 in DCs, mice receiving OVA-loaded *Tyro3*$^{-/-}$ PDL2$^+$ DCs exhibited increased LN cellularity and type 2 cytokine production (Fig. 3, B and C). Note that similar percentages of WT and *Tyro3*$^{-/-}$ PDL2$^+$ DCs were detected in the draining LNs,

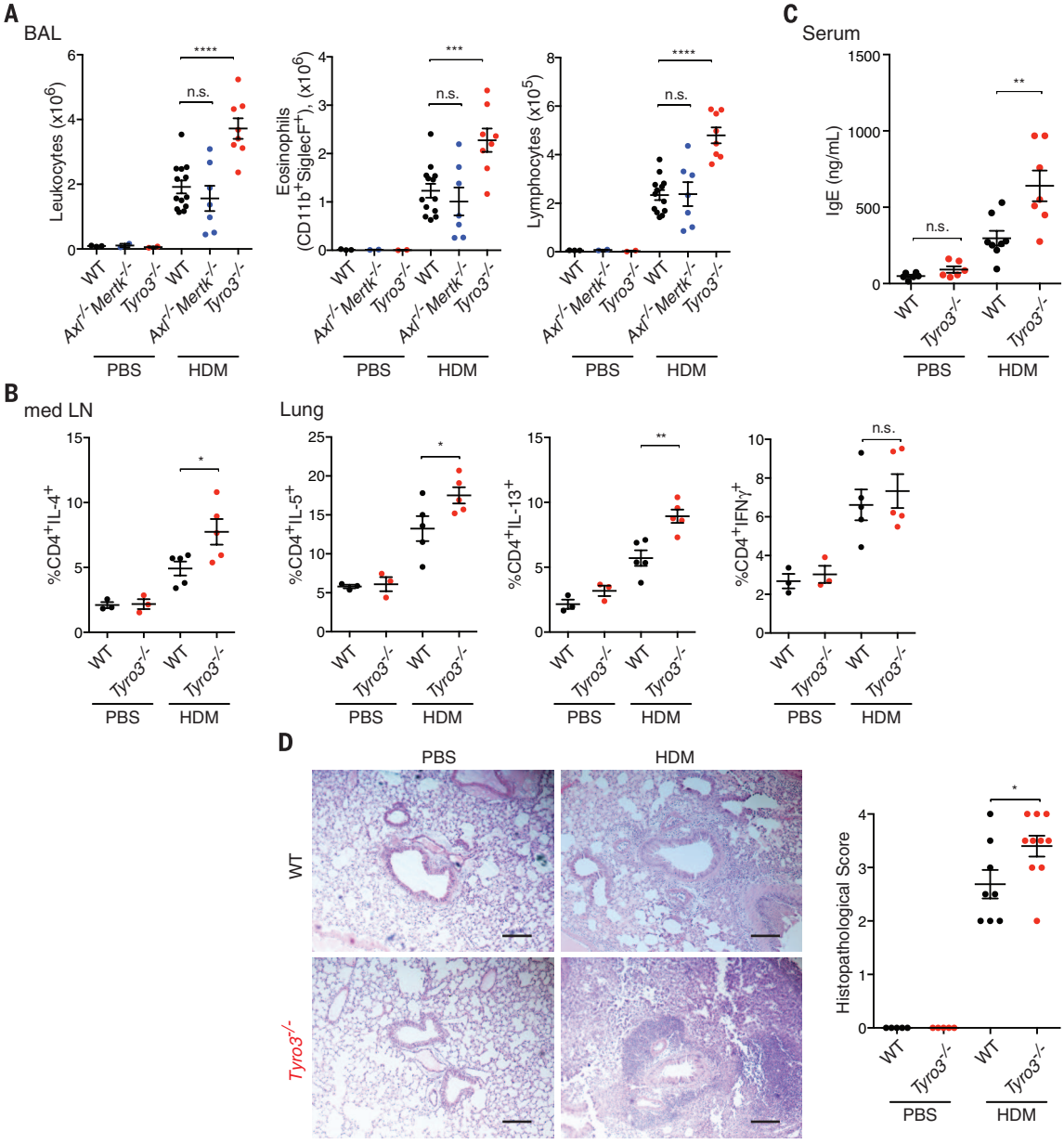


Fig. 1. *Tyro3*$^{-/-}$ mice hyperrespond to HDM-induced asthma. (**A**) Total numbers of infiltrating leukocytes (CD45$^+$), eosinophils (CD45$^+$CD3$^-$Ly6G$^-$CD11c$^-$CD11b$^+$SiglecF$^+$) and lymphocytes (CD45$^+$CD3$^+$) in the BAL of HDM-challenged WT, *Axl*$^{-/-}$*Mertk*$^{-/-}$, and *Tyro3*$^{-/-}$ mice. (**B**) Percentage of CD4$^+$IL-4$^+$, CD4$^+$IL-5$^+$, CD4$^+$IL-13$^+$, and CD4$^+$IFNγ$^+$ cells in medLNs and lung as indicated from phosphate-buffered saline (PBS) controls and HDM-treated mice. (**C**) Concentration of circulating IgE antibodies as determined by enzyme-linked immunosorbent assay (ELISA) in PBS controls and HDM-treated WT and *Tyro3*$^{-/-}$ mice. (**D**) Representative images and independent histological scores of lung sections stained with hematoxylin and eosin from PBS controls and HDM-treated WT and *Tyro3*$^{-/-}$ mice. Scale bar, 5 μm. Data are representative of two or three independent experiments. In all panels, each data point is from a different animal, and bars indicate means ± SEM. Data were analyzed with analysis of variance (ANOVA) and Bonferroni multiple comparison test (A) and unpaired Student's *t* test [(B) to (D)]. *P 0.05; **P < 0.01; ***P < 0.001; ****P < 0.0001; n.s., nonsignificant.

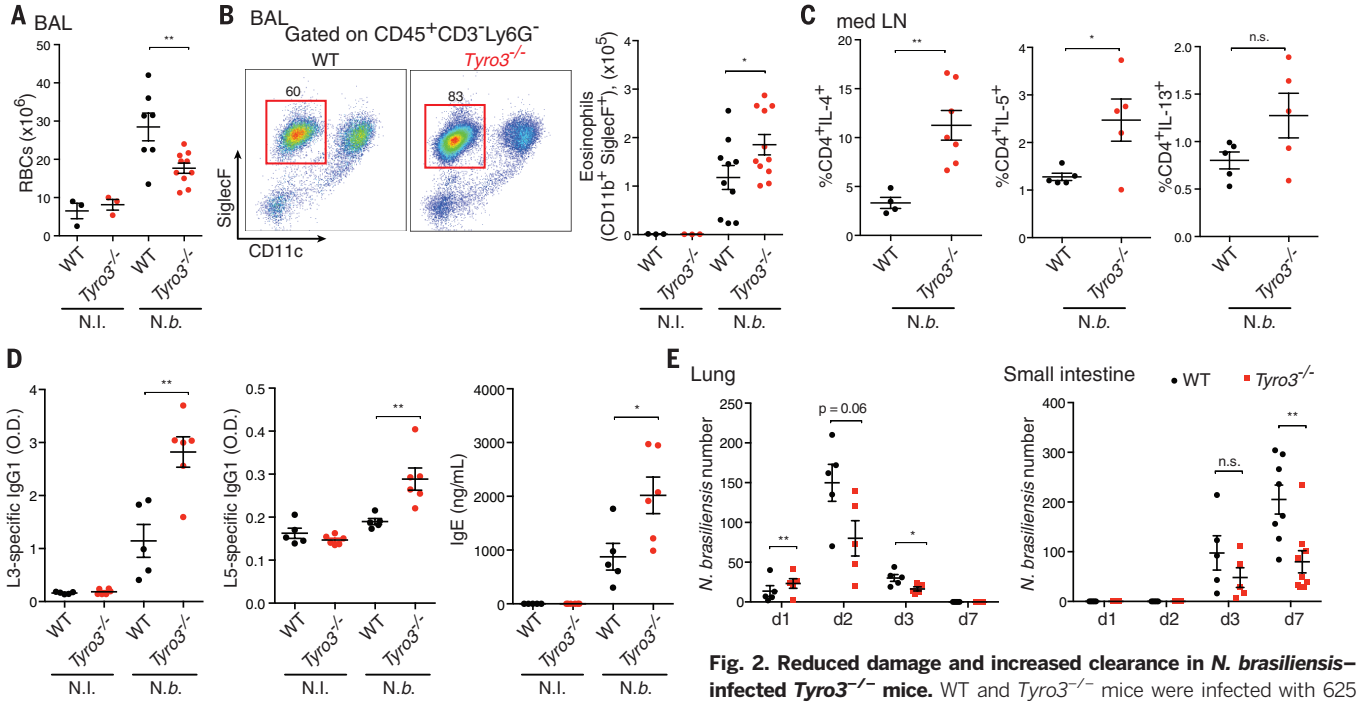


Fig. 2. Reduced damage and increased clearance in *N. brasiliensis*–infected *Tyro3*$^{-/-}$ mice. WT and *Tyro3*$^{-/-}$ mice were infected with 625 *N. brasiliensis* larvae. NI., noninfected; *N.b.*, *N. brasiliensis*. (**A**) RBC total numbers in BAL at 7 dpi. (**B**) Representative fluorescence-activated cell sorting (FACS) plots of eosinophil ($CD45^+CD3^-Ly6G^-CD11c^-CD11b^+SiglecF^+$) percentages and total numbers of eosinophils in BAL at 7 dpi. (**C**) Percentage of $CD4^+IL\text{-}4^+$, $CD4^+IL\text{-}5^+$, and $CD4^+IL\text{-}13^+$ cells from medLNs at 2 dpi. (**D**) Circulating L3- and L5-specific IgG1 antibodies and total IgE antibodies as determined by ELISA. O.D., optical density. (**E**) Kinetics of the total parasite numbers in the lung and small intestine (SI.) at 1 dpi, 2 dpi, 3 dpi, and 7 dpi. Data are representative of two or three independent experiments. In all graphs, each data point is from a different animal, means ± SEM. Data were analyzed using unpaired Student's *t* test [(A) to (E)]. *$P < 0.05$; **$P < 0.01$; n.s., nonsignificant.

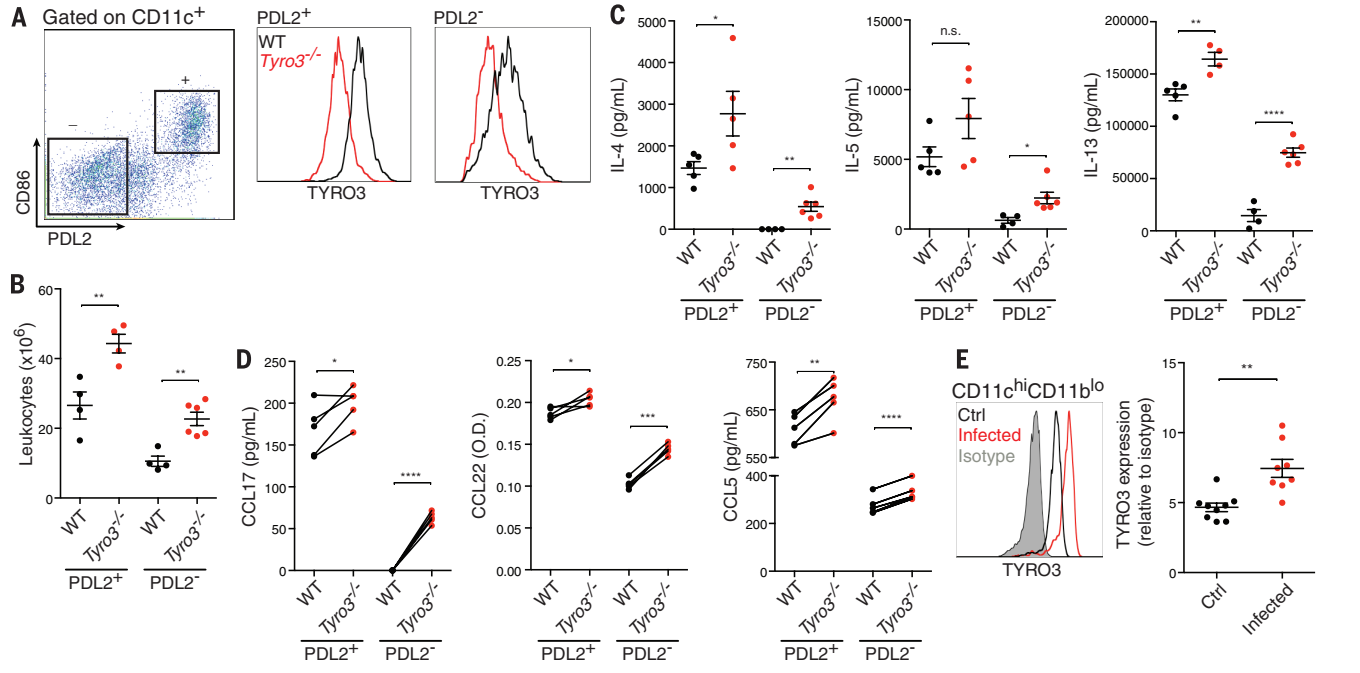


Fig. 3. TYRO3 is expressed by and functions in mouse and human DCs. (**A**) TYRO3 expression by FACS in sorted $PDL2^+$ and $PDL2^-$ DCs from BM DC cultures. (**B**) Total number of leukocytes from draining LNs of mice receiving WT or *Tyro3*$^{-/-}$ $PDL2^+$ or $PDL2^-$ OVA-loaded DCs. (**C**) OVA recalls production of IL-4, IL-5, and IL-13 from $CD4^+$ T cells in the draining LNs of mice receiving indicated DCs as measured by ELISA. (**D**) WT or *Tyro3*$^{-/-}$ $PDL2^+$ or $PDL2^-$ DCs as indicated were cocultured with naïve $CD4^+$ T cells for 24 hours in the presence of α-CD3; CCL17, CCL22, and CCL5 were measured in the supernatant by ELISA. (**E**) TYRO3 expression by FACS on human circulating DCs ($CD11c^{hi}CD11b^{lo}CD14^{lo}$) from healthy controls and parasite-infected patients. Data are representative of two or three independent experiments. In all panels, each data point is from a different mouse or human. Means ± SEM. Data were analyzed using unpaired Student's *t* test [(B), (C), and (E)] or paired Student's *t* test (D). *$P < 0.05$; **$P < 0.01$; ***$P < 0.001$; ****$P < 0.0001$; n.s., nonsignificant.

which indicated that WT and *Tyro3*$^{-/-}$ DCs migrated and survived to equal degree (fig. S7B). The type 2 immune response in mice receiving OVA-loaded WT PDL2^{-} DCs was negligible. In contrast loss of TYRO3 in PDL2^{-} DCs resulted in an enhanced type 2 immune response yet lower in magnitude relative to mice receiving *Tyro3*$^{-/-}$ PDL2^{+} DCs (Fig. 3, B and C). When OVA-loaded WT or *Tyro3*$^{-/-}$ DCs were transferred during priming, only *Tyro3*$^{-/-}$ PDL2^{+} DCs led to an enhanced response in recipient mice (fig. S8).

Comparison of the most differentially transcribed genes between DCs that can induce type 2 immunity and those that cannot revealed that a subset of chemokines—CCL22, CCL17, and CCL5—are highly expressed in PDL2^{+} DCs (*11*). Some of these chemokines actively promote type 2 immunity, as neutralization of their function results in a reduction of the response (*15*, *16*). We detected a significant increase in the production of these chemokines when either *Tyro3*$^{-/-}$ PDL2^{+} or PDL2^{-} DCs were cocultured with activated CD4^{+} T cells in comparison with respective WT DCs (Fig. 3D). Consistent with the requirement for OX40L in inducing T_H2 responses (*12*), *Tyro3*$^{-/-}$ PDL2^{+} DCs had higher expression of OX40L after transfer relative to WT PDL2^{+} DCs, whereas CD86 and CD40 levels were comparable (fig. S7, C and D). Finally, circulating human CD11c^{hi}CD11b^{lo} DCs also expressed TYRO3. This expression was significantly increased in DCs from helminth-infected patients in comparison with healthy controls (Fig. 3E). In summary, our results indicate that the absence of TYRO3 in both PDL2^{+} and PDL2^{-} DCs leads to enhanced production of type 2 chemokines and costimulatory molecules, resulting in exacerbated type 2 immune response.

We have recently described that T cells, once activated, produce the TAM receptor agonist PROS1 (*2*, *17*). PROS1 is also an agonist for TYRO3 (*2*, *17*). However, the expression profile of PROS1

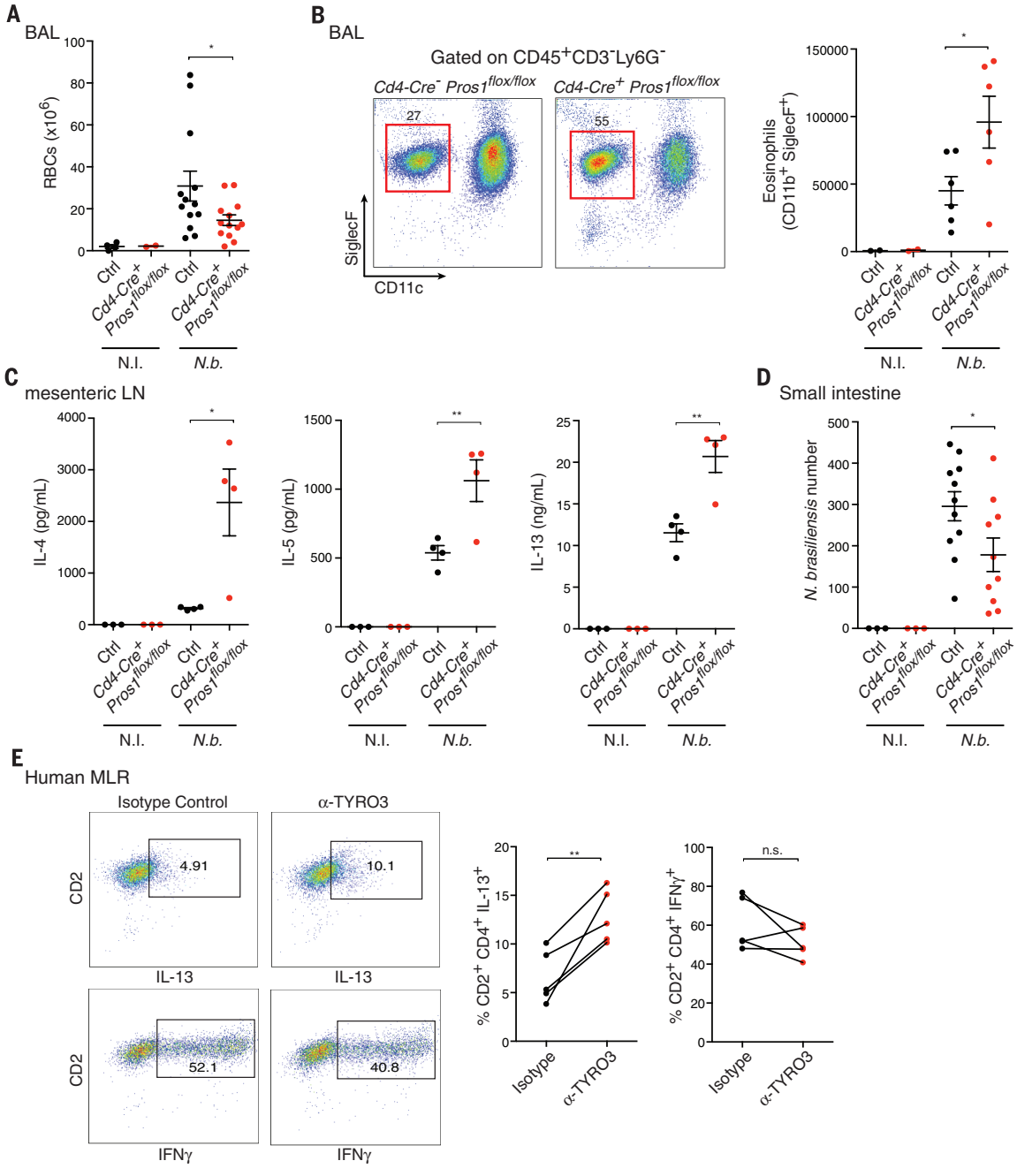


Fig. 4. T cell–derived PROS1 mediates TYRO3 regulation of type 2 immunity. (**A** to **D**) *Cd4-Cre*$^{-}$*Pros1*$^{flox/flox}$ (Ctrl) and *Cd4-Cre*$^{+}$*Pros1*$^{flox/flox}$ mice were infected with 625 *N. brasiliensis* larvae, and all parameters are shown at 7 dpi. (**A**) RBC total numbers in BAL. (**B**) Representative FACS plots of eosinophil (CD45^{+}CD3^{-}Ly6G^{-}CD11c^{-}CD11b^{+}SiglecF^{+}) percentages and total numbers of eosinophils in the BAL. (**C**) mLNs were restimulated in vitro with antibody against CD3 for 48 hours, and cytokines were measured in the supernatant by ELISA. (**D**) Total parasite numbers in the small intestine. (**E**) Representative FACS plots and independent data of the percentage of CD2^{+}CD4^{+}IL-13^{+} and CD2^{+}CD4^{+}IFNγ^{+} cells after treating an MLR of human monocyte-derived DCs cocultured with human CD4^{+} T cells with either isotype antibody or antibody against TYRO3 (α-TYRO3) for 10 days. Data are representative of two or three independent experiments. In all panels, each data point is from a different mouse or human, means ± SEM. Data were analyzed using unpaired Student's *t* test [(A) to (D)] or paired Student's *t* test (E).*P < 0.05, **P < 0.01, ***P < 0.001, ****P < 0.0001, n.s., nonsignificant.

in differentiated T helper subsets was unknown. Remarkably, T_H2 cells expressed PROS1 in vitro and in vivo, whereas T_H1 and T_H17 cells did not (fig. S9, A and B). These results indicated that T cells differentiating toward the T_H2 lineage sustain PROS1 expression, whereas expression is lost during T_H1 or T_H17 commitment. *Gas6*, the only other known agonist for TYRO3 (*17*, *18*), is not expressed in murine T cells (*2*). Activation of T cell–receptor (TCR) signaling leads to the expression of PROS1 (*2*). This depends on intrinsic IL-4 production as *IL-4*$^{-/-}$ -naïve CD4$^+$ T cells failed to up-regulate *Pros1* after TCR stimulation, but exogenous addition of IL-4 rescued this defect (fig. S9C). *Pros1* up-regulation was also STAT6-dependent (fig. S9C). Because IL-4 expression is sustained in T_H2, but not in T_H1 or T_H17 cells, only T_H2 cells maintained PROS1 expression. Only IL-4 and not IL-2, IL-5, IL-7, IL-10, IFN-γ, or transforming growth factor β induced *Pros1* expression in naïve CD4$^+$ T cells (fig. S9D).

To address whether PROS1 produced by T cells inhibits type 2 immune responses, we infected *Cd4-Cre*$^-$ *Pros1*$^{flox/flox}$ (control) and *Cd4-Cre*$^+$ *Pros1*$^{flox/flox}$ mice with *N. brasiliensis*. Activated lung CD4$^+$ T cells of infected mice expressed PROS1 (fig. S9E). *Cd4-Cre*$^+$ *Pros1*$^{flox/flox}$ mice had fewer RBCs, increased BAL eosinophils, greater type 2 cytokine production from mLNs, and lower worm burden (Fig. 4, A to D). Furthermore, OVA-papain immunization resulted in increased leukocytes and type 2 cytokine production by antigen-specific T cells in *Cd4-Cre*$^+$ *Pros1*$^{flox/flox}$ mice (fig. S10, A to C). Last, *Cd4-Cre*$^+$ *Pros1*$^{flox/flox}$ mice hyperresponded in a model of atopic dermatitis (fig. S10, D to F). Altogether, these findings demonstrate that IL-4 leads to sustained expression of PROS1 after T_H2 differentiation. This, in turn, maintains the optimal degree of the type 2 immune response.

To explore whether this PROS1-TYRO3 axis functions in the regulation of type 2 immune responses in humans, we performed mixed-lymphocyte reactions (MLR) in the presence of an TYRO3-specific antibody or isotype control. We previously showed that human T cells express PROS1 upon activation (*2*). The neutralization of TYRO3 led to a significant increase in the production of IL-13 but not IFN-γ by the T cells, which underscores a selective inhibitory role of TYRO3 in type 2, but not type 1, immunity (Fig. 4E). These results demonstrate that the TYRO3-PROS1 axis is an evolutionarily conserved negative regulator of the magnitude of the type 2 immune response.

A physiological immune response that limits the pathogen or pathogen-induced damage but avoids immunopathology has to be scalable. Such a response should have built-in sensors to monitor activation level and rheostats that vary the magnitude of the response. Here, we report the identification of a molecular mechanism that controls the intensity of type 2 immunity. In this mechanism, a RTK in DCs and its ligand produced by T_H2 cells function in concert to regulate the ensuing response. The same cytokine required for T_H2 commitment after T cell priming—IL-4 (*19*)—induces the sustained expression of *Pros1* in T cells. This leads to the activation of the RTK TYRO3, expressed on DCs, which provides an inducible feedback mechanism at the DC–T cell interface. The overall effect of PROS1-TYRO3 signaling is to limit the magnitude of the type 2 immune response.

The critical role of TYRO3 in negatively regulating T_H2 responses makes this RTK an attractive pharmacological target for small molecules or biologics that activate or inhibit its function. The innate immune sensing mechanisms for the vast array of allergen and helminth products remain largely unknown. Therefore, therapeutic interventions in allergic disorders are currently limited to targeting downstream effectors of the type 2 immune response, such as histamine and leukotrienes, or to making use of broad immunosuppressive drugs, i.e., corticosteroids (*20*). Our discovery of a self-limiting process intrinsic to type 2 immunity provides a novel opportunity to either enhance or inhibit this response. For example, activating TYRO3 would specifically lower allergic responses by preventing adaptive immune responses that function upstream of the generation of IgE, as well as the subsequent degranulation of eosinophils and mast cells. It could be equally attractive to extend this paradigm to parasitic infections where blocking TYRO3 may heighten type 2 response and improve expulsion of the parasites.

REFERENCES AND NOTES

1. L. Bosurgi *et al*., *Proc. Natl. Acad. Sci. U.S.A.* **110**, 13091–13096 (2013).
2. E. A. Carrera Silva *et al*., *Immunity* **39**, 160–170 (2013).
3. C. V. Rothlin, E. A. Carrera-Silva, L. Bosurgi, S. Ghosh, *Annu. Rev. Immunol.* **33**, 355–391 (2015).
4. C. V. Rothlin, S. Ghosh, E. I. Zuniga, M. B. Oldstone, G. Lemke, *Cell* **131**, 1124–1136 (2007).
5. T. Fujimori *et al*., *Mucosal Immunol.* **8**, 1021–1030 (2015).
6. T. Shibata *et al*., *J. Immunol.* **192**, 3569–3581 (2014).
7. H. Hammad *et al*., *J. Exp. Med.* **207**, 2097–2111 (2010).
8. B. León *et al*., *Nat. Immunol.* **13**, 681–690 (2012).
9. A. T. Phythian-Adams *et al*., *J. Exp. Med.* **207**, 2089–2096 (2010).
10. K. A. Smith *et al*., *Infect. Immun.* **80**, 3481–3489 (2012).
11. Y. Gao *et al*., *Immunity* **39**, 722–732 (2013).
12. Y. Kumamoto *et al*., *Immunity* **39**, 733–743 (2013).
13. R. Murakami *et al*., *PLOS ONE* **8**, e73270 (2013).
14. B. Vander Lugt *et al*., *Nat. Immunol.* **15**, 161–167 (2014).
15. T. Y. Halim *et al*., *Nat. Immunol.* **17**, 57–64 (2016).
16. F. Perros, H. C. Hoogsteden, A. J. Coyle, B. N. Lambrecht, H. Hammad, *Allergy* **64**, 995–1002 (2009).
17. E. D. Lew *et al*., *eLife* **3**, (2014).
18. A. Zagórska, P. G. Través, E. D. Lew, I. Dransfield, G. Lemke, *Nat. Immunol.* **15**, 920–928 (2014).
19. W. E. Paul, J. Zhu, *Nat. Rev. Immunol.* **10**, 225–235 (2010).
20. M. Portelli, I. Sayers, *Expert Rev. Respir. Med.* **6**, 223–236 (2012).

ACKNOWLEDGMENTS

We thank G. Tokmulina for cell sorting and A. Iwasaki, R. Medzhitov, J. Nussbaum, and R. Locksley for scientific discussion. The data presented in this manuscript are tabulated in the main paper and in the supplementary materials. C.V.R. is a shareholder of Kolltan Pharmaceuticals. This research was supported by grants from the American Asthma Foundation (C.V.R. and E.G.B.), NIH (R01 AI089824 to C.V.R., T32 AI007019 to P.Y.C., T32 GM007205 to D.D.K., and HL088133, HL078885, HL004464, HL104608, and HL117004 to E.G.B), the National Institute on Minority Health and Health Disparities (MD006902 to E.G.B.), Kolltan Pharmaceuticals (C.V.R.) and the Yale University Gershon-Trudeau Fellowship (P.Y.C.).

SUPPLEMENTARY MATERIALS

www.sciencemag.org/content/352/6281/99/suppl/DC1
Materials and Methods
Figs. S1 to S10
Table S1
References (*21*–*32*)

21 December 2015; accepted 24 February 2016
10.1126/science.aaf1358

BOYALIFE

Science & Science Translational Medicine Award in Stem Cells and Regenerative Medicine

The first global award for stem cells and regenerative medicine



Stem cells and regenerative medicine is the new frontier in life sciences. *Boyalife, Science, and Science Translational Medicine* jointly establish a global award to recognize and reward scientists in the fields of stem cells and/or regenerative medicine with a focus on developing cell-based treatments for cancer, degenerative disorders, immunotherapy and stem cells transplantation.

The 2016 award ceremony will be held in San Francisco, on 23rd June, 2016.

The winners will receive:

☆A Grand Prize of $25,000 and a Runner-Up Prize of $5,000 will be awarded.

☆The Grand Prize Winning Essay will be published in Science; a brief abstract of the Runner-Up Essay will be published in Science.

Learn more about the Prize,
visit : *www.sciencemag.org/prize/boyalife/rules*

BOYALIFE Stem Cell

Science AAAS

Science Translational Medicine AAAS

BOYALIFE
博雅控股集团

All about Biotechnology and Health Improvement

Boyalife Group is an enterprise centered on innovation in the biotechnology field covering stem cell technology and bio-pharm. Founded in 2009, Boyalife Group has more than 30 wholly-owned subsidiaries and holding companies currently, becoming the leading brand in healthcare and pharmaceutical center in China.

Our operative segments all for better health are including:

- Stem Cell Technology
- Regenerative Medicine & Anti-aging
- Cancer Immunotherapy
- Genomics & Precision Medicine
- Healthcare Management
- Cloning Technology
- Innovative Drug Discovery
- Disease Model Research

We are inviting gifted candidates from around the world to join us, we will offer you a dynamic environment to develop work of globe consequence.

Become a member! Contact: *career@boyalife.com*
For more information, visit : *www.boyalifegroup.com*

NEW ENGLAND BioLabs® Inc.

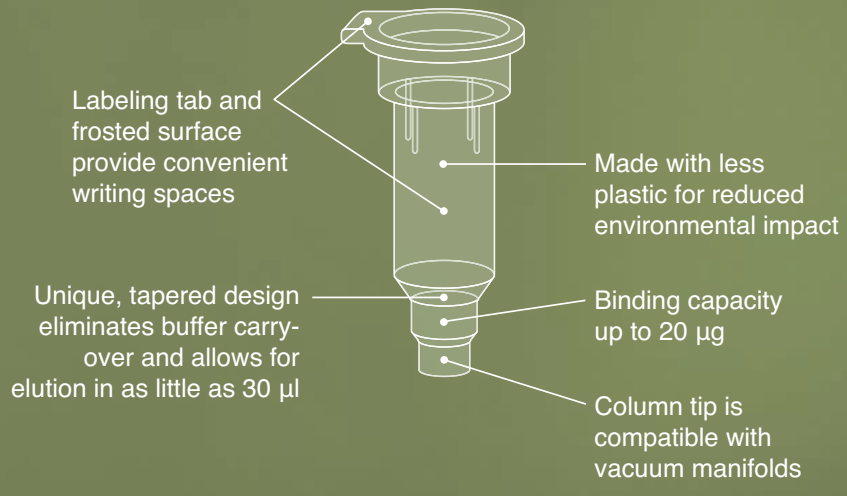
Time for change.

Introducing Monarch™ Nucleic Acid Purification Kits

It's time to transform your DNA purification experience. NEB's Monarch Nucleic Acid Purification Kits are optimized for maximum performance and minimal environmental impact. With an innovative column design, buffer retention is prevented, eliminating risk of carryover contamination and enabling elution in smaller volumes. The result – highly pure DNA for your downstream applications.

Make the change and migrate to Monarch today.

Optimized design of Monarch Miniprep Columns



Request your free sample at **NEBMonarch.com**

NEW ENGLAND BIOLABS® and NEB® are registered trademarks of New England Biolabs, Inc.
MONARCH™ is a trademark of New England Biolabs, Inc.

2016 MRS® FALL MEETING & EXHIBIT

November 27 – December 2, 2016 | Boston, Massachusetts

CALL FOR PAPERS

Abstract Submission Opens
May 16, 2016

Abstract Submission Deadline
June 16, 2016

BROADER IMPACT

BI1 Today's Teaching and Learning in Materials Science—Challenges and Advances
BI2 The Business of Materials Technology

BIOMATERIALS AND SOFT MATERIALS

BM1 Spatiotemporally and Morphologically-Controlled Biomaterials for Medical Applications
BM2 Stimuli Responsive Organic and Inorganic Nanomaterials for Biomedical Applications and Biosafety
BM3 Biomaterials for Regenerative Medicine
BM4 Materials and Manufacturing of Biointerfaces Devices and Stretchable Electronics
BM5 Materials for Biointegrated Photonic Systems
BM6 Fabrication, Characterization and Applications of Bioinspired Nanostructured Materials
BM7 Functional Nanostructured Polymers for Emerging Energy Technologies

ELECTROCHEMISTRY

EC1 Redox Activity on the Molecular Level—Fundamental Studies and Applications
EC2 Facilitating Charge Transport in Electrochemical Energy Storage Materials
EC3 Catalytic Materials for Energy and Sustainability
EC4 Material, Devices and Systems for Sustainable Conversion of Solar Energy to Fuels
EC5 Proton Transfer and Transport—From Biological Systems to Energy Applications

ELECTRONICS, MAGNETICS AND PHOTONICS

EM1 Materials Issues for Quantum Computing
EM2 Rare-Earths in Advanced Photonics and Spintronics
EM3 Electronic and Ionic Dynamics at Solid-Liquid Interfaces
EM4 Structure-Property Relationships of Organic Semiconductors
EM5 Materials and Mechanisms of Correlated Electronic Phenomena in Oxide Heterostructures
EM6 Thin-Film Transistors—New Materials and Device Concepts
EM7 Functional Plasmonics
EM8 Spin Dynamics in Nonmagnetic Materials and Devices
EM9 Materials and Nanostructures for Magnetic Skyrmions
EM10 Emerging Materials and Technologies for Nonvolatile Memories
EM11 Wide-Bandgap Materials for Energy Efficiency—Power Electronics and Solid-State Lighting
EM12 Diamond Electronics, Sensors and Biotechnology—Fundamentals to Applications

ENERGY AND SUSTAINABILITY

ES1 Materials Science and Chemistry for Grid-Scale Energy Storage
ES2 Materials Challenges for Flow-Based Energy Conversion and Storage
ES3 Perovskite Solar Cell Research from Material Properties to Photovoltaic Function
ES4 Thermoelectric Polymers and Composites—Nontraditional Routes to High Efficiency
ES5 Materials Research and Design for A Nuclear Renaissance
ES6 Scientific Basis for Nuclear Waste Management

MECHANICAL BEHAVIOR AND FAILURE MECHANISMS OF MATERIALS

MB1 Intermetallic-Based Alloys—From Fundamentals to Applications
MB2 Materials under Mechanical Extremes
MB3 High-Entropy Alloys
MB4 Glassy, Nanocrystalline and Other Complex Alloy Systems and Their Applications
MB5 Size Effects and Small-Scale Mechanical Behavior of Materials
MB6 Cyclic Deformation and Fracture at the Nanoscale
MB7 Shear Transformation Mechanisms and Their Effect on Mechanical Behavior of Crystalline Materials

NANOMATERIALS

NM1 Semiconducting Nanowires, Nanoribbons and Heterostructures—Synthesis, Characterizations and Functional Devices
NM2 2D Layers and Heterostructures beyond Graphene—Theory, Preparation, Properties and Devices
NM3 Nanotubes and Related Nanostructures
NM4 Nanomaterials-Based Solar Energy Conversion
NM5 Nanomembrane Materials—From Fabrication to Application
NM6 Nanoscale Materials and Devices by High-Temperature Gas-Phase Processes

PROCESSING AND MANUFACTURING

PM1 Ion Beam-Enabled Nanoscale Fabrication, Modification and Synthesis
PM2 Plasma Processing via Liquid for Life Sciences and Environmental Applications
PM3 Science-Enabled Advances in Materials- and Manufacturing-Technologies
PM4 Novel Materials, Fabrication Routes and Devices for Environmental Monitoring
PM5 Hierarchical, Hybrid and Roll-to-Roll Manufacturing for Device Applications

THEORY, CHARACTERIZATION AND MODELING

TC1 *In Silico* Materials Chemistry
TC2 Design, Discovery and Understanding of Materials Guided by Theory, Computation and Data Mining
TC3 Materials Issues in Art and Archaeology
TC4 Advances in Spatial, Energy and Time Resolution in Electron Microscopy

www.mrs.org/fall2016

Meeting Chairs

Bernard Bewlay, General Electric–Global Research Center
Silvija Gradečak, Massachusetts Institute of Technology
Sarah Heilshorn, Stanford University
Ralph Spolenak, ETH Zürich
T. Venky Venkatesan, National University of Singapore

Don't Miss These Future MRS Meetings!

2017 MRS Spring Meeting & Exhibit
April 17 – 21, 2017
Phoenix, Arizona

2017 MRS Fall Meeting & Exhibit
November 26 – December 1, 2017
Boston, Massachusetts

MRS MATERIALS RESEARCH SOCIETY®
Advancing materials. Improving the quality of life.
506 Keystone Drive • Warrendale, PA 15086-7573
Tel 724.779.3003 • Fax 724.779.8313
info@mrs.org • www.mrs.org

CALL FOR APPLICATIONS

CHANEL

RECHERCHE ET TECHNOLOGIE

RESEARCH AND TECHNOLOGY

CHANEL-CERIES RESEARCH AWARD 2016

The CHANEL-CERIES Research Award of 40,000€ is intended to honor a scientific researcher with a proven track record in fundamental or clinical research work, for a one-year period, on the subject of

PHYSIOLOGY OR BIOLOGY OF HEALTHY SKIN AND/OR ITS REACTIONS TO ENVIRONMENTAL FACTORS

Previous Award Winners

2015 Emi Nishimura M.D., Ph.D., Japan
2014 Julia A. Segre, Ph.D., Bethesda, USA
2013 Robert L. Modlin, M.D., Los Angeles, USA
2012 Martin Röcken, M.D., Ph.D., Tübingen, Germany
2011 Joke A. Bouwstra, Ph.D., Leiden, Netherlands
2010 Howard Y. Chang, M.D., Ph.D., Stanford, USA
2009 Sabine Werner, Ph.D., Zurich, Switzerland
2008 Paul A. Khavari, M.D., Ph.D., Stanford, USA
2007 Richard L. Gallo, M.D., Ph.D., San Diego, USA
2006 Irwin McLean, Ph.D., D.Sc., FRSE, Scotland, UK
2005 Masayuki Amagai, M.D., Ph.D., Tokyo, Japan
2004 Thomas Schwarz, M.D., Kiel, Germany
2003 Angela M. Christiano, Ph.D., New York, USA
2002 Dennis R. Roop, Ph.D., Houston, USA
2001 Fiona M. Watt, D.Phil., London, UK
2000 Michael Karin, Ph.D., San Diego, USA
1999 Jonathan Rees, M.D., Edinburgh, UK
1998 Jean Krutmann, M.D., Düsseldorf, Germany
1997 Jens-Michael Schröder, Ph.D., Kiel, Germany
1996 Akira Takashima, M.D., Ph.D., Dallas, USA

DEADLINE FOR APPLICATIONS: JUNE 1, 2016

http://research-technology.chanel.com/research-awards

HIV Cure Funding Opportunity

Gilead Sciences has spent 25 years working to improve treatments for people living with HIV, with an ultimate goal in mind: finding a cure.To that end, we've set aside fundingto support academic institutions,nonprofit organizations and communitygroups committed to HIV cure activities.

Visit www.gilead.com/HIV-Cure-FOA to learn more and apply for funding.

GILEAD

AAAS *Travels*

Botanical Iceland



Land of Fire & Ice & Nature's Paradise!
July 2-11, 2016

Outdoors enthusiasts grab your cameras and field guides, and come explore Iceland! Discover Iceland in all of its great natural beauty. Iceland has captured the imagination of people all over the world since Jules Verne wrote the "Journey to the Center of the Earth" in 1871. Iceland has a proud heritage—it is the world's oldest democracy. Its plant life and the natural wonders are truly magical! This trip is a tremendous introduction to the heritage of Iceland, from geology to history and landscapes with many fascinating plants. $4,295 pp + air.

For a detailed brochure, call (800) 252-4910
All prices are per person twin share + air

BETCHART EXPEDITIONS Inc.
17050 Montebello Rd, Cupertino, CA 95014
Email: AAASInfo@betchartexpeditions.com
www.betchartexpeditions.com

Advance your career with expert advice from *Science* Careers.

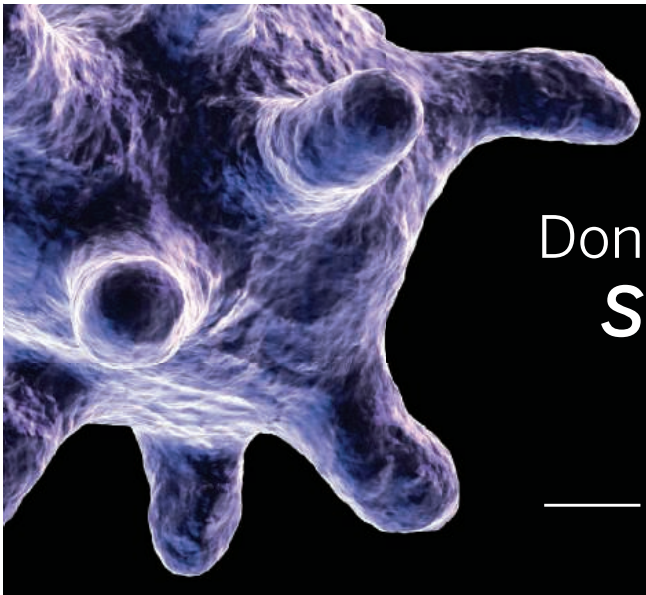


Download Free Career Advice Booklets!
ScienceCareers.org/booklets

Featured Topics:
- Networking
- Industry or Academia
- Job Searching
- Non-Bench Careers
- And More



ScienceCareers
FROM THE JOURNAL SCIENCE AAAS



Don't miss the debut of
Science Immunology.

NOW ACCEPTING PAPERS

Image: Eraxion / iStockPhoto

Science is expanding its reach into immunology—now offering the newest online-only, weekly journal in the *Science* family of publications. *Science Immunology* will provide original, peer-reviewed research articles that report critical advances in all areas of immunological research.

Be a part of the *Science Immunology* debut issue publishing Summer 2016!

Submit your manuscript today at **ScienceImmunology.org.**

ScienceImmunology

qPCR Assays

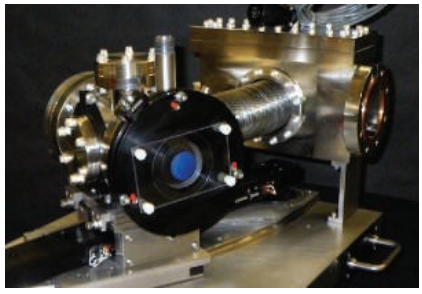
The PrimeTime Gene Expression Master Mix is an optimized enzyme mix for probe-based quantitative polymerase chain reaction (qPCR). This newest product enhances the Integrated DNA Technologies (IDT) PrimeTime qPCR product line, as researchers can economically obtain both assays and a master mix that are optimized and validated to work together. PrimeTime qPCR Assays are available with a choice of dyes and quenchers, and the predesigned assays are backed by a performance guarantee. The versatile, stable master mix easily integrates into new and existing experimental workflows, because it is also compatible with all commercially available 5' nuclease gene expression assays. The PrimeTime qPCR Assays and Master Mix deliver accurate, sensitive gene expression analysis with efficiencies >90% in two-step reverse transcription (RT)-qPCR under both fast and standard cycling conditions. This provides the reproducibility that gives researchers confidence in the quality of their data, whether it be from singleplex or duplex reactions.

Integrated DNA Technologies
For info: 800-328-2661
www.idtdna.com

HPLC Column

The Thermo Scientific Acclaim AmG C18 high-performance liquid chromatography (HPLC) column is a high-performance, reversed-phase column designed for ion-pairing chromatographic separations and optimized for various aminoglycoside (AmG) antibiotics analyses, including drug purity and impurity characterization and quantification, therapeutic drug monitoring, and residual control testing in different matrices. AmG analysis requires columns that are robust to withstand harsh, low-pH conditions. The new Acclaim AmG C18 columns have been engineered specifically for this application. Our unique silica surface chemistry provides a layer of protection during the separation process and extends column longevity.

Thermo Fisher Scientific
For info: 800-532-4752
www.thermofisher.com



XUV Spectrometer

McPherson's new grazing incidence wavelength dispersive optical spectrometer allows rapid analysis of spectral light in the ~1-nm to 300-nm wavelength region (4 eV to 1,200 eV.) In addition to performing high-harmonic laser generation experiments, the Model 248/310 is also useful for measuring ion- or discharge light sources and for astrophysics detector calibration. At FLASH, the free electron laser experiment conducted by DESY in Hamburg, Germany, the McPherson 248/310 ultrahigh vacuum (UHV) model assisted in analysis of the 2.3-nm to 4.4-nm water window (a region transparent to light). Space scientists and plasma physicists who need an instrument for vacuum ultraviolet and extreme ultraviolet (EUV/XUV) capitalize on the 248/310's range and flexibility. Configured in reverse, it operates as a tunable light source. This is useful for spectral calibration and spectroscopy in the vacuum ultraviolet and the extreme and soft X-ray wavelength region (EUV and SXR respectively). Direct detection charge-coupled devices (CCDs), image intensifiers, microchannel plates, or electron multipliers provide wide range and flexible detection.

McPherson
For info: 978-256-4512
www.mcphersoninc.com

Microscope

Streamlining the cell-culture workflow in a range of application areas, Olympus' renowned optical expertise has given rise to the new CKX53 microscope, offering a novel inversion contrast (IVC) imaging technique. While a variety of capabilities enable the CKX53 to deliver high-quality images over a wide field of view for live-cell and fluorescence imaging, the system is also tailored to the cell-culture process with optimized ergonomics and fast, intuitive operation. Fast processing is vital to minimize the time precious live cells are removed from optimal incubation conditions, and Olympus' unique integrated Phase Contrast (iPC) system simplifies and speeds up phase contrast observations with the CKX53, removing the need to prepare or center the objectives when moving between 4X and 40X magnification. Phase contrast observations are also enhanced with the new IVC technique, enabling 3D views devoid of halos or directional shadows.

Olympus
For info: +49-(0)-40-23773-5913
www.olympus-lifescience.com

Benchtop Workstation

The CleneCab Workstation is a low-cost, benchtop alternative to a cleanroom. For those who wish to create a local cleanroom or safe environment to prevent contamination when working with samples, this is the ideal solution. The CleneCab provides a bench top size environment of 62 × 42 × 77 cm. Constructed from 10-mm acrylic glass, the workstation protects the sample from external contamination and the user from biohazards. It can also be used for other situations in which a high demand for cleanliness or protection is required, as with radioactive labeling of DNA. Its construction provides ideal shielding from radioactive substances like ^{32}P. Five powerful, timer-controlled ultraviolet (UV) tubes combined with special reflectors efficiently irradiate the entire working surface. The workstation is also equipped with a microprocessor to control the energy of the UV tubes. The UV dose can be preset very easily in energy (mJ) or time units (s).

Herolab
For info: +44-(0)-1223-515440
www.herolab.de

Electronically submit your new product description or product literature information! Go to www.sciencemag.org/about/new-products-section for more information.

Newly offered instrumentation, apparatus, and laboratory materials of interest to researchers in all disciplines in academic, industrial, and governmental organizations are featured in this space. Emphasis is given to purpose, chief characteristics, and availability of products and materials. Endorsement by *Science* or AAAS of any products or materials mentioned is not implied. Additional information may be obtained from the manufacturer or supplier.



Join the Conversation!

Twitter is a great way to connect with AAAS members and staff about the issues that matter to you most. Be a part of the discussion while staying up-to-date on the latest news and information about your personal member benefits.

Follow us @AAASmember and join the conversation with #AAAS

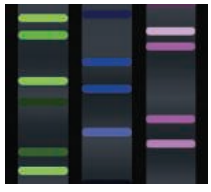
AAAS MemberCentral

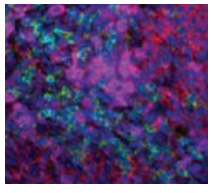
MemberCentral.aaas.org

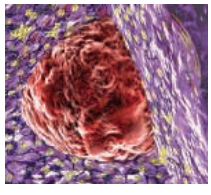
want new technologies?

antibodies
apoptosis
biomarkers
cancer
cytometry
data
diseases
DNA
epigenetics
genomics
immunotherapies
medicine
microbiomics
microfluidics
microscopy
neuroscience
proteomics
sequencing
toxicology
transcriptomics









watch our webinars

Learn about the latest breakthroughs, new technologies, and ground-breaking research in a variety of fields. Our expert speakers explain their quality research to you and answer questions submitted by live viewers.

VIEW NOW!
webinar.sciencemag.org

Science
AAAS

Brought to you by the *Science*/AAAS Custom Publishing Office

@SciMagWebinars

R&D SYSTEMS
a bio-techne brand

What's in Your Sample?



Choose the right immunoassay to get your answers!

Learn more | rndsystems.com/immunoassays

bio-techne®
Global info@bio-techne.com bio-techne.com/find-us/distributors TEL +1 612 379 2956
North America TEL 800 343 7475 **Europe | Middle East | Africa** TEL +44 (0)1235 529449
China info.cn@bio-techne.com TEL +86 (21) 52380373
bio-techne.com



Science Careers Advertising

For full advertising details, go to ScienceCareers.org and click For Employers, or call one of our representatives.

Tracy Holmes
Worldwide Associate Director
Science Careers
Phone: +44 (0) 1223 326525

THE AMERICAS

E-mail: advertise@sciencecareers.org
Fax: +1 (202) 289 6742

Tina Burks
Phone: +1 (202) 326 6577

Nancy Toema
Phone: +1 (202) 326 6578

Online Job Posting Questions
Phone: +1 (202) 312 6375

EUROPE / INDIA / AUSTRALIA / NEW ZEALAND / REST OF WORLD

E-mail: ads@science-int.co.uk
Fax: +44 (0) 1223 326532

Sarah Lelarge
Phone: +44 (0) 1223 326527

Kelly Grace
Phone: +44 (0) 1223 326528

Online Job Posting Questions
Phone: +44 (0) 1223 326528

JAPAN

Katsuyoshi Fukamizu (Tokyo)
E-mail: kfukamizu@aaas.org
Phone: +81 3 3219 5777

Hiroyuki Mashiki (Kyoto)
E-mail: hmashiki@aaas.org
Phone: +81 75 823 1109

CHINA / KOREA / SINGAPORE / TAIWAN / THAILAND

Ruolei Wu
E-mail: rwu@aaas.org
Phone: +86 186 0082 9345

All ads submitted for publication must comply with applicable U.S. and non-U.S. laws. *Science* reserves the right to refuse any advertisement at its sole discretion for any reason, including without limitation for offensive language or inappropriate content, and all advertising is subject to publisher approval. *Science* encourages our readers to alert us to any ads that they feel may be discriminatory or offensive.

ScienceCareers
FROM THE JOURNAL SCIENCE AAAS

ScienceCareers.org

UCSF
University of California San Francisco

Seeking Scientist with expertise in Cell and Molecular Biology broadly relevant to Asthma

The UCSF Division of Pulmonary, Critical Care, Allergy and Sleep Medicine, in the Department of Medicine, and the Sandler Basic Research Center invite applications for a joint faculty position at the Assistant or Associate Professor level. Preferred candidates will have demonstrated expertise in Cell and Molecular Biology broadly relevant to Asthma.

Candidates must have a Ph.D., M.D., or M.D. Ph.D. and must have outstanding written and communication skills. The candidate should have a record of success or significant promise in basic research that is broadly applicable to Asthma.

UCSF is an Equal Opportunity/Affirmative Action Employer. The University undertakes affirmative action to assure equal employment opportunity for underutilized minorities and women, for persons with disabilities, and for covered veterans. All qualified applicants are encouraged to apply, including minorities and women. All qualified applicants will receive consideration for employment without regard to race, color, religion, sex, sexual orientation, gender identity, national origin, disability, age or protected veteran status.

Please apply online at: **http://apptrkr.com/767258**
For more information, contact the Chair of the search committee Prescott Woodruff, M.D., M.P.H. at prescott.woodruff@ucsf.edu.

University of Colorado Denver

School of Medicine

Infectious Disease Research Faculty Positions

The Division of Infectious Diseases at the University of Colorado Denver School of Medicine is recruiting outstanding infectious disease scientists. Scientists (MD, MD-PhD or PhD) with ability to build and/or maintain an internationally recognized, extramurally funded laboratory based research program will be provided with strongly competitive start-up packages. The division is interested in emerging infectious diseases and researchers investigating pathogens of global health importance are invited to apply, as are investigators who diversify and complement us in HIV research. **Valued:** scientific accomplishment and drive backed by primary research publications, collaborative and interpersonal skills, peer-reviewed funding consistent with seniority. The Anschutz Medical Campus provides state of the art facilities and Denver and the Colorado Front Range offer exceptional quality of life.

Apply electronically at **www.cu.edu/cu-careers**, job number **03734** such that you provide four specific items: (1) cover letter explaining record, interests and qualifications; (2) C.V. [US applicants please also provide your NIH biosketch]; (3) description of anticipated research direction; (4) three references. In addition, please email these documents to brandi.dolan@ucdenver.edu, and entitle the email **"Strategic Recruitment."**



Faculty Position
Computational Genomics

UNC CHARLOTTE

Department of Bioinformatics and Genomics

College of Computing and Informatics
University of North Carolina at Charlotte

The Department of Bioinformatics and Genomics at the University of North Carolina at Charlotte seeks a tenure-track professor at any career stage to work at our location in the North Carolina Research Campus (NCRC) in Kannapolis. The NCRC is a public-private partnership between corporations, universities and healthcare organizations advancing science at the intersection of human health, nutrition and agriculture.

The NCRC hosts,UNC Charlotte, six other UNC system universities as well as Duke University. UNC Charlotte has a leadership position at the NCRC in bioinformatics. We seek applicants wishing to develop a research program in bioinformatics, computational biology and/or computational genomics. This position is part of a larger university-wide research initiative in Data Science and Analytics. The successful applicant will have an earned doctorate with an exceptional record of achievement and will be expected to maintain an externally funded research program that will catalyze a larger group of interdisciplinary scientists. The responsibilities of the position include teaching quantitative skills such as programming and statistical modeling at the graduate and undergraduate level.

We offer a collegial environment, excellent facilities, a competitive start up package, and a competitive nine-month salary commensurate with experience.

Preliminary inquiries about the position can be made to **Dan Janies** via email **djanies@uncc.edu**. However, formal applications must be made electronically at **https://jobs.uncc.edu** (position **#1074**) and must include a CV, contact information for 4 references, and statements on research and teaching.

The University of North Carolina at Charlotte is an EOE/AA Employer and an NSF ADVANCE institution.

For additional information, please visit our websites at http://bioinformatics.uncc.edu and http://transforming-science.com.

Faculty Position

UNC CHARLOTTE

Department of Bioinformatics and Genomics

College of Computing and Informatics
University of North Carolina at Charlotte

The University of North Carolina at Charlotte invites applications for faculty at the Assistant or Associate level in the Department of Bioinformatics and Genomics in the College of Computing and Informatics. The Department seeks candidates with a proven research record in Computational Systems Biology, directed toward the theoretical modeling and simulation of complex biological systems, alone or in combination with experimental approaches. The successful candidate should have an earned doctorate and be eligible for appointment at the rank of Assistant or Associate professor. We seek applicants with a commitment to excellence in graduate and undergraduate teaching and mentorship who have exceptional computational/analytic skills to meet teaching requirements in one or more of the following areas: Statistics, Programming, Structural Biology, Big Data Analytics as applied to biological datasets, Machine Learning, and Integrative Systems Biology.

Research areas of interest include the development and application of data analytic and theoretical methods, mathematical modeling, and simulation techniques. Research should address important biological data analysis needs such as structural and functional modeling of biomolecules and molecular interactions, or integration of heterogeneous data sets into models of complex systems, to address issues of health, agricultural productivity, and the environment.

We offer a collegial environment, excellent facilities, a competitive start-up package, and a competitive nine-month salary commensurate with experience. Applications must be made electronically at **https://jobs.uncc.edu** (position **#1732**) and must include a CV, contact information for 4 references, and statements on research and teaching. Preliminary inquiries may be addressed to **Dr. Cynthia Gibas** (**cgibas@uncc.edu**).

The University of North Carolina at Charlotte is an EOE/AA Employer and an NSF ADVANCE Institution.

For additional information, please visit our website at http://bioinformatics.uncc.edu.

新潟大學腦研究所
BRAIN RESEARCH INSTITUTE
NIIGATA UNIVERSITY
IN HONOR OF MIZUHO NAKATA
1957

Information about Applying for Faculty Positions in System Pathology for Neurological Disorders in Brain Research Institute, Niigata University

[URL: http://www.bri.niigata-u.ac.jp/en/ info/news/000529.html]

1. Research fields / Position / Number of people
Neuroscience, Neuropathology / Professor or Associate Professor / 2

2. Required qualifications
Applicants must have a doctoral degree, research experience in neurological disorders, and a strong desire to conduct creative, innovative research.

3. Terms of employment
From June 1, 2016 (tentative) – March 31, 2021 (tentative)

4. Deadline for applying
17:00 on Saturday, April 30, 2016 (Japan Standard Time)

5. Where to make inquiries
Brain Research Institute, Niigata University
E-mail: noukenshomu@adm.niigata-u.ac.jp

Please refer to the following URL for detailed information
http://www.bri.niigata-u.ac.jp/en/info/bri-employment2016.pdf

AWARDS

HFSP

HUMAN FRONTIER SCIENCE PROGRAM (HFSP)

CALL FOR NOMINATIONS FOR THE 2017 HFSP NAKASONE AWARD

In keeping with its mission to promote innovative international research, HFSP invites nominations for the 2017 Nakasone Award which honors ground-breaking contributions in the life sciences. Typically these will be breakthroughs in understanding the complex mechanisms of living organisms that have important consequences for scientists throughout the world. Experimental, conceptual and technological contributions are eligible. This award recognizes the vision of former Prime Minister Nakasone of Japan in the creation of HFSP.

The joint winners of the 2016 award were Emmanuelle Charpentier, Max Planck Institute for Infection Biology, Berlin, Germany and Jennifer Doudna, University of California at Berkeley, USA, for their pioneering work on the CRISPR-Cas9 system.

The competition is open; it is not limited to HFSP awardees and there is no age limit for candidates. However the jury will pay particular attention to recent breakthroughs by younger scientists. Nominations should be made before 13 May 2016 by submitting the standard one-page nomination form and the nominee's CV (see the HFSP website for more information). The selection will be made by the HFSP Council of Scientists at its meeting in July 2016.

The awardee will receive an unrestricted research grant of 10.000 USD, a commemorative medal and an invitation to deliver the Nakasone lecture at the 2017 HFSP Awardees Meeting.

HFSP, 12 quai Saint-Jean, 67080 STRASBOURG Cedex, France, **www.hfsp.org/awardees**

Science Careers online @sciencecareers.org

ScienceCareers online @sciencecareers.org



Special Job Focus:

Immunology

Issue date: May 6

Book ad by April 19 to guarantee space

Ads accepted until April 29 if space allows

For recruitment in science, there's only one *Science*.

What makes *Science* the best choice?

- Read and respected by 400,00 readers around the globe
- 75% of readers read *Science* more often than any other journal
- Your ad dollars support AAAS and its programs, which strengthens the global scientific community.

Why choose this Immunology Focus for your advertisement?

- Relevant ads lead off the career section with special immunology banner
- Bonus distribution to Immunology 2016 (AAI), May 13–17, Seattle, WA.

Expand your exposure. Post your print ad online to benefit from:

- Link on the job board homepage directly to immunology jobs
- Dedicated landing page for jobs in immunology
- Additional marketing driving relevant job seekers to the job board.

Deliver your message to a global audience of targeted, qualified scientists.

129,574
subscribers in print every week

37,942
unique active job seekers searching for **immunology** positions in 2015

41,047
applications submitted for **immunology** positions in 2015



SCIENCECAREERS.ORG

Produced by the *Science*/AAAS Custom Publishing Office.

ScienceCareers
FROM THE JOURNAL SCIENCE AAAS

To book your ad: **advertise@sciencecareers.org**

The Americas
+202 326 6582
Japan
+81 3 3219 5777
Europe/RoW
+44 (0) 1223 326500
China/Korea/Singapore/Taiwan
+86 186 0082 9345

ERA Chair in Cellular and Molecular Biology of Ageing

The **Faculty of Medicine of the University of Coimbra** announces a Senior Scientist position (ERA Chair holder) for the ERA@UC 2.5 M€ project funded by Widespread 2014-ERA Chairs. The position foresees an initial 4 years full-time appointment and the recruitment of the ERA Chair team, to develop research, advanced teaching and science management in the field of Cellular and Molecular Biology of Ageing. The outstanding performance of the team will support a tenure position for the Senior Scientist at University of Coimbra.
The ERA Chair team will be the first top-quality research group of the strategic project "Multidisciplinary Research Institute of Ageing-MIA" and "Vitality Campus Ageing@Coimbra", funded by the program Spreading Excellence and Widening Participation (Teaming). This is a flagship project of "Centro" Region of Portugal, as Health and Ageing are top priorities of its Smart Specialization Strategy.

Requirements
-Preference given to internationally leading and highly competitive scientist in ageing research, using simple model organisms (not exclusive)
-Proven experience in science and education management
-Solid experience in securing competitive funds from international agencies (eg. ERC, H2020, 7FP, NIH and others)
-Established international network of collaborators

Application
Submit a detailed proposal according to the template provided at the website **http://www.uc.pt/en/fmuc/ibili/erachair**, including a short CV and two-pages (max.) research plan. The template should be submitted in .pdf format to the email **ggp@fmed.uc.pt** no later than **May 31st, 2016**.

For additional information please send an email to **ggp@fmed.uc.pt** or visit **http://www.uc.pt/en/fmuc/ibili/erachair.**

Prospero BioSciences

CIC nanoGUNE
nanoscience cooperative research center

Prospero Biosciences S.L., a spin-off company of the Nanoscience Cooperative Research Center CIC nanoGUNE (**www.nanogune.eu**), invites applications and nominations for the position of

Chief Technical Officer (CTO)

Prospero Biosciences S.L., which is based at the nanoGUNE facilities in San Sebastian, Basque Country (Spain), has been launched recently with the mission of producing and commercializing a novel detector for protein mass spectrometry.

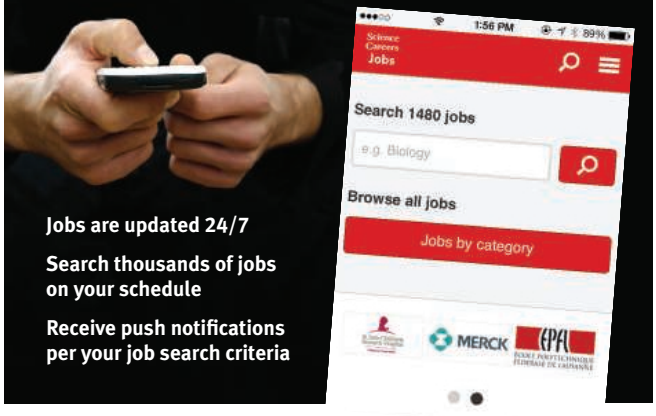
The Chief Technical Officer (CTO) will be responsible for the fabrication of ultra-thin large-scale semiconductor nanomembranes based on dry- and wet-etching techniques. The aim is to incorporate those membranes into a novel protein mass-spec detector covering an unprecedented mass range. The CTO is also expected to connect with existing and potential clients in order to promote our products and our research activities in terms of an application in the field of life sciences.

Candidates should have a PhD in Physics or Materials Science with a strong background in cleanroom fabrication technologies, i.e. optical lithography, dry- and wet-etching techniques, metal layer deposition, and possibly atomic layer definition for super-adhesive metal deposition. Furthermore, candidates should be skilled in handling both fundamental problems and engineering devices to the application level. Proficency in spoken and written English is compulsory.

Applicants should forward their CV and a list of at least three references to **director@nanogune.eu**, quoting the position reference **prosp_cto**.

Closing date: 10 April 2016

Download the *Science* Careers jobs app from Science



Jobs are updated 24/7

Search thousands of jobs on your schedule

Receive push notifications per your job search criteria

Get a job on the go.
Search worldwide for thousands of scientific jobs in academia, industry, and government. The application process is seamless, linking you directly to job postings from your customized push notifications.

Scan this code to download app or visit **apps.sciencemag.org** for information.

ScienceCareers | AAAS
FROM THE JOURNAL SCIENCE

ScienceCareers.org

Center for Immunology & Microbial Disease
Albany Medical College

Assistant/Associate Professor

The Center for Immunology & Microbial Disease at Albany Medical College invites applications for a tenure-track faculty position from individuals who have a doctoral degree, postdoctoral experience, and demonstrated research productivity. The successful candidate will be expected to establish an independent, extramurally-funded research program and participate in the teaching of medical and graduate students. The basic science departments at Albany Medical College are organized as interdisciplinary research centers and the Center for Immunology & Microbial Disease has a focus on microbial pathogenesis and immune defense, particularly as related to host-pathogen interactions. Faculty at the Albany Medical College receive competitive salaries, attractive start-up packages, and access to the Center's ABSL-3/BSL-3, Microbiology and Immunology Core Labs. In addition, we have established a close relationship with the New York State Department of Health Wadsworth Laboratories, providing a diverse environment that is rich in infectious disease expertise. Albany Medical College is located in a mid-sized city within the upstate New York Capital Region, and has easy access to Boston, New York City, and the Adirondack Mountains.

Applicants should send their curriculum vitae, a statement of research plans, and three letters of reference to:

Faculty Search Committee
Center for Immunology & Microbial Disease
Albany Medical College
47 New Scotland Avenue, MC-151
Albany, NY 12208

For further information about the Center, visit
http://www.amc.edu/Research/IMD/

An Equal Opportunity/Affirmative Action Employer.
Women and minorities are encouraged to apply.

By **Adam Ruben**

Of mice and mics

Years ago, I stood on stage at the Laugh Factory in midtown Manhattan, telling jokes about toys, driving, and foreign language workbooks. But all I could think about was the Band-Aid on my index finger covering the spot where, earlier in the day, I had accidentally injected myself with mouse malaria. As part of my Ph.D. research, I was testing novel malaria drugs in mice, a process that began with administering a syringe of blood infected with the parasite *Plasmodium vinckei*. I had done it dozens of times before, but this time I stuck the needle into my own finger. My first thoughts were, "I need to contact the Centers for Disease Control and Prevention. And I need to write a joke about this."

I didn't start college knowing I wanted to be a science comedian. But freshman year, I entered a stand-up comedy contest on a whim and ended up enjoying it. By the time I graduated with my molecular biology degree, I had even been asked to perform on campus a few times, opening for real comedians and a student band in a coffee shop. In graduate school, I started performing at open mic nights, and as the years passed, I said yes to any comedy-like opportunity that arose. I was poisoned at corporate murder mystery parties. Dressed as an orthodox rabbi, I made fun of elderly relatives at bar mitzvahs. I held doors in a tux at a Kenny Loggins concert, wrote humor pieces for *National Lampoon*, joined an improv group, and appeared as a thug in a Korean soap opera. I even convinced the school to let me teach a stand-up comedy class for undergraduates.



"I said yes to any comedy-like opportunity that arose."

All the while, I tried to keep the science and the comedy separate—no science jokes, and no joking while doing science. I didn't want to be the comedian for whom comedy was clearly a minor hobby, and I didn't want to be the scientist who was perceived as not serious enough. I also enjoyed feeling like Batman: leaving the lab, putting on my black T-shirt and jeans, and slipping into a completely different world—or driving home late from a comedy show, opening my laptop, and digging through dissertation references.

In retrospect, building a wall between science and comedy was the wrong choice. I tell my stand-up students to think about what specialized knowledge they have that sets them apart from other comics. For me, that niche was science, but I was ignoring it. Then I slowly began merging science and comedy. I published a book called *Surviving Your Stupid, Stupid Decision to Go to Grad School*, which led to a monthly science humor column. I landed roles as a TV scientist. I began touring grad schools and scientific conferences, telling jokes about liquid nitrogen, grant funding, and the absolute hell of proctoring undergraduate exams. Suddenly I realized that audiences—even nonscientific ones—want to hear about science. To me, lab work is the everyday default; to others, it's exotic.

My two careers haven't merged completely. Not all of my scientific colleagues have viewed my hobby positively, and in my day job as an industry biologist, I don't go around writing jokes into lab protocols. But I find that stand-up has made me comfortable communicating science, helping with everything from simple interpersonal interactions to larger presentations.

Having a day job and a Batman job also means that I do a lot of juggling. It means red-eye flights and writing after my kids are asleep and working through new jokes during my commute and a periodically nagging fear that I'm neglecting something (typically sleep, occasionally hygiene). And I love it.

As for the mouse malaria, I'm fine—though I did suffer the side effect of several hours spent filling out occupational safety paperwork. Over the years, I've learned that comedy and science don't always mix, but they're not completely incompatible either. On stage at the Laugh Factory that night, my vinyl Band-Aid sticking slightly to the microphone, I knew I'd still be doing that in 10 years. And I also knew I had no intention of, as they say, quitting my day job. ■

Adam Ruben is a molecular biologist, science comedian, and the author of the Science *Careers "Experimental Error" column. Learn more at adamruben.net.*

ILLUSTRATION: ROBERT NEUBECKER

Downloaded from on March 31, 2016

Published by AAAS